Imaging Probes Targeted to Pancreatic Beta-Cells: Design, Synthesis and Testing

Thomas Joseph Clough

January 2021

Imperial College London

Department of Chemistry

Thesis submitted in partial fulfilment of the requirements for the degree of Doctor of Philosophy in Chemistry

Declaration of Originality

I hereby declare that the work described in this thesis conducted between October 2017 and January 2021 is my own unless otherwise stated or referenced. Contributions from others have been clearly acknowledged within the text.

Copyright Declaration

The copyright of this thesis rests with the author. Unless otherwise indicated, its contents are licensed under a Creative Commons Attribution Non-Commercial 4.0 International Licence (CC BY-NC).

Under this licence, you may copy and redistribute the material in any medium or format. You may also create and distribute modified versions of the work. This is on the condition that: you credit the author and do not use it, or any derivative works, for a commercial purpose.

When reusing or sharing this work, ensure you make the licence terms clear to others by naming the licence and linking to the licence text. Where a work has been adapted, you should indicate that the work has been changed and describe those changes.

Please seek permission from the copyright holder for uses of this work that are not included in this licence or permitted under UK Copyright Law.

Publications Arising from This Thesis

Thomas J. Clough, Nicoleta Baxan, Emma J. Coakley, Charlotte Rivas, Lan Zhao, Isabelle Leclerc, Aida Martinez-Sanchez, Guy A. Rutter and Nicholas J. Long, "Synthesis and in vivo behaviour of an exendin-4-based MRI probe capable of β-cell-dependent contrast enhancement in the pancreas", *Dalton Transactions*, 2020, **49**, 4732-4790.

Thomas J. Clough, Lijun Jiang, Ka-Leung Wong and Nicholas J. Long, "Ligand design strategies to increase stability of gadolinium-based magnetic resonance imaging contrast agents", *Nature Communications*, 2019, **10**, 1420

Acknowledgements

First and foremost, I'd like to thank my supervisor, Prof. Nick Long, for giving me the opportunity to pursue my PhD. Your support and guidance have kept me engaged and motivated, and studying at Imperial has continued to spark my curiosity and has widened my horizons over the past 3 years, enabling me to become the successful chemist that I am today. Your leadership of the group has created an atmosphere where every group member can reach their full potential, from the trials of the move to White City through to the pandemic and hopefully for many more years. Thank you.

Secondly, I'd like to acknowledge the invaluable contributions to this work of the analytical staff at Imperial, particularly Peter Haycock and Dr Lisa Haigh for their support throughout my PhD, and for putting up with my often-excessive sample submission. Dr Nicoleta Baxan, Dr Aida-Martinez Sanchez and Dr Ben Jones from the School of Medicine have all been extremely helpful thanks to their expertise in *in vivo* and *in vitro* analysis, as well as being excellent company when sitting at an MRI scanner for hours in the basement of Hammersmith Hospital or providing me with frozen human serum, which is not as ominous as it sounds.

The members of the Long group have made my postgraduate career so very enjoyable. Special mentions go to Troy for our endless political scheming, Steph for all of the tequila shots, Megan and Rhiannon for surviving THAT flight to Montréal, Sammy for every single slice of cake, Brad for filling the lab with Boney M and Rick Astley, Chloe for being equally as obsessed with running, Ed and Marie for endless Brexit debates, Lijun for your chemistry wisdom, Saul for propping me up at that infamous Christmas party, Tom for sharing my LCMS woes, Shane for sharing in email etiquette criticisms, and Jin for staining the lab just as pink as I have. Adam, Lucy, Tamara, Javi, Luke and Emma were always on hand with chemistry know-how in my early days in the group and the newer members Charlie, Angelo, Ben and William have helped make my final few months in the lab as enjoyable as ever.

To Howard, Troy and Siriney, thank you for putting up with me from the scary basement of Rosaline Road to the vegetable garden on the balcony of Downbury Mews. I couldn't have asked for better housemates.

To Mum, Dad, Rosie and Corrie, thank you for your love and support throughout this venture.

Finally, to Abbee, thank you for changing my life. I couldn't have done this without you and your steadfast love and affection. You mean the world to me.

Abstract

Diabetes Mellitus is a widely recognised yet still poorly understood disease which afflicts hundreds of millions around the globe. The disease is characterised by a decline in both mass and functionality of pancreatic β-cells, which are responsible for insulin production. Currently, type 2 diabetes is diagnosed at a late stage of progression, limiting clinical opportunities for treatment. There is a clear unmet need for improved early detection of diabetes, which can come in the form of molecular imaging probes designed to image pancreatic β-cell loss.

The work described within this thesis is primarily focussed on the development of imaging probes targeted directly to these cells. This is through the incorporation of agonists for the receptors GLP-1R and GPR40 which are enriched by pancreatic β-cells. A significant body of work involved the peptide exendin-4, a potent agonist of GLP-1R which is utilised in the clinic for the treatment of diabetes. Exendin-4 was conjugated to a gadolinium(III) complex to generate the MRI contrast agent **GdEx**, which was shown to exhibit pancreas-specific contrast enhancement in both wild-type and disease-model mice. An additional family of optical imaging agents based on terbium(III)- and rhodamine-exendin-4 conjugates of exendin-4 were also generated. These were shown to provide receptor-level information about GLP-1R *in vitro*.

An alternative targeting method was employed in the development of the ligand **GPR-L1**. This ligand was designed to bind to the receptor GPR40. The ligand was found to be reasonably versatile, with chelation to a number of lanthanide(III) centres successfully carried out. During characterisation of these complexes, it was found that the aromatic nature of the GPR40 targeting moiety could sensitise both Eu(III) and Tb(III) luminescence. Additionally, the fluorescence of the indole was utilised to verify the GPR40 targeting ability of the ligand through *in vitro* analysis.

Zinc(II) ions play a critical role in the stabilisation of insulin storage and a final avenue of this body of work explored cyanine dyes capable of responding to the presence of Zn^{2+}. These compounds were found to exhibit some versatility, with a series of alternative zinc-sensing moieties examined. Some steps were taken towards the development of dual-modal imaging probes based on these cyanine frameworks as well as targeted fluorescent optical agents.

Table of Contents

Declaration..... 2

Acknowledgements..... 3

Abstract..... 4

Table of Contents..... 5

List of Abbreviations..... 12

List of Key Compounds..... 16

Chapter 1 - Introduction..... 19

1.1. Diabetes Mellitus..... 20

1.1.1. Epidemiology, Symptoms and Disease Development..... 20

1.1.1.1. Global Incidence and Epidemiology..... 20

1.1.1.2. Disease Sub-Types, Causes and Symptoms..... 21

1.1.2. Pancreatic β-Cells..... 22

1.1.3. β-Cell Receptors: Targets for Imaging Probes..... 23

1.1.3.1. The Glucagon-Like Peptide-1 Receptor..... 23

1.1.3.2. G-Protein Coupled Receptor 40..... 24

1.1.4. Diabetes and Zinc..... 26

1.2. Molecular Imaging..... 27

1.2.1. The Lanthanides in Molecular Imaging..... 27

1.2.1.1. Lanthanide(III) Ions..... 28

1.2.1.2. Ligands for Lanthanide(III) Ions..... 28

1.2.2. Magnetic Resonance Imaging..... 29

1.2.2.1. Contrast Agents for MRI..... 30

1.2.2.2. Critical Factors in MRI Contrast Agent Design..... 33
1.2.3. Optical Imaging..... 37
1.2.3.1. Principles of Luminescence..... 38
1.2.3.2. Organic Chromophores and Fluorophores..... 40
1.2.3.3. Lanthanides for Optical Imaging..... 41
1.2.4. PET Imaging..... 42
1.2.5. Dual-Modal Imaging..... 44
1.2.5.1. Dual-Modal MRI-Optical Contrast Agents..... 45
1.2.5.2. Dual-Modal Optical-Nuclear Imaging Agents..... 47
1.2.6. Towards Next-Generation Imaging Agents..... 48
1.2.6.1. Zinc-Sensing MRI Contrast Agents..... 48
1.2.6.2. Zinc-Sensing Fluorescence Contrast Agents..... 51
1.2.6.3. Mechanisms of Zinc-Sensing in Fluorescence..... 51
1.2.6.4. Zinc-Receptor Moieties..... 52
1.3. Aims and Objectives..... 56
1.4. References..... 57

Chapter 2 – GdEx: An Exendin-4 Based Probe for Pancreas-Specific MRI Contrast Enhancement..... 70
2.1. Introduction..... 71
2.1.1. Exendin-4 and GLP-1..... 71
2.1.2. Probes Incorporating Exendin-4..... 71
2.1.3. Ligand Design and Methodology..... 75
2.1.4. Aims and Objectives..... 76

2.2. Results and Discussion..... 76

2.2.1. Synthesis of **GdEx**..... 76

2.2.2. *In Vivo* Studies with **GdEx**: Methodology and Practicalities..... 81

2.2.2.1. Experimental Rationale..... 81

2.2.2.2. Prior Work..... 81

2.2.3. Summary of *In Vivo* Data..... 82

2.2.3.1. Examination of **GdEx** in Wild-Type Mice..... 82

2.2.3.2. Examination of **GdEx** in Diabetic-Model Mice..... 84

2.3. A Zinc-Sensing, Targeted Contrast Agent **GdZn**..... 85

2.3.1. Probe Synthesis..... 87

2.3.2. *In Vivo* Studies with **GdZn**..... 88

2.4. Conclusions and Outlook..... 89

2.5. References..... 91

Chapter 3 – Synthesis of GPR-L1, a Ligand Targeted to GPR40, and its Lanthanide(III) Complexes..... 96

3.1. Introduction..... 97

3.1.1. G-Protein Coupled Receptor 40 (GPR40)..... 97

3.1.2. Agonists for GPR40 and Their Uses..... 97

3.1.3. Ligand Design..... 98

3.1.4. Aims and Objectives..... 101

3.2. Results and Discussion..... 101

3.2.1. Synthesis of Yoon's Indole-5 Propanoic Acid Derivative..... 101

3.2.2. Synthesis of **GPR-L1**..... 102

3.2.3. Lanthanide(III) Complexes of **GPR-L1** 109

3.2.3.1. Complex Properties and Characterisation 113

3.3. *In Vitro* Data 121

3.4. Conclusions and Outlook 125

3.5. References 127

Chapter4 – Exploring Agonist Interactions with the Glucagon-Like Peptide-1 Receptor (GLP-1R) 130

4.1. Introduction 131

4.1.1. The Glucagon-Like Peptide-1 Receptor (GLP-1R) 131

4.1.2. GLP-1R in Cell Membranes 131

4.1.3. Optical Imaging Systems 132

4.1.3.1. Fluorescence Resonance Energy Transfer (FRET) 132

4.1.3.2. Lanthanides in FRET: Time-Resolved Systems 133

4.1.3.3. Rhodamine-Based Chemosensors 134

4.1.4. Aims and Objectives 137

4.2. Results and Discussion 138

4.2.1. Synthesis of Terbium(III)-Exendin-4 Conjugates 139

4.2.1.1. *In Vitro* Receptor Binding Investigations 142

4.2.1.2. FRET Studies and Receptor Interactions 143

4.2.2. Synthesis of Rhodamine-Exendin-4 Conjugates 148

4.2.2.1. Photophysical Properties 150

4.2.2.2. Synthesis of Sterically-Encumbered Rhodamine Derivatives 154

4.2.2.3. Towards Reduced-Rhodol Derivatives 156

4.3. Conclusions and Outlook..... 157

4.4. References..... 159

Chapter 5 – Cyanine Compounds Designed for Zinc Sensing and Fluorescence Imaging..... 162

5.1. Introduction..... 163

5.1.1. Cyanine Dyes..... 163

5.1.1.1. General Structure of and Modifications to Cyanines..... 164

5.1.2. Zinc-Sensing..... 166

5.1.2.1. Mechanisms of Zinc-Sensing..... 166

5.1.2.2. Zinc Receptor Moieties..... 167

5.1.3. Dual-Modal Imaging Agents..... 167

5.1.4. Aims and Objectives..... 168

5.2. Results and Discussion..... 168

5.2.1. Exploration of Alternative Zinc-Sensing Moieties..... 168

5.2.1.1. Fluorescence Spectroscopy and Zinc-Binding Titrations..... 173

5.2.2. Towards Dual-Modal Imaging Agents..... 176

5.2.2.1. Fluorination of Cyanine Dyes..... 177

5.2.2.2. Zinc-Binding Titrations of Compound **5.14**..... 183

5.2.2.3. Radiolabelling of Tosylated Cyanine Dyes..... 185

5.2.2.4. Macrocyclic Metal Chelates for MR and PET Imaging..... 188

5.2.2.5. Towards Targeted Fluorescence Imaging Probes..... 191

5.3. Conclusions and Outlook..... 192

5.4. References..... 194

Chapter 6 – Conclusions and Outlook..... 198

6.1. General Comments..... 199

6.2. MRI Contrast Agents Targeting GLP-1R..... 199

6.3. Lanthanide(III) Complexes of a Ligand Targeted to GPR40..... 201

6.4. Exploration of Agonist Binding in GLP-1R..... 205

6.5. Near-Infrared Emissive Fluorescent Cyanine Dyes for Multi-Modal Imaging..... 208

6.6. Final Remarks..... 210

6.7. References..... 211

Chapter 7 – Experimental Procedures..... 213

7.1. General Experimental Considerations..... 214

7.2. General Spectroscopic Methods..... 214

7.2.1. Photophysical Methods..... 214

7.2.2. Relaxometric Measurements..... 215

7.3. *In Vitro* Procedures.....215

7.3.1. *In Vitro* Toxicity Tests..... 215

7.3.2. *In Vitro* Confocal Imaging..... 215

7.4. *In Vivo* Procedures..... 215

7.4.1. Magnetic Resonance Imaging..... 216

7.4.2. MR Data Analysis..... 216

7.5. Synthesis of Compounds in Chapter 2..... 217

7.6. Synthesis of Compounds in Chapter 3..... 217

7.7. Synthesis of Compounds in Chapter 4..... 230

7.7.1. General Considerations..... 230

7.7.2. Experimental Procedures..... 231

7.8. Synthesis of Compounds in Chapter 5..... 244

7.9. References..... 260

Chapter 8 – Appendix: Table of Rights and Permissions.....262

List of Abbreviations

18-FDG - [^{18}F]-fluorodeoxyglucose

2D – 2 Dimensional

3D – 3 Dimensional

Ac - Acetyl

ANOVA – Analysis of Variance

AIBN - Azobisisobutyronitrile

ATP – Adenosine Triphosphate

AUC – Area Under the Curve

Boc – *Tert*-butoxycarbonyl

BODIPY – Boron Dipyrromethane

cAMP – Cyclic Adenosine Monophosphate

CNR – Contrast to Noise Ratio

CT – Computed Tomography

CuAAC - Copper-Catalysed Alkyne-Azide Cycloaddition

Cy - Cyanine

DAST – Diethylamino Sulfur Trifluoride

DNA - Deoxyribose Nucleic Acid

DCM – Dichloromethane

Dicer-Ctrl - Dicer-Ctrl, Dicerfl/fl, Cre-ER negative

Dicer-KO - Dicer-Ctrl, Dicerfl/fl, Cre-ER positive

DIPA - Diisopropylamine

DIPEA – Diisopropylethylamine

DMF – Dimethylformamide

DMSO - Dimethylsulfoxide

DPA – Dipicolylamine

EC_{50} – Effective Concentration

EDDA - Ethylenediamine Diacetic Acid

EDC – 1-Ethyl-3-(3-dimethylaminopropyl) Carbodiimide

EMA – European Medicines Agency

Et - Ethyl

Ex4 – Exendin-4

FDA – Food and Drug Administration

FFA – Free Fatty Acid

FRET – Fluorescence Resonance Energy Transfer

GBCA – Gadolinium-Based Contrast Agent

GLP-1 – Glucagon-Like Peptide-1

GLP-1R – Glucagon-Like Peptide-1 Receptor

GPCR – G-Protein Coupled Receptor

GPR40 – G-Protein Coupled Receptor 40

H_2do2a - 1,4,7,10-Tetraazacyclododecane-1,7-diacetic Acid

H_3do3a - 1,4,7,10-Tetraazacyclododecane-1,4,7-triacetic Acid

H_3nota - 1, 4, 7-Triazacyclononane-1,4,7-triacetic Acid

H_4dota - 1,4,7,10-Tetraazacyclododecane-1,4,7,10-tetraacetic Acid

H_4dota(ga) - 2-(4,7,10-Tris(carboxymethyl)-1,4,7,10-tetraazacyclododecan-1-yl)pentanedioic Acid

H_5dtpa - Diethylenetriamine Pentaacetic Acid

hAGT - O^6-Alkylguanine-DNA Alkyltransferase

HATU - 1-[Bis(dimethylamino)methylene]-1*H*-1,2,3-triazolo[4,5-b]pyridinium 3-oxide Hexafluorophosphate

HBTU - 2-(1*H*-Benzotriazol-1-yl)-1,1,3,3-tetramethyluronium Hexafluorophosphate

HEK – Human Embryonic Kidney

HEPES - 4-(2-Hydroxyethyl)-1-piperazineethanesulfonic Acid

HOBt - Hydroxybenzotriazole

HOMO – Highest Occupied Molecular Orbital

HOPO – Hydroxypyrodinate

HPLC – High Performance Liquid Chromatography

HSA – Human Serum Albumin

HSAB – Hard-Soft Acid-Base

HYNIC - hydrazine nicotinamide

IC_{50} – Median Inhibitory Concentration

ICG -Indocyanine Green

ICT – Internal Charge Transfer

IR - Infrared

ISC – Inter-System Crossing

K_{222} - Kryptofix222

LCMS – Liquid Chromatography-Mass Spectrometry

LD – Liquid Disordered

LD_{50} – Median Lethal Dose

LFSE – Ligand Field Stabilisation Energy

LO – Liquid Ordered

LSD – Least Significant Difference

LUMO – Lowest Unoccupied Molecular Orbital

MALDI-MS: Matrix-Assisted Laser Desorption Ionisation- Mass Spectrometry

Me – Methyl

MS – Mass Spectrometry

MW – Molecular Weight

MRI – Magnetic Resonance Imaging

MTT - 3-(4,5-Dimethylthiazol-2-yl)-2,5-diphenyltetrazolium Bromide

NBS – *N*-Bromosuccinimide

NIR – Near Infrared

NIS – *N*-Iodosuccinimide

NMR – Nuclear Magnetic Resonance

NSF – Nephrogenic Systemic Fibrosis

PBS – Phosphate-Buffered Saline

PeT – Photoinduced Electron Transfer

PET – Positron Emission Tomography

Pra – Propargyl Alkyne Amino Acid

q – Hydration State

QD – Quantum Dots

quant. – Quantitative

ROS – Reactive Oxygen Species

SAP – Square Antiprismatic

SAR – Structure-Activity Relationship

S_n – Singlet State

SPECT – Single Photon Emission Computed Tomography

SPION – Superparamagnetic Iron Oxide Nanoparticles

T1D – Type 1 Diabetes Mellitus

T2D – Type 2 Diabetes Mellitus

TAK-875 - [(3*S*)-6-({2′,6′-dimethyl-4′-[3-(methylsulfonyl)-propoxy]biphenyl-3-yl}methoxy)-2,3-dihydro-1-benzofuran-3-yl]acetic acid hydrate

TES - *N*-[Tris(hydroxymethyl)methyl]-2-aminoethanesulfonic Acid

TFA – Trifluoroacetic Acid

TLC – Thin Layer Chromatography

TMS - Trimethylsilyl

T_n – Triplet State

TOF – Time of Flight

TPEN - *N*,*N*,*N*′,*N*′-tetrakis(2-pyridinylmethyl)-1,2-ethanediamine

TR-FRET – Time-Resolved Fluorescence Resonance Energy Transfer

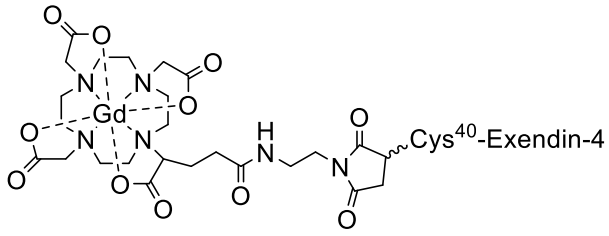
TSAP – Twisted Square Antiprismatic

US – Ultrasound

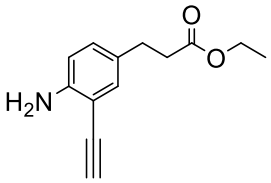
UV - Ultraviolet

WT – Wild Type

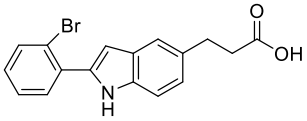
List of Key Compounds



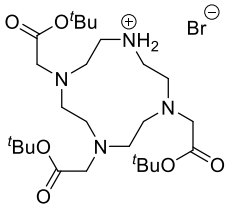
GdEx



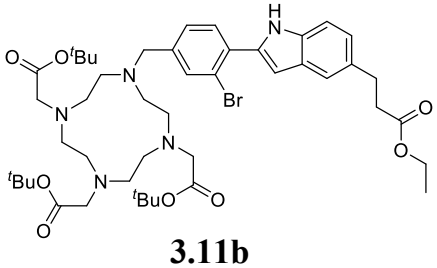
3.4



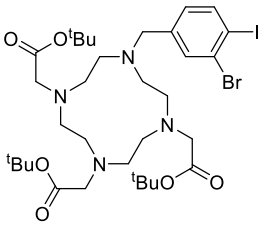
3.7



3.8



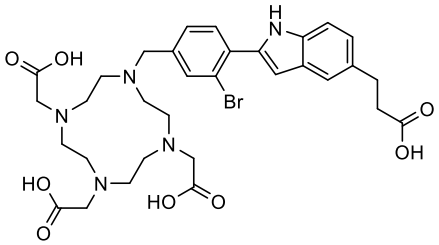
3.11b

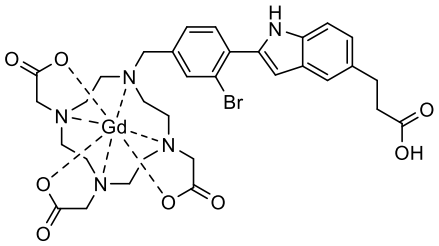


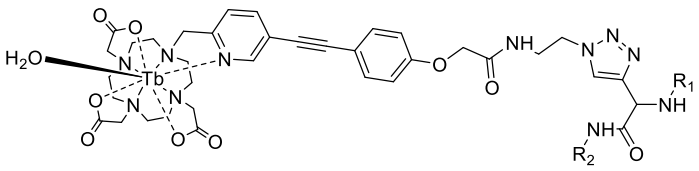
3.14

3.16, GPR-L1

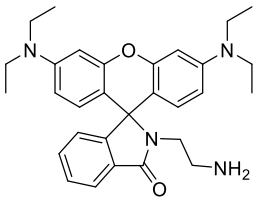
3.18, [Gd(GPR-L1)]



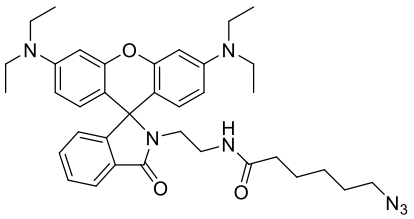




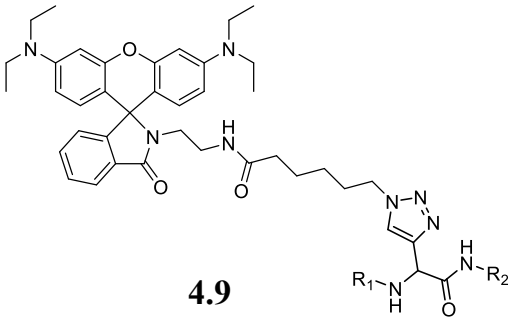
General Structure of Tb(III)-Peptide Conjugates 4.1 – 4.5



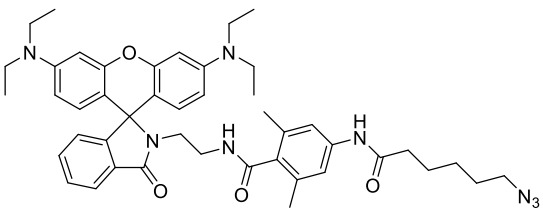
4.6



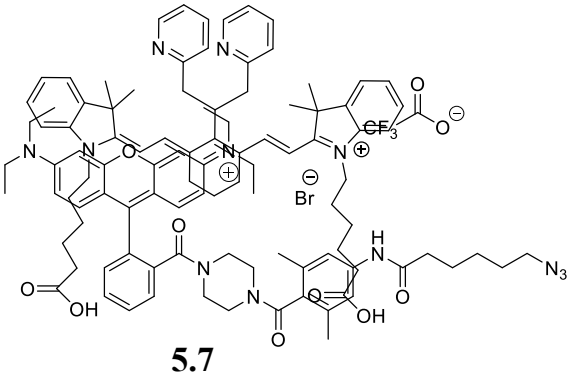
4.8



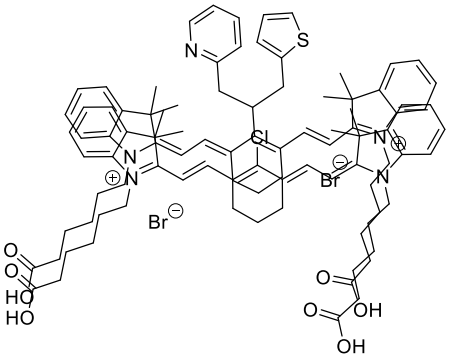
4.9



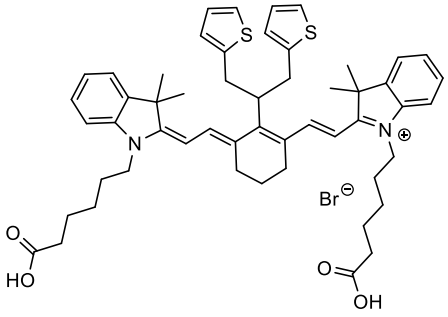
4.16



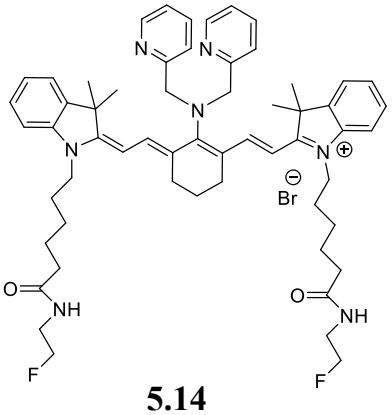
5.7



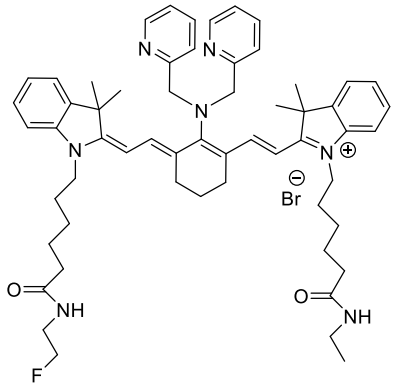
5.8



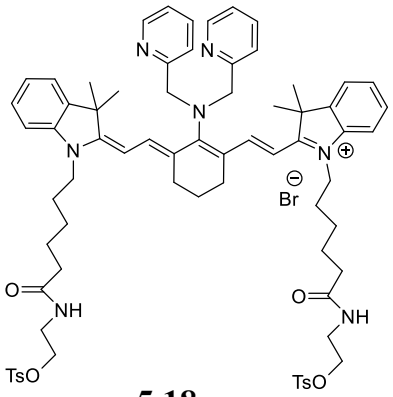
5.9



5.14



5.16



5.18

Chapter 1

Introduction

Diabetes mellitus is an increasingly alarming global health concern. However, current diagnostic ability is limited in its ability to detect development of the disease at the early stage. This thesis describes the development of imaging probes for a range of modalities which, through specific targeting of the insulin-producing cells of the pancreas, aim to improve *in vivo* imaging of this vital organ. Both peptide and small molecule-based targeting approaches are employed, and a substantial range of synthetic chemistry and methodology discussed. This introductory chapter seeks to provide context to this synthetic work, describing the disease diabetes and its underlying biology, the principles of molecular imaging and the techniques that these probes were designed for, notably magnetic resonance and optical imaging, a discussion on cation sensing with a focus on Zn^{2+}, which plays a critical role in insulin storage, and summarising the aims and objectives of this body of work.

Briefly, chapter 2 outlines the development of an MRI contrast agent based on the peptide exendin-4, **GdEx**, its *in vivo* behaviour and the synthesis of a closely related zinc-sensing probe, **GdZn**. Chapter 3 discusses the generation of a ligand targeting the receptor GPR40, its complexation to lanthanide(III) ions of interest in the molecular imaging field and the properties and characterisation of these complexes. The synthesis of exendin-based probes capable of exploring agonist binding interactions at the receptor GLP-1R through Tb(III) and rhodamine incorporating compounds is explored in chapter 4. Chapter 5 focuses on the development of a range of zinc-sensing cyanine dyes capable of optical imaging.

1.1. Diabetes Mellitus

1.1.1. Epidemiology, Symptoms and Disease Development

1.1.1.1. Global Incidence and Epidemiology

In just 6 years between 2008 and 2014, the estimated number of people living with diabetes mellitus rose by more than 70 million to reach 420 million[1,2]. By 2035, that number is expected to exceed 600 million – greater than the population of any country in the world excluding China and India[3,4]. Diabetes, which was once regarded primarily as a disease of adults in advanced economies of the Western world associated with sedentary lifestyles, unhealthy diets and obesity may now be truly considered a pandemic which is the 9th most common cause of death globally[5–7]. Indeed, the rise in living standards and spread of urbanisation across the world, in conjunction with ever-increasing rates of obesity and an aging global population has seen diabetes affect every region of the planet in some unexpected ways: as many as 1 in 4 Micronesians and Saudi Arabians are sufferers; and 25% of healthcare spending by Latin American governments goes towards treatment and mediation of the disease[7,8]. Here in the U.K., recent analysis has shown that there are around 3.8 million diabetics in the country, who will unfortunately exhibit double the mortality rate of their non-diabetic peers of a similar age[9,10]. More than £23 billion was spent on diagnosing and treating diabetes in 2011 and, with the number of diabetic

Britons projected to rise to around 6.3 million by 2035, the disease is expected to consume as much as 17% of British healthcare expenditure[10].

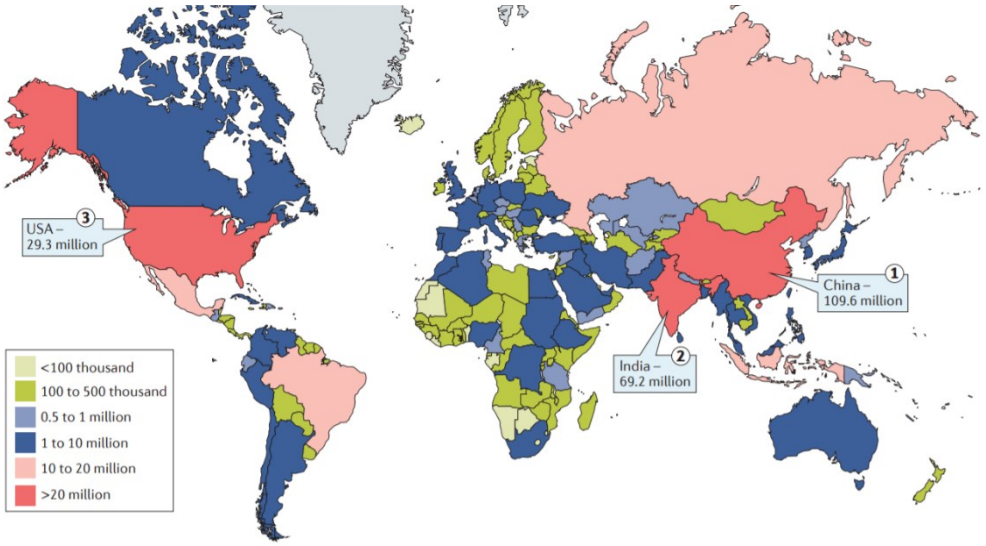


Figure 1.1: Map showing estimated national totals of diabetic adults in each country. The 3 countries with the highest totals are highlighted. Adapted from reference 7, with permissions[7].

1.1.1.2. Disease Sub-types, Causes and Symptoms

Diabetes mellitus is a chronic metabolic disease attributed to either a lack of functional insulin, or an insufficient response by the body to insulin secretion[11]. Insulin is a hormone which is responsible for the regulation of glucose storage: its release occurs in response to elevated blood glucose levels, such as those after ingesting a meal, triggering the conversion of glucose into glycogen[12,13]. Glycogen is a polymer of glucose which acts as a storage molecule in the liver and muscle tissue[13]. In addition, insulin release initiates the synthesis and storage of triglycerides in adipose tissue[14]. Improper storage of glucose results in an individual's blood glucose levels becoming unusually high: a state known as hyperglycaemia. In the short term, acute hyperglycaemia is associated with thirst and a frequent need to urinate, as well as fatigue following excretion of glucose from the body[11]. Persistent, chronic, untreated hyperglycaemia can lead to the development of several debilitating conditions including blindness, kidney failure and severe nerve damage to the extremities, with the latter even occasionally resulting in the need for amputation[11,13].

There are many contributary factors to the development of diabetes which may be genetic, environmental and even socio-economic, with the complex relationships between these rendering diabetes a challenging disease to grasp[4,6–8,11,13,15]. Efforts to understand diabetes and enable its treatment have led to its broad classification into 2 sub-types: type 1 diabetes (T1D) and type 2 diabetes (T2D), although recent work has attempted to reflect the complexity of the illness and move towards as many as 5 different sub-groups[16].

Making up around 10% of cases of diabetes, T1D is an autoimmune disease in which T-cells of the immune system attack β-cells of the islets of Langerhans within the pancreas; the insulin production centre[8,11,13,17–20]. Destruction of these cells removes the body's ability to secrete insulin, triggering the symptoms discussed above. T1D is often referred to colloquially as early-onset diabetes, given that it typically manifests in early childhood or adolescence and is almost exclusively caused by genetic predisposition[21]. The mechanisms behind the development of T2D are less well established, but it is suspected that there is a progressive decline in β-cell mass and functionality, with the extent of the latter currently a subject of debate amongst leading researchers in the field[13,18,22–26]. Sufferers of T2D have either become resistant to insulin, i.e. their bodies cannot respond effectively to insulin secretion, or produce insulin at insufficient quantities or in a dysfunctional form[11,13,27]. What has been discovered is that there is a strong link between numerous lifestyle and environmental factors and susceptibility to T2D. Smoking, excessive alcohol consumption and sedentary behaviour have all been shown to increase an individual's risk of developing T2D – primarily as these behaviours can lead to obesity: adipose tissue secretes fatty acids, glycerol, cytokines and hormones which can interfere with insulin signalling pathways and trigger β-cell apoptosis and dysfunction[6–8,11,28]. Environmental factors are not exclusively responsible for T2D: a family history of the disease and ethnic background can also predispose an individual to developing the condition[4,7].

1.1.2. Pancreatic β-Cells

The pancreas is found deep within the abdomen, located close to the stomach and spleen[29]. The organ is predominantly comprised of the exocrine pancreas, where digestive enzymes are produced, although a series of around 1 million microstructures known as the islets of Langerhans can be found dispersed throughout pancreatic tissue[29]. These islet cells make up the endocrine pancreas, responsible for hormone production, and β-cells are the dominant cell type in these islets, comprising up to 80% of islet cell mass[12,29]. Despite making up the bulk of the islets of Langerhans, β-cells actually only account for around 1% of the volume of the pancreas, although there is quite a wide variation in this proportion amongst non-diabetic individuals[12,30]. As the cells responsible for insulin production, pancreatic β-cells are the key to understanding both types of diabetes and their progression.

Current understanding in the mechanism of T2D development suggests than in response to insulin resistance, the pancreas is able to compensate by increasing insulin secretion to help ensure glucose homeostasis[29]. Over a prolonged period, β-cell functionality decreases and the cells become unable to compensate for increased levels of insulin resistance, resulting in an impaired ability to moderate glucose levels and generation of T2D[29]. This presents a major challenge in the diagnosis of diabetes: although blood glucose levels can be measured to identify whether a patient is persistently hyperglycaemic, this often only becomes apparent several years after a decline in β-cell mass and functionality begins: sometimes as much as 80% of cell function can be lost during the asymptomatic

period of diabetes yet remains undetected due to the highly resilient nature of the organ[15,19,23,27,29]. This diagnosis typically comes at an advanced stage of disease progression. As a result, treatment typically consists of regular blood glucose monitoring, insulin injections and a strict diet and exercise regime[13]. Ideally, diabetes would be treated either through transplantation of healthy β-cells or some kind of pharmacological stimulation which would trigger β-cell regeneration, or at least slow β-cell degradation[22,27,31]. This would provide a long-term solution for patients, removing the need for daily monitoring of blood glucose and insulin injections. An early stage detection of β-cell mass loss, as well as a means to determine cell functionality both non-invasively and quantitatively over an extended time period would enable such an approach to be taken. Clinicians could utilise this method to determine which treatment pathway for an individual would be most effective. Currently, no such method has been developed[18,23].

Imaging of pancreatic β-cells and attaining quantitative data on them remains challenging for multiple reasons: predominantly the low proportion of the pancreas they occupy, but also their non-uniform size distribution and uneven sizes, all of which can lead to specificity issues in targeting[15,23,30]. There is a clear and present need for a β-cell specific imaging agent to allow for cell quantification which could help stem the spread of the pandemic levels of diabetes.

1.1.3. β-Cell Receptors: Targets for Imaging Probes

One well-established technique to develop imaging agents for specific organs or tissues is to synthesise a compound which incorporates a molecule, such as a peptide or other biomolecule, which binds to an over-expressed receptor within the tissue of interest. This can favourably influence the biodistribution of the agent, enhancing the image of the biological target and potentially reducing both undesired off-target effects of the agent or the quantity of the imaging probe required[32–34]. The introduction of a targeting moiety can improve the clinical utility of an imaging probe, enhancing target to background signal ratio, improve agent specificity and uptake by and retention in the tissue of interest, as well as potentially opening the door for multimodal imaging and theranostics through intelligent probe design[34,35].

1.1.3.1. The Glucagon-Like Peptide-1 Receptor

The human genome codes for the synthesis of proteins. Amongst these, the G-protein coupled receptor family, defined by the presence of seven transmembrane helices, is the largest group of peptides which is encoded for[36]. The glucagon-like peptide-1 receptor (GLP-1R) falls into this family[36,37]. A wide variety of tissues express this receptor, ranging from adipose tissue to the heart, lungs and kidneys[37,38]. Critically for diabetes, GLP-1R is also found in pancreatic islets: specifically β-cells, and the brain[37–40]. In the brain, activation of GLP-1R has been shown to increase feelings of satiety and slow the rate of gastric emptying, leading collectively to a reduction in appetite[22,37,38,40]. Stimulation of pancreatic GLP-

1R results in a plethora of actions, including an increase in insulin biosynthesis and secretion, enhanced β-cell proliferation and reductions in both β-cell apoptosis and glucagon release[22,37,38,40].

Due to the effects of GLP-1R activation, agonists for the receptor have found success as clinical treatment agents for diabetes in the forms of exenatide and lixisenatide[15,41]. Ample evidence exists in the literature that GLP-1R agonists, in particular the peptide exendin-4, are utilised with great success in the development of imaging probes specifically for pancreatic β-cells across a wide range of imaging modalities[3,15,27,42–52]. In addition to the quantification of islet cell mass through the acquisition of single photon emission computed tomography (SPECT) images, these agents also include dual-modal fluorescence-PET probes and functionalised nanoparticles, showing the wide variety of compounds which have been made possible through the modification of ligands for GLP-1R. These compounds and their applications, along with the analysis of **GdEx**, a probe synthesised by the Long group for the *in vivo* assessment of β-cell mass in healthy and disease-model animals, are discussed further in chapter 2.

1.1.3.2. G-Protein Coupled Receptor 40

Despite the well-known abundance of GLP-1R in pancreatic islets, recent work has established that it is not the most prolific on β-cells. In fact, the relatively recently discovered receptor G-protein coupled receptor 40 (GPR40) is the most commonly found receptor on the membranes of these critical, insulin producing cells[53–59]. Prior to the revelation that GPR40 is enriched in the pancreas, alongside the ileum and parts of the brain, the function of the receptor in biological systems posed a challenge to researchers, especially as it had been discovered *via* amplification of the human genome rather than observation of any physiological processes[60–63].

Polyunsaturated fatty acids have been shown to act as agonists for GPR40, with its activation triggering release of Ca^{2+} in β-cells and therefore augmenting insulin secretion, although the biological mechanisms behind this process remain unclear[53–55,58,61,63]. This positive effect on insulin release, which is known to occur in a glucose-dependent fashion has caught the eye of groups seeking to develop pharmaceutical methods of treating T2D[64–66]. Several notable reviews have been devoted to the discussion of developments in this field, and it has been observed that propionic acid species with polar aromatic appendages exhibit strong binding to GPR40, with several of these compounds progressing to clinical trials and even more in preclinical development[64–66]. **Figure 1.2** shows a selection of these agonists, as well as examples of thiazolidinediones and diacylphloroglucionols, both of which have also been shown to be capable of acting as ligands for GPR40[66].

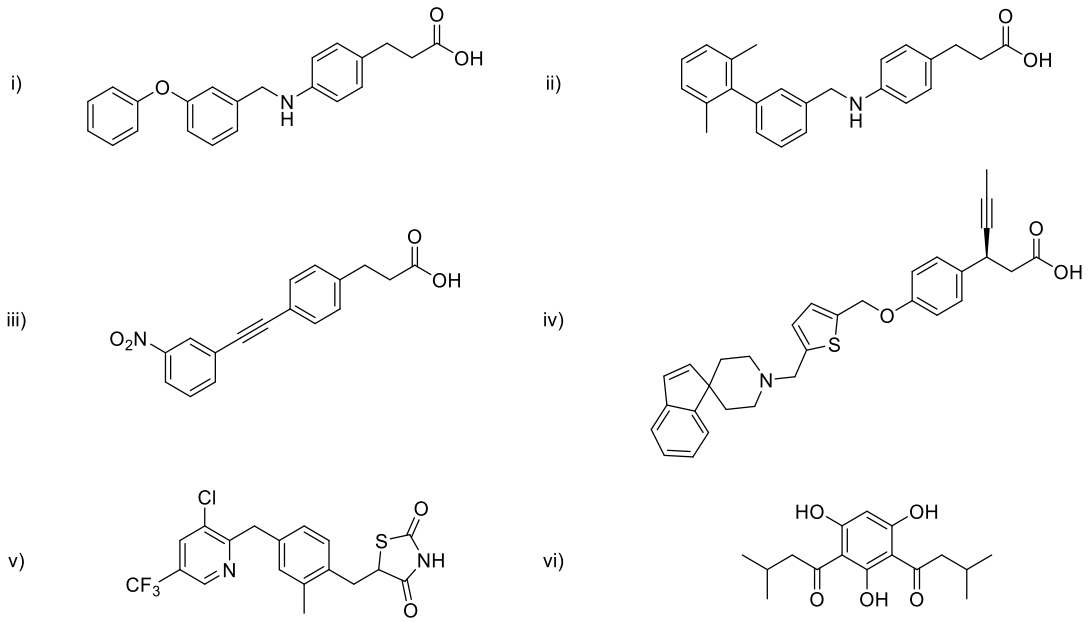


Figure 1.2: A selection of phenyl propionic acid-based GPR40 agonists reported by i) Mckeown *et al.*[67], ii) Yasuma *et al.*[66], iii) Christiansen *et al.*[68], iv) Hamdouchi *et al.*[69], v) a thiazolidinedione agonist synthesised by Tan *et al.*[70] and vi) a diacylphloroglucinol published by Bharate *et al.*[71].

Amongst the many classes of compound which have been developed as agonists for GPR40, the aromatic propionic acid species have shown the most promise in terms of progression to and through clinical trials. One of these, [(3*S*)-6-({2′,6′-dimethyl-4′-[3-(methylsulfonyl)-propoxy]biphenyl-3-yl}methoxy)-2,3-dihydro-1-benzofuran-3-yl]acetic acid hydrate, (TAK-875), developed by Negoro *et al*. reached phase III clinical trials, although was discontinued in December 2013 due to concerns over hepatotoxicity[64,69,72]. Despite this TAK-875 did show significant promise, including high potency, sufficient oral bioavailability and selectivity over the plethora of other similar receptors[72]. Furthermore, TAK-875 was shown to avert hyperglycaemia in diabetic patients *via* GPR40 activation and subsequent insulin secretion[72–74].

Understanding of the relationship between the structure of a compound and its function in biological systems is key in medicinal chemistry and in the design of targeting moieties. Several critical interactions between TAK-875 and GPR40 have been established through the investigation of the structure-activity relationship (SAR)[59,72]. Hydrogen bonding from the carboxylic acid group has been shown to play a vital role in receptor binding, perhaps explaining the success of these compounds in the pursuit of pharmaceutical remedies for diabetes, as well as π-stacking from the aromatic rings and polar interaction from the methanesulfonate group[59,72].

In 2017, a series of indole-propionic acid compounds were published by Yoon *et al.*[59]. These compounds were shown to bind to GPR40 with an even greater affinity than TAK-875 and utilised many of the key binding interactions discussed above[59]. One compound in particular showed heightened

receptor binding ability, and it was hypothesised that this structure could be harnessed as a targeting group for imaging compounds developed to study and quantify pancreatic β-cells (**Figure 1.3**).

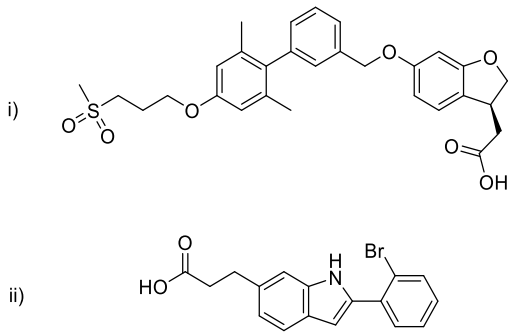


Figure 1.3: i) TAK-875, ii) the compound synthesised by Yoon *et al*.[59,72].

The design, synthesis and testing of compounds aiming to harness the strong interactions between these compounds and GPR40 in imaging probes has formed an extensive part of work within this thesis. Chapters 3 details the synthetic work towards such compounds with potential applications in magnetic resonance and optical imaging, as well as the introduction of zinc chemosensing ability.

1.1.4. Diabetes and Zinc

Zinc is the second most abundant metal found in the human body and has a number of extensive and varied biological roles[75]. The metal is involved in over 300 cellular processes, including the function of at least 200 enzymes, and dysfunction in its metabolism has been linked to a vast array of diseases including diabetes, cancer, immune system disorders and liver cirrhosis[75–78].

Almost a century ago, in 1926, it was established that the pancreas contained large quantities of zinc when compared to many other organs[79]. Shortly afterwards, ground-breaking work by Scott resulted in the discovery that zinc(II) ions are responsible for the crystallisation of insulin as hexameric structures, and also that the level of pancreatic zinc was lower in diabetic individuals[80,81].

This early suggestion of a link between low levels of zinc and diabetes has been extensively examined in the 95 years since it was first reported. During this period it has been established that, within the pancreas itself, the islet β-cells are extremely rich in Zn^{2+} when compared to the rest of the organ[18,78,82,83]. Additionally, zinc(II) ions are intimately involved in insulin biosynthesis and release, as well as its storage[76,77,84]. Diabetic humans and animals have been shown to exhibit enhanced zinc loss through excretion, and it is now widely accepted in the field that there is an association between depleted zinc levels and the progression of T2D[76–78,84]. The exact underlying mechanisms for this correlation are debated, although there are several prominent theories: zinc deficiency has been shown to be related to oxidative stress, which may then lead to β-cell degradation[77]. Zinc(II) ions have been shown to have insulinomemetic effects and a deficiency may also result in impaired insulin secretion, interference in insulin receptor binding and a decrease in the biosynthesis of these receptors, or abnormal glucose

carrier structure formation[76,77]. Additionally, there is some suggestion that Zn^{2+} ions released during insulin secretion may subsequently be involved in the inhibition of glucagon release from α-cells[84]. Although the exact reasons behind the link between depleted zinc levels and diabetes remain undefined – i.e. whether the disruption to zinc homeostasis is the cause of β-cell functionality decline or vice versa - it is apparent that there is a clear link between the two, and that understanding the role played by Zn^{2+} in pancreatic β-cells may lead to greater clarity in our diagnosis and treatment of diabetes.

The high concentration of Zn^{2+} in insulin secretory granules results in co-release of the ions alongside insulin[78]. It has been hypothesised that this zinc release could be quantified through ratiometric imaging probes: these could be fluorescent compounds or magnetic resonance imaging (MRI) contrast agents incorporating a zinc-chelating moiety which would undergo a change in fluorescence intensity or relaxivity proportional to the amount of zinc(II) present[18,83,85]. The images obtained using these agents could be quantifiably processed and used to calculate the functional β-cell mass in the organ and therefore potentially be utilised as an early diagnosis system for diabetes[86]. Zinc transporter proteins and the maintenance of zinc homeostasis and metabolism have also become increasingly relevant as pharmacological and therapeutic targets for diabetes and a whole host of other disorders[75,78]. The introduction of a zinc-binding unit to a molecule has also been promoted as a method of probe targeting: despite zinc(II) being highly abundant in biological systems, it is concentrated in the brain, pancreas and spermatozoa[83,87]. If a compound is able to bind to zinc ions, it is likely to localise in these zinc-rich areas of the body, potentially enhancing the specificity of the imaging probe.

1.2. Molecular Imaging

The identification and diagnosis of diseases within the human body are typically carried out through the monitoring of anatomical or morphological changes[88,89]. These physical symptoms of a disease are caused by changes in metabolism or physiological processes which begin at a much earlier point in time and the detection of these alterations could result in earlier detection of disease[88,89]. The field of molecular imaging seeks to identify and monitor these failures of biological processes at the cellular and sub-cellular level and enable this to be done *in vivo*, rather than simply examining the end stage of disruption to specific molecular pathways[88–90]. Being able to study the development of pre-disease states in a living organism in a non-invasive, quantifiable way would provide more meaningful, relevant information than *in vitro* analysis obtained from biopsies or other methods of pathology or tissue sampling[88–90].

1.2.1. The Lanthanides in Molecular Imaging

Elements within the lanthanide series possess several unique properties which have been harnessed for a broad spectrum of applications within the molecular imaging field[91]. Although many lanthanides have been used to great effect, the most well-established in molecular imaging are gadolinium, terbium and

europium due to their magnetic and optical properties, which are discussed below and elsewhere in this thesis[91,92].

The useful properties of the lanthanides which lend themselves to imaging applications derive from the unique properties of their ions.

1.2.1.1. Lanthanide(III) Ions

Almost all of the lanthanides are most commonly found in the +3 oxidation state in their compounds[91–93]. These ions, represented as Ln^{3+} or Ln(III), have the electronic configuration $[Xe]4f^n$, where n = 0 – 14[92]. The 4f orbitals are diffuse in nature and are energetically below the occupied 5s and 5p orbitals, resulting in a shielding effect which renders the 4f electrons core-like – i.e. the energy of these orbitals is mostly unaffected by the ion's chemical environment and the 4f electrons do not make a large contribution to bonding in lanthanide(III) complexes[91–93]. This results in a phenomenon known as the 'lanthanide contraction': moving across the lanthanide series, the size of the Ln^{3+} decreases as the valence electrons in the 5s and 5p sub-shells, which penetrate the 4f orbital to some degree, are more strongly attracted by the increased nuclear charge that comes with each additional proton[91]. Despite this change in size across the period, there is only a 0.15 Å difference in ionic radius between La^{3+} and Lu^{3+} in a 9-coordinate environment, and the ions behave remarkably similarly in terms of their complexation properties[92].

The shielded nature of the 4f orbitals results in the Ln^{3+} ions being uniformly large, hard and spherical, which causes bonding in Ln(III) complexes to be predominantly ionic and non-directional[92,93]. Variable coordination numbers are possible, with coordination complexes between 6 and 12 reported most often in the literature, although 8 or 9 coordinate structures are the most commonly adopted[91].

1.2.1.2. Ligands for Lanthanide(III) Ions

As hard, Lewis acidic metal centres, the Ln^{3+} ions prefer anionic ligands with electronegative, negatively charged donor atoms such as oxygen or strongly Lewis basic atoms like nitrogen[91]. The variable coordination geometries and high coordination numbers desired by these ions can present a challenge to synthetic chemists. However, macrocyclic ligands such as the octadentate 1,4,7,10-tetraazacyclododecane-1,4,7,10-tetraacetic acid (H_4dota) provide the high denticity and desired donor atom combination necessary for thermodynamically stable and kinetically inert complexes to be formed. Furthermore, macrocycles may be readily modified through synthetic alterations to the ligand backbone or acetate arms, which can allow the properties of the Ln(III) complexes (such as biodistribution) to be favourably altered. As such, macrocyclic chelates have proven themselves to be versatile scaffolds for use in lanthanide(III) complexes designed for molecular imaging[92].

Other considerations beyond the necessary complex stability must be taken into account, particularly for the luminescent ions Eu^{3+} and Tb^{3+}. These are discussed further in **section 1.2.3**.

1.2.2. Magnetic Resonance Imaging

Nuclear magnetic resonance (NMR) is a critical part of any synthetic chemist's toolkit, where it is harnessed to aid in the elucidation and identification of molecular structure. Charged nuclei have a characteristic motion, resulting in a small magnetic moment. When a magnetic field is applied to these nuclei, a phenomenon called Larmor precession occurs[90]. This phenomenon manifests as the altered motion of a charged particle after the application of a magnetic field to it[94]. The Larmor frequency (ω_0) is proportional to the applied magnetic field and the gyromagnetic ratio (γ), a nucleus-specific constant[90].

In the absence of a magnetic field, nuclei with a non-zero spin, such as protons, are randomly aligned. When a field, B_0, is applied, these nuclei align so that the direction of the spin and the field are parallel. If a radio frequency is then applied to these nuclei, a second magnetic field, B_1, is induced, resulting in the alignment of the nuclei shifting away from the direction of B_0. The radio frequency utilised is the same as the Larmor frequency (**Equation 1.1**)[90].

Equation 1.1: $\omega_0 = \gamma B_0$

When the radio pulse is removed, the nuclei can realign, returning to their parallel alignment with B_0. This realignment is done *via* longitudinal and transverse relaxation. The times taken to relax along the longitudinal and transverse axes are referred to T_1 and T_2 respectively, and the rate of relaxation is dependent upon the environment of the nucleus. During this relaxation, the nuclei lose energy through the emission of radio frequencies, and this energy is used to generate a signal[15,90]. In NMR spectra this signal is in the form of peaks which can give information on the structural identity of a chemical compound through its chemical shift, multiplicity, coupling constant and integral.

In an MRI scan, the signals given from relaxing nuclei are used to generate grayscale images of a patient, an anatomical sample as opposed to a chemical one. The nucleus of interest in MRI is hydrogen. Human tissues are predominantly composed of fat and water, and therefore contain large numbers of hydrogen nuclei which can be used to generate an image[90]. Fourier transform processes the emitted radio frequencies and generates a signal which is proportional to the density of hydrogen atoms at a particular location, enabling image construction[90]. As the relaxation rate of excited nuclei is dependent on their environment, water molecules in different biological tissues will relax at different rates. For T_1 relaxation, a reduced relaxation time results in a brighter image after Fourier transform and faster T_2 relaxation will result in darker images. These contrast differences, coupled with excellent depth penetration and high resolution of the images obtained through MRI scans enable detailed anatomical data to be collected[15,18,95]. In addition, it avoids exposing the patient to any ionising radiation and allows physiological and anatomical data to be acquired simultaneously[90].

However, MRI is not without its drawbacks. Most notable amongst these is its lack of sensitivity: only a small fraction of hydrogen atoms are able to absorb the radiofrequency required to generate a signal[18,90,96,97]. This can render the imaging of some biological targets challenging. With respect to diabetes, pancreatic β-cells make up an extremely small fraction of the organ's volume (1%)[12,30]. The prospect of imaging these cells is already difficult enough, and the low sensitivity of MRI adds to this challenge.

1.2.2.1. Contrast Agents for MRI

In order to overcome the issue of low sensitivity in MRI scans, a contrast agent is often administered during a scan. Contrast agents shorten the T_1 and T_2 relaxation times of water molecule protons in their immediate vicinity, resulting in greater differences in the brightness of the resulting image and therefore enabling these tissues to be more readily distinguished from one another[90,96,98–103]. In the clinic, contrast agents are administered to improve contrast in images between healthy and abnormal tissue or enhance certain regions of the anatomy[98]. Around 1 in 3 patients undergoing an MRI scan are administered with a contrast agent[98].

MRI contrast agents can be grouped according to their magnetic properties. Ferromagnetic contrast agents, typically iron-oxide nanoparticles and their functionalised analogues, distort the B_0 around the agent, thus altering the T_2* and creating contrast[90,104]. Several such agents have been utilised in the clinic, although many nanoparticulate contrast agents are no longer commercially viable[105,106]. The fact that T_2 contrast agents generate negative contrast in obtained images, which is more challenging to interpret, is possibly behind the limited popularity of these agents. Paramagnetic contrast agents act by promoting T_1 relaxation of water molecules, which creates brighter images[90,103]. The f-block element gadolinium forms trivalent ions with 7 unpaired electrons which are highly paramagnetic (μ = 7.94 BM) and rendering gadolinium-based contrast agents (GBCAs) extremely popular[103,107]. GBCAs have been in clinical usage for over 30 years, with the compound Magnevist® first synthesised in 1981 and clinically approved in 1988[103,108–110]. In the intervening decades, a total of 11 GBCAs (**Figure 1.4**) have been approved for use and Magnevist® itself has been used over 100 million times[103,111].

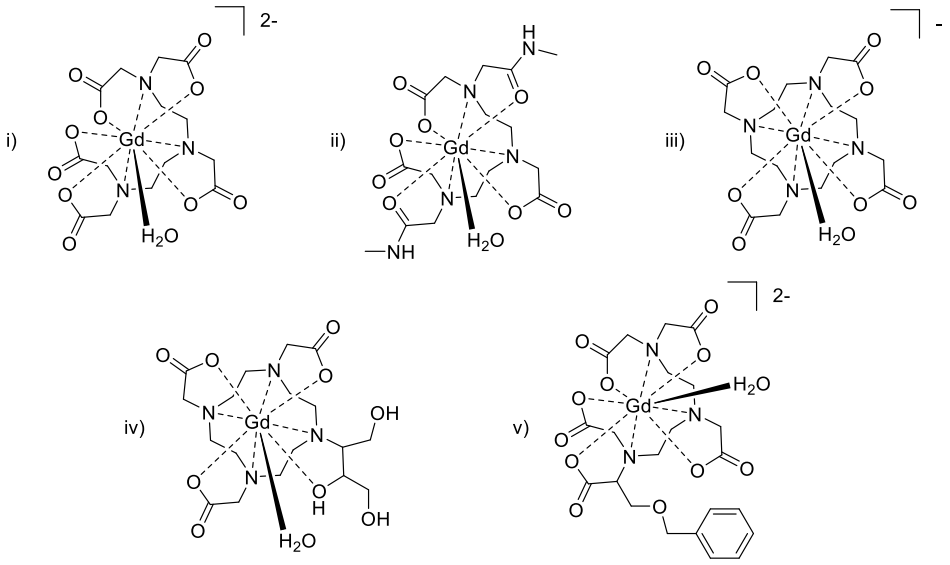


Figure 1.4: Structures of the five most commonly administered GBCAs in clinical use worldwide[112] i) Magnevist®, $[Gd(OH_2)(dtpa)]^{2-}$, ii) Omniscan®, $[Gd(OH_2)(dtpa\text{-}bma)]$, iii) Dotarem®, $[Gd(OH_2)(dota)]^{-}$, iv) Gadovist®, $[Gd(OH_2)(do3a\text{-}butrol)]$ and v) Multihance®, $[Gd(OH_2)(bopta)]^{2-}$. Adapted from reference 103, with permissions[103].

Magnevist® is the gadolinium(III) complex of diethylenetriaminepentaacetic acid (H_5dtpa). Despite the early promise of this species, and other related ligands such as the bis-amide derivative H_3dtpa-bma, the field now focuses predominantly on the use of macrocyclic ligands. Acyclic species tend to form more kinetically labile complexes with metal ions, which has been associated with toxicity concerns in patients, as discussed below. Indeed, the log K values for the Gd(III) complexes of H_4dota and H_5dtpa are 24.7 and 22.3 respectively[103,113]. The rate constants for demetallation at pH 1 show this difference in stability more drastically, with values of 3-5 x 10^{-7} and 1.2 x 10^{-3} respectively[114]. Although research into acyclic ligands for GBCAs does continue, macrocyclic derivatives form the most stable and inert complexes with gadolinium(III) and are therefore most appropriate for patient safety and clinical translation.

The contrast agent Dotarem® is the Gd^{3+} complex of the macrocycle H_4dota, which has been widely referred to in the literature as the "gold standard" for gadolinium(III) ligands[32,103]. H_4dota forms extremely thermodynamically stable and kinetically inert complexes with a host of metal ions, including many lanthanides, which exhibit a range of interesting behaviour in solution with possible formation of 4 different stereoisomers[114]. These isomers differ from one another in terms of the position of the pendant acetate arms (Δ or Λ according to whether the complex twists in a right- or left-handed helix respectively) and the orientation of the macrocycle's ethylene bridges (λλλλ or δδδδ)[103,114,115]. Geometrically, the shapes adopted by these isomers may be described as square antiprismatic (SAP) and twisted square antiprismatic (TSAP), with the twist angle between the planes of nitrogen and

oxygen donor atoms used to characterise these two geometries[115]. Interconversion between these macrocyclic isomeric species is possible and occurs on the NMR timescale, resulting in the complex, broad shapes seen in ^{1}H NMR spectra of complexes of H_4dota and its derivatives with lanthanide(III) ions[103,116]. The interconversion between these isomers can impact on complex stability, and strategies to mitigate this have formed a significant part of the literature discussion[103].

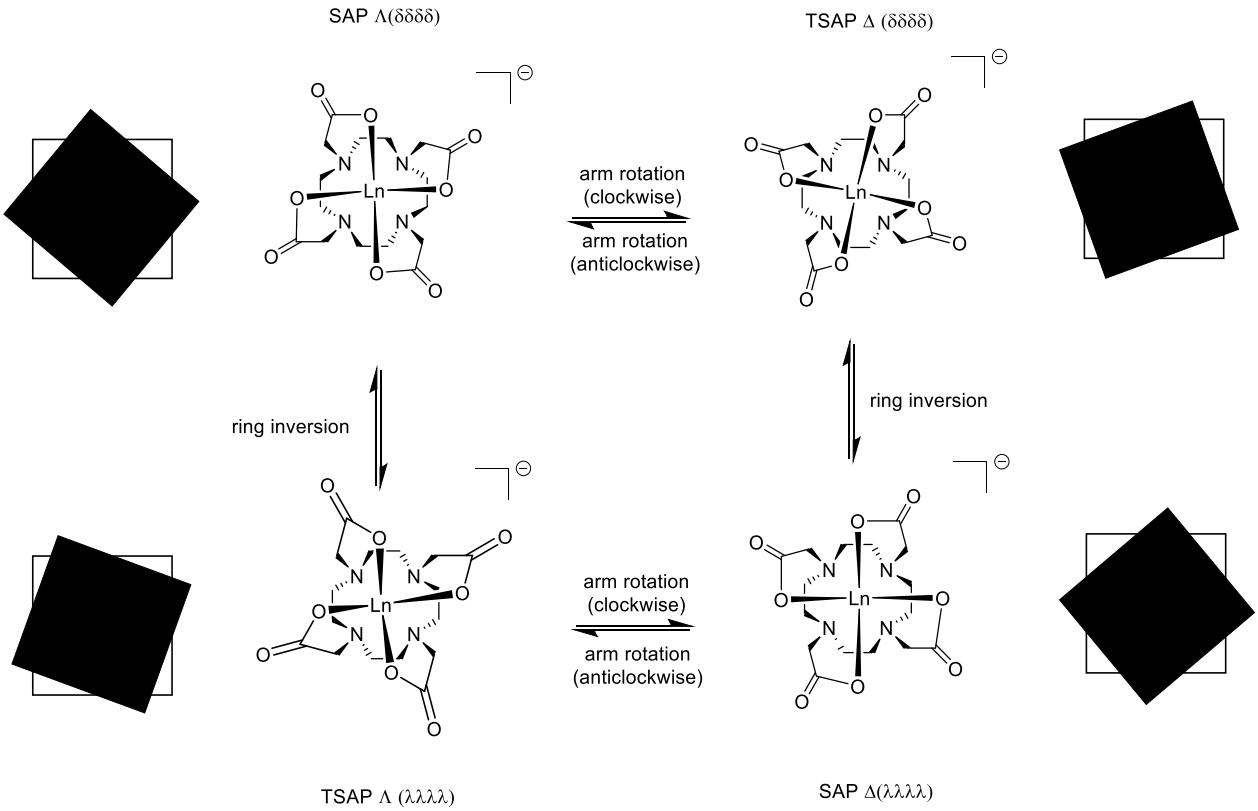


Figure 1.5: The four possible stereoisomers for [Ln(dota)]$^-$ and their interconversion mechanisms. Visualisation of the SAP and TSAP shapes is achieved by considering planes of the macrocyclic N4 donors (white square) acetate O4 donors (black square). Pairs of enantiomers are diagonally opposite one another. Coordinated water molecules are omitted for clarity. Adapted from reference 103, with permissions[103].

Due to the low sensitivity of MRI, large quantities of contrast agent, sometimes even several grams, are often required in order to obtain useful images from scans of patients[103]. In the early 2000s, there were early indications of a potential link between the administration of GBCAs and the potentially fatal disease nephrogenic systemic fibrosis (NSF)[117,118]. Since Marckmann's observations in 2006, NSF patients who have undergone MRI scans with a GBCA have been found to have gadolinium metal deposits in their heart, kidneys and skin and, perhaps even more concerning, individuals with healthy kidney function have suffered from gadolinium deposits in the brain[103,110,119–122]. Although a recent study has sought to quell rising concerns over the usage of GBCAs[123], free Gd^{3+} ions have been found to be extremely toxic (LD_{50} = 0.2 mmol kg^{-1}) due to their similar ionic radius to Ca^{2+}, which results in

interference in signalling pathways mediated by the release of calcium(II) ions[103,124,125]. Due to the increased concern over the toxicity of GBCAs, the European Medicines Agency (EMA) has begun to restrict the administration of gadolinium(III) complexes of acyclic ligands and the U.S. Food and Drug Administration (FDA) has issued warnings of its own[121,126,127]. Due to these concerns, and others about gadolinium(III) which have been covered extensively in the literature, the focus in the field is now almost exclusively on macrocyclic ligands for Gd^{3+} and how these may be modified to reduce toxicity concerns and optimise biodistribution through the use of targeting groups to grant favourable biodistribution[103,128–130].

Chapters 2 and 3 of this thesis deal with the synthesis of gadolinium(III) complexes based on two macrocyclic ligands which have incorporated targeting moieties for GLP-1R and GPR-40. These complexes, which are designed for use as MRI contrast agents, aim to harness the stability and inertness provided by macrocyclic ligands, in addition to maximising delivery of the probes to the biological target of interest and therefore minimising toxicity concerns.

1.2.2.2. Critical Factors in MRI Contrast Agent Design

As discussed above, the contrast enhancement in an MRI scan using a contrast agent is achieved through the enhancement of the relaxation rate of local water molecules. The ability of a compound to increase this relaxation rate, and therefore generate better contrast, is its relaxivity, with greater values associated with more effective contrast agents[102,103,114,131]. The discussion in this section will focus on factors involved in the design of GBCAs, which are the focus of this thesis.

There are a number of factors which determine the relaxivity of a compound, and these are shown in **Equation 1.2**[132]. The optimisation of each of these factors is critical in the successful design of MRI probes, and has been the subject of much discussion in the literature[96,101,103,107,133,134].

$$\textbf{\textit{Equation}}\ \mathbf{1.2}\text{:}\ r_1 = \left(\frac{cq}{55.6}\right)\left(\frac{1}{T_{1m} + \tau_m}\right)$$

In the above equation, r_1 is the longitudinal relaxivity of the compound, c is its concentration, q is the hydration state (the number of inner sphere water molecules, those which are directly bonded to a metal centre), T_{1m} is the longitudinal relaxation time and τ_m is the water exchange lifetimes (the amount of time that the water molecule spends coordinated to the metal centre)[96,103]. Of these factors, the synthetic chemist is able to influence relaxivity through careful manipulation of q and τ_m and attempts to do so are discussed further below.

Hydration state can typically be increased by a reduction in ligand denticity. Gadolinium(III) is known to favour 9 coordinate structures in solution[107]. All currently clinically approved GBCAs are based on octadentate polyaminocarboxylate ligands such as H_4dota[103]. Logically, reducing the number of donor atoms in a ligand designed for use in a GBCA will open up coordination sites at the metal centre which

can then be occupied by water molecules, therefore increasing *q* and relaxivity of the contrast agent. Unfortunately, this often results in a reduction in both thermodynamic stability and kinetic inertness of the complex, presenting challenges for their use *in vivo* in light of the toxicity concerns around NSF[103].

Several different strategies have been employed throughout the literature in order to counter this negative impact on complex stability encountered with reduced ligand denticity. Lanthanide(III) complexes of macrocyclic ligands based on H_4dota are known to exist as four different stereoisomers, as shown above (**Figure 1.5**). Demetallation is possible during the interconversion between these different enantiomers, which occurs *via* two mechanisms: rotation of the acetate binding arms and inversion of the macrocyclic ring[114–116,135,136]. The introduction of chirality to the backbone of the macrocycle and to the acetate arms of the ligand has been shown to reduce the fluxionality of the resultant lanthanide(III) complexes and therefore compensate for the reduction in stability associated with reduced ligand denticity[103]. An innovative example of this approach was shown by Messeri *et al*., who stereoselectively introduced a butanoic acid chain at the α position of the acetate arm[137]. The gadolinium complex of this ligand, shown in **Figure 1.6**, had a hydration state of 2 and a high relaxivity value of 12.3 $mM^{-1}s^{-1}$, approximately 3.6 times higher than that of $[Gd(dota)]^-$ (r_1 = 3.4 $mM^{-1}s^{-1}$ at 0.47 T)[138,139].

Increasing the basicity of the ligand has also been shown to reduce fluxionality between different isomers of the macrocycle, and it has been shown that there is a linear relationship between ligand basicity and thermodynamic stability of the Gd(III) complex[103,140]. Maximising ligand basicity can be achieved through the inclusion of oxygen donors, which also helps to exploit the oxophilicity of Ln(III) ions[102,141]. This strategy has been put to use to maximise hydration state in acyclic ligands, such as the hydroxypyrodinate (HOPO) family which has been developed (**Figure 1.6**)[141].

Furthermore, restriction of ligand rotation has been shown to enhance the kinetic inertness of the Gd(III) complexes. Rotation results in an interruption of the donor atom-Gd interaction and can therefore result in demetallation. Introduction of rigid structures such as cyclohexyl rings, or even non-coordinating macrocycles, has been shown to enable complexes with *q* values as high as 3 to be synthesised[103]. A selection of these ligands, and the hydration states of their corresponding gadolinium(III) complexes, are shown in **Figure 1.6**.

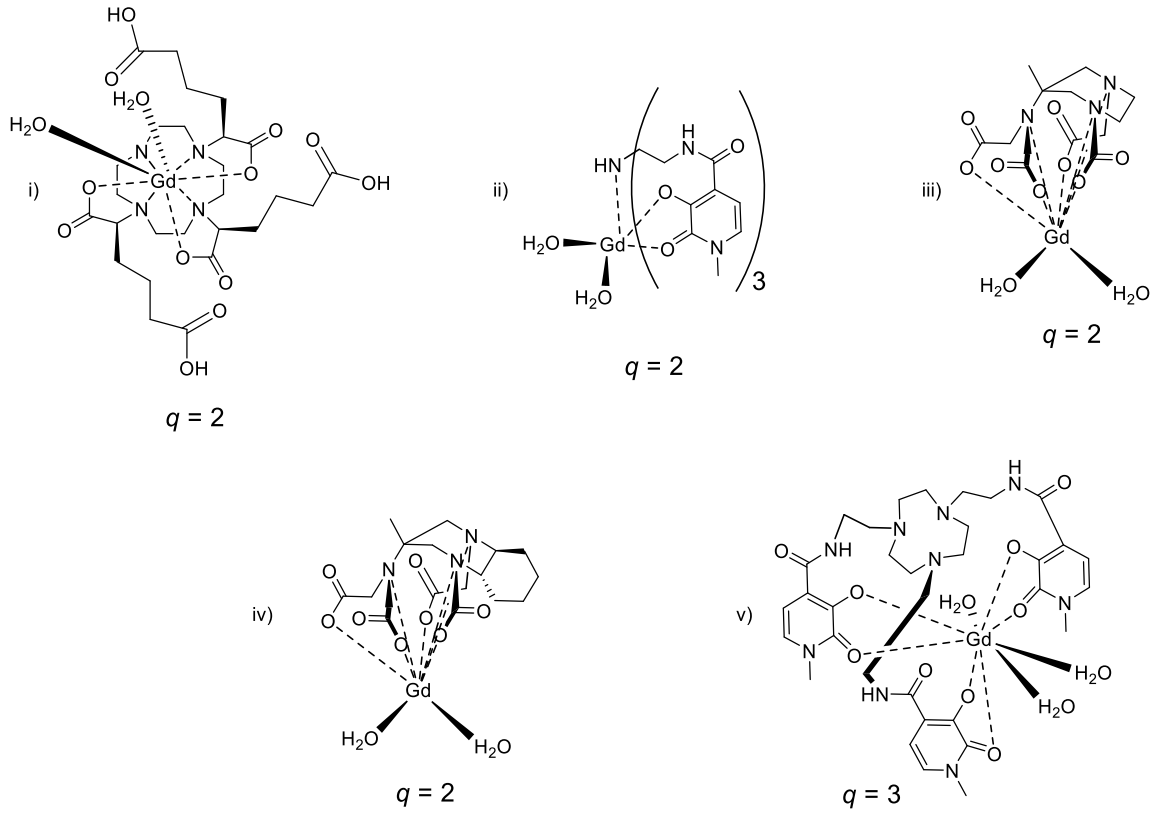


Figure 1.6: A selection of ligands designed to form Gd(III) complexes with elevated hydration states and the hydration state of these: i) H_6*R,R,R*da-do3a[137], ii) H_3-tren-Me-3,2-hopo[141], iii) H_4aazta[142], iv) H_4cyaazta[143] and v) H_3-tacn-3,2-hopo[144].

Due to the lanthanide contraction, the size of lanthanide(III) ions decreases from left to right across the 4f period, resulting in a decrease in the preferred coordination number for each ion[102]. Gadolinium is near to the centre of this period, resulting in a relatively small barrier to conversion between 8- and 9-coordinate complexes in solution and opening up the possibility for rapid water molecule exchange in MRI contrast agents[102]. Enhancing the rate of water exchange would correspond to a reduction in water residence lifetime, τ_m, and therefore increase the relaxivity of the contrast agent. One method which has been employed to increase water exchange rate is to increase steric crowding around the metal centre and prejudice the system towards releasing inner-sphere water molecules *via* dissociative exchange[102]. This tactic has been employed with some derivatives of H_5dtpa and H_4dota, which are shown below in **Figure 1.7**, although this results in a decrease in thermodynamic stability of the resultant Gd(III) complexes[102].

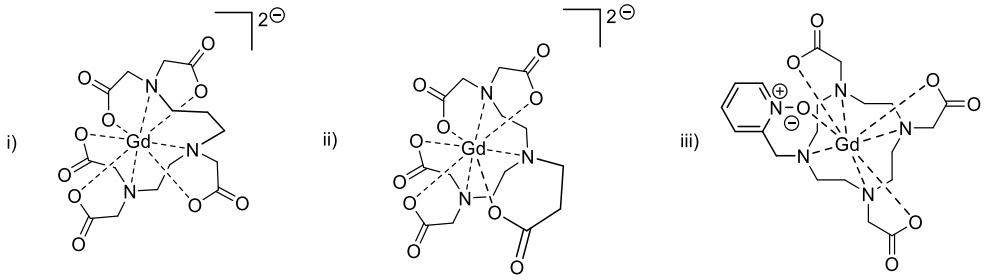


Figure 1.7: Ligands designed to form sterically crowded Gd(III) complexes with decreased τ_m values: i) H_5eptpa[145], ii) H_5dtta-Nprop[145] and iii) H_3do3a-pyNox[146].

One of the mechanisms involved in paramagnetic relaxation is dipole-dipole coupling between the paramagnetic metal ion and the proton of any coordinated inner-sphere water molecules[147]. This contribution to T_1 relaxation may be described by **Equation 1.3**, in which T_1^{DD} is the dipolar contribution to longitudinal relaxation[147].

$$\textbf{\textit{Equation}}\ \textbf{1.3}\text{: } \frac{1}{T_1^{DD}} = \frac{2}{15}\left(\frac{\mu_0}{4\pi}\right)\left(\frac{{\gamma_H}^2 {g_e}^2 {\mu_B}^2 S(S+1)}{{r_{MH}}^6}\right)\left(\frac{3\tau_c}{1+\ {\omega_H}^2{\tau_c}^2}\right)$$

In this equation, μ_0 is the magnetic permeability of free space (4π x 10^{-7} NA^{-2}), γ_H is the proton gyromagnetic ratio (2.675 x 10^8 rad $s^{-1}T^{-1}$), g_e is the electronic g factor of the paramagnetic metal centre (2 for Gd(III)), μ_B is the Bohr magneton (9.274 x 10^{-24} JT^{-1}), S is the spin quantum number, r_{MH} is the distance between the proton and the metal centre, ω_H is the Larmor frequency of a proton and τ_c is the correlation time[147].

Correlation time has been shown to have a relationship with water residence lifetime (τ_m) and molecular rotational correlation time (τ_R), which is essentially a description of the tumbling rate of the compound, i.e. how fast it rotates in solution[148]. This relationship is shown by **Equation 1.4**[147].

$$\textbf{\textit{Equation}}\ \textbf{1.4}\text{: } \frac{1}{\tau_c} = \frac{1}{\tau_R} + \frac{1}{\tau_m}$$

Molecular rotational correlation time itself depends on many factors, as shown by **Equation 1.5**[149].

$$\textbf{\textit{Equation}}\ \textbf{1.5}\text{: } \tau_R = \frac{4\pi a^3 \eta}{3kT}$$

The variables above are solvent viscosity (η), temperature (T), k: the Boltzmann constant (1.381 JK^{-1}) and, critically, molecular volume, approximated by $\frac{4}{3}\pi a^3$ in which a is the radius of the molecule[149]. Molecular volume corresponds roughly to molecular weight[150]. As this is also within the control of synthetic chemists, manipulation of molecular weight to slow molecular rotation, and therefore increase relaxivity, has also been employed by those in the field who seek to develop effective MRI contrast agents[147,148,151].

Many in the field have sought to increase the molecular weight, and therefore τ_R, through conjugation to nanoparticles[152], dendrimers[153] and biological macromolecules such as polysaccharides and peptides[96,102]. Interaction between GBCAs and the peptide human serum albumin (HSA) has been used to result in drastic increases in relaxivity, as seen with the blood pool imaging agent MS-325[114]. This compound contains a large, lipophilic phenyl cyclohexyl ester which enabled peptide binding and improved *in vivo* circulation time of the probe and its relaxivity[154,155].

Zinc-sensing MRI probes, such as that reported in 2009 by Esqueda *et al*., exploit the interaction between HSA and lipophilic GBCAs[151]. The concept of zinc-sensing is discussed further below, but in principle, relies on the synthesis of a chemosensor which alters its properties in the presence of Zn^{2+} ions. Esqueda *et al*. produced a macrocyclic ligand which contained two dipicolylamine (DPA) moieties capable of binding to zinc(II) ions. When this took place, the ternary complex was then able to form a macromolecular species through coordination to HSA, resulting in a dramatic increase in relaxivity from the increased molecular weight[86,148,151].

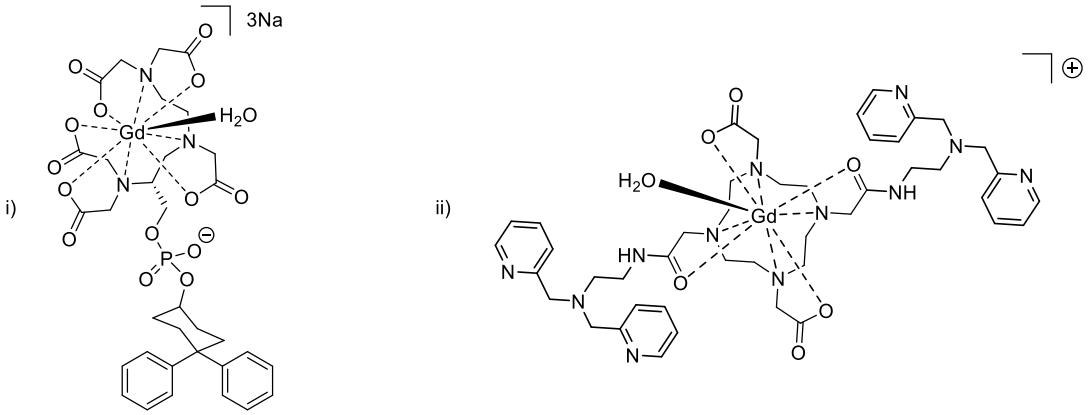


Figure 1.8: Two compounds designed to exhibit a significant relaxivity increase *via* an interaction with the peptide HSA and corresponding increase in molecular rotational correlation time: i) MS-325[155] and ii) Gd-DOTA-diBPEN[151].

It is clear that there are many factors to be considered in the development of GBCAs to be utilised as MRI contrast agents. There is often a subtle interplay between these different factors, with the pursuit of greater hydration state or water residence time frequently associated with a reduction in complex thermodynamic stability or kinetic inertness. Coordination between GBCAs and macromolecules is also often associated with a reduction in aqueous solubility, which could present problems *in vivo*[102]. Each of these factors were taken into consideration in the design and synthesis of compounds to be used as MRI contrast agents, which is discussed in chapters 2, 3 and 4 of this thesis.

1.2.3. Optical Imaging

Due to the simplicity of the techniques involved, the use of light to generate contrast was harnessed early in the field of molecular imaging – indeed, optical microscopy was invented in the mid-17th

century, with the invention of the microscope and its early usage in the study of biological organisms[156,157]. Biologists have utilised optical imaging to study cellular structure and biological processes since then, and it remains one of the dominant tools in the medical sciences today, allowing both qualitative and quantitative data to be obtained[90,156].

1.2.3.1. Principles of Luminescence

Luminescence, a term which applies to two phenomena – fluorescence and phosphorescence, may be harnessed through advanced microscopy techniques to acquire images with greater contrast and signal-to-noise ratio than simple optical microscopy, which relies on reflected or transmitted light[158]. Fluorescence, which is short-lived with a lifetime of less than 10^{-8} seconds, is a property of certain molecules which may absorb specific wavelengths of light[159]. These molecules, known as fluorophores, absorb a photon of light and emit another photon at a different, specific, characteristic wavelength[90,160]. In phosphorescence the emission is typically less intense, longer-lived and can continue after the removal of the excitation source[159]. The photophysical properties of luminescent compounds can be explained and described through consideration of their electronic states. For many organic molecules, singlet (S_n) and triplet (T_n) electronic states are typical. In the former, the spins of all electrons in the system are paired, whereas in the latter one set of electron spins remain unpaired. Different vibrational and rotational energy levels exist within these electronic states and, although these impact little on the photophysics of the system, help to fully describe luminescent systems energetically[90,159–161].

In fluorescence processes, a molecule is promoted from the ground state (S_0) to an excited singlet state (S_n) by absorption of a photon with an energy equal to or greater than the energy gap between the two levels[160]. **Equation 1.6** describes the critical relationship between this energy gap (E) and the wavelength of the absorbed photon (λ) in terms of Planck's constant ($h = 6.626 \times 10^{-34}$ Js), frequency of the photon (ν) and the speed of light ($c = 2.998 \times 10^{8}$ ms^{-1})[160].

$$\textbf{\textit{Equation}}\ \mathbf{1.6}: E = h\nu = h\frac{c}{\lambda}$$

The excitation process will typically populate the first excited singlet state (S_1), with the population of the vibrational and rotational energy levels with this state described by a Boltzmann distribution – i.e. most molecules within the system will occupy the lowest vibrational level within the S_1 state[160]. Non-radiative decay processes allow molecules at greater vibrational energy levels to relax to the lowest vibrational energy state *via* vibrational motion without the emission of a photon[90,160,161]. Internal conversion processes can also take place to populate the S_1 state from higher energy excited singlet states (S_2, S_3 etc.)[159]. The molecule then remains at this energy level for a short time period (ps to ns) before undergoing radiative decay in which a photon of light is emitted to return the system to the ground state (S_0). Fluorescence emission always occurs from the S_1 excited state[159]. The difference in wavelength between the absorbed and emitted photons is known as the Stokes shift[158,160]. Fluorescence

is short-lived due to the spin-allowed nature of the $S_1 \rightarrow S_0$ process and typically occurs in wholly organic fluorophores[156,158].

Phosphorescence is a similar process, but the radiative decay is associated with a transition between electronic states with different spin multiplicities[159]. Furthermore, phosphorescence processes have a much longer lifetime than fluorescence as the transition is spin-forbidden and phosphorescence is typically much less intense[159]. The excitation process is similar to that observed in fluorescence, with absorption of a photon enabling excitation of the molecule ($S_0 \rightarrow S_1$). However, a process known as inter-system crossing (ISC) then takes place to populate the first excited triplet state of the system ($S_1 \rightarrow T_1$). Further non-radiative decay processes may then take place within the T_1 state before radiative decay *via* emission of a photon returns the system to the ground state ($T_1 \rightarrow S_0$)[159]. Both fluorescence and phosphorescence may be described through the use of a Jablonski diagram (**Figure 1.9**)[162].

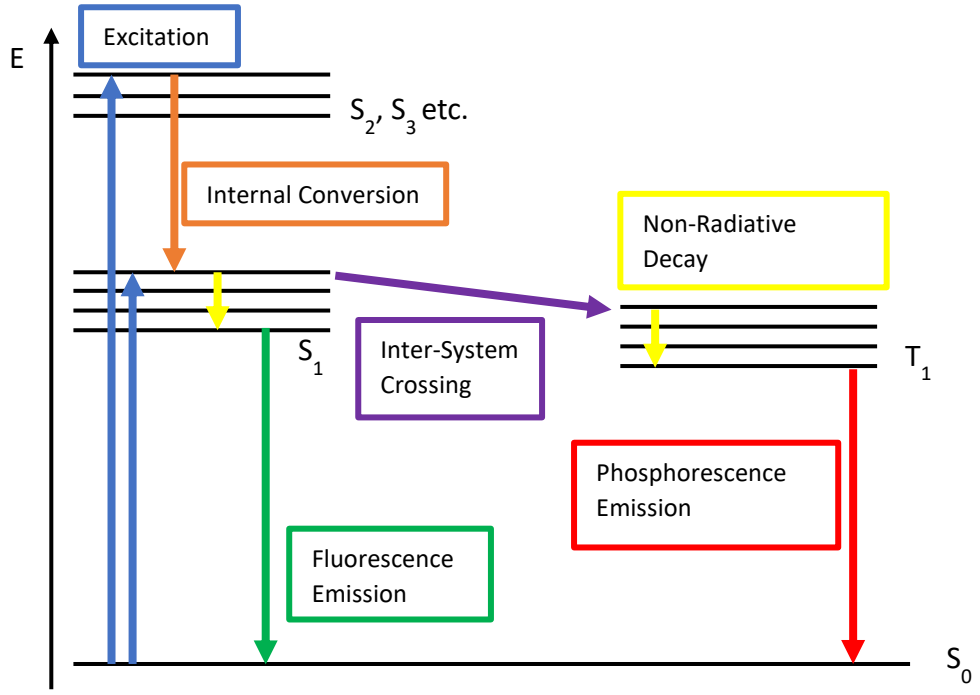


Figure 1.9: Jablonski diagram showing the processes involved in fluorescence and phosphorescence[159,162].

Radiative decay *via* these two mechanisms are harnessed in optical imaging in order to obtain information on biological systems. Fluorescence and phosphorescence may be quantified by the quantum yield of the emission – the ratio of emitted photons to absorbed photons – and the emission lifetime[90,163].

Whilst many biomolecules have luminescent properties, the majority of intracellular components do not possess useful photophysical properties for facile observation of biological systems, necessitating the use of staining agents or exogenous chromophores to be applied to cells to enable their study. Prior

to the 20th century, these agents were typically coloured dyes derived from natural sources such as saffron, carminic acid or hematoxylins (derived from cochineal beetles and wood respectively) which would stain cellular components differently according to their composition and therefore generate contrast[156,164,165]. After the development of fluorescence microscopy in 1904, the field of agents rapidly expanded – early work utilised naturally occurring fluorophores such as aromatic amino acids, although these suffered from low quantum yields and reduced photostability[156]. As such, there arose a need for alternative fluorescent imaging agents and a novel area of organic chemistry was born.

1.2.3.2. Organic Chromophores and Fluorophores

Mauveine, the earliest artificial dye, was first synthesised serendipitously in 1856 by William Henry Perkin at Imperial College London[166], and found applications as a staining agent for optical microscopy in the 1860s. Other azine compounds and the related thiazine family has been used to stain and identify cells since the 1880s[156,167–169]. Other early developments of fluorescent dye compounds included the xanthene family, of which fluorescein was the first isolated in 1871. Since then, the field has expanded rapidly, generating an enormous range of compounds (**Figure 1.10**). Perhaps the largest family of these dyes is the polymethines, which consist of an electron donor and an electron acceptor separated by a conjugated spacer such as an unsaturated carbon chain[156]. This family includes triarylmethines, styryls and cyanines, amongst others.

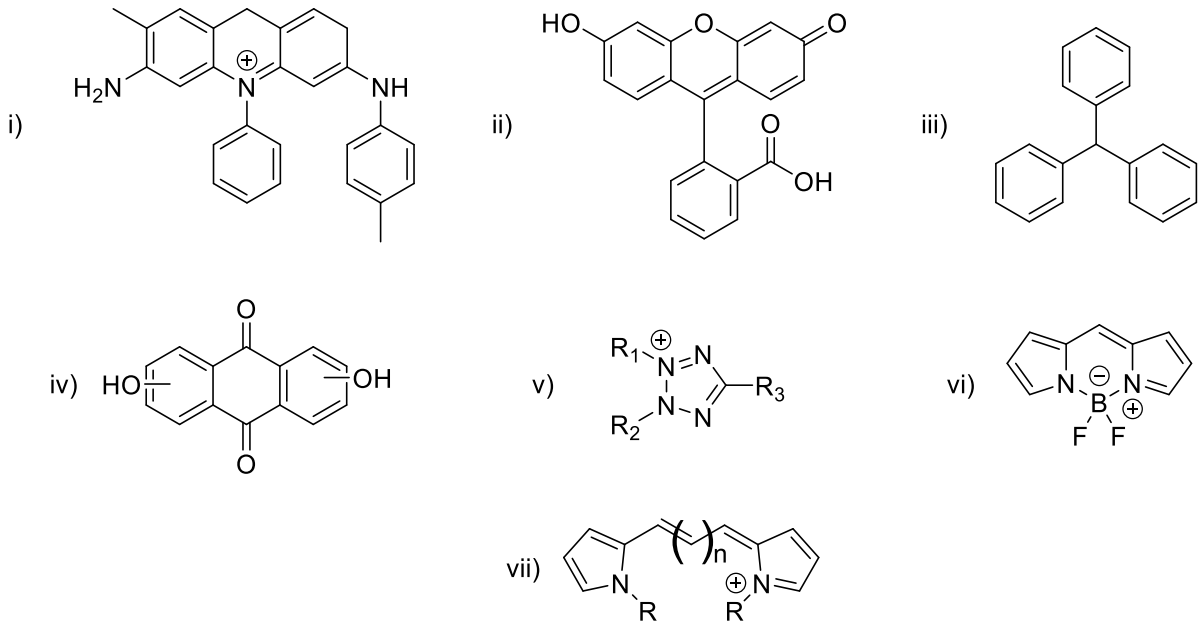


Figure 1.10: Structures of various fluorescent compounds i) Mauveine, ii) Fluorescein, iii) a triarylmethane, iv) dihydroxyanthraquinone general structure, v) tetrazolium general structure, vi) BODIPY core structure, vii) closed cyanine general core structure.

These fluorescent compounds have been widely utilised, and the field has developed to try to garner as much information as possible from optical imaging. This has included the conjugation of biomolecules

and synthetic fluorophores, either covalently or non-associatively, which allows the chemical nature of fluorescent probes to direct their cellular localisation. In addition, some have been developed into chemosensors which exhibit a change in photophysical properties such as fluorescence intensity or wavelength indicating a recognition event. This could include ion sensing or enable the probing of enzymatic activity[156]. Cyanine (Cy) dyes are a classic example of this, with Cy3 and Cy5 having been used as tagging agents for nucleic acids, peptides and a whole host of other biomolecules[156].

Many of the compounds above fluoresce in the visible region. There are several problems associated with this, most notably that biomolecules will often autofluoresce in the same region, which can result in increased background noise and detract from the useful information being acquired. As such, the field is moving towards organic fluorescent compounds which emit in the near-infrared region (λ_{em} = 700 – 1000 nm)[87,170]. Chapter 5 of this thesis focuses on some near-infrared emitting cyanine dyes and attempts to produce multi-modal imaging agents capable of quantifying Zn^{2+} levels in the pancreas.

1.2.3.3. Lanthanides for Optical Imaging

As discussed above, there are some issues with the use of organic fluorophores as optical imaging agents. Often, this is a difficulty in differentiating between the signal and background noise from luminescent biological materials due to similar emission lifetimes or wavelengths[158]. Photobleaching is an additional concern associated with the use of organic compounds – the excited states of organic fluorophores can often react *in vivo* with oxygen or reactive oxygen species to produce non-emissive compounds and reduce overall signal intensity[158]. Luminescent metal ions are less prone to photobleaching due to different structures of their excited states, and typically exhibit longer luminescence lifetimes than their organic counterparts, and therefore offer an ideal alternative to help bypass these problems.

Although some imaging capabilities are possible with the d-block metals, notably rhenium and ruthenium, the majority of the trivalent lanthanides ([Xe]$4f^n$, n = 0 - 14) are luminescent and more inert than their transition metal counterparts. Due to the core nature of the 4f orbitals, the lanthanides typically adopt similar coordination chemistry and geometry across the series, with much weaker ligand field effects observed when compared to the transition metals[158]. Luminescence of the Ln^{3+} ions results from 4f → 4f transitions, which are parity forbidden and therefore exhibit large Stokes shifts and lifetimes on the micro- to milli-second scale[158]. The emission spectra recorded from these ions are also characteristic of the metal centre involved, allowing it to be readily distinguished from any background autofluorescence[158]. This field is still in its infancy compared to the use of organic optical imaging agents, with some of the earliest examples of optical imaging with Ln^{3+} complexes published in the late 1990s[158,171].

Due to the forbidden nature of the 4f → 4f transitions responsible for lanthanide(III) luminescence, the associated molar absorptivities for these emissions are very low for direct excitation of the metal ion. In order to avoid this, a sensitising chromophore, also referred to as an antenna, is required[158]. The antenna structure, which may be covalently attached to the Ln^{3+} chelator, absorbs light in order to become excited before transferring this energy to the 4f excited state, which then undergoes non-radiative decay and emission, resulting in characteristic, long-lived luminescence[158]. This antenna group must effectively absorb light but must also have a triplet state of a suitable energy in order to sensitise the lanthanide(III) centre and not simply exhibit short-lived fluorescence[158]. The triplet state should typically be >2000 cm^{-1} higher in energy than the lanthanide ion acceptor state – this thesis focuses on complexes of Eu(III) and Tb(III), which have acceptor states of $^5D_0$ (E ~ 17200 cm^{-1}) and $^5D_4$ (E ~ 20400 cm^{-1}) respectively[158]. Generally, these antenna absorb in the region of 350 – 410 nm and are polyaromatic or heterocyclic[158].

The vibrational oscillation of O-H, N-H and C-H bonds can enable non-radiative decay of excited states. This can result in reduction of quantum yields of many Ln(III) complexes[158]. This can be counteracted through increasing denticity, hydrophobicity and rigidity of the ligand encapsulating the metal centre, which inhibits the approach of water and other solvent molecules and therefore can enhance emission intensity. Accordingly, many of the existing lanthanide-based imaging agents are based on highly thermodynamically stable and kinetically inert macrocyclic ligands, including some shown below (**Figure 1.11**)[158].

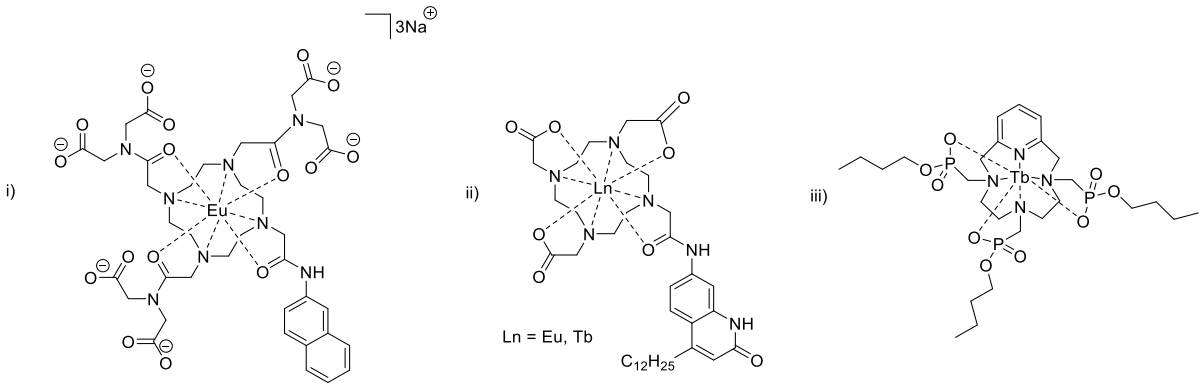


Figure 1.11: Examples of complexes of macrocyclic ligands with the lanthanide ions Eu^{3+} and Tb^{3+}, synthesised by i) Bornhop *et al*., ii) McMahon *et al*. and iii) Lee *et al*.[171–173].

1.2.4. PET Imaging

Positron emission tomography (PET) is a nuclear imaging technique which is highly regarded in the imaging field for its extremely high sensitivity. PET has been utilised to analyse and monitor physiological processes *in vivo* and, in addition to its enhanced sensitivity over techniques such as MRI, there is no need for an external excitation source which can enable more facile imaging in a clinical setting, although there are concerns about the limited spatial resolution of the technique due to the short

distance travelled by positrons prior to annihilation, which is discussed below[90,174–177]. In addition, there are many readily available radioactive isotopes with a range of half-lives which may be utilised to monitor changes in metabolic or physiological processes at the cellular level, which can often be the early stages of disease development[90].

PET imaging relies on the use of radioactive imaging agents. These agents incorporate radionuclides which decay with the emission of a positron, the antimatter component of an electron. These positrons will travel a short distance through a tissue, typically less than 2 mm, until it encounters an electron and undergoes an annihilation process which results in the emission of two γ-rays at 180° to one another, which are then detected externally and used to generate a three dimensional image of the sample[90].

Currently, the isotope ^{18}F dominates in the clinic, primarily due to its 110 minute half-life, which is long enough to allow for radiochemical syntheses and imaging agent distribution, but short enough to avoid excessive radiation dose delivery to the patient in the form[90,178]. This half-life is far more useful in the clinic than other organic radioisotopes such as ^{15}O, ^{13}N and ^{11}C, which exhibit half-lives of 2, 10 and 20 minutes respectively[90,179]. The decay of ^{18}F is shown in **Equation 1.7**.

$$\textbf{\textit{Equation}}\ \mathbf{1.7}\text{: } {}^{18}_{9}F \rightarrow {}^{18}_{8}O + {}^{0}_{+1}\beta$$

When considering the uptake of a radiotracer into cells, there are additional advantages to the use of ^{18}F. Chief amongst these is that the C-F bond acts as a bioisotere for C-H and C-OH moieties and that the latter can be replaced with the former with minimal changes to a compound's *in vivo* behaviour[178]. Many successful PET radiopharmaceuticals are based on this principle, and three examples, including the widely used [^{18}F]-fluorodeoxyglucose (18-FDG) are shown in **Figure 1.12**.

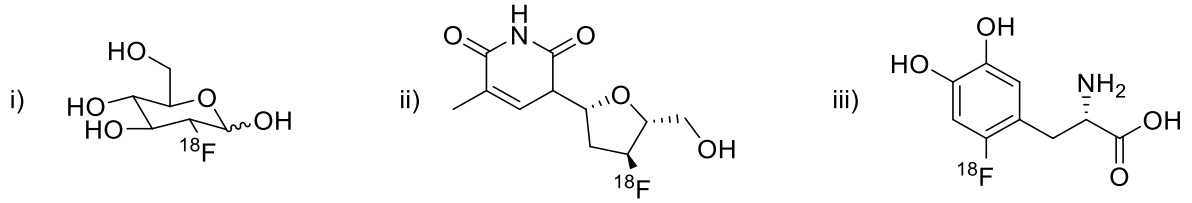


Figure 1.12: Widely used PET imaging agents incorporating ^{18}F: i) 18-FDG, ii) 3'-[^{18}F]fluoro-3'-deoxythymidine and iii) 6-[^{18}F]fluoro-L-DOPA[178].

Radioactive fluorine may be conveniently introduced into organic molecules through nucleophilic substitution reactions, typically displacing sulphonate, triflate, mesylate or tosylate groups[178]. The use of chelating units for radiolabelled AlF_3 units is also an attractive area of the field[180].

The use of organic elements in PET radiotracers is extremely widespread. However, there is an increasing interest in radiometals, which can be readily introduced into a chelate without potentially difficult organic bond formation[181]. Furthermore, many metallic positron emitters exhibit much longer half-lives than their organic counterparts, lending themselves to antibody conjugation and potentially

allowing patient imaging over a longer time period, which could enable more information to be acquired following administration of a single radiotracer[181]. Two radioisotopes of interest are ^{64}Cu and ^{89}Zr, which have half-lives of 12.7 and 78.5 hours respectively[181]. Both of these metals emit low-energy positrons, allowing high resolution images to be obtained.

Chapter 5 discusses some attempts to introduce ^{18}F to a family of zinc-sensing cyanine dyes to enable PET imaging, as well as steps towards the chelation of zirconium and copper by these compounds.

1.2.5. Dual-Modal Imaging

Although each of the imaging techniques discussed above are powerful and have been successfully used in the clinic for decades, they are not without their drawbacks. Optical imaging is known to suffer from poor tissue penetration, rendering sub-surface imaging challenging[170,182–184].

MRI is renowned for its low sensitivity, requiring contrast agents to be administered in large quantities compared to other imaging modalities and presenting a particular challenge when trying to distinguish targets which are present at low levels in the body[18,95,96,183,184]. Furthermore, PET is associated with a high cost and synthetic difficulties in probe synthesis with short time frames required, as well as low spatial resolution and concerns over radiation dose to the pateint[32,183–185].

The development of imaging agents which are capable of multi-modality has been widely explored in the literature[183,184,186]. These compounds and materials seek to harness the benefits of specific imaging techniques and overcoming their limitations by synthesising individual probes with the structure or properties to allow different imaging types to be exploited. This is favourable to simply administering two different agents which may have different biodistribution profiles and could result in toxicity or data fusion issues[186]. Other benefits include potential development of theranostic agents, cross-validation of probe accumulation, treatment response and an overall improved understanding of the subcellular processes which are the initial steps in disease development[183,184,186].

In the design of multi-modal imaging agents, due consideration must be made to the imaging techniques which the probe will be capable of. Ideally, these modalities will either have some complementary properties – i.e. nuclear imaging techniques such as PET and SPECT share a high sensitivity with optical imaging and so the concentration of probe could remain constant no matter which detection technique was employed[186] – or one will compensate for the shortcomings of another and *vice versa* – consider the low sensitivity of MRI being made up for the sensitivity of optical probes which themselves suffer from poor depth penetration[183,184]. The components of an imaging probe or contrast agent must also be chemically compatible and synthetically accessible. **Table 1.1** shows the properties, common imaging probes, advantages and disadvantages of imaging techniques which dominate in the clinic.

Modality	Spatial Resolution	Depth Penetration	Probes	Advantages	Disadvantages
Optical	1-3 mm	mm	Organic dyes, QDs, Ln(III) complexes	High sensitivity, avoidance of ionising radiation	Poor penetration
MRI	10 – 100 μM	No limit	Gd(III) and Mn(II) complexes, iron oxide nanoparticles	High resolution, avoidance of ionising radiation, information on physiological and anatomical processes	Low sensitivity, high cost
CT	50 - 200 mm	No limit	Iodine, Ln(III) and Au compounds	High resolution	Exposure to ionising radiation, high cost
SPECT/PET	0.5 – 2 mm	No limit	Radioactive isotopes: ^{18}F, ^{11}C, ^{64}Cu etc.	Quantitative, information on metabolic processes	Exposure to ionising radiation, low resolution
Ultrasound	50 – 500 mm	mm - cm	Microbubbles	Low cost, safe and fast	Low resolution

Table 1.1: A summary of the properties and contrast agents employed in a variety of imaging techniques[184].

1.2.5.1. Dual-Modal MRI-Optical Contrast Agents

Later in this thesis, notably in chapter 5, the synthesis of some optical-PET and optical-MRI imaging agents is discussed. The Long group has successfully developed several dual-modal optical-MRI probes, one of which, reported by Stasiuk *et al.* in 2015, was shown to favourably accumulate in pancreatic β-cells and shown to act as a zinc chemosensor[18]. Another, synthesised by Rivas *et al*. in 2013, exhibited pH sensing ability *via* the rhodamine group appended to the macrocyclic chelator[95].

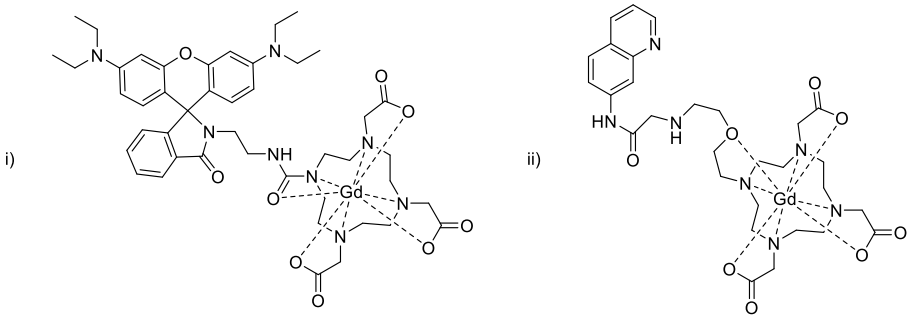


Figure 1.13: Two dual-modal optical-MRI probes synthesised by i) Rivas *et al.*[95] and ii) Stasiuk *et al.*[18].

MR-optical agents are often based on H_4dota and its related macrocycles to avoid the toxicity issues associated with the release of the highly paramagnetic Gd^{3+} ion *in vivo*. These chelates can be covalently attached to organic dyes or other luminescent moieties to introduce the capability for optical imaging to these paramagnetic complexes. **Figure 1.14** shows further examples of these from elsewhere in the literature.

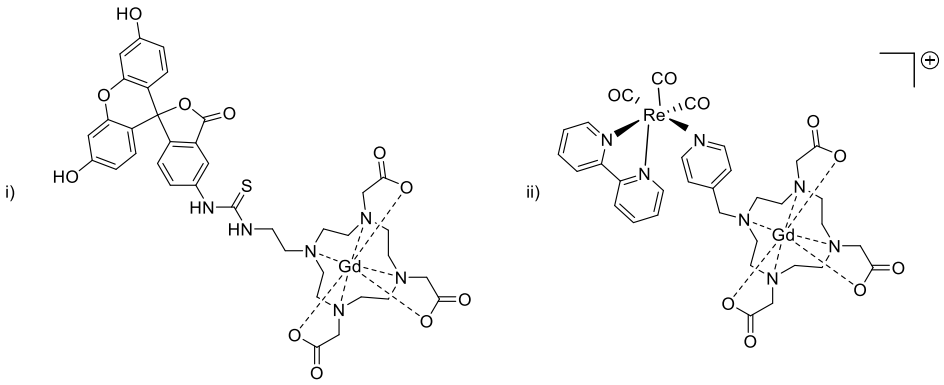


Figure 1.14: Additional optical-MRI probes synthesised by i) Mishra *et al*[187]. and ii) Koullourou *et al.*[188].

Extensive work has been focussed on the development of optical-MR probes based on nanoparticles and quantum dots (QDs), each of which have a large surface area available for functionalisation. Many of these are based on superparamagnetic iron oxide nanoparticles (SPIONs) which provide T_2 contrast enhancement and therefore negative contrast in images, leading to potential issues in image analysis in the clinic[183,184].

One particularly innovative approach to the application of dual-modal MRI probes is the administration of complexes of Gd^{3+} and another lanthanide(III) ion with the same ligand. The ratio of metals may be tuned to make up for the low sensitivity of MRI. This has been successfully employed by Laurent *et al.* and Malikidogo *et al.* to enable dual-modal imaging with Gd^{3+}/Eu^{3+} and $Gd^{3+}/^{165}Er^{3+}$ complexes of pyridine-polyaminocarboxylate ligands for MR-optical and MR-SPECT imaging respectively[183,189,190]. Malikidogo's compound was also capable of zinc-sensing, exhibiting a change in relaxivity in the presence of Zn^{2+}. These two compounds are shown in **Figure 1.15.**

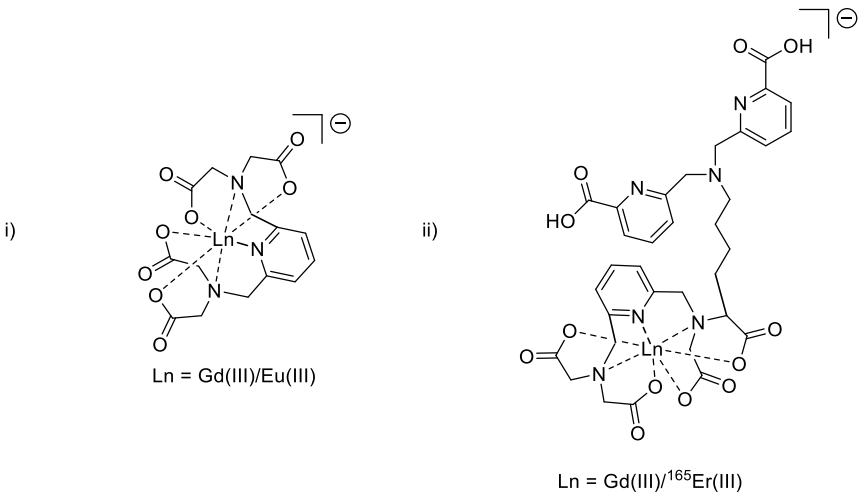


Figure 1.15: The ligands utilised to administer dual-modal "cocktails" by i) Laurent *et al.*[190] and ii) Malikidogo *et al.*[189].

1.2.5.2. Dual-Modal Optical-Nuclear Imaging Agents

The combination of optical and nuclear imaging agents is routinely employed in the diagnosis and management of disease[183,186,191]. Both modalities are extremely sensitive, and the excellent depth penetration of PET can make up for the poor tissue penetration of fluorescence imaging. Optical images can also be used to cross-validate nuclear images and also to trace dual modal probes after their radioactivity has declined[183,186]. Most of the work in this area has focussed on the use of radiometal chelates which are conjugated to organic dyes in an analogous fashion to the MR-optical agents discussed above[183]. However, there is great potential in the use of organic radionuclides such as ^{11}C and ^{18}F which can be used to radiolabel organic compounds without affecting their biodistribution[183].

Due to the increased penetration of photons in the near-infrared (NIR) window, cyanine dyes have begun to be incorporated into dual-modal optical-nuclear imaging agents[183]. One notable example incorporating the cyanine dye indocyanine green and a chelator for ^{111}In, utilised in SPECT imaging, was developed by Xu *et al*. in 2007 and is also capable of bioconjugation to enhance its distribution *in vivo*[191]. Although designed as an optical/SPECT compound, this chelator could also be used to bind to ^{86}Y to form a PET-optical dual modal probe.

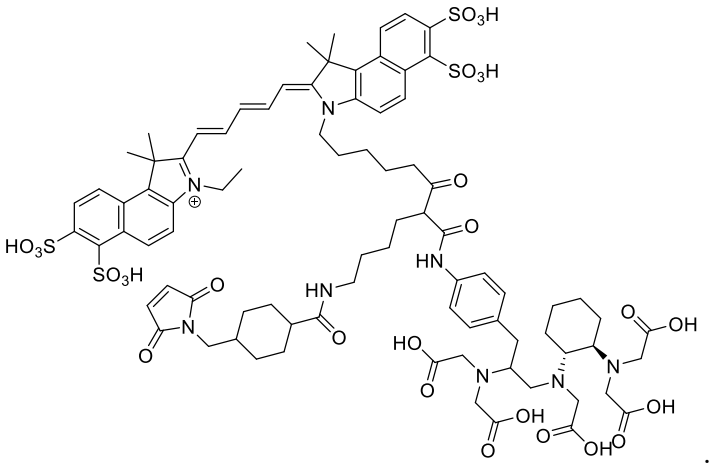


Figure 1.16: The ligand, based on indocyanine green, synthesised by Xu *et al*.[191].

Chapter 5 discusses the synthesis of a range of cyanine dye compounds and steps towards their functionalisation as dual-modal fluorescence-PET imaging agents.

1.2.6. Towards Next-Generation Imaging Agents

As collective understanding of dual-modal imaging agents develops, attention in the field has begun to turn towards more advanced probes. It is hotly anticipated that theranostics will be a growing area in future, where a single probe can be adapted to enable diagnosis and treatment of a disease condition at a cellular level[183]. Furthermore, the design and synthesis of probes which are sensitive to their environment, such as ion concentration, is of increasing interest as a means to probe the physiological processes which occur prior to disease development. An example of an ion-sensing dual modal optical-MRI probe was reported by Jang *et al*. in 2013 and is shown in **Figure 1.17**. Chapter 5 also discusses the concept of ion-sensing and responsive dual modal probes.

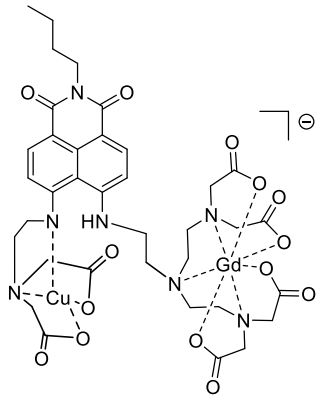


Figure 1.18: The smart dual modal probe synthesised by Jang *et al*.[192].

1.2.6.1. Zinc-Sensing MRI Contrast Agents

As discussed above, zinc(II) is especially abundant within pancreatic β-cells, and its release could be monitored as a means of β-cell quantification. For many years, the low sensitivity of MRI was considered a major obstacle to the detection of physiological levels of zinc(II)[18,193]. However, many in

the field have sought to explore the concept of Zn^{2+} sensing through the use of optimisation of factors contributing to contrast agent relaxivity. The earliest example of this strategy was published by Hanaoka *et al*. in 2002, who synthesised a family of bis-amide derivatives of H_5dtpa incorporating the zinc-binding unit DPA (**Figure 1.18**)[194].

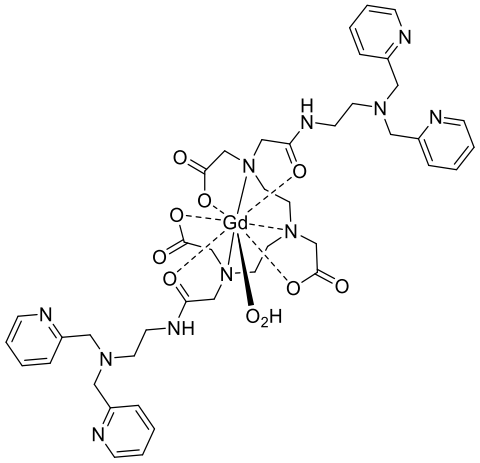


Figure 1.18: One of the first published zinc-sensing MRI contrast agents[194].

An understanding of one of the mechanisms critical to an increase in relaxivity was first reported by Major *et al*[195,196]. Major's probes were based on a macrocyclic framework but incorporated two additional acetate arms. In the absence of Zn^{2+}, these arms were coordinated to the gadolinium(III) metal centre, saturating the ion's coordination sphere and preventing coordination of any water molecules[195,196]. The relaxivity of this probe in the absence of Zn^{2+} was 2.3 $mM^{-1}s^{-1}$, corresponding to a hydration state of 0[195]. In the presence of zinc(II) ions, the two acetate arms not directly bonded to the macrocycle move from the Gd^{3+} ion to the Zn^{2+}, opening up additional coordination sites on the gadolinium(III) centre and allowing inner sphere water molecules to approach[195,196]. The authors reported that the relaxivity of the probe increased to 5.1 $mM^{-1}s^{-1}$ during zinc binding, which suggested a *q* value of 1 and implied that this mechanism was taking place[195].

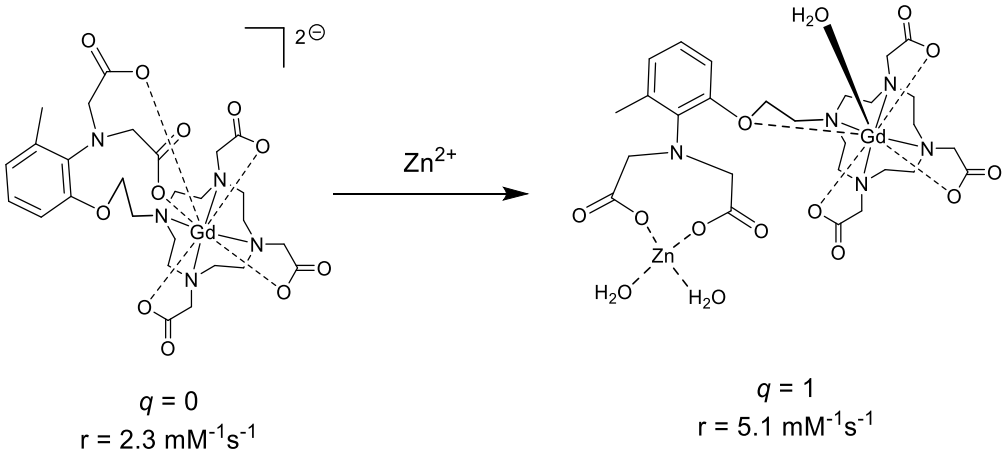


Figure 1.19: The compound synthesised by Major *et al*. and its increase in hydration state in the presence of Zn^{2+} [195].

This technique has been utilised previously in the Long group to produce zinc-sensing MRI contrast agents, such as that reported by Stasiuk *et al*. (see above, **section 1.2.5.1**)[18]. In addition to this compound's dual-modal capabilities, zinc binding through its aminoaquinoline moiety resulted in an increase in *q* from 1 to 2 and a corresponding enhancement in relaxivity[18]. Stasiuk's probe was also shown to be capable of pancreas-specific contrast enhancement, with an increased retention in the organ compared to that of $[Gd(dota)]^-$. This could be due to some degree of targeting conferred on the probe by its zinc-binding: Zn^{2+} is found in large quantities in the pancreas compared to other organs. Indeed, it may be possible to use the change in relaxivity of zinc binding MRI contrast agents to assess pancreatic function – the role of zinc(II) in insulin storage is well-known and extensively discussed above (section **1.1.4**). The co-release of Zn^{2+} alongside insulin results in a ten-fold increase in serum concentration of zinc(II) ions, and presents an opportunity for the exploration of β-cell function[148,193].

The examples of zinc-sensing MRI contrast agents mentioned above utilise an increase in hydration state to trigger relaxivity enhancement. A different approach, based on coordination to HSA and a subsequent slowing of molecular rotation and increase in τ_R and therefore relaxivity, was first reported by Esqueda *et al*.[151]. This probe, shown above in **section 1.2.2.2**, exhibited a low affinity for the peptide HSA in the absence of Zn^{2+}, but could form a ternary complex after ion coordination[151,193]. This group have extensively studied this probe's interaction with HSA and used it to image glucose-stimuated insulin secretion *in vivo*[86,148,151,193]. A recent publication in 2018 by Martins *et al*. synthesised a compound with a lower affinity for Zn^{2+} than that reported by Esqueda, with this reduction in affinity achieved from the introduction of an additional methylene unit in the zinc-sensing DPA arm and resulting in a better signal-to-noise ratio in the images obtained *in vivo*[86]. This concept is explored further in chapter 2 of this thesis.

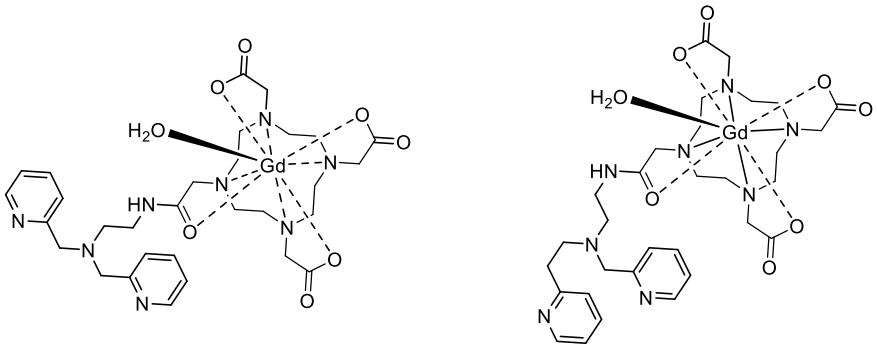


Figure 1.20: The two compounds produced by Martins *et al*., with the compound on the right exhibiting a reduced affinity for Zn^{2+} but an improved signal to noise ratio *in vivo*[86].

Zinc-sensing MRI contrast agents present a powerful opportunity to explore the functionality of pancreatic β-cells. Although the first example of assessment of β-cell function utilised a manganese(II) species and many other high-spin manganese-based zinc-binding contrast agents exist in the literature, it was decided to pursue zinc sensing through GBCAs[148,193,197]. This was for a number of reasons, primarily the greater magnetic moment of Gd(III) compared to Mn(II) (although there is increasing interest in the latter in contrast agents[198]), the wide application of GBCAs in the clinic and the well-established coordination chemistry of Gd^{3+}, which can be readily translated to other lanthanide(III) centres with imaging applications. Furthermore, it was hoped that the work described in this thesis could build on previous successes in the Long group, which dealt with zinc-binding in GBCAs.

1.2.6.2. Zinc-Sensing Fluorescence Imaging Agents

The electronic configuration of Zn^{2+} is d^{10} and prefers tetrahedral coordination geometry[199,200]. This renders the ion spectroscopically silent – many of the techniques used to examine other metal ions such as UV-visible light spectroscopy and electron paramagnetic resonance cannot be used in its detection[201]. Techniques such as X-ray photoelectron and fluorescence spectroscopy are used in zinc(II) detection[201,202]. Fluorescence spectroscopy lends itself to this detection due to its high sensitivity, on-off switchability, ease of use and accuracy[202–204]. A fluorescent chemosensor is a compound which is capable of transferring environmental information, such as the presence of an analyte or pH changes, into a change in its photophysical properties – for example, a change in emission intensity or a shift in emission wavelength[200,202,205]. This change could be binary – i.e. an on-off sensor which can act as a molecular switch indicating the presence of an ion or a pH value below a certain value – or it could be ratiometric and proportional to the concentration of the analyte of interest[204]. Structurally, these chemosensors consist of a fluorophore which is linked to a receptor for the analyte of interest[205].

1.2.6.3. Mechanisms of Zinc-Sensing in Fluorescence

Molecular probes intended to sense Zn^{2+} ions are typically designed to harness two specific fluorescence processes. These are internal charge transfer (ICT) and photoinduced electron transfer (PeT)[200,202,204–206]. In the presence of zinc(II), a probe designed to signal a recognition event *via* ICT will undergo a

spectroscopic band shift, i.e. a change in its absorption and emission wavelengths, and compounds designed to make use of PeT will signal the presence of Zn^{2+} through an emission intensity increase[206]. The desired photophysical behaviour in the event of zinc binding directs probe design and synthesis according to which mechanism is required.

ICT chemosensors consist of a fluorophore which is covalently bonded to a receptor without the inclusion of any spacer group. This forms an extended, conjugated π system with an uneven distribution of electron density – i.e. a dipole moment exists across the π system and there is an electron rich and an electron poor terminal[204–206]. Charge transfer can occur from the electron-rich region of the π system to the electron-poor region, and this process is enhanced by photon absorption[204–206]. A binding event will generate a partial positive charge at the terminal of the π system where the receptor is – this occurs due to the Lewis acidic nature of Zn^{2+}, which results in a withdrawal of electron density from the cation receptor[204]. As a result, the energy levels of the frontier molecular orbitals of the π system, which are involved in the fluorescence process, will change, resulting in a shift in both the absorption and emission wavelengths of the system, which can be ratiometric and in proportion to the concentration of the ion which is in the probe's microenvironment[200,206].

Cation sensors which harness the PeT detection mechanism have a spacer between the ion receptor site and the fluorophore. This receptor typically contains a high energy, non-bonding electron pair and, as such, nitrogen atoms are commonly seen in PeT systems[205]. In the absence of Zn^{2+}, chemosensors of this type are either non-emissive or only fluoresce weakly due to quenching of the fluorophore excited state by the receptor moiety[205]. This occurs through PeT: in a cation-free system, photon absorption triggers promotion of an electron from the highest occupied molecular orbital (HOMO) to the lowest unoccupied molecular orbital (LUMO) of the fluorophore (i.e. the ground to excited state $S_0 \rightarrow S_1$). The HOMO of the receptor moiety, which remains distinct from the conjugated system due to the inclusion of the spacer group, is of a similar energy to the unoccupied HOMO of the fluorophore and is therefore able to non-radiatively transfer an electron to the fluorophore[205,206]. This results in a quenching of the fluorescence process. After binding to Zn^{2+}, the HOMO of the receptor is lowered in energy, sitting below the energy level of the fluorophore HOMO. This prevents transfer of an electron after fluorophore excitation and therefore eliminates quenching[206]. Chemosensors which utilise the PeT process therefore signal recognition events through a dramatic increase in fluorescence intensity[200,202,204,205].

1.2.6.4. Zinc Receptor Moieties

In addition to a probe's desired photophysical response to the presence of Zn^{2+}, there are several other factors to consider in the development of cation chemosensors. From a basic chemical standpoint, due consideration must be given to the nature of the atoms in any receptor group, as this can help improve affinity of the probe for Zn^{2+}, as well as confer some degree of selectivity over other metal ions.

According to hard-soft acid base (HSAB) theory, Zn^{2+} has a borderline hard-soft Lewis acidic nature and will therefore favour coordination to borderline bases such as pyridine over hard, charged species such as oxygen[199]. Oxygen donors are often used to chelate alkali metal ions such as Na^{+} and K^{+}, which are widely found in biological systems, so HSAB theory suggests that the use of aromatic nitrogen or sulphur donors may be more appropriate and result in the development of probes with greater selectivity and stronger binding[199]. Furthermore, Zn^{2+} is a d^{10} metal ion which, unlike many transition metal ions, has no specific coordination geometry preferences determined from ligand field stabilisation energy (LFSE) – tetrahedral zinc complexes are widespread in the literature and in natural systems because of this and therefore tetradentate receptor systems may also be preferable[199,200]. Specificity is also a key factor, and interactions with other endogenous metals such as Ca^{2+} should be minimised to avoid disruption to cell signalling pathways[207].

These considerations have given rise to a plethora of different zinc-sensing moieties. There are many examples from the literature of substituted quinolines being employed as Zn^{2+} receptors, including from previously within the Long group and in the pursuit of compounds capable of dual modality. This unit and examples from Stasiuk *et al*. and Luo *et al*. are shown in **Figure 1.21**.

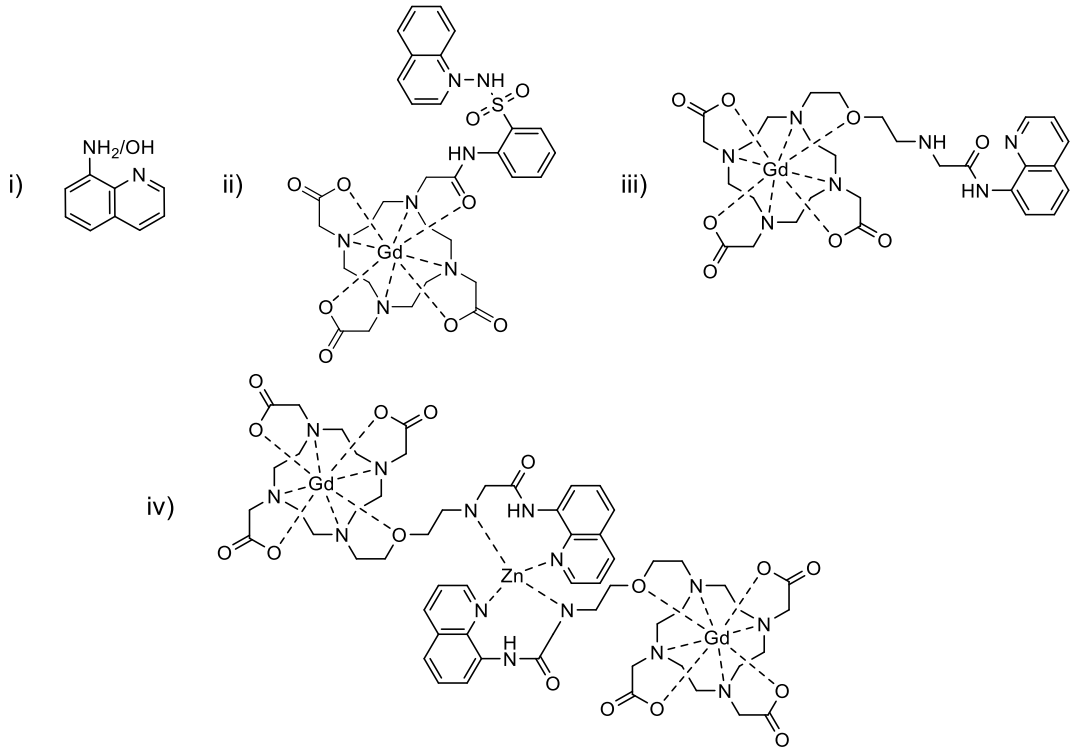


Figure 1.21: i) The substituted quinoline receptor unit commonly employed in Zn^{2+} chemosensors and the compounds synthesised by ii) Luo *et al*. and iii) Stasiuk *et al*., as well as the 2:1 complex formed by the interaction of this compound and Zn(II)[18,207,208].

Both of these compounds exhibit ratiometric Zn^{2+} sensing behaviour. In Stasiuk's, there was an increase in relaxivity of the compound up to a maximum at 0.5 equivalents of zinc(II) due to the formation of a

2:1 complex. This relaxivity increase also came alongside a ratiometric spectroscopic window shift due to the ICT mechanism[18,208]. However, both probes emit in the visible light window (380 nm – 740 nm), Luo's at 500 nm and Stasiuk's at 410 nm, which presents problems *in vivo* due to the autofluorescence of biological compounds and light scattering, as discussed above[18,208–210]. Additionally, many other probes incorporating quinoline-based sensing moieties require excitation in the ultraviolet (UV) region of the electromagnetic spectrum, which could result in cell damage[207].

Macrocyclic chelates have also been explored as zinc(II) chelators, as reported by Lim *et al*., who published a PeT-based chemosensor which exhibited a 4.4 fold-fluorescence increase in the presence of Zn^{2+}[211]. Despite its selectivity over many other endogenous metal ions, this species also emitted in the visible light region and, exhibited extremely slow binding to Zn^{2+} with a half-life of 60 minutes[202,211].

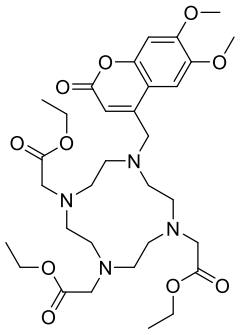


Figure 1.22: The macrocyclic zinc-sensing fluorescent chemosensor developed by Lim *et al*.[211].

As can be expected from the HSAB behaviour of zinc(II), aromatic amines dominate the field. One early option was the chelating unit *N*,*N*,*N*′,*N*′-tetrakis(2-pyridinylmethyl)-1,2-ethanediamine (TPEN), which is widely used in the field due to its strong zinc-binding ability[199,207,212]. Despite being widely thought of as highly selective, TPEN itself has a greater affinity for Cu^{2+} than Zn^{2+} (although the former is present at much lower levels in humans than the latter) and exhibits strong binding to Fe^{2+}, the most common transition metal in biological systems, which could be of concern when seeking to develop selective probes[199,213]. As such, many derivatives of TPEN has been explored as alternatives, most notably dipicolylamine (DPA), which forms an extremely strong complex with Zn^{2+} (K_d = 70 nM)[214]. Indeed, the first published compound designed to sense Zn^{2+}, Newport Green, was a fluorescein derivative which utilised DPA as a zinc receptor unit[206,215–217]. The use of DPA also extends beyond its incorporation into organic dye systems, with several examples of its chelating abilities being harnessed in lanthanide(III) species designed for time-resolved fluorescence systems[218–220]. Lanthanide(III) luminescence, discussed extensively in chapter 3 of this thesis, is longer-lived than the emission from organic fluorophores, allowing time-gated techniques to be employed and minimise interference from biological autofluorescence[219]. However, excitation of the antenna unit often requires UV light, which could result in cell damage. **Figure 1.23** shows DPA and some examples of its incorporation into fluorescent zinc chemosensors.

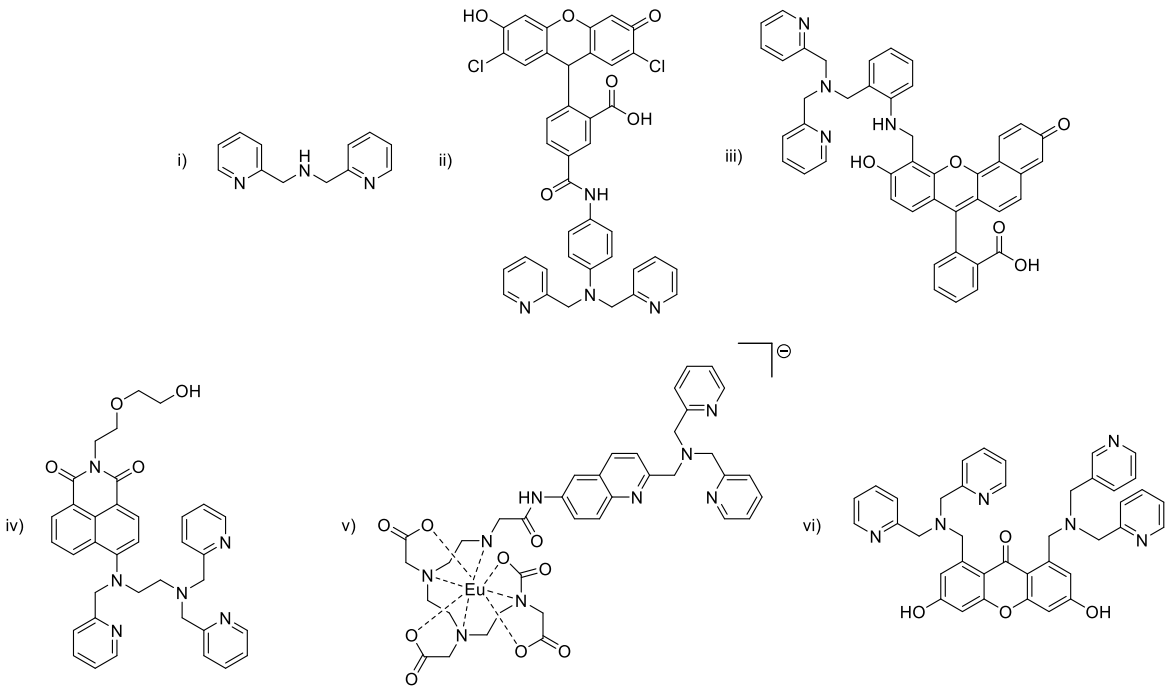


Figure 1.23: i) DPA, ii) Newport Green[216,217], iii) a fluorescein-DPA conjugate synthesised by Cheng *et al*[221], iv) a chemosensor utilising a TPEN receptor from Hanaoka *et al.*[222], v) a lanthanide(III) chelator also developed by Hanaoka *et al*.[219] and vi) a xanthone derivative reported by Ojida *et al*.[223].

Cyanine dyes are widely used in optical imaging due to their emission in the NIR window of the electromagnetic spectrum, large Stokes shifts and impressive quantum yields and molar extinction coefficients. These properties render polymethine cyanines an attractive family for the development of NIR zinc(II) chemosensors, and this has been exploited by many in the field. In 2006, Kiyose *et al*. produced a rigidified heptamethine cyanine structure which utilised a DPA-ethylenediamine unit as a Zn^{2+} receptor and exhibited a 44 nm red shift in its emission wavelength during cation binding due to an ICT process[200,224]. This compound was emissive in the NIR region at 760 nm but had a reduced receptor affinity for Zn(II), perhaps due to the presence of the ethylene bridge[224]. More recently in 2012, Guo *et al*. published an analogous species which was designed as a PeT chemosensor[225]. In the presence of Zn^{2+}, solutions of this compound were seen to change colour from blue to red, corresponding to a dramatic shift in the absorption band from 670 nm to 510 nm and emission from 730 nm to 585 nm[225]. The authors proposed that this was indicative of ICT, rather than PeT taking place, and that this was due to an interaction between the secondary amine in the receptor unit and Zn^{2+} resulting in subsequent deprotonation and imine formation, resulting in conjugation between the receptor and fluorophore[225]. Despite the compound possessing a greater affinity for Zn^{2+} than DPA itself (K_d = 1.2 nm), the fact that its emission during a recognition event shifts into the visible window could present issues *in vivo*[225]. A particularly notable example was reported by Tang *et al*., which was also based on a heptamethine cyanine dye and used a DPA sensor and PeT sensing mechanism[214]. This species exhibited a 20-fold increase in emission intensity (λ = 780 nm) in the presence of Zn^{2+}, which remained independent of pH

at physiologically relevant values (6.4 to 7.5)[205,214]. Furthermore, the probe was selective for Zn^{2+} over many other endogenous cations (**Figure 1.24**)[214].

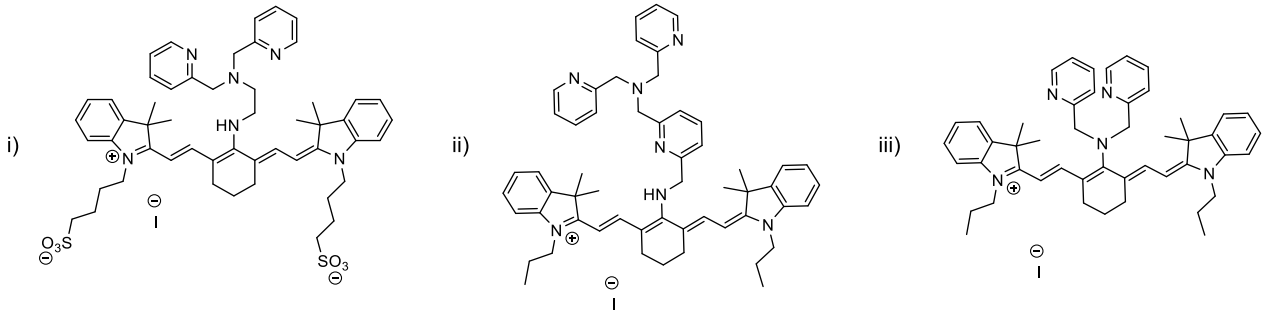


Figure 1.24: The zinc-sensing cyanine compounds produced by i) Kiyose *et al.*[224], ii) Guo *et al.*[225] and iii) Tang *et al.*[214].

One issue with Tang's compound was its interaction with Cu^{2+}, which was found to quench the fluorescence of the system[214]. Indeed, DPA is known to act as a receptor for Cu^{2+} ions and cyanine-DPA derivatives bound to copper(II) have been utilised as anion sensors[203]. Although both Zn^{2+} and Fe^{2+} are found at much higher levels *in vivo*, copper is the third most prevalent transition metal present in humans, presenting issues with the use of DPA as a zinc(II) ion receptor[213].

1.3. Aims and Objectives

The aims of this thesis were extensive and broad. Chiefly, it has been the design, synthesis and testing of targeted imaging probes. Targeted, specific delivery of probes to pancreatic β-cells could allow better imaging of these important, yet, in terms of overall organ volume, relatively scarce islet components. Furthermore, targeting of compounds delivered to biological systems can help optimise probe delivery and enable smaller quantities to be utilised. This can help reduce toxicity concerns around the administration of some compounds: GBCAs for example.

The peptide exendin-4, a ligand for the receptor GLP-1R, has found applications in therapeutic treatment of diabetes and has formed the basis of many β-cell-specific agents designed for applications in optical, PET and SPECT. However, there is a lack of exendin-mediated MRI contrast agents, which, due to its high resolution and strongly penetrative nature could be critical in the study of diabetes development. Indeed, the technique is being used by some in the field to quantify β-cell mass *via* insulin-stimulated insulin secretion[86]. The synthesis of a GBCA incorporating exendin-4 was pursued, followed by its testing *in vivo* in both healthy and disease-model mice. This work is described in chapter 2.

Small molecules possess some advantages over peptides in terms of reduced cost, synthetic flexibility and accessibility and the ability to be extensively characterised. The relatively recent elucidation of the receptor GPR40, which, alongside GLP-1R, is over-expressed by β-cells, presents an opportunity in this regard. GPR40 is activated by small molecules such as fatty acids and some aromatic species.

Although some agonists for the receptor are currently in clinical trials, there are very few imaging probes designed to target GPR40. Of these, most utilise the compound TAK-875 as a targeting moiety[226,227], a therapeutic compound which was withdrawn from clinical trials due to its hepatotoxic effects. It was hoped that imaging agents with an alternative targeting group could be successfully designed and synthesised. This involved the development of a ligand which could act as a lanthanide chelator, making use of the magnetic and luminescent properties of those elements and enabling a range of different imaging modalities to be employed. Furthermore, this work could enable a comparison between the merits of small molecule targeting and peptide targeting, as explored in chapter 2. This is detailed further in chapter 3.

Recent work has shown that, after agonist binding, GLP-1R is involved in a process of cell internalisation[228–230]. This internalisation is thought to be involved in the activation of insulin secretion. As such, there is great interest in the field in exploring the interactions between GLP-1R and its agonists and what difference the structure of these agonists makes on the efficacy of receptor binding and activation. This can be explored through luminescent lanthanide(III) systems and receptors labelled with organic fluorophores capable of a fluorescence resonance energy transfer (FRET) process. As a potent agonist for GLP-1R, it was hypothesised that the synthesis of compounds which could incorporate FRET capability to exendin-4 could be used to explore this interaction and complement the work done on exendin-targeted GBCAs discussed in chapter 2. This work is built upon in chapter 4.

Zinc(II) ions are known to be closely associated with insulin storage and secretion, and it has been hypothesised that a decline in pancreatic Zn^{2+} levels may be associated with the progression of diabetes development. Smart imaging probes which exhibit a change in their characteristics in the presence of certain analytes are of keen research interest. There are many different chemical mechanisms which can be employed to give enhanced imaging and Zn^{2+} quantification: relaxivity increases can be caused by changes in chelating modes or molecular rotation, and there are many different zinc-sensing strategies employed in optical imaging. Chapters 2, 3 and 5 discuss the concept of zinc-binding and seek to synthesise probes with this capability, in addition to some steps towards dual-modality imaging.

1.4. References

1 G. Danaei, M. M. Finucane, Y. Lu, G. M. Singh, M. J. Cowan, C. J. Paciorek, J. K. Lin, F. Farzadfar, Y. H. Khang, G. A. Stevens, M. Rao, M. K. Ali, L. M. Riley, C. A. Robinson and M. Ezzati, *Lancet*, 2011, **378**, 31–40.

2 M. Ezzati, *Lancet*, 2016, **387**, 1513–1530.

3 H. Kimura, N. Fujita, K. Kanbe, H. Matsuda, H. Watanabe, K. Arimitsu, H. Fujimoto, K. Hamamatsu, Y. Yagi, M. Ono, N. Inagaki and H. Saji, *Bioorg. Med. Chem.*, 2017, **25**, 5772–5778.

4 M. C. Thomas, M. E. Cooper and P. Zimmet, *Nat. Rev. Nephrol.*, 2016, 12, 73–81.

5 F. B. Hu, *Diabetes Care*, 2011, **34**, 1249–1257.

6 S. N. Bhupathiraju and F. B. Hu, *Circ. Res.*, 2016, **118**, 1723–1735.

7 Y. Zheng, S. H. Ley and F. B. Hu, *Nat. Rev. Endocrinol.*, 2018, 14, 88–98.

8 S. H. Ley and J. B. Meigs, in *Diabetes Epidemiology, Genetics, Pathogenesis, Diagnosis, Prevention, and Treatment*, eds. E. Bonora and R. A. DeFronzo, Springer Nature Switzerland, Cham, Switzerland, 2018, pp. 55–80.

9 H. E. Mulnier, H. E. Seaman, V. S. Raleigh, S. S. Soedamah-Muthu, H. M. Colhoun and R. A. Lawrenson, *Diabet. Med.*, 2006, **23**, 516–521.

10 N. Hex, C. Bartlett, D. Wright, M. Taylor and D. Varley, *Diabet. Med.*, 2012, **29**, 855–862.

11 J. Marx, *Science (80-.).*, 2002, **296**, 686–689.

12 G. A. Rutter, T. J. Pullen, D. J. Hodson and A. Martinez-Sanchez, *Biochem. J.*, 2015, 466, 203–218.

13 A. Awasthi, N. Parween, V. K. Singh, A. Anwar, B. Prasad and J. Kumar, *Adv. Diabetes Metab.*, 2016, **4**, 10–23.

14 E. Ferrannini and R. A. DeFronzo, in *International Textbook of Diabetes Mellitus*, 2015, pp. 211–233.

15 A. Jodal, R. Schibli and M. Béhé, *Eur. J. Nucl. Med. Mol. Imaging*, 2017, **44**, 712–727.

16 E. Ahlqvist, P. Storm, A. Käräjämäki, M. Martinell, M. Dorkhan, A. Carlsson, P. Vikman, R. B. Prasad, D. M. Aly, P. Almgren, Y. Wessman, N. Shaat, P. Spégel, H. Mulder, E. Lindholm, O. Melander, O. Hansson, U. Malmqvist, Å. Lernmark, K. Lahti, T. Forsén, T. Tuomi, A. H. Rosengren and L. Groop, *Lancet Diabetes Endocrinol.*, 2018, **6**, 361–369.

17 A. Pugliese, in *International Textbook of Diabetes Mellitus*, 2015, pp. 442–453.

18 G. J. Stasiuk, F. Minuzzi, M. Sae-Heng, C. Rivas, H. Juretschke, L. Piemonti, P. R. Allegrini, D. Laurent, A. R. Duckworth, A. Beeby, G. A. Rutter and N. J. Long, *Chem. – A Eur. J.*, 2015, **21**, 5023–5033.

19 M. Knip, H. Siljander, J. Ilonen, O. Simell and R. Veijola, *Pediatr. Diabetes*, 2016, **17**, 17–24.

20 S. T. Azar, H. Tamim, H. N. Beyhum, M. Zouhair Habbal and W. Y. Almawi, *Clin. Diagnositc Lab. Immunol.*, 1999, **6**, 306–310.

21 M. A. Atkinson, G. S. Eisenbarth and A. W. Michels, *Lancet*, 2014, 383, 69–82.

22 U. Werner, G. Haschke, A. W. Herling and W. Kramer, *Regul. Pept.*, 2010, **164**, 58–64.

23 M. J. Kim, J. H. Yu, M. H. Oh, Y. S. Nam and D. Y. Lee, *J. Ind. Eng. Chem.*, 2017, **45**, 404–411.

24 C. Chen, C. M. Cohrs, J. Stertmann, R. Bozsak and S. Speier, *Mol. Metab.*, 2017, **6**, 943–957.

25 J. Rahier, Y. Guiot, R. M. Goebbels, C. Sempoux and J.-C. Henquin, *Diabetes, Obes. Metab.*, 2008, **10**,

32–42.

26 A. E. Butler, J. Janson, S. Bonner-Weir, R. Ritzel, R. A. Rizza and P. C. Butler, *Diabetes*, 2003, **52**, 102–110.

27 D. Laurent, L. Vinet, S. Lamprianou, M. Daval, G. Filhoulaud, A. Ktorza, H. Wang, S. Sewing, H. -P Juretschke, H. Glombik, P. Meda, R. Boisgard, D. L. Nguyen, G. J. Stasiuk, N. J. Long, X. Montet, P. Hecht, W. Kramer, G. A. Rutter and J. Hecksher-Sørensen, *Diabetes, Obes. Metab.*, 2016, **18**, 6–15.

28 B. Mukherjee, C. M. Hossain, L. Mondal, P. Paul and M. K. Ghosh, *Lipid Insights*, 2013, **6**, 1–11.

29 F. Souza, M. Freeby, K. Hultman, N. Simpson, A. Herron, P. Witkowsky, E. Liu, A. Maffei and P. Harris, *Curr. Med. Chem.*, 2006, **13**, 2761–2773.

30 R. Hernandez, S. A. Graves, T. Gregg, H. R. VanDeusen, R. J. Fenske, H. N. Wienkes, C. G. Engl, H. F. Valdovinos, J. J. Jeffery, T. E. Barnhart, G. W. Severin, R. J. Nickles, M. E. Kimple, M. J. Merrins and W. Cai, *Diabetes*, 2017, **66**, 2163–2174.

31 O. Eriksson, M. Laughlin, M. Brom, P. Nuutila, M. Roden, A. Hwa, R. Bonadonna and M. Gotthardt, *Diabetologia*, 2016, **59**, 1340–1349.

32 C. Ramogida and C. Orvig, *Chem. Commun.*, 2013, **49**, 4720–4739.

33 J. Wahsner, E. M. Gale, A. Rodríguez-Rodríguez and P. Caravan, *Chem. Rev.*, 2019, 119, 957–1057.

34 S. Lee, J. Xie and X. Chen, *Biochemistry*, 2010, **49**, 1364–1376.

35 Z. Y. Chen, Y. X. Wang, Y. Lin, J. S. Zhang, F. Yang, Q. L. Zhou and Y. Y. Liao, *Biomed Res. Int.*, 2014, 2014.

36 S. Runge, H. Thøgersen, K. Madsen, J. Lau and R. Rudolph, *J. Biol. Chem.*, 2008, **283**, 11340–11347.

37 L. J. Miller, P. M. Sexton, M. Dong and K. G. Harikumar, *Int. J. Obes. Suppl.*, 2014, **4**, S9–S13.

38 J. P. Gutzwiller, B. Göke, J. Drewe, P. Hildebrand, S. Ketterer, D. Handschin, R. Winterhalder, D. Conen and C. Beglinger, *Gut*, 1999, **44**, 81–86.

39 A. E. Adriaenssens, B. Svendsen, B. Y. H. Lam, G. S. H. Yeo, J. J. Holst, F. Reimann and F. M. Gribble, *Diabetologia*, 2016, **59**, 2156–2165.

40 D. J. Drucker and M. A. Nauck, *Lancet*, 2006, 368, 1696–1705.

41 M. A. Pfeffer, B. Claggett, R. Diaz, K. Dickstein, H. C. Gerstein, L. V. Køber, F. C. Lawson, L. Ping, X. Wei, E. F. Lewis, A. P. Maggioni, J. J. V. McMurray, J. L. Probstfield, M. C. Riddle, S. D. Solomon and J.-C. Tardif, *N. Engl. J. Med.*, 2015, **373**, 2247–2257.

42 L. Joosten, M. Brom, H. Peeters, S. Heskamp, M. Béhé, O. Boerman and M. Gotthardt, *Mol. Pharm.*, 2018, **15**, 486–494.

43 A. Sowa-Staszczak, M. Trofimiuk-Müldner, A. Stefańska, M. Tomaszuk, M. Buziak-Bereza, A. Gilis-Januszewska, A. Jabrocka-Hybel, B. Głowa, M. Małecki, T. Bednarczuk, G. Kamiński, A. Kowalska, R. Mikołajczak, B. Janota and A. Hubalewska-Dydejczyk, *PLoS One*, 2016, **11**, 1–13.

44 M. Gotthardt, G. Lalyko, J. van Eerd-Vismale, B. Keil, T. Schurrat, M. Hower, P. Laverman, T. M. Behr, O. C. Boerman, B. Göke and M. Béhé, *Regul. Pept.*, 2006, **137**, 162–167.

45 T. Reiner, G. Thurber, J. Gaglia, C. Vinegoni, C. W. Liew, R. Upadhyay, R. H. Kohler, L. Li, R. N. Kulkarni, C. Benoist, D. Mathis and R. Weissleder, *Proc. Natl. Acad. Sci.*, 2011, **108**, 12815–12820.

46 D. O. Kiesewetter, H. Gao, Y. Ma, G. Niu, Q. Quan, N. Guo and X. Chen, *Eur J Nucl Med Mol Imaging*, 2012, **39**, 463–473.

47 L. Vinet, S. Lamprianou, A. Babič, N. Lange, F. Thorel, P. L. Herrera, X. Montet and P. Meda, *Diabetologia*, 2014, **58**, 304–312.

48 R. K. Selvaraju, I. Velikyan, L. Johansson, Z. Wu, I. Todorov, J. Shively, F. Kandeel, O. Korsgren and O. Eriksson, *J Nucl Med*, 2013, **54**, 1458–1463.

49 P. Wang, B. Yoo, J. Yang, X. Zhang, A. Ross, P. Pantazopoulos, G. Dai and A. Moore, *Diabetes*, 2014, **63**, 1465–1474.

50 Y. Luo, Q. Pan, S. Yao, M. Yu, W. Wu, H. Xue, D. O. Kiesewetter, Z. Zhu, F. Li, Y. Zhao and X. Chen, *J. Nucl. Med.*, 2016, **57**, 715–720.

51 H. Kimura, Y. Ogawa, H. Fujimoto, E. Mukai, H. Kawashima, K. Arimitsu, K. Toyoda, N. Fujita, Y. Yagi, K. Hamamatsu, T. Murakami, A. Murakami, M. Ono, Y. Nakamoto, K. Togashi, N. Inagaki and H. Saji, *Bioorg. Med. Chem.*, 2018, **26**, 463–469.

52 L. Joosten, M. Brom, H. Peeters, D. Bos, E. Himpe, L. Bouwens, O. Boerman and M. Gotthardt, *Mol. Pharm.*, 2019, **16**, 4024–4030.

53 S. Edfalk, P. Steneberg and H. Edlund, *Diabetes*, 2008, **57**, 2280–2287.

54 P. Steneberg, N. Rubins, R. Bartoov-Shifman, M. D. Walker and H. Edlund, *Cell Metab.*, 2005, **1**, 245–258.

55 H. Shapiro, S. Shachar, I. Sekler, M. Hershfinkel and M. D. Walker, *Biochem. Biophys. Res. Commun.*, 2005, **335**, 97–104.

56 M. G. Latour, T. Alquier, E. Oseid, C. Tremblay, T. L. Jetton, J. Luo, D. C-H Lin and V. Poitout, *Diabetes*, 2007, **56**, 1087–1094.

57 I. Syed, J. Lee, P. M. Moraes-Vieira, C. J. Donaldson, A. Sontheimer, P. Aryal, K. Wellenstein, M. J. Kolar, A. T. Nelson, D. Siegel, J. Mokrosinski, I. S. Farooqi, J. J. Zhao, M. M. Yore, O. D. Peroni, A. Saghatelian and B. B. Kahn, *Cell Metab.*, 2018, **27**, 419-427.e4.

58 M. Z. Khan and L. He, *Neuropharmacology*, 2017, 113, 639–651.

59 D. O. Yoon, X. Zhao, D. Son, J. T. Han, J. Yun, D. Shin and H. J. Park, *ACS Med. Chem. Lett.*, 2017, **8**, 1336–1340.

60 M. Sawzdargo, S. R. George, T. Nguyen, S. Xu, L. F. Kolakowski and B. F. O'Dowd, *Biochem. Biophys. Res. Commun.*, 1997, **239**, 543–547.

61 J. J. Chen, Y. H. Gong and L. He, *J. Drug Target.*, 2019, 27, 347–354.

62 Y. Itoh, Y. Kawamata, M. Harada, M. Kobayashi, R. Fujii, S. Fukusumi, K. Ogi, M. Hosoya, Y. Tanaka, H. Uejima, H. Tanaka, M. Maruyama, R. Satoh, S. Okubo, H. Kizawa, H. Komatsu, F. Matsumura, Y. Noguchi, T. Shinohara, S. Hinuma, Y. Fujisawa and M. Fujino, *Nature*, 2003, **422**, 173–176.

63 C. P. Briscoe, M. Tadayyon, J. L. Andrews, W. G. Benson, J. K. Chambers, M. M. Eilert, C. Ellis, N. A. Elshourbagy, A. S. Goetz, D. T. Minnick, P. R. Murdock, H. R. Sauls, U. Shabon, L. D. Spinage, J. C. Strum, P. G. Szekeres, K. B. Tan, J. M. Way, D. M. Ignar, S. Wilson and A. I. Muir, *J. Biol. Chem.*, 2003, **278**, 11303–11311.

64 Z. Li, Q. Qiu, X. Geng, J. Yang, W. Huang and H. Qian, *Expert Opin. Investig. Drugs*, 2016, **25**, 871–890.

65 C. Eleazu, A. Charles, K. Eleazu and N. Achi, *Chem. Biol. Interact.*, 2018, 289, 32–39.

66 S. B. Bharate, K. V. Nemmani and R. A. Vishwakarma, *Expert Opin. Ther. Pat.*, 2009, **19**, 237–264.

67 S. C. McKeown, D. F. Corbett, A. S. Goetz, T. R. Littleton, E. Bigham, C. P. Briscoe, A. J. Peat, S. P. Watson and D. M. B. Hickey, *Bioorganic Med. Chem. Lett.*, 2007, **17**, 1584–1589.

68 E. Christiansen, C. Urban, N. Merten, K. Liebscher, K. K. Karlsen, A. Hamacher, A. Spinrath, A. D. Bond, C. Drewke, S. Ullrich, M. U. Kassack, E. Kostenis and T. Ulven, *J. Med. Chem.*, 2008, **51**, 7061–7064.

69 C. Hamdouchi, S. D. Kahl, A. Patel Lewis, G. R. Cardona, R. W. Zink, K. Chen, T. E. Eessalu, J. V. Ficorilli, M. C. Marcelo, K. A. Otto, K. L. Wilbur, J. P. Lineswala, J. L. Piper, D. S. Coffey, S. A. Sweetana, J. V. Haas, D. A. Brooks, E. J. Pratt, R. M. Belin, M. A. Deeg, X. Ma, E. A. Cannady, J. T. Johnson, N. P. Yumibe, Q. Chen, P. Maiti, C. Montrose-Rafizadeh, Y. Chen and A. Reifel Miller, *J. Med. Chem.*, 2016, **59**, 10891–10916.

70 C. P. Tan, Y. Feng, Y.-P. Zhou, G. J. Eiermann, A. Petrov, C. Zhou, S. Lin, G. Salituro, P. Meinke, R. Mosley, T. E. Akiyama, M. Einstein, S. Kumar, J. P. Berger, S. G. Mills, N. A. Thornberry, L. Yang and A. D. Howard, *Am Diabetes Assoc*, , DOI:10.2337/db08-0130.

71 S. B. Bharate, A. Rodge, R. K. Joshi, J. Kaur, S. Srinivasan, S. Senthil Kumar, A. Kulkarni-Almeida, S. Balachandran, A. Balakrishnan and R. A. Vishwakarma, *Bioorganic Med. Chem. Lett.*, 2008, **18**, 6357–6361.

72 N. Negoro, S. Sasaki, S. Mikami, M. Ito, M. Suzuki, Y. Tsujihata, R. Ito, A. Harada, K. Takeuchi, N.

Suzuki, J. Miyazaki, T. Santou, T. Odani, N. Kanzaki, M. Funami, T. Tanaka, A. Kogame, S. Matsunaga, T. Yasuma and Y. Momose, *Chem. Lett*, 2010, **1**, 290–294.

73 T. Araki, M. Hirayama, S. Hiroi and K. Kaku, *Diabetes, Obes. Metab.*, 2012, **14**, 271–278.

74 H. Naik, M. Vakilynejad, J. Wu, P. Viswanathan, N. Dote, T. Higuchi and E. Leifke, *J. Clin. Pharmacol.*, 2012, **52**, 1007–1016.

75 S. L. Kelleher, N. H. Mccormick, V. Velasquez and V. Lopez, *Adv. Nutr*, 2011, **2**, 101–111.

76 J. Jansen, W. Karges and L. Rink, *J. Nutr. Biochem.*, 2009.

77 M. J. Salgueiro, N. Krebs, M. B. Zubillaga, R. Weill, E. Postaire, A. E. Lysionek, R. A. Caro, T. De Paoli, A. Hager and J. Boccio, *Biol. Trace Elem. Res.*, 2001, **81**, 215–228.

78 J. Rungby, *Diabetologia*, 2010, 53, 1549–1551.

79 R. E. Lutz, *J. Ind. Hyg.*, 1926, **8**, 177–207.

80 D. A. Scott, *Biochem. J.*, 1934, **28**, 1592-1602.1.

81 D. A. Scott and A. M. Fisher, *J. Clin. Invest.*, 1938, **17**, 725–728.

82 L. G. Sondergaard, M. Stoltenberg, P. Doering, A. Flyvbjerg and J. Rungby, *Histol. Histopathol.*, 2006, **21**, 619–625.

83 K. Kikuchi, K. Komatsu and T. Nagano, *Curr. Opin. Chem. Biol.*, 2004, **8**, 182–191.

84 C. G. Taylor, in *BioMetals*, 2005, vol. 18, pp. 305–312.

85 E. V Antina, N. A. Bumagina, A. I. V'yugin and A. V Solomonov, *Dye. Pigment.*, 2017, **136**, 368–381.

86 A. F. Martins, V. Clavijo Jordan, F. Bochner, S. Chirayil, N. Paranawithana, S. Zhang, S. T. Lo, X. Wen, P. Zhao, M. Neeman and A. D. Sherry, *J. Am. Chem. Soc.*, 2018, **140**, 17456–17464.

87 J. Zhang, Michigan Technological University, 2015.

88 R. Weissleder and U. Mahmood, *Radiology*, 2001, **219**, 316–333.

89 J. K. Willmann, N. van Bruggen, L. M. Dinkelborg and S. S. Gambhir, *Nat. Rev. Drug Discov.*, 2008, 7, 591–607.

90 G.-L. Law and W.-T. Wong, in *The Chemistry of Molecular Imaging*, eds. N. J. Long and W.-T. Wong, John Wiley & Sons, Hoboken, U.S.A., 2015, pp. 1–24.

91 S. Cotton, *Lanthanide and Actinide Chemistry*, 2006.

92 J. C. G. Bünzli and C. Piguet, *Chem. Soc. Rev.*, 2005, 34, 1048–1077.

93 J. C. G. Bünzli, *Chem. Lett.*, 2009, 38, 104–109.

94 D. T. Edmonds, *Bioelectrochemistry Bioenerg.*, 1993, **30**, 3–12.

95 C. Rivas, G. J. Stasiuk, J. Gallo, F. Minuzzi, G. A. Rutter and N. J. Long, *Inorg. Chem.*, 2013, **52**, 14284–14293.

96 P. Caravan, *Chem. Soc. Rev.*, 2006, **35**, 512–523.

97 C. Rivas, G. J. Stasiuk, M. Sae-Heng and N. J. Long, *Dalt. Trans.*, , DOI:10.1039/c4dt02981j.

98 J. A. Peters, J. Huskens and D. J. Raber, *Prog. Nucl. Magn. Reson. Spectrosc.*, 1996, **28**, 283–350.

99 P. Caravan, J. J. Ellison, T. J. McMurry and R. B. Lauffer, *Chem. Rev.*, 1999, **99**, 2293–2352.

100 M. Bottrill, L. Kwok and N. J. Long, *Chem. Soc. Rev.*, 2006, **35**, 557.

101 S. Aime, M. Botta and E. Terreno, *Adv. Inorg. Chem.*, 2005, **57**, 173–237.

102 E. J. Werner, A. Datta, C. J. Jocher and K. N. Raymond, *Angew. Chemie - Int. Ed.*, 2008, 47, 8568–8580.

103 T. J. Clough, L. Jiang, K. L. Wong and N. J. Long, *Nat. Commun.*, 2019, 10.

104 J. Gallo and N. J. Long, in *The Chemistry of Molecular Imaging*, eds. N. J. Long and W.-T. Wong, John Wiley & Sons, Hoboken, U.S.A., 2015, pp. 199–224.

105 H. Bin Na, I. C. Song and T. Hyeon, *Adv. Mater.*, 2009, **21**, 2133–2148.

106 Y. D. Xiao, R. Paudel, J. Liu, C. Ma, Z. S. Zhang and S. K. Zhou, *Int. J. Mol. Med.*, 2016, **38**, 1319–1326.

107 A. D. Sherry, P. Caravan and R. E. Lenkinski, *J. Magn. Reson. Imaging*, 2009, **30**, 1240–1248.

108 D. H. Carr, J. Brown, G. M. Bydder, R. E. Steiner, H.-J. Weinmann, U. Speck, A. S. Hall and I. R. Young, *Am. J. Roentgenol.*, 1984, **143**, 215–224.

109 H. P. Niendorf, *Bristol Medico-Chirurgical J.*, 1988, **103**, 34–34.

110 S. Aime and P. Caravan, *J. Magn. Reson. Imaging*, 2009, **30**, 1259–1267.

111 European Medicines Agency, *Assessment report for Gadolinium-containing contrast agents*, London, U.K., 2010, vol. 44.

112 A. Z. Khawaja, D. B. Cassidy, J. Al Shakarchi, D. G. Mcgrogan, N. G. Inston and R. G. Jones, *Insights Imaging*, 2015, **6**, 553–558.

113 A. D. Sherry, W. P. Cacheris and K. -T Kuan, *Magn. Reson. Med.*, 1988, **8**, 180–190.

114 S. Faulkner and O. A. Blackburn, in *The Chemistry of Molecular Imaging*, eds. N. Long and W.-T. Wong, John Wiley & Sons, Hoboken, U.S.A., 2015, pp. 179–197.

115 L. Frullano, J. Rohovec, J. A. Peters and C. F. G. C. Geraldes, *Top. Curr. Chem.*, 2002, **221**, 25–60.

116 J. F. Desreux, *Inorg. Chem.*, 1980, **19**, 1319–1324.

117 P. Marckmann, L. Skov, K. Rossen, A. Dupont, B. Damholt, J. G. Heaf and H. S. Thomsen, *J Am Soc Nephrol*, 2006, **17**, 2359–2362.

118 T. Grobner, *Nephrol Dial Transpl.*, 2006, **21**, 1104–1108.

119 R. McDonald, J. McDonald, D. Kallmes, M. Jentoft, D. Murray, K. Thielen, E. Williamson and L. Eckel, *Radiology*, 2015, **275**, 772–782.

120 T. Kanda, H. Oba, K. Toyoda, K. Kitajima and S. Furui, *Jpn. J. Radiol.*, 2016, **34**, 3–9.

121 I. A. Dekkers, R. Roos and A. J. Van Der Molen, *Eur. Radiol.*, 2018, **28**, 1579–1584.

122 V. Gulani, F. Calamante, F. G. Shellock, E. Kanal and S. B. Reeder, *Lancet Neurol.*, 2017, **16**, 564–70.

123 L. K. Young, S. Z. Matthew and J. G. Houston, *Eur. Radiol.*, 2019, **29**, 1922–1930.

124 D. W. Darnall and E. R. Birnbaum, *Biochemistry*, 1973, **12**, 3489–3491.

125 A. Spencer, S. Wilson and E. Harpur, *Hum. Exp. Toxicol.*, 1998, **17**, 633–637.

126 L. Yang, I. Krefting, A. Gorovets, L. Marzella, J. Kaiser, R. Boucher and D. Rieves, *Radiology*, 2012, **265**, 248–253.

127 G.E. Healthcare, *Brief. Doc. MIDAC*, 2017, 1–91.

128 J. Ramalho, R. C. Semelka, M. Ramalho, R. H. Nunes, M. Alobaidy and M. Castillo, *Am. J. Neuroradiol.*, 2016, **37**, 1192–1198.

129 R. C. Semelka, J. Ramalho, A. Vakharia, M. Alobaidy, L. M. Burke, M. Jay and M. Ramalho, *Magn. Reson. Imaging*, 2016, **34**, 1383–1390.

130 M. Rogosnitzky and S. Branch, *BioMetals*, 2016, **29**, 365–376.

131 E. Toth, L. Helm and A. E. Merbah, in *Contrast Agents 1 - Topics in Current Chemistry*, ed. W. Krause, Springer, Berlin, Germany, 2002, pp. 61–101.

132 C. F. G. C. Geraldes, in *NMR in Supramolecular Chemistry*, Springer Netherlands, Dordrecht, The Netherlands, 1999, pp. 133–154.

133 V. C. Pierre, M. J. Allen and P. Caravan, *J Biol Inorg Chem*, 2014, **19**, 127–131.

134 P. Caravan, J. J. Ellison, T. J. McMurry and R. B. Lauffer, *Chem. Rev.*, 1999, **99**, 2293–2352.

135 S. Aime, M. Botta and G. Ermondi, *Inorg. Chem.*, 1992, **31**, 4291–4299.

136 S. Aime, M. Botta, S. G. Crich, G. B. Giovenzana, G. Jommi, R. Pagliarin and M. Sisti, *Inorg. Chem.*, 1997, **36**, 2992–3000.

137 D. Messeri, M. P. Lowe, D. Parker and M. Botta, *Chem. Commun.*, 2001, **1**, 2742–2743.

138 D. Messeri, M. P. Lowe, D. Parker and M. Botta, *Chem. Commun.*, 2001, **1**, 2742–2743.

139 M. Rohrer, H. Bauer, J. Mintorovitch, M. Requardt and H.-J. Weinmann, *Comparison of Magnetic Properties of MRI Contrast Media Solutions at Different Magnetic Field Strengths*, 2005, vol. 40.

140 K. Kumar, T. Jin, X. Wang, J. F. Desreux and M. F. Tweedle, *Inorg. Chem.*, 1994, **33**, 3823–3829.

141 D. M. J. Doble, M. Melchior, B. O'Sullican, C. Siering, J. Xu, V. C. Pierre and K. N. Raymond, *Inorg. Chem.*, 2003, **42**, 4930–4937.

142 S. Aime, L. Calabi, C. Cavallotti, E. Gianolio, G. B. Giovenzana, P. Losi, A. Maiocchi, G. Palmisano and M. Sisti, *Inorg. Chem.*, 2004, **43**, 7588–7590.

143 A. Vágner, E. Gianolio, S. Aime, A. Maiocchi, I. Tó, Z. Baranyai and L. Tei, *Chem. Commun.*, 2016, **52**, 11235–11238.

144 E. J. Werner, S. Avedano, M. Botta, B. P. Hay, E. G. Moore, S. Aime and K. N. Raymond, *J Am Chem Soc*, 2007, **129**, 1870–1871.

145 S. Laus, R. Ruloff, É. Tóth and A. E. Merbach, *Chem. - A Eur. J.*, 2003, **9**, 3555–3566.

146 M. Polášek, J. Rudovský, P. Hermann, I. Lukeš, L. Vander Elst and R. N. Muller, *Chem. Commun.*, 2004, **10**, 2602–2603.

147 P. Caravan, C. T. Farrar, L. Frullano and R. Uppal, *Contrast Media Mol. Imaging*, 2009, **4**, 89–100.

148 L. De Leon-Rodriguez, A. Josue, M. Lubag and A. D. Sherry, *Inorganica Chim. Acta*, 2012, **393**, 12–23.

149 L. Vander Elst, S. Laurent, H. M. Bintoma and R. N. Muller, *Magma Magn. Reson. Mater. Physics, Biol. Med.*, 2001, **12**, 135–140.

150 D. Lee, C. Hilty, G. Wider and K. Wüthrich, *J. Magn. Reson.*, 2006, **178**, 72–76.

151 A. C. Esqueda, J. A. López, G. Andreu-de-Riquer, J. C. Alvarado-Monzón, J. Ratnakar, A. J. M. Lubag, A. D. Sherry and L. M. De León-Rodríguez, *J. Am. Chem. Soc.*, 2009, **131**, 11387.

152 M. Yon, C. Billotey and J. D. Marty, *Int. J. Pharm.*, , DOI:10.1016/j.ijpharm.2019.118577.

153 D. A. Tomalia and H. D. Durst, in *Supramolecular Chemistry I — Directed Synthesis and Molecular Recognition*, Springer, Berlin, Heidelberg, 1993, pp. 193–313.

154 P. Caravan, C. Comuzzi, W. Crooks, T. J. Mcmurry, G. R. Choppin and S. R. Woulfe, *Inorg. Chem.*, 2001, **40**, 2170–2176.

155 Z. Tyeklár, S. U. Dunham, K. Midelfort, D. M. Scott, H. Sajiki, K. Ong, R. B. Lauffer, P. Caravan and T. J. Mcmurry, *Inorg. Chem.*, 2007, **46**, 6621–6631.

156 M. H.-W. Lam, G.-L. Law, C.-S. Lee and K.-L. Wong, in *The Chemistry of Molecular Imaging*, eds. N. J. Long and W.-T. Wong, John Wiley & Sons, Ltd, Hoboken, U.S.A., 2015, pp. 245–274.

157 F. N. Egerton, *Bull. Ecol. Soc. Am.*, 2006, **87**, 47–58.

158 M. P. Coogan and S. J. A. Pope, in *The Chemistry of Molecular Imaging*, eds. N. J. Long and W.-T. Wong, John Wiley & Sons, Ltd, Hoboken, U.S.A., 2015, pp. 275–298.

159 G. Baryshnikov, B. Minaev and H. Ågren, *Chem. Rev.*, 2017, **117**, 6500–6537.

160 J. C. Croney, D. M. Jameson and R. P. Learmonth, *Biochem. Mol. Biol. Educ.*, 2001, **29**, 60–65.

161 J. W. Lichtman and J. A. Conchello, *Nat. Methods*, 2005, **2**, 910–919.

162 A. Jabłoński, *Nature*, 1933, 131, 839–840.

163 A. T. Rhys Williams, S. A. Winfield and J. N. Miller, *Analyst*, 1983, **108**, 1067–1071.

164 F. N. Egerton, *Bull. Ecol. Soc. Am.*, 2006, 87, 47–58.

165 F. N. Egerton, *J. Hist. Biol.*, 1968, **1**, 1–22.

166 I. Holme, *Color. Technol.*, 2006, **122**, 235–251.

167 P. Ehrlich, *Die Anaemte,* HoÌˆlder, Wien, 2. Aufl., 1909.

168 D. Wittekind, *Clin. Lab. Haematol.*, 1979, 1, 247–262.

169 R. W. Horobin and K. J. Walter, *Histochemistry*, 1987, **86**, 331–336.

170 J. V Frangioni, *Curr. Opin. Chem. Biol.*, 2003, **7**, 626–634.

171 D. J. Bornhop, D. S. Hubbard, M. P. Houlne, C. Adair, G. E. Kiefer, B. C. Pence and D. L. Morgan, *Anal. Chem.*, 1999, **71**, 2607–2615.

172 B. McMahon, P. Mauer, C. P. McCoy, T. C. Lee and T. Gunnlaugsson, *J. Am. Chem. Soc.*, 2009, **131**, 17542–17543.

173 M. Lee, M. S. Tremblay, S. Jockusch, N. J. Turro and D. Sames, *Org. Lett.*, 2011, **13**, 2802–2805.

174 M. D. Seemann, S. Nekolla, S. Ziegler, F. Bengel and M. Schwaiger, *Eur. J. Med. Res.*, 2004, **9**, 241–246.

175 T. Ido, C. -N Wan, V. Casella, J. S. Fowler, A. P. Wolf, M. Reivich and D. E. Kuhl, *J. Label. Compd. Radiopharm.*, 1978, **14**, 175–183.

176 T. G. Turkington, *J. Nucl. Med. Technol.*, 2001, 29, 4–11.

177 M. M. Ter Pogossian, M. E. Phelps and E. J. N. A. Hoffman andMullani, *Radiology*, 1975, **114**, 89–98.

178 D. Roeda and F. Dollé, in *The Chemistry of Molecular Imaging*, eds. N. J. Long and W.-T. Wong, John Wiley & Sons, Ltd, Hoboken, U.S.A., 2015, pp. 55–78.

179 N. Blow, *Nat. Methods*, 2009, **6**, 465–469.

180 R. Bhalla, C. Darby, W. Levason, S. K. Luthra, G. McRobbie, G. Reid, G. Sanderson and W. Zhang, *Chem. Sci.*, 2014, **5**, 381–391.

181 E. W. Price and C. Orvig, in *The Chemistry of Molecular Imaging*, eds. N. J. Long and W.-T. Wong, John Wiley & Sons, Ltd, Hoboken, U.S.A., 2015, pp. 105–136.

182 C. Brand, D. Abdel-Atti, Y. Zhang, S. Carlin, S. M. Clardy, E. J. Keliher, W. A. Weber, J. S. Lewis and T. Reiner, *Bioconjugate Chem*, 2014, **25**, 1323–1330.

183 L. E. Jennings and N. J. Long, *Chem. Commun.*, 2009, 0, 3511–3524.

184 L. Zhang, R. Liu, H. Peng, P. Li, Z. Xu and A. K. Whittaker, *Nanoscale*, 2016, 8, 10491–10510.

185 P. W. Miller, N. J. Long, R. Vilar and A. D. Gee, *Angew Chem Int Ed*, 2008, **47**, 8998–9003.

186 J. Culver, W. Akers and S. Achilefu, *J. Nucl. Med.*, 2008, **49**, 169–172.

187 A. Mishra, J. Pfeuffer, R. Mishra, J. Engelmann, A. K. Mishra, K. Ugurbil and N. K. Logothetis, *Bioconjug. Chem.*, 2006, **17**, 773–780.

188 T. Koullourou, L. S. Natrajan, H. Bhavsar, S. J. A. Pope, J. Feng, J. Narvainen, R. Shaw, E. Scales, R. Kauppinen, A. M. Kenwright and S. Faulkner, *J. Am. Chem. Soc.*, 2008, **130**, 2178–2179.

189 K. P. Malikidogo, I. Da Silva, J. F. Morfin, S. Lacerda, L. Barantin, T. Sauvage, J. Sobilo, S. Lerondel, É. Tóth and C. S. Bonnet, *Chem. Commun.*, 2018, **54**, 7597–7600.

190 S. Laurent, L. Vander Elst, M. Wautier, C. Galaup, R. N. Muller and C. Picard, *Bioorganic Med. Chem. Lett.*, 2007, **17**, 6230–6233.

191 H. Xu, K. Baidoo, A. J. Gunn, C. A. Boswell, D. E. Milenic, P. L. Choyke and M. W. Brechbiel, *J. Med. Chem.*, 2007, **50**, 4759–4765.

192 J. H. Jang, S. Bhuniya, J. Kang, A. Yeom, K. S. Hong and J. S. Kim, *Org. Lett.*, 2013, **15**, 4702–4705.

193 A. J. M. Lubag, L. M. De Leon-Rodriguez, S. C. Burgess and A. D. Sherry, *Proc. Natl. Acad. Sci. U. S. A.*, 2011, **108**, 18400–18405.

194 K. Hanaoka, K. Kikuchi, Y. Urano, M. Narazaki, T. Yokawa, S. Sakamoto, K. Yamaguchi and T. Nagano, *Chem. Biol.*, 2002, **9**, 1027–1032.

195 J. L. Major, G. Parigi, C. Luchinat and T. J. Meade, *Proc. Natl. Acad. Sci. U. S. A.*, 2007, **104**, 13881–13886.

196 J. L. Major, R. M. Boiteau and T. J. Meade, *Inorg. Chem.*, 2008, **47**, 10788–10795.

197 P. F. Antkowiak, S. A. Tersey, J. D. Carter, M. H. Vandsburger, J. L. Nadler, F. H. Epstein and R. G. Mirmira, *Am. J. Physiol. Metab.*, 2009, **296**, E573–E578.

198 D. Pan, A. Schmieder, S. Wickline and G. Lanza, *Tetrahedron*, 2011, **67**, 8431–8444.

199 K. L. Haas and K. J. Franz, *Chem. Rev.*, 2009, **109**, 4921–4960.

200 P. Carol, S. Sreejith and A. Ajayaghosh, *Chem. – An Asian J.*, 2007, **2**, 338–348.

201 O. McCubbin Stepanic, J. Ward, J. E. Penner-Hahn, A. Deb, U. Bergmann and S. Debeer, *Inorg. Chem.*, 2020, **59**, 13551–13560.

202 N. C. Lim, H. C. Freake and C. Brückner, *Chem. - A Eur. J.*, 2005, **11**, 38–49.

203 X. Yang, L. Shen, H. Bao, X. Fang, J. Xu, Y. Zhao and W. Yang, *Sensors Actuators, B Chem.*, 2015, **220**, 1361–1367.

204 A. P. De Silva, H. Q. N. Gunaratne, T. Gunnlaugsson, A. J. M. Huxley, C. P. McCoy, J. T. Rademacher and T. E. Rice, *Chem. Rev.*, 1997, **97**, 1515–1566.

205 Z. Xu, J. Yoon and D. R. Spring, *Chem. Soc. Rev.*, 2010, **39**, 1996–2006.

206 P. Jiang and Z. Guo, *Coord. Chem. Rev.*, 2004, 248, 205–229.

207 R. J. Radford and S. J. Lippard, *Curr. Opin. Chem. Biol.*, 2013, 17, 129–136.

208 J. Luo, W. S. Li, P. Xu, L. Y. Zhang and Z. N. Chen, *Inorg. Chem.*, 2012, **51**, 9508–9516.

209 A. N. Bashkatov, E. A. Genina, V. I. Kochubey and V. V Tuchin, *J. Phys. D Appl. Phys*, 2005, **38**, 2543–2555.

210 Z. Guo, S. Park, J. Yoon and I. Shin, *Chem. Soc. Rev.*, 2014, 43, 16–29.

211 N. C. Lim, L. Yao, H. C. Freake and C. Brückner, *Bioorganic Med. Chem. Lett.*, 2003, **13**, 2251–2254.

212 K. D. Kröncke, *Arch. Biochem. Biophys.*, 2007, 463, 183–187.

213 M. A. Zoroddu, J. Aaseth, G. Crisponi, S. Medici, M. Peana and V. M. Nurchi, *J. Inorg. Biochem.*, 2019, 195, 120–129.

214 B. Tang, H. Huang, K. Xu, L. Tong, G. Yang, X. Liu and L. An, *Chem. Commun.*, 2006, 3609–3611.

215 S. Wuertz, E. Mü Ller, R. Spaeth, P. Pfleiderer and H.-C. Flemming, *Detection of heavy metals in bacterial biofilms and microbial flocs with the fluorescent complexing agent Newport Green*, 2000, vol. 24.

216 L. M. T. Canzoniero, S. L. Sensi and D. W. Choi, *Neurobiol. Dis.*, 1997, **4**, 275–279.

217 R. P. Haugland, *Methods Mol Biol*, 2002, 966.

218 O. Reany, T. Gunnlaugsson and D. Parker, *Chem. Commun.*, 2000, **0**, 473–474.

219 K. Hanaoka, K. Kikuchi, H. Kojima, Y. Urano and T. Nagano, *J. Am. Chem. Soc.*, 2004, **126**, 12470–12476.

220 O. Reany, T. Gunnlaugsson and D. Parker, *J. Chem. Soc. Perkin Trans. 2*, 2000, **0**, 1819–1831.

221 C. J. Chang, J. Jaworski, E. M. Nolan, M. Sheng and S. J. Lippard, *Proc. Natl. Acad. Sci. U. S. A.*, 2004, **101**, 1129–1134.

222 K. Hanaoka, Y. Muramatsu, Y. Urano, T. Terai and T. Nagano, *Chem. - A Eur. J.*, 2010, **16**, 568–572.

223 A. Ojida, H. Nonaka, Y. Miyahara, S. Tamaru, K. Sada and I. Hamachi, *Angew. Chemie Int. Ed.*, 2006, **45**, 5518–5521.

224 K. Kiyose, H. Kojima, Y. Urano and T. Nagano, *J. Am. Chem. Soc.*, 2006, **128**, 6548–6549.

225 Z. Guo, G. H. Kim, I. Shin and J. Yoon, *Biomaterials*, 2012, **33**, 7818–7827.

226 R. Bertrand, A. Wolf, Y. Ivashchenko, M. Löhn, M. Schäfer, M. Brönstrup, M. Gotthardt, V. Derdau and O. Plettenburg, *ACS Chem. Biol.*, 2016, **11**, 1745–1754.

227 R. Bertrand, I. Hamp, M. Brönstrup, R. Weck, M. Lukacevic, A. Polyak, T. L. Ross, M. Gotthardt, O. Plettenburg and V. Derdau, *J. Label. Compd. Radiopharm.*, 2016, **59**, 604–610.

228 T. Buenaventura, N. Kanda, P. C. Douzenis, B. Jones, S. R. Bloom, P. Chabosseau, I. R. Corrêa, D. Bosco, L. Piemonti, P. Marchetti, P. R. Johnson, A. M. J. Shapiro, G. A. Rutter and A. Tomas, *Diabetes*, 2018, **67**, 385–399.

229 B. Jones, T. Buenaventura, N. Kanda, P. Chabosseau, B. M. Owen, R. Scott, R. Goldin, N. Angkathunyakul, I. R. Corrêa, D. Bosco, P. R. Johnson, L. Piemonti, P. Marchetti, A. M. J. Shapiro, B. J. Cochran, A. C. Hanyaloglu, A. Inoue, T. Tan, G. A. Rutter, A. Tomas and S. R. Bloom, *Nat. Commun.*

230 T. Buenaventura, S. Bitsi, W. E. Laughlin, T. Burgoyne, Z. Lyu, A. I. Oqua, H. Norman, E. R. McGlone, A. S. Klymchenko, I. R. Corrêa, A. Walker, A. Inoue, A. Hanyaloglu, J. Grimes, Z. Koszegi, D. Calebiro, G. A. Rutter, S. R. Bloom, B. Jones and A. Tomas, *PLoS Biol.*, 2019, **17**, e3000097.

Chapter 2

GdEx: An Exendin-4 Based Probe for Pancreas-Specific MRI Contrast Enhancement

2.1. Introduction

2.1.1. Exendin-4 and GLP-1

Glucagon-like peptide 1 (GLP-1) is a 30 amino acid-long peptide secreted from epithelial endocrine L-cells[1]. Secretion of GLP-1 is meal-stimulated, being released during food transit through the gastrointestinal tract[1,2]. *Via* binding to the class B G-protein coupled glucagon-like peptide 1 receptor (GLP-1R), GLP-1 acts as an incretin, resulting in amplification of insulin release, inhibition of glucagon secretion and facilitation of glucose-dependent adenosine triphosphate (ATP) production[1–3]**.** Additionally, there is evidence that GLP-1 acts as an appetite suppressant and induces feelings of satiety[1]. GLP-1R is strongly enriched in pancreatic β-cells, but its presence in other neuroendocrine islet cells is negligible[4–7], which renders it an attractive target for imaging agents designed to examine the insulin production centre.

As an endogenous ligand, GLP-1 itself would be a logical choice for a targeting moiety in the design of these imaging agents, one major limitation is its biological lifetime. The peptide is extremely metabolically unstable, with an apparent half-life of approximately 2 minutes in blood plasma[1]. Exendin-4 is a peptide comprised of 39 amino acid residues, first isolated from the Gila monster, which shares 53% homology with GLP-1[8]. Due to the shared homology of the two proteins, exendin-4 acts as a ligand for GLP-1R and has been shown to induce insulin release. Additionally, its half-life is more than 10 times longer than that of GLP-1, making exendin-4 a highly potent insulinotropic agent[9]. Alongside many other GLP-1R agonists, exendin-4 has been clinically approved for use in therapeutics for the treatment of type 2 diabetes such as exenatide (a synthetic variant of exendin-4) and lixisenatide[10–12]. To add to its therapeutic credentials, exendin-4 results in an in increase β-cell mass and reduction in the number of apoptotic cells in the mouse pancreas[13,14]. Therefore, exendin-4 has been shown to be an attractive targeting moiety for pancreatic β-cells.

2.1.2. Probes Incorporating Exendin-4

A vast spectrum of probes based on the use of exendin-4 as a targeting group have been synthesised and their biological behaviour explored utilising a range of imaging modalities[10,15–26]. Chief amongst these have been probes for the radiochemical techniques positron emission tomography (PET) and single photon emission computed tomography (SPECT).

Probes for PET imaging have incorporated both organic elements and chelators for radiometals. In 2012, a series of ^{18}F-labelled exendin-4 analogues were synthesised by Kiesewetter *et al*., with a cysteine residue added to the C- and N- termini to enable introduction of ^{18}F *via* a maleimide-based chelating goup: [^{18}F]FBEM-[Cys^{40}]-exendin-4 and [^{18}F]FBEM-[Cys^{0}]-exendin-4 respectively[15]. The authors subsequently evaluated these compounds for their affinity for GLP-1R in an insulinoma tumour xenograph model, finding that the Cys^{40} isomer exhibited much greater cellular uptake[15].

Advances towards radiometal chelation with exendin-4 based probes have been made by Wu *et al*., who in 2011 demonstrated the use of a ^{64}Cu-labelled H_4dota analogue ^{64}Cu-do3a-VS-Cys^{40}-exendin-4 for quantification of GLP-1R in the pancreas[27]. The uptake of the probe in healthy and diabetic mice was compared through a competitive binding study with exendin-4 itself in which it was shown that synthetic modifications of exendin-4 to incorporate metal binding regions did not interfere with its affinity for GLP-1R[27]. The authors also reported that probe uptake was significantly reduced in diseased mice compared with the healthy ones, providing a method of β-cell mass quantification and monitoring through PET imaging[27]. A simple analogue to this probe, although utilising the alternative radioisotope ^{68}Ga, ^{68}Ga-do3a-exendin-4, has been shown to have a difference in pancreatic uptake of rats and non-human primates before and after the administration of streptozotocin, an agent capable of inducing β-cell destruction[10,19]. More recently, conjugates of 1, 4, 7-triazacyclononane-1,4,7-triacetic acid (H_3nota) and Cys^{40}-exendin-4 have been utilised in radiolabelling with ^{68}Ga, enabling the detection of localised insulinomas[28]. Many other probes designed for radiometal chelation have been designed and synthesised[10,12,29]. One particularly synthetically impressive example of these is the compound reported in 2014 by Brand *et al*., which incorporated an exendin-based targeting moiety, a cryptand for ^{64}Cu chelation and a cyanine fluorophore, unlocking dual-modal imaging of pancreatic islets[29].

An additional radioimaging technique which has made use of exendin derivatives is that of SPECT. A number of these probes have been synthesised and have also been used to quantify β-cell mass[10,20–22,25,26,30–32]. In 2006, Wild *et al*. utilised a synthetic exendin variant incorporating an additional lysine residue as the backbone of a SPECT probe which included diethylene triamine pentaacetic acid (H_5dtpa) as a chelator for ^{111}In [33]. Since then, this probe and analogues of it have been shown to bind exclusively to β-cells of the pancreas and to target insulinomas, validating the development of SPECT probes with exendin as a targeting group for GLP-1R[33–35]. In 2014, [^{111}In-Lys^{40}((Ahx)-DTPA)-exendin-4] was shown to have a reduced uptake in the pancreas of diabetic humans patients when compared to healthy individuals, suggesting that SPECT probes based on exendin-4 could be used for quantitative assessment of β-cell mass[36]. It has been recently established by Gotthardt *et al.* that loss of β-cell mass can monitored and determined through quantitative analysis of SPECT images recorded with the use of these indium chelates as the relevant imaging agent[20,22]. It has also been recorded by this group that GLP-1R expression is reduced during periods of hyperglycaemia, corresponding with a reduced uptake of exendin-based probes during periods of elevated blood glucose levels[20,22]. A host of additional ligands for ^{111}In based on modifications to exendin-4 have also been reported, notably those from Gotthardt *et al.*, Reiner *et al*. and Kimura *et al.*, which have shown specific binding to receptor tissues expressing GLP-1R[10,21,25,26].

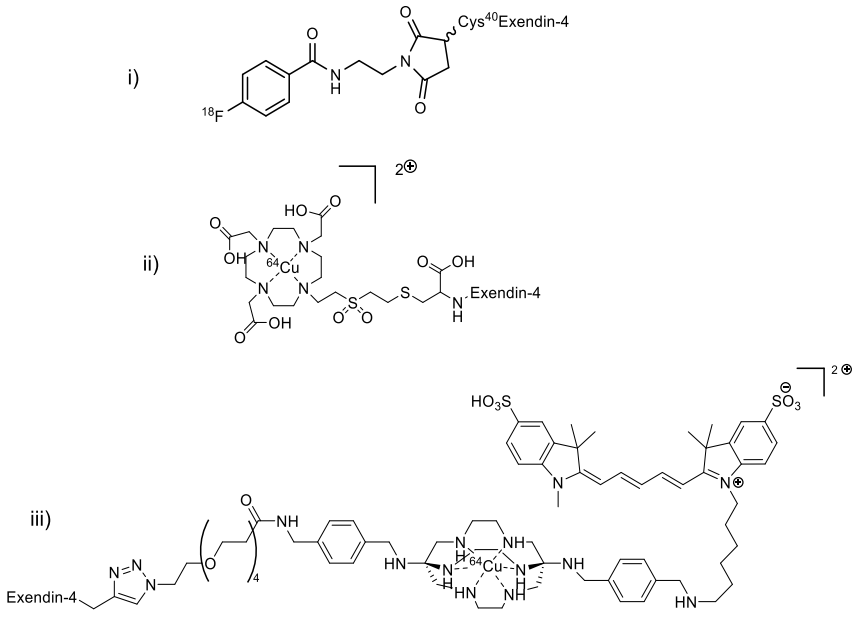


Figure 2.1: Probes incorporating exendin-4 which have been designed for PET imaging, synthesised by i) Kiesewetter *et al*., ii) Wu *et al*. and iii) Brand *et al*.[15,27,29,37]

SPECT imaging agents incorporating exendin derivatives have also been increasingly important in an innovative potential treatment for type-1 diabetes – the monitoring of islet graft volume[30]. The use of SPECT and PET probes for this purpose has been widely reported in recent literature[27,30,31,35,36,38], and several initial forays into the area utilised MRI as the imaging modality of choice, albeit with a focus on superparamagnetic iron oxide nanoparticles as a contrast agent[39–41]. This signals another potential use of these compounds, and a possible developing role for gadolinium-based contrast agents incorporating exendin-4 in both the diagnosis and treatment of diabetes.

A further example of the modification of exendin-4 to produce a SPECT imaging agent is one designed to be a technetium chelator incorporating both a hydrazine nicotinamide (HYNIC) and an ethylenediamine diacetic acid (EDDA) moiety: Lys^{40}(Ahx-HYNIC-^{99m}Tc/EDDA)NH_2-exendin-4. This probe was developed by Wild *et al*.[23] and has been studied in humans, where it exhibited localised insulinoma uptake. What was particularly impressive about the studies carried out with this compound is that it enabled biochemically proven tumours to be visualised where other probes had failed to do so[10,42–44]. This probe has also been explored for the study of thyroid tumours [10,23,44].

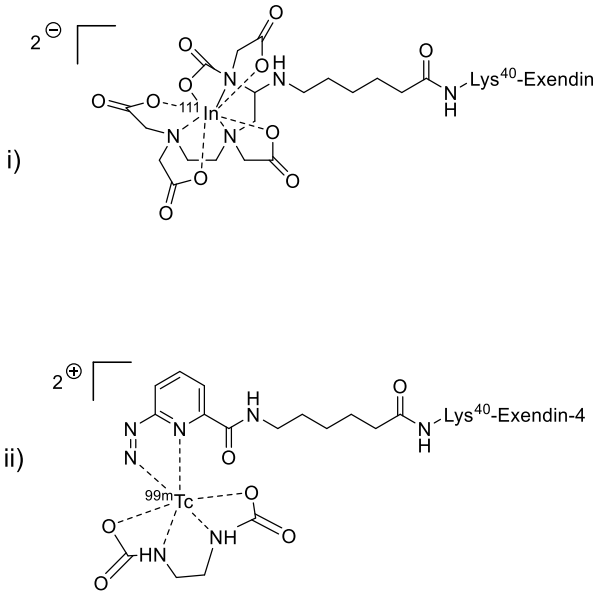


Figure 2.2: SPECT probes conjugated to exendin derivatives: i) [^{111}In-Lys^{40}((Ahx)-DTPA)-exendin-4] and ii) : [Lys^{40}(Ahx-HYNIC-^{99m}Tc/EDDA)NH$_2$-exendin-4][23,33,36,45]. The Tc centre in ii has an oxidation state of +5[46].

Exendin-4 has been successfully utilised as a targeting moiety in both PET and SPECT imaging probes, enabling the study of pancreatic insulinomas originating from β-cells and significant progress towards β-cell mass quantification and islet graft monitoring. Despite the high sensitivity offered by radiochemical imaging techniques, magnetic resonance imaging (MRI) offers much greater spatial resolution and depth penetration, as well as allowing the avoidance of ionising radiation and the time constraints involved in radiochemical syntheses[47]. However, fruitful targeting and visualisation utilising magnetic resonance techniques is less well established. Some work in this area does exist, although this has been largely limited to the conjugation of iron oxide nanoparticles to exendin-4. Notable examples of this strategy have been published by Wang *et al*. and Vinet *et al*., who have recorded differences in contrast enhancement *in vivo* between wild-type mice and disease models[16,17]. Wang *et al*. also incorporated a cyanine fluorophore, Cy5.5, into their scaffold to enable dual modal imaging, which was utilised to identify β-cell uptake of the probe through histological analysis *ex vivo*.

Despite the early promise of nanoparticle contrast agents targeted using exendin-4, there are a number of issues arising from the use of iron oxide species in the clinic. Currently, most clinically-approved nanoparticle based contrast agents have been withdrawn from the market due to a combination of safety concerns, fairly high incidence of painful side effects and poor market share compared to gadolinium-based species[48,49]. Additionally, iron oxide nanoparticles are T_2 contrast agents, which results in negative contrast and a decrease in image brightness, opposed to T_1 agents which result in positive contrast and image brightening[50]. Clinicians prefer the latter as it renders image interpretation easier: signal loss observed with iron oxide nanoparticles can make direct tissue analysis challenging and present difficulties in distinguishing between targeted cells and image artefacts[48,50,51]. *In vivo*, iron oxide

nanoparticles exhibit a high degree of liver and spleen uptake, which can make the targeting of other organs challenging, in spite of the addition of a targeting group[48,50]. Due to the location of the pancreas, in close proximity to the spleen, this could make specific pancreatic imaging particular difficult.

As a highly paramagnetic f-block metal ion with seven unpaired electrons, Gd^{3+} is a prime candidate for the enhancement of T_1 relaxation of water molecules, which results in positive contrast enhancement and therefore image brightening in obtained MR images[47,52]. Polyaminocarboxylate ligands such as 2-[bis[2-[bis(carboxymethyl)amino]ethyl]amino]acetic acid, also referred to as diethylenetraiminepentaacetic acid, (H_5dtpa) are well suited to gadolinium(III) chelation: the first ever clinically-approved MRI contrast agent was $[Gd(OH_2)(dtpa)]^{2-}$ (Magnevist®), which was developed in 1981 and clinically approved in 1988[53]. Forty years further down the line, all current MRI contrast agents in clinical use are gadolinium(III) complexes of this ligand family, which can be accessibly and extensively functionalised [54,55].

2.1.3. Ligand Design and Methodology

Previously, work in the Long group successfully synthesised a dual-modal fluorescent-MRI contrast agent which included a zinc-sensing moiety[56]. This zinc binding capability resulted in uptake of the probe by pancreatic β-cells due to the high levels of zinc(II) ions associated with insulin granule storage[56–58]. We hypothesised that the introduction of a targeting group, such as exendin-4, would enable us to build on this work.

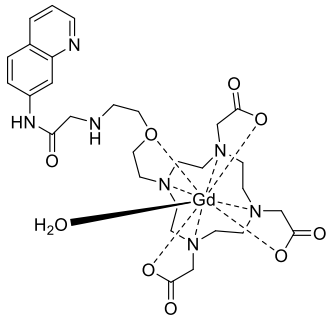


Figure 2.3: The MRI contrast agent developed by Stasiuk *et al*., **Gd1**.[56]

The extensive body of work on exendin-4 derivatives as targeted imaging agents for pancreatic β-cells discussed above has proven the peptide as an effective and reliable targeting moiety. It has been shown that the introduction of a metal chelator does not interrupt the receptor-binding properties of any exendin conjugate, and indeed that a wide variety of metals capable of a host of imaging modalities may be

utilised. In addition, it has been shown that modifications can be made to exendin under mild conditions to produce a range of varied imaging probes.

Former researchers in the Long group, Dr Charlotte Rivas and Dr Emma Coakley, hoped to synthesise an MRI contrast agent which was targeted to the pancreas *via* exendin-4 and incorporated a Gd(III) chelate. A chelator was designed which was based on the ubiquitous Gd(III) ligand 1,4,7,10-tetraazacyclododecane-1,4,7,10-tetraacetic acid, (H_4dota), which was modified with a maleimide group. The maleimide can act as an electrophile, enabling conjugation with a modified variant of exendin-4 with an additional cysteine residue at the 40th position, analogous to the procedures developed by Kiesewetter *et al.*[15]. This agent, **GdEx**, was successfully produced, and its behaviour examined *in vivo* in healthy, wild-type C57BL6/J mice, where initial work showed some contrast enhancement in the pancreas.

2.1.4. Aims and Objectives

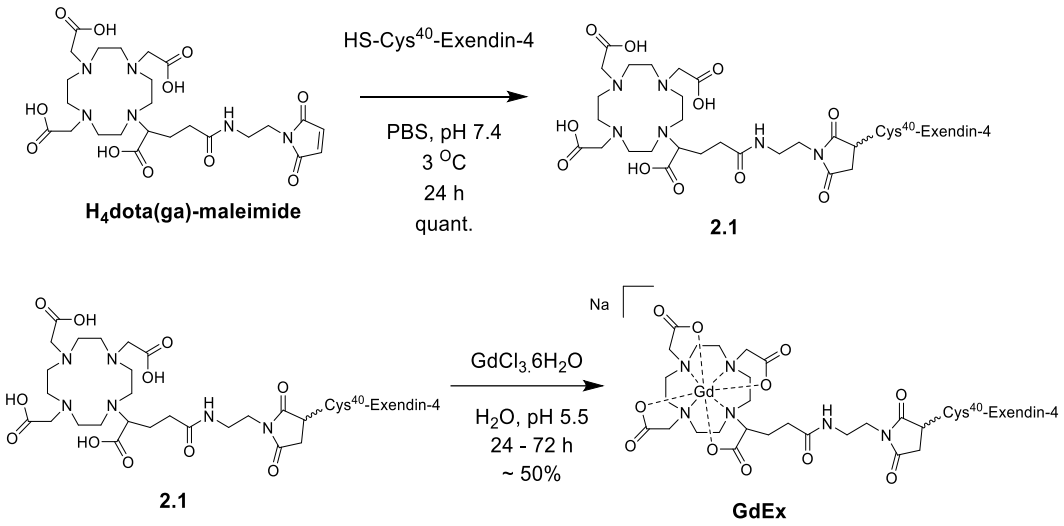
Building on from the success had in the early stages of the development of **GdEx**, this portion of the project hoped to refine the synthetic methodology of the probe's formation to render it a better use of time and resources. Additionally, it was hoped that **GdEx** could be studied in additional mice, both wild-type and a disease model to quantitatively analyse the uptake of the probe in individual animals with a depleted β-cell count. This would assess the compound's capabilities for use in the clinic as a diagnostic tool for diabetes development and open the door to the use of exendin-4 in other metal chelates for MRI contrast agents. Building on the prior work in the group on the zinc-sensing contrast agent **Gd1** (**Figure 2.3**), it was also hoped that a targeted, zinc sensing contrast agent could be produced and tested using the same rationale.

2.2. Results and Discussion

2.2.1. Synthesis of GdEx

The synthetic pathway towards **GdEx** which was devised was simple and straightforward. Similar methodology was employed to that utilised by Kiesewetter *et al.*[15], in which a maleimide group was the key functionality employed to link the targeting moiety to the component of the molecule responsible for imaging. A synthetic route towards H_4dota(ga)-maleimide had previously been developed by Dr Emma Coakley[59], although it was discovered that this compound could be purchased commercially. In the interests of time, the commercial source of H_4dota(ga)-maleimide was utilised throughout this work. Due to the planned *in vivo* work necessary to examine the behaviour of **GdEx** in animals with a depleted β-cell count, it was necessary to improve the yields of this synthetic route, especially as this had

historically relied upon purification by preparative liquid chromatography-mass spectrometry (LCMS), which resulted in very scare amounts of the probe being isolated.



Scheme 2.1: The complete synthetic pathway utilised to isolate **GdEx**.

Electrophilic maleimides are susceptible to attack by nucleophiles such as thiols. As such, the same modified exendin-4 variant with a cysteine residue introduced at the C-terminus (HGEGTFTSDLSKQMEEEAVRLFIEWLKNGGPSSGAPPPS-[C]) can be used to conjugate the peptide to a metal chelator. This was achieved through incubation of the maleimide and Cys^{40}-exendin-4 in PBS (pH 7.4) at 3 °C overnight, giving the free ligand, compound **2.1**, at quantitative yields. Progress of the reaction was monitored by LCMS, which was also used to confirm the extent of conversion.

Complexation of **2.1** to Gd(III) proved to be somewhat more challenging than its synthesis. Early attempts at producing **GdEx** were hampered by only partial complexation of the free ligand to the metal centre. Any free ligand injected into animals for *in vivo* investigation would result in occupation of the GLP-1R receptor sites but provide no contrast enhancement due to the lack of a paramagnetic Gd(III) ion. This would therefore result in a lower signal being recorded in the pancreas, which would result in an underestimate of the binding ability of **GdEx**. As such, the optimisation of the complexation procedure was a key concern.

Early synthetic attempts utilised an initial portion of between 1.5 and 2 equivalents of $GdCl_3 \cdot 6H_2O$ being added to an aqueous solution of **2.1**, which would then be left to stir overnight at pH 5.5. This frequently resulted in only around 50% of the ligand binding to Gd^{3+}, as seen by LCMS. Both **2.1** and **GdEx** would coelute from a C_{18} silica cartridge, rendering isolation of **GdEx** from these reaction mixtures extremely challenging.

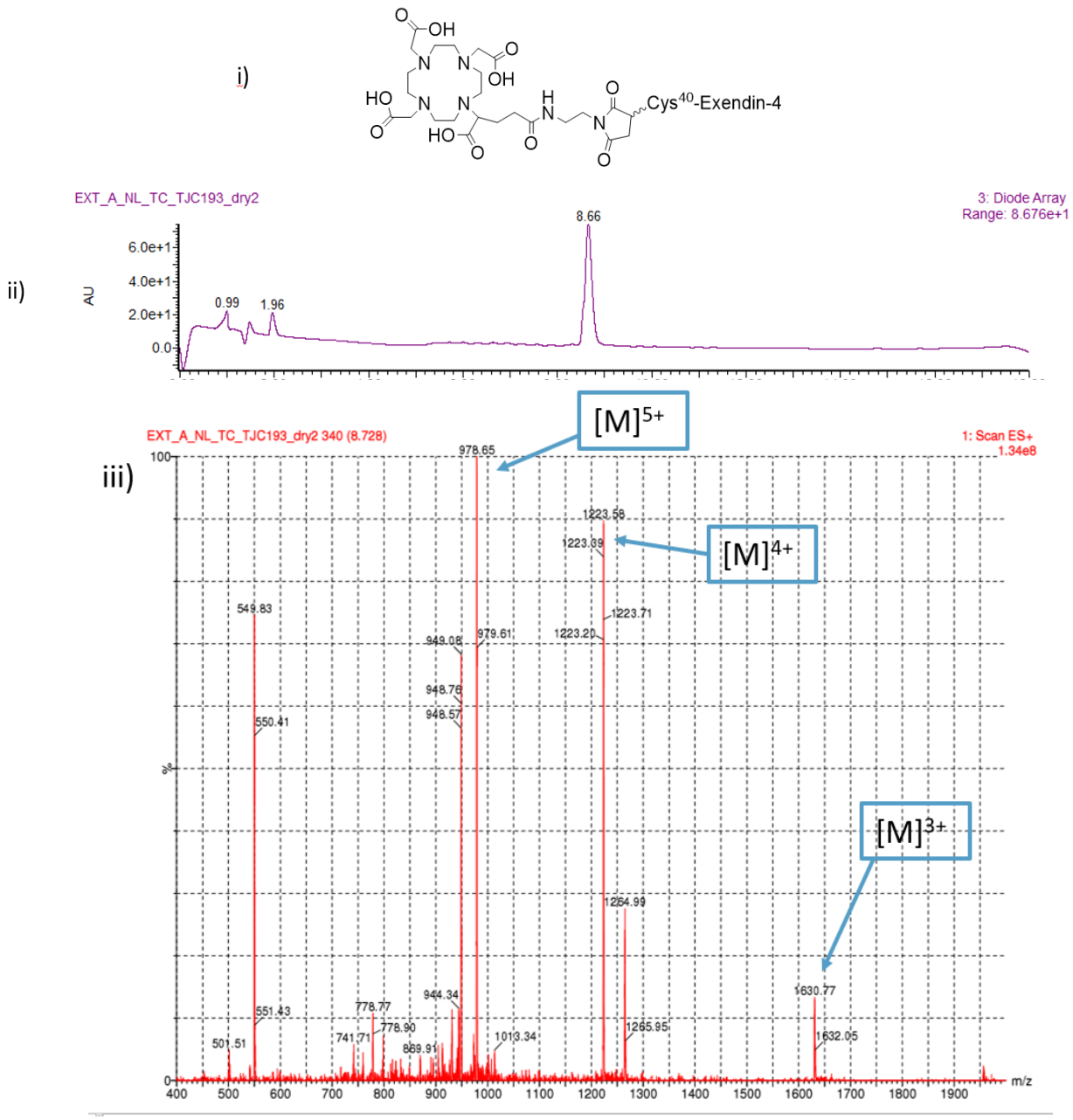


Figure 2.4: **:** Characterisation data (i) structure of the free ligand, compound **2.1**., (ii) LCMS UV absorption trace (5% MeCN/95% H_2O to 95% MeCN/5%H_2O), and (iii) MS of the peak with retention time of 8.66 minutes showing the $[M]^{3+}$, $[M]^{4+}$ an $[M]^{5+}$ peaks at *m/z* = 1630.99, 1223.58 and 978.65 respectively.

Ultimately, it was decided that driving the reaction to completion would provide a more robust synthetic route to **GdEx**. Extreme care had to be taken with this route: one early trial which involved the addition of 3 equivalents of $GdCl_3{\cdot}6H_2O$ resulted in cleavage of the four terminal amino acids from the exendin chain (determined from a peak in the mass spectrum at *m/z* = 1540, corresponding to $[M\text{-}420]^{4+}$), potentially hindering its GLP-1R affinity. This was theorised to be due to the slight Lewis acidity of lanthanide(III) salts which, in excess, could possibly result in cleavage of the amide bonds holding the peptide together.

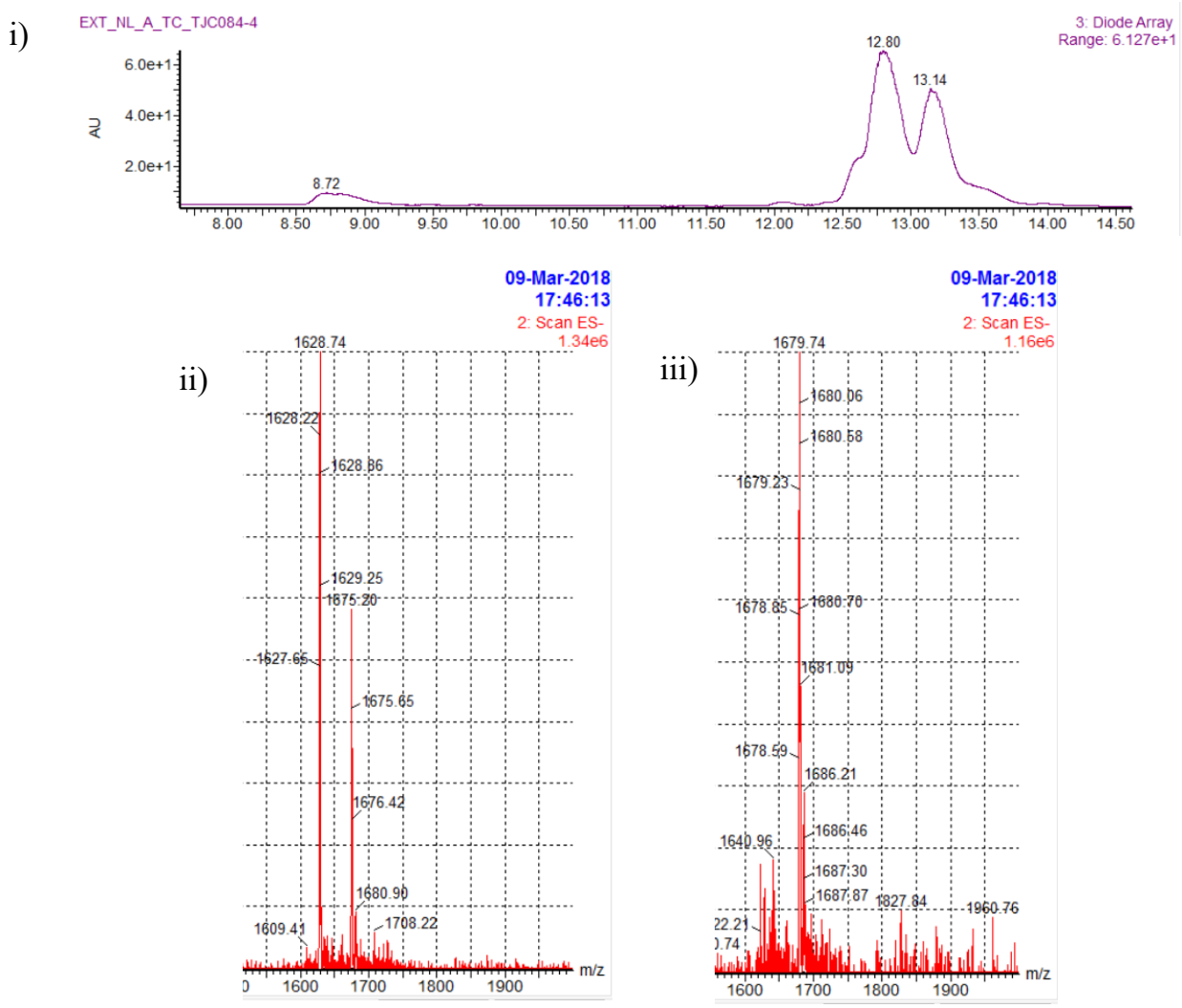


Figure 2.5: i) LCMS trace for an early attempt at **GdEx** synthesis showing the two overlapping peaks ii) the *m/z* spectrum for the peak with a retention time of 12.80 minutes, showing the presence of **2.1** and **GdEx**, iii) the *m/z* spectrum for the peak at 13.14 minutes, showing **GdEx**.

Success was ultimately achieved through portion-wise addition of $GdCl_3{\cdot}6H_2O$ to the reaction mixture alongside continuous monitoring by LCMS and pH adjustment, keeping it in the range of 5.5 to 6.5 consistently. This approach resulted in complete conversion of **2.1** to **GdEx** after between 24 and 72 hours, depending on the scale at which the reaction was carried out. Once LCMS indicated that **2.1** had been consumed, the reaction mixture was lyophilised before being purified *via* reverse phase automated flash chromatography using C_{18} silica. Yields were typically around 50% for this process, with the loss attributed to the purification process: collection during the automated chromatography process was triggered by UV absorbance, which could have resulted in some of **GdEx** being lost. Ultimately however, the probe could reliably be produced at sufficient quantities for the required *in vivo* work utilising this approach. The complete route towards **GdEx** is shown in **Scheme 2.1**.

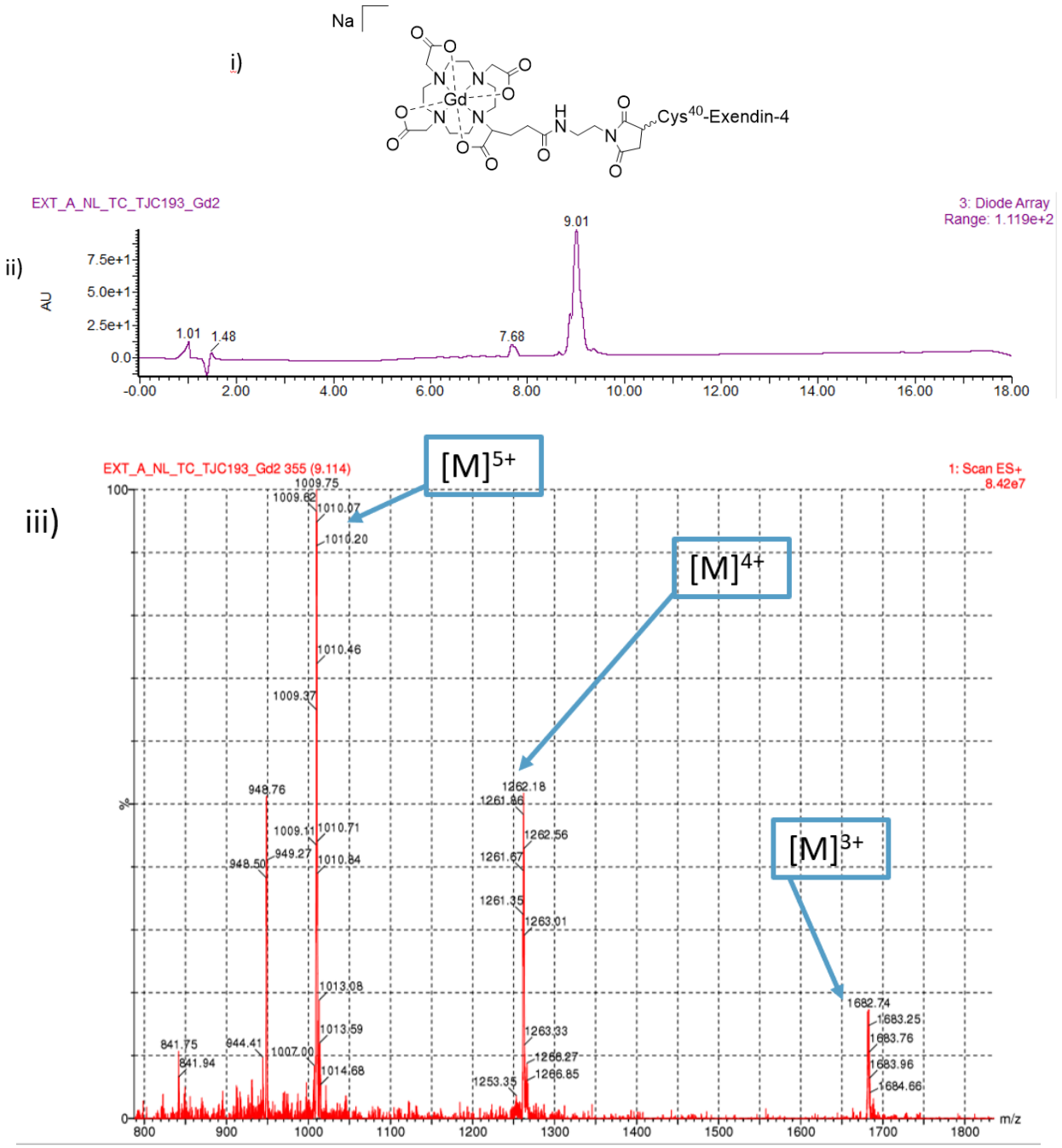


Figure 2.6: Characterisation data (i) LCMS UV absorption trace (5% MeCN/95% H_2O to 95% MeCN/5%H_2O), (ii) MS of the peak with retention time of 9.90 minutes showing the $[M]^{3+}$, $[M]^{4+}$ an $[M]^{5+}$ peaks at *m/z* = 1683.22, 1262.09 and 1009.83 respectively) and (iii) structure of **GdEx**.

The relaxivity of **GdEx** was calculated to be 6.1 mM^{-1} s^{-1}, greater than that of $[Gd(dota)]^-$ which is 4.3 mM^{-1} s^{-1} at 400 MHz[60], an increase likely attributed to the increased molecular weight and rotational correlation time of **GdEx**[61].

2.2.2. *In Vivo* Studies with GdEx: Methodology and Practicalities

2.2.2.1. Experimental Rationale

GdEx was designed to be utilised as an MRI contrast agent capable of pancreas-specific contrast enhancement. Hypothetically, upon translation to the clinic, the agent could be used to scan patients at risk of diabetes over a period of time, with any reduction in contrast enhancement in the pancreas taken to be indicative of a reduction in the number of β-cells in that patient. Falling β-cell mass is known to occur in the progression of type-2 diabetes, and therefore **GdEx** could help identify individuals at risk of developing the disease at an earlier stage compared to existing diagnostic tests. This could enable them to make lifestyle changes to reduce or remove factors known to exacerbate the condition, such as smoking, drinking and a sedentary lifestyle.

Accordingly, it would be necessary to assess the ability of **GdEx** to target the pancreas. This could be done through the injection of the probe into several wild-type mice, the commercially available C57BL6/J. The MR images obtained from these animals would be analysed and the contrast to noise ratio (CNR) in the pancreas measured, with an increase in the signal in the pancreas taken to be indicative of binding between **GdEx** and GLP-1R. The significance of this contrast enhancement could be examined through a comparison with the ubiquitous MRI contrast agent $[Gd(dota)]^-$, which was to be synthesised and taken *in vivo* in the same animal group. Long term, if **GdEx** were to be suitable for use in the diagnosis of diabetes, it should also be able to produce contrast enhancement in the pancreas of individuals with a reduced β-cell count. As such, it was decided to test the probe as a contrast agent in mice with a β-cell specific Dicer deletion (Dicer-KO), which can be induced by the injection of tamoxifen. Dicer is an RNAseIII enzyme which is critical in the production of miRNA essential for the development of functional β-cells[62,63]. Previous work with this mouse strain has shown that Dicer-KO mice exhibit extreme hyperglycaemia and glucose intolerance following a period of four weeks of tamoxifen injections, in conjunction with up to an 80% reduction in mass of β-cells[62]. A sophisticated model developed by the Rutter group utilising these mice has been devised: Dicer-control mice may be bred (Dicer-Ctrl, Dicerfl/fl, Cre-ER negative) which would not express the enzyme Cre-recombinase and therefore, although injected with tamoxifen, should not experience a reduction in β-cell mass. Littermate Dicer-KO (Dicerfl/fl, Cre-ER positive) do express Cre-recombinase, and therefore should have a depletion in the number of β-cells compared to both wild-type and Dicer-Ctrl mice. Scanning of both of these mouse groups with GdEx would be useful in the examination of its ability to target the pancreas in diseased mice.

2.2.2.2. Prior Work

Previous *in vivo* work in the group had been carried out utilising **GdEx** synthesised by Dr Charlotte Rivas and Dr Emma Coakley. These studies were carried out alongside Dr Aida Martinez-Sanchez and Dr Nicoleta Baxan within the Faculty of Medicine, who were responsible for animal maintenance and

study and MRI scanning and data interpretation respectively. The necessary dose of **GdEx** required for pancreatic contrast enhancement, 5.65 mg/mouse, approximately 0.5 mmol kg^{-1}, was established during these experiments. In addition, MRI scans of 5 healthy, wild-type C57BL6/J (WT) mice were carried out using **GdEx**. These scans did show some pancreas specific contrast enhancement, although the data were not fully analysed: a thorough, quantitative analysis of the obtained images had not been carried out, nor had the data been processed to allow for comments to made on the significance of the contrast enhancement. Further to this, it was felt that it would be necessary to draw comparisons between **GdEx** and an untargeted contrast agent to examine the specificity of the probe and to confirm and validate the success of its targeting ability.

2.2.3. Summary of *In Vivo* Data

2.2.3.1. Examination of GdEx in Wild-Type Mice

It was hoped that the specificity, efficacy and targeting ability of **GdEx** could be thoroughly examined by studying its biodistribution and behaviour *in vivo*. Initially, this was pursued by injection of **GdEx** into five male WT mice aged between 12 and 14 weeks. T_1 weighted MRI scans of each of the mice were recorded up to 54 minutes post-injection. The CNR in the pancreas of each mouse was recorded and normalised compared to the signal seen in the spleen. Preliminary results from these scans indicated an increase in CNR in the pancreas, which suggested successful targeting of the β-cells by **GdEx**. To explore whether this CNR increase was due to the exendin-4 moiety and not simply due to the use of a gadolinium-based contrast agent, it was decided to compare the results of these scans with images obtained utilising the ubiquitous MRI contrast agent Na[Gd(dota)]. An additional 5 WT mice were injected with Na[Gd(dota)] at the same molar dosage as **GdEx** and the same scanning procedure carried out. **Figure 2.7** shows an exemplar scan utilising **GdEx** and the defined region of interest: the pancreas.

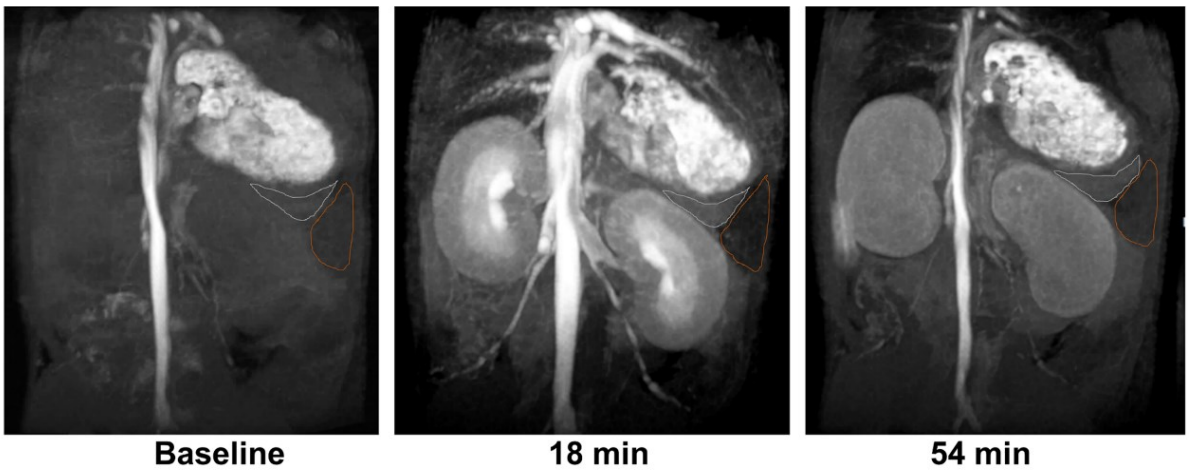


Figure 2.7: MR images of a WT C57BL/6J mouse before (baseline and at 18 and 54 minutes after injection of GdEx. The pancreas is outlined in white and the screen in brown. Some contrast enhancement may be visibly observed in the pancreas. Image produced by Dr Nicoleta Baxan and adapted from reference 63, with permissions[64].

When quantitatively comparing the mice analysed with **GdEx** and Na[Gd(dota)], the CNR in the pancreas observed at baseline levels, i.e. before injection, was considered to be 100%. In the mice scanned with Na[Gd(dota)], there was an observed increase in CNR to around 130%, which occurred at around 18 minutes post-injection. Following this was a steady, gradual decline with a return to baseline contrast levels after 54 minutes. In contrast, the mice injected with **GdEx** showed much stronger contrast enhancement, reaching a peak CNR value of around 175% approximately 20 minutes after contrast agent injection. Whilst this also showed a subsequent decline, the decrease in CNR for the mice scanned with **GdEx** was much slower and CNR values remained consistently higher compared to the usage of Na[Gd(dota)] throughout the duration of the scan. These data can be seen in **Figure 2.8.**

Consistently, a maximum CNR value was observed at between 18 and 21 minutes post-injection. This may coincide with full accumulation of the probes in the pancreas following normal biodistribution pathways. It appears as though this peak is followed by full clearance of the non-specific contrast agent, Na[Gd(dota)], but that there is some significant retention of **GdEx** in the β-cells. The results presented here indicate that the exendin-4 targeting moiety incorporated in **GdEx** is responsible for the contrast enhancement taking place specifically in the pancreas, rather than simply the presence of a highly paramagnetic Gd^{3+} ion. This suggests that, as expected, the introduction of exendin-4 has resulted in improved targeted uptake and retention by pancreatic β-cells, conferring selectivity to a GBCA.

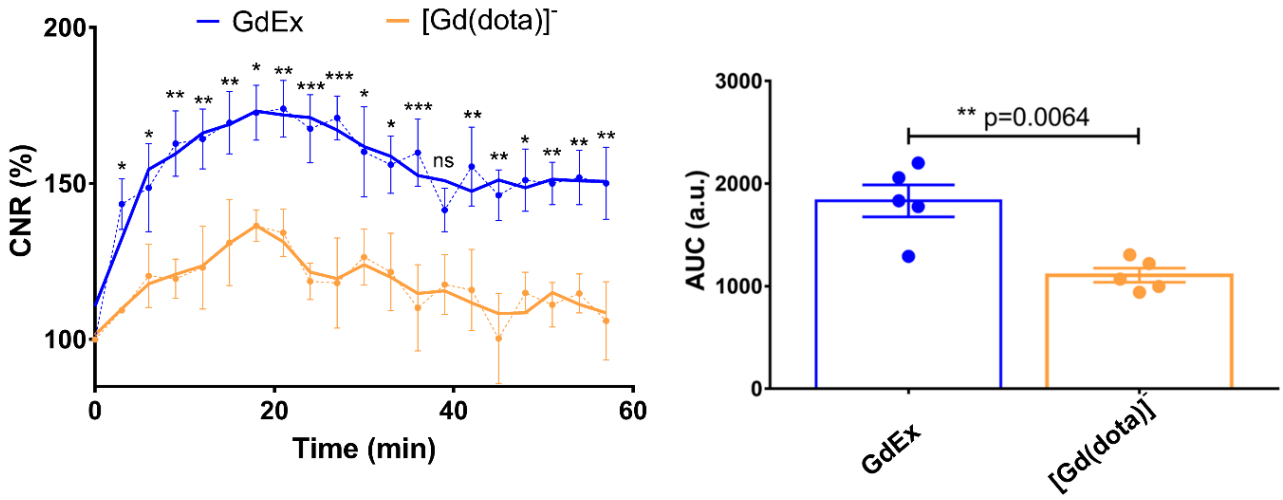


Figure 2.8: Left: CNR in the pancreas over time observed in WT mice injected with **GdEx** (blue) and Na[Gd(dota)] (yellow). Right: The respective areas under each curve. Data: mean ± S.E.M., n=5 animals, *p<0.05, **p<0.01, ***p<0.001, two-way ANOVA (repeated measures), Fisher's LSD test (Time-courses), Student's t test (AUC) using GraphPad Prism 7.0. It is clear that scanning with **GdEx** gives greater contrast enhancement than a non-specific contrast agent. Image produced by Dr Nicoleta Baxan and adapted from reference 63, with permissions[63].

2.2.3.2. Examination of GdEx in Diabetic-Model Mice

As discussed above, if **GdEx** were to be utilised as a contrast agent in the diagnosis monitoring of diabetes progression, it should be able to exhibit some form of ratiometric change in contrast enhancement which is proportional to the β-cell mass. The individuals chosen for examination were Dicer-KO mice – these have an extremely low number of β-cells due to a tamoxifen-induced Dicer deletion (see **2.2.2.1.**).

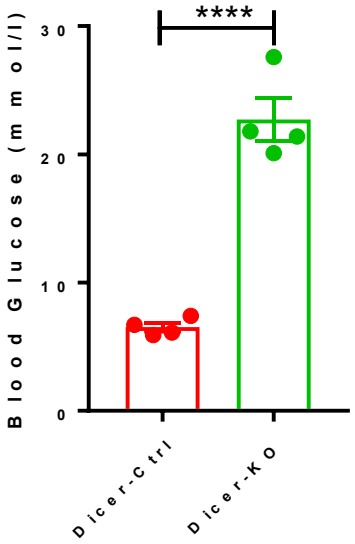


Figure 2.9: Glycemia after MRI in Dicer-KO (green) and littermate controls (Dicer-Ctrl, red). N = 4/genotype. Each dot represents a single mouse. ****p<0.0001, Student's t test. Image produced by Dr Aida Martinez-Sanchez and adapted from reference 63, with permissions[63].

To explore whether **GdEx** is able to detect the associated changes in β-cell mass observed in the Dicer-KO model, 4 Dicer-Ctrl and 4 Dicer-KO mice were injected with tamoxifen before being scanned with **GdEx** 4 weeks later. At the time the MRI scans were carried out, the Dicer-KO mice were strongly hyperglycaemic (**Figure 2.9**), suggesting successful imitation of diabetes. In both sets of Dicer mice, the maximum CNR value was observed at around 21 minutes after injection, as had been seen previously with the WT mice. In the Dicer-Ctrl mice this peak was at a CNR of approximately 145%, whereas in Dicer-KO mice this was at 120%, although the data at these early time points did not show statistical significance. Additionally, the area under the curve (AUC) of CNR against time for both sets of animals did not show any major differences in the first 21 minutes of the scan. As seen in the WT animals, this peak in signal enhancement was followed by a steady decline, presumably as **GdEx** was cleared from the pancreas. What was interesting to note at this time was that there was a marked decline in CNR in the Dicer-KO animals, with the CNR values approaching baseline levels after 45 minutes. In the Dicer-Ctrl mice this was not observed, with CNR values of around 130% seen up until the end of the scan at 54 minutes post-injection. This could also be seen from the AUC analysis, which showed

around a 1.8-fold greater retention of **GdEx** in the Dicer-Ctrl group compared to the Dicer-KO mice. These data suggest that the elimination and washout of **GdEx** from the pancreas occurred more rapidly in Dicer-KO individuals, in combination with the lower overall contrast enhancement.

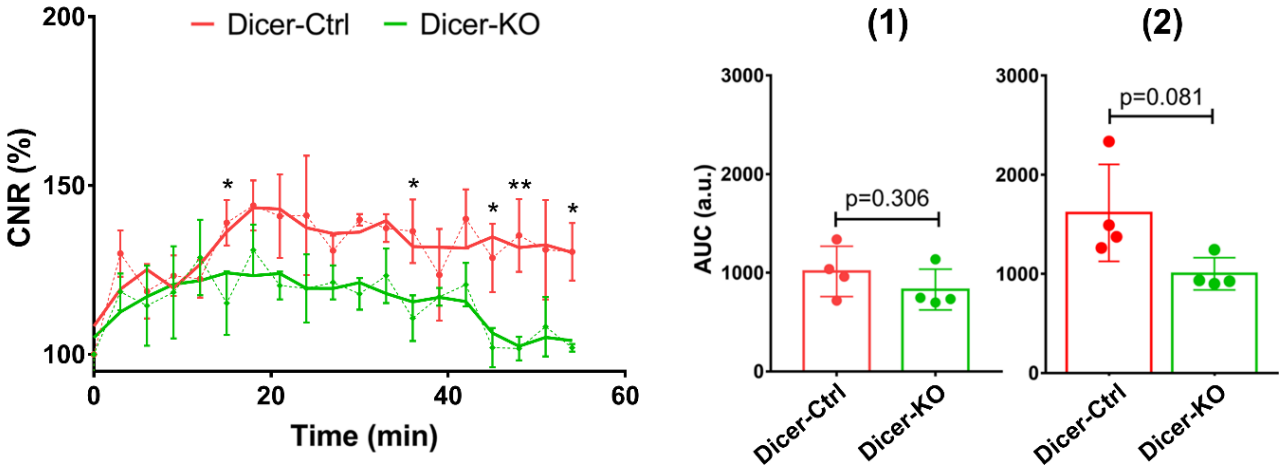


Figure 2.10: Left: CNR over time for Dicer-Ctrl (red) and Dicer-KO (green) mice after injection with **GdEx**. Data: mean ± S.E.M, N = 4/phenotype. Right: AUC analysis at 1) 0 to 21 minutes, 2) 21 to 54 minutes post-injection with **GdEx**. Each dot is the AUC for a single mouse. *p<0.05, **p<0.01, ***p<0.001, two-way ANOVA (repeated measures), Fisher's LSD test (Time-courses), Student's t test (AUC) using GraphPad Prism 7.0. Image produced by Dr Nicoleta Baxan and adapted from reference 63, with permissions[63].

The apparent improved retention of **GdEx** in the pancreas of the WT and Dicer-Ctrl mice compared to the Dicer-KO and in WT mice injected with Na[Gd(dota)] suggest that the exendin-4 targeting moiety is responsible for binding to the GLP-1R receptors in pancreatic β-cells and preventing elimination of the probe from the pancreas, resulting in contrast enhancement over a longer period of time and potentially leading towards β-cell quantification through changes in CNR.

It is noteworthy that the CNR values observed in the Dicer-Ctrl mice were considerably lower than in the WT mice. This was unexpected as the Dicer-Ctrl animals did not present any undue hyperglycaemia and are expected to have a normal, healthy β-cell count. In addition, the Dicer-Ctrl mice share a genetic origin (C57BL/6J), age and sex with the WT animals. One possible explanation is that the Dicer-Ctrl animals were intraperitoneally injected with tamoxifen dissolved in a large volume of corn oil: 100µL every day for 5 days for each individual. It could be that this resulted in a large presence of corn oil around the organs in both Dicer mouse sets, which could have interfered with local tissue relaxivity and resulted in a non-specific reduction in CNR around the pancreas.

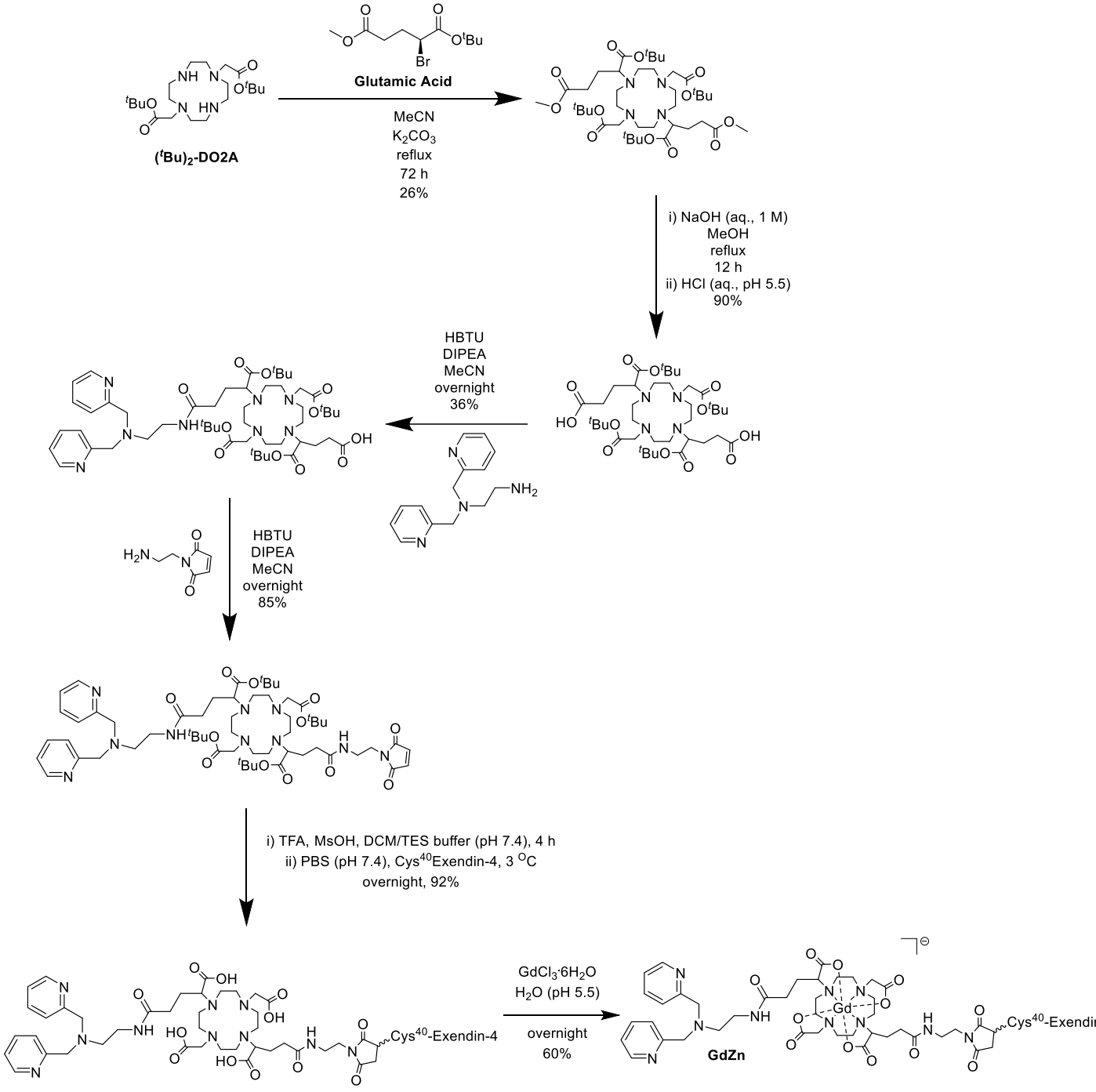
2.3. A Zinc-Sensing, Targeted Contrast Agent, GdZn

Both types of diabetes mellitus are known to be associated with a decrease in the mass and functionality of pancreatic β-cells and assessing any change in mass of these cells has the potential to allow for earlier diagnosis of the disease, in addition to monitoring the response to any treatment[4,6,56,65,66].

Zinc(II) ions aid the stabilisation of insulin hexamers, and therefore highly abundant in β-cells when compared to the rest of the pancreas[56–58]. Indeed, zinc deficiency has also been proposed as a contributary factor in the development of type-2 diabetes[58].

It has been hypothesised that an imaging probe incorporating a zinc-binding moiety could enhance its selectivity *in vivo* – although Zn^{2+} is the second most abundant ion in biological systems, it is most highly concentrated in the brain, pancreas and spermatozoa[57,67]. A probe capable of chelating to zinc(II) ions may localise to these zinc-rich regions of the body, avoiding its accumulation in organs and tissues which are not of interest. Quantitative assessment of β-cell mass is possible through the use of zinc sensors: for MRI, binding to a zinc(II) ion typically accompanies a ratiometric increase in relaxivity of the probe and therefore greater contrast enhancement[56,57,68,69]. To date, the majority of the work on zinc sensors has used amine-based chelating group and, amongst these, the dipicolylamine (DPA) moiety has risen to prominence due to its high affinity and selectivity for zinc(II) ions[56,67,70].

2.3.1. Probe Synthesis



Scheme 2.2: The synthesis of **GdZn**.

Aa zinc-sensing probe was designed which utilised exendin-4 as a targeting moiety, **GdZn**. The total synthetic route taken towards this probe, which is shown above, followed a similar methodology to **GdEx**, with a maleimide group being introduced to allow bioconjugation to a modified exendin-4 variant. The probe also incorporated a DPA moiety which could act as a zinc sensor. The synthesis of the probe, detailed below, was carried out by Dr Emma Coakley.

The macrocyclic chelator 1,4,7,10-tetraazacyclododecane-1,7-diacetic acid (H_2do2a) was used as the starting framework for the synthesis of **GdZn**. Its di-tertbutyl protected analogue, (^{t}Bu)$_2$-do2a, was prepared following literature procedures[71]. Alkylation of the two free amine nitrogen atoms was then carried out, introducing two arms of the ligand which were based on an orthogonally protected analogue of glutamic acid, which was also synthesised following literature procedures[72,73]. Deprotection of the two methyl esters on this compound was achieved through a standard basic hydrolysis and producing two free carboxylic acid groups. DPA was introduced in the form of *N*-*N*-bis(2-pyridyl-methyl)ethylenediamine, which contains an ethylenediamine bridge. This amine was coupled to the free carboxylic acids on the macrocycle using the coupling reagent 2-(1*H*-benzotriazol-1-yl)-1,1,3,3-tetramethyluronium hexafluorophosphate (HBTU), producing a mono-substituted variant incorporating the necessary zinc-sensing capability. Subsequent coupling of this compound to the maleimide-containing *N*-2(aminoethyl)maleimide (also prepared *via* literature procedures[74]) gave the fully protected ligand.

Deprotection of this ligand was necessary to introduce gadolinium and enable the compound to be used as an MRI contrast agent. This was achieved by subjecting the protected ligand to a mixture of trifluoroacetic acid (TFA) and MsOH in a buffer solution of *N*-[tris(hydroxymethyl)methyl]-2-aminoethanesulfonic acid (TES) at pH 7.4, liberating all of the carboxylic acids remaining in the ligand. Due to concerns about hydrolysis of the maleimide group, purification was not carried out at this stage and, after confirming that deprotection had been successful through LCMS, Cys^{40}exendin-4 was immediately introduced under the same conditions as in the synthesis of **GdEx** – incubation in PBS overnight at 3 °C. This targeted ligand could then be complexed to Gd(III) through typical macrocyclic chelation conditions to produce the targeted, zinc-sensing contrast agent **GdZn**.

2.3.2. *In Vivo* Studies with GdZn

As with **GdEx**, it was decided to explore the biodistribution of **GdZn** *in vivo* to establish its suitability as an MRI contrast agent and ability at quantitative assessment of β-cell mass through changes in relaxivity. Initially, the probe was injected at the same dose as **GdEx**, (0.5 mmol kg^{-1}) into two WT mice, each of which were scanned for a period of at least 60 minutes.

What was surprising in the scans utilising **GdZn** was that minimal T_1 contrast enhancement was observed in the pancreas: there was no increase above baseline levels and indeed some negative CNR values at short times immediately after injection, indicating that the brightness of the pancreas was lower than that in the surrounding tissues. The only contrast enhancement which was seen was in the kidneys, likely due to washout of the saline solution which the probe was injected in. Additionally, a darkening in the liver, which had been observed in mice administered with **GdEx** (likely due to a T_2 effect observed at high concentrations of Gd^{3+}) was also not seen in these mice. What was striking in these mice was a darkening of the blood vessels was observed. It is possible that this was indicative of

a large concentration of gadolinium(III) ions in the bloodstream, causing the T_2 effect which had been expected in the liver. It is possible that an interaction between the probe and serum albumins within the mouse could be responsible for the probe's retention in the blood vessels. This could have resulted in a size increase, with **GdZn** and serum proteins forming a large complex which could then potentially prevent the probe from crossing the blood vessel walls. Such interactions have been observed before by other groups working with zinc-sensing MR contrast agents[56,68,75].

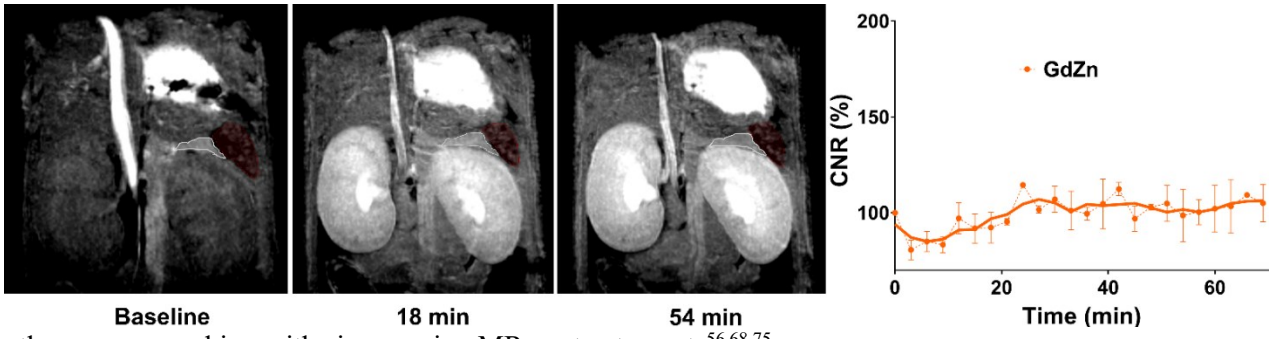


Figure 2.11: Left: Representative MRI of a healthy C57BL/6J mouse abdomen before (baseline) and at 18 min. and 54 min. after **GdZn** injection. The pancreas is outlined in white, the spleen in brown. Right: CNR against time in the pancreas vs spleen (n = 2) indicating no pancreatic signal enhancement above baseline levels. Image produced by Dr Nicoleta Baxan.

Due to the lengthy synthesis and expensive nature of the probe, in conjunction with the disappointing contrast enhancement observed with **GdZn**, no further experiments were carried out. Alterations in probe design, perhaps through substituting the dipicolylamine zinc sensing moiety, could also be carried out, or the *in vivo* behaviour of this probe further explored in future work with exendin-targeted probes.

2.4. Conclusions and Outlook

This Chapter has described an improved synthesis of **GdEx**, in comparison to the longer pathway which was previously developed in the Long group[59]. This synthesis is both simple and straightforward and could be further developed to allow complexation to other metal centres for use in MRI contrast agents, such as manganese(II). This short reaction pathway results in the production of **GdEx** at moderate yields, providing sufficient probe for *in vivo* analysis.

Building on the initial promising *in vivo* studies carried out with **GdEx**, which suggested pancreas-specific contrast enhancement in WT mice, further experiments were carried out utilising Na[Gd(dota)] as a contrast agent, to assess whether this CNR increase was statistically significant. These experiments showed that **GdEx** resulted in superior contrast enhancement, up to 40% higher than Na[Gd(dota)], the current gold standard of MRI contrast agents. This contrast enhancement was as high as 70% over baseline levels, indicative of successful targeting of the GLP-1R receptor and therefore pancreatic β-cells through the inclusion of the exendin-4 targeting moiety. This also confirms that the incorporation

of exendin-4 into a bifunctional chelator for GBCAs does not interfere with the biological properties of the peptide.

Critically, in addition to a CNR increase in the pancreas of healthy WT mice, **GdEx** exhibits a reduced level of retention in Dicer-KO compared to Dicer-Ctrl animals. As Dicer-KO mice have an extremely low β-cell mass, this is indicative that **GdEx** is able to detect deterioration of these cells *in vivo*. There is currently some debate in the field around the contribution of β-cell mass to the progression of T2D, primarily due to a lack of reliable methods of measuring β-cell mass in living organisms. **GdEx** is both stable and non-toxic *in vivo* and therefore could act as a potent tool could help settle this debate amongst the research community. Aiding the quantification of these vital cells using MRI could help indicate whether individuals are at risk of diabetes development, or monitor the success of islet grafts, as successfully employed with SPECT and PET.

One major limitation of **GdEx** is the large quantity necessary for successful scans, especially when compared to other imaging modalities. Despite extensive dose optimisation studies previously in the group showing that half the concentration of **GdEx** may be used compared to that of Na[Gd(dota)] in the clinic (0.05 mmol kg^{-1} and 0.1 mmol kg^{-1} respectively)[59]. However, due to the large molecular weight of the exendin-4 moiety, each of these scans utilised 5.65 mg of **GdEx** per mouse. Extrapolating this dose regime to humans could result in more than as much as 20 g of the probe being required per scan, although this would involve reduced patient exposure to gadolinium. Whilst the mice in this work did not exhibit any excessive hypoglycaemia after injection, it is almost certain that the intravenous administration of such a large quantity of compound would result in numerous adverse effects in human subjects: exenatide treatment has been shown to result in nausea and vomiting even at the μg kg^{-1} level[76]. The low sensitivity of MRI is a well-established problem within the field but is counteracted by the excellent spatial resolution and depth penetration of the technique, which radiochemical techniques cannot compete with. As such, this work acts as proof of principle: the development of exendin-4 targeted GBCAs for MRI which are capable of pancreatic β-cell quantification is possible. This opens the door for the development of alternative GBCAs which are targeted to the pancreas, which could allow the measurement of β-cell mass whilst avoiding the exposure of patients to ionising radiation and the synthetic challenges associated with radiochemistry. It is hoped that **GdEx** could represent a foundation for the development of future probes that could be used for early diagnosis and monitoring of diabetes in the clinic.

After validation of the specificity of **GdEx** and indication that it is possible to quantify β-cells through its usage, future work in this area will focus on the development of GBCAs targeted to pancreatic β-cells through a variety of methods. Indeed, there are many other potent, stable agonists of GLP-1R which could be explored, and the targeting of other receptors over-expressed by pancreatic β-cells is discussed in other Chapters of this thesis. In addition, this bioconjugation strategy and synthetic route

could be extended to incorporate other metal centres; or diverged to examine other chelators for gadolinium(III). Other animal strains, such as alternative models for diabetes, could also be explored to further probe the retention of **GdEx** in the pancreas, and this could also be assessed through *ex vivo* analysis.

The design and synthesis of **GdZn** was carried out successfully. Despite the probe's relative complexity, it can be derived from a robust synthetic pathway, albeit with a yield of just 4% over 6 steps. Despite the hopes that **GdZn** would complement **GdEx** as a zinc-sensing, exendin-targeted contrast agent to enable improved β-cell mass quantification, the *in vivo* work which was carried out failed to show the probe leaving the bloodstream of healthy, wild-type mice, resulting in no pancreas-specific contrast enhancement. It was hypothesised that this was due to an interaction between **GdZn** and some serum albumin proteins, resulting the formation of a large ternary complex which was not then able to enter the cells of the pancreas, despite the zinc-sensing and exendin moieties. Whilst this was disappointing, it may be that these results could aid our understanding of interactions *in vivo* between zinc-chelating species and endogenous peptides. Additionally, there is the potential for modifications to this probe to be made to try and explore its *in vivo* interactions further – for example, this could be by altering the zinc-sensing moiety, perhaps introducing one with a lower affinity for zinc(II) ions.

2.5. References

1 J. J. Holst, *Physiol. Rev.*, 2007, 87, 1409–1439.

2 Y. Seino, M. Fukushima and D. Yabe, *J Diabetes Invest*, 2010, **1**, 8–23.

3 L. J. Miller, P. M. Sexton, M. Dong and K. G. Harikumar, *Int. J. Obes. Suppl.*, 2014, **4**, S9–S13.

4 K. Mikkola, C. Bin Yim, V. Fagerholm, T. Ishizu, V. V. Elomaa, J. Rajander, J. Jurttila, T. Saanijoki, T. Tolvanen, M. Tirri, E. Gourni, M. Béhé, M. Gotthardt, J. C. Reubi, H. Mäcke, A. Roivainen, O. Solin and P. Nuutila, *Mol. Imaging Biol.*, 2014, **16**, 255–263.

5 H. Abe, T. Uchida, A. Hara, H. Mizukami, K. Komiya, M. Koike, N. Shigihara, Y. Toyofuku, T. Ogihara, Y. Uchiyama, S. Yagihashi, Y. Fujitani and H. Watada, *Endocrinology*, 2013, **154**, 4512–4524.

6 U. Werner, G. Haschke, A. W. Herling and W. Kramer, *Regul. Pept.*, 2010, **164**, 58–64.

7 A. E. Adriaenssens, B. Svendsen, B. Y. H. Lam, G. S. H. Yeo, J. J. Holst, F. Reimann and F. M. Gribble, *Diabetologia*, 2016, **59**, 2156–2165.

8 J. P. Raufman, *Regul. Pept.*, 1996, 61, 1–18.

9 D. Parkes, C. Jodka, P. Smith, S. Nayak, L. Rinehart, R. Gingerich, K. Chen and A. Young, *Drug Dev. Res.*, 2001, **53**, 260–267.

10 A. Jodal, R. Schibli and M. Béhé, *Eur. J. Nucl. Med. Mol. Imaging*, 2017, **44**, 712–727.

11 M. A. Pfeffer, B. Claggett, R. Diaz, K. Dickstein, H. C. Gerstein, L. V. Køber, F. C. Lawson, L. Ping, X. Wei, E. F. Lewis, A. P. Maggioni, J. J. V. McMurray, J. L. Probstfield, M. C. Riddle, S. D. Solomon and J.-C. Tardif, *N. Engl. J. Med.*, 2015, **373**, 2247–2257.

12 B. Manandhar and J. M. Ahn, *J. Med. Chem.*, 2015, **58**, 1020–1037.

13 Q. Wang and P. Brubaker, *Diabetologia*, 2002, **45**, 1263–1273.

14 L. Farilla, H. Hui, C. Bertolotto, E. Kang, A. Bulotta, U. Di Mario and R. Perfetti, *Endocrinology*, 2002, **143**, 4397–4408.

15 D. O. Kiesewetter, H. Gao, Y. Ma, G. Niu, Q. Quan, N. Guo and X. Chen, *Eur J Nucl Med Mol Imaging*, 2012, **39**, 463–473.

16 L. Vinet, S. Lamprianou, A. Babič, N. Lange, F. Thorel, P. L. Herrera, X. Montet and P. Meda, *Diabetologia*, 2014, **58**, 304–312.

17 P. Wang, B. Yoo, J. Yang, X. Zhang, A. Ross, P. Pantazopoulos, G. Dai and A. Moore, *Diabetes*, 2014, **63**, 1465–1474.

18 Y. Luo, Q. Pan, S. Yao, M. Yu, W. Wu, H. Xue, D. O. Kiesewetter, Z. Zhu, F. Li, Y. Zhao and X. Chen, *J. Nucl. Med.*, 2016, **57**, 715–720.

19 R. K. Selvaraju, I. Velikyan, L. Johansson, Z. Wu, I. Todorov, J. Shively, F. Kandeel, O. Korsgren and O. Eriksson, *J Nucl Med*, 2013, **54**, 1458–1463.

20 M. Brom, L. Joosten, C. Frielink, H. Peeters, D. Bos, M. Van Zanten, O. Boerman and M. Gotthardt, *Diabetes*, 2018, **67**, 2012–2018.

21 H. Kimura, N. Fujita, K. Kanbe, H. Matsuda, H. Watanabe, K. Arimitsu, H. Fujimoto, K. Hamamatsu, Y. Yagi, M. Ono, N. Inagaki and H. Saji, *Bioorg. Med. Chem.*, 2017, **25**, 5772–5778.

22 L. Joosten, M. Brom, H. Peeters, D. Bos, E. Himpe, L. Bouwens, O. Boerman and M. Gotthardt, *Mol. Pharm.*, 2019, **16**, 4024–4030.

23 D. Wild, A. Wicki, R. Mansi, M. Behe, B. Keil, P. Bernhardt, G. Christofori, P. J. Ell and H. R. Macke, *J. Nucl. Med.*, 2010, **51**, 1059–1067.

24 A. Sowa-Staszczak, M. Trofimiuk-Müldner, A. Stefańska, M. Tomaszuk, M. Buziak-Bereza, A. Gilis-Januszewska, A. Jabrocka-Hybel, B. Głowa, M. Małecki, T. Bednarczuk, G. Kamiński, A. Kowalska, R. Mikołajczak, B. Janota and A. Hubalewska-Dydejczyk, *PLoS One*, 2016, **11**, 1–13.

25 M. Gotthardt, G. Lalyko, J. van Eerd-Vismale, B. Keil, T. Schurrat, M. Hower, P. Laverman, T. M. Behr, O. C. Boerman, B. Göke and M. Béhé, *Regul. Pept.*, 2006, **137**, 162–167.

26 T. Reiner, G. Thurber, J. Gaglia, C. Vinegoni, C. W. Liew, R. Upadhyay, R. H. Kohler, L. Li, R. N. Kulkarni, C. Benoist, D. Mathis and R. Weissleder, *Proc. Natl. Acad. Sci.*, 2011, **108**, 12815–12820.

27 Z. Wu, I. Todorov, L. Li, J. R. Bading, Z. Li, I. Nair, K. Ishiyama, D. Colcher, P. E. Conti, S. E. Fraser, J. E. Shively and F. Kandeel, *Bioconjug. Chem.*, 2011, **22**, 1587–1594.

28 Y. Luo, Q. Pan, S. Yao, M. Yu, W. Wu, H. Xue, D. O. Kiesewetter, Z. Zhu, F. Li, Y. Zhao and X. Chen, *J Nucl Med*, 2016, **57**, 715–720.

29 C. Brand, D. Abdel-Atti, Y. Zhang, S. Carlin, S. M. Clardy, E. J. Keliher, W. A. Weber, J. S. Lewis and T. Reiner, *Bioconjugate Chem*, 2014, **25**, 1323–1330.

30 W. A. Eter, I. Van Der Kroon, K. Andralojc, M. Buitinga, S. M. A. Willekens, C. Frielink, D. Bos, L. Joosten, O. C. Boerman, M. Brom and M. Gotthardt, *Sci. Rep.*, , DOI:10.1038/s41598-017-07815-3.

31 I. Van Der Kroon, L. Joosten, B. A. Nock, T. Maina, O. C. Boerman, M. Brom and M. Gotthardt, *Mol. Pharm.*, 2016, **13**, 3478–3483.

32 L. Joosten, M. Brom, H. Peeters, S. Heskamp, M. Béhé, O. Boerman and M. Gotthardt, *Mol. Pharm.*, 2018, **15**, 486–494.

33 D. Wild, B. Martin, G. Christofori, J. C. Reubi and R. M. Helmut, *J. Nucl. Med.*, 2006, **40**, 2025–2034.

34 M. Brom, W. J. G. Oyen, L. Joosten, M. Gotthardt and O. C. Boerman, *Eur. J. Nucl. Med. Mol. Imaging*, 2010, **37**, 1345–1355.

35 M. Brom, L. Joosten, C. Frielink, O. Boerman and M. Gotthardt, *Diabetes*, 2015, **64**, 1324–1328.

36 M. Brom, W. Woliner-Van Der Weg, L. Joosten, C. Frielink, T. Bouckenooghe, P. Rijken, K. Andralojc, B. J. Göke, M. De Jong, D. L. Eizirik, M. Béhé, T. Lahoutte, W. J. G. Oyen, C. J. Tack, M. Janssen, O. C. Boerman and M. Gotthardt, *Diabetologia*, 2014, **57**, 950–959.

37 H. Gao, G. Niu, M. Yang, Q. Quan, Y. Ma, E. N. Murage, J.-M. Ahn, D. O. Kiesewetter and X. Chen, *Mol. Pharm.*, 2011, **8**, 1775–1782.

38 F. Pattou, J. Kerr-Conte and D. Wild, *N. Engl. J. Med.*, 2010, 363, 1289–1290.

39 D. Jirák, J. Kríz, V. Herynek, B. Andersson, P. Girman, M. Burian, F. Saudek and M. Hájek, *Magn. Reson. Med.*, 2004, **52**, 1228–1233.

40 F. Saudek, D. Jirák, P. Girman, V. Herynek, M. Dezortová, J. Kříž, J. Peregrin, Z. Berková, K. Zacharovová and M. Hájek, *Transplantation*, 2010, **90**, 1602–1606.

41 N. V Evgenov, Z. Medarova, G. Dai, S. Bonner-Weir and A. Moore, *Nat. Med.*, 2006, **12**, 144–148.

42 K. Senica, A. Tomazic, A. Skvarca, P. Kolenc Peitl, R. Mikolajczak, A. Hubalewska-Dydejczyk and L. Lezaic, *Mol. Imaging Biol.*, 2020, **22**, 165–172.

43 A. Carollo, S. Papi, C. M. Grana, L. Mansi and M. Chinol, *Curr. Radiopharm.*, 2019, **12**, 107–125.

44 D. Pach, A. Sowa-Staszczak, A. Jabrocka-Hybel, A. Stefańska, M. Tomaszuk, R. Mikołajczak, B. Janota, M. Trofimiuk-Müldner, E. Przybylik-Mazurek and A. Hubalewska-Dydejczyk, *Int. J.*

Endocrinol., 2013, **2013**, e384508.

45 A. Sowa-Staszczak, M. Trofimiuk-Müldner, A. Stefańska, M. Tomaszuk, M. Buziak-Bereza, A. Gilis-Januszewska, A. Jabrocka-Hybel, B. Głowa, M. Małecki, T. Bednarczuk, G. Kamiński, A. Kowalska, R. Mikołajczak, B. Janota and A. Hubalewska-Dydejczyk, *PLoS One*, 2016, **11**, 1–13.

46 R. C. King, M. Bashir-Uddin Surfraz, S. C. G Biagini, P. J. Blower and S. J. Mather, , DOI:10.1039/b705111e.

47 G.-L. Law and W.-T. Wong, in *The Chemistry of Molecular Imaging*, eds. N. J. Long and W.-T. Wong, John Wiley & Sons, Hoboken, U.S.A., 2015, pp. 1–24.

48 D. Kim, J. Kim, Y. Il Park, N. Lee and T. Hyeon, , DOI:10.1021/acscentsci.7b00574.

49 Y.-X. J. Wang, *Quant. Imaging Med. Surg.*, 2011, **1**, 35–40.

50 J. Gallo and N. J. Long, in *The Chemistry of Molecular Imaging*, eds. N. J. Long and W.-T. Wong, John Wiley & Sons, Hoboken, U.S.A., 2015, pp. 199–224.

51 J. W. M. Bulte and D. L. Kraitchman, *NMR Biomed.*, 2004, 17, 484–499.

52 A. D. Sherry, P. Caravan and R. E. Lenkinski, *J. Magn. Reson. Imaging*, 2009, **30**, 1240–1248.

53 H. P. Niendorf, *Bristol Medico-Chirurgical J.*, 1988, **103**, 34–34.

54 S. Faulkner and O. A. Blackburn, in *The Chemistry of Molecular Imaging*, eds. N. Long and W.-T. Wong, John Wiley & Sons, Hoboken, U.S.A., 2015, pp. 179–197.

55 T. J. Clough, L. Jiang, K. L. Wong and N. J. Long, *Nat. Commun.*, 2019, 10.

56 G. J. Stasiuk, F. Minuzzi, M. Sae-Heng, C. Rivas, H. Juretschke, L. Piemonti, P. R. Allegrini, D. Laurent, A. R. Duckworth, A. Beeby, G. A. Rutter and N. J. Long, *Chem. – A Eur. J.*, 2015, **21**, 5023–5033.

57 K. Kikuchi, K. Komatsu and T. Nagano, *Curr. Opin. Chem. Biol.*, 2004, **8**, 182–191.

58 L. G. Sondergaard, M. Stoltenberg, P. Doering, A. Flyvbjerg and J. Rungby, *Histol. Histopathol.*, 2006, **21**, 619–625.

59 E. Coakley, Imperial College London, 2018.

60 S. Aime, M. Botta, S. G. Crich, G. Giovenzana, R. Pagliarin, M. Sisti and E. Terreno, *Magn. Reson. Chem.*, 1998, **36**, S200–S208.

61 P. D. Garimella, A. Datta, D. W. Romanini, K. N. Raymond and M. B. Francis, *J. Am. Chem. Soc.*, 2011, **133**, 14704–14709.

62 A. Martinez-Sanchez, M. S. Nguyen-Tu and G. A. Rutter, *Mol. Endocrinol.*, 2015, **29**, 1067–1079.

63 T. Melkman-Zehavi, R. Oren, S. Kredo-Russo, T. Shapira, A. D. Mandelbaum, N. Rivkin, T. Nir, K. A.

Lennox, M. A. Behlke, Y. Dor and E. Hornstein, *EMBO J.*, 2011, **30**, 835–845.

64 T. J. Clough, N. Baxan, E. J. Coakley, C. Rivas, L. Zhao, I. Leclerc, A. Martinez-Sanchez, G. A. Rutter and N. J. Long, *Dalt. Trans.*, 2020, **49**, 4732–4740.

65 R. Hernandez, S. A. Graves, T. Gregg, H. R. VanDeusen, R. J. Fenske, H. N. Wienkes, C. G. Engl, H. F. Valdovinos, J. J. Jeffery, T. E. Barnhart, G. W. Severin, R. J. Nickles, M. E. Kimple, M. J. Merrins and W. Cai, *Diabetes*, 2017, **66**, 2163–2174.

66 M. J. Kim, J. H. Yu, M. H. Oh, Y. S. Nam and D. Y. Lee, *J. Ind. Eng. Chem.*, 2017, **45**, 404–411.

67 J. Zhang, Michigan Technological University, 2015.

68 A. F. Martins, V. Clavijo Jordan, F. Bochner, S. Chirayil, N. Paranawithana, S. Zhang, S. T. Lo, X. Wen, P. Zhao, M. Neeman and A. D. Sherry, *J. Am. Chem. Soc.*, 2018, **140**, 17456–17464.

69 E. V Antina, N. A. Bumagina, A. I. V'yugin and A. V Solomonov, *Dye. Pigment.*, 2017, **136**, 368–381.

70 E. M. Nolan and S. J. Lippard, *Inorg. Chem.*, 2004, **43**, 8310–8317.

71 L. M. De León-Rodríguez, Z. Kovacs, A. C. Esqueda-Oliva and A. D. Miranda-Olvera, *Tetrahedron Lett.*, 2006, **47**, 6937–6940.

72 J. Henig, É. Tóth, J. Engelmann, S. Gottschalk and H. A. Mayer, *Inorg. Chem.*, 2010, **49**, 6124–6138.

73 F. Kielar, L. Tei, E. Terreno and M. Botta, *J. Am. Chem. Soc.*, 2010, **132**, 7836–7837.

74 Y. Arano, T. Uezono, H. Akizawa, M. Ono, K. Wakisaka, M. Nakayama, H. Sakahara, J. Konishi and A. Yokoyama, *J. Med. Chem.*, 1996, **39**, 3451–3460.

75 J. Yu, A. F. Martins, C. Preihs, V. Clavijo Jordan, S. Chirayil, P. Zhao, Y. Wu, K. Nasr, G. E. Kiefer and A. D. Sherry, *J. Am. Chem. Soc.*, 2015, **137**, 14173–14179.

76 M. S. Fineman, L. Z. Shen, K. Taylor, D. D. Kim and A. D. Baron, *Diabetes. Metab. Res. Rev.*, 2004, **20**, 411–417.

Chapter 3

Synthesis of GPR-L1, a Ligand Targeted to GPR40, and its Lanthanide(III) Complexes

3.1. Introduction

3.1.1. G-Protein Coupled Receptor 40 (GPR-40)

Developments in biochemistry throughout the 1980s enabled explosive growth in the number of known G-protein coupled receptors (GPCRs). These were discovered through the cloning and amplification of human gene sequences from deoxyribose nucleic acid (DNA) databases using the polymerase chain reaction[1–3]. In 1997, Sawzdargo *et al*. successfully elucidated the genes coding for, and corresponding structure of, G-protein coupled receptor 40 (GPR40)[2,3]. Initially, the receptor was considered an "orphan" – its ligands remained unidentified and its biological role and physiological significance was unclear[1–5]. Since these early years in limbo, it has been discovered that GPR40 is enriched in the ileum, some areas of the brain and, notably, pancreatic β-cells – it is in fact the most abundant GPCR expressed in islet β-cells, surpassing the well-known glucagon-like peptide receptor 1 (GLP-1R)[6–12].

3.1.2. Agonists for GPR40 and Their Uses

GPR40 is activated by, amongst other ligands, polyunsaturated fatty acids[5,6]. This stimulation has been shown to result in increased Ca^{2+} ion release, which can result in enhanced levels of insulin secretion, although the exact mechanisms for this process are a subject of debate in the literature at present[2,7,8,11]. What has been established is that stimulation of GPR40 is able to promote glucose-dependent insulin secretion, which has rendered the development of agonists for the receptor an attractive area in the pursuit of medical treatments for type 2 diabetes[7,13–16]. One compound of note which has been devised as part of this endeavour is [(3S)-6-({2′,6′-dimethyl-4′-[3-(methylsulfonyl)-propoxy]biphenyl-3-yl}methoxy)-2,3-dihydro-1-benzofuran-3-yl]acetic acid hydrate, (TAK-875). TAK-875 acts as a GPR40 agonist, showing selectivity over other members of the vast G-protein coupled receptor family and additionally is highly potent with oral bioavailability[13]. Clinical trials on diabetic patients have shown that administration of TAK-875 can result in the avoidance of hyperglycaemia *via* stimulation of GPR40, which subsequently triggers insulin secretion in the presence of elevated glucose levels[13,16,17].

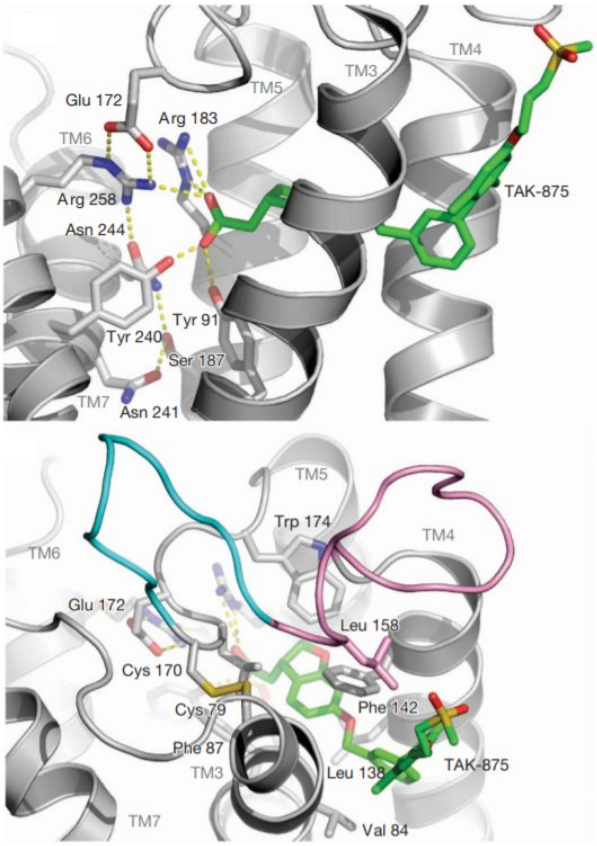


Figure 3.1: Diagram showing the interaction between TAK-875 and GPR-40. It can be seen that the hydrogen bonding between the carboxylic acid group and the receptor are key in binding[18]. Figure reproduced with permissions from reference 18.

3.1.3. Ligand Design

As discussed above, agonists of GPR-40 are of keen interest in the field as potential therapeutic agents, some of which have reached clinical trials[11,13,16]. The first of these agonists to be taken to clinical trials is the notable example of TAK-875, (**Figure 3.2**), which was produced in 2010 by Negoro *et al*. and has been shown to act selectively and with a high affinity for GPR40[13,19]. TAK-875 was ultimately withdrawn from phase III clinical trials due to hepatotoxicity concerns[19–22]. The precise mechanism of this toxicity towards hepatocytes is yet to be firmly established, with proposals ranging from inhibition of hepatobiliary transporters and generation of reactive oxygen species[20–22]. A comprehensive review of potential toxicity mechanisms published by Otieno *et al*. in 2018 hypothesised that the primary reason for the compound's toxicity towards hepatocytes is through acylation of its carboxylic acid group, forming reactive metabolites and transporter channel inhibitors[20]. The authors state that this was more of a concern at higher concentrations of TAK-875, and therefore it may be that lower dosages of a more potent compound could help avoid these[20]. TAK-875 was shown to bind to GPR40 through several key interactions: hydrogen bonding from its carboxylate moiety, a π-π stacking interaction *via* the numerous aromatic rings and a polar interaction through the methanesulfonate group[13,18]. The exploitation of these interactions inspired the development of other compounds which could also act as agonists for GPR40. In 2017, Yoon *et al.* carried out a study of the structure-activity relationship of the receptor and its

interactions with a range of similar compounds with these capabilities[12]. The authors found that a derivative of indole-5-propanoic acid (**Figure 3.2**) exhibited greater affinity for GPR40 than TAK-875 (EC_{50} = 9.4 nM compared to 14 nM) and could be used in the future as an anti-diabetic agent, potentially avoiding the toxicity concerns encountered with its predecessor.

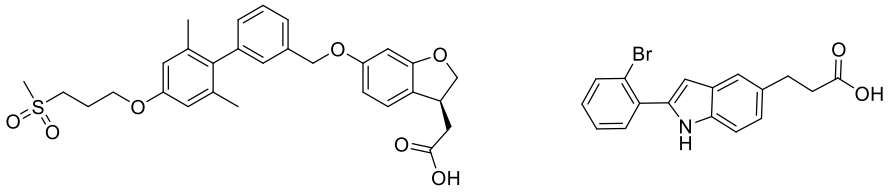


Figure 3.2: The structures of TAK-875 (L) and the indole derivative developed by Yoon *et al*. (R)[12,13]

It was hypothesised that the potency of this indole could render it useful as a targeting moiety for GPR40. Currently, compounds which are modified to target the receptor GLP-1R are the most prolific in the field, and the majority of these utilise peptides as the targeting moiety[23]. Whilst peptide-based receptor agonists have been fairly successful, the manufacturing of some peptides, such as modified variants of the ubiquitous exendin-4, can be both time consuming and expensive. Probes designed for β-cell imaging *via* GPR-40 or making use of small molecule ligands remain under-explored[12].

The macrocycle 1,4,7,10-tetraazacyclododecane-1,4,7,10-tetraacetic acid (H_4dota) is a robust chelator for many metal ions with applications in the imaging field, notably the lanthanide gadolinium(III), the corresponding complex has been in clinical use for decades[24,25]. This ligand has been shown to be extremely versatile and a ready scaffold for modification, with extensive work in the field exploring the effect of different structural changes or donor atoms and the effect that these alterations have on complex stability, inertness and biodistribution[25,26]. Due to its promise and the precedent set by prior work in the area, it was decided to initially introduce an indole-based targeting group to a macrocyclic ligand comparable to H_4dota in an attempt to develop an imaging probe targeted to GPR-40. 1,4,7,10-Tetraazacyclododecane-1,4,7-triacetic acid (H_3do3a) was selected due to its structural similarity to H_4dota – the only difference being that H_3do3a has one fewer acetic acid arm. The loss of this acetic acid arm results in H_3do3a possessing a free amine, which may be easily deprotonated and act as a nucleophile, allowing ready functionalisation of the macrocycle.

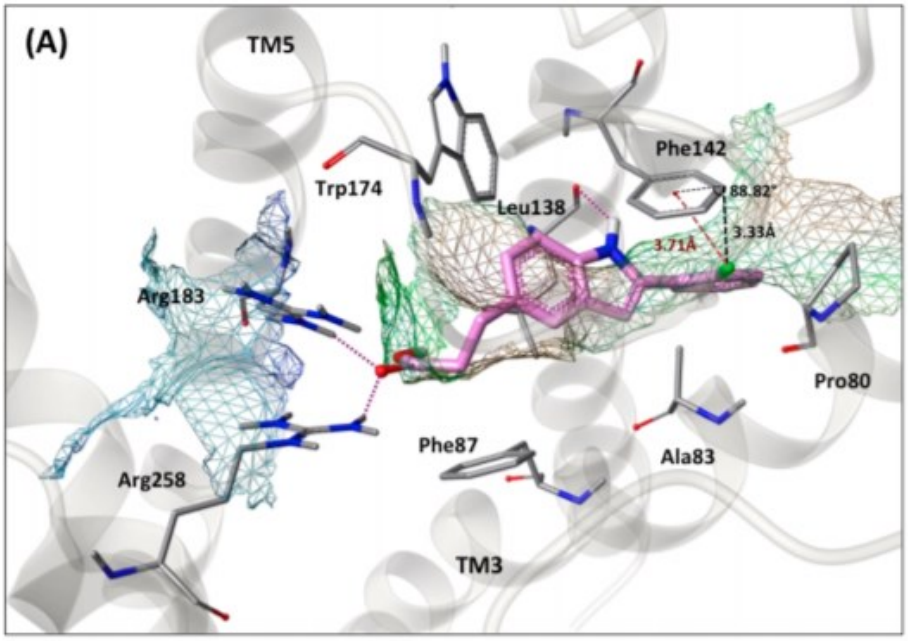


Figure 3.3: Computational image of the indole compound developed by Yoon, binding to GPR-40. Hydrophilic regions of the peptide are shaded blue and hydrophobic regions in brown. Several key interactions can be seen: hydrogen bonding between the carboxylic acid and two arginine residues, hydrophobic interactions between the indole and receptor binding site and an unusual π-Br interaction with an aromatic phenylalanine residue. These are the same interactions observed with GPR40 and TAK-875[18]. Additionally, a hydrogen bonding interaction between the indole NH group and a leucine residue may be seen. Image reproduced with permissions from ref. 12, Copyright (2017) American Chemical Society)[12].

The synthetic route published by Yoon *et al*. was straightforward and relied on well-established synthetic chemistry[12]. Through the examination of the agonist and its SAR, the authors established that the most important functional groups in their derivative were the carboxylic acid, indole and brominated aromatic ring[12]. It was hypothesised that an electrophile could be introduced as a substituent to the aromatic ring, which would then allow the macrocyclic structure to be incorporated *via* a simple S_N2 reaction. This could be done at a fairly late stage of the synthesis, allowing only minimal adaptations to be made to the published procedure and enabling rapid generation of a first-generation probe targeted to GPR40. The structure of the target compound is shown in **Figure 3.4**.

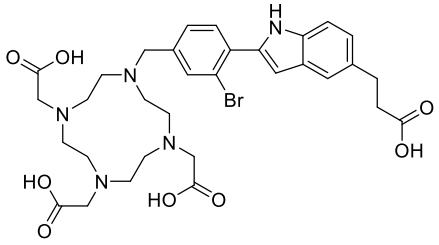


Figure 3.4: The structure of the target ligand, **GPR-L1**.

3.1.4. Aims and Objectives

The aim of the work which formed the basis of this Chapter was to develop, carry out and optimise a synthetic route towards **GPR-L1**. This ligand would then be fully characterised and complexed to a series of metal ions with imaging applications, and these complexes analysed to assess their suitability for imaging against criteria for magnetic resonance and optical imaging, depending on the metal complex.

These metal complexes would then be assessed for their suitability as imaging probes through *in vitro* work assessing their receptor affinity and providing proof of successful interaction *via* the indole-based targeting group. Following validation of the receptor-binding abilities of the synthesised complexes, it was hoped that at least one of them could be taken *in vivo*, assessing their biodistribution and exploring whether the probe could be able to quantify pancreatic β-cell mass in animals or even hypothetically in the clinic.

Successfully taking **GPR-L1** *in vivo* would enable a comparison between a small-molecule-based imaging probe targeted to GPR40, and one which utilised a peptide moiety to target the receptor GLP-1R, **GdEx**, which is discussed in Chapter 2. This could help conclusions to be drawn on which method of targeting, and which biological target, is most effective and could best aid the assessment of β-cell mass, functionality and diabetes progression.

3.2. Results and Discussion

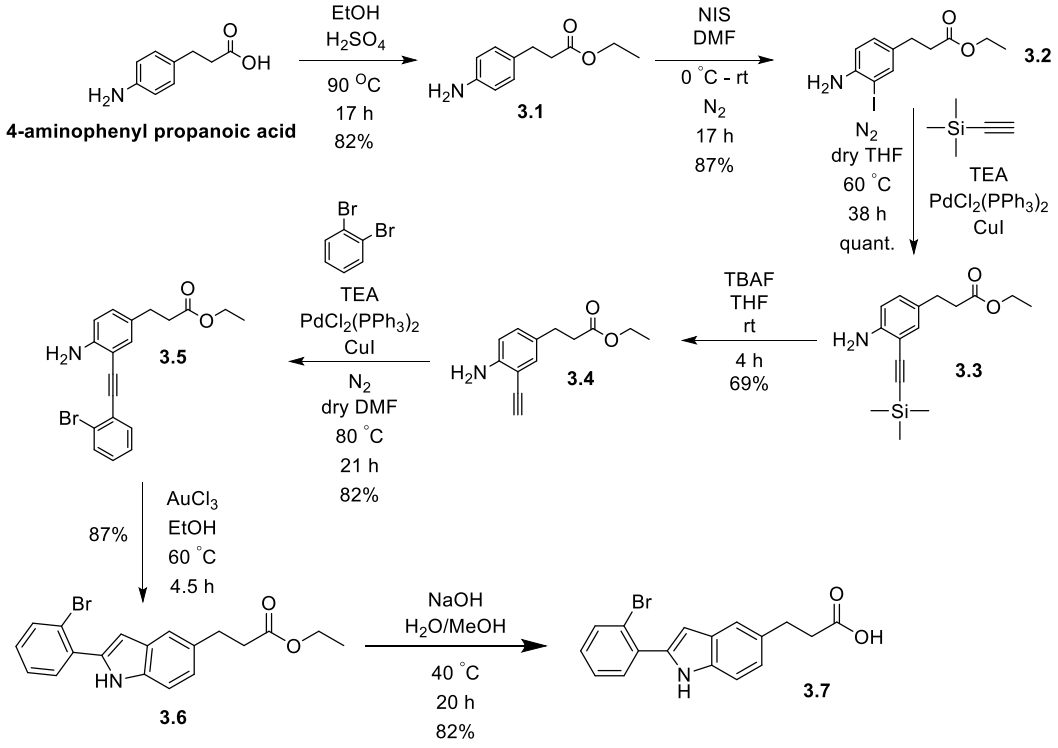
3.2.1. Synthesis of Yoon's Indole-5-Propanoic Acid Derivative

It was decided initially to replicate the synthesis of the compound developed by Yoon *et al*., in order to assess the viability of the synthetic route and determine whether or not the necessary modifications to produce **GPR-L1** could be accomplished[12].

Commercially available 4-aminophenyl propanoic acid was utilised as the starting point of the synthesis. This acid may be readily converted to its corresponding ethyl ester, **3.1** at a high yield of 72% by refluxing in ethanol in the presence of an H_2SO_4 catalyst. Mono-iodination of **3.1** to give the *ortho*-substituted variant **3.2** could be achieved by portion-wise addition of *N*-iodosuccinimide (NIS) at 0 °C. The rate of addition had to be carefully adjusted: immediate addition of 1 equivalent of NIS resulted in isolation of the disubstituted analogue and unreacted starting material – possibly from mesomeric electron donation from the iodide substituent into the aromatic ring **3.2** rendering subsequent addition more favourable. Ultimately, this synthetic step could be achieved at a high yield of 87%. The following Sonogashira reaction between **3.2** and trimethylsilylacetylene (TMS) gave the protected alkyne derivative **3.3** at a quantitative yield. Rapid deprotection of the TMS group to liberate the alkyne **3.4** could be readily accomplished using tetrabutylammonium fluoride solution, giving the desired compound at a high yield of 69% in as little as 30 minutes. A second Sonogashira reaction with 1,2-

dibromobenzene produced compound **3.5** at a high yield of 82%. The most interesting chemistry in this synthetic route was a gold-catalysed cyclisation reaction, which enabled formation of the indole **3.6** at a high yield of 87%. This compound could then be easily deprotected *via* ester hydrolysis under basic conditions to give the indole derivative **3.7** at a good yield of 80%. Purification at each stage was extremely straightforward, with flash chromatography in petroleum ether and ethyl acetate, or water and acetonitrile in the case of **3.7**. The complete synthesis is shown in **Scheme 3.1**. The total yield was 29% over 7 steps.

Once Yoon's synthetic route had been successfully replicated, the focus of the work could shift to modifications in pursuit of an imaging chelate.

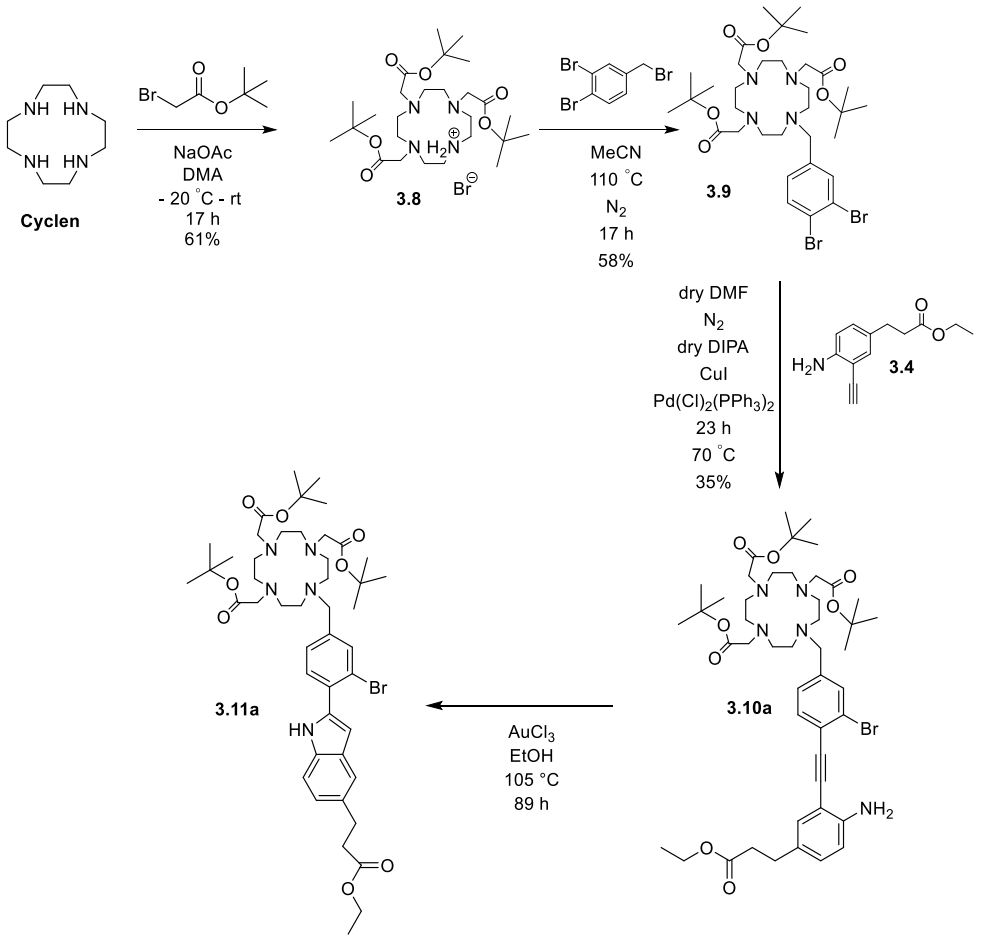


Scheme 3.1: Synthesis of the GPR-40 targeting indole derivative **3.7**.

3.2.2. Synthesis of GPR-L1

After successfully isolating the targeting moiety, it was decided to pursue its functionalisation to introduce imaging modalities. As can be seen in **Scheme 3.1**, a palladium-catalysed Sonogashira reaction with 1,2-dibromobenzene and compound **3.4** was required in the synthesis of Yoon's compound. It was hoped that replacing 1,2-dibromobenzene with the analogous 1,2-dibromo-4(bromomethyl)benzene would allow a macrocyclic chelator to be introduced *via* a simple nucleophilic substitution reaction. T*ert*-butyl protected H_3do3a could be synthesised from the macrocycle cyclen, which may be alkylated selectively by dropwise addition of 3 equivalents of *tert*-butyl bromoacetate at – 20 °C, followed by stirring at room temperature overnight to give compound **3.8** at a moderate yield of 61%. Refluxing 4(bromomethyl)benzene in acetonitrile and in the presence of an excess of K_2CO_3,

gave the alkylated derivative **3.9** at a moderate yield of 58% after 17 hours. Initial attempts at replicating the Sonogashira reaction with the alkyne **3.4** were unsuccessful when triethylamine was used, and substitution of this amine for dry diisopropylamine (DIPA) gave the corresponding cyclisation precursor, **3.10a**, at disappointing yields of between 10 and 35%. The success of this reaction step seemed to be dependent on its scale: larger scale syntheses tended to result in higher yields. Cyclisation of this compound utilising $AuCl_3$ was attempted and, despite some evidence that a reaction had taken place, nothing that could be identified as the desired indole product could be isolated. These reactions are summarised in **Scheme 3.2**.



Scheme 3.2: Synthesis of **3.10a** and the conditions used in its subsequent cyclisation.

Despite the cyclisation conditions published by Yoon *et al*. proving successful in the replication of their work, no success was had when attempting to isolate the indole shown above in **Scheme 3.2**. There was evidence of some reaction progress: the disappearance of the starting material spot through monitoring by thin layer chromatography (TLC), a distinct shift in the aromatic region of the proton NMR spectrum and the absence of an alkyne stretch in the infrared (IR) spectrum of the crude residue isolated from the cyclisation reaction.

Difficulty in interpretation of some of the obtained mass spectrometry (MS) results during the purification of compound **3.11a** led to this reaction pathway being abandoned. These results are shown in **Figure 3.5.** Following flash chromatography of crude **3.11a**, two different compounds were isolated. The two compounds had extremely different R_f values, yet the same values could be seen in the mass spectra of the two different spots. The base ion peak for the two compounds was at an *m/z* value of 787.1. It was hypothesised that this peak corresponded to two different, deprotected analogues of the target compound **3.11a**, which are shown in **Figure 3.5**. As neither isolated compound could be definitively identified, this synthetic route was no longer pursued.

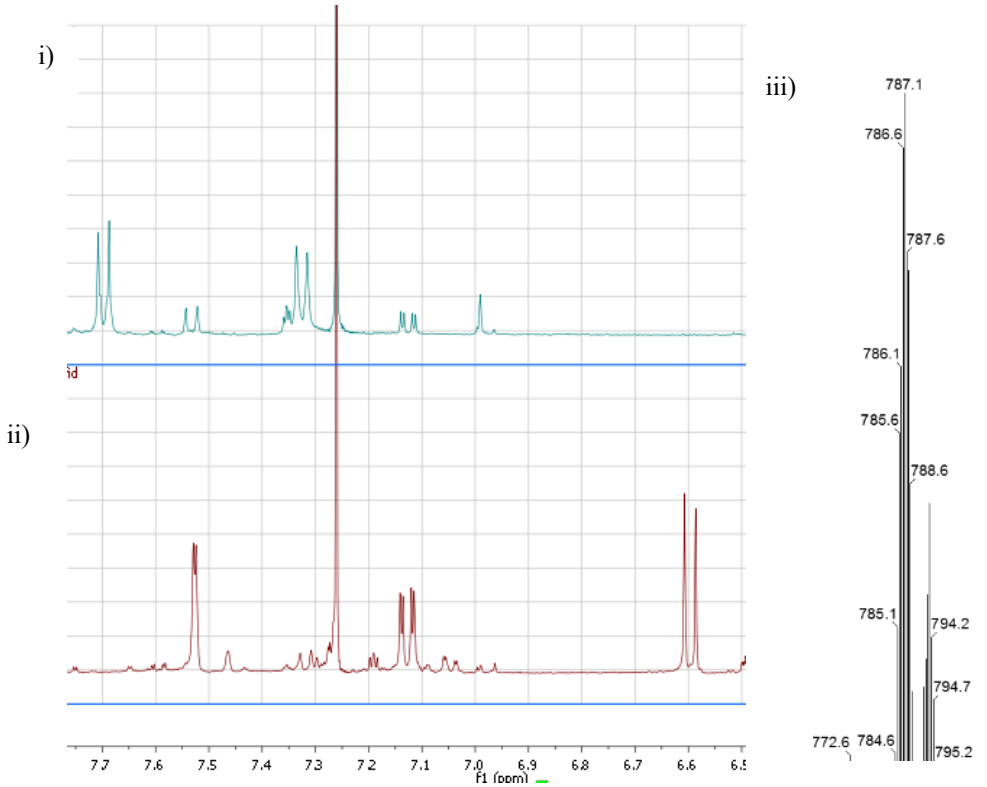
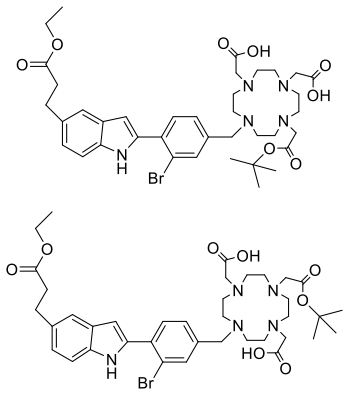


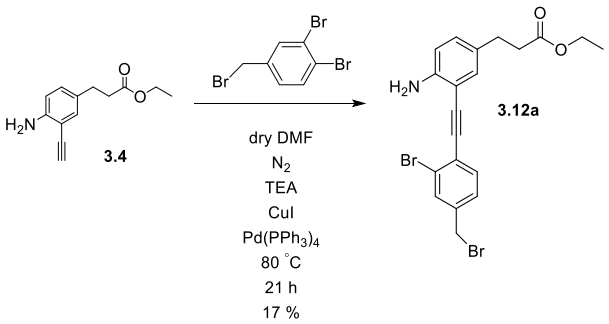
Figure 3.5: i) Aromatic region of ^{1}H NMR spectrum ($CDCl_3$, 400 MHz) of crude **3.11a**, ii) Aromatic region of ^{1}H NMR spectrum ($CDCl_3$, 400 MHz) of compound **3.10a**, iii) ESI-MS of one of the isolated fractions from purification of **3.11a**



Molecular Weight: 786.77

Figure 3.6: Proposed possible structures of **3.11a**.

It was theorised that the macrocyclic unit may have been interfering with the reaction process in some way, possibly by making cyclisation less favourable due to the large steric bulk of the ring. It was also considered that the macrocycle could be chelating to some of the available Au^{3+} in solution, which could have provided a Lewis acidic site for water coordination, therefore promoting hydrolysis of the *tert*-butyl ester protecting groups and liberating the free carboxylic acids in the two proposed structures of **3.11a** shown in **Figure 3.5**. An attempt to form the indole using a zinc catalyst was also unsuccessful. In order to try to avoid any potential interference from the macrocycle, it was decided to re-attempt the synthesis of **3.11a** in a different order, by building up the targeting group first and then introducing the metal binding region. This was attempted using the same Sonogashira reaction conditions reported by Yoon *et al.* to try and promote a reaction between **3.4** and 1,2-dibromo-4-(bromomethyl)benzene, which successfully gave the alkyne compound **3.12a**, albeit at a low yield of 17%. Due to the presence of two aromatic bromine atoms, there was some concern that two possible isomers of compound **3.12a** could be produced. Despite this, only one was isolated. This was identified as the *para* isomer, which was formed selectively perhaps due to both steric influence and the *ortho*/*para* directing effect of the bromomethyl substituent. The cyclisation step was attempted but to no avail, and a reassessment of the methodology employed in this pathway was carried out at this stage.



Scheme 3.3: Synthesis of compound **3.12a**.

In the synthetic work which had been carried out up to this point, aromatic compounds containing bromide substituents had been exclusively utilised as substrates for the various attempted Sonogashira

reactions. These had been hampered by low yields and difficult purifications. It was hypothesised that this could be due to a possible selectivity issue resulting from use of a di-brominated compound and its use in palladium-catalysed cross coupling processes, although no evidence for this had been collected. Buchwald-Hartwig reactions are also known to take place between amines and aromatic bromides in the presence of palladium catalysts, and this competing process could have been taking place in various attempts to build on **3.4**, resulting in low yields of the desired products[27,28]. To try to avoid this possible competing process, and in conjunction with the fact that iodide substituents react favourably to bromides in similar reactions elsewhere in the literature[29,30]. The pursuit of an iodo- variant of the compounds synthesised thus far was carried out in order to obtain a ligand capable of GPR40 targeted imaging.

1-Iodo-2-bromo-4-(bromomethyl)benzene is commercially available but extremely expensive. It was decided to synthesise the compound from 3-bromo-4-iodotoluene *via* a radical reaction with *N*-bromosuccinimide and the radical initiator azobisisobutyronitrile (AIBN). Stirring these compounds overnight in chloroform at 80 °C gave **3.13** at a moderate yield of 37%. This reaction was routinely carried out on a large scale and proved more viable than purchasing **3.13**. Subsequent reaction between the electrophilic **3.13** and the nucleophile **3.8** gave the (^{t}Bu)$_3$do3a analogue **3.14** at a good yield of 80% after refluxing for between 2 and 3 days. The Sonogashira reaction between this compound and **3.4** was then carried out, which enabled **3.10b** to be produced at a moderate yield of 66%. It had been hypothesised that the use of an aromatic iodide substrate would avoid possible issues in stereoselectivity and competing Buchwald-Hartwig processes and lead to higher yields of the desired product, so it was pleasing to see an improvement. Additionally, the purification process was more straightforward, with better separation occurring on the column. It was therefore decided to persevere with this synthetic approach. Cyclisation of the alkyne to form the indole **3.11b** *via* the previously discussed $AuCl_3$-catalysed reaction could be achieved at a good yield of 69%. Difficulty in determining the success of this reaction had been had with MS results which were challenging to interpret, suggesting that some degree of deprotection had occurred during the cyclisation process. The higher yields achieved earlier in the synthesis thanks to the use of iodo- rather than bromo- compounds had enabled the indole formation to be attempted on a much larger scale than had previously been trialled. It may have been that the larger scale made characterisation of **3.11b** more feasible and accurate. For example, the disappearance of an alkyne peak in the IR spectrum (**Figure 3.7**) was a key piece of characterisation evidence.

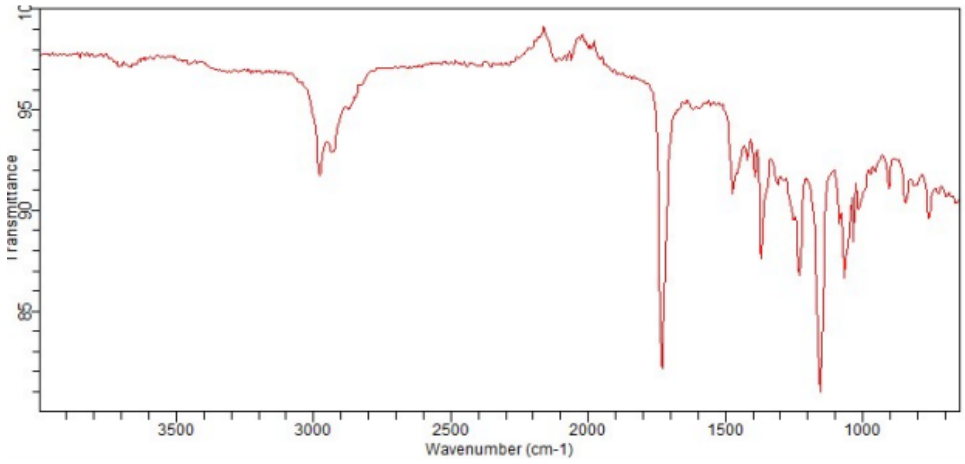
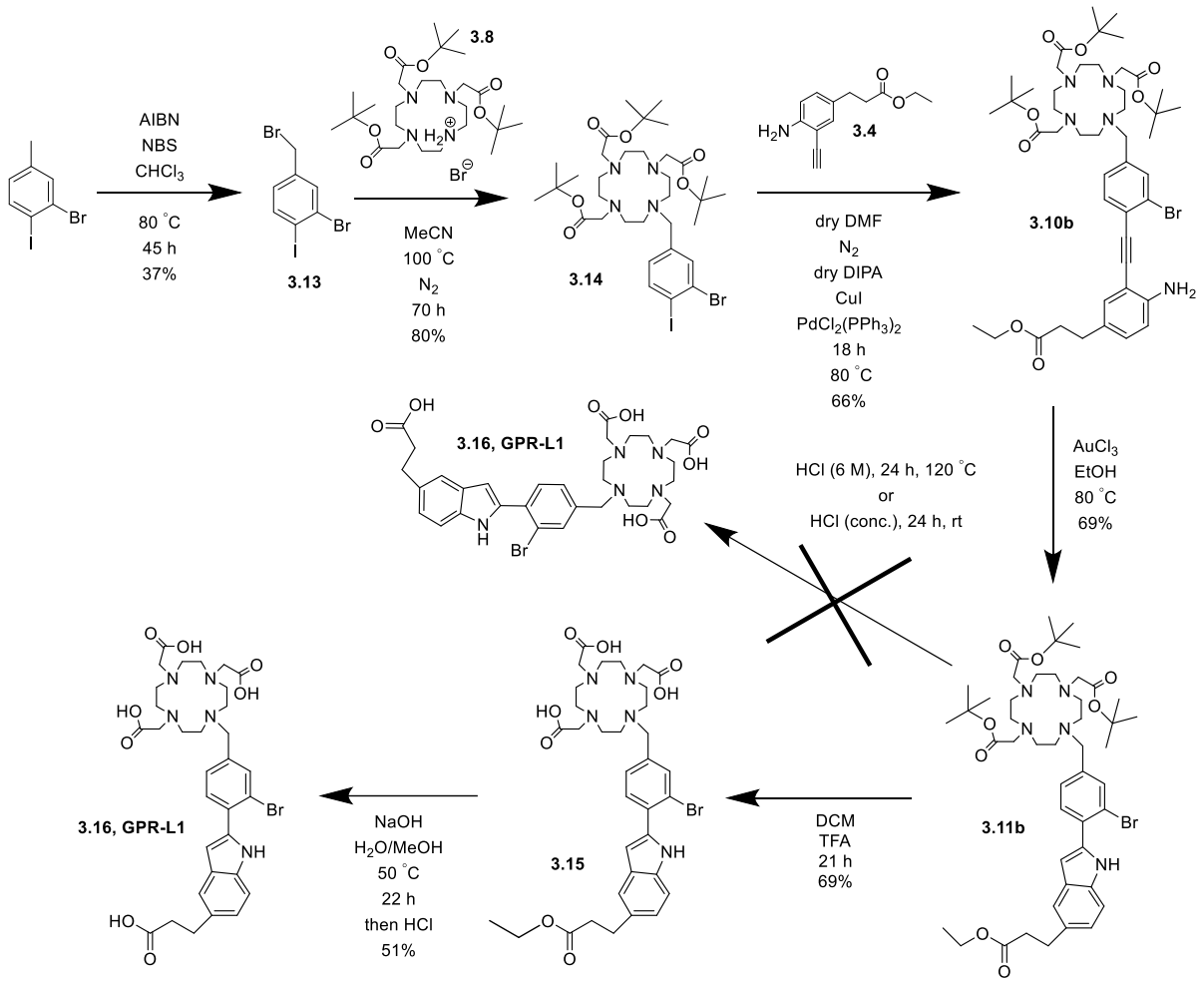


Figure 3.7: Solid state infrared spectrum of compound **3.11b** (Cary 630 FTIR).

Once indole formation had been confirmed, the next step required to enable metal complexation was deprotection of the *tert*-butyl esters on the acetic acid arms of the macrocyclic ring. In addition to this, hydrolysis of the ethyl ester on the propanoic acid arm of the indole was also necessary to allow sufficient interaction between the targeting moiety and the binding site of GPR40. Initially, it was decided to attempt deprotection of all of the esters simultaneously, minimising the number of synthetic steps required. Refluxing compound **3.11b** in HCl (aq., 6.0 M) overnight did not allow any compound to be isolated which could be successfully identified or characterised, nor did stirring at room temperature in concentrated HCl, despite attempting extraction with multiple different organic solvents. Reduction of the aqueous phase *in vacuo* did not allow anything to be isolated. With these routes not proving viable, it was decided to deprotect the esters sequentially under more mild conditions. Stirring compound **3.11b** in a 1:1 mixture of dichloromethane (DCM) and TFA for 21 hours gave compound **3.15**, the deprotected macrocyclic ligand at a yield of 69%. Hydrolysis of the ethyl ester using sodium hydroxide allowed the fully deprotected ligand, compound **3.16, GPR-L1,** at a moderate yield of 51%. The complete synthetic route towards **GPR-L1** is shown in **Scheme 3.4**. The total yield of the ligand was 5% over 6 steps, showing a clear need for optimisation of the reaction pathway. However, the isolation of the ligand from a relatively short synthetic route was encouraging and allowed the ligand to be remade in a short timeframe when necessary.



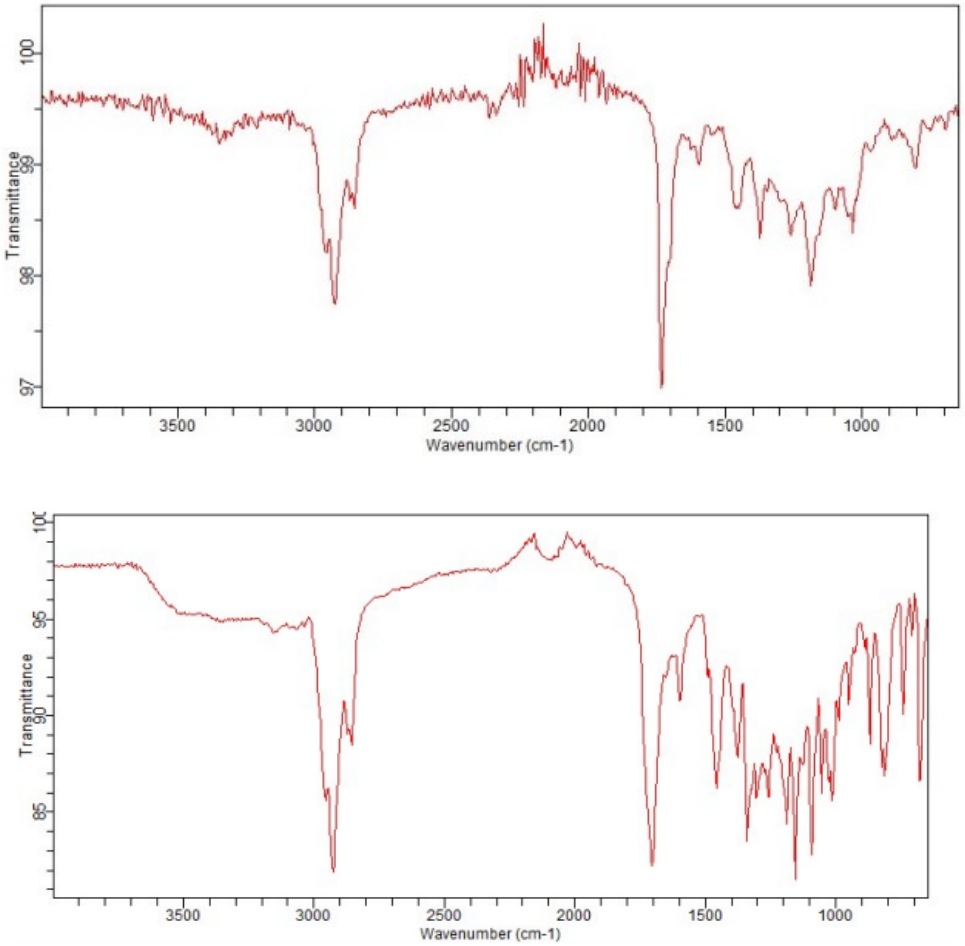
Scheme 3.4: The complete synthetic route towards the free ligand, **GPR-L1**, **3.16**.

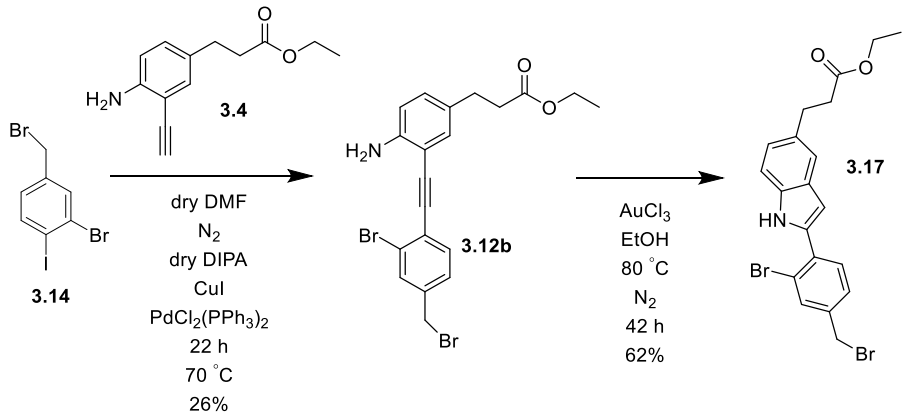
An alternative route towards this ligand had been devised previously in which the targeting moiety was built up before subsequently being attached to the macrocyclic ring. It was decided to try to repeat this synthesis but utilising the iodo- variant, compound **3.13**, to explore whether higher yields could be achieved. Some success was had with this reaction pathway, with the cross-coupling between the alkyne scaffold **3.4** and **3.13** giving analogue **3.12b** at a low yield of 26%. This was slightly higher than the 17% achieved when working from the bromide derivative, possibly due to the reduced extent of competing reactions like the Buchwald-Hartwig. The indole **3.17** could also be obtained at moderate yields of 62% after heating **3.12b** in the presence of $AuCl_3$ in ethanol. Cyclisation was confirmed by comparing the IR spectra of compounds **3.12b** and **3.17** (**Figure 3.8**). An absorption peak at around 2300 cm^{-1}, corresponding to alkyne functionality can be seen in the spectrum of **3.12b**, but not that of **3.17**. The IR spectrum of compound **3.12b** also appears to show two weak peaks at around 3300 cm^{-1}, corresponding to the symmetric and asymmetric stretch of a primary amine, whereas only one weak peak appears to be present in the same region for compound **3.17** – although the latter sample may have been slightly wet, resulting in a large O-H stretch in this region, obscuring any second peak. A slight shift in the aromatic region of the proton NMR spectra could also be observed. Perhaps more telling

was a colour change from yellow to red, which could suggest a change in the chromophore of the molecule.

Figure 3.8: Solid state IR spectra (Cary 630 FTIR) of compounds **3.12b** (top) and **3.17** (bottom).

Despite successful synthesis and characterisation of the indole **3.17**, the compound could not be successfully conjugated to the macrocyclic compound **3.8**. This was despite employing standard conditions for nucleophilic substitution reactions. Having isolated **GPR-L1** successfully through the route described previously, it was decided to no longer pursue the ligand through this strategy.





Scheme 3.5: Synthetic route towards compound **3.17.**

3.2.3. Lanthanide(III) Complexes of GPR-L1

Once **GPR-L1** had been successfully synthesised, it was decided to attempt to complex it to a series of lanthanide(III) centres of interest in the imaging field. The chosen metal ions were Gd^{3+}, Tb^{3+} and Eu^{3+}. With seven unpaired electrons, gadolinium(III) is highly paramagnetic and therefore capable of enhancing longitudinal (T_1) relaxation rate of water molecules[26,31,32]. Within biological systems, gadolinium(III) complexes have been used as contrast agents for magnetic resonance imaging, with their magnetic properties resulting in differences in brightness between various tissue types, enabling the elucidation of more useful anatomical data. Gadolinium-based contrast agents (GBCAs) dominate the contrast agent field – 11 are currently in clinical usage, with the earliest first approved in 1988[26,33,34]. In addition to gadolinium, the lanthanides europium and terbium were chosen as target metal centres. Both metals have applications in *in vitro* luminescent imaging due to their notable photophysical properties, which are discussed in the introduction to this thesis[35–37]. Further to this, the luminescence of Eu(III) and Tb(III) ions, when appropriately sensitised *via* a ligand chromophore, may be utilised to accurately determine the inner sphere hydration state, q, of the complex[36–39]. Due to the similar coordination environments preferred across the lanthanide series, these data can be exploited to determine the hydration state of the corresponding Gd(III) complex[36]. Hydration state is a critical component in the relaxivity of any MRI contrast agent, and its assessment would help fully characterise the gadolinium(III) complex of **GPR-L1**, enabling judgements to be made about its suitability for use as an MRI contrast agent.

The synthesis of a macrocyclic Gd(III) complex had been accomplished previously with $GdCl_3{\cdot}6H_2O$ as the lanthanide source, see Chapter 2, and it was decided to repeat this approach with **GPR-L1**. Complexation was attempted by dissolving the ligand in water and adding a slight excess (1.5 equivalents) of each of the corresponding $LnCl_3{\cdot}xH_2O$ salts before leaving the reaction mixture to stir overnight at a pH between 5 and 7. LCMS was utilised to monitor the reactions in order to confirm the identity of any complex prior to working up the reaction mixture. After 24 hours, LCMS indicated that

no sequestration of Gd^{3+} or Eu^{3+} had occurred and suggested that only partial complexation of Tb^{3+} could be observed (**Figure 3.9**). After a further 24 hours, the gadolinium(III) complexation was heated to 40 °C and a new Gd^{3+} source ($Gd(OTf)_3$) added. However, no subsequent LCMS results could be fully assigned to any of the complexes or the ligand itself.

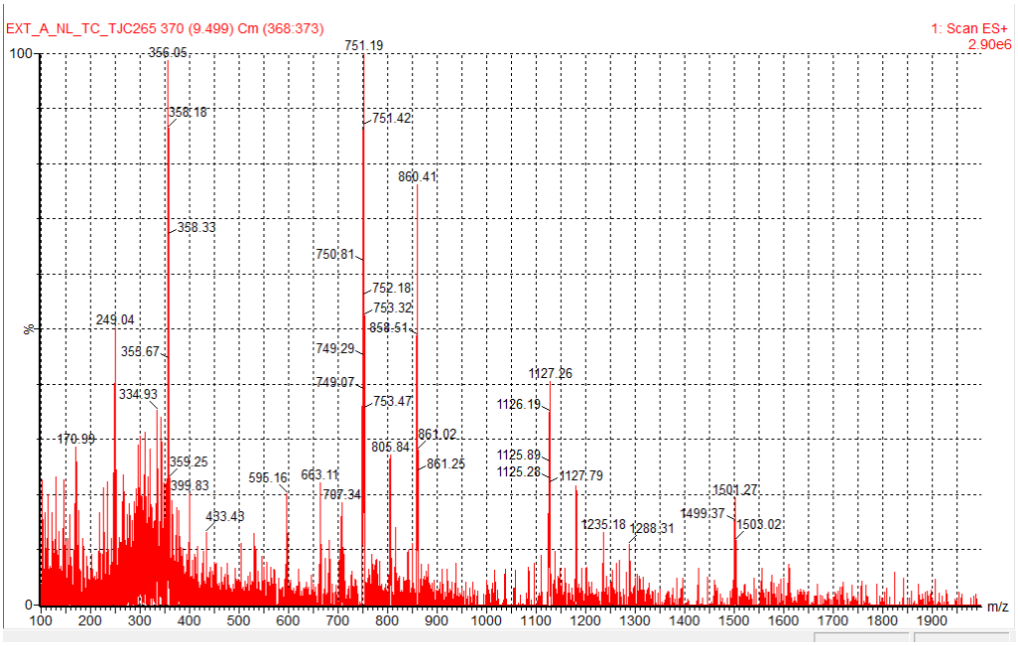


Figure 3.9: Mass spectrum from an LCMS run of the reaction mixture for the terbium(III) complex of **GPR-L1** suggesting successful complexation: MW = 858.50 and 702.60 respectively.

Despite no explicit evidence that complexation had occurred, it was decided to work up and purify each of the reaction mixtures to try and assess what, if anything, had taken place. Each solution was lyophilised and the resulting white solids desalted to remove any free lanthanide(III) ions. This was done by dissolving the compounds in water and bringing the pH to 10 by addition of sodium hydroxide solution. This resulted in the precipitation of $Ln(OH)_3$. The solution was centrifuged and the supernatant isolated and tested for the presence of free Ln^{3+} ions using xylenol orange as an indicator. Purification was carried out using automated reverse-phase flash chromatography and the resultant compounds submitted for MS analysis to establish whether complexation had been successful.

As complexation utilising the $LnCl_3$ salts had proved fairly challenging, it was decided to attempt new methodologies to try to attain lanthanide(III) complexes of **GPR-L1**. Efforts were initially focussed on the formation of a gadolinium(III) complex due to its potential application as an MRI contrast agent. Having unsuccessfully attempted complexation with the chloride and triflate salts of Gd(III), the nitrate was utilised as the next lanthanide(III) source. Carrying out the reaction in aqueous conditions at pH 6 did not result in any complex formation. Rather than continuing to substitute the metal salt, it was decided to explore the effect of solvent and temperature on the complexation reaction. Alcohols have a lower donor number than water molecules, and have been shown to have a reduced Ln^{3+} solvating ability compared to water[40]. Substitution of water for methanol resulted in successful chelation of Gd^{3+}

by **GPR-L1** when a slight excess of $Gd(NO_3)_3$ was introduced and the reaction mixture left to stir overnight at pH 6.5 and 50 °C.

Given the difficulties encountered previously when LCMS was used to monitor the progression of the reaction, the Evans method was used to determine the extent of complex formation. This entailed removing the solvent *in vacuo* before removing excess salts from the reaction mixture using automated reverse-phase flash chromatography. The solid obtained after purification was then dissolved in H_2O and a series of solutions prepared at known concentrations, assuming that all of the isolated compound was the target complex. These solutions were placed into capillaries and then inserted into an NMR tube containing D_2O. A ^1H NMR spectrum was recorded and the difference in chemical shift between the H_2O and D_2O peaks (Δx) in the spectrum for each concentration measured and used to calculate the actual gadolinium concentration (c) using **Equation 3.1**. Using this quantification method for the reaction conditions discussed above, complexation was shown to have reached 100% after 48 hours[41]. The gadolinium(III) complex of **GPR-L1**, **3.18**, was isolated at a disappointing yield of just 18% after desalting and purification. However, it was reassuring that complex formation could be achieved.

$$\boldsymbol{Equation\ 3.1}: \Delta x = 10^3 \left(\frac{4\pi cS}{T}\right)\left(\frac{\mu_{eff}}{2.84}\right)^2$$

For Gd^{3+}: μ_{eff} = 7.94. S = 1/3 for a solution parallel to the applied magnetic field.

Utilisation of methanol and an elevated temperature was trialled for other metal ions. In the absence of terbium nitrate the triflate salt was utilised. On this occasion, LCMS successfully identified terbium(III) complexation, with compound **3.19** ultimately being isolated at a 50% yield.

In the case of europium, no complex formation could be confirmed from the nitrate salt. All that was obtained after leaving the reaction mixture for 4 days was a white solid which gave inconclusive results from MS (**Figure 3.10**). The base peak in this spectrum appeared to correspond to a europium isotope pattern, but came at an *m/z* value approximately 100 below the mass of the complex. Attempts were made to crystallise this compound in order to further characterise it, but this could not be done successfully.

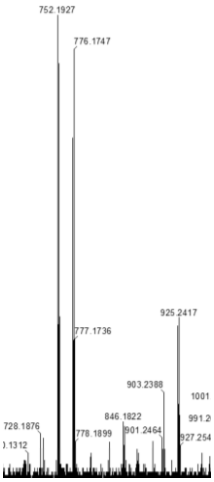
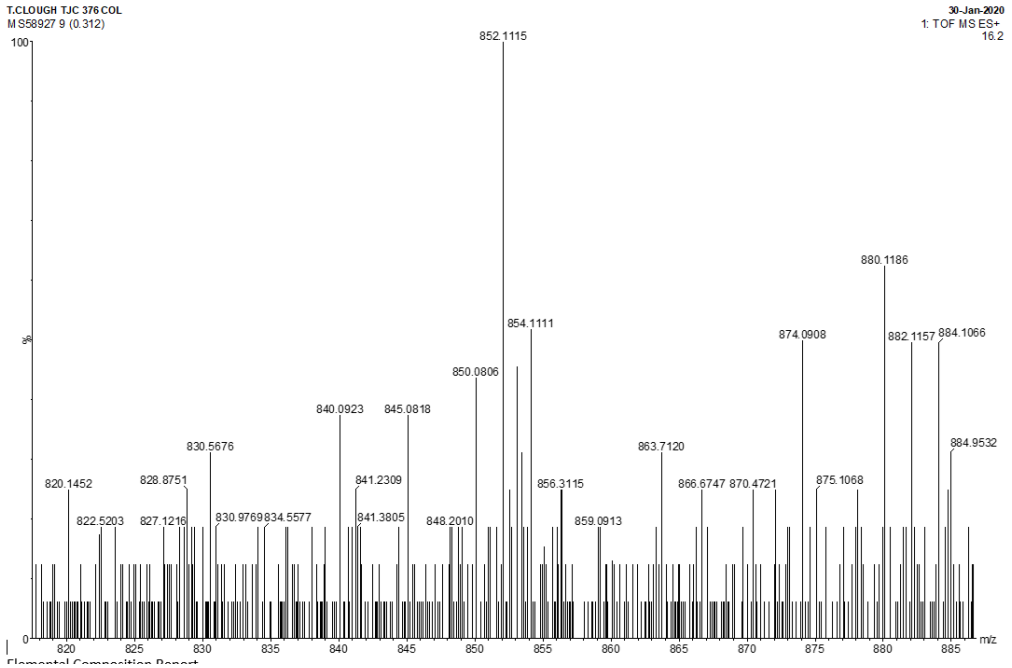


Figure 3.10: The mass spectrum obtained after attempting to complex **GPR-L1** with $Eu(NO_3)_3$. The peaks at around 752 and 776 respectively appear to correspond to an unknown species plus H^+ and Na^+ respectively. MW for [Eu(GPR-L1)] = 851.54.

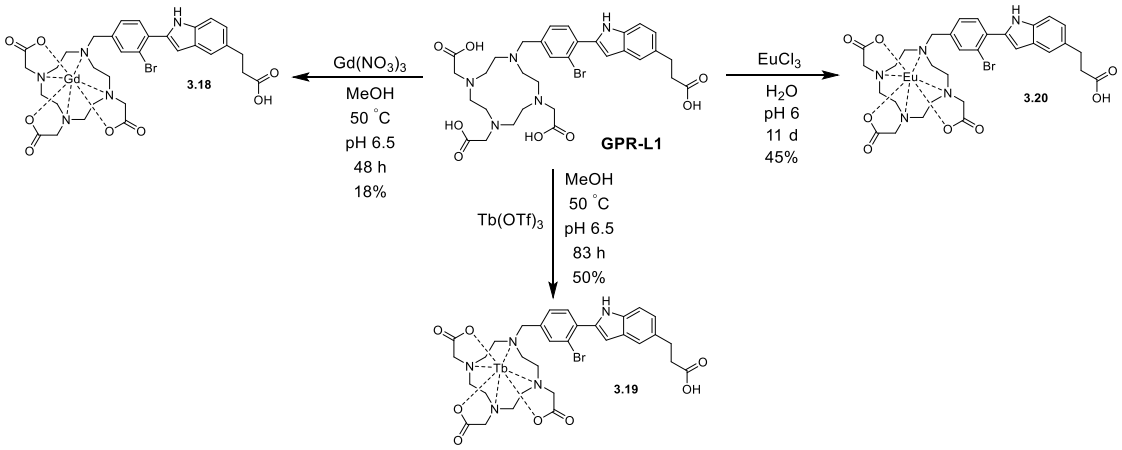
It was hypothesised that the kinetics involved in complexation of these metal ions may be vastly different, which is very possible given the differences in the rate of formation of the gadolinium(III) and terbium(III) complexes. This could account for the apparent lack of success in europium(III) complex formation. Several alternative europium(III) sources were trialled, namely the triflate, trifluoroacetate and completely anhydrous chloride, all to no avail.

It was hypothesised that the application of heat could have caused some ligand degradation or possible coordination from the carboxylic acid arm of **GPR-L1**. As such, complexation utilising anhydrous $EuCl_3$ at pH 6 in water was attempted again. Anhydrous $EuCl_3$ was added portion-wise, up to a total 15 equivalents over a period of 11 days before LCMS and MALDI-MS suggested product formation. After lyophilisation and subsequent reverse-phase column chromatography, the Eu(III) complex of **GPR-L1**, **3.20** could finally be isolated at a yield of 45%. **Scheme 3.6** shows the formation of the three isolated lanthanide(III) complexes of **GPR-L1**.



Mass	Calc. Mass	mDa	PPM	DBE	i-FIT	i-FIT (Norm)	Formula
852.1115	852.1116	-0.1	-0.1	16.5	31.3	0.7	C32 H38 N5 O8 Br 153Eu

Figure 3.11: Mass spectrum of compound **3.20** and the associated accurate mass calculated indicating successful europium(III) complex formation.



Scheme 3.6: Synthesis of the lanthanide(III) complexes of **GPR-L1.**

The vastly different rates of formation between these ions could be due to the metal salt used as the lanthanide source, or possibly due to intrinsic properties of the lanthanide(III) ions themselves. These kinetics could be investigated as part of future work on this project.

3.2.3.1. Complex Properties and Characterisation

Relaxivity is a key factor in consideration of any compounds which is to be used as an MRI contrast agent and, accordingly, it was decided to determine the relaxivity of compound **3.18**. This was done through the measurement of T_1 values of aqueous solutions of the complex at varying concentrations, which was carried out by Peter Haycock. Plotting the inverse of T_1 against [Gd] gave a linear plot from which the r_1 of compound **3.18** could be calculated as 9.22 $mM^{-1}s^{-1}$.

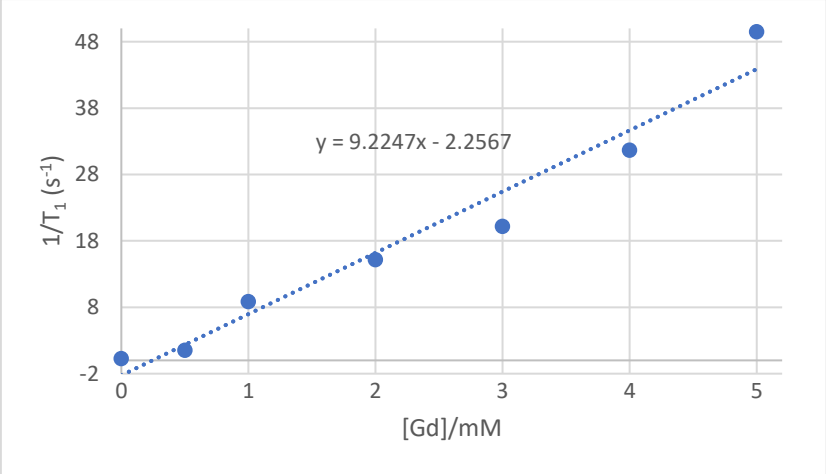


Figure 3.12: Plot used to determine relaxivity value of compound **3.18**.

This relaxivity is fairly high, especially when compared with many clinically approved gadolinium-based contrast agents: for example $[Gd(dota)]^-$ has had r_1 values of between 3.5 and 4.8 $mM^{-1}s^{-1}$ reported[25]. However, it is important to consider that **GPR-L1** is heptadentate and its complexes with trivalent lanthanide ions are likely to have a hydration state of 2, rather than 1. Comparing this to other $q = 2$ complexes, such as [Gd(tren-1,2-HOPO)], which has a relaxivity of 10.5 $mM^{-1}s^{-1}$, reveals that this r_1 value is not unrealistic or unexpected[25,42]. The hydration state of compound **3.18** could theoretically be calculated from the quantum yields and luminescent lifetimes of the Eu(III) or Tb(III) complexes and used to confirm that this relaxivity value is sensible.

As the luminescence of Ln(III) ions is due to 4f-4f transitions, which are Laporte forbidden, direct excitation of the metal centre is associated with a low molar absorptivity and often requires high-powered laser excitation[35,36]. In order to exploit the unique photophysical properties of the Eu^{3+} and Tb^{3+} ions, a sensitising chromophore should be used to excite the metal centre *via* the antenna effect[35,36]. Ligands which are typically used as antennae are polyaromatic or heterocyclic species which absorb light with a wavelength between 350 and 410 nm[35]. Although **GPR-L1** is not a classical polyaromatic, it was decided to investigate its optical properties to explore whether the ligand itself could be capable of sensitising Eu(III) or Tb(III) luminescence. **GPR-L1** was dissolved in water at a concentration of 1.85 mmol dm^{-3} and its UV absorbance spectrum recorded. This spectrum is shown in **Figure 3.13**. A small peak in absorbance could be seen at around 293 nm, although with absorption taking place at reasonable levels between 300 and around 375 nm.

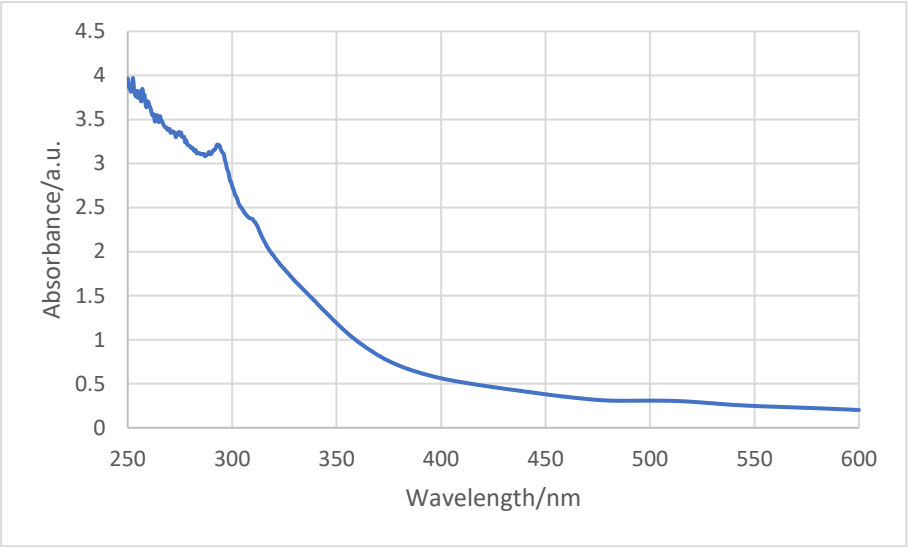


Figure 3.13: UV-vis absorption spectrum of **GPR-L1** in H_2O.

With some absorption occurring in the ligand in the relevant window for lanthanide sensitisation, it was decided to explore the fluorescence properties of the ligand. The fluorescence of the ligand was investigated at the same concentration as the UV data and the relevant spectrum is shown in **Figure 3.14**.

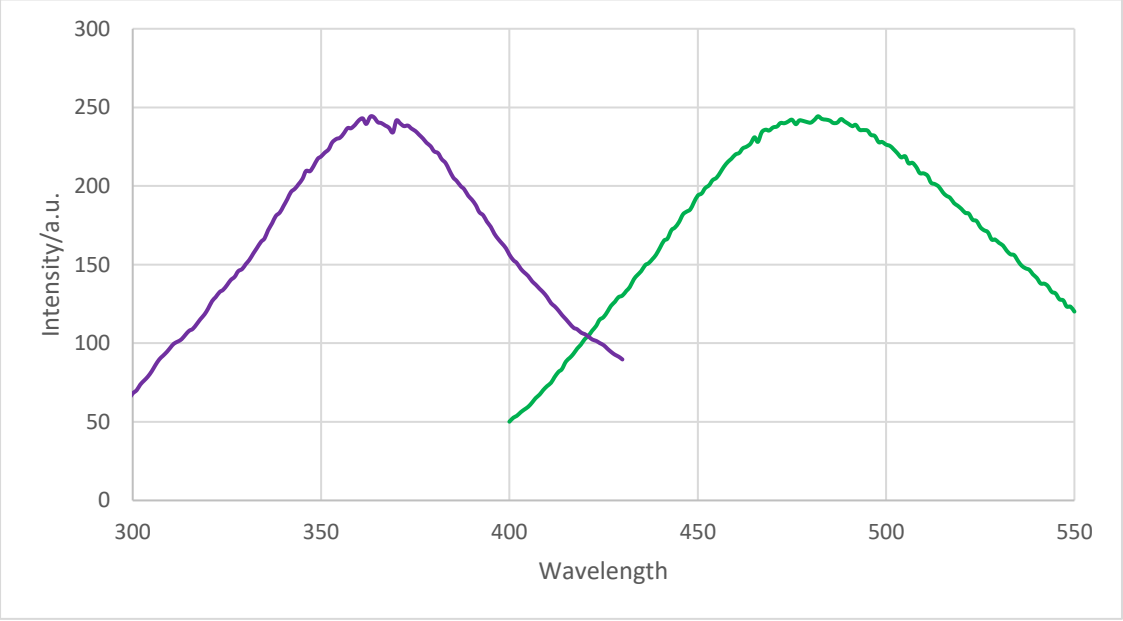


Figure 3.14: Fluorescence spectra of **GPR-L1** in H_2O showing excitation (purple) and emission (green).

It was found that the ligand could be excited at 366 nm, resulting in emission at around 484 nm. Given that this excitation wavelength fell within the window necessary for lanthanide(III) sensitisation, it was hoped that the photophysical properties of [Tb(GPR-L1)], **3.19**, could be used to calculate the hydration state of the gadolinium(III) complex, **3.18**, and draw conclusions about the suitability of the latter for use as an MRI contrast agent. In addition, the fluorescent nature of the ligand could also lend itself to *in vitro* studies of cells which over-express GPR40. This could be used to validate the efficacy of the

targeting moiety, and to confirm that the modification of the indole agonist developed by Yoon does not interfere with its affinity for the receptor target.

The luminescent properties of the Tb^{3+} complex **3.19** were explored by preparing a solution of the compound in water at a concentration of 2.43 mmol dm^{-3}. The complex could be excited at 391 nm, resulting in emission at 468 nm. This excitation wavelength also fell within the window appropriate for Tb(III) sensitisation, so it was decided to examine the phosphorescent properties of the complex. It was pleasing to see that the characteristic terbium(III) emission peaks were seen when this was explored, although these were extremely weak when compared to the intensity of the fluorescence. This would limit the usage of **3.19** as a luminescent probe in practice but suggested that the ligand **GPR-L1** could indeed be used to sensitise the emission of trivalent lanthanide ions and confirmed that a terbium complex had been formed. The fluorescence and phosphorescence spectra for **3.19** can be seen in **Figure 3.15**.

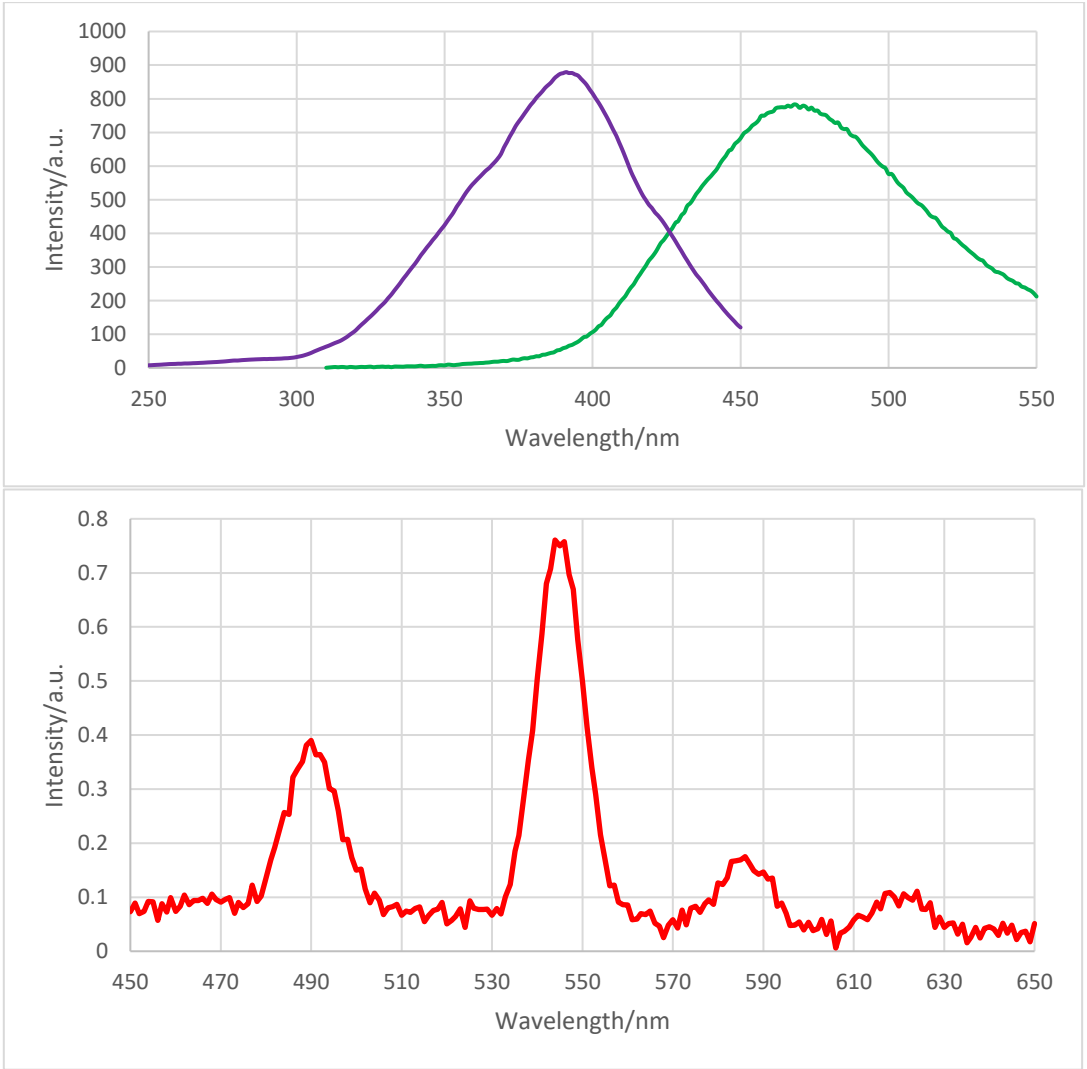


Figure 3.15: Top – emission (green) and excitation (purple) spectra of **3.19** in H_2O. Bottom – phosphorescence spectrum of **3.19** displaying the classic terbium(III) emission peaks.

Following successful isolation of [Eu(GPR-L1)], it was also decided to investigate the antenna effect and luminescence of this complex to establish if **GPR-L1** could sensitise emission from Eu^{3+}. This was done through recording the excitation and emission spectra of an aqueous solution of **3.20** (0.82 mmol dm^{-3}), which showed that the complex could be excited around 323 nm, resulting in emission at 401 nm (**Figure 3.16**).

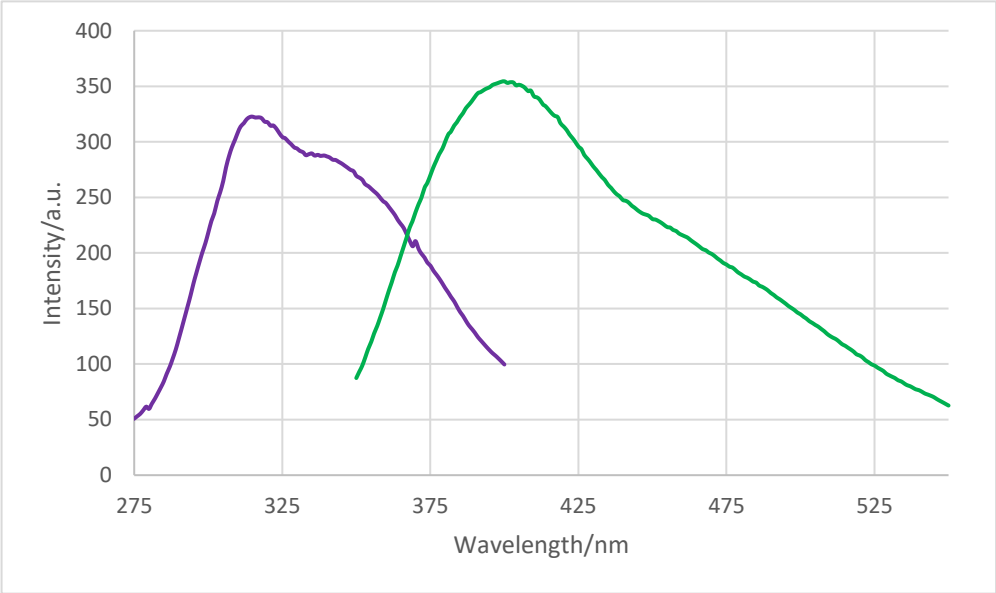


Figure 3.16: Excitation (purple) and emission (green) spectra of **3.20** in H_2O.

Given that **3.20** could be excited across a broad range of wavelengths, including within the window typically used for lanthanide(III) antennae, it was also decided to explore the phosphorescence of this compound. Excitation at around 350 nm resulted in a classical Eu(III) emission spectrum, which can be seen below in **Figure 3.17**.

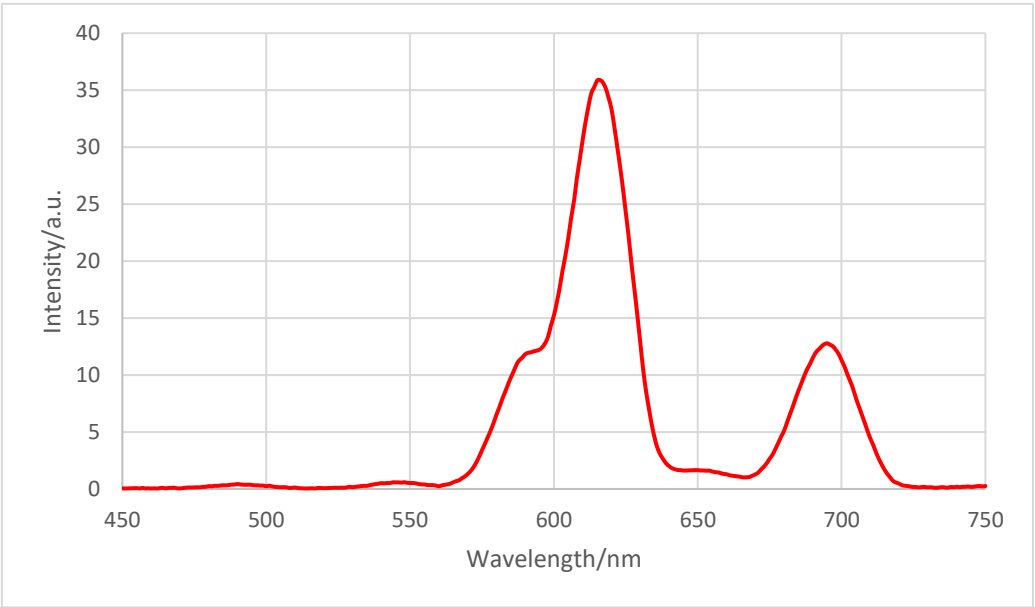


Figure 3.17: Time-gated emission spectrum of **3.20** in H_2O.

With some suggestion that **GPR-L1** could sensitise lanthanide(III) emission, it was decided to try and calculate the excited state lifetime of the lanthanide(III) centres of **3.19** and **3.20** in both H_2O and D_2O, as this would allow calculation of the hydration state of the complex and confirm the *q* value of 2 which was assigned to the gadolinium(III) complex. Quenching of lanthanide(III) excited states can occur non-radiatively, which reduces emission intensity. This quenching can occur through energy transfer to O-H oscillators in solvent molecules when these are in close proximity to the excited metal centre – i.e. they occupy the ion's inner coordination sphere[43,44]. In deuterated solvents, the quenching process is less pronounced as there is less effective overlap between the excited state and O-D vibrational energy levels, resulting in reduced efficiency of energy transfer and therefore a marked increase in the lifetime of the excited state and longer-lived emission[45,46]. In 1981, Horrocks *et al*. proposed an equation relating these different quenching effects to the hydration state of the metal ion, with different constants accounting for how readily the excited state can be quenched by nearby osciallators[47,48]. Since then, a series of iterative changes to the equation have been made to account for any excited state quenching from the Ln(III) complex's outer coordination sphere[43,48].

Equations 3.2 and **3.3** show the relationship between these lifetimes (τ) and hydration state for Eu^{3+} and Tb^{3+} respectively.

$$\boldsymbol{Equation\ 3.2}: q = 1.2\left(\frac{1}{\tau_{H_2O}} - \frac{1}{\tau_{D_2O}} - 0.25\right)$$

$$\boldsymbol{Equation\ 3.3}: q = 5\left(\frac{1}{\tau_{H_2O}} - \frac{1}{\tau_{D_2O}} - 0.06\right)$$

Solutions of both **3.19** and **3.20** were prepared in both H_2O and D_2O, initially at 100 μM. The relevant lifetimes were recorded on a Varian Cary Eclipse fluorescence spectrophotometer in the phosphorescence mode and the intensity of the emission after a 0.15 ms time gate applied was recorded and plotted against time. Compound **3.19** was excited at 391 nm and the lifetime of the emission peak at 545 nm recorded. Compound **3.20** was excited at 350 nm and the lifetime of the emission at 618 nm measured. The resulting decay curves (up to t = 20 ms) were fit to an exponential decay using Origin, which assumed an ideal relationship between the intensity of emission and time, such as that shown by **Equation 3.4.**

$$\boldsymbol{Equation\ 3.4}: I(t) = I(0)e^{-\frac{t}{\tau}}$$

From the first set of measurements, lifetimes for the lanthanide(III) luminescence were calculated. For the europium(III) centre in **3.20**, τ(H_2O) was found to be 0.76 ms and τ(D_2O) 1.21 ms and for the terbium(III) ion in **3.19** τ(H_2O) was found to be 0.25 ms and τ(D_2O) 1.26 ms. At first glance this was reassuring: both luminescent lifetimes in aqueous solution fell within the expected window (0.1 – 1.0 ms for Eu^{3+} and 0.4 -5.0 ms for Tb^{3+}, dependent on ligand environment) and both lifetimes were longer

in D_2O than H_2O[49]. Unfortunately, when these lifetimes were put into **Equations 3.1** and **3.2** respectively, *q* values of 0.29 and 4.19 were obtained for compound **3.20** and **3.19**. These were vastly different from the expected values, closer to 2, expected for these complexes based on the relaxivity data obtained from **3.18**. It was hypothesised that the obtained results could have been inaccurate due to the low concentration used to record the emission lifetimes. Subsequently, 1 mM solutions each of **3.19** and **3.20** were prepared and the measurements taken again. This time, *q* values of 0.30 and 6.74 were calculated. Even with the large associated error with Horrocks' equation, (± 0.5)[47] it was surprising that these values were so different from the expected results. There have been reports in the literature of excited state quenching by O_2[50]. This has been observed in a range of systems, such as porphyrins complexed to Pd and Pt, but also in Tb(III) complexes, some of which have been designed as oxygen sensors[50–54]. In these systems, removing oxygen from the system has been shown to significantly increase emission lifetime and quantum yield of the luminescent metal centre[50]. It was therefore decided to degas each solution (1 mM) by bubbling through nitrogen gas for a period of 90 minutes before subsequently measuring the lifetime. The obtained results are summarised in **Table 3.1**.

Compound (Ln^{3+})	Conditions	$\tau(H_2O)$/ms	$\tau(D_2O)$/ms	Calculated *q* Value
3.19 (Tb^{3+})	100 µM	0.25	0.32	4.19
	1 mM	0.31	0.55	6.74
	1 mM, degassed solvent	0.68	0.70	-0.10
3.20 (Eu^{3+})	100 µM	0.76	1.21	0.29
	1 mM	0.70	1.07	0.30
	1 mM, degassed solvent	0.74	1.26	0.37

Table 3.1: Summarised lanthanide(III) luminescence lifetime data for **3.19** and **3.20**.

Although repeating the measurements in degassed solvents resulted in a slight increase in the calculated *q* value for **3.20**, it can be seen that it resulted in no meaningful data being obtained for **3.19**. It is possible that, due to the extremely weak sensitisation of the terbium(III) luminescence by **GPR-L1**, (see **Figure 3.15**), the recorded lifetime data is unreliable – this seems incredibly likely due to its inconsistency. For **3.20**, both the lifetime and calculated *q* values seemed fairly consistent, with values ranging from between 0.70 – 0.76 ms in H_2O and 1.07 – 1.26 ms in D_2O for the former and 0.29 and 0.37 for the latter. However, whilst these values are consistent with one another, they are much lower than the expected value of 2 based on the relaxivity of compound **3.18**. The increase in the calculated value for *q* after the use of degassed solvents suggests that there could be some oxygen quenching processes involved which could lead to a lower than expected emission lifetime and therefore hydration state. Some additional credence is leant to this hypothesis by the observed increase in the lifetime of both complexes when recorded at 1 mM in glycerol. Glycerol is known to have low oxygen solubility, considerably lower than water, and any increase in excited state lifetime of the complexes in glycerol

could be indicative of some oxygen-mediated quenching process[55]. The lifetime values obtained for **3.19** and **3.20** respectively under these conditions were 0.55 ms and 0.87 ms. These represent substantial increases in excited state lifetime for both complexes when compared to the same concentration in water, suggesting that there may indeed by some degree of quenching by O_2. Further degassing of solvents may be required in order to increase the accuracy of the obtained results. There may also be some relationship between solvent viscosity and excited state lifetimes of terbium(III) complexes[55–57]. It has been proposed by Placide *et al*. that reduced solvent viscosity enables increased aryl-aryl rotations in antenna systems[57]. This increases the number of non-radiative pathways available to the excited state, which can lead to reduced luminescence lifetimes[56,57]. This phenomenon could explain the discrepancies in the recorded lifetimes and calculated *q* values for **3.19** and could also be occurring with **3.20**, as well as explaining the increased values of τ for both complexes in glycerol, a much more viscous solvent than water which would result in slower molecular rotation. In order to further explore this, low temperature measurements could be carried out, with an increase in lifetimes at lower temperatures indicative of a non-radiative rotational relaxation process being behind the unexpected results observed.

As discussed above, the europium(III) complex of **GPR-L1** was extremely difficult to form, requiring a much longer reaction time than both the Tb(III) and Gd(III) complexes. It may be that **3.20** exhibits markedly different behaviour in solution to other complexes of this ligand, dimer formation for example, which results in alternative hydration states being adopted. There are a number of ways in which this could be verified – crystallography is one example. Additionally, the complete lanthanide(III) series could be synthesised and their luminescent properties explored to gain more insight on the behaviour of this ligand and its complexes. Furthermore, it is possible that the carboxylic acid arm of the targeting group incorporated into the ligand could be responsible for the unusual observations of **3.20** – i.e. this carboxylic acid on one molecule could be chelating to the Eu(III) centre of another molecule given the heptadentate nature of **GPR-L1**. This could leave a free coordination site for a water molecule which could then be associated with both metal centres and give the reduced calculated hydration state. One way in which this could be explored is through complexation of the ligand precursor **3.15** to europium(III). Compound **3.15** has this carboxylic acid ethyl protected, so reducing its chelating ability could enable exploration of the unusual solution behaviour observed.

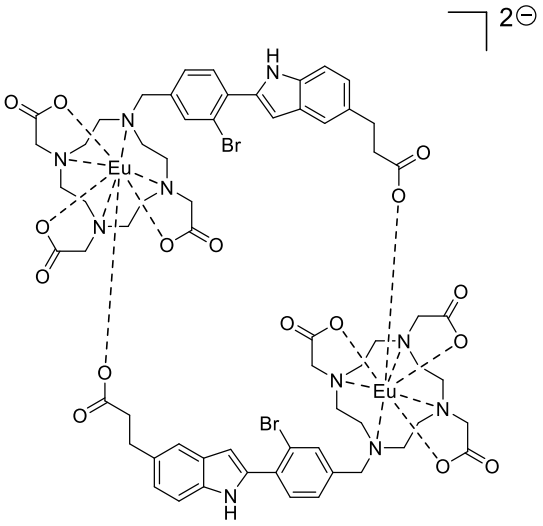


Figure 3.18: Possible dimer formation in compound **3.20**, which could account for a lower than expected hydration state due to increased steric hindrance at the metal centre.

3.3. *In Vitro* Data

It was hypothesised that the fluorescent nature of **GPR-L1** could be used to examine *in vitro* behaviour of the ligand's complexes and to confirm their affinity for the GPR40 receptor. The fluorescence spectra of **3.18** were recorded in order to assess the viability of this work. It was found that **3.18** could be excited at 326 nm with emission then occurring at 430 nm. There is a notable difference of around 40 nm between this compound, the gadolinium(III) complex, and the terbium(III) complex. This is quite possibly due to the different excited electronic states at the two metal centres.

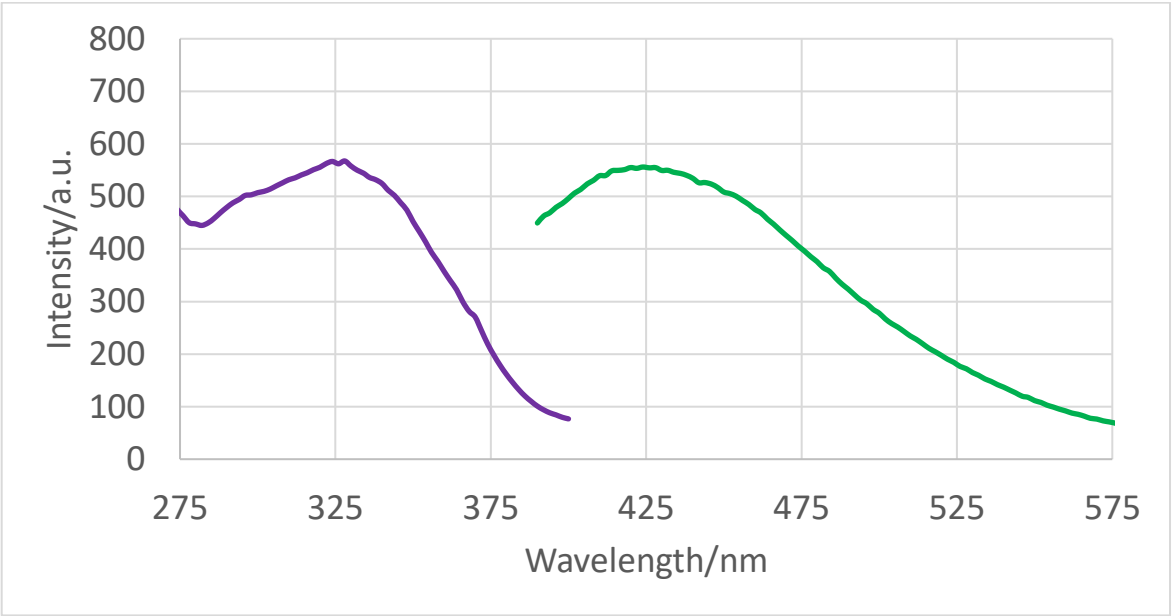


Figure 3.19: Fluorescence spectra of **3.18** in H_2O showing excitation (purple) and emission (green).

A set of *in vitro* experiments were carried out by Dr Shuai Zha at Hong Kong Baptist University. The initial round of these experiments sought to assess the toxicity of the compound towards cells and give an indication of whether it would be appropriate for future *in vivo* applications or use as a contrast agent. Compound **3.18** was incubated alongside human embryonic kidney-293 (HEK293) cells transfected with the plasmid FFA1-Tango at a range of concentrations (0 – 500 µM) for 24 hours. The plasmid, which was provided by Addgene, enables expression of human GPR40 and HEK293 cells have been used to express mammalian peptides[58,59]. The proportion of surviving cells after 24 hours incubation, expressed as cell viability, was utilised to assess compound toxicity.

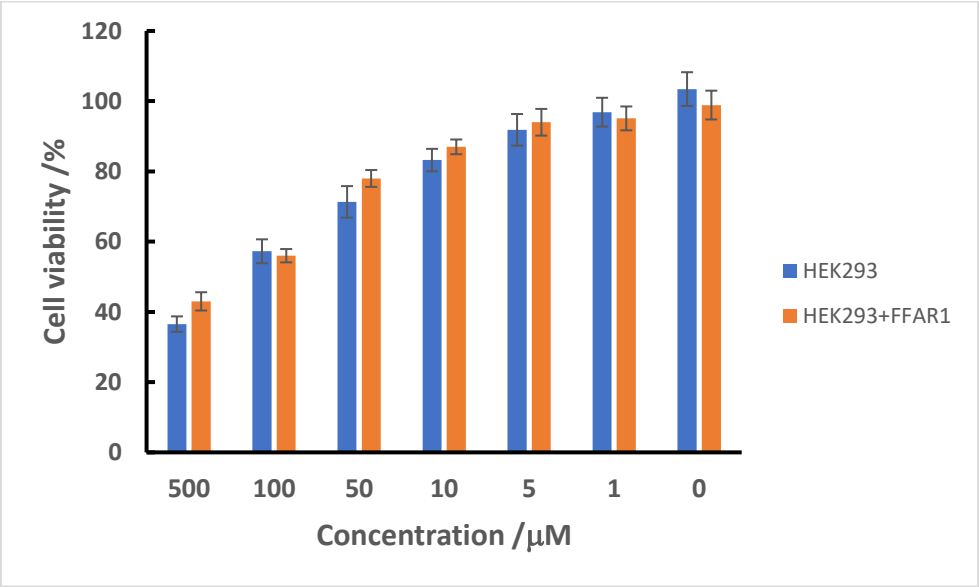


Figure 3.20: Viability of transfected (orange) and native (blue) HEK293 cells at varying concentrations of **3.18**. Figure prepared by Dr Shuai Zha.

The cell toxicity results were reassuring, with **3.18** showing minimal toxicity towards human cells expressing GPR40. Cell viability remained at or above 90% when the cells were incubated for 24 hours with **3.18** at concentrations at or below 5 µM, far above the length and dose which would be required for *in vivo* experimentation. There was limited cell death at even high concentrations, with cell viability remaining as high as 70-80% at 50 µM of **3.18**. The IC_{50} value of **3.18** was calculated to be 336 µM in native HEK293 cells and 380 µM in transfected cells expressing GPR40. These values are relatively high, indicating a low level of compound toxicity *in vitro*.

Further experiments were devised in order to assess the receptor-binding ability of **3.18**. The methodology was adapted from an exploration of GPR40 agonists published by Bertrand *et al.*, in which HEK293 cells were used as a control against those modified to express the receptor[60]. The native cells showed no fluorescence after incubation with a fluorescent GPR40 agonist, but those expressing GPR40 did[60]. Due to relatively weak emission from the aromatic targeting moiety, two-photon fluorescence excitation was used for confocal imaging of both HEK293 and the transfected variant cells. Two-photon

excitation involves the use of two photons of higher wavelength, typically from the infrared region of the spectrum, which are applied simultaneously to an organic compound in lieu of a single photon of visible light[61]. Proponents of two-photon excitation suggest that the use of lower energy photons can avoid damaging living cells[61]. Additionally, the use of infrared photons results in reduced background interference due to scattering, as well as more efficient detection of fluorescent photons, which enables ultrasensitive detection of weakly-emissive systems or molecules at low concentrations, even down to the single molecule level[61,62].

Dr Zha conducted a further round of *in vitro* imaging experiments. In order to assess specific binding of **3.18**, the compound was incubated at a concentration of 50 μM with both HEK293 and transfected HEK293 cells overexpressing GPR40, as with the toxicity studies. Confocal imaging was carried out with excitation at 700 nm and an emission window set at 400 – 550 nm to correspond to the emission profile of **3.18**, visible in **Figure 3.19**. Images were acquired at 6, 12 and 24 hours. The complete imaging sets are shown below in **Figure 3.21** and **3.22**.

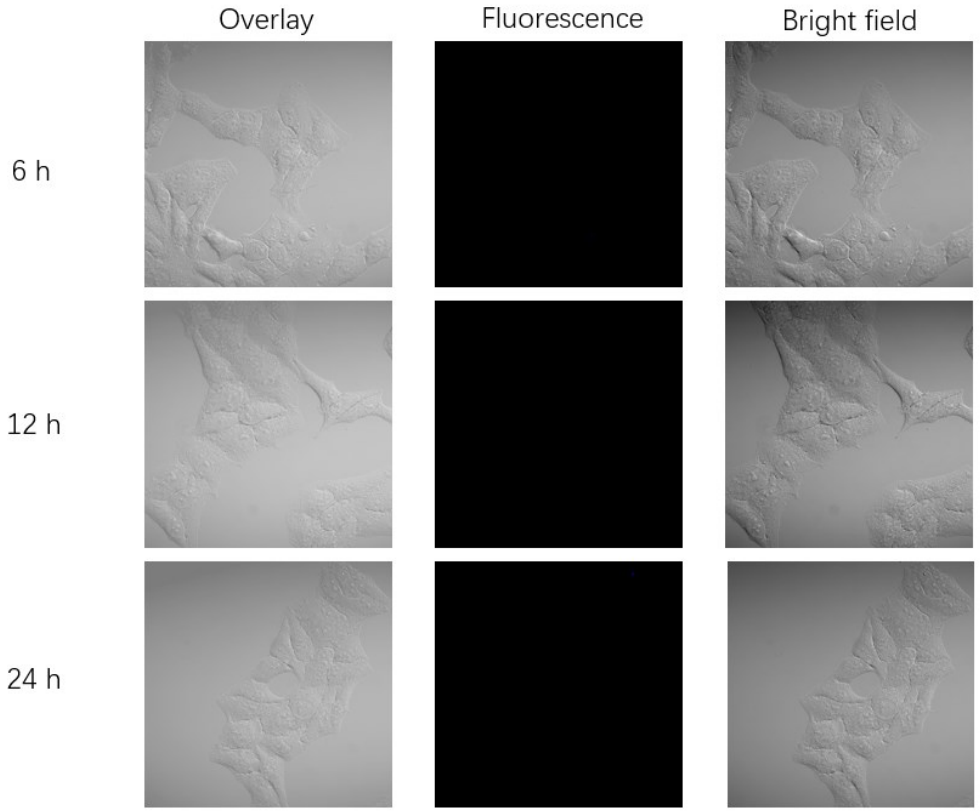


Figure 3.21: Microscope images obtained of native HEK293 cells incubated with **3.18** (50 μM). For fluorescence: λ_{ex} = 700 nm, λ_{em} = 400 – 550 nm. Image prepared by Dr Shuai Zha.

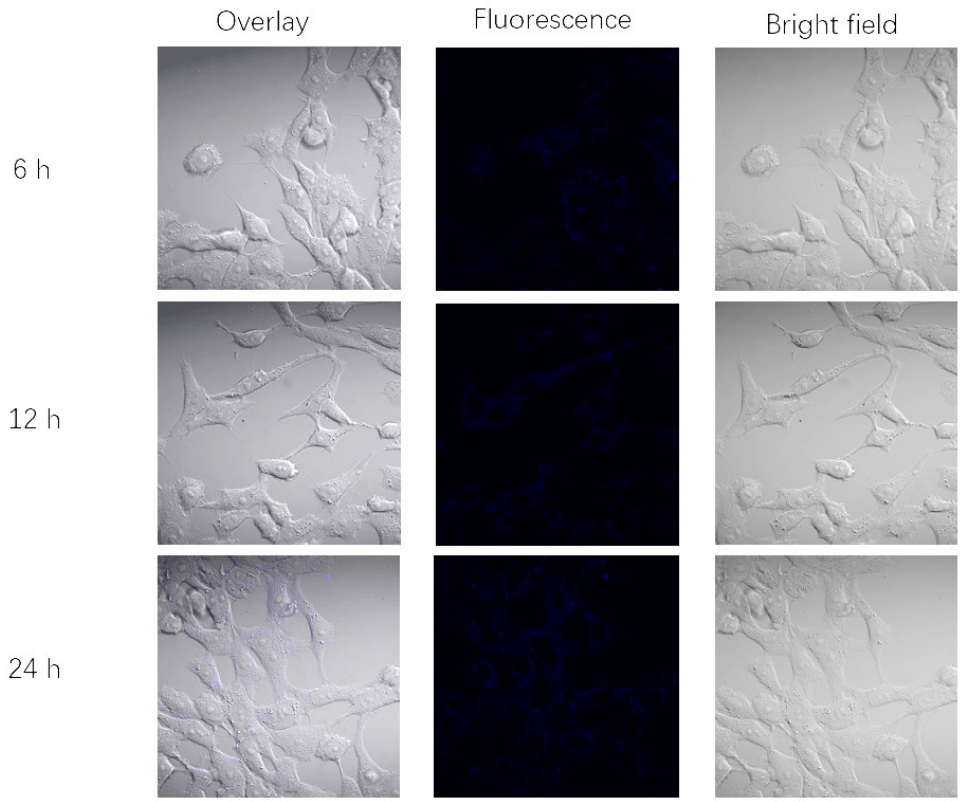


Figure 3.22: Microscope images obtained of transfected HEK293 cells expressing GPR40 incubated with **3.18** (50 μM). For fluorescence: λ_{ex} = 700 nm, λ_{em} = 400 – 550 nm. Image prepared by Dr Shuai Zha.

No fluorescence could be observed in the HEK293 cells incubated with **3.18**, indicating no uptake. This was expected as there was no receptor for the probe to bind to. Some fluorescence could be observed in the transfected cells, although this was fairly weak, perhaps due to the low efficiency of the two-photon excitation system. Despite the weak emission, a clear difference can be observed, with fluorescence observed at the plasma membrane of the transfected cells. This is indicative of receptor binding, suggesting that **3.18** was binding to GPR40 receptors and therefore that the designed targeting group could successfully be applied.

Following this indication that the targeting group devised by Yoon *et al*. did bind to the GPR40 receptor *in vitro* when incorporated into an imaging probe, there is certainly scope to carry out *in vivo* experiments assessing the use of **3.18** as an MRI contrast agent, or the luminescent species **3.19** and **3.20** as optical agents. *In vivo* work examining the uptake of **3.18** in the pancreas of wild-type mice is currently taking place, courtesy of Dr Zuo Rui at Sun Yat-sen University.

3.4. Conclusions and Outlook

A novel ligand, **GPR-L1**, targeted to the G-protein coupled receptor GPR40 has been designed and synthesised. **GPR-L1** incorporates an indole moiety functionalised with a propanoic acid arm, which has been shown to exhibit greater potency for GPR40 than TAK-875, an agonist which successfully reached phase 3 clinical trials. In addition, the ligand is based on the macrocycle H_4dota, introducing versatility and enabling a diverse range of metal centres to be explored. **GPR-L1** can be produced at moderate yields *via* a short, straightforward synthetic pathway with yields of 5% over 6 reaction steps. Whilst this is fairly low, there is certainly scope for optimisation of the reactions involved, and the sufficient quantities of the ligand required for complexation and preliminary *in vitro* work could be regularly and reliably produced. Due to the high affinity of the indole moiety for GPR-40, it is hoped that any complexes of **GPR-L1** could be used as diagnostic, or possibly even therapeutic agents for the diagnosis and treatment of diabetes.

Both the terbium(III) and gadolinium(III) complexes of **GPR-L1** have been isolated. The properties of these complexes have been thoroughly explored. The relaxivity of [Gd(GPR-L1)], 9.22 $mM^{-1}s^{-1}$ is similar to that of other heptadentate gadolinium(III) complexes which have been synthesised and suggests a hydration state of 2. This would enable reduced quantities of the complex to be utilised, which could help avoid some of the toxicity risks associated with gadolinium-based contrast agents. In attempts to validate this hydration state, it was discovered that **GPR-L1** was fluorescent, and that it could very weakly sensitise Tb^{3+} luminescence, enabling [Tb(GPR-L1)] to possibly be used for *in vitro* imaging of β-cell assays. However, the sensitisation was extremely weak, and it may not be realistic for *in vitro* applications. The europium(III) complex was ultimately isolated after utilisation of alternative metal salts, solvents and the application of heat, with success ultimately coming with a vast excess of anhydrous $EuCl_3$ after a period of 11 days. It may be that the kinetics associated with each of the lanthanide(III) ions and **GPR-L1** are vastly different, and some unusual behaviour occurs with Eu^{3+}. This could have been exacerbated by increasing the temperature of the reaction, which could have resulted in interaction with the carboxylic acid arm of the ligand.

It was found that **GPR-L1** could sensitise Eu^{3+} emission resulting in more intense lanthanide luminescence when compared to the terbium(III) complex, likely due to more favourable energy level overlap between the ligand and metal molecular orbitals. It was hoped that the lifetime of this luminescence could be used to calculate the hydration state of the complex and therefore validate the results obtained through measuring the relaxivity values of the gadolinium complex. However, the lifetime data obtained from the Tb(III) and Eu(III) complexes did not provide much clarity in this area.

The hydration state value calculated from the europium(III) complex of **GPR-L1** was calculated to be an average of 0.32, far removed from the expected value of 2 found from the relaxivity value of the gadolinium(III) complex. This may be due to some unusual behaviour in solution of the Eu(III) complex, perhaps dimer formation, which could also explain the difficulty had in formation of this complex. Further synthetic work and crystallographic studies could help explore or explain this further. The *q* value calculated from the lifetime of the terbium complex's luminescence lifetime could not be reliably calculated, perhaps due to only weak sensitisation of the Tb^{3+} emission. The increase in the calculated hydration state of the Eu(III) complex after solvent degassing suggested that there may be some degree of O_2 quenching of the excited states in the system, which could be further explored using alternative solvents with reduced oxygen solubilities.

Early *in vitro* work established that compound **3.18**, a potential gadolinium-based MRI contrast agent formed from **GPR-L1**, exhibited low toxicity towards human cells expressing GPR40. This paved the way for further *in vitro* analysis, which established that the targeting moiety incorporated into the ligand could allow the probe to target these cells specifically. As pancreatic β-cells overexpress GPR40, the complexes of **GPR-L1** have the potential to be used for the imaging of the pancreas alongside the previously discussed **GdEx**.

Future work in this area would involve extensive *in vivo* analysis of the complexes of **GPR-L1**, exploring a range of metal centres capable of a variety of imaging modalities and possibly even moving into therapeutic agents through radiometal chelation *via* the macrocycle. Subsequently, this could even be extended to clinical trials or studies in human patients. Additionally, the successful synthetic work and accomplishments had in the introduction of the targeting moiety to a metal chelator paves the way for further structural modifications to be made. These could include zinc-sensing capabilities in order to assess β-cell functionality, analogous to the work carried out by Martins *et al.*[63], such as those in **Figure 3.23** below.

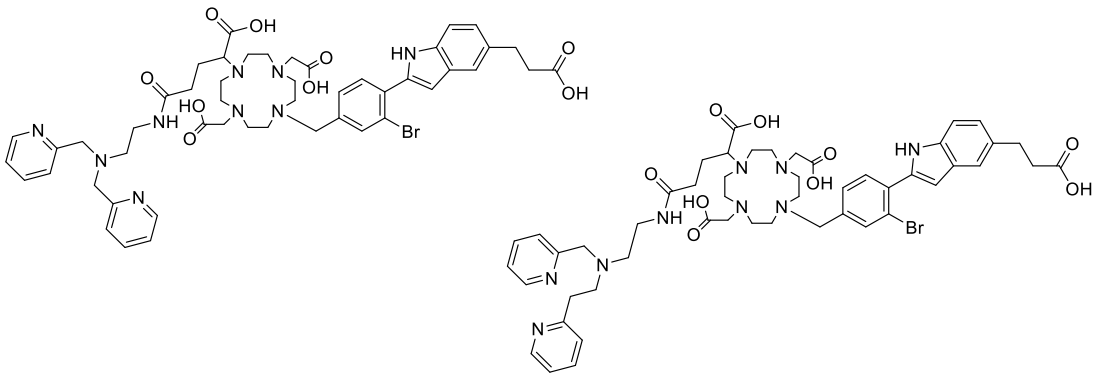


Figure 3.23: Possible alterations to **GPR-L1** which could exhibit relaxivity changes in the presence of Zn^{2+} and therefore give an indication of β-cell functionality.

3.5. References

1 J. M. Stadel, S. Wilson and D. J. Bergsma, *Trends Pharmacol. Sci.*, 1997, **18**, 430–437.

2 J. J. Chen, Y. H. Gong and L. He, *J. Drug Target.*, 2019, 27, 347–354.

3 M. Sawzdargo, S. R. George, T. Nguyen, S. Xu, L. F. Kolakowski and B. F. O'Dowd, *Biochem. Biophys. Res. Commun.*, 1997, **239**, 543–547.

4 Y. Itoh, Y. Kawamata, M. Harada, M. Kobayashi, R. Fujii, S. Fukusumi, K. Ogi, M. Hosoya, Y. Tanaka, H. Uejima, H. Tanaka, M. Maruyama, R. Satoh, S. Okubo, H. Kizawa, H. Komatsu, F. Matsumura, Y. Noguchi, T. Shinohara, S. Hinuma, Y. Fujisawa and M. Fujino, *Nature*, 2003, **422**, 173–176.

5 C. P. Briscoe, M. Tadayyon, J. L. Andrews, W. G. Benson, J. K. Chambers, M. M. Eilert, C. Ellis, N. A. Elshourbagy, A. S. Goetz, D. T. Minnick, P. R. Murdock, H. R. Sauls, U. Shabon, L. D. Spinage, J. C. Strum, P. G. Szekeres, K. B. Tan, J. M. Way, D. M. Ignar, S. Wilson and A. I. Muir, *J. Biol. Chem.*, 2003, **278**, 11303–11311.

6 S. Edfalk, P. Steneberg and H. Edlund, *Diabetes*, 2008, **57**, 2280–2287.

7 P. Steneberg, N. Rubins, R. Bartoov-Shifman, M. D. Walker and H. Edlund, *Cell Metab.*, 2005, **1**, 245–258.

8 H. Shapiro, S. Shachar, I. Sekler, M. Hershfinkel and M. D. Walker, *Biochem. Biophys. Res. Commun.*, 2005, **335**, 97–104.

9 M. G. Latour, T. Alquier, E. Oseid, C. Tremblay, T. L. Jetton, J. Luo, D. C-H Lin and V. Poitout, *Diabetes*, 2007, **56**, 1087–1094.

10 I. Syed, J. Lee, P. M. Moraes-Vieira, C. J. Donaldson, A. Sontheimer, P. Aryal, K. Wellenstein, M. J. Kolar, A. T. Nelson, D. Siegel, J. Mokrosinski, I. S. Farooqi, J. J. Zhao, M. M. Yore, O. D. Peroni, A. Saghatelian and B. B. Kahn, *Cell Metab.*, 2018, **27**, 419-427.e4.

11 M. Z. Khan and L. He, *Neuropharmacology*, 2017, 113, 639–651.

12 D. O. Yoon, X. Zhao, D. Son, J. T. Han, J. Yun, D. Shin and H. J. Park, *ACS Med. Chem. Lett.*, 2017, **8**, 1336–1340.

13 N. Negoro, S. Sasaki, S. Mikami, M. Ito, M. Suzuki, Y. Tsujihata, R. Ito, A. Harada, K. Takeuchi, N. Suzuki, J. Miyazaki, T. Santou, T. Odani, N. Kanzaki, M. Funami, T. Tanaka, A. Kogame, S. Matsunaga, T. Yasuma and Y. Momose, *Chem. Lett*, 2010, **1**, 290–294.

14 K. Nagasumi, R. Esaki, K. Iwachidow, Y. Yasuhara, K. Ogi, H. Tanaka, M. Nakata, T. Yano, K. Shimakawa, S. Taketomi, K. Takeuchi, H. Odaka and Y. Kaisho, *Diabetes*, 2009, **58**, 1067–1076.

15 M. Kebede, T. Alquier, M. G. Latour, M. Semache, C. Tremblay and V. Poitout, *Diabetes*, 2008, **57**, 2432–2437.

16 T. Araki, M. Hirayama, S. Hiroi and K. Kaku, *Diabetes, Obes. Metab.*, 2012, **14**, 271–278.

17 H. Naik, M. Vakilynejad, J. Wu, P. Viswanathan, N. Dote, T. Higuchi and E. Leifke, *J. Clin. Pharmacol.*, 2012, **52**, 1007–1016.

18 A. Srivastava, J. Yano, Y. Hirozane, G. Kefala, F. Gruswitz, G. Snell, W. Lane, A. Ivetac, K. Aertgeerts, J. Nguyen, A. Jennings and K. Okada, *Nature*, 2014, **513**, 124–127.

19 J. F. Marcinak, M. S. Munsaka, P. B. Watkins, T. Ohira and N. Smith, *Drug Saf.*, 2018, **41**, 625–640.

20 M. A. Otieno, J. Snoeys, W. Lam, A. Ghosh, M. R. Player, A. Pocai, R. Salter, D. Simic, H. Skaggs, B. Singh and H. K. Lim, *Toxicol. Sci.*, 2018, **163**, 374–384.

21 M. Kim, G. J. Gu, Y. S. Koh, S. H. Lee, Y. R. Na, S. H. Seok and K. M. Lim, *Biomol. Ther.*, 2018, **26**, 599–607.

22 X. Li, K. Zhong, Z. Guo, D. Zhong and X. Chen, *Drug Metab. Dispos.*, 2015, **43**, 1751–1759.

23 A. Jodal, R. Schibli and M. Béhé, *Eur. J. Nucl. Med. Mol. Imaging*, 2017, **44**, 712–727.

24 A. Bianchi, L. Calabi, F. Corana, S. Fontana, P. Losi, A. Maiocchi, L. Paleari and B. Valtancoli, *Coord. Chem. Rev.*, 2000, **204**, 309–393.

25 S. Faulkner and O. A. Blackburn, in *The Chemistry of Molecular Imaging*, eds. N. Long and W.-T. Wong, John Wiley & Sons, Hoboken, U.S.A., 2015, pp. 179–197.

26 T. J. Clough, L. Jiang, K. L. Wong and N. J. Long, *Nat. Commun.*, 2019, 10.

27 Y. Sunesson, E. Limé, S. O. Nilsson Lill, R. E. Meadows and P. O. Norrby, *J. Org. Chem.*, 2014, **79**, 11961–11969.

28 C. L. McMullin, B. Rühle, M. Besora, A. G. Orpen, J. N. Harvey and N. Fey, *J. Mol. Catal. A Chem.*, 2010, **324**, 48–55.

29 R. Chinchilla and C. Nájera, *Chem. Rev.*, 2007, 107, 874–922.

30 D. Yang, B. Li, H. Yang, H. Fu and L. Hu, *Synlett*, 2011, 702–706.

31 G.-L. Law and W.-T. Wong, in *The Chemistry of Molecular Imaging*, eds. N. J. Long and W.-T. Wong, John Wiley & Sons, Hoboken, U.S.A., 2015, pp. 1–24.

32 A. D. Sherry, P. Caravan and R. E. Lenkinski, *J. Magn. Reson. Imaging*, 2009, **30**, 1240–1248.

33 H. P. Niendorf, *Bristol Medico-Chirurgical J.*, 1988, **103**, 34–34.

34 A. Z. Khawaja, D. B. Cassidy, J. Al Shakarchi, D. G. Mcgrogan, N. G. Inston and R. G. Jones, *Insights Imaging*, 2015, **6**, 553–558.

35 M. P. Coogan and S. J. A. Pope, in *The Chemistry of Molecular Imaging*, eds. N. J. Long and W.-T. Wong, John Wiley & Sons, Ltd, Hoboken, U.S.A., 2015, pp. 275–298.

36 E. G. Moore, A. P. S. Samuel and K. N. Raymond, *Acc. Chem. Res.*, 2009, **42**, 542–552.

37 A. Aebischer, F. Gumy and J. C. G. Bünzli, *Phys. Chem. Chem. Phys.*, 2009, **11**, 1346–1353.

38 W. D. Horrocks and D. R. Sudnick, *J. Am. Chem. Soc.*, 1979, **490**, 334–340.

39 R. M. Supkowski and W. D. W. Horrocks, *Inorganica Chim. Acta*, 2002, **340**, 44–48.

40 P. Di Bernardo, A. Melchior, M. Tolazzi and P. L. Zanonato, *Coord. Chem. Rev.*, 2012.

41 D. M. Corsi, C. Platas-Iglesias, H. Van Bekkum and J. A. Peters, *Magn. Reson. Chem.*, 2001, **39**, 723–

726.

42 S. Hajela, M. Botta, S. Giraudo, J. Xu, K. N. Raymond and S. Aime, *J. Am. Chem. Soc.*, 2000, 122, 11228–11229.

43 A. Beeby, I. M. Clarkson, R. S. Dickins, S. Faulkner, D. Parker, L. Royle, A. S. De Sousa, J. A. G. Williams and M. Woods, *J. Chem. Soc. Perkin Trans. 2*, 1999, 493–503.

44 J. L. Kropp and M. W. Windsor, *J. Chem. Phys.*, 1963, **39**, 836.

45 Y. Haas and G. Stein, *Chem. Phys. Lett.*, 1972, **15**, 12–16.

46 A. Thibon and V. C. Pierre, *Anal. Bioanal. Chem.*, 2009, 394, 107–120.

47 W. DeW Horrocks and D. R. Sudnick, *Acc. Chem. Res*, 1981, **14**, 384–392.

48 S. Faulkner, S. J. A. Pope and B. P. Burton-Pye, *Appl. Spectrosc. Rev.*, 2005, **40**, 1–31.

49 F. S. Richardson, *Chem. Rev.*, 1982, **82**, 541–552.

50 D. Parker, *Coord. Chem. Rev.*, 2000, **205**, 109–130.

51 A. Mills and M. Thomas, *Analyst*, 1997, **122**, 63–68.

52 A. Beeby, D. Parker and J. A. G. Williams, *J. Chem. Soc. Perkin Trans. 2*, 1996, **8**, 1565–1579.

53 D. Parker and J. A. G. Williams, *J. Chem. Soc. Perkin Trans. 2*, 1996, **8**, 1581–1586.

54 I. Klimant and O. S. Wolfbeis, *Anal. Chem.*, 1995, **67**, 3160–3166.

55 E. R. H. Walter, J. A. G. Williams and D. Parker, *Chem. Commun*, 2017, **53**, 13344.

56 A. T. Bui, A. Grichine, A. Duperray, P. Lidon, F. Riobé, C. Andraud and O. Maury, *J. Am. Chem. Soc.*, 2017, **139**, 7693–7696.

57 V. Placide, A. T. Bui, A. Grichine, A. Duperray, D. Pitrat, C. Andraud and O. Maury, *Dalt. Trans.*, 2015, **44**, 4918–4924.

58 W. K. Kroeze, M. F. Sassano, X. P. Huang, K. Lansu, J. D. McCorvy, P. M. Giguère, N. Sciaky and B. L. Roth, *Nat. Struct. Mol. Biol.*, 2015, **22**, 362–369.

59 P. Thomas and T. G. Smart, *J. Pharmacol. Toxicol. Methods*, 2005, **51**, 187–200.

60 R. Bertrand, A. Wolf, Y. Ivashchenko, M. Löhn, M. Schäfer, M. Brönstrup, M. Gotthardt, V. Derdau and O. Plettenburg, *ACS Chem. Biol.*, 2016, **11**, 1745–1754.

61 J. M. Squirrell, D. L. Wokosin, J. G. White and B. D. Bavister, *Long-term two-photon fluorescence imaging of mammalian embryos without compromising viability*, 1999, vol. 17.

62 C. Xu, W. Zipfel, J. B. Shear, R. M. Williams and W. W. Webb, *Multiphoton fluorescence excitation: New spectral windows for biological nonlinear microscopy*, 1996, vol. 93.

63 A. F. Martins, V. Clavijo Jordan, F. Bochner, S. Chirayil, N. Paranawithana, S. Zhang, S. T. Lo, X. Wen, P. Zhao, M. Neeman and A. D. Sherry, *J. Am. Chem. Soc.*, 2018, **140**, 17456–17464.

Chapter 4

Exploring Agonist Interactions with the Glucagon-Like Peptide-1 Receptor (GLP-1R)

4.1. Introduction

4.1.1. The Glucagon-Like Peptide 1 Receptor (GLP-1R)

The physiological effects of stimulation of the glucagon-like peptide 1 receptor are discussed extensively in the introduction to and Chapter 2 of this thesis. Structurally, GLP-1R is a member of the G-protein-coupled receptor (GPCR) superfamily, which is the most commonly encoded for by the human genome[1]. Within this superfamily, GLP-1R is part of the class B subclassification[1–4]. Class B GPCRs, of which 15 are known to exist, are characterised by three key regions: an extracellular domain at the *N*-terminus of the receptor, an intracellular domain at the *C*-terminus and a transmembrane domain which consists of 7 α helices[1–4].

The extracellular domain of GLP-1R is involved in agonist binding[1,2]. For peptide agonists, the *C*-terminus of the ligand interacts with the extracellular *N*-terminus of the receptor whilst the agonist's *N*-terminus binds to the transmembrane helices. This results in a conformational change to the receptor structure and activates it towards intracellular G-protein binding *via* the *C*-terminus of the receptor[1,2].

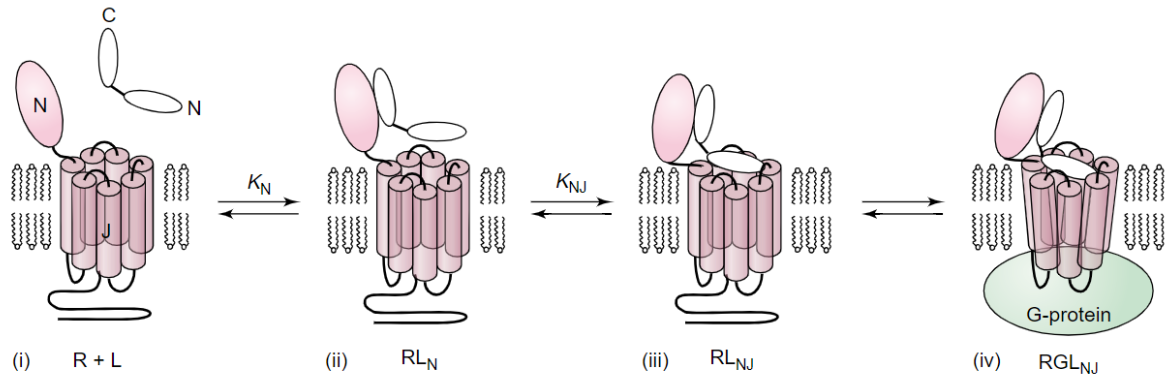


Figure 4.1: Simplified model of a peptide agonist binding to a class B GPCR. Adapted from reference 2, with permissions[2].

4.1.2. GLP-1R In Cell Membranes

Cell plasma membranes are principally composed of proteins and lipids, with some carbohydrate content[5]. The lipid fraction of these membranes, composed primarily of phospholipids and cholesterol, dictates the membrane structure and function[5,6].

In association with the phospholipid sphingomyelin, cholesterol forms tightly-packed, highly ordered structures within the plasma membrane – these are referred to as liquid ordered (LO) nanodomains or lipid rafts[6,7]. GPCRs are known to localise within these lipid rafts, which is thought to aid coupling to G-proteins and organisation of signalling molecules[7].

Upon agonist binding, a conformational change in the receptor structure takes place[7,8]. This change is often outward movement of one of the transmembrane helices, which enables G-protein binding but can result in an energetically unfavourable hydrophobic interaction between the receptor and structures

within the plasma membrane[7,8]. This may be the trigger for association between the activated receptor and cholesterol-rich lipid rafts[7]. After G-protein binding, the receptor undergoes a series of processes including phosphorylation before being taken into the cell through endocytosis[7,9,10]. The effect of GLP-1R internalisation is not fully understood, with conflicting evidence that it promotes[11] or reduces[9,12] intracellular signalling events coupled to insulin release. Different agonists for GLP-1R have been shown to impact this endocytosis process to varying degrees: GLP-1 and exendin-4 are 10 times more potent at inducing internalisation than the therapeutic compound liraglutide and GLP-1 triggers recycling of the receptor to the cell membrane 2 to 3 times faster than exendin-4[12]. So-called "biased agonists" for GLP-1R that show a reduced propensity for internalisation appear to enhance insulin release with prolonged agonist exposure times[9]. The mechanisms behind these differences are unclear and may be due to the varied effects on receptor conformational changes triggered by the binding of each agonist.

Due to the suspected role of this cell internalisation process and the differences between agonists, there is scope for extensive investigation of the process of agonist binding to GLP-1R. Ligand-receptor interactions have been explored previously using fluorescence resonance energy transfer (FRET) spectroscopic methods[8].

4.1.3. Optical Imaging Systems

The principles behind fluorescence and organic and lanthanide(III) systems for optical imaging are explored in great detail in the introduction to this thesis. There is some discussion below on the principles of time-resolved fluorescence resonance energy transfer (TR-FRET), the application of lanthanide(III) luminescence in these systems, and the chemical properties of rhodamine, which have all found use in the exploration of the exendin-4 derivatives synthesised in this Chapter.

4.1.3.1. Fluorescence Resonance Energy Transfer (FRET)

FRET has long been established as a technique that can be used to measure distances on the angstrom scale, indeed, it is often referred to as a spectroscopic ruler[13–15]. The process involved is based on the principles of fluorescence and luminescence. Essentially, the system consists of a donor fluorophore and an acceptor fluorophore which exhibit some degree of spectral overlap, i.e. some wavelengths which correspond to donor emission overlap with the absorption spectrum of the acceptor fluorophore[13,14,16].

As with typical fluorescent systems, photon absorption excites the donor fluorophore from the ground state to a higher vibrational energy level with an excited electronic state. The molecule obtains thermal equilibrium with its surrounding media, returning it to the lowest vibrational energy level of the excited electronic state[16]. The molecule remains in this energy state for the rest of its lifetime which, for organic fluorophores is around 10^{-8} s, before undergoing spontaneous radiative or non-radiative decay processes to return it to the ground state[16]. With sufficient spectral overlap, the energy gap associated with one of

these processes can match the energy gap associated with absorption required to excite an acceptor molecule[16]. This then results in emission from the acceptor system.

FRET is distinct from simple re-absorption of an emitted photon: resonance energy transfer occurs without fluorescence of the donor fluorophore occurring. Additionally, the process can only occur over short distances, as can be seen by the equation for the amount of energy transferred (**Equation 4.1**)[13,16].

$$\textbf{\textit{Equation}}\ \mathbf{4.1}: E = \frac{1}{1 + (\frac{R}{R_0})^6}$$

In **Equation 4.1**, E is the amount of energy transferred from the donor to the acceptor, R is the distance between donor and acceptor and R_0 is the distance between donor and acceptor at which half the maximum energy transfer is achieved[13]. R_0 can be either known or calculated and is typically 20 – 60 Å[14].

As an additional distinction between reabsorption of an emitted photon, there is a relationship between the emission intensities of the donor and acceptor systems. With more effective energy transfer there is a reduction in intensity of fluorescence from the donor system and an increase in intensity of the acceptor emission[13–16]. This change in intensity is quantifiable and can be used to calculate the distance between the donor and acceptor, and the term of a "molecular ruler" is often used in discussions of FRET[14]. A common example of an application of FRET is to monitor changes in biological systems. For example, conformational changes in biomolecules which contain a donor and acceptor will result in an alteration in distance and therefore a substantial difference in energy transfer[13]. As such, FRET presents itself as an attractive tool for examining conformational changes associated in agonist binding of GLP-1R.

4.1.3.2. Lanthanides in FRET: Time-Resolved Systems

In classical FRET systems, energy-transfer sensitised acceptor emission is accompanied by emission resulting directly from excitation of the acceptor fluorophore – this is a side effect of the spectral overlap between donor and acceptor necessary for FRET pairs: some light intended to excite the donor will inevitably excite the acceptor, resulting in fluorescence[15]. In order to avoid this and therefore acquire more accurate information about the degree of resonance energy transfer, TR-FRET can be used. This requires selection of a FRET donor and acceptor that have different excited state lifetimes – if the donor lifetime is much longer than the acceptor then a temporal distinction will exist between sensitised emission and that resulting from direct excitation[15]. The use of a time-gate in TR-FRET allows the FRET emission to be isolated, giving more accurate information.

Lanthanide(III) ions such as Tb^{3+} and Eu^{3+} present ideal donor systems for TR-FRET. As discussed in Chapters 1 and 3, the lifetime of lanthanide(III) luminescence is typically on the millisecond timescale, much more than the nanoseconds usually observed for organic fluorophores[14,17]. Furthermore,

terbium(III) and europium(III) have sharp emission spectra and exhibit high quantum yields[14]. Coupled with the ability to reduce background fluorescence, and therefore reduce signal to noise ratio, TR-FRET using lanthanide(III) systems can allow more accurate data acquisition in the examination of biomolecular systems. Some examples of such probes, designed to allow Tb(III) chelation, are shown in **Figure 4.2**.

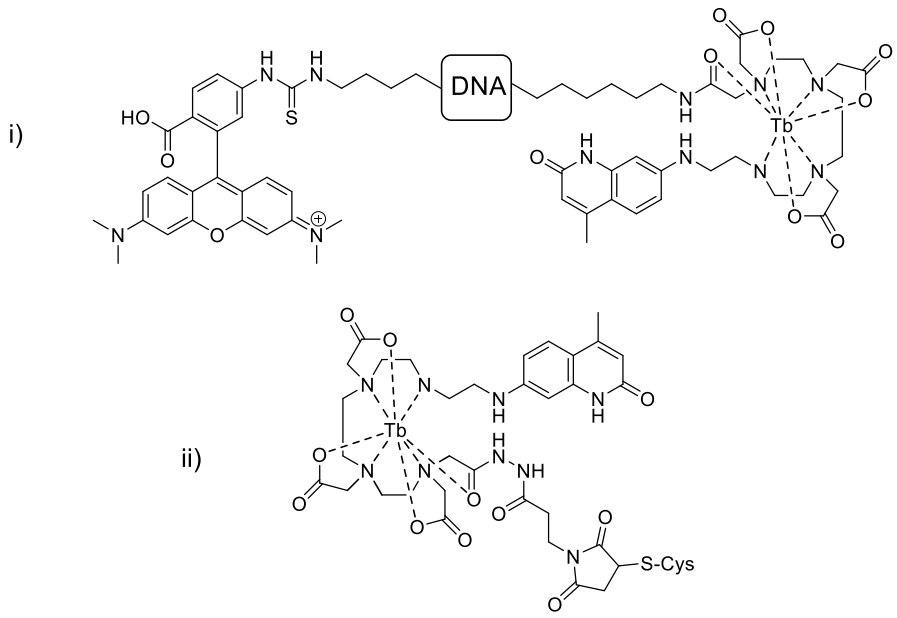


Figure 4.2: Bioconjugate systems designed for TR-FRET applications reported by i) Selvin *et al.*[18] and ii) Cha *et al.*[19].

In the compounds shown above, Selvin *et al*. utilised a DNA sequence of 10, 12 or 14 base pairs, using TR-FRET between the terbium(III) donor and the carboxytetramethyl rhodamine acceptor to measure the length of the sequences. Cha *et al*. used a cysteine residue to link the Tb(III) chelating unit to a voltage-gated ion channel labelled with a series of organic fluorophores which acted as FRET acceptors[19]. These examples show innovative usage of TR-FRET to measure distances in biological systems *via* a Tb(III)-organic fluorophore FRET pair and show that this principle could also be harnessed to study ligand-receptor interactions. Indeed, there are several examples in recent literature of TR-FRET systems being used to study GLP-1R[12,20,21].

4.1.3.3. Rhodamine-Based Chemosensors

Maintenance of intracellular pH is critical to a range of biological processes including apoptosis, cell proliferation and endocytosis[22–25]. Furthermore, specific organelles and cell structures such as mitochondria, vesicles and endosomes are known to have a pH that deviates from the rest of the cell[22,23,25]. Fluctuations in typical pH values within cells has also been shown to be involved in disease states[22]. As such, there has been an increasing interest into the development of compounds capable of indicating and monitoring changes in intracellular pH. Intraluminal pH is known to fall along the endocytic and post-endocytic pathways, and this could be explored as part of the investigation into the

effects of agonist binding on endocytosis[26]. Fluorescent chemosensors, the principle of which are discussed extensively in Chapter 5 of this thesis, possess many advantages for the detection of pH *in vitro* as fluorescence microscopy is highly sensitive and can be performed rapidly and non-destructively, making it highly attractive as a technique for use in biological systems[23].

Rhodamine was first synthesised in 1905 by Noelting and Dziewónksi[23,27]. It is a xanthene derivative which exhibits high molar absorptivity, good quantum yields, biocompatibility and high photostability[22–24]. Interest in the application of rhodamine derivatives as chemosensors began in 1997 when Dujols *et al*. reported that a derivative of the species rhodamine B exhibited "turn-on" fluorescence in the presence of Cu^{2+} ions: the compound was non-fluorescent in the absence of the ions, but the introduction of copper(II) under aqueous conditions resulted in liberation of rhodamine B itself[23,28]. It was found that this chemosensing ability was due to opening of its spirolactam ring. This has since been adapted by many in the field to produce a range of spirolactam and spriolactone rhodamine species which are capable of acting as sensors for a wide range of analytes including metal ions and nucleic acids[23–25].

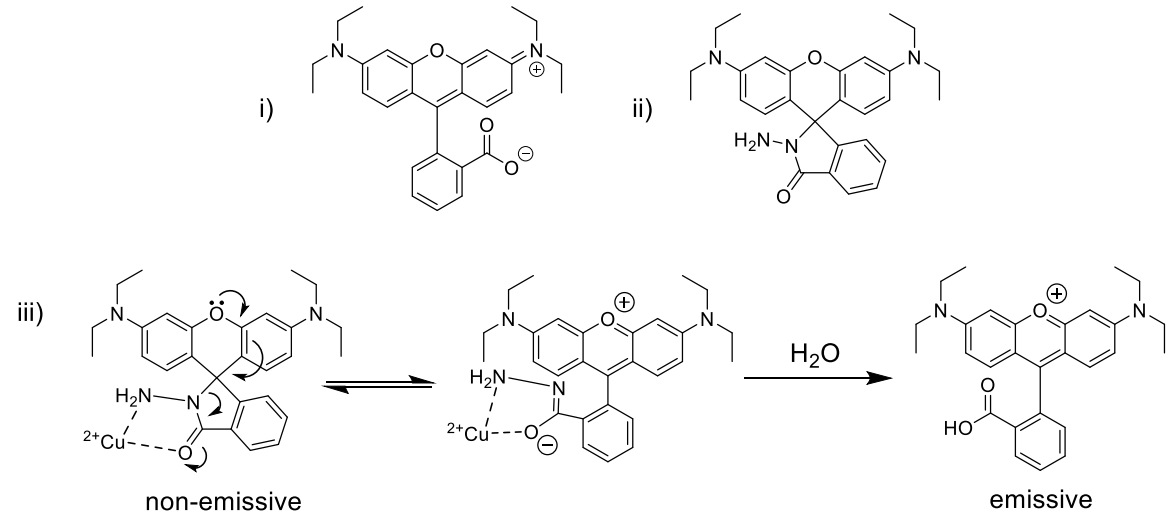


Figure 4.3: i) Rhodamine B, ii) Dujols' compound - the first rhodamine-based chemosensor featuring a spirolactam ring, iii) the mechanism of Dujol's interaction with Cu^{2+}[28].

The binary nature of rhodamine's fluorescence response has presented it as an attractive system for the detection of differences in pH. Historically, ratiometric pH sensors had been developed around systems which exhibited a Stokes shift during pH changes[22]. These compounds can suffer from a small Stokes shift and frequently only function in a narrow pH range, rendering their use to obtain accurate information difficult[22]. The "off-on" nature of rhodamine derivatives overcomes these limitations. From a chemical perspective, it has been found that spirocyclic rhodamine compounds are highly fluorescent at acidic pH, when this ring is open, and non-emissive under neutral or basic conditions[22–25]. The mechanism responsible for this is shown in **Figure 4.4**.

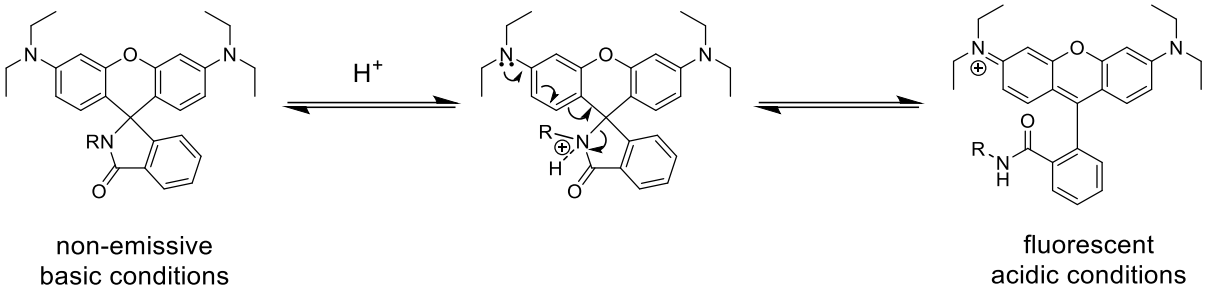


Figure 4.4: The equilibrium between the non-emissive and fluorescent derivatives of a rhodamine spirolactam compound[25].

This equilibrium found in spirocyclic systems has been harnessed by many in the field to produce a series of compounds which act as "on-off" sensors to monitor and detect pH changes. Some of these are shown below in **Figure 4.5**.

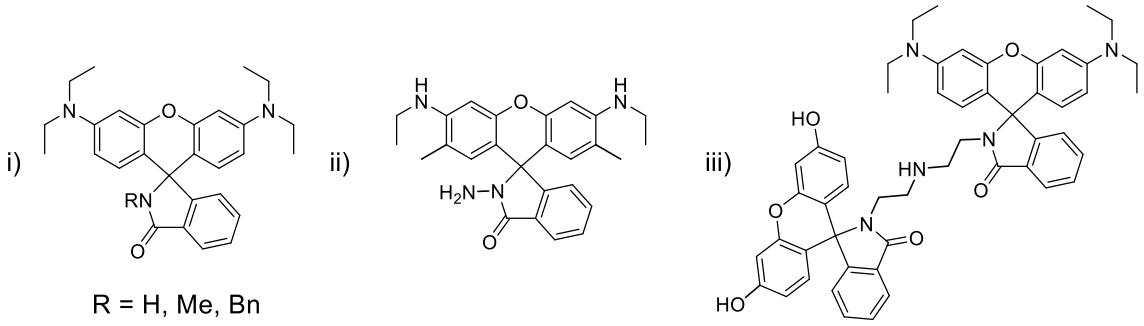


Figure 4.5: i) Markush structure of the family of compounds developed by Best *et al*.[25], ii) a pH sensitive compound reported by Kang *et al*.[29] and iii) a dual-colour species synthesised by Lee *et al*.[22].

Of the compounds depicted above, the family produced by Best *et al*. are notable for what they revealed about the contributing factors to the equilibrium shown in **Figure 4.5**. The authors found that increasing the nucleophilicity of the amine, alongside reducing steric hindrance, resulted in a shift in the position of equilibrium towards the ring-opened system at higher pH values, introducing a mechanism through which the pH sensitivity of these compounds may be finely tuned[25].

Additionally, the compound synthesised by Lee *et al*. is uniquely interesting as it utilises two fairly similar, xanthene-based moieties to act as a pH sensor across a wide range of pH values[22]. Fluorescein exhibits analogous behaviour to rhodamine derivatives based on spirocyclic systems but this is inverted, with these compounds being highly fluorescent under basic conditions and relatively non-emissive in acid[22]. The authors harnessed the complementary behaviour of rhodamine and fluorescein to produce a probe with two alternately coloured emissive regions of the same compound, with the rhodamine moiety exhibiting pink fluorescence in acid, fluorescein emitting green light under basic conditions, and both colours observable at varying degrees within intermediate pH values[22].

The “off-on” switchable nature of the fluorescence of rhodamine derivatives capable of acting as pH chemosensors, their previous use in the Long group and successful incorporation into protein labels rendered the development of a series of exendin-4-rhodamine conjugates desirable as these could monitor any endocytosis taking place after binding to GLP-1R through changes in pH within the probe’s environment, giving an insight into the potential for agonist cell internalisation[24,30].

4.1.4. Aims and Objectives

The aim of the work described in this Chapter was to synthesise a family of compounds which could be used to investigate specific GLP-1R agonist behaviours. Building on the success had utilising exendin-4 as a targeting peptide for the probes discussed in Chapter 2, it was theorised that this series should be based on this well known, potent ligand for GLP-1R. Synthesising a range of compounds which would have different affinities for GLP-1R, as well as potentially being able to localise to other parts of the cell membrane, would also be desirable. These compounds should be able to harness the phenomenon of FRET to allow examination of their interaction with the receptor, which would give an indication of the conformational changes taking place within the receptor’s transmembrane helices.

Due to the changes in endosomal pH associated with the endocytosis process, there is substantial interest in probes which can act as chemosensors, responding to the acidic conditions experience by receptors and agonists during endocytosis. Fluorescent compounds, particularly those based on rhodamine, have found many applications as pH sensors due to the spirocyclic ring opening equilibrium which they can include. As such, it was theorised that a rhodamine-exendin-4 derivative could act as a complementary probe to the FRET-based systems and allow a thorough investigation of agonist binding and receptor endocytosis.

The interaction between these probes and GLP-1R was explored. For the pH sensitive compounds, their photophysical properties at different pH values were analysed to establish whether they are suitable for *in vitro* and *in vivo* applications.

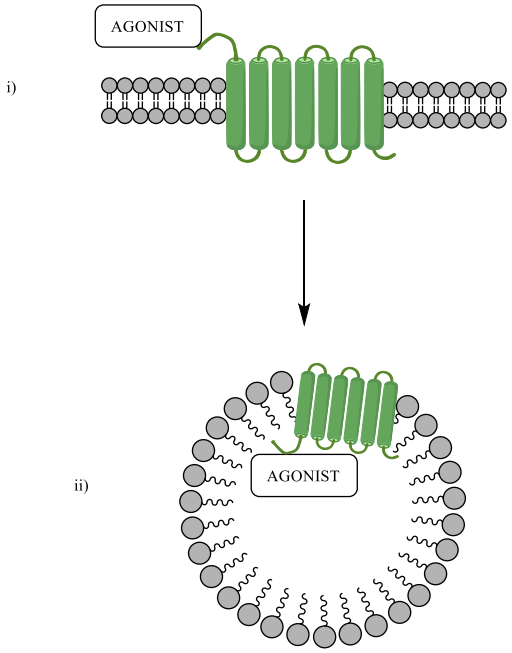


Figure 4.6: Simplified diagram of agonist binding and subsequent endosome formation involved with GLP-1R. These processes can be examined through i) FRET based probes looking at conformational receptor changes *via* its distance dependence and ii) pH sensitive fluorescent compounds which exhibit different responses as the endosomal pH drops during cell internalisation.

4.2. Results and Discussion

Variants of exendin-4 have been widely utilised to image pancreatic β-cells using a wide array of modalities[31–35]. Frequently, modifications to the peptide have taken place at the terminus of the amino acid chain, which is known to have a limited involvement in receptor binding[36]. In 2014, Clardy *et al.* produced a series of exendin-4 derivatives which explored the effect of modifications at different positions of the amino acid chain on receptor binding affinity[37]. This work established that the addition of fluorophores to the 12th amino acid in the peptide sequence was well-tolerated, with only a small reduction in affinity of these probes for the GLP-1R receptor[37].

It was hypothesised that ligand interactions with GLP-1R could be explored through TR-FRET experiments – FRET is distance dependent so the energy transfer efficiency could reveal nanoscale information about the proximity of the receptor and its agonist[13]. These would consist of assessing the energy transfer from a FRET donor-labelled exendin derivative to a FRET acceptor-labelled GLP-1R. Time-resolved spectroscopy is advantageous in studying biological systems as it enables background fluorescence to be excluded, enhancing signal-to-noise ratio[17]. Lanthanide(III) complexes, for example those with Tb(III), are a prime example of species which are suitable for this application.

Furthermore, it was also theorised that the role of GLP-1R in vesicle formation and cell internalisation could be explored through the incorporation of a pH-switchable probe. The pH of endosomes is known to drop during the cell internalisation process, and it was hypothesised that modifying exendin-4 at the 12th amino acid position with a pH-dependent fluorophore could explore this and assess whether the broader family of probes were taken up into cells expressing GLP-1R[26]. Rhodamine derivatives are highly fluorescent and can be modified to introduce a level of pH dependence, as has been previously achieved in the Long group, so they presented an attractive option for this approach[24].

4.2.1. Synthesis of Terbium(III)-Exendin-4 Conjugates

As discussed above, Tb(III) complexes with an appropriate antenna ligand present a suitable FRET system for the study of ligand-receptor binding in GLP-1R. In order to conjugate a complex to a peptide such as exendin-4, the conditions required should be mild and enable this to be done selectively.

Copper-catalysed alkyne-azide cycloaddition (CuAAC) is a technique which has been widely used in synthetic chemistry to enable covalent bond formation under mild conditions[38]. Typically, all that is required is for azide and alkyne functionality to be present in the two molecular fragments which are to be conjoined. This can be done under aqueous conditions and in the presence of a copper(I) centre at room temperature, and this route, which was also utilised by Clardy, was chosen as the synthetic method to develop the Tb(III)-exendin-4 analogues synthesised in this Chapter[37,39,40]. Other groups have also utilised Cu(II) catalysts for this process[41–43]. Utilisation of CuAAC, rather than amide coupling, also presented a selective route to avoid addition at the many NH_2 groups present in exendin-4: Clardy *et al*. had used a modified amino acid variant including a propargyl alkyne chain, which is shown in **Figure 4.7**[37].

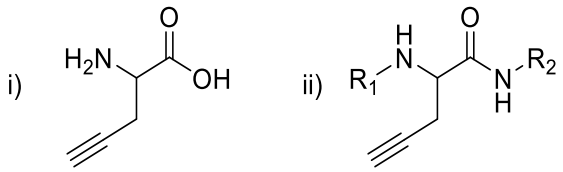


Figure 4.7: i) Pra, the modified propargyl alkyne amino acid (Pra) utilised by Clardy *et al*.[37] and ii) general structure of peptides incorporating this amino acid.

Dr Ben Jones of the Section of Endocrinology at Imperial College London provided a series of exendin-4 variants which incorporated this amino acid at the 12th position in the sequence. An exception to these is a modified derivative of exendin-9, a shorter peptide which acts as an antagonist of GLP-1R[44]. The nomenclature applied to these peptides and their amino acid sequences in relation to the structure shown in **Figure 4.7** are displayed in **Table 4.1**.

Peptide	R_1	R_2
Ex4-Pra^{12}	HisGlyGluGlyThrPhe ThrSerAspLeuSer	GlnMetGluGluGluAlaValArgLeuPheIleGluTrpLeuLysAsnGlyGlyProSerSer GlyAlaProProProSerNH$_2$
Ex4-Pra^{12}-C$_{16}$	HisGlyGluGlyThrPhe ThrSerAspLeuSer	GlnMetGluGluGluAlaValArgLeuPheIleGluTrpLeuLysAsnGlyGlyProSerSer GlyAlaProProProSerGlyLys-hexadecanoic acid
Ex9-Pra^{12}	AspLeuSer	GlnMetGluGluGluAlaValArgLeuPheIleGluTrpLeuLysAsnGlyGlyProSerSer GlyAlaProProProSerNH$_2$
Ex4-Phe^1-Pra^{12}	PheGlyGluGlyThrPhe ThrSerAspLeuSer	GlnMetGluGluGluAlaValArgLeuPheIleGluTrpLeuLysAsnGlyGlyProSerSer GlyAlaProProProSerNH$_2$
Ex4-Asp^3-Pra^{12}	HisGlyAspGlyThrPhe ThrSerAspLeuSer	GlnMetGluGluGluAlaValArgLeuPheIleGluTrpLeuLysAsnGlyGlyProSerSer GlyAlaProProProSerNH$_2$

Table 4.1: Nomenclature and amino acid sequences of the peptides discussed in this Chapter.

Another collaborator, Yue Wu, working with Professor Gary Ka-Leung Wong at Hong Kong Baptist University, was able to provide a terbium(III) complex incorporating azide functionality. This compound is shown below.

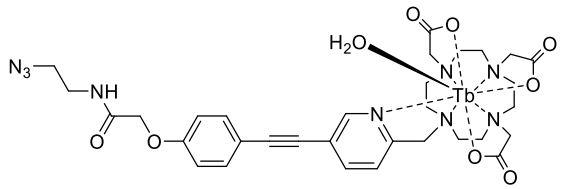


Figure 4.8: The Tb(III) complex provided by Yue Wu.

It was decided to employ CuAAC chemistry to join this complex and the peptides. The first two peptides chosen were Ex4-Pra^{12} and Ex4-Pra^{12}-C$_{16}$.The former has the same sequence as the native peptide, bar substitution of the lysine residue at the 12th position for the propargyl alkyne shown above. This same modification is employed in the latter, with the addition of a fatty acid chain containing 16 methylene units. This addition was expected to direct the ligand to bind to the receptor in particular membrane nanodomains.

The terbium(III) complex and Ex4-Pra^{12} could be successfully conjugated using $CuSO_4$ as the copper source and sodium ascorbate. Reaction progress was monitored by LCMS, carried out by Dr Lisa Haigh. Once the LCMS trace suggested that the reaction had reached completion, the reaction mixture was lyophilised and reverse phase flash chromatography used to isolate the conjugate, Ex4-Pra^{12}-Tb, compound **4.1** at an impressive yield of 94%. These same conditions could not successfully give the Ex4-Pra^{12}-C$_{16}$-Tb analogue, possibly due to reduced solubility of the peptide containing the fatty acid chain. Use of copper(I) iodide and addition of NaOH solution (0.1 M) did improve solubility and enable the conjugate, **4.2**, to be isolated, albeit at a much lower yield of just 50%.

Variations on each of these conditions were employed to synthesise Tb(III) conjugates of the five peptides supplied by Dr Jones. The copper catalyst, reaction time and other reaction conditions for these species are summarised in **Table 4.2**.

Peptide	Product	Reaction Conditions	Reaction Time	Yield
Ex4-Pra^{12}	Ex4-Pra^{12}-Tb, **4.1**	Cu(SO_4), sodium ascorbate	24 hours	94%
Ex4-Pra^{12}-C_{16}	Ex4-Pra^{12}-C_{16}-Tb, **4.2**	CuI, NaOH	22 hours	50%
Ex9-Pra^{12}	Ex9-Pra^{12}-Tb, **4.3**	Cu(SO_4), sodium ascorbate	39 hours	91%
Ex4-Phe^{1}-Pra^{12}	Ex4-Phe^{1}-Pra^{12}-Tb, **4.4**	Cu(SO_4), sodium ascorbate, NaOH	6 days	72%
Ex4-Asp^{3}-Pra^{12}	Ex4-Asp^{3}-Pra^{12}-Tb, **4.5**	Cu(SO_4), sodium ascorbate	6 days	28%

Table 4.2: Summary of reaction conditions employed in the synthesis of exendin-Tb conjugates.

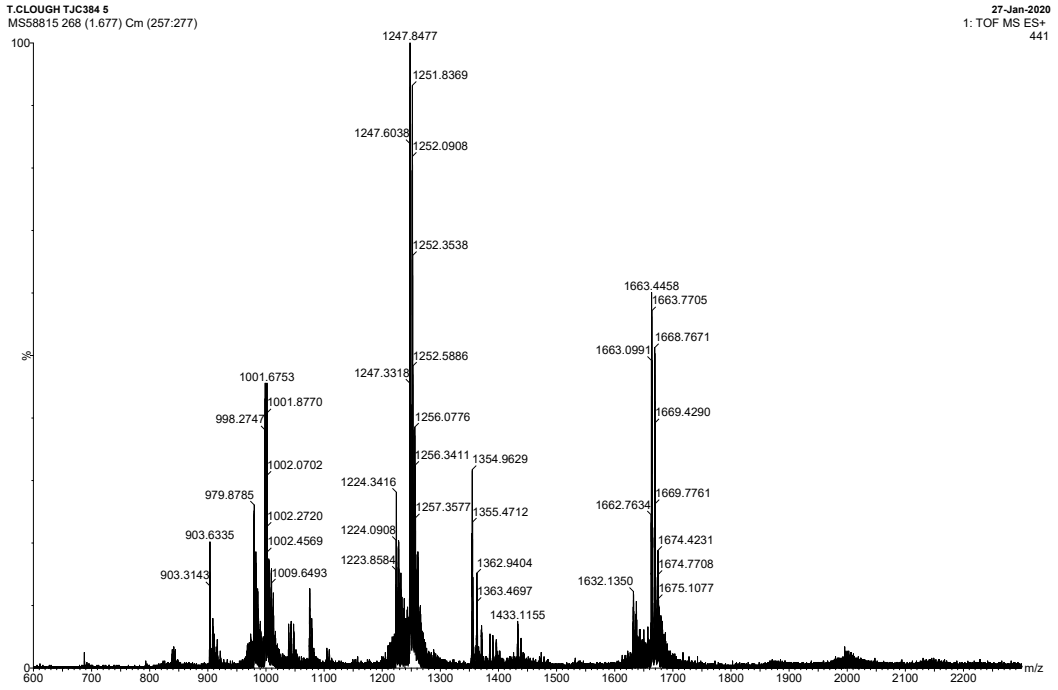


Figure 4.9: Mass spectrum of compound **4.1** with peaks at 1001.6753 $[M]^{5+}$, 1247.8477 $[M]^{4+}$, 1663.4458 $[M]^{3+}$.

The addition of NaOH solution was required for peptides with lower solubility in aqueous conditions. In general, there was little variation in the reactions, although there were much longer reaction times necessary for the phenylalanine and aspartic acid derivatives **4.4** and **4.5**. In general, it was pleasing

that a wide variety of compounds, the general structure of which is shown below in **Figure 4.10**, could be produced from these mild, straightforward reaction conditions.

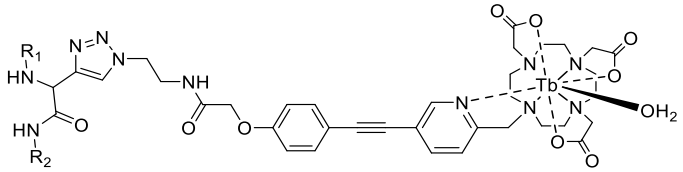


Figure 4.10: General structure of the conjugates synthesised.

The lifetime of the luminescence of the Tb(III) centres of each of these conjugates was measured to examine the impact of the peptide. These results are displayed in **Table 4.3**.

Compound	Lifetime/ms
Yue286	0.1093
4.1	0.2161
4.2	0.2905
4.3	0.2533
4.4	0.3928
4.5	0.3624

Table 4.3: Lifetime data for compounds **4.1** – **4.5** and the Tb(III) complex **Yue286** (1 μM, H_2O, n = 3).

The lifetime data for these compounds showed a large increase luminescence lifetime of the Tb(III) complex in each of the peptide conjugates. This increased lifetime is likely to be due to shielding of the Tb(III) centre from solvent molecules and O_2 which can quench the excited state of lanthanides. Differences between the peptides are likely due to different peptide structures resulting from the alternative amino acid sequences, although the dramatic differences seen in compounds **4.4** and **4.**5 compared to **4.1** may warrant further investigations. These data show that the probes could have applications in optical imaging, and that there was not a negative effect of conjugation.

4.2.1.1. In Vitro Receptor Binding Investigations

It was decided to explore the impact of the conjugation of a Tb(III) complex to exendin-4 on its ability to activate GLP-1R. Exendin-4 has been shown to trigger the production of cyclic adenosine monopohosphate (cAMP) *via* its activation of GLP-1R *in vivo*[45,46]. The signalling potency of the compounds **4.1** and **4.2** for GLP-1R was investigated by measuring the level of cAMP produced in HEK293-SNAP-GLP-1R cells[7] after incubation with different concentrations of the ligands. As stated earlier, this work was carried out by Dr Ben Jones in the Section of Endocrinology, Imperial College London.

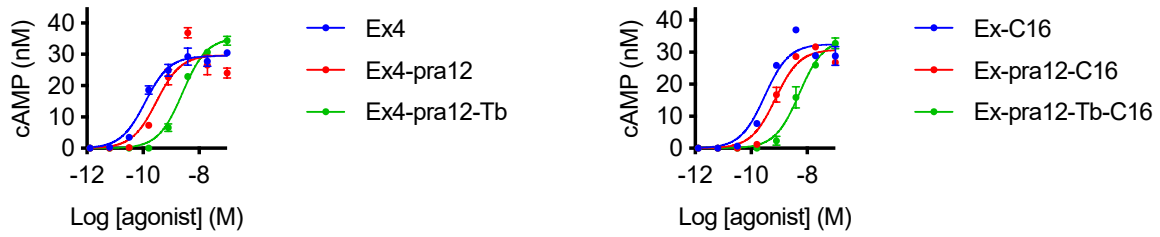


Figure 4.11: Dose-response curves showing *in vitro* concentration of cAMP produced after administration of exendin-4, Ex4-Pra^{12} and **4.1** (left), and the fatty acid chain analogues exendin-4-C$_{16}$, Ex4-Pra^{12}-C$_{16}$ and **4.2** (right).

Effective concentration (EC$_{50}$) is a measure of receptor affinity, which represents the concentration of a substance required to elicit half the maximum response of the receptor it activates[47]. Using the dose-response curves shown above, Dr Jones was able to calculate EC$_{50}$ values for **4.1** and **4.2**, which are displayed alongside the non-conjugated derivatives in **Table 4.4**.

Compound	**Exendin-4**	**Ex4-Pra^{12}**	**4.1**	**Ex4-C$_{16}$**	**Ex4-Pra^{12}-C$_{16}$**	**4.2**
EC$_{50}$/nM	0.1	0.3	2.4	0.3	0.9	5.6

Table 4.4: EC$_{50}$ values obtained from the dose-response curves above in **Figure 4.10**.

The EC$_{50}$ values obtained show that modification to the exendin-4 structure resulted in a reduction in receptor affinity. An increase in EC$_{50}$ indicates that a greater concentration was required to elicit the same response. These data show that incorporation of the fatty acid chain, or substitution of lysine for the modified propargyl amino acid resulted in a three-fold reduction in receptor affinity of the peptide. Inclusion of both of these modifications resulted in a nine-fold potency reduction, as seen in the EC$_{50}$ value for Ex4-Pra^{12}-C$_{16}$. Coupling to the Tb(III) complex resulted in a further eight-fold potency decrease for **4.1** compared to Ex4-Pra^{12} (24 times less than the native agonist) and approximately a six-fold reduction for **4.2** compared to Ex4-Pra^{12}-C$_{16}$ (56 times lower than exendin-4). Although these affinities are much lower than the native peptide, and also clinically approved drugs which are based on exendin-4[48,49], it was reassuring to see that a response could still be obtained, indicative of receptor binding, and that modifications to the peptide did not complete remove any receptor binding ability.

4.2.1.2. FRET Studies and Receptor Interaction

After it was established that compounds **4.1** and **4.2** could bind successfully with GLP-1R, it was decided to explore whether the Tb(III) complex could act as a FRET donor to explore any conformational changes in GLP-1 which take place on agonist binding. The photophysical properties of the Tb(III) complex synthesised by Yue Wu alongside **4.1** and **4.2** were explored, with the excitation spectrum of the former and time-gated emission spectra of the latter two displayed in **Figure 4.12**. These were recorded by Dr. Jones.

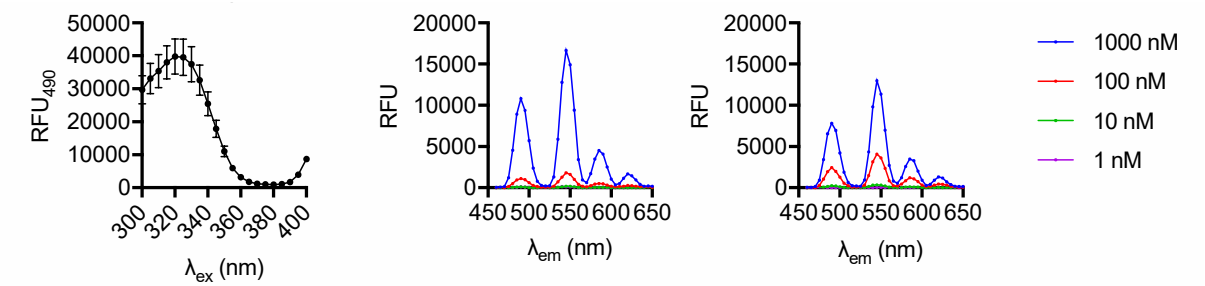


Figure 4.12: Excitation spectrum of the Tb(III) complex provided by Yue Wu (left) and the time-gated emission spectra of **4.1** (centre) and **4.2** (right), displaying classical Tb(III) emission patterns. Spectra recorded by Dr Ben Jones.

It was concluded that the Tb(III) luminescence of both **4.1** and **4.2** showed that the two compounds could be used as FRET donors for near-infrared emissive organic fluorophores conjugated to GLP-1R. This strategy has been widely reported in the literature as a strategy for exploring protein behaviour *in vitro*[50–53]. The organic compound BG-649 (**Figure 4.13**) was chosen as the fluorophore of interest.

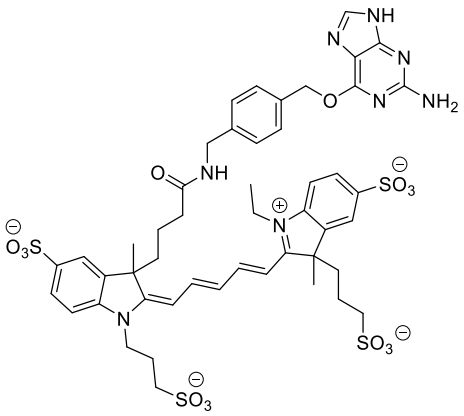


Figure 4.13: Structure of BG-649[51].

BG-649 could be appended to GLP-1R *via* a SNAP tag. This is a well-established technique for site-specific peptide labelling which used the species O^6-alkylguanine-DNA alkyltransferase (hAGT), which forms a covalent thioether bond between the O-alkyl group and a cysteine residue within hAGT[54,55]. Compounds **4.1** and **4.2** were incubated with SNAP-labelled HEK293-BG-649-GLP-1R[7]. This resulted in observable FRET taking place from the donor Tb(III) system and the acceptor cyanine fluorophore, indicating that ligand binding to GLP-1R could be detected through TR-FRET.

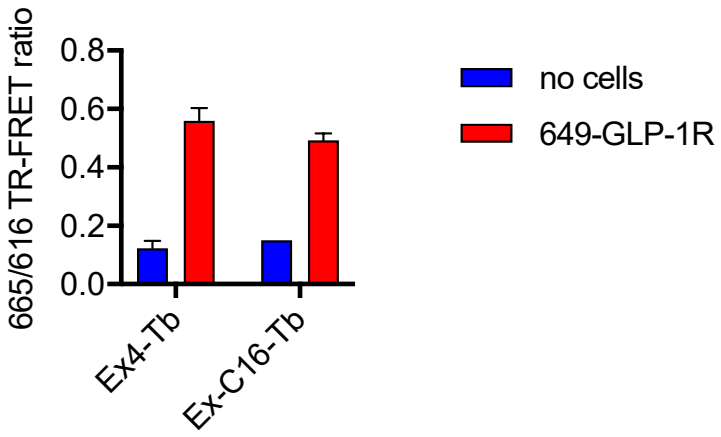


Figure 4.14: TR-FRET ratios for compounds **4.1** and **4.2** in the presence and absence of SNAP-labelled GLP-1R containing cells, prepared by Dr Ben Jones.

BG-649 is a FRET acceptor which can be excited by the transition in Tb^{3+} associated with the emission peak at around 620 nm. The Figure above shows the ratio of the intensity of the BG-649 sensitised emission at 665 nm to the intensity of the Tb(III)-centred emission at 616 nm. In the absence of cells containing the labelled receptor, i.e. only with BG-649 present, some FRET occurred, as observed from the small ratio value. When cells containing the labelled GLP-1R were introduced, FRET can be observed: the increase in the ratio of emission intensities (665 nm:616 nm) shows that there was a decrease in donor emission intensity and an increase in acceptor emission, indicative of a FRET process. Due to the strong distance dependence of FRET, this suggests that the Tb(III) labelled peptide and fluorophore-labelled GLP-1R are being brought into close proximity, which is thought to be due to receptor binding.

These exciting results indicate that TR-FRET can be used to monitor receptor-agonist binding processes for both compounds **4.1** and **4.2**, with the former exhibiting slightly more effective resonance energy transfer, as can be seen by the greater acceptor:donor intensity ratio seen in **Figure 4.14**. This could be due to the greater affinity of **4.1** for the GLP-1R receptor, which may result in receptor conformational changes bringing the donor and acceptor fluorophores into closer proximity after agonist-receptor binding. It is hoped that in the future this same study can be carried out with compounds **4.3**, **4.4** and **4.5**. This would give an insight into the different conformational changes occurring during the interaction between GLP-1R and its ligands.

An additional investigation has been proposed to explore the impact of the fatty acid chain present in **4.2** on the localisation of the probe within plasma membranes. As discussed above, GLP-1R is known to associate with cholesterol-rich, liquid ordered (LO) lipid rafts within cell membranes[7,8]. Regions of the plasma membrane which have a lower cholesterol content are less tightly packed and are referred to as liquid disordered (LD)[6]. These areas have an enhanced phospholipid content. It was hypothesised that the inclusion of the C_{16} chain in **4.2** would result in distribution to these liquid-disordered, non-raft

regions of the membrane. This could be investigated through the use of the compound NR12S, which was reported by Kucherak *et al*. in 2010[6]. NR12S contains a Nile Red fluorophore, a hydrocarbon chain and an anionic terminal group, therefore acting as a structural mimic of a phospholipid, and inserts uniformly across the plasma membrane[6]. The structure of NR12S is shown in **Figure 4.15**.

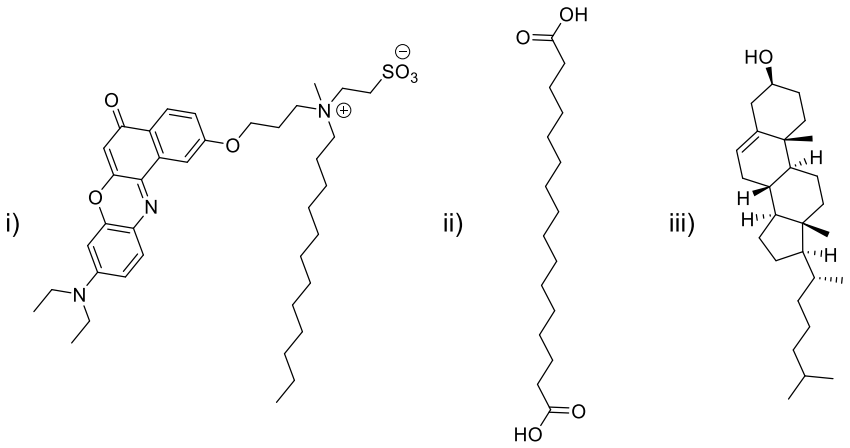


Figure 4.15: The structures of i) NR12S[6], ii) the hexadecenoic acid chain appended to **4.2** and iii) cholesterol.

NR12S has several interesting photophysical properties which are relevant to the investigation of the structure of cell membranes. Its emission wavelength changes dramatically according to the polarity and order within its environment[6]. Kucherak *et al*. extensively studied this and showed that NR12S exhibited a blue shift when incorporated into LO domains and a red shift when taken into LD regions[6].

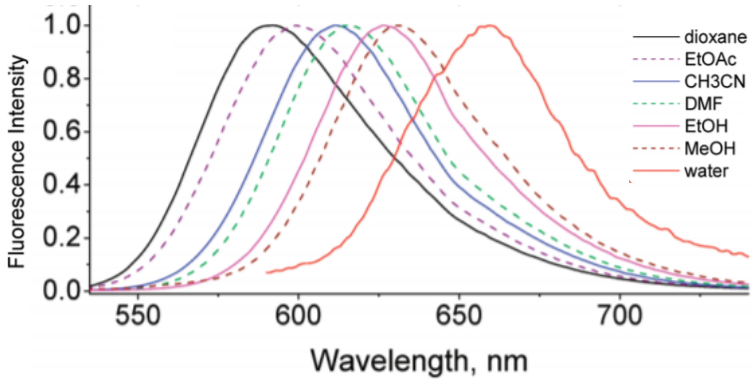


Figure 4.16: Emission spectra of NR12S in a range of solvents. A clear red shift can be observed in more polar solvent systems and a blue shift in non-polar systems. Adapted from reference 6, with permissions, Copyright (2010) American Chemical Society[6].

Cholesterol is a relatively non-polar compound, therefore regions of the plasma membrane which are rich in it (the LO lipid rafts) would be expected to result in a blue shift in the emission spectrum of NR12S.

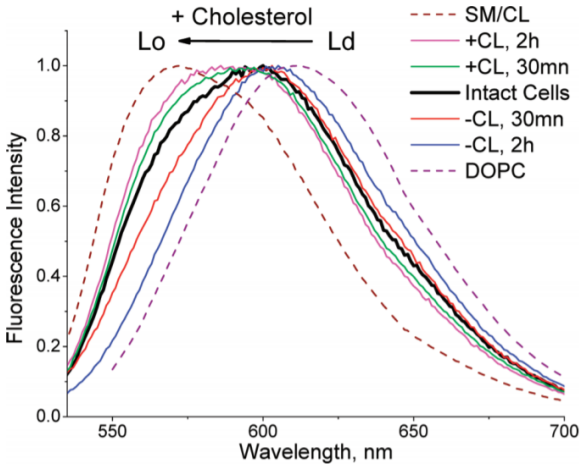


Figure 4.17: Emission spectrum of NR12S in cells with different cholesterol levels (±CL) and in model plasma membranes with LO (SM/CL) and LD (DOPC) phases showing the corresponding blue and red shifts. Adapted from reference 6, with permissions, Copyright (2010) American Chemical Society[6].

NR12S can be excited at 490 nm, therefore has the potential to act as a FRET acceptor from the emission of Tb(III)[6]. Due to the relationship between the structure of the plasma membrane (i.e. LO or LD) and emission wavelength of NR12S, it was hypothesised that incubation of cells with the dye and either **4.1** or **4.2**, then seeing if any FRET was taking place, could allow the distribution of the probes on cell membranes to be explored.

It was expected that **4.1** would bind to GLP-1R in LO regions, where it is known to be compartmentalised. This would result in a blue shift seen from any FRET emission from NR12S in close proximity. Comparatively, **4.2** was predicted to be taken up slightly more by LD regions with a lower cholesterol content, resulting in red shifted FRET emission from NR12S. This investigation was carried out by Dr. Jones.

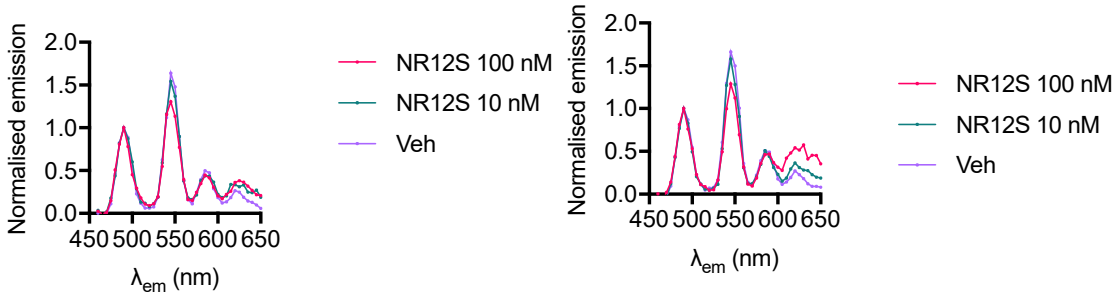


Figure 4.18: Emission spectra of **4.1** (left) and **4.2** (right) in aqueous solution at different concentrations of NR12S, normalised to the emission at 490 nm. Spectra acquired by Dr. Ben Jones.

The obtained results showed that a FRET process was taking place between each of the Tb(III) containing probes and NR12S. This can be seen from a reduction in the intensity of the emission peak at around 550 nm, which is more prevalent at higher concentrations of NR12S. There was an increase in the emission around 630 nm observed with both compounds, although more so with **4.2**. This may

be due to the fatty acid chain of **4.2** allowing hydrophobic interactions between the probe and NR12S, enabling the two compounds to come into closer proximity and resulting in more effective FRET.

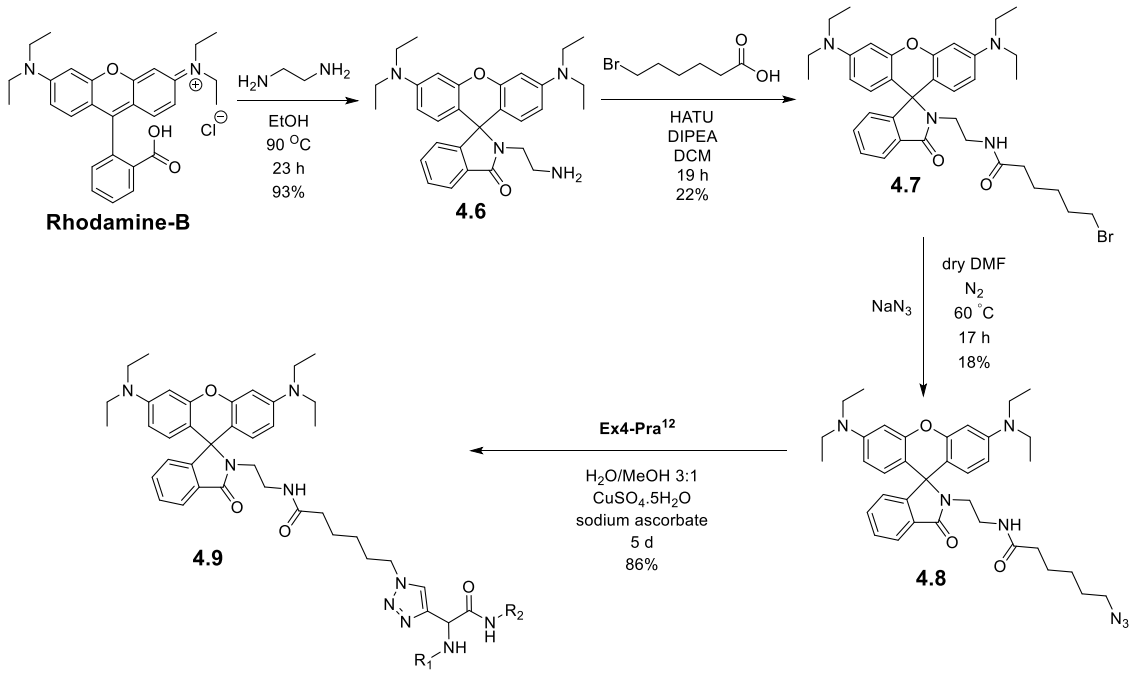
Having seen that FRET was possible between both **4.1** and **4.2**, the next step in this investigation would be to explore the behaviour of these compounds in cells labelled with NR12S. This would help establish whether the incorporation of the acid chain to **4.2** had an impact on its distribution within plasma membranes, and whether this could be recorded through a change in emission wavelength associated with NR12S. Some *in vitro* work exploring this concept, and the different cell internalisation profiles of the Phe[1] and Asp[3] conjugates synthesised, is currently being carried out by Waygen Thor and Antony Ho Fai Chau at Hong Kong Baptist University.

4.2.2. Synthesis of Rhodamine-Exendin-4 Conjugates

As mentioned above, pH-sensitive rhodamine derivatives can be synthesised[24]. In order to explore whether ligands binding to GLP-1R could then be internalised, it was decided to produce modified exendin-4 analogues which could utilise properties of these rhodamine compounds. One of these contained a spirolactam ring that would be susceptible to acid-catalysed opening and a corresponding "switching on" of the fluorescence of the compound. It was hypothesised that, if cell-internalisation was occurring, the associated drop in pH would result in an enhancement in emission intensity and suggest that these probes could be internalised. Another compound that did not exhibit this pH-dependence on emission intensity would be synthesised to act as a standard for comparison. It was also decided to employ the same CuAAC chemistry that had successfully been utilised to generate the terbium(III) chelates discussed above. As such, an azide group would need to be introduced to this rhodamine compounds.

The synthesis of the pH-sensitive rhodamine compound was carried out first. The initial step in this synthetic pathway was a procedure published by Zhang *et al*., which required stirring a solution of rhodamine-B and an excess of ethylenediamine in ethanol overnight[56]. This was successfully carried out to give compound **4.6** at an impressive yield of 93% with no further purification needed. One early indicator of the success of this reaction was a distinct colour change: rhodamine-B is bright pink in solution, indicative of its intense emission, whereas compound **4.6** was pale orange, due to its non-emissive state. It was necessary to introduce a leaving group that could be readily converted to an azide through a nucleophilic substitution reaction. The distance between the rhodamine fluorophore and this leaving group was critical – too close and there was the risk of steric hindrance preventing any conversion to the azide taking place. Other work within the Long group, as yet unpublished, has suggested that the length and nature of this chain can also impact on the pH sensitivity of the spirolactam ring opening[57]. 6-Bromohexanoic acid was chosen as the tool to introduce this leaving group a suitable distance away from the fluorophore coupled with the fact that standard chemistry techniques could be used to couple it to amine **4.6**. This reaction was carried out using 1-[bis(dimethylamino)methylene]-

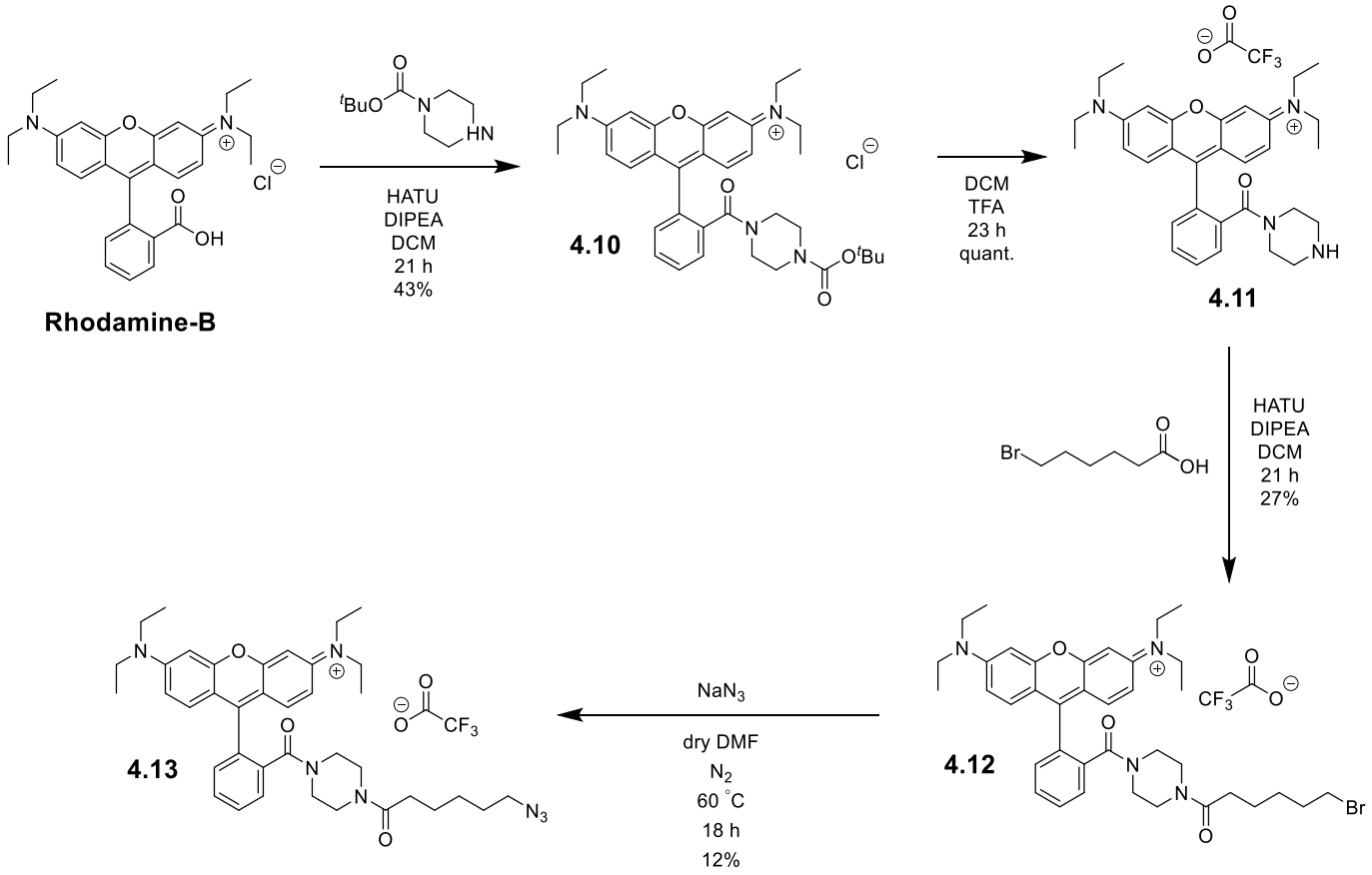
1*H*-1,2,3-triazolo[4,5-b]pyridinium 3-oxide hexafluorophosphate (HATU) and diisopropylethylamine (DIPEA), typical conditions for amide couplings, and gave the bromide **4.7** at a low yield of 22%. Conversion of this bromide to the azide **4.8** necessary for CuAAC chemistry through its reaction with NaN_3 in anhydrous dimethylformamide (DMF) was completed, again at a low yield of just 18%. Reaction of this azide with Ex4-Pra[12] could be carried out with $CuSO_4$ and sodium ascorbate to give the peptide conjugate **4.9** at a high yield of 86%, although this reaction was left running for a fairly long time (5 days) before LCMS results indicated successful product formation. **Scheme 4.1** shows the synthetic route towards this compound.



Scheme 4.1: Synthesis of the rhodamine-peptide conjugate **4.9**. R_1 and R_2 correspond to the amino acid sequences in Ex4-Pra[12] displayed in **table 4.1**.

Following the successful isolation of the switchable rhodamine-exendin-4 conjugate, it was decided to start synthesis of a non-switchable derivative. This would be "always on" and contain a tertiary amide group which would prevent any spirolactam ring formation from taking place.

An amide coupling between rhodamine-B and *N*-Boc-piperazine allowed the necessary tertiary amide functionality to be incorporated into the rhodamine framework and lock the compound into "always-on" fluorescence. This was carried out using HATU and DIPEA and gave the protected amide **4.10** at a satisfactory yield of 43%. Deprotection of the Boc group to liberate the amine was based on an analogous procedure carried out by Yuan *et al.*[58] and enabled **4.11** to be obtained quantitatively. Coupling of this compound to 6-bromohexanoic acid using HATU gave the bromide **4.12** at a yield of 27%, with subsequent conversion to the azide **4.13** being achieved at a yield of 12%. It is possible that the strong N_3^- nucleophile could also attack the amide bonds in each of the compounds, resulting in the low yields. **Scheme 4.2** shows that synthesis of the "always-on" rhodamine derivative.



Scheme 4.2: Synthesis of the azide **4.13**.

Subsequent conjugation to an alkyne-functionalised exendin-4 variant could not be carried out due to time constraints, but in future this should be a routine procedure.

4.2.2.1. Photophysical Properties

Having successfully synthesised a fluorophore-exendin-4 conjugate which should exhibit pH-sensitive changes in fluorescence emission intensity, it was decided to explore the photophysical properties of **4.9** and examine its response to changes in pH.

Initially, the UV-vis absorbance of **4.9** was recorded. The spectrum is shown in **Figure 4.19**.

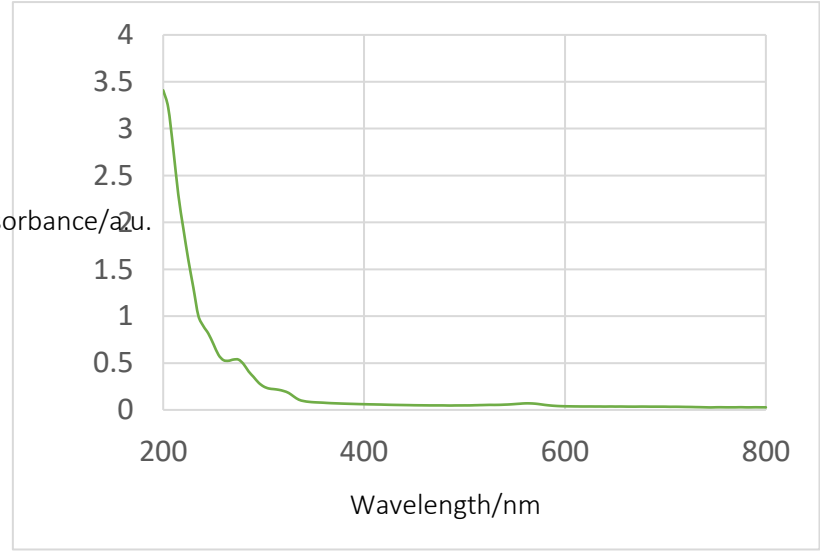


Figure 4.19: UV-vis absorbance of **4.9** (300 µM, H_2O).

Peptides are known to absorb UV light, and as LCMS had been used to characterise the conjugates discussed above (**4.1** – **4.5**) and the exendin-based probes synthesised in Chapter 2, the intense absorbance below around 375 nm was anticipated. Initially, the low absorbance of **4.9** in the visible region of the spectrum was surprising, as the compound was visibly coloured pink and all characterisation suggested that the rhodamine unit had been attached. Upon closer inspection of the visible window, an absorbance pattern corresponding to typical rhodamine absorption could be seen.

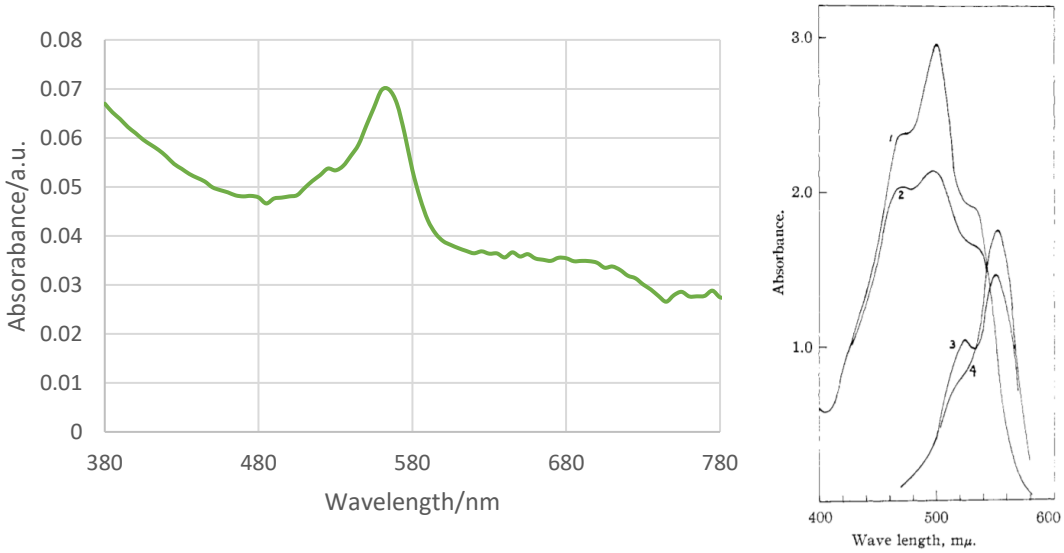


Figure 4.20: Left - Highlighted visible region of the absorbance spectrum of **4.9**, showing an absorption maximum at 570 nm. Right – exemplar absorbance spectrum of rhodamine-B with curves 3 and 4 exhibiting similar shapes and absorption maxima at 580 nm (pH 8, aq. NH_4Cl buffer, 0.2 mM and 20 µM respectively), adapted from reference 59, with permissions, Copyright (1956) American Chemical Society[59].

Following successful indication that the rhodamine moiety was present, the fluorescence of the system was explored. This was done by exciting the compound at 560 nm, which resulted in emission at 580 nm. Excitation at 570 nm was not carried out – the small amount of **4.9** isolated meant that the intensity of the fluorescence emission was extremely weak when 5 nm emission and excitation slits were used.

Increasing this to 10 nm allowed more intense spectra to be recorded but meant that excitation at 570 nm could not be used.

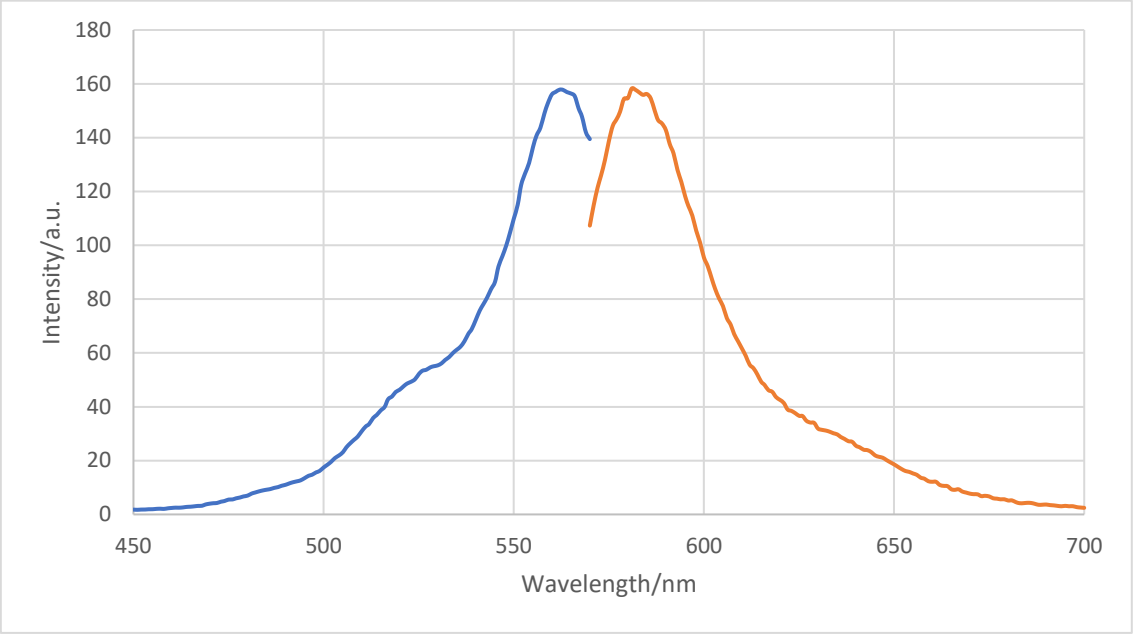


Figure 4.21: Excitation (blue) and emission (orange) spectra of **4.9** (300 µM, H_2O).

It was decided to explore the changes in fluorescence emission of **4.9** at different pH values. A range of solutions with pH values between 3 and 8 were prepared using 0.1 M KCl, 0.1 M HCl and 0.1 M KOH, with KCl solution used to ensure the ionic strength of the solutions was kept constant at different pH values. The pH of each solution was measured using a pH probe. 15 µM solutions of **4.9** were prepared at each of these pH values and left overnight to equilibrate, accounting for the possibly slow kinetics involved in spirolactam ring opening. After allowing for equilibration, the emission spectrum of each solution was recorded.

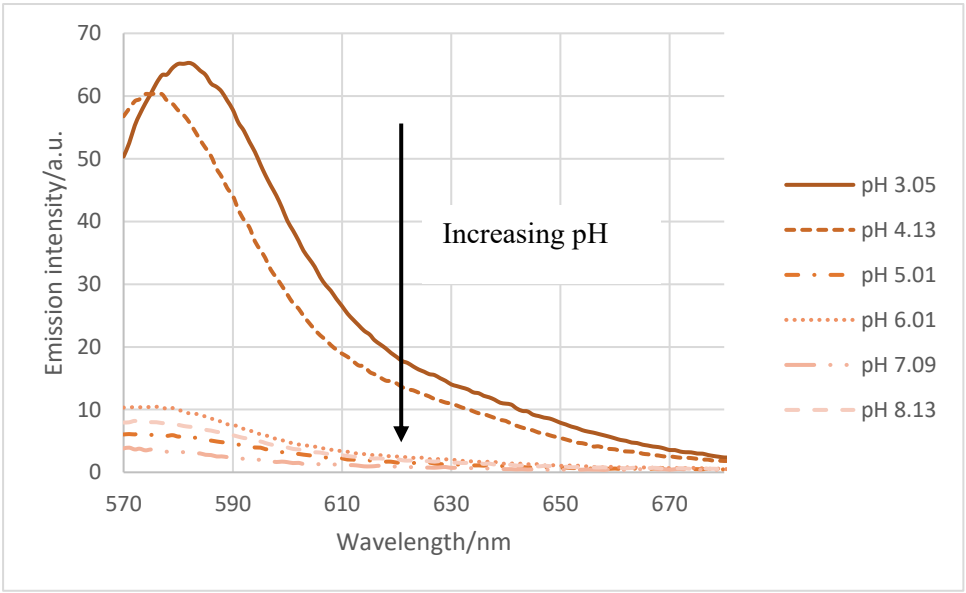


Figure 4.22: Emission spectra from the pH titration of compound **4.9** (15 µM, 0.1 M KCl, n = 3, λ_{ex} = 550 nm).

As can be clearly seen from **Figure 4.22**, the emission intensity of **4.9** markedly decreased as the pH of the solutions increased. This was in line with the expected behaviour, with higher pH values being associated with shifting the position of equilibrium associated with spirolactam ring opening from the open, emissive state to the closed, non-emissive isomer. This is discussed in more detail above. It is possible that a shift in emission wavelength could be observed at pH 3, with the emission maximum occurring at 580 nm rather than 575 nm. The clear pH switchable behaviour observed was pleasing to see, as it validated the inclusion of the spirolactam moiety in **4.9** and suggested that the probe could be used as a way to monitor whether or not the formation of endosomes and vesicles was occurring.

It was decided to determine the pK_a of the compound in order to have an indication of the precise pH value at which it becomes strongly emissive. This was done by taking the average emission intensity at 580 nm and plotting this against pH in Origin. The resulting curve was fitted to a sigmoidal curve according to a Boltzmann distribution (**Figure 4.23**). The pH value corresponding to half the maximum emission intensity was found to be 4.19, which was taken as the pK_a of compound **4.9**.

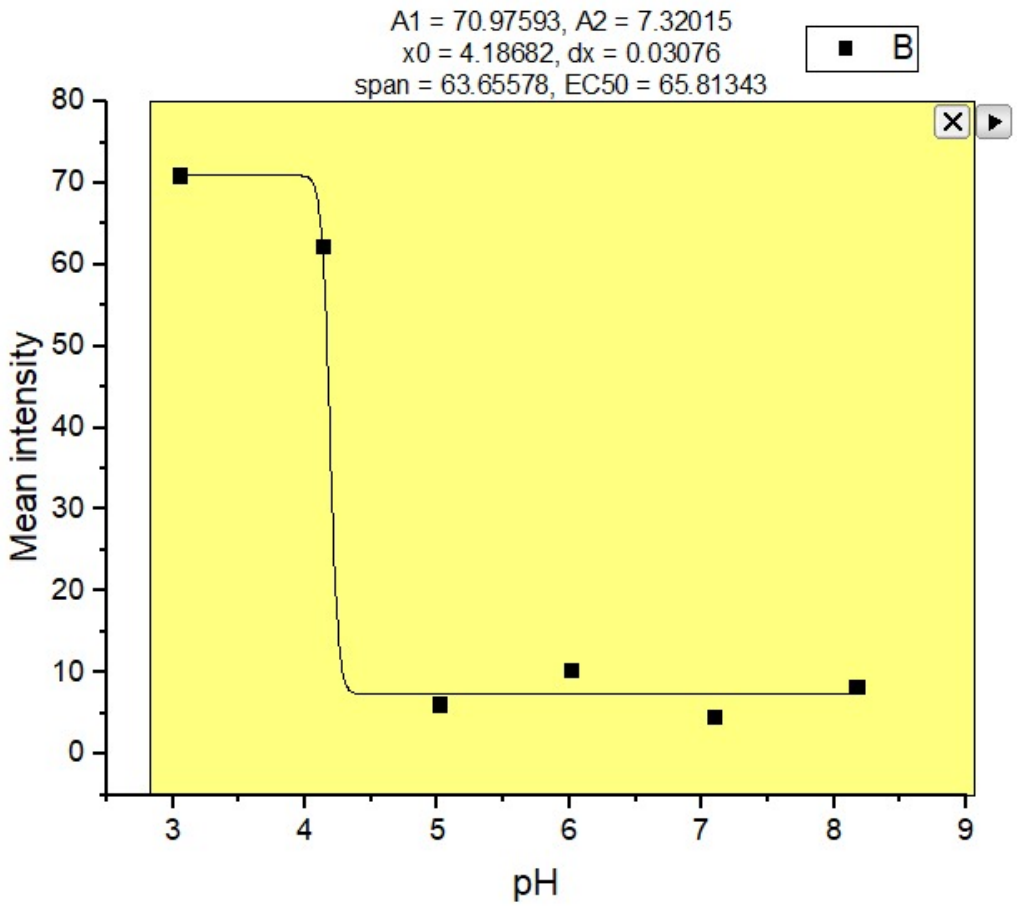


Figure 4.23: The plot used to calculate the pK_a of compound **4.9**.

Whilst endosome formation is associated with a drop in the internal pH of the intracellular fluid, these typically have average pH values of 5, with young endosomes having pH values closer to 6[60,61]. The data obtained for compound **4.9** suggest that the pH at which the fluorescence is "turned on" is too low

– indeed it can be seen above that the compound is virtually non-emissive at pH values above 4. Further work in this area would no doubt involve modifications to the probe to increase the pH at which it rearranges to form the ring-open state and become emissive. This could possibly be achieved by an increase in steric hindrance or basicity of the amide chain[23,25]. As can be seen from the mechanism discussed above, a more sterically hindered position, as well as one which is more readily protonated, will cause the spirolactam ring to sit more towards the open, emissive side of the equilibrium at the same pH when compared to a less sterically encumbered, less basic moiety[23,25]. Care would have to be taken to ensure that this does not impact on the ability of the compound to act as a pH sensor.

It will also be necessary to carry out a series of pH titrations on any peptide conjugate which is synthesised based on the "always-on" fluorophore, compound **4.13**, to ensure that it does not exhibit any pH response and can act as an appropriate control.

4.2.2.2. Synthesis of Sterically Encumbered Rhodamine Derivatives

As discussed above, enhancement of steric hindrance close to the spirolactam position can affect the position of the equilibrium between the emissive ring-open and non-emissive ring-closed analogues of rhodamine derivatives, raising the pH at which the switch from non-emissive to fluorescent occurs. It was decided to synthesise two analogues incorporating a 2,6-dimethyl aryl system. These compounds would have more steric hindrance than **4.8** and **4.13**, so theoretically the switchable derivative would become emissive at higher pH values. These two target compounds are shown in **Figure 4.24**.

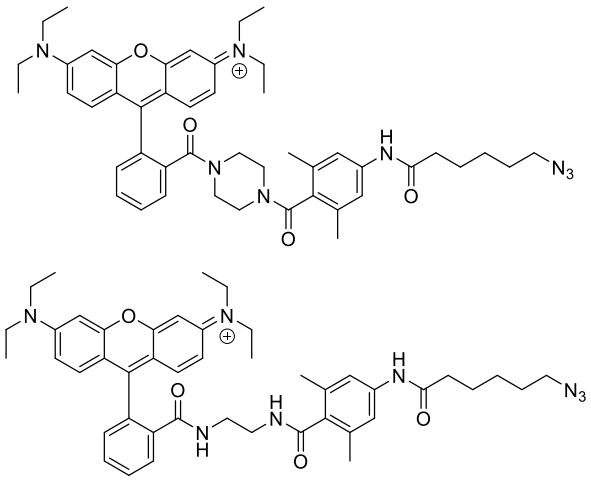
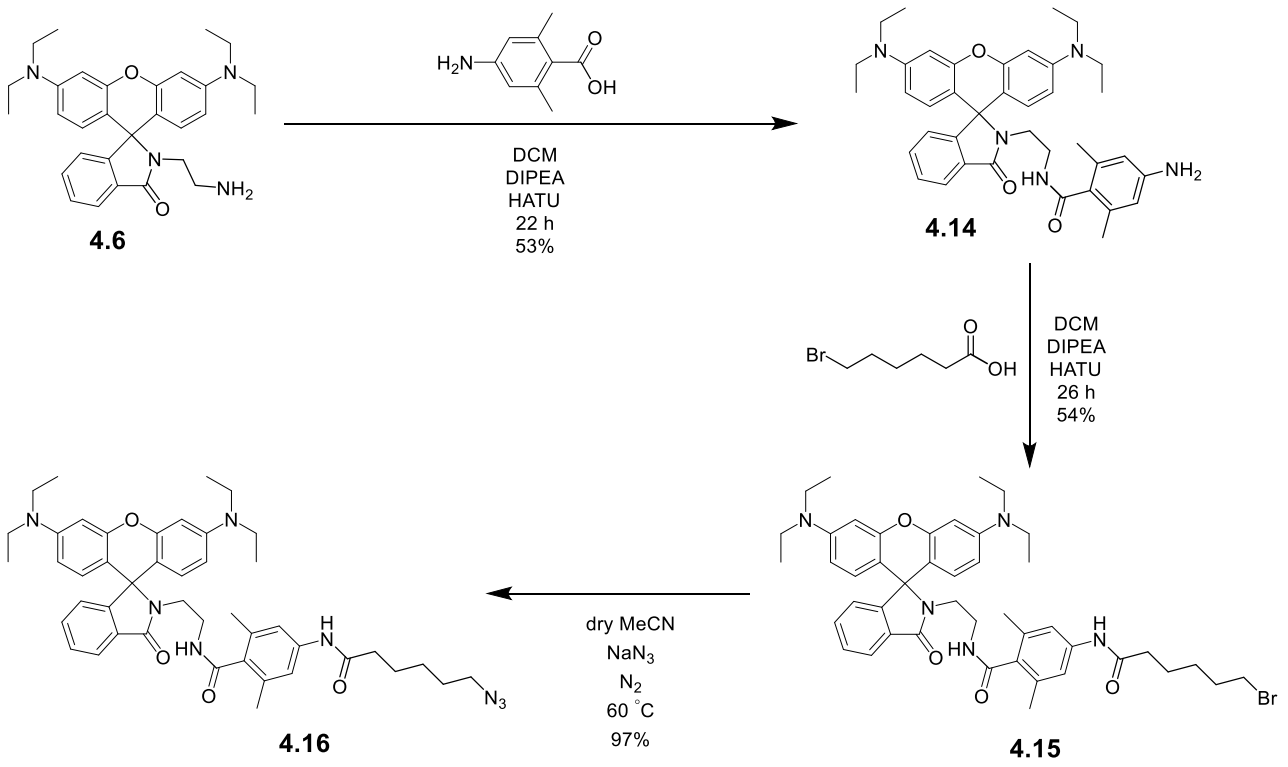
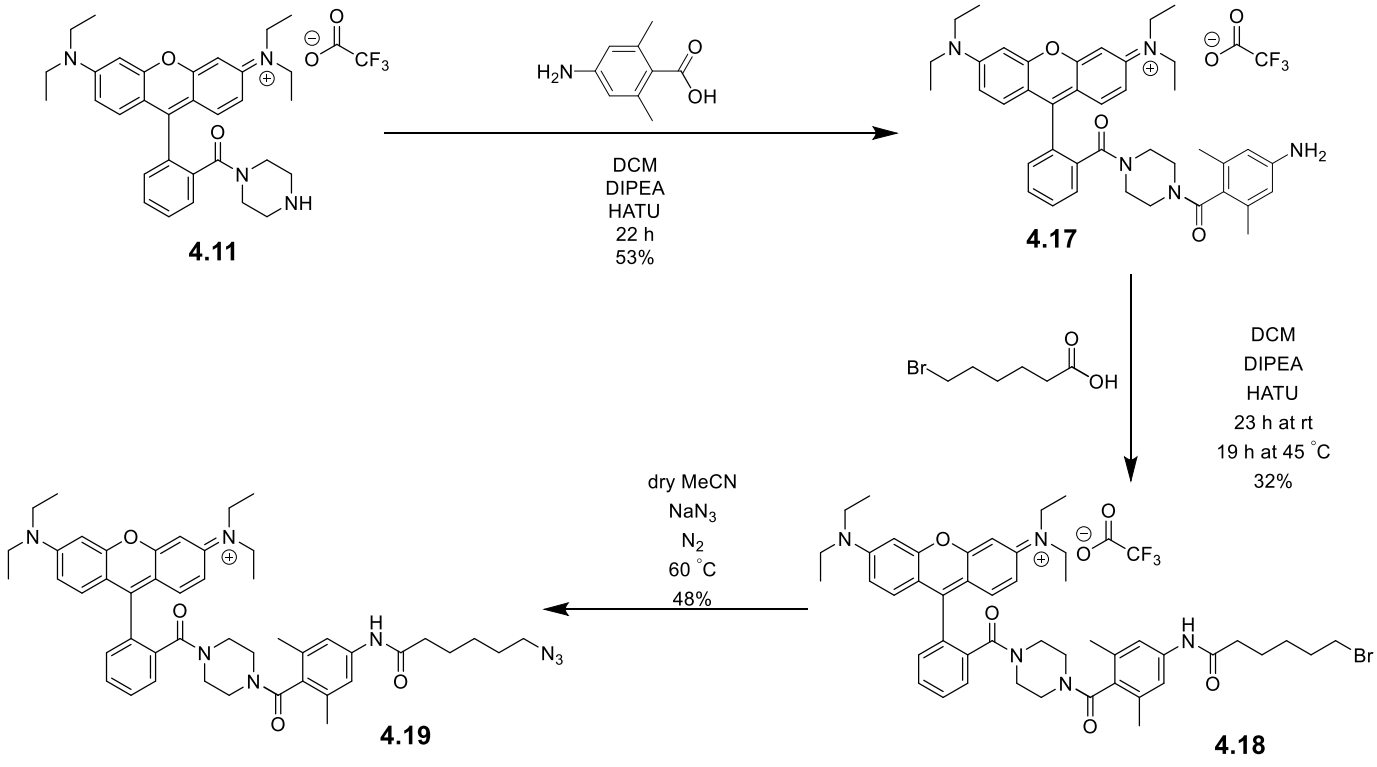


Figure 4.24: The two target 2,6-dimethyl aryl compounds based on "always-on" (top) and switchable (bottom) rhodamine systems.

The piperazine ring and ethylenediamine chain were retained in both target compounds in order to ensure the "always-on" and switchable nature of the fluorophore emission. The synthetic pathways chosen began from compounds **4.6** and **4.11** and are outline in **Schemes 4.3** and **4.4**.



Scheme 4.3: Synthesis of the azide derivative **4.16**.



Scheme 4.4: Synthetic steps towards the "always-on" derivative.

Compound **4.6** could be successfully coupled with 4-amino-2,6-dimethyl benzoic acid to give the derivative **4.14**, with increased steric hindrance at the spirolactam position, at a moderate yield of 53%. Subsequent functionalisation with 6-bromohexanoic acid was achieved using standard amide coupling

conditions, yielding the bromide **4.15**. This bromide was readily converted to the azide **4.16** at an impressive yield of 97%, producing a substrate which could be conjugated *via* CuAAC methods to several of the exendin analogues mentioned above.

A similar procedure was carried out with compound **4.11**, with the "always-on" di-methyl aryl species **4.17** obtained through an amide coupling at a moderate 53% yield. As with the pH sensitive derivative, coupling with 6-bromohexanoic acid followed by conversion to the azide **4.19** could be achieved, providing a control for peptide conjugates to be compared to the switchable **4.16**.

4.2.2.3. Towards Reduced Rhodol Derivatives

Subsequent coupling of compounds **4.19** and **4.16** to the alkyne-functionalised peptides discussed in this Chapter proved challenging, despite the utilisation of a wide variety of catalysts and the application of temperature. In order to try and avoid this, it was decided to synthesise a family of reduced rhodol-based pH-sensitive fluorophores which could be employed to examine the endocytotic pathway of GLP-1R at pancreatic β-cell membranes. Rhodols are a family of compounds analogous to both rhodamine and fluorescein, two widely-used fluorophores, and, in their reduced alcohol form, also exhibit pH dependent spirocyclic ring opening, which has leant itself to lysosome imaging[62,63]. **Figure 4.25** shows the general structure of reduced rhodols, as well as the acid-catalysed ring opening process which results in a dramatic increase in fluorescence intensity[62].

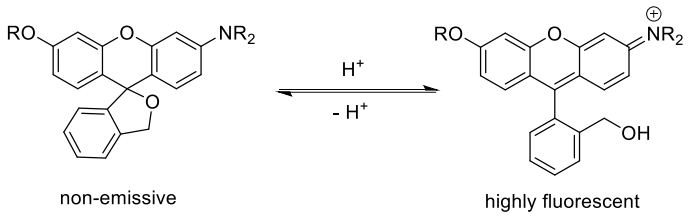


Figure 4.25: The pH-dependent ring opening of reduced rhodols.

It was also decided to attempt to synthesise a compound where the azide functionality was further away from the alcohol group, in case this interfered with the cyclisation mechanism. The proposed target compound is shown below in **Figure 4.26**.

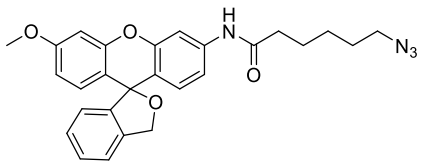
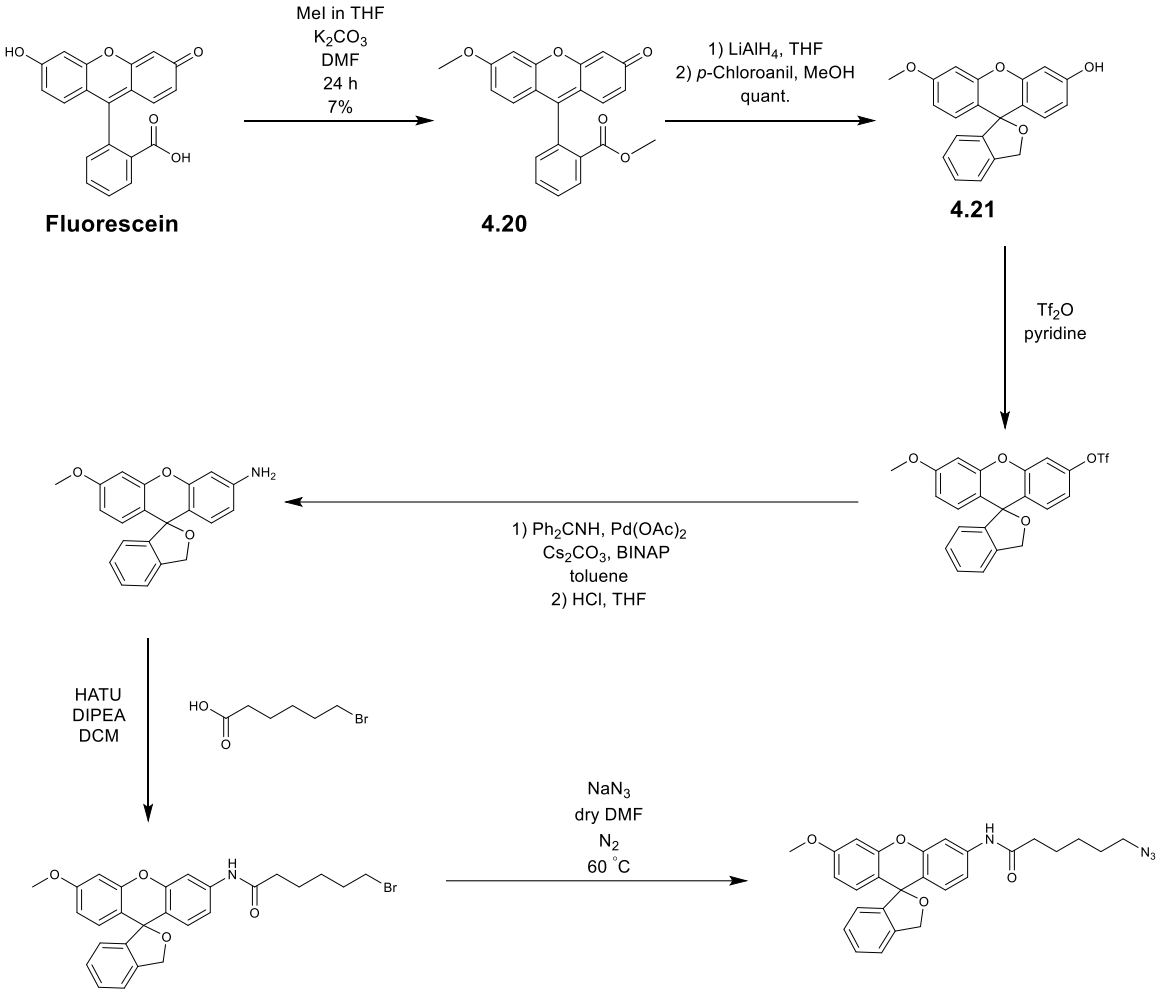


Figure 4.26: The target reduced rhodol compound.

Both More *et al.* and Kamiya *et al*. have synthesised reduced rhodol compounds with methoxy rather than hydroxyl substituents on the aromatic system[62,63]. This was found to bring the pK_a of their compounds to a range of 5.66 – 6.60, an appropriate range for the emission turn-on to be triggered by lysosome formation[62,63]. More *et al*. published an accessible synthetic route, which could be readily

adapted to reach the target compound. This utilised fluorescein as the starting material, after which methylation could be readily achieved through the use of methyl iodide to give derivative **4.20**, albeit at a low yield of just 7%. Subsequent reduction and cyclisation to give the reduced rhodol **4.21** could be achieved using $LiAlH_4$ at quantitative yields. **Scheme 4.5** shows this synthetic pathway, as well as the proposed future work towards the target compound.



Scheme 4.5: Synthesis of compound **4.21** and proposed future work towards the reduced rhodol azide.

Although good progress was made with this synthesis, time constraints prevented further functionalisation of the cyclised reduced rhodol **4.21**. Future work will no doubt focus on the development of these compounds.

4.3. Conclusions and Outlook

In conclusion, several probes which could be useful in investigating agonist binding to GLP-1R were synthesised. Five of these probes, conjugated to a luminescent Tb(III) complex, are capable of acting as FRET donors, which could be utilised to explore the proximity of agonist and receptor in a binding event, and to examine the effect that different agonists with different amino acid substitutions have on the conformational changes involved. These probes could be used to explore the relationship between

the affinity of probes for receptors and the physiological effects of receptor stimulation with different ligands.

Following similar work by Clardy *et al*., which showed that modifications to the 12th amino acid in the exendin-4 sequence do not significantly impact on ligand potency, dose-response curves of two of these compounds (**4.1** and **4.2**) were recorded. However, these dose-response curves showed that, although there was a reduction in affinity for GLP-1R compared to exendin-4, this was not substantial enough to completely disrupt receptor binding, with EC_{50} values for **4.1** and **4.2** recorded as 2.4 and 5.6 nM respectively.

Having confirmed that both **4.1** and **4.2** could bind to GLP-1R, their ability to act as FRET donors to a receptor labelled with a FRET acceptor was studied. The probes were both found to be capable of acting as FRET donors, indicating that this strategy could be applied to the study of ligand-receptor interactions for exendin-4 variants and GLP-1R. Future work in this area would involve examination of the remaining three compounds' interaction with donor-labelled GLP-1R, followed by comparison of the FRET ratios to explore whether or not the amino acid substitutions made impact on receptor affinity, or whether antagonist compounds result in different conformational changes to GLP-1R.

Some preliminary work exploring the effect of fatty acid incorporation on plasma membrane localisation of these probes has been carried out. It was shown that both compounds **4.1** and **4.2** can act as FRET donors towards the phospholipid-mimicking fluorophore NR12S, which exhibits polarity-dependent changes in fluorescence emission wavelength. *In vitro* studies involving cells expressing GLP-1R and labelled with NR12S should be carried out as the next stage of this investigation to explore whether the inclusion of a fatty acid chain in **4.2** results in localisation away from cholesterol-rich regions of the plasma membrane. This could help explain the role of lipid rafts in receptor activation. Synthesis of other fatty acid labelled derivatives could help give a complete picture of the complex interactions involved in this process. There has been some suggestion in the literature that the presence of serum albumin proteins can promote leakage of NR12S from cell membranes, so future investigations into the nature of lipid rafts could involve an alternative compound, bNR10S, which has a high affinity for LD membrane phases[64].

An exendin-4-rhodamine conjugate containing a spirolactam ring was successfully isolated. This compound was found to exhibit pH-responsive fluorescent emission, with a dramatic decrease in fluorescence intensity at pH values of 5 and above. There was also a possible Stokes shift at pH values close to 3, which could also be used to analyse endosomal formation. The pK_a of the compound was calculated as 4.19, which is likely too low to act as an on-off switchable fluorophore in endosomes, as these typically have a pH of around 5 or 6. Future work may be to explore modifications to the rhodamine side chain to optimise the pK_a of the compound and make it more applicable to monitoring

cell internalisation. A non-switchable compound based on piperazine was also synthesised which could act as a control to the switchable rhodamine analogue. In future, this "always-on" fluorophore will need to be conjugated to the propargyl-functionalised exendin-4 derivative and pH titrations carried out to establish that it does not exhibit pH sensitive emission and can act as a suitable control for the switchable compound. Additionally, further reduced rhodol compounds can be expanded upon.

The need to understand the biological mechanisms behind diseases such as diabetes mellitus is extremely prescient. The compounds synthesised and analysed in this Chapter could go towards developing our collective knowledge of agonist binding, receptor activation and internalisation which take place at the GLP-1R receptor.

4.4. References

1 S. Runge, H. Thøgersen, K. Madsen, J. Lau and R. Rudolph, *J. Biol. Chem.*, 2008, **283**, 11340–11347.

2 S. R. J. Hoare, *Drug Discov. Today*, 2005, 10, 417–427.

3 C. R. Underwood, P. Garibay, L. B. Knudsen, S. Hastrup, G. H. Peters, R. Rudolph and S. Reedtz-Runge, *J. Biol. Chem.*, 2010, **285**, 723–730.

4 D. Donnelly, *Br. J. Pharmacol.*, 2012, **166**, 27–41.

5 A. H. Maddy, *Int. Rev. Cytol.*, 1966, **20**, 1–65.

6 O. A. Kucherak, S. Oncul, Z. Darwich, D. A. Yushchenko, Y. Arntz, P. Didier, Y. Mély and A. S. Klymchenko, *J. Am. Chem. Soc.*, 2010, **132**, 4907–4916.

7 T. Buenaventura, S. Bitsi, W. E. Laughlin, T. Burgoyne, Z. Lyu, A. I. Oqua, H. Norman, E. R. McGlone, A. S. Klymchenko, I. R. Corrêa, A. Walker, A. Inoue, A. Hanyaloglu, J. Grimes, Z. Koszegi, D. Calebiro, G. A. Rutter, S. R. Bloom, B. Jones and A. Tomas, *PLoS Biol.*, 2019, **17**, e3000097.

8 S. Gahbauer and R. A. Böckmann, *Front. Physiol.*, 2016, 7, 494.

9 B. Jones, T. Buenaventura, N. Kanda, P. Chabosseau, B. M. Owen, R. Scott, R. Goldin, N. Angkathunyakul, I. R. Corrêa, D. Bosco, P. R. Johnson, L. Piemonti, P. Marchetti, A. M. J. Shapiro, B. J. Cochran, A. C. Hanyaloglu, A. Inoue, T. Tan, G. A. Rutter, A. Tomas and S. R. Bloom, *Nat. Commun.*

10 T. Buenaventura, N. Kanda, P. C. Douzenis, B. Jones, S. R. Bloom, P. Chabosseau, I. R. Corrêa, D. Bosco, L. Piemonti, P. Marchetti, P. R. Johnson, A. M. J. Shapiro, G. A. Rutter and A. Tomas, *Diabetes*, 2018, **67**, 385–399.

11 R. S. Kuna, S. B. Girada, S. Asalla, J. Vallentyne, S. Maddika, J. T. Patterson, D. L. Smiley, R. D. DiMarchi and P. Mitra, *Am. J. Physiol. Metab.*, 2013, **305**, E161–E170.

12 M. M. Fletcher, M. L. Halls, P. Zhao, L. Clydesdale, A. Christopoulos, P. M. Sexton and D. Wootten, *Biochem. Pharmacol.*, 2018, **156**, 406–419.

13 T. Ha, *Methods*, 2001, **25**, 78–86.

14 P. R. Selvin, *Nat. Struct. Biol.*, 2000, **7**, 730–734.

15 L. E. Morrison, *Anal. Biochem.*, 1988, **174**, 101–120.

16 T. Förster, *Discuss. Faraday Soc.*, 1959, 27, 7–17.

17 M. P. Coogan and S. J. A. Pope, in *The Chemistry of Molecular Imaging*, eds. N. J. Long and W.-T. Wong, John Wiley & Sons, Ltd, Hoboken, U.S.A., 2015, pp. 275–298.

18 P. R. Selvin and J. E. Hearst, *Proc. Natl. Acad. Sci. U. S. A.*, 1994, **91**, 10024–10028.

19 A. Cha, G. E. Snyder, P. R. Selvin and F. Bezanilla, *Nature*, 1999, **946**, 809–813.

20 P. Pickford, M. Lucey, Z. Fang, S. Bitsi, J. Broichhagen and B. Jones, *bioRxiv*, 2019, 803833.

21 S. N. Roed, P. Wismann, C. R. Underwood, N. Kulahin, H. Iversen, K. A. Cappelen, L. Schäffer, J. Lehtonen, J. Hecksher-Soerensen, A. Secher, J. M. Mathiesen, H. Bräuner-Osborne, J. L. Whistler, S. M. Knudsen and M. Waldhoer, *Mol. Cell. Endocrinol.*, 2014, **382**, 938–949.

22 M. H. Lee, J. H. Han, J. H. Lee, N. Park, R. Kumar, C. Kang and J. S. Kim, *Angew. Chemie Int. Ed.*, 2013, **52**, 6206–6209.

23 X. Chen, T. Pradhan, F. Wang, J. S. Kim and J. Yoon, *Chem. Rev.*, 2012, 112, 1910–1956.

24 C. Rivas, G. J. Stasiuk, J. Gallo, F. Minuzzi, G. A. Rutter and N. J. Long, *Inorg. Chem.*, 2013, **52**, 14284–14293.

25 Q. A. Best, R. Xu, M. E. McCarroll, L. Wang and D. J. Dyer, *Org. Lett.*, 2010, **12**, 3219–3221.

26 M. J. Geisow and W. H. Evans, *Exp. Cell Res.*, 1984, **150**, 36–46.

27 E. Noelting and K. Dziewoński, *Berichte der Dtsch. Chem. Gesellschaft*, 1905, **38**, 3516–3527.

28 V. Dujols, F. Ford and A. W. Czarnik, *J. Am. Chem. Soc.*, 1997, **119**, 7386–7387.

29 S. Kang, S. Kim, Y. K. Yang, S. Bae and J. Tae, *Tetrahedron Lett.*, 2009, **50**, 2010–2012.

30 R. Bandichhor, A. D. Petrescu, A. Vespa, A. B. Kier, F. Schroeder and K. Burgess, *J. Am. Chem. Soc.*, 2006, **128**, 10688–10689.

31 T. J. Clough, N. Baxan, E. J. Coakley, C. Rivas, L. Zhao, I. Leclerc, A. Martinez-Sanchez, G. A. Rutter and N. J. Long, *Dalt. Trans.*, 2020, **49**, 4732–4740.

32 D. O. Kiesewetter, H. Gao, Y. Ma, G. Niu, Q. Quan, N. Guo and X. Chen, *Eur J Nucl Med Mol Imaging*, 2012, **39**, 463–473.

33 L. Joosten, M. Brom, H. Peeters, D. Bos, E. Himpe, L. Bouwens, O. Boerman and M. Gotthardt, *Mol. Pharm.*, 2019, **16**, 4024–4030.

34 K. Mikkola, C. B. Yim, V. Fagerholm, T. Ishizu, V. V Elomaa, J. Rajander, J. Jurttila, T. Saanijoki, T. Tolvanen, M. Tirri, E. Gourni, M. Behe, M. Gotthardt, J. C. Reubi, H. Macke, A. Roivainen, O. Solin and P. Nuutila, *Mol. Imaging Biol.*, 2014, **16**, 255–263.

35 C. Brand, D. Abdel-Atti, Y. Zhang, S. Carlin, S. M. Clardy, E. J. Keliher, W. A. Weber, J. S. Lewis and T. Reiner, *Bioconjugate Chem*, 2014, **25**, 1323–1330.

36 A. Kirkpatrick, J. Heo, R. Abrol and W. A. Goddard, *Proc. Natl. Acad. Sci. U. S. A.*, 2012, **109**, 19988–19993.

37 S. M. Clardy, E. J. Keliher, J. F. Mohan, M. Sebas, C. Benoist, D. Mathis and R. Weissleder, *Bioconjug. Chem.*, 2014, **25**, 171–177.

38 L. Liang and D. Astruc, *Coord. Chem. Rev.*, 2011, 255, 2933–2945.

39 Y. Wang, C. Cong, W. Chern Chai, R. Dong, L. Jia, D. Song, Z. Zhou and S. Ma, *Bioorganic Med. Chem. Lett.*, 2017, **27**, 3872–3877.

40 D. Wang, M. Zhao, X. Liu, Y. Chen, N. Li and B. Chen, *Org. Biomol. Chem.*, 2012, **10**, 229–231.

41 T. Gong, B. J. Adzima and C. N. Bowman, *Chem. Commun.*, 2013, **49**, 7950–7952.

42 S. Mohammed, A. K. Padala, B. A. Dar, B. Singh, B. Sreedhar, R. A. Vishwakarma and S. B. Bharate, *Tetrahedron*, 2012, **68**, 8156–8162.

43 B. J. Adzima, Y. Tao, C. J. Kloxin, C. A. DeForest, K. S. Anseth and C. N. Bowman, *Nat. Chem.*, 2011, **3**, 256–259.

44 R. Göke, H. C. Fehmann, T. Linn, H. Schmidt, J. Eng and B. Göke, *Digestion*, 1993, 54, 347.

45 H. Ligumsky, I. Wolf, S. Israeli, M. Haimsohn, S. Ferber, A. Karasik, B. Kaufman and T. Rubinek, *Breast Cancer Res. Treat.*, 2012, **132**, 449–461.

46 G. Skoglund, M. A. Hussain and G. G. Holz, *Diabetes*, 2000, **49**, 1156–1164.

47 J. L. Sebaugh, *Pharm. Stat.*, 2011, **10**, 128–134.

48 S. A. Doggrell, *Expert Opin. Drug Metab. Toxicol.*, 2018, **14**, 371–377.

49 K. Kyhl, J. Lønborg, B. Hartmann, H. Kissow, S. S. Poulsen, H. El Ali, A. Kjær, F. Dela, T. Engstrøm and M. Treiman, *Peptides*, 2017, **93**, 1–12.

50 A. Keppler, H. Pick, C. Arrivoli, H. Vogel and K. Johnsson, *Proc. Natl. Acad. Sci. U. S. A.*, 2004, **101**, 9955–9959.

51 B. A. Smith, S. B. Padrick, L. K. Doolittle, K. Daugherty-Clarke, I. R. Corrêa, M. Q. Xu, B. L. Goode, M. K. Rosen and J. Gelles, *Elife*, 2013, **2013**, e01008.

52 A. Gavalas, T.-H. Lan, Q. Liu, I. R. Corrêa, J. A. Javitch and N. A. Lambert, *Mol. Pharmacol. Mol Pharmacol*, 2013, **84**, 346–352.

53 I. R. Corrêa, *Curr. Opin. Chem. Biol.*, 2014, 20, 36–45.

54 X. Sun, A. Zhang, B. Baker, L. Sun, A. Howard, J. Buswell, D. Maurel, A. Masharina, K. Johnsson, C. J. Noren, M. Q. Xu and I. R. Corrêa, *ChemBioChem*, 2011, **12**, 2217–2226.

55 A. Keppler, S. Gendreizig, T. Gronemeyer, H. Pick, H. Vogel and K. Johnsson, *Nat. Biotechnol.*, 2003, **21**, 86–89.

56 X. Zhang, Y. Shiraishi and T. Hirai, *Org. Lett.*, 2007, **9**, 5039–5042.

57 M. Midson, *Unpubl. Thesis*.

58 L. Yuan, W. Lin, Z. Cao, J. Wang and B. Chen, *Chem. - A Eur. J.*, 2012, **18**, 1247–1255.

59 R. W. Ramette and E. B. Sandell, *J. Am. Chem. Soc.*, 1956, **78**, 4872–4878.

60 J. Kneipp, H. Kneipp, B. Wittig and K. Kneipp, *J. Phys. Chem. C*, 2010, **114**, 7421–7426.

61 R. F. Murphy, S. Powers and C. R. Cantor, *J. Cell Biol.*, 1984, **98**, 1757–1762.

62 K. N. More, S. K. Mun, J. Kang, J. J. Kim, S. T. Yee and D. J. Chang, *Dye. Pigment.*, 2021, **184**, 108785.

63 M. Kamiya, D. Asanuma, E. Kuranaga, A. Takeishi, M. Sakabe, M. Miura, T. Nagano and Y. Urano, *J. Am. Chem. Soc*, 2011, **133**, 12960–12963.

64 R. Kreder, K. A. Pyrshev, Z. Darwich, O. A. Kucherak, Y. Mély and A. S. Klymchenko, *ACS Chem. Biol.*, 2015, **10**, 1435–1442.

Chapter 5

Cyanine Compounds Designed for Zinc-Sensing and Fluorescence Imaging

5.1. Introduction

Fluorescence imaging is a powerful, sensitive, non-invasive technique which allows rapid acquisition of high-resolution images[1–4]. There has been a longstanding interest in the development of optical imaging agents which emit in the near-infrared (NIR) window of the electromagnetic spectrum (λ_{ex} = 700 – 1000 nm) and the field is currently dominated by polymethine cyanine dyes[1,2,5,6].

As discussed in other Chapters of this thesis, Zn^{2+} is known to have a critical role in several areas of human biochemistry[7–12]. With respect to diabetes, zinc(II) plays a critical role in the stabilisation of insulin storage and the two components are co-released from pancreatic β-cells[13–16]. As such, the assessment and quantification of Zn^{2+} levels in the pancreas is an exciting and highly promising field, and it has been hypothesised that ratiometric chemosensors could be used to gain an insight into the progression of diabetes, as well as the body's response to any treatment[17–19].

The literature is rich with examples of zinc-sensing probes and in-depth explorations of this vast field[7–9,20,21]. However, there is an ongoing discussion about the suitability of different zinc-binding motifs, the development of probes with suitable photophysical properties for *in vivo* applications, overcoming some limitations of fluorescence imaging through the synthesis of multi-modal imaging agents and the introduction of probe specificity through targeting moieties.

5.1.1. Cyanine Dyes

Many organic dyes emit in the visible light window. Whilst this presents few issues for *in vitro* imaging, it renders the study of living systems through *in vivo* analysis challenging for a number of reasons. Chief amongst these is the phenomenon of autofluorescence, with many biological components exhibiting this behaviour and emitting visible light, which can impact negatively on signal to noise ratio[2,22–24]. The penetrating ability of photons in the visible light region (380 nm – 740 nm) is fairly limited and they are highly susceptible to scattering by biological tissues such as skin, which can reduce the amount of useful information acquired and make non-invasive imaging challenging[2,5,25]. Photons in the NIR region (> 740 nm) have been shown to exhibit minimal scattering, in addition to high depth penetration in biological tissues (up to 6 cm) and the avoidance of interference from autofluorescence[22,23,25–28]

Since their initial synthesis in 1856, polymethine cyanine dyes have risen to prominence as NIR emissive fluorescent imaging agents, amongst a wide range of other fields, including in semiconductors, industrial paints, laser materials and light harvesting[1,5,6,29]. These compounds exhibit high molar extinction coefficients and quantum yields (> 150,000 M^{-1} cm^{-1} and > 50% respectively) in addition to a high degree of chemical versatility and tunability[5,6,27,29]. These properties present cyanine dyes as an attractive scaffold for development of zinc-sensing, β-cell targeted compounds for dual-modal imaging.

The cyanine compound indocyanine green (ICG) is the only FDA-approved cyanine compound and has been in clinical use for over 60 years[22,30]. Despite its applications in the assessment of liver function and tumour visualisation in surgical procedures, there are several issues associated with ICG, namely its limited tissue penetration compared to other NIR fluorophores (typically 5 -10 nm), the quenching of its fluorescence which occurs upon serum protein binding and its limited potential for bioconjugation or other modifications[22,30,31]. The successful translation of ICG from the lab to the clinic is an example of the potential of this family of compounds, but a reminder that constant refinement and improvement is required in the molecular imaging field.

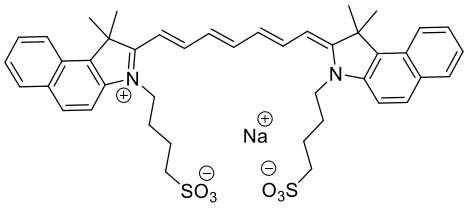


Figure 5.1: The structure of ICG.

5.1.1.1. General Structure of and Modifications to Cyanines

Cyanine dyes consist of two nitrogen atoms linked by an unsaturated carbon chain. One of these nitrogen atoms is formally positively charged, although in reality there is an extensive degree of delocalisation throughout the system[6]. The number of carbon atoms – methine units - in the conjugated chain is always odd, and the number of these dictates the nomenclature of the cyanine dye.

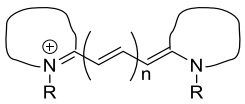


Figure 5.2: General structure of a cyanine dye. The number of methine units determines dye nomenclature: n = 1: trimethine, n = 2: pentamethine, n = 3: heptamethine.

Each additional methine unit in the cyanine backbone results in a red-shift in the compound's emission wavelength, rendering heptamethine dyes perhaps the most suitable as NIR fluorophores[6,23,32]. However, the extension of this carbon chain renders the dye more susceptible to nucleophilic attack, as well as decreasing photo- and thermostability of the cyanine, which can prevent problems in dye synthesis and application[1,23,24]. Other issues associated with cyanine dyes include their poor aqueous solubility, a significant obstacle to *in vivo* applications, and aggregation in solution due to π-stacking[6,29].

The reduced photostability associated with increase polymethine backbone length can be attributed to there being an increased number of positions at which the compound may be attacked by reactive oxygen species (ROS) such as singlet oxygen ($^1O_2$) or superoxide ions (O_2^-)[23,24,33]. The processes involved are fairly straightforward from a photophysical perspective. After photon absorption, a cyanine dye becomes excited to an excited singlet state ($S_0 \rightarrow S_1$). The dye can then undergo intersystem crossing *via* an internal conversion mechanism to reach an excited triplet state ($S_1 \rightarrow T_1$). This T_1 state,

represented as dye*, can then interact with ground state triplet oxygen, as shown below[23,24,34]. Equations **5.1** and **5.2** show the formation of these two species in systems where a dye molecule has been excited by a photon.

$$\textbf{\textit{Equation}}\ \mathbf{5.1}\text{: } {}^3O_2 + dye^* \rightarrow dye + {}^1O_2$$

$$\textbf{\textit{Equation}}\ \mathbf{5.2}\text{: } O_2 + dye^* \rightarrow O_2^- + dye^+$$

Singlet oxygen reacts with a cyanine dye to form a ketone and an aldehyde species. This aldehyde is then oxidised by the superoxide anion, leading to irreversible photobleaching[24].

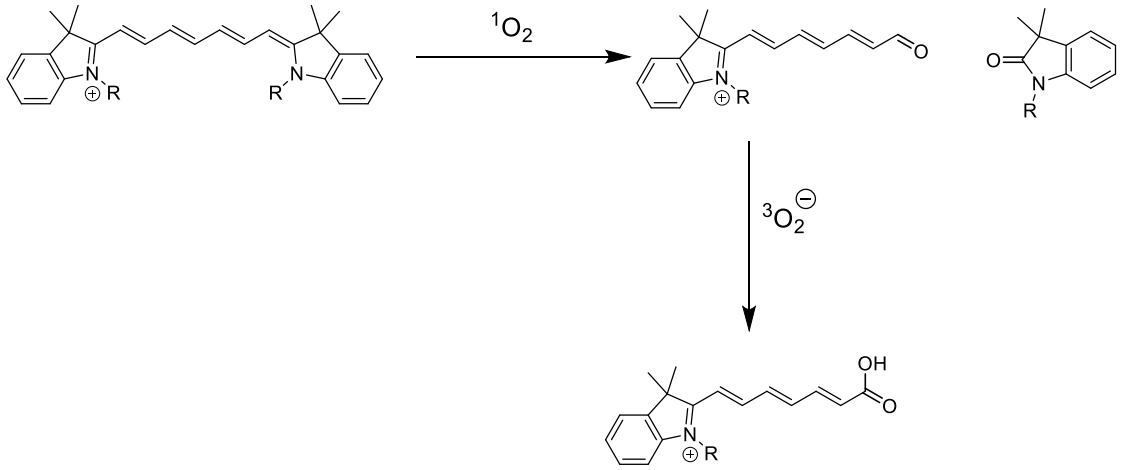


Figure 5.3: Photodegradation pathway for a heptamethine cyanine dye[24].

One way in which the photostability of cyanine compounds can be improved is through backbone rigidification, which reduces the efficiency of internal conversion in these systems[24]. A classic example of this has been the introduction of a cyclohexyl ring, which was reported by Strekowski *et al*. in 1992[23,35,36]. The cyclohexyl ring of choice had the added benefit of enabling further functionalisation *via* its chloride substituent, which could allow nucleophiles to be introduced in close proximity to the cyanine fluorophore[35,37].

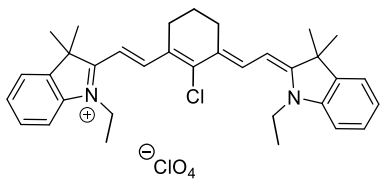


Figure 5.4: The compound synthesised by Strekowski *et al*.

The introduction of electron-donating substituents such as long alkyl on the nitrogen atoms of cyanine dyes has been shown to enhance photostability of cyanines with minimal impact on their photophysical properties[23,29]. Photostability is enhanced through this method by making the system less electrophilic and therefore less susceptible to oxidation. Furthermore, the incorporation of sulphonic or carboxylic

acids to the end of alkyl chains on these positions may enable an intramolecular dimerization process to take place which can further increase backbone rigidity and prevent aggregation, leading to enhanced photostability[29,32]. These groups also act to increase water solubility of cyanines and introduce the ability for bioconjugation and other functionalisation techniques to be carried out[6].

The extensive body of research surrounding cyanine dyes suggests that heptamethine compounds are best placed to act as foundation for NIR emissive compounds. Although there is a decrease in stability associated with longer carbon chains in these compounds, this can be counteracted by backbone rigidification and *N*-substitution, with acidic groups also introducing the possibility of extensive functionalisation.

5.1.2. Zinc-Sensing

After iron, zinc is the most abundant transition metal in the human body, with an average of 2 g being present in the average person[12,20]. In biological systems it is ubiquitously found as Zn^{2+}, where it performs a number of critical functions including as an enzyme cofactor, a protein structural feature, neurotransmitter and regulator of apoptosis, amongst others[7,9–11,21,38,39]. The dysfunction of zinc(II) homeostasis is associated with a wide array of diseases and disorders including Alzheimer's, epilepsy, Parkinson's and, as discussed above and extensively in the introduction to this thesis, diabetes[8,20]. As such, the analysis and quantification of Zn^{2+} in biological systems is of keen interest.

As discussed in the introduction to this thesis, the traditional methods used for the detection of metal ions, such as UV-visible light spectroscopy, is challenging when applied to Zn^{2+} due to the ion's d^{10} configuration[7,8,9]. Fluorescence spectroscopy and fluorescent chemosensors provide a mechanism for the detection of zinc(II) through change in their photophysical properties – for example, a change in emission intensity or a shift in emission wavelength[8,9,40].

5.1.2.1. Mechanisms of Zinc-Sensing

The introduction to this thesis outlines the underlying mechanisms involved in changes in photophysical properties of zinc(II) responsive optical imaging agents. Broadly, these two mechanisms are internal charge transfer (ICT) and photoinduced electron transfer (PeT)[8,9,20,40,41]. Probes designed to indicate the presence of Zn^{2+} in their microenvironment through ICT will undergo a ratiometric shift in its absorption and emission wavelengths and consist of a fluorophore covalently bonded to a zinc binding receptor, forming an extended π system[20]. Fluorescent PeT-based chemosensors will undergo a large increase in emission intensity in the presence of zinc(II) [20]. These compounds include a spacer unit between the fluorophore and the zinc-sensing unit, which is often comprised of a series of nitrogen donors as the ligating atoms.

The compounds discussed in this Chapter were designed and synthesised to sense Zn^{2+} through a PeT mechanism. Whilst the design of ratiometric sensors, possible through an ICT mechanism, is highly desirable as it enables quantification of Zn(II) *in vivo*, PeT sensors exhibit more distinctive sensing

behaviour through dramatic increases in fluorescence intensity. Small Stokes shifts observed in ICT may be insufficient to detect small changes in the levels of Zn^{2+} in the pancreas, and larger ones could push the emission wavelength into an unfavourable window – i.e. the visible region of the spectrum or further into the IR region, which could then present challenges in detection.

5.1.2.2. Zinc Receptor Moieties

Judicious choice of the sensing unit for zinc(II) in a fluorescent chemosensor is critical to ensure selectivity and efficacy of the probe. The range of sensing units exploited in the literature is discussed at length in the introduction to this thesis and these include pyridine based moieties such as dipicolylamine (DPA) and *N*,*N*,*N*′,*N*′-tetrakis(2-pyridinylmethyl)-1,2-ethanediamine (TPEN), as well as macrocyclic chelates[7,21,38,42]. **Figure 5.7** shows DPA and some examples of its incorporation into fluorescent zinc chemosensors.

The selectivity of DPA for Zn^{2+} over other endogenous metal ions such as Cu^{2+} is one issue with its widespread use[43, 44]. Some alternatives to it are discussed further below.

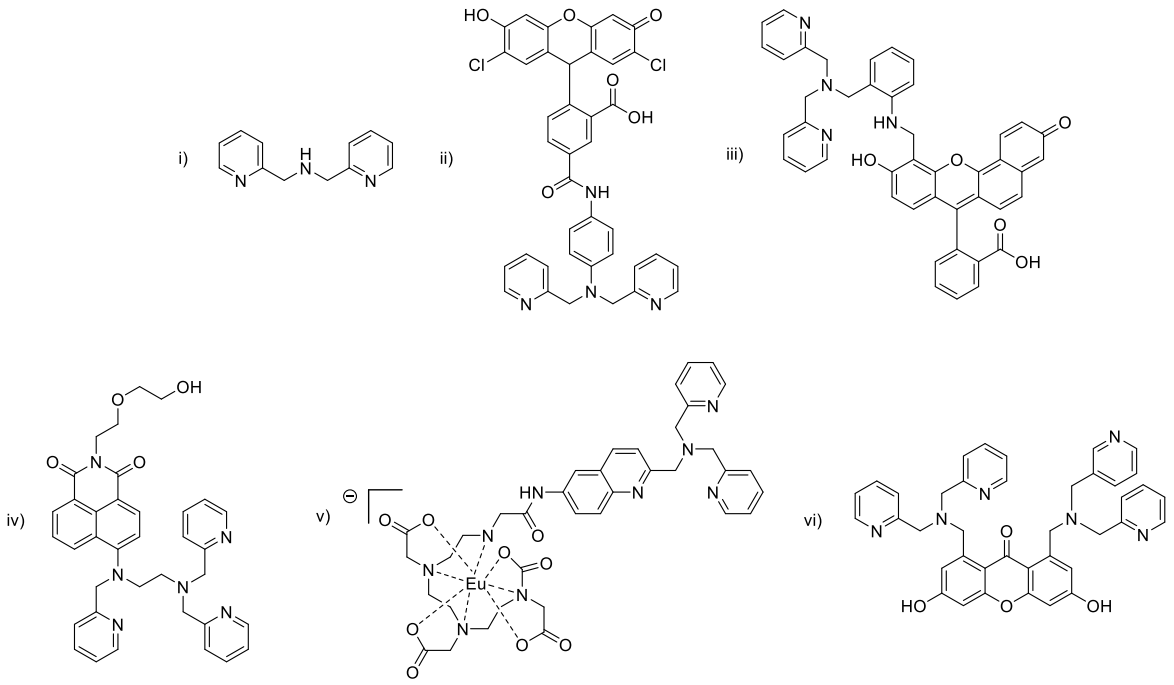


Figure 5.7: i) DPA, ii) Newport Green[45,46], iii) a fluorescein-DPA conjugate synthesised by Cheng *et al*[47], iv) a chemosensor utilising a TPEN receptor from Hanaoka *et al.*[48], v) a lanthanide(III) chelator also developed by Hanaoka *et al*.[10] and vi) a xanthone derivative reported by Ojida *et al*.[49].

5.1.3. Dual Modal Imaging Agents

As briefly mentioned above, there are many examples of dual-modal imaging agents incorporating zinc-sensing capabilities. This strategy seeks to maximise the individual strengths of multiple imaging techniques to allow enhanced understanding of biological materials through improved visualisation and data collection[50,51]. Dual-modal imaging has been discussed extensively elsewhere in this thesis. There

are many notable examples of cyanine-based multi-modality probes, some of which are mentioned below (see **5.2.2.**). The literature is rich with further examples incorporating cyanine dyes, with examples of both PET and MRI capabilities being introduced[50–53].

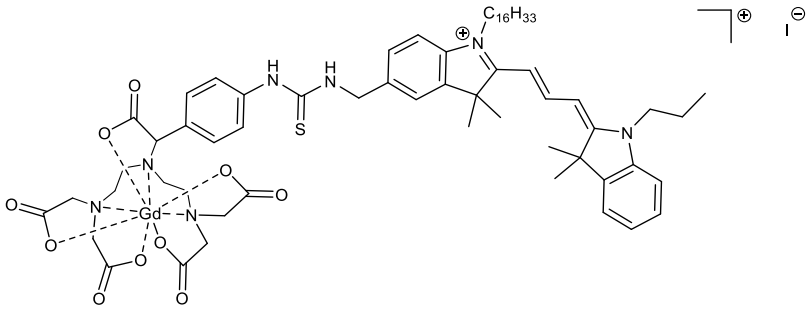


Figure 5.8: An example of a dual-modal optical-MRI probe incorporating a cyanine dye[50].

5.1.4. Aims and Objectives

The work described in this Chapter hopes to build on the already extensive field of NIR cyanine dyes and harness their potent optical properties to generate compounds capable of acting as zinc(II) chemosensors which emit in this biologically useful window. Vast research effort has been employed to explore a range of different zinc receptors, and although DPA has seen much success, it may have issues with selectivity. The development of alternative Zn^{2+} binding moieties was seen as a key part of this body of work.

Furthermore, introducing the capability for dual-modality in cyanine compounds was highly desirable. This would enable the issues associated with optical imaging to be countered – principally by introducing the capability for more penetrative *in vivo* techniques such as MRI and PET.

Additionally, it was hoped that some form of targeting group could be added to the synthesised compounds to produce a series of multi-modal imaging agents which could be delivered directly to pancreatic β-cells and assess their functionality through their interaction with Zn^{2+}.

5.2. Results and Discussion

5.2.1. Exploration of Alternative Zinc-Sensing Moieties

As discussed above, DPA is widely utilised as a zinc-sensing moiety in the imaging field[54,55]. Whilst many of these imaging agents have been shown to be highly successful in their ability to sense Zn^{2+} ions, there are some concerns around the use of DPA. Chief amongst these is its selectivity – whilst DPA does indeed bind strongly to Zn(II), it has also been shown to have a high affinity for all of the divalent first row transition metal ions, some of which (notably Fe^{2+}) are found in biological systems[56]. This, coupled with the notable interaction between DPA and both Ca^{2+} and Mg^{2+}, which are involved in cell signalling and DNA storage respectively[18], could interfere with the selectivity of a zinc-sensing probe *in vivo* and therefore disrupt attempts to selectively target pancreatic β-cells and measure their

functionality. Calcium(II) is also found in high proportions in β-cells, which could further complicate the measure of their functionality[57].

In addition to these selectivity concerns, the *in vivo* results from the probe **GdZn** (see **Chapter 2**) suggested that the use of DPA resulted in a strong interaction between the compound and serum albumin proteins in mice. This caused **GdZn** to remain in the bloodstream and resulted in no successful pancreatic contrast enhancement.

It was hypothesised that both of these concerns could be tackled by utilising an alternative zinc-sensing moiety. A family of compounds incorporating both pyridine and thiophene rings has been developed by the Lippard group, named the Zinspy family by the authors[56,58,59]. These compounds, which built upon the group's previous work on the DPA-based Zinpyr family, exhibited a reduced affinity for Zn^{2+} when compared to Zinpyr compounds but showed selectivity for divalent zinc over a wide array of other M^{2+} ions, particularly Ca^{2+} and Mg^{2+} [56,58,59]. One (**Figure 5.9**) was successfully utilised to monitor Zn^{2+} ion flow *in vivo*[58].

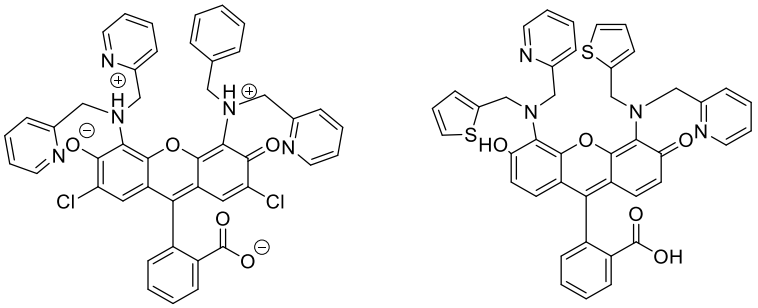


Figure 5.9: The Zinspy compound developed by Nolan *et al.* employing a thiophene-based zinc sensor which was utilised to monitor Zn^{2+} levels *in vivo* (right) and its Zinpyr predecessor, which used a DPA receptor (left).

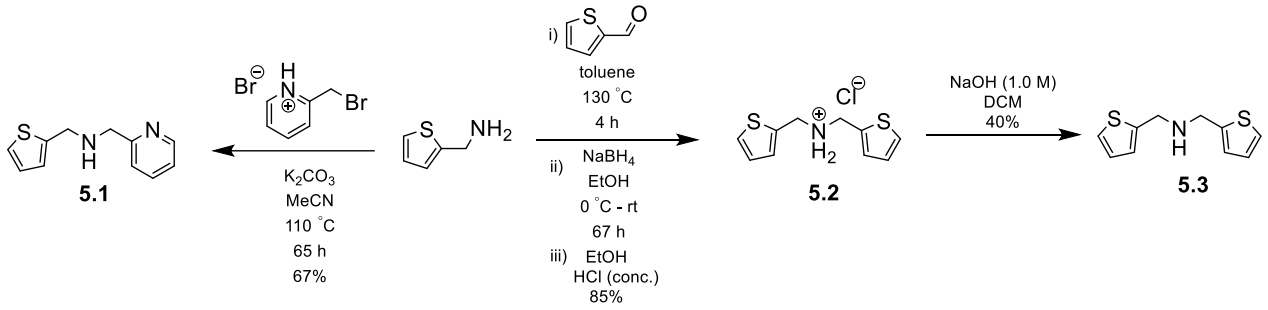
It was decided to synthesise a family of cyanine dyes which employed several different zinc-sensing moieties based on thiophenes in analogous work to the Zinspy family. These cyanine dyes could be compared to a derivative which utilised DPA to assess their affinity and selectivity for Zn^{2+}, as well as on their photophysical properties. It was hoped that this would enable an optimised imaging agent capable of fluorescing in the NIR window which could ratiometrically detect zinc(II). The two derived synthetic targets are shown in **Figure 5.10**.



Figure 5.10: The two analogues of DPA synthesised as alternative zinc sensors.

The amine thiophen-2-ylmethanamine was identified as a key intermediate in the synthesis of each of these target compounds. The pyridine-incorporating zinc sensor could be readily produced from this amine through a nucleophilic substitution reaction with 2-bromomethylpyridine hydrochloride, which

enabled the amine **5.1** to be produced at a satisfactory yield of 67%. The synthetic route towards the di-thiophene compound was slightly longer, but still fairly straightforward. Initially, a condensation reaction between thiophen-2-ylmethanamine and thiophene-2-carboxaldehyde was utilised, following reduction of the imine intermediate with sodium borohydride overnight. Addition of ethanol and hydrochloric acid resulted in precipitation of the hydrochloride salt **5.2** at a good yield of 85%. This salt could be basified using sodium hydroxide to liberate the free amine **5.3** at a moderate yield of 40%. **Scheme 5.1** shows the synthesis of the two zinc-sensing moieties.

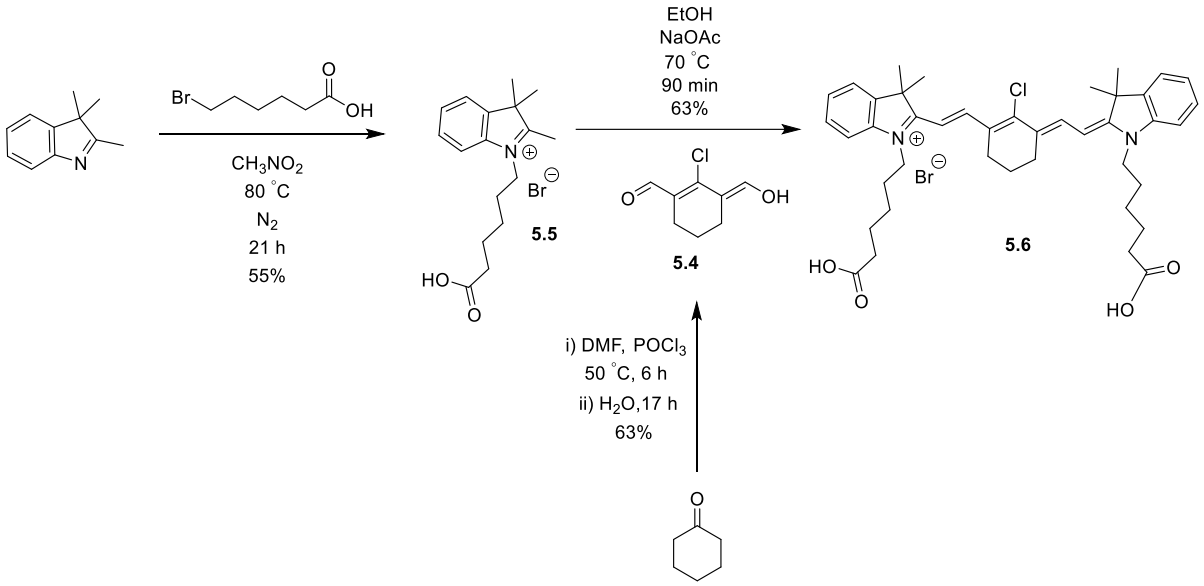


Scheme 5.1.: Synthesis of the two zinc-sensing moieties **1** and **3** from the common starting material thiophene-2-methylamine.

Once these two alternative zinc sensors had been produced, it was decided to incorporate them into a cyanine dye alongside DPA. The cyanine framework chosen was IR-808, a compound reported by Luo *et al*. in 2013[37]. IR-808 is a heptamethine cyanine which was shown to exhibit tumour targeting ability and was chosen due to its emission in the NIR region at 808 nm[37]. The synthesis of IR-808 is also fairly short. The free chloride substituent within the heptimethine backbone of the dye was also attractive as a potential leaving group, enabling the zinc-sensing moieties to be introduced through nucleophilic substitution reactions.

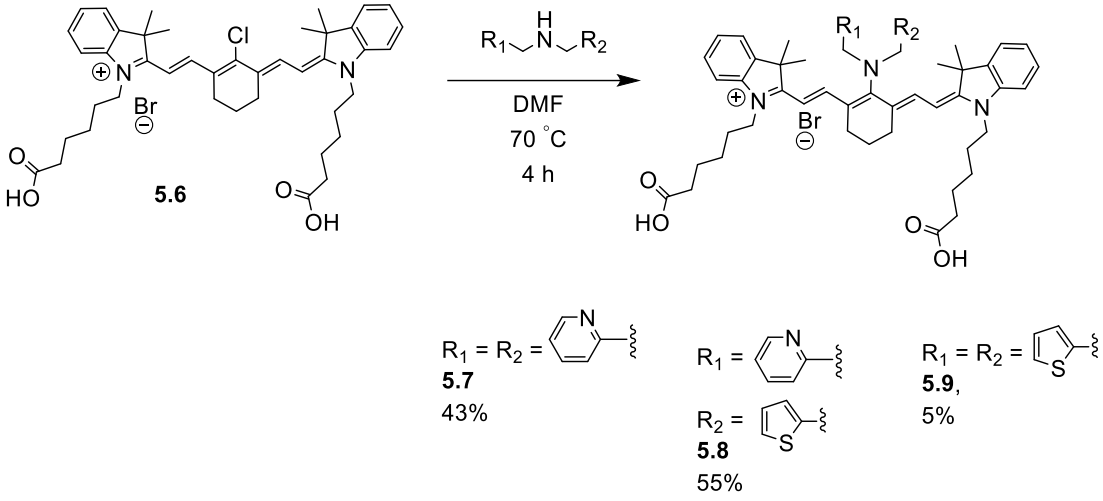
The initial step in the synthesis of IR-808 was a reaction between cyclochexanone and $POCl_3$. This reaction employed conditions analogous to a Vilsmeir-Haack formylation: $POCl_3$ was added dropwise to DMF and left to stir for 30 minutes before the addition of cyclohexanone. Allowing the reaction mixture to stir for 6 hours before pouring the reaction mixture into ice-cold water, resulting in the formation of a precipitate. This precipitate was then recrystallised from DCM to give the chloride species **5.4** at a moderate yield of 63%. The carboxylic acid arms of IR-808 could be synthesised from 2,3,3-trimethylindolenine and 6-bromohexanoic acid, which reacted *via* a nucleophilic substitution to give the deep purple indolium salt **5.5** at a satisfactory yield of 55%. 6-Bromohexanoic acid was chosen for several reasons – chiefly the introduction of a carboxylic acid group. The presence of this group would enable functionalisation of this family of cyanine dyes through the introduction of targeting moieties or allow the capability for other imaging techniques to be explored further and to prevent aggregation of the dye in solution, thereby improving solubility, by increasing interactions with solvent molecules[24]. The carbon chain length was chosen to distance this reaction site from the potentially

vulnerable conjugated system and prevent against degradation of the cyanine backbone. Additionally, as discussed above, the substitution of electron-donating alkyl chains helps to improve photostability of cyanine compounds[23]. Heating an ethanolic solution of **5.4** and **5.5** in the presence of sodium acetate for 90 minutes enabled the isolation of IR-808, **5.6**, at a yield of 63%. **Scheme 5.2** shows the synthesis of compound **5.6**.



Scheme 5.2: Synthesis of **5.6** (IR-808)[37].

It was decided to introduce the zinc-sensing moieties through nucleophilic substitution reactions. Due to concerns over the sensitivity of the cyanine backbone, it was hypothesised that these reactions may be more successful without the addition of an inorganic base and that an excess of the zinc-sensing amines could be utilised to drive the reactions to completion. This was first attempted with DPA, which was stirred in solution in DMF with **5.6** at a 10:1 ratio. After 4 hours, the reaction mixture was poured into Et_2O and left to stir for one hour, resulting in the formation of a blue precipitate which could be purified by flash chromatography to give compound **5.7** at an adequate yield of 43%. This same procedure was carried out with compound **5.2**, giving the corresponding zinc-sensing dye, **5.8** at a yield of 55% and with **5.3** to give the thiophene-based compound **5.9**, although this was at a poor yield of just 5%. **Scheme 5.3** shows the synthesis of these three different zinc-sensing cyanine dyes.



Scheme 5.3: Synthesis of the three different zinc-sensing cyanine dyes.

The low yield of **5.9** compared to the other analogues may be due to reduced basicity of compound **5.3** – the π system of 6 membered heteroaromatic rings does not include the lone pair of the heteroatom, leaving it available to react further. On the other hand, 5-membered heteroaromatics do involve the lone pair of the heteroatom in the π system, rendering it less available. It may be that, as DPA and **5.1** both contain at least one pyridinyl substituent they are able to deprotonate the free amine moiety and allow the nucleophilic substitution to proceed. Compound **5.3** only contains thiophenyl substituents, and therefore is likely to be much less basic. This will have an effect on the position of equilibrium in any self-deprotonation and may explain the reduced overall yield.

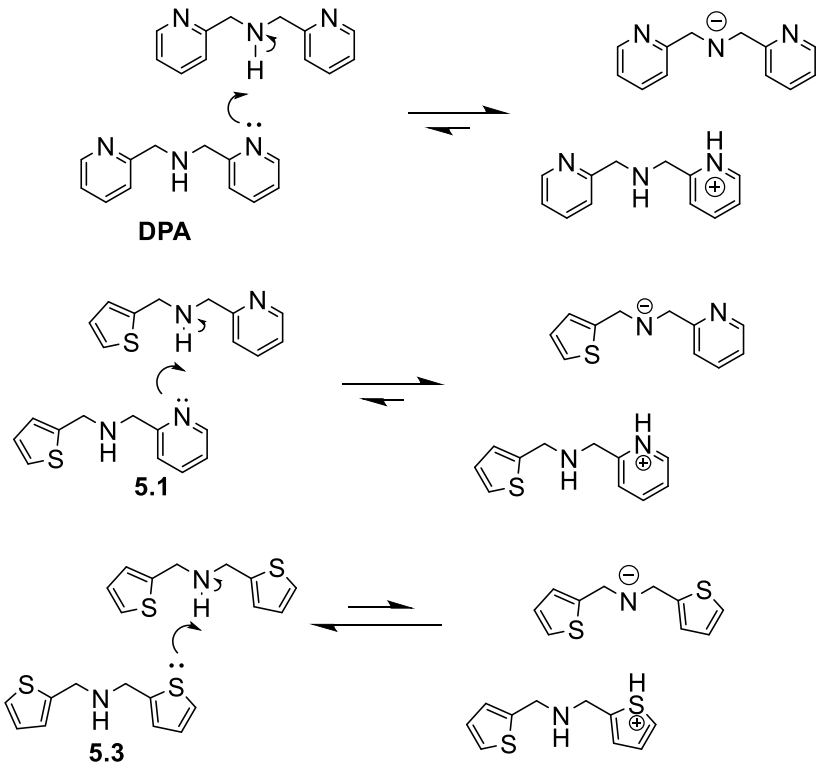
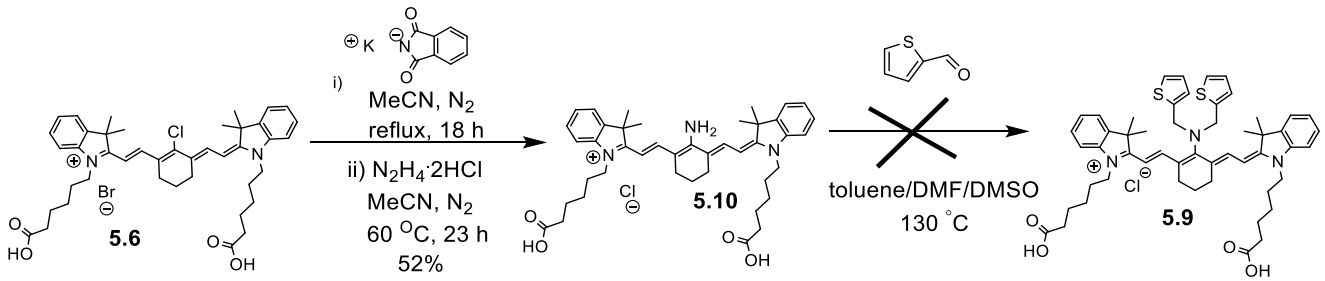


Figure 5.11: Self-deprotonation reactions for **DPA**, **5.1** and **5.3.** It may be that **5.3** has a reduced basicity compared to **DPA** and **5.1** due to its lack of pyridinyl group.

Several attempts were made to improve the yield of **5.9**. One of these was by avoiding the de-salting step in the isolation of the amine **5.3**, by attempting direct reaction of the hydrochloride salt **5.2** and the chloride **5.6**. Unfortunately, this resulted in no reaction progress when monitoring by TLC, even after 5 hours and with 10 equivalents of **5.2** added. Addition of DIPEA, a commonly used non-nucleophilic base, was also attempted to try and liberate the free amine **5.3** *in situ*¸ but again these conditions gave no reaction.

An alternative route to compound **5.9** was devised. This synthetic pathway would introduce the thiophene moiety *via* a condensation reaction, with the amine group being incorporated initially into the cyanine framework. The first step in this synthesis was conversion of **5.6** to an amine. This was done by modifying a synthesis published by Lee *et al*., which used potassium phthalimide and hydrazine hydrate to convert a chloride in a conjugated system to an amine[60]. Formation of the phthalimide intermediate was carried out using potassium phthalimide in acetonitrile under reflux and N_2. After stirring overnight, hydrazine dihydrochloride in H_2O was added and the reaction left to stir for a further 23 hours. A colour change was seen from dark green to dark blue. Flash chromatography gave the amine product, **5.10**, at a moderate yield of 52%, with the resulting solid a deep purple colour. Despite success in the first step of this procedure, all attempts to carry out the condensation reaction with thiophene-2-carboxaldehyde, in a range of solvents, failed. It is possible that the lone pair on the nitrogen atom of **5.10**, critical for condensation reactions, is less available due to its conjugation with the extended unsaturated system in the dye, which is implied by the dramatic colour change between **5.6** and **5.10**. **Scheme 5.4** depicts the formation of the amine **5.10** and the attempts made to reach **5.9** *via* condensation reactions.



Scheme 5.4: The successful synthesis of the amine-functionalised cyanine dye, **5.10** and unsuccessful attempts to convert that to the target compound **5.9**.

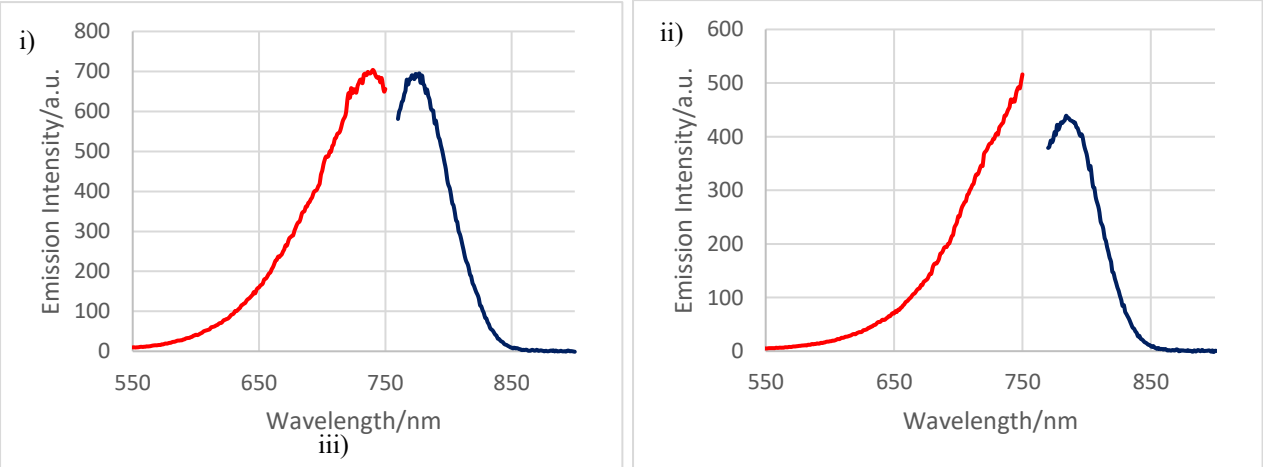
It was decided not to continue the pursuit of **5.9** by alternative means and to explore its photophysical properties and metal binding abilities. The ability to produce each of the cyanine dyes under the same synthetic conditions was advantageous, although the amine derivative **5.10** could have future synthetic applications which may be further explored.

5.2.1.1. Fluorescence Spectroscopy and Zinc-Binding Titrations

Biological systems often auto-fluoresce in the visible region of the electromagnetic spectrum. This presents an issue in fluorescence imaging as there can be increased background noise and it can be harder to distinguish between a fluorescent agent and the cells or tissues being studied[61–63]. The use of fluorophores which are emissive in the NIR region are desirable for this reason, which directed the selection of heptamethine cyanine dyes and IR-808 in particular as the basic framework for these zinc-sensing compounds. It was necessary to examine the photophysical properties of each of these compounds and examine whether their emission still fell within the NIR window after the inclusion of a zinc sensing moiety. In addition, the interaction of these compounds with Zn^{2+} ions was explored in order to assess whether they could be used as zinc sensors. A successful fluorescent ion sensing compound should exhibit a change in its photophysical properties in the presence of the ion it is designed to detect. This change could be a change in emission intensity, or possibly a difference in Stokes shift which may be proportional to the amount of the target ion present in the system[17–19].

With respect to pancreatic β-cells, where there is an abundance of zinc(II) in comparison to the rest of the organ, a fluorescent sensor could be used to potentially quantify the mass of these islet cells and, over a prolonged period of time, monitor progression or development of diabetes, or the response of the body to any successful treatment to be evaluated[57,64,65].

To examine the fluorescent properties of each of the three compounds, 5 μM solutions of each of **5.7**, **5.8** and **5.9** were prepared in an aqueous solution of 4-(2-hydroxyethyl)-1-piperazineethanesulfonic acid (HEPES) buffer (100 mM) and acetonitrile (9:1 ratio) and their excitation and emission spectra recorded (**Figure 5.12**).



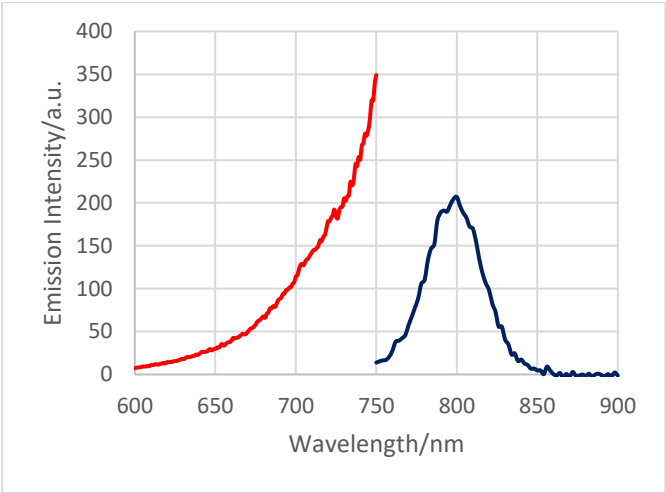
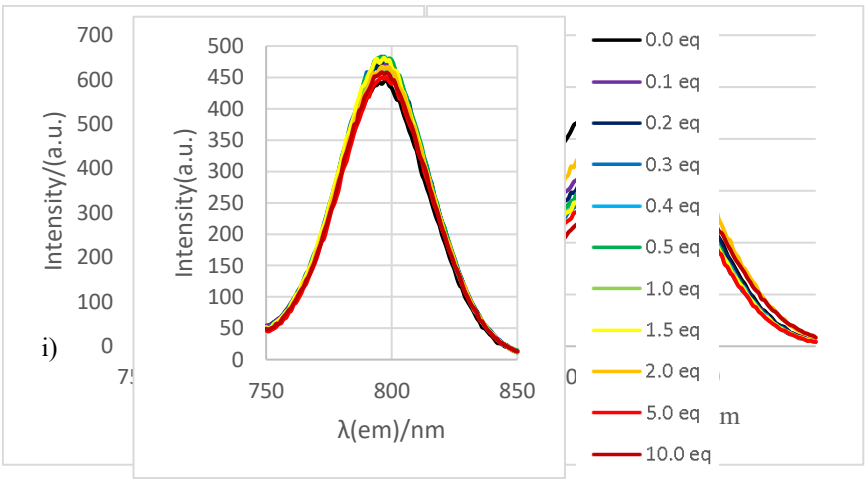


Figure 5.12: Excitation (red) and emission (blue)fluorescence spectra for the dyes i) **5.7** (λ_{ex} = ,721 nm λ_{em} = 780 nm), ii) **5.8** (λ_{ex} = 778 nm λ_{em} = 792 nm) and iii) **5.9** (λ_{ex} = 782 nm λ_{em} = 802 nm), (5 µM, HEPES/MeCN (100 mM aq. HEPES, 9:1 ratio).

These initial experiments showed that all three compounds emitted in the NIR window. Compound **5.7**, which contained DPA as its zinc-sensor, had a peak in its emission spectrum at 780 nm. The emission wavelength of these cyanine compounds was pushed further into the NIR with the substitution of pyridine rings for thiophenes in the zinc-sensing moiety. Compound **5.8** contained a sensor consisting of one of each of these aromatic rings and showed a peak in its emission spectrum at 792 nm. Employing a di-thiophene based moiety shifted the emission peak of compound **5.9** to 802 nm. Although the latter two compounds exhibited fluorescence further into the NIR region, there was a large reduction in the Stokes shift seen in these two compounds, with much higher wavelengths being needed to excite them than **5.7**. Compound **5.7** could be excited at 721 nm, with excitation for **5.8** and **5.9** occurring at 778 nm and 782 nm respectively. These small Stokes shifts (14 nm and 20 nm respectively, compared to 59 nm for **5.7**) could potentially cause problems in any fluorescent imaging applications, and this is exemplified by the lack of any definitive peak in the excitation peaks in **Figure 5.13**.

Despite these potential issues in application, it was decided to assess the binding ability of each of these compounds for Zn^{2+} ions. This was done through a titration method. A range of solutions containing



varied concentrations of $ZnCl_2$ (0 μM to 50 μM) were prepared in an aqueous solution of HEPES buffer (pH 7.4, 100 mM) and acetonitrile (9:1 ratio). An aliquot of the cyanine to be investigated was then added to the solution to give a cyanine concentration of 5μM and the emission spectrum of the solution recorded. The averaged emission spectra of each of the three compounds are shown below in **Figure 5.13**.

Figure 5.13: Fluorescence emission spectra dyes i) **5.7** (λ_{ex} = ,721 nm λ_{em} = 780 nm), ii) **5.8** (λ_{ex} = 778 nm λ_{em} = 792 nm) and iii) **5.9** (λ_{ex} = 782 nm λ_{em} = 802 nm) at different concentrations of Zn^{2+} (5 μM, HEPES, aq., 100mM + 10% MeCN, pH 7.4, n = 3).

The zinc binding titrations showed that compound **5.7** appeared to have the greatest affinity for Zn^{2+}. This was shown by an increase in its fluorescence intensity of up to around 20% in the presence of 10 equivalents of zinc(II), indicative of a PeT mechanism of cation sensing, expected with a DPA receptor. There is also evidence of a possible slight Stokes shift, with the emission wavelength appearing to increase slightly at higher Zn^{2+} concentrations. The same cannot be said for **5.8** and **5.9**. The former appeared to show a decrease in emission intensity at greater zinc concentrations, along with a possible Stokes shift. However, there did not appear to be any definitive or obvious trend in this data. In the case of **5.9**, there was no real change in emission intensity or wavelength as the concentration of zinc(II) ions increased. This is likely due to the lower affinity of the two zinc-sensing moieties employed in these compounds, which was expected, although it was not foreseen that the difference would be so dramatic. With no obvious positive trends visible in the data for **5.8** or **5.9**, it was decided that DPA would be the best zinc-sensing moiety for any cyanine-based imaging agents which were to be explored throughout the project. Issues such as selectivity or albumin binding could potentially be overcome through synthetic modifications of other parts of the molecule, perhaps by tuning lipophilicity, and it was decided that it would be favourable to have some definite interaction with Zn^{2+} than none at all, or a decrease in emission intensity.

The presence of the two free carboxylic acid groups in all three compounds could also have impacted on the results of these titrations as carboxylate groups are known to interact with Zn^{2+}. The use of HEPES buffer at a pH of 7.4 had been chosen to mimic physiological conditions and should have been basic enough to keep the carboxylic acid groups protonated and lessen any binding interaction with the added zinc(II) ions, although it is possible that this still took place, preventing any interaction and modulation of the fluorescence processes *via* the DPA or thiophene units. One attempt was made to form the methyl ester of compound **5.8**, although this was unsuccessful with the addition of H_2SO_4 as a catalyst causing the compound to be destroyed. Further work in this area could form an ester of 6-bromohexanoic acid prior to its incorporation into the cyanine framework, which would then enable a further investigation of these zinc-sensing moieties.

5.2.2. Towards Dual-Modal Imaging Agents

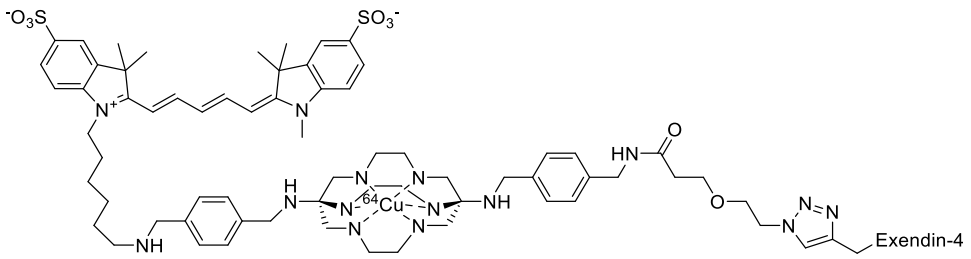
Fluorescence imaging is certainly a powerful, highly sensitive imaging technique which enables rapid collection of high resolution images, even at subcellular levels[53,61,66]. However, it also suffers from poor tissue penetration – this renders sub-surface imaging of organs challenging and clinical use would require the need for invasive tissue biopsies[53,61]. Indeed, many optical fluorescent imaging agents, including the clinically approved cyanine dye indocyanine green, have primarily found use in the field of image guided surgery as opposed to diagnostic agents[67–69]. Other imaging modalities have their own drawbacks too: the low sensitivity of MRI and difficulties in synthetic techniques, radioisotope acquisition and patient exposure to radiation associated with both PET and SPECT imaging are just some examples[70,71].

No imaging technique is perfect, and the development of dual-modal imaging agents is a key part in attempts to overcome the intrinsic problems associated with the techniques listed above when used in isolation. Utilising the same chemical agent for different imaging modalities can enable improved resolution and result in the acquisition of improved local information and validate biodistribution and tissue localisation[19,66]. Indeed, being able to use the same agent for both fluorescence and PET imaging could avoid variation in biodistribution which would of course be an issue with two different compounds.

It was hypothesised that dual-modality could be harnessed in the pursuit of zinc-sensing imaging agents. Zinc-binding could act as a targeting methodology of sorts, allowing localisation of a dual-modal compound at pancreatic β-cells. The high sensitivity and 3D images obtained through PET imaging could further explore this localisation and potentially identify islet clusters. Due to the extremely low volume (~1%) of the pancreas which is occupied by islet β-cells, this could be extremely helpful[72,73]. These identified regions of high β-cell density could then be explored further with the fluorescent Zn^{2+} sensing ability of the compound, i.e. using ratiometric changes in fluorescence emission intensity to monitor cell functionality changes, which could be useful in diagnosing diabetes progression or assessing any response to treatment, be it pharmacological or through islet grafting.

5.2.2.1. Fluorination of Cyanine Dyes

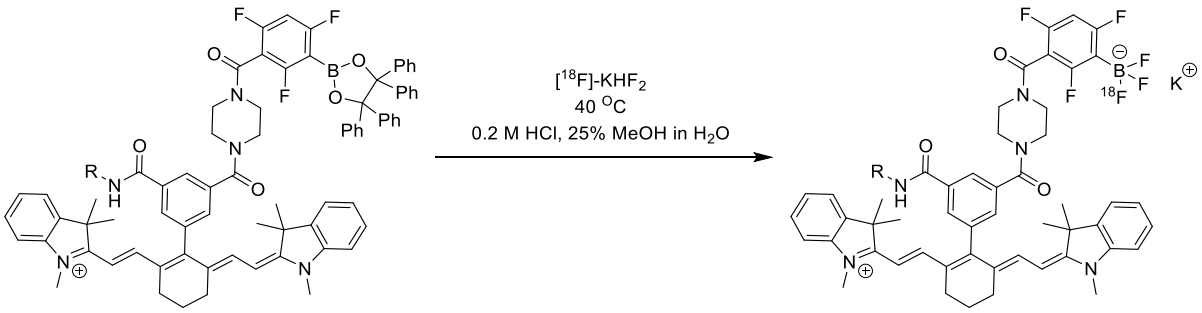
One particularly notable dual-modal imaging agent based on a cyanine dye was synthesised by Brand *et al.* in 2014[53]. This compound, which incorporated the NIR fluorophore indocyanine green as a



fluorophore and a sarcophogine copper chelator, was coupled to the glucagon-like peptide 1 receptor (GLP-1R) agonist exendin-4, which targets β-cells and is extensively discussed in Chapter 2 of this thesis. Brand's compound (**Figure 5.14**) was designed to be used as an agent to detect tumour growth in GLP-1R expressive insulinomas, and was able to delineate between these and healthy cells[53]. This successful dual-modal imaging agent successfully based on a cyanine dye was envisioned as the basis for dual modal compounds based on compound **5.7**.

Figure 5.14: The dual-modal (optical-PET), cyanine-based compound synthesised by Brand *et al*.[53].

In contrast to Brand's work, it was hypothesised that the use of any radiometal, such as the commonly used PET isotopes ^{64}Cu or ^{68}Ga, could present some issues due to the inclusion of a metal binding DPA moiety – i.e. that during radiolabelling the DPA could bind to a radiometal in addition to any specific ligand or chelate in the molecule, which could disrupt the ion-sensing ability of the compound or result in toxicity issues and radiation exposure *in vivo*. As such, it was decided to synthesise a dual-modal PET-optical imaging agent which incorporated an organic radionuclide rather than a radiometal. The radioisotope ^{18}F is a positron emitter which has risen to the forefront of PET imaging agents. Its half-life of 110 minutes is much longer than other organic positron emitting nuclei, alleviating some of the synthetic concerns associated with radiochemistry[74,75]. Success had also been had in radiofluorination of cyanine compounds by Ting *et al*. in 2010, who used cleavage of a boronate ester bonded to a heptamethine cyanine dye to produce a dual-modal imaging probe capable of bioconjugation[76]. Ting's compound and the radiolabelling conditions are shown in **Scheme 5.5**. The success of this work gave some reassurance that the process of cyanine radiolabelling was possible without destroying the sensitive conjugated backbone.



Scheme 5.5: The cyanine dye radiolabelled by Ting *et al*. in 2010[81]. The authors used the carbohydrate Lymphoseek (DTPA-mannosyl-dextran) as a targeting group, represented by R.

In 2018, the synthesis of an ^{18}F labelled zinc-sensing fluorescent probe was published by Price *et al*.[77]. This compound was shown to selectively bind to Zn^{2+} over other metal ions through its aminoquinoline moiety and exhibited a large quantum yield enhancement in the presence of zinc(II)[77]. These zinc-sensing abilities of the compound were successfully used to quantify and compare levels of Zn^{2+} in prostate cancer and healthy cells[77]. The synthetic chemistry employed in the pursuit of this compound,

shown in Figure **5.15**, was fairly straightforward – simply employing nucleophilic substitution and amide coupling - and appeared to be an accessible way in which fluorine could be introduced to a fluorescent compound to produce a cold analogue of a dual modal agent. Previously within the Long group, microwave reactions and click chemistry have been employed to introduce C-F bonds into PET imaging agents[78]. However, there was concern about the robustness of cyanine dyes under these conditions, due to the highly sensitive nature of the compounds.

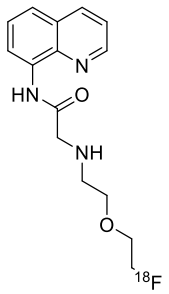
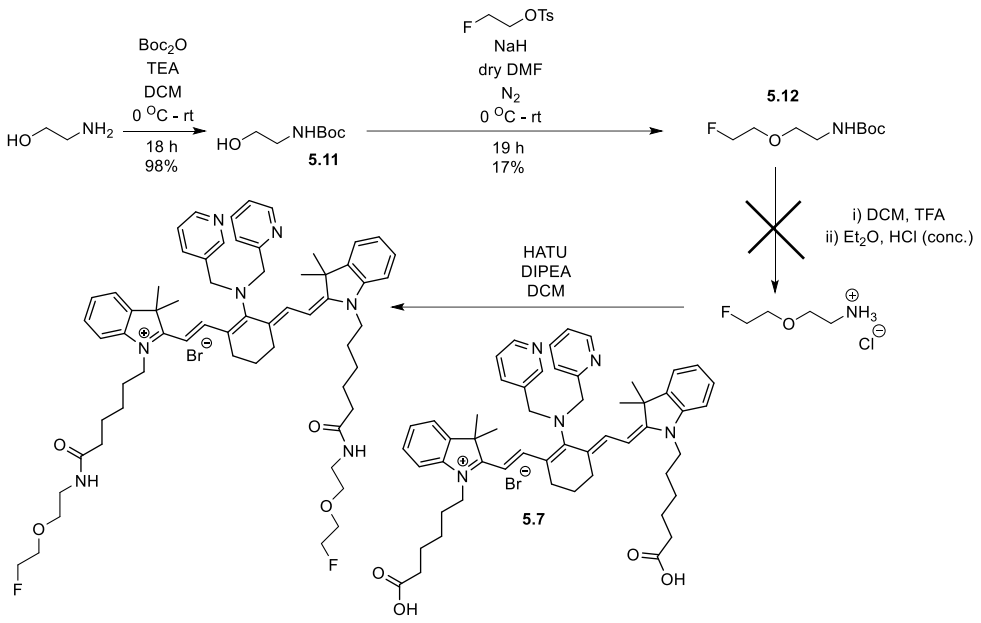


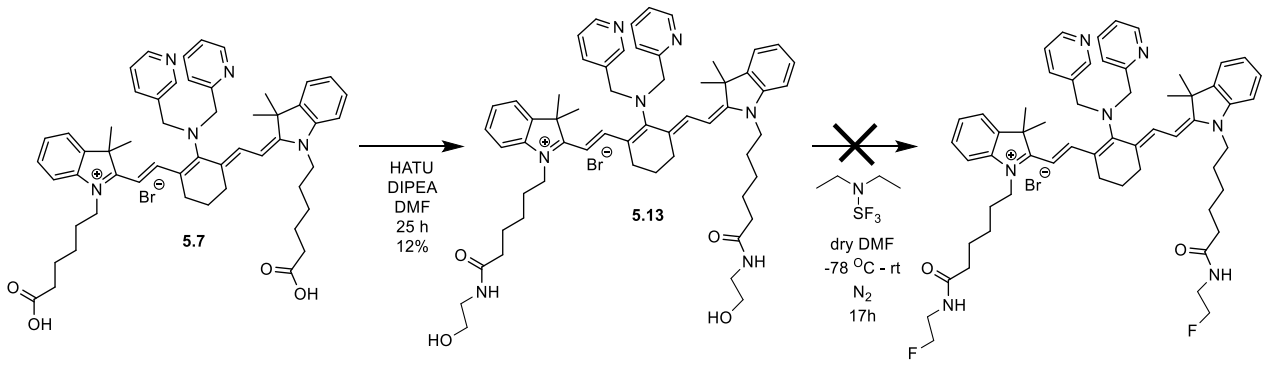
Figure 5.15: The dual modal, zinc-sensing probe synthesised by Price *et al*.[77]

It was decided to replicate the method of fluorination utilised by Price *et al*. to introduce fluorine into a series of cyanine compounds. The first step in this synthesis was to protect ethanolamine with a *tert*-butoxycarbonyl (Boc) group. This could be easily achieved overnight using Boc_2O to give compound **5.11** at yields of up to 98% following a simple aqueous extraction. Subsequently, this compound was used as a nucleophile through deprotonation with sodium hydride which enabled displacement of a tosylate group from 2-fluoroethyl *p*-toluenesulfonate. The yield of this reaction, which produced compound **5.12**, was low at just 17%. Unfortunately, the necessary deprotection step required to liberate the amine in this compound could not be successfully be carried out, despite several attempts. During work-up, Price *et al*. isolated the free amine through precipitation, and it is possible that the fairly small scale of this reaction hindered the work-up procedure. Typically, only around 150 mg of **5.12** could be produced each time and, ultimately, it was decided that the low yield of this compound and difficulties in further synthesis rendered this synthetic pathway unsuitable. **Scheme 5.6** shows the successful steps carried out in this route and the intended future synthesis.



Scheme 5.6: The successful replication of Price's work and the desired future synthesis.

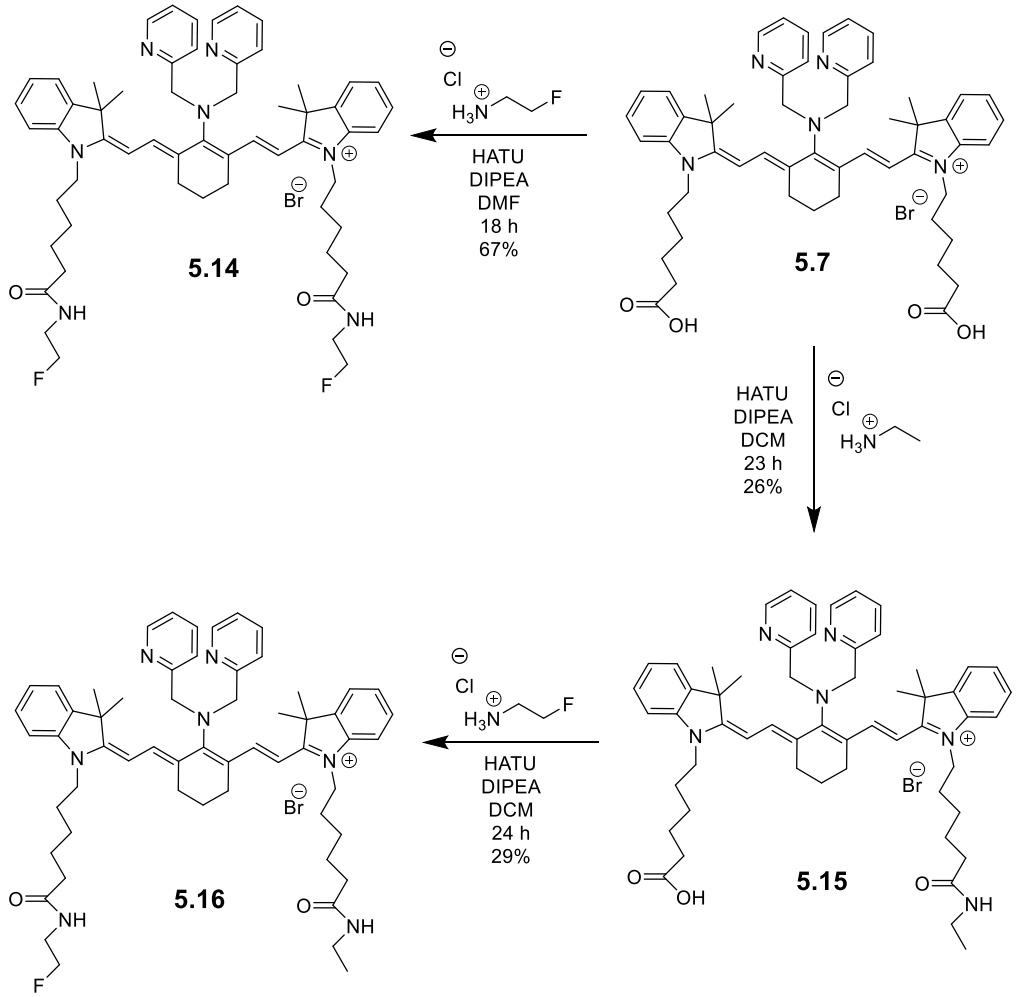
Following the difficulties encountered in the ethanolamine-based approach, it was decided to pursue an alternative route towards fluorinated cyanine dyes. One approach which was considered was the use of the fluorinating reagent diethylamino sulphur trifluoride (DAST). This compound converts primary alcohols to fluorides, and so it was decided to couple compound **5.7** to ethanolamine, giving the di-alcohol **5.13** at a disappointing yield of just 12%. Unfortunately, carrying out the fluorination reaction with DAST resulted in degradation of the cyanine. It is possible that, as the by-product of any DAST reaction is HF, an extremely strong acid which could have destroyed the sensitive conjugated backbone of compound **5.13**. These reactions are summarised in **Scheme 5.7**.



Scheme 5.7: The successful coupling of 5.7 to ethanolamine and the unsuccessful DAST reaction.

To avoid the harsh conditions encountered during the DAST reaction, more mild conditions were employed to introduce fluorine-containing substituents. Compound **5.7** could be successfully coupled to 2-fluoroethylamine hydrochloride using the coupling reagent HATU, giving the difluorinated compound **5.14** at a good yield of 67%.

Many imaging agents incorporate targeting groups to enhance their delivery to the biological target of interest. The two carboxylic acid arms of **5.7** lend themselves to bi-functionalisation of the cyanine dye, with different groups being added to each arm. As a long term goal, it was considered that one of the arms could be used to introduce a targeting group, such as the G-protein coupled receptor 40 (GPR40) agonists discussed in Chapters 3 and 4. Any such dual-modal compound produced in this way would be mono-, rather than di-fluorinated and so it was decided to synthesise a mono-fluorinated compound which could be compared to **5.14** for *in vivo* applications, as well as assess how the quantity of any probe required for PET imaging could change. Ethylamine was chosen as a simple placeholder to essentially act as a stand-in for any targeting group which could be introduced and essentially act as a protecting group for one of the carboxylic acid groups. The mono-alkylated compound **5.15** could be produced from **5.7** through a typical amide coupling with HATU. The yield of this reaction was low at just 26%. This was primarily due to formation of the disubstituted analogue of **5.15** as the major product, despite control of equivalents and temperature: use of sub-stoichiometric amounts of ethylamine hydrochloride and allowing the reaction to stir for 6 hours at 0 °C instead of overnight at room temperature still did not prevent reaction at both carboxylic acid positions from occurring. The amide coupling reagents 1-ethyl-3-(3-dimethylaminopropyl)carbodiimide (EDC) and hydroxybenzotriazole (HOBt), considered as potentially less effective than uronium compounds resulted in lower yields, typically around 15%, but still did not prevent formation of the disubstituted compound. Subsequent coupling with 2-fluroethylamine hydrochloride could then be carried out to give the mono-fluorinated cyanine dye **5.16** at a satisfactory yield of 29%. **Scheme 5.8** shows the synthesis of the two fluorinated compounds.



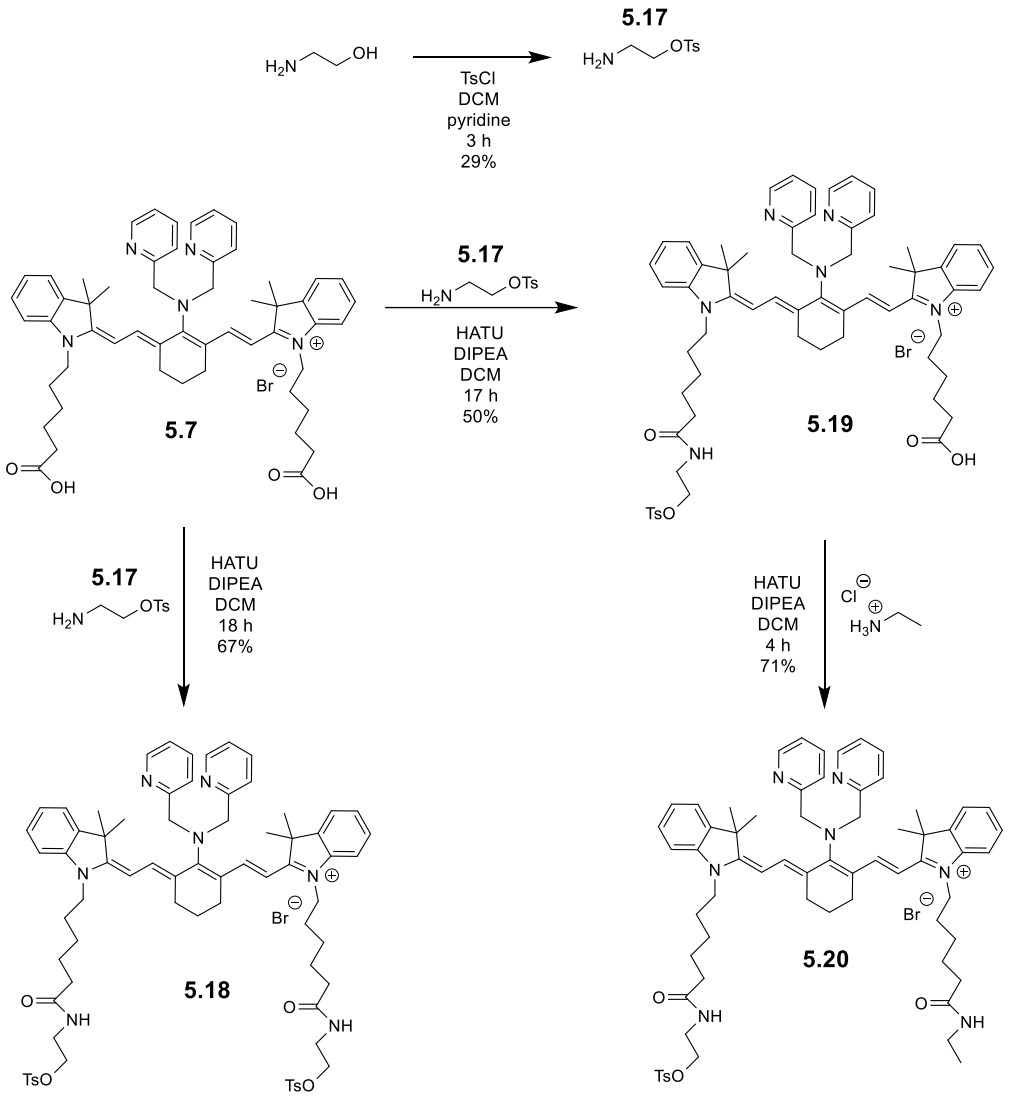
Scheme 5.8: Synthesis of the fluorinated cyanine dyes **5.14** and **5.16.**

Both compounds **5.14** and **5.16** are cold analogues of potential PET imaging agents incorporating ^{18}F. A cold compound has the same structure and chemical formula as a radioactive species but contains no radioactive nuclei. A radiolabelled compound, which is radioactive, is referred to as hot. Radiolabelling procedures must take into account the time-sensitive nature of the whole process: extensive purification and characterisation of the product are undesirable as they can be time-consuming and reduce the radioactivity count of the compound, reducing its utility as a PET imaging probe. Practically, the success of the radiolabelling procedure is monitored by high performance liquid chromatography (HPLC): the retention time of a cold analogue of the product is measured and, after radiolabelling, the HPLC trace of the product is compared to that of the cold compound to validate that the compound has been successfully radiolabelled. As such, neither **5.14** nor **5.16** could be used as radiolabelling precursors as there would not be a sufficient difference in HPLC retention time to definitively say that radiolabelling had taken place, although their HPLC traces could be used to validate successful radiolabelling.

Price *et al*. synthesised a tosylate derivative of their compound as the radiolabelling precursor[77]. Indeed, it is well established in the literature that sulfonate groups such as triflates, mesylates and tosylates are labile leaving groups for the introduction of electrophilic radioactive fluoride[75]. Typical conditions for this process involve the cryptand Kryptofix222 (K_{222}), which coordinates to the cation of the fluoride salt (typically K^+ or Cs^+) produced in a cyclotron and essentially leaves the [^{18}F]-fluoride anion naked and therefore extremely nucleophilic[79]. As such, it was decided to synthesise tosylate analogues of compounds **5.14** and **5.16** to act as precursors for radiolabelling.

The synthetic pathway which was undertaken towards these compounds was very similar to that used to isolate the two fluorinated cyanines. Initially, ethanolamine was tosyl protected by reaction with tosyl chloride, producing compound **5.17** at a satisfactory yield of 29% after 3 hours. This could then undergo an amide coupling reaction with the free carboxylic arms of **5.7** to give the ditosylate **5.18** at a good yield of 67%. An initial attempt at this reaction gave a low yield of just 11% - this was attributed to difficulties in the work-up procedure: most of the cyanine compounds explored up until this point could be isolated from a reaction mixture by pouring into a vast excess of Et_2O, avoiding the need to wash off DMF and non-nucleophilic amines present in the amide coupling reactions. However, it appears that the aromatic tosyl rings resulted in increased solubility in relatively non-polar solvents.

Due to the difficulties encountered in selective synthesis of **5.15** and avoiding reaction at both positions, it was decided to reverse the order of the coupling reactions involved to produce the monotosylated species. Compound **5.7** was coupled with **5.17** using the standard coupling conditions employed elsewhere in this Chapter: HATU being the coupling reagent of choice. This successfully gave **5.19** at a moderate yield of 50%, with the monotosylate subsequently reacted with ethylamine hydrochloride to give the radiolabelling precursor **5.20** at a high yield of 71%. **Scheme 5.9** shows the synthesis of the tosylated precursors.



Scheme 5.9: The synthesis of the two tosylate precursors (**5.18** and **5.20**) for radiolabelling.

5.2.2.2. Zinc-Binding Titrations of Compound 5.14

This family of cyanine dyes have been designed to act as sensors for Zn^{2+} ions *via* the DPA moiety in order to explore the declining functionality of pancreatic β-cells in diabetes development. It was decided to examine the interaction between compound **5.14** and these ions to judge its suitability as a ratiometric fluorescent probe.

The procedure followed in the exploration of a range of alternative zinc sensors (discussed above in **5.2.1.1**) was adapted to carry out the zinc-binding titrations. A 100 μM solution of **5.14** was prepared in a mixture of HEPES buffer solution (aq., 100 mM) and MeCN (9:1 ratio) and aliquots of an aqueous solution of $ZnCl_2$ added to give a range of solutions with between 0.1 and 10 equivalents of Zn(II). Each solution was excited at 728 nm, resulting in emission at 770 nm. The complete titration data are shown in **Figure 5.16**.

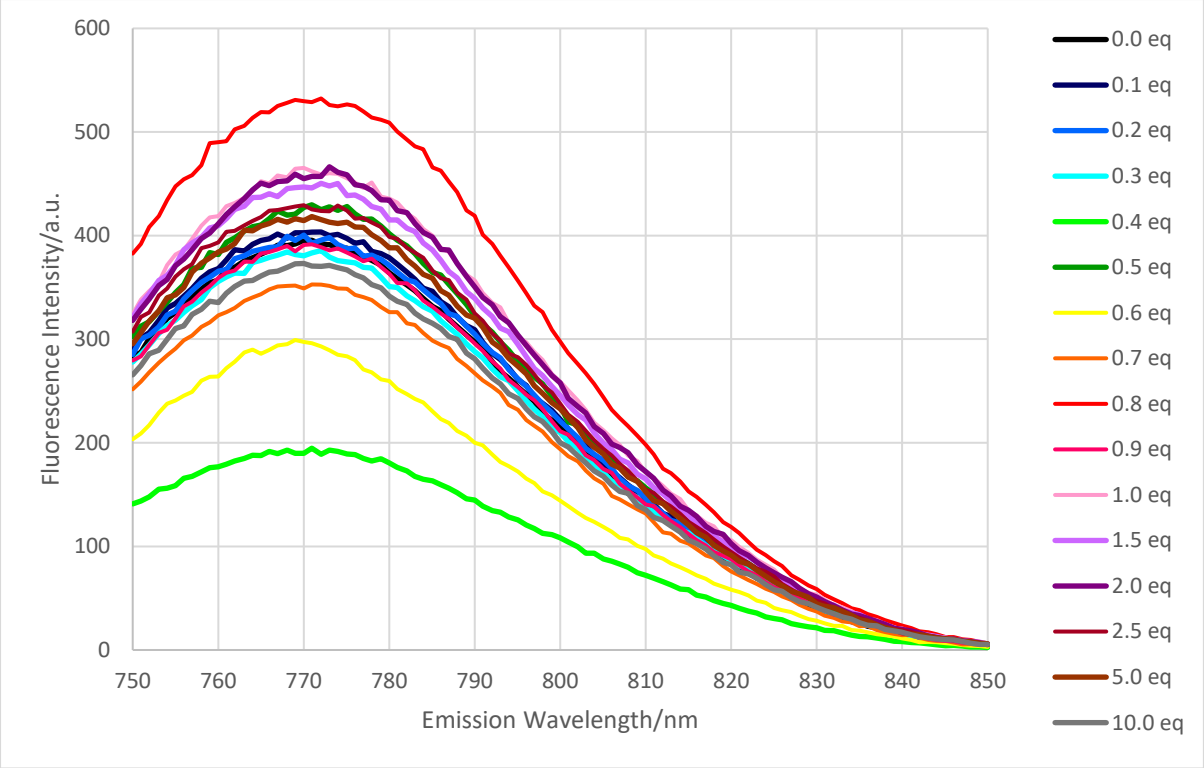


Figure 5.16: Fluorescence data from zinc-binding titrations of compound **5.14** (n = 3, HEPES/MeCN (9:1), λ_{ex}= 728 nm).

No obvious or immediate conclusions could be drawn from the titration data, with no clear relationship between the number of Zn^{2+} equivalents and emission intensity. As a general inference, it appeared that there is some enhancement of emission intensity of **5.14** when between 0.8 and 5.0 equivalents of Zn^{2+} are present, although this was by no means ratiometric it could give some kind of qualitative indication of ion levels. The increase in emission intensity in the presence of Zn(II) suggests that a PeT mechanism is taking place. However, there was actually a marked decrease in emission intensity when the number of equivalents was increased to 10. The reasons for this are unclear – it is possible that the probe does have a very low affinity for Zn^{2+} which does allow some chelation to take place *via* the DPA moiety, resulting in modulation of the fluorescent properties of the cyanine through photoinduced electron transfer (PeT) and internal charge transfer (ICT) processes and subsequent emission intensity enhancement, as discussed extensively in the introduction to this thesis[9,80–82]. The peak in emission intensity in the presence of 0.8 equivalents could be due to formation of a Zn:**5.14** unit. Furthermore, the lack of a trend may be due to the solution behaviour of the compound. Cyanine dyes are known to be fairly hydrophobic and can aggregate in aqueous solution by stacking into regular arrangements – this can be attributed to the presence of their extended aromatic systems and the corresponding strong intermolecular π-stacking and attractive forces that exist between them[6,29,83].

Figure 5.17 highlights selected data sets from the titration to indicate the general increase in emission intensity in the presence of higher numbers of Zn^{2+} equivalents and the unexpected decrease in intensity when 10 equivalents were present.

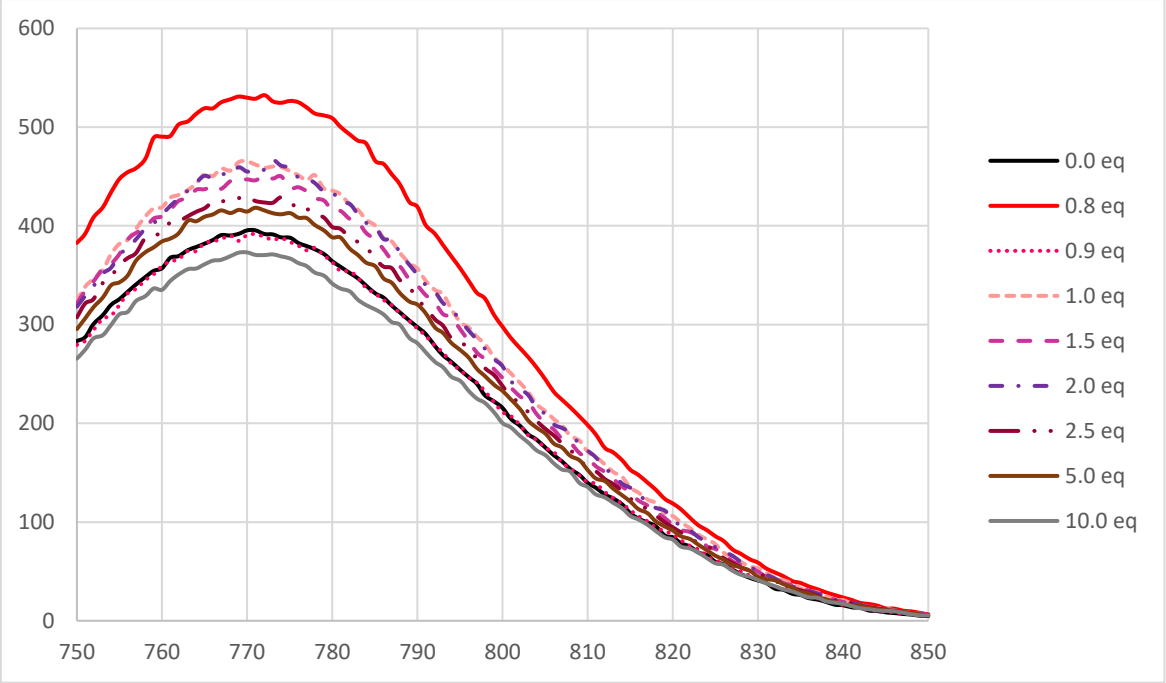


Figure 5.17: Selected data series from the zinc-binding titrations of **5.14**.

There may have been a methodology problem resulting in the unexpected results observed here – for example a Stokes shift could have occurred in the excitation wavelength of **5.14** in the presence of Zn^{2+}. This could be explored further in future work by recording the UV-vis absorption spectrum in the presence of a large excess of Zn^{2+}, along with the selectivity of the probe for other metal ions. This could not be carried out due to time constraints.

5.2.2.3. Radiolabelling of Tosylated Cyanine Dyes

Success of any radiolabelling process is determined by a change in HPLC retention time between precursor and product, with the retention time of the isolated hot product compared to that of a cold analogue and a match indicating that the desired outcome has been achieved. **Figure 5.18** shows the HPLC traces of the cold difluorinated cyanine **5.14** and its tosylate precursor **5.18**, recorded on an Aglient 6200 TOF LC-MS.

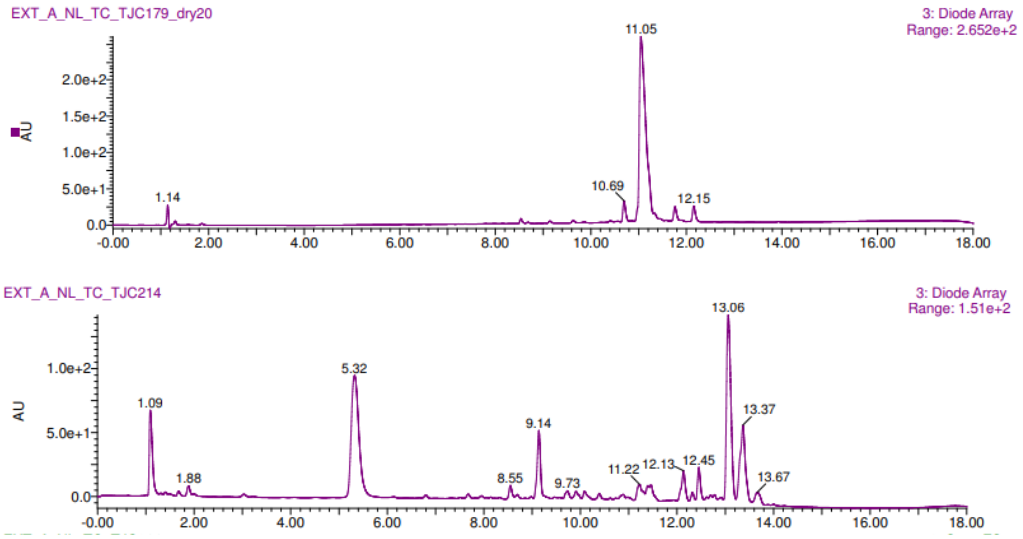
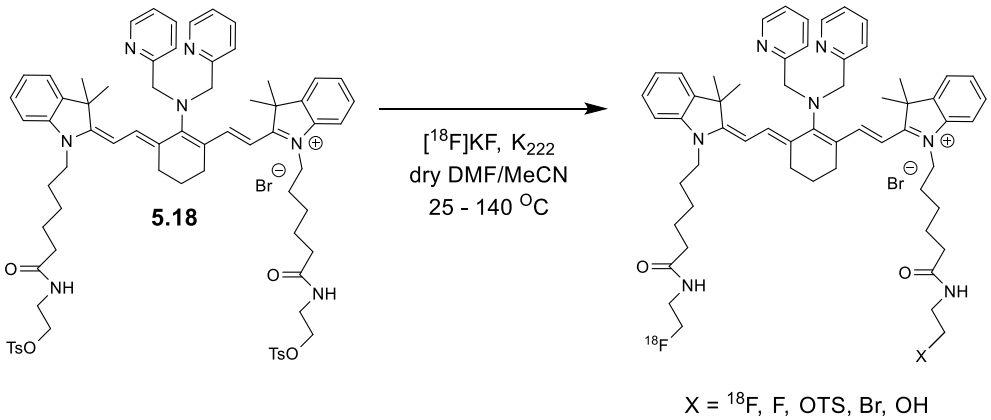


Figure 5.18: The LCMS traces of compounds **5.14** (top) and **5.18** (bottom) (95:5 H_2O:MeCN to 100% MeCN +0.1% formic acid). The peak at 13.06 minutes corresponds to **5.18**.

Compound **5.18** was chosen for initial radiolabelling due to its improved synthetic accessibility over **5.20**, which was more challenging to make. There was some apprehension about this due to the range of different products which can be produced when radiolabelling at multiple positions, but it was also theorised that if **5.18** was shown to be successfully radiolabelled, then the process should prove more straightforward for **5.20**. Compound **5.18** was subjected to radioactive ^{18}F-labelled KF in the presence of K_{222} in a solution of anhydrous DMF or MeCN. **Scheme 5.10** summarises these conditions and the possible product formations.



Scheme 5.10: Radiolabelling conditions for **5.18** and the expected range of products.

Prior to radiolabelling, comparisons were made between the compound reported by Price *et al*. in 2018 and **5.18** to assess its suitability for the chosen conditions. There were several similarities between the two compounds – notably the tosylate leaving group, presence of an amide bond and a basic pyridine moiety[77]. Differences between the two that were judged to possibly impact on the radiolabelling process were the tertiary amine in **5.18**, compared to a carbamate protected amine in Price's compound and,

perhaps critically, the positive charge in the cyanine backbone and corresponding bromide counter ion. Ultimately, it was judged that similar conditions could be employed in the radiolabelling process.

Radiolabelling of compound **5.18** was carried out by Dr Graeme Stasiuk and Dr Tom Price at the University of Hull. The first radiolabelling attempt was carried out by introducing [^{18}F]KF/K_{222} to a solution of **5.18** in DMF at a concentration of 19.60 mM at 140°C . After 15 minutes, the solution had changed from the characteristic blue associated with these cyanine compounds to brown, suggesting decomposition of the dye. Use of MeCN instead of DMF gave the same colour change, even at a lower temperature of 110°C. Additionally, the radio-HPLC traces from both reaction mixtures showed no peak with a retention time corresponding to the cold analogue **5.14**, indicating that now radiolabelling had taken place. The UV-vis spectrum of each sample was also extremely messy and complex, further implying complete degradation of the precursor. These traces are shown in **Figure 5.19**.

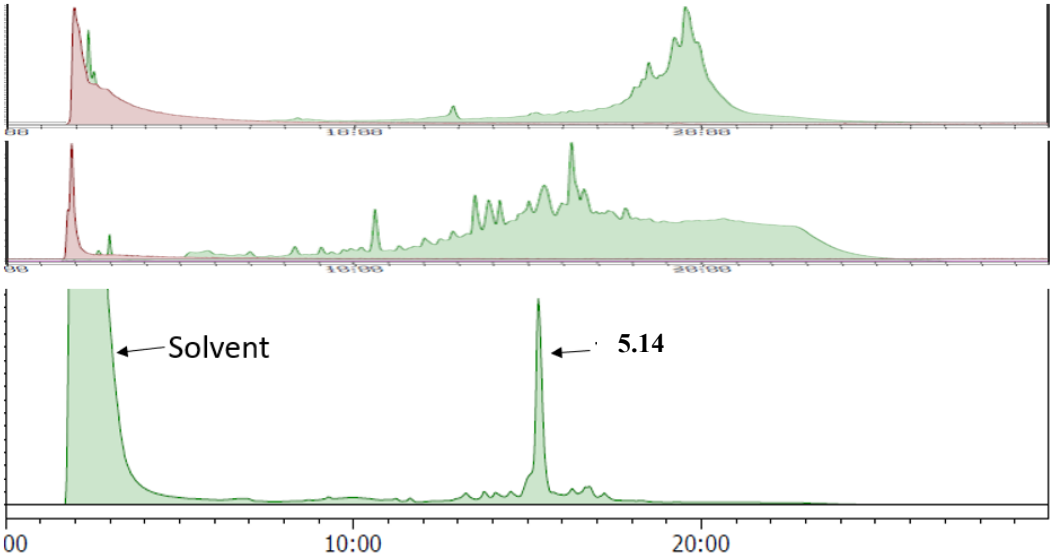


Figure 5.19: HPLC traces from radiolabelling of compound **5.18**. Red = radiotrace, Green = UV trace. Gradient: 3 minutes 95:5 H_2O:MeCN + 0.1% TFA to 5:95 H_2O:MeCN + 0.1% TFA over 15 minutes, followed by washing. Top: 110 °C in MeCN middle: 140 °C in DMF, bottom: HPLC trace of cold compound **5.14**.

It was suspected that the high temperatures used in these initial attempts were responsible for the degradation of the precursor. Accordingly, it was decided to attempt the radiolabelling at lower temperatures to see if this could be avoided. Compound **5.18** was dissolved in DMF at a concentration of 29 mM and stirred in the presence of K_{222} and ^{18}F-labelled KF at 25 °C for 15 minutes. The temperature was then increased in 20 °C increments up to a maximum of 105 °C, stirring for a period of 30 minutes at each temperature. An aliquot of the solution was taken and analysed at each temperature after dilution with H_2O. The same colour change from blue to orange was observed in the solution after 30 minutes. These traces are shown in **Figure 5.20**.

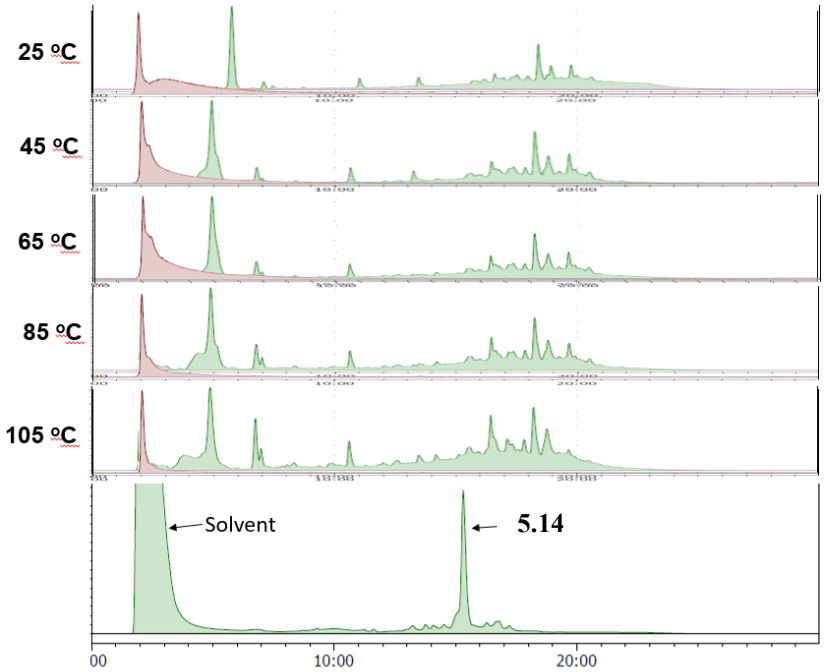


Figure 5.20 Traces from variable temperature radiolabelling attempts of compound **5.18**. Red = radiotrace, Green = UV trace. Gradient: 3 minutes 95:5 H_2O:MeCN + 0.1% TFA to 5:95 H_2O:MeCN + 0.1% TFA over 15 minutes, followed by washing. Bottom: HPLC trace of cold compound **5.14**.

As can be seen from the full set of radiotraces above, no successful labelling of **5.18** was achieved to give a hot analogue of **5.14**. This was disappointing, especially as similar compounds had successfully been radiolabelled in prior work, as discussed above[76,77]. The failure of the process could be due to deprotonation of an acidic proton from the cyanine dye, i.e. it is possible that the amide proton or those at the α positions in the arms of the compound could be removed by F^-, especially as the highly reactive naked anion. Furthermore, there may be some interaction between the powerful nucleophile and the extended system of conjugation present in these dyes resulting in substantial degradation at ambient temperatures.

Due to the disappointing results obtained at this stage, it was decided not to pursue further radiolabelling of compounds **5.18** or **5.20**. The significant decomposition of the precursor seen at low temperatures was thought to be due to intrinsic properties of this family of compounds, and therefore radiofluorination was unlikely to work. Alternative routes towards the synthesis of dual-modal imaging probes were to be based on the incorporation of radiometals, and this is discussed further below.

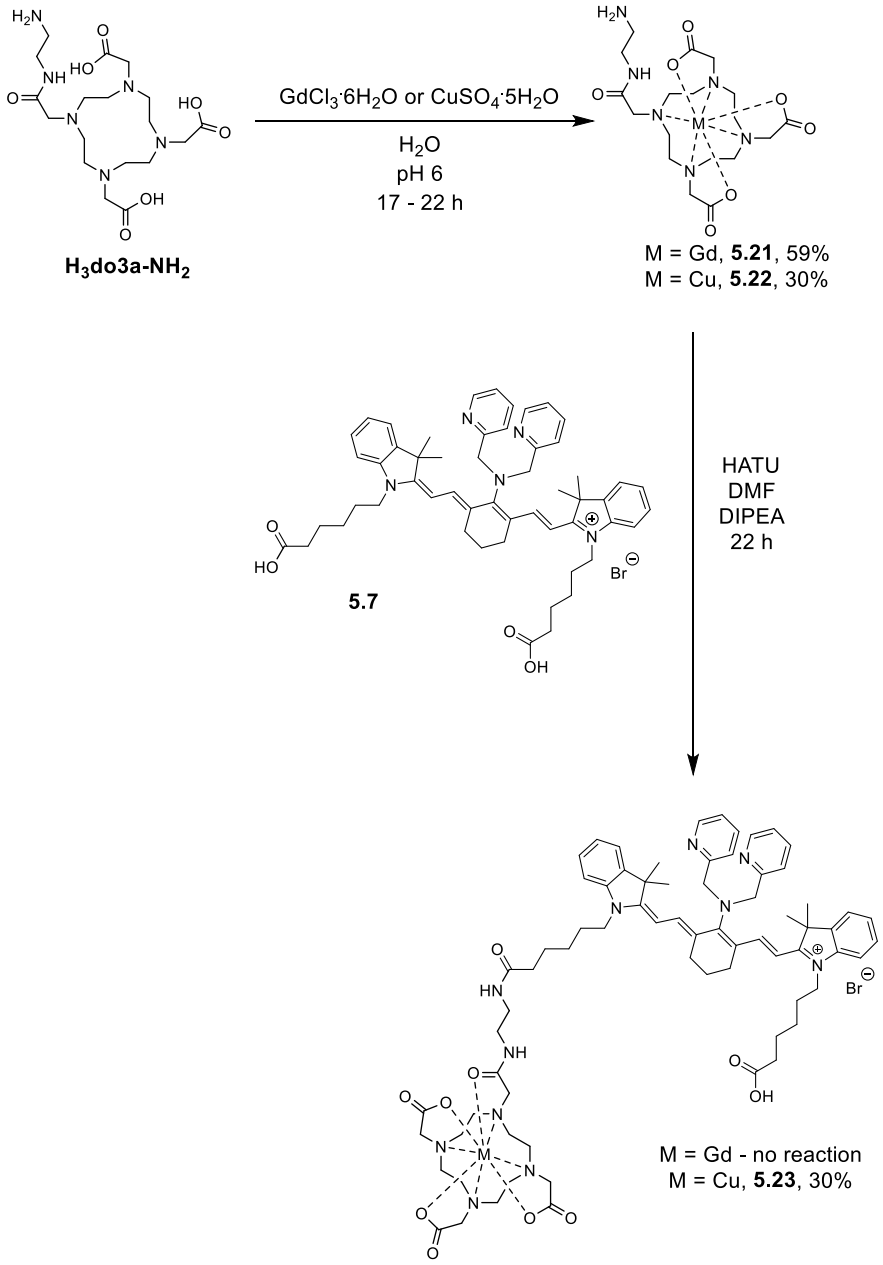
5.2.2.4. Macrocyclic Metal Chelators for MR and PET Imaging

As the use of fluorine-18 seemed non-viable, it was decided to introduce a macrocyclic metal binding unit to compound **5.7**, which could then act as a versatile ligand for a wide range of medicinally useful ions such as copper, which has a positron emitting radioisotope, or gadolinium, widely exploited in the field of MRI. It was also hoped that some kind of targeting moiety could be introduced to these cyanine compounds in order to enhance their distribution *in vivo* and form a group of targeted bimodal probes.

The targeting group of choice was the indole-propionic acid moiety developed by Yoon *et al*. which was exploited in the synthesis of lanthanide(III) based probes and discussed in Chapter 3 of this thesis[84].

Initially, the chelator H_4dota(ga)NH_2 was chosen as the metal binding unit. Its octadentate nature could allow thermodynamically stable and kinetically inert complexes to be synthesised, as well as enabling a large array of metal ions to be sequestered and increasing the versatility of the cyanine dye family. Due to the sensitive nature of the cyanine backbone, especially its susceptibility to pH variations, it was decided to first introduce the metals to the ligand and couple the resultant complex to **5.7** in order to minimise the risk of cyanine degradation. Whilst the complexes of these metals and H_4dota(ga)NH_2 could be successfully isolated, neither could be successfully coupled to **5.7**. Due to the long and complex synthetic route needed to produce H_4dota(ga)NH_2, in addition to the difficulties encountered in any further functionalisation, it was decided to use an alternative metal binding unit. The ligand chosen was H_3do3a-NH_2, which can be readily synthesised from H_3-do3a *via* sequential reactions with chloroacetyl chloride and ethylenediamine. The synthesis of H_3do3a-NH_2 was carried out by Dr Tamara Boltersdorf, who provided the necessary quantity of ligand to enable complexation with Gd(III) and Cu(II). This could be successfully achieved through utilisation of the salts $GdCl_3 \cdot 6H_2O$ and $CuSO_4 \cdot 5H_2O$ to give the complexes **5.21** and **5.22** at moderate yields of 59% and 50% respectively.

Subsequent amide coupling to **5.7** used HATU and DMF, which had successfully been utilised in prior work for cyanine functionalisation *via* the carboxylic acid arms. Whilst this could not be achieved using compound **5.21** (**5.7** was completely consumed, but the isolated product could not be identified), the cyanine dye-copper chelate compound **5.23** could be produced under these conditions at a moderate yield of 30%. This synthesis is shown in **Scheme 5.10.**



Scheme 5.10: Complexation of H_3do3a-NH_2 and subsequent reaction with **5.7**.

Chapter 3 of this thesis discusses the introduction of a targeting group designed to bind to GPR40. The ligands synthesised in that Chapter had the targeting group brought in through nucleophilic substitution reactions in which the electrophile was compound **3.14**, an aromatic bromide with an iodo- substituent on the phenyl ring which was subsequently used to build on the targeting moiety through a Sonogashira reaction. It was hoped that this some methodology could be repeated in the pursuit of targeted cyanine dyes, albeit with one small alteration: compound **3.14** was to be converted to an amine to enable an amide coupling reaction to take place with the free carboxylic acid arm in compound **5.23**. This was successfully achieved using the same reaction conditions used in the production of the amine

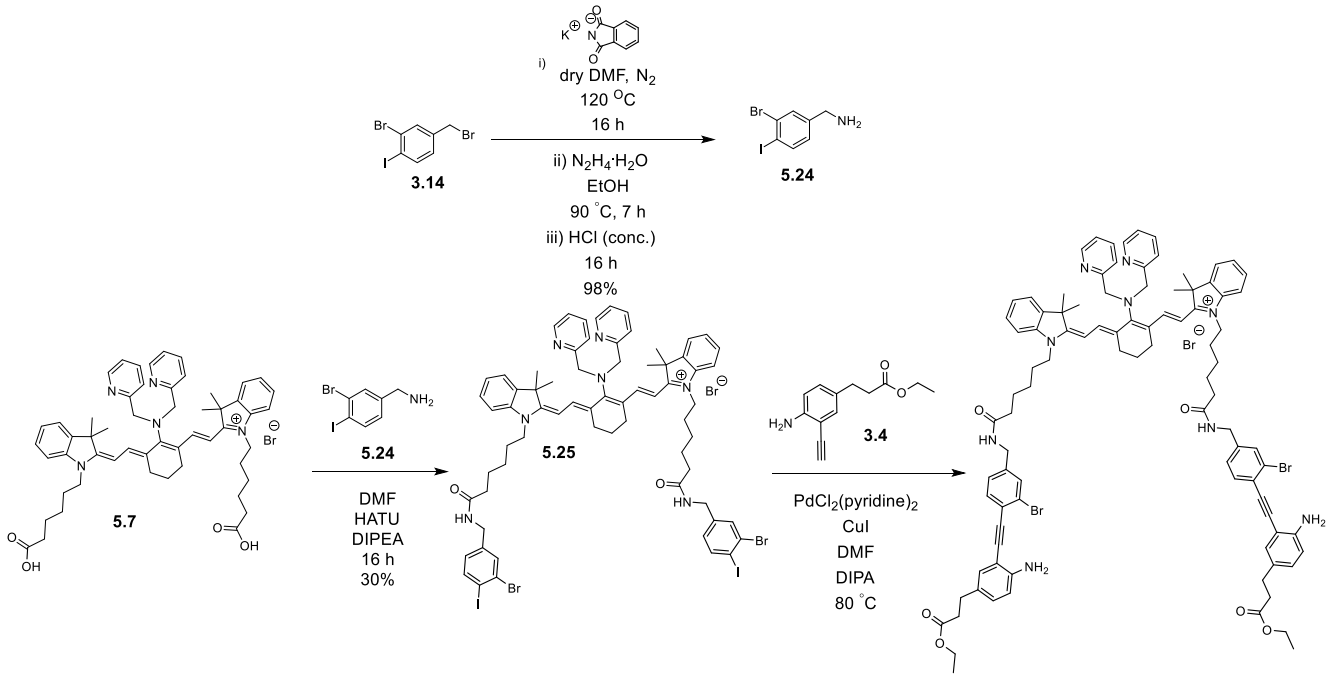
functionalised cyanine dye **5.10** – the bromide was converted to a phthalimide and then reduced to the primary amine **5.24** using hydrazine hydrate (**Scheme 5.11**). Unfortunately, attempts to couple this compound to **5.23** using both HBTU and HATU were unsuccessful, resulting only in degradation of the cyanine.

5.2.2.5 Towards Targeted Fluorescence Imaging Probes

Due to difficulties encountered in synthetic chemistry involving the metal complexes, it was decided to attempt the introduction of the targeting group first, in case the presence of charged metal chelates were interfering with subsequent amide coupling processes.

Compounds **5.7** and **5.24** could be successfully coupled using HATU. As has been discussed above, there were issues controlling the extent of reaction on the carboxylic acid arms – despite just one equivalent of **5.24** being added, all that could be isolated was the disubstituted compound **5.25** at a moderate yield of 30%, alongside some unreacted starting material. It was decided that this could be carried forward to produce a cyanine dye with two targeting moieties. Hypothetically, the aromatic propionic acid group (compound **3.4**) which forms the basis of the targeting group could then be introduced *via* a Sonogashira coupling to begin the development of a targeted probe. Unfortunately, this coupling reaction could not be carried out due to time constraints. **Scheme 5.11** summarises the work towards the introduction of some targeting ability to cyanine dyes.

Future work could explore alternatives to the gold-catalysed indole formation reaction, as it the previously utilised conditions may be incompatible with the sensitive cyanine dye framework. Should these be found, it is hoped that the GPR-40 targeting group could be introduced to the cyanine dye alone and dual-modal probes incorporating metal chelates for a range of imaging modalities. What may be most successful for this route is the initial synthesis of the targeting moiety prior to coupling to the cyanine framework, which avoids the use of a gold catalyst in the presence of the conjugated backbone which may trigger degradation. This would have been carried out if not for time constraints.



Scheme 5.11: Synthetic work towards targeted cyanine dye derivatives and the proposed future Sonogashira reaction towards introducing a targeting moiety.

5.3. Conclusions and Outlook

In summation, a substantial body of work has been dedicated to the synthesis of a family of heptamethine cyanine dye compounds and the exploration of how each iteration and modification has impacted on the properties of these derivatives, notably their photophysical behaviour in the NIR window, which is of increasing interest in the optical imaging field.

Previous work within the Long group, as discussed earlier in this thesis, coupled with concerns about the selectivity of DPA for Zn^{2+} over other endogenous metal ions, directed the initial direction of the syntheses described in this Chapter. Following successful work by Nolan *et al.* where thiophene moieties were incorporated into fluorescent, zinc-sensing probes and utilised to monitor zinc(II) flow *in vivo*[56,58,59], a family of three heptamethine dyes based on the NIR emissive compound IR-808[37] were synthesised to study the effect of substituting pyridine rings for thiophenes. Replacing a pyridine ring with a thiophene was found to shift the emission wavelength of cyanines further into the NIR, although these novel compounds appeared to have a much lower affinity for zinc(II) ions. Whilst it was disappointing to see that only the DPA sensing unit resulted in a notable change in fluorescence emission intensity in the presence of Zn^{2+}, hence its application throughout the rest of this Chapter, future work could involve the use of other NIR fluorophores and thiophene-based zinc sensing units to synthesise highly selective fluorescent zinc sensors which exploit the advantages of this critical window in the electromagnetic spectrum. Other practical work in this area could explore the selectivity of these different moieties – there is evidence in the literature to suggest that thiophene units confer greater bias towards Zn^{2+} over other metal centres, and this should be confirmed through further metal binding

titrations. Additionally, due to concerns about possible interactions between the carboxylic acid arms of these dyes and Zn^{2+}, the esterification of the dye precursor could be carried out prior to synthesis and subsequent metal binding titrations.

The benefits of dual-modality in molecular imaging are now widely known. It was hypothesised that a bimodal PET-fluorescent imaging agent coupled with the ability to respond quantitatively to the presence of zinc(II) ions would be a worthwhile addition to the field of imaging pancreatic β-cells. Two fluorinated cyanine dyes were synthesised to act as cold analogues of the corresponding ^{18}F-labelled PET emitters which could be used as an imaging agent. The tosylate precursors of these two compounds were also produced, all at satisfactory yields, although these syntheses could be further optimised. One of these compounds, the di-fluorinated analogue, was shown to exhibit an increase in fluorescence emission intensity in the presence of between 0.8 and 5.0 equivalents of Zn(II). Whilst this was by no means ratiometric and no clear trend could be observed, this could suggest an interaction between the probe and Zn^{2+} which could be harnessed to give a qualitative indication of the presence of these ions. The lack of any clear trend could be due to the unique behaviour of cyanine dyes and other conjugated systems in solution, and this should be investigated in future work through the use of alternative, less polar solvents. Additionally, the selectivity of this probe should be studied using an analogous procedure to that exploring the affinity of different zinc-sensing moieties.

Radiolabelling of the tosylate compounds to give the hot analogues of the di-fluorinated cyanine dyes was attempted, although this could not be carried out successfully. Degradation of the di-tosylate was observed at all temperatures, even as low as 25 °C. It is possible that this was due to an attack on the conjugated, unsaturated cyanine backbone by the naked fluoride anion, a powerful nucleophile, although recent work used a similar heptamethine compound which could be successfully radiolabelled through the hydrolysis of a boronate ester by $^{18}F^-$ [76]. Another potential reason for the failure is acidity of its hexanoic acid arms, which contained an amide bond and a CH_2 group at an α position to a carbonyl. Deprotonation at these positions could have occurred and led to subsequent decomposition of the cyanine. Future work in this area would involve a synthetic re-design: perhaps by using shorter carboxylic acid arms analogous to those employed by Ting *et al*. in their cyanine radiolabelling[76]. The long carbon chain had originally been chosen to distance the leaving group from the unsaturated system due to concerns about possible fluoride attack there during the radiolabelling process. Reducing the length of this chain could increase steric hindrance around the acidic protons and make them less accessible to the extremely basic fluoride anion. Future work could explore this systematically and establish whether there is in fact an optimal chain length for these compounds which could in fact reduce their sensitivity. That would subsequently enable a family of fluorinated cyanine dyes to be produced and investigated to assess their suitability for application as dual-modal imaging agents.

It has been observed that the presence of cyclodextrin species can help shield cyanine dyes from the approach of ROS[85]. It is possible that aggregation of other widely used and highly stable cyanines such as IR-808 and ICG in solution may have a similar effect. In comparison, **5.18** may not aggregate well in solution and could therefore be more exposed to ROS. It may be that modification to try and coax the system into more effective aggregation could improve stability. This could be achieved by the extension of the aromatic system, which could invoke additional π-stacking and may explain the enhanced stability of ICG and its derivatives. Furthermore, a recent study by Hernandez *et al*. reported that degradation of cyanine dyes during the radiolabelling process was due to the generation of ROS from water by isotopes such as ^{68}Ga, ^{111}In and ^{213}Bi[86]. Re-attempting the radiolabelling procedures here with a radical scavenger present may help improve the results.

Attempts were made to introduce macrocyclic metal chelating units which could allow incorporation of the highly paramagnetic Gd^{3+}, ubiquitous amongst MRI contrast agents, or cold metal centres such as copper or zirconium which have positron-emitting radioisotopes. Furthermore, it was hoped that a targeting moiety could be added to these compounds. Despite successful synthesis of a cyanine-copper chelate, this could not be achieved with gadolinium and no targeting moiety could be successfully built on to this conjugate or the parent cyanine framework. The sensitive nature of the cyanine itself could have been degraded due to the use of some of the metal catalysts needed to synthesise the targeting group, and future work in this area could focus on sidestepping these and avoiding damage to the sensitive core of these molecules.

Overall, the cyanine dye framework based on IR-808 has been shown to be extremely versatile. Introducing and adopting thiophene based zinc-sensing units was shown to push the emission of the cyanine unit further into the NIR, a strategy which could be adapted in future. In addition, tosylated and fluorinated analogues which could act as dual modal imaging agents and their precursors which, despite problems during the radiolabelling process, could be modified to try and reduce sensitivity of the dye. Attempts were made to synthesise a targeted cyanine dye, which would aid favourable biodistribution, although again the sensitivity of the conjugated system hindered this work. Shorter cyanine dyes, such as pentamethine compounds, may well be more robust but emit in the visible, rather than NIR region, which presents problems in biological systems. However, it could be that the addition of thiophene rings could modify the emissive properties of these dyes to more useful wavelengths. Additionally, there could be systematic approaches employed to try and reduce the sensitivity of the heptamethine compounds to the conditions involved in the synthetic routes discussed in this Chapter, or by modifying these pathways to account for the fragile nature of the dyes.

5.4. References

1 K. Umezawa, D. Citterio and K. Suzuki, *Anal. Sci.*, 2014, 30, 327–349.

2 Z. Guo, S. Park, J. Yoon and I. Shin, *Chem. Soc. Rev.*, 2014, 43, 16–29.

3 T. Xia, N. Li and X. Fang, *Annu. Rev. Phys. Chem.*, 2013, **64**, 459–480.

4 J. Luo, W. S. Li, P. Xu, L. Y. Zhang and Z. N. Chen, *Inorg. Chem.*, 2012, **51**, 9508–9516.

5 J. R. Johnson, N. Fu, E. Arunkumar, W. M. Leevy, S. T. Gammon, D. Piwnica-Worms and B. D. Smith, *Angew. Chemie Int. Ed.*, 2007, **46**, 5528–5531.

6 A. Mishra, R. K. Behera, P. K. Behera, B. K. Mishra and G. B. Behera, *Chem. Rev.*, 2000, **100**, 1973–2011.

7 K. L. Haas and K. J. Franz, *Chem. Rev.*, 2009, **109**, 4921–4960.

8 P. Carol, S. Sreejith and A. Ajayaghosh, *Chem. – An Asian J.*, 2007, **2**, 338–348.

9 N. C. Lim, H. C. Freake and C. Brückner, *Chem. - A Eur. J.*, 2005, **11**, 38–49.

10 K. Hanaoka, K. Kikuchi, H. Kojima, Y. Urano and T. Nagano, *J. Am. Chem. Soc.*, 2004, **126**, 12470–12476.

11 G. K. Walkup, S. C. Burdette, S. J. Lippard and R. Y. Tsien, *J. Am. Chem. Soc.*, 2000, 122, 5644–5645.

12 M. A. Zoroddu, J. Aaseth, G. Crisponi, S. Medici, M. Peana and V. M. Nurchi, *J. Inorg. Biochem.*, 2019, 195, 120–129.

13 J. Rungby, *Diabetologia*, 2010, 53, 1549–1551.

14 C. G. Taylor, in *BioMetals*, 2005, vol. 18, pp. 305–312.

15 M. J. Salgueiro, N. Krebs, M. B. Zubillaga, R. Weill, E. Postaire, A. E. Lysionek, R. A. Caro, T. De Paoli, A. Hager and J. Boccio, *Biol. Trace Elem. Res.*, 2001, **81**, 215–228.

16 J. Jansen, W. Karges and L. Rink, *J. Nutr. Biochem.*, 2009.

17 K. Kikuchi, K. Komatsu and T. Nagano, *Curr. Opin. Chem. Biol.*, 2004, **8**, 182–191.

18 E. V Antina, N. A. Bumagina, A. I. V'yugin and A. V Solomonov, *Dye. Pigment.*, 2017, **136**, 368–381.

19 G. J. Stasiuk, F. Minuzzi, M. Sae-Heng, C. Rivas, H. Juretschke, L. Piemonti, P. R. Allegrini, D. Laurent, A. R. Duckworth, A. Beeby, G. A. Rutter and N. J. Long, *Chem. – A Eur. J.*, 2015, **21**, 5023–5033.

20 P. Jiang and Z. Guo, *Coord. Chem. Rev.*, 2004, 248, 205–229.

21 R. J. Radford and S. J. Lippard, *Curr. Opin. Chem. Biol.*, 2013, 17, 129–136.

22 M. Ogawa, N. Kosaka, P. L. Choyke and H. Kobayashi, *Cancer Res.*, 2009, **69**, 1268–1272.

23 X. Chen, X. Peng, A. Cui, B. Wang, L. Wang and R. Zhang, *J. Photochem. Photobiol. A Chem.*, 2006, **181**, 79–85.

24 M. Henary and M. Mojzych, in *Heterocyclic Polymethine Dyes*, Springer Berlin Heidelberg, 2008, pp. 221–238.

25 A. N. Bashkatov, E. A. Genina, V. I. Kochubey and V. V Tuchin, *J. Phys. D Appl. Phys*, 2005, **38**, 2543–2555.

26 R. J. Gillies, *J. Cell. Biochem.*, 2002, **87**, 231–238.

27 K. Licha, Springer, Berlin, Heidelberg, 2002, pp. 1–29.

28 F. Jobsis, *Science (80-.).*, 1977, **198**, 1264–1267.

29 V. E. Shershov, M. A. Spitsyn, V. E. Kuznetsova, E. N. Timofeev, O. A. Ivashkina, I. S. Abramov, T. V. Nasedkina, A. S. Zasedatelev and A. V. Chudinov, *Dye. Pigment.*, 2013, **97**, 353–360.

30 S. G. Sakka, *Curr. Opin. Crit. Care*, 2007, **13**, 207–214.

31 N. Kokudo and T. Ishizawa, *Liver Cancer*, 2012, **1**, 15–21.

32 T. L. Dost, M. T. Gressel and M. Henary, *Anal. Chem. Insights*, 2017, **12**, 1–6.

33 S. Weiss, *Science (80-.).*, 1999, 283, 1676–1683.

34 C. Chen, B. Zhou, D. Lu and G. Xu, *J. Photochem. Photobiol. A Chem.*, 1995, **89**, 25–29.

35 L. Strekowski, M. Lipowska and G. Patonay, *J. Org. Chem.*, 1992, 57, 4578–4580.

36 F. Song, X. Peng, E. Lu, R. Zhang, X. Chen and B. Song, *J. Photochem. Photobiol. A Chem.*, 2004, **168**, 53–57.

37 S. Luo, X. Tan, Q. Qi, Q. Guo, X. Ran, L. Zhang, E. Zhang, Y. Liang, L. Weng, H. Zheng, T. Cheng, Y. Su and C. Shi, *Biomaterials*, 2013, **34**, 2244–2251.

38 K. D. Kröncke, *Arch. Biochem. Biophys.*, 2007, 463, 183–187.

39 H. Haase, S. Hebel, G. Engelhardt and L. Rink, *Metallomics*, 2015, **7**, 97–106.

40 Z. Xu, J. Yoon and D. R. Spring, *Chem. Soc. Rev.*, 2010, **39**, 1996–2006.

41 A. P. De Silva, H. Q. N. Gunaratne, T. Gunnlaugsson, A. J. M. Huxley, C. P. McCoy, J. T. Rademacher and T. E. Rice, *Chem. Rev.*, 1997, **97**, 1515–1566.

42 N. C. Lim, L. Yao, H. C. Freake and C. Brückner, *Bioorganic Med. Chem. Lett.*, 2003, **13**, 2251–2254.

43 X. Yang, L. Shen, H. Bao, X. Fang, J. Xu, Y. Zhao and W. Yang, *Sensors Actuators, B Chem.*, 2015, **220**, 1361–1367.

44 B. Tang, H. Huang, K. Xu, L. Tong, G. Yang, X. Liu and L. An, *Chem. Commun.*, 2006, 3609–3611.

45 L. M. T. Canzoniero, S. L. Sensi and D. W. Choi, *Neurobiol. Dis.*, 1997, **4**, 275–279.

46 R. P. Haugland, *Methods Mol Biol*, 2002, 966.

47 C. J. Chang, J. Jaworski, E. M. Nolan, M. Sheng and S. J. Lippard, *Proc. Natl. Acad. Sci. U. S. A.*, 2004, **101**, 1129–1134.

48 K. Hanaoka, Y. Muramatsu, Y. Urano, T. Terai and T. Nagano, *Chem. - A Eur. J.*, 2010, **16**, 568–572.

49 A. Ojida, H. Nonaka, Y. Miyahara, S. Tamaru, K. Sada and I. Hamachi, *Angew. Chemie Int. Ed.*, 2006, **45**, 5518–5521.

50 L. Frullano and T. J. Meade, *J. Biol. Inorg. Chem.*, 2007, 12, 939–949.

51 L. E. Jennings and N. J. Long, *Chem. Commun.*, 2009, 0, 3511–3524.

52 V. S. R. Harrison, C. E. Carney, K. W. MacRenaris, E. A. Waters and T. J. Meade, *J. Am. Chem. Soc.*, 2015, **137**, 9108–9116.

53 C. Brand, D. Abdel-Atti, Y. Zhang, S. Carlin, S. M. Clardy, E. J. Keliher, W. A. Weber, J. S. Lewis and T. Reiner, *Bioconjugate Chem*, 2014, **25**, 1323–1330.

54 A. C. Esqueda, J. A. López, G. Andreu-de-Riquer, J. C. Alvarado-Monzón, J. Ratnakar, A. J. M. Lubag, A. D. Sherry and L. M. De León-Rodríguez, *J. Am. Chem. Soc.*, 2009, **131**, 11387.

55 L. De Leon-Rodriguez, A. Josue, M. Lubag and A. D. Sherry, *Inorganica Chim. Acta*, 2012, **393**, 12–23.

56 E. M. Nolan and S. J. Lippard, *Inorg. Chem.*, 2004, **43**, 8310–8317.

57 D. Laurent, L. Vinet, S. Lamprianou, M. Daval, G. Filhoulaud, A. Ktorza, H. Wang, S. Sewing, H. -P Juretschke, H. Glombik, P. Meda, R. Boisgard, D. L. Nguyen, G. J. Stasiuk, N. J. Long, X. Montet, P. Hecht, W. Kramer, G. A. Rutter and J. Hecksher-Sørensen, *Diabetes, Obes. Metab.*, 2016, **18**, 6–15.

58 E. M. Nolan, J. W. Ryu, J. Jaworski, R. P. Feazell, M. Sheng and S. J. Lippard, *J. Am. Chem. Soc.*, 2006, **128**, 15517–15528.

59 E. M. Nolan and S. J. Lippard, *Acc. Chem. Res.*, 2009, **42**, 193–203.

60 J. Lee, H. Kim and M. J. Park, *Chem. Mater.*, 2016, **28**, 2408–2416.

61 J. V Frangioni, *Curr. Opin. Chem. Biol.*, 2003, **7**, 626–634.

62 J. Zhang, Michigan Technological University, 2015.

63 S. Zhang, R. Adhikari, M. Fang, N. Dorh, C. Li, M. Jaishi, J. Zhang, A. Tiwari, R. Pati, F.-T. Luo and H. Liu, *ACS Sensors*, 2016, **1**, 1408–1415.

64 U. Werner, G. Haschke, A. W. Herling and W. Kramer, *Regul. Pept.*, 2010, **164**, 58–64.

65 O. Eriksson, M. Laughlin, M. Brom, P. Nuutila, M. Roden, A. Hwa, R. Bonadonna and M. Gotthardt, *Diabetologia*, 2016, **59**, 1340–1349.

66 C. Rivas, G. J. Stasiuk, J. Gallo, F. Minuzzi, G. A. Rutter and N. J. Long, *Inorg. Chem.*, 2013, **52**, 14284–14293.

67 B. E. Schaafsma, J. S. D. Mieog, M. Hutteman, J. R. van der Vorst, P. J. K. Kuppen, C. W. G. M. Löwik, J. V. Frangioni, C. J. H. van de Velde and A. L. Vahrmeijer, *J. Surg. Oncol.*, 2011, **104**, 323–332.

68 S. L. Gibbs, *Quant. Imaging Med. Surg.*, 2012, **2**, 177–17787.

69 S. Keereweer, J. D. F. Kerrebijn, P. B. A. A. Van Driel, B. Xie, E. L. Kaijzel, T. J. A. Snoeks, I. Que, M. Hutteman, J. R. Van Der Vorst, J. S. D. Mieog, A. L. Vahrmeijer, C. J. H. Van De Velde, R. J. Baatenburg De Jong and C. W. G. M. Löwik, *Mol. Imaging Biol.*, 2011, 13, 199–207.

70 P. W. Miller, N. J. Long, R. Vilar and A. D. Gee, *Angew Chem Int Ed*, 2008, **47**, 8998–9003.

71 C. Ramogida and C. Orvig, *Chem. Commun.*, 2013, **49**, 4720–4739.

72 G. A. Rutter, T. J. Pullen, D. J. Hodson and A. Martinez-Sanchez, *Biochem. J.*, 2015, 466, 203–218.

73 R. Hernandez, S. A. Graves, T. Gregg, H. R. VanDeusen, R. J. Fenske, H. N. Wienkes, C. G. Engl, H. F. Valdovinos, J. J. Jeffery, T. E. Barnhart, G. W. Severin, R. J. Nickles, M. E. Kimple, M. J. Merrins and W. Cai, *Diabetes*, 2017, **66**, 2163–2174.

74 G.-L. Law and W.-T. Wong, in *The Chemistry of Molecular Imaging*, eds. N. J. Long and W.-T. Wong, John Wiley & Sons, Hoboken, U.S.A., 2015, pp. 1–24.

75 D. Roeda and F. Dollé, in *The Chemistry of Molecular Imaging*, eds. N. J. Long and W.-T. Wong, John Wiley & Sons, Ltd, Hoboken, U.S.A., 2015, pp. 55–78.

76 R. Ting, T. A. Aguilera, J. L. Crisp, D. J. Hall, W. C. Eckelman, D. R. Vera and R. Y. Tsien, *Bioconjug. Chem.*, 2010, **21**, 1811–1819.

77 T. W. Price, G. Firth, C. J. Eling, M. Kinnon, N. J. Long, J. Sturge and G. J. Stasiuk, *Chem. Commun.*, 2018, **54**, 3227–3230.

78 A. Haslop, L. Wells, A. Gee, C. Plisson and N. Long, *Mol. Pharm.*, 2014, **11**, 3818–3822.

79 M. Constantinou, F. I. Aigbirhio, R. G. Smith, C. A. Ramsden and V. W. Pike, *J. Am. Chem. Soc.*, 2001, 123, 1780–1781.

80 W. Jiang, Q. Fu, H. Fan and W. Wang, *Chem. Commun.*, 2008, **0**, 259–261.

81 Z. Guo, G. H. Kim, J. Yoon and I. Shin, *Nat. Protoc.*, 2014, **9**, 1245–1254.

82 K. Kiyose, H. Kojima, Y. Urano and T. Nagano, *J. Am. Chem. Soc.*, 2006, **128**, 6548–6549.

83 A. Louie, *Chem. Rev.*, 2010, **110**, 3146–3195.

84 D. O. Yoon, X. Zhao, D. Son, J. T. Han, J. Yun, D. Shin and H. J. Park, *ACS Med. Chem. Lett.*, 2017, **8**, 1336–1340.

85 R. Guether and M. V. Reddington, *Tetrahedron Lett.*, 1997, **38**, 6167–6170.

86 R. Hernandez, S. Heskamp, M. Rijpkema, D. L. Bos, D. M. Goldenberg, W. J. Mcbride, A. Morgenstern, F. Bruchertseifer, W. Cai and O. C. Boerman, *Theranostics*, 2017, **7**, 1–8.

Chapter 6

Conclusions and Outlook

6.1. General Comments

The work described in this thesis explores a wide variety of concepts critical to the design of molecular imaging probes. Primarily, the focus has been on the synthesis and testing, both *in vitro* and *in vivo* of compounds targeted to pancreatic β-cells. Two different approaches were employed: the use of the peptide exendin-4, a ligand for the receptor GLP-1R, and a chelator incorporating an indole propionic acid moiety designed to have a high affinity for the receptor GPR40. Both families of probes synthesised using these two chelators had their properties extensively explored, with this discussed in further detail below. Exendin-4 has been shown to be an effective therapeutic agent for diabetes treatment, and there is currently great interest in the field around the investigation of the mechanisms involved in receptor binding, including conformational receptor changes and endocytosis, and how this could affect the physiological processes involved in diabetes[1–3]. A series of analogues of exendin-4 were conjugated to luminescent optical probes to investigate the process involved in receptor binding and membrane localisation.

The development of dual-modal imaging agents is of substantial interest in the field due to its ability to combine the strengths of myriad imaging techniques. A significant body of work discussed in this thesis dealt with the synthesis of compounds designed to be utilised for dual-modal imaging. Many of these agents also included the ability to respond selectively to Zn^{2+} ions, which could enable visualisation of β-cell functionality through non-invasive imaging techniques.

The successes achieved with each of these objectives in mind is discussed below, with reflections on the methodology and consideration of possible future pathways for this project.

6.2. MRI Contrast Agents Targeting GLP-1R

The functionalisation of the peptide exendin-4 was achieved through its conjugation to a chelator based on the macrocycle H_4dota. The resulting ligand was complexed to the highly paramagnetic Gd^{3+} to form the MRI contrast agent **GdEx**. This probe was found to have a high relaxivity value of 6.1 $mM^{-1}s^{-1}$, which is greater than that of the ubiquitous $[Gd(dota)]^-$. Analysis of **GdEx** *in vivo* showed that the probe localised in the pancreas of healthy mice, indicative of successful targeting of the pancreas *via* the exendin unit and its high potency for the GLP-1R receptor. The contrast to noise ratio observed in the pancreases of mice administered with **GdEx** was compared to those scanned with $[Gd(dota)]^-$ as the contrast agent. It was found that use of **GdEx** resulted in a 40% increase in CNR over that seen with $[Gd(dota)]^-$, up to a maximum of 70% over baseline levels.

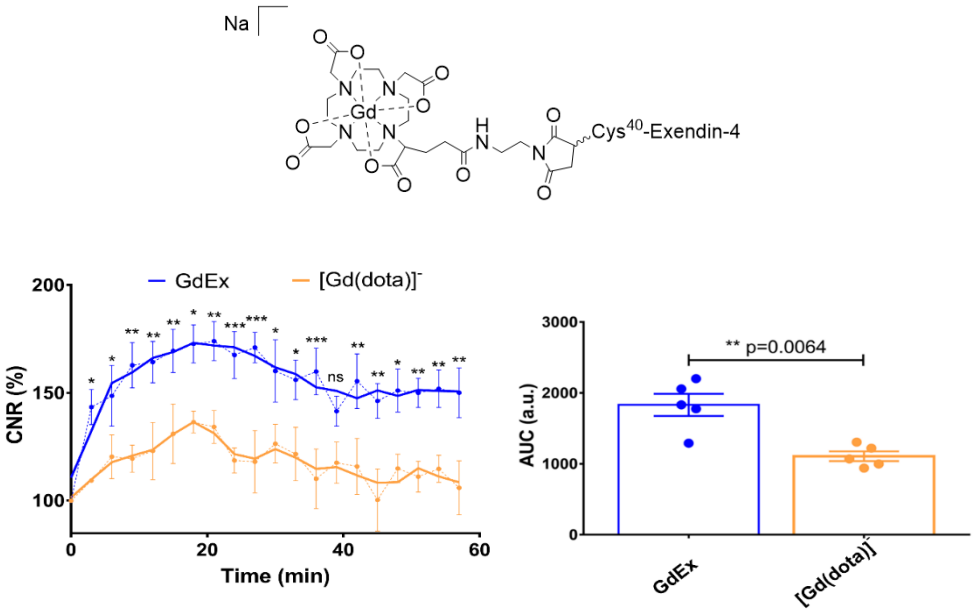


Figure 6.1: Structure of **GdEx** (top) and the observed CNR compared to that seen in C57BL/6J WT mice (bottom).

Following validation that **GdEx** could successfully be utilised to give pancreas-specific contrast enhancement and that the incorporation of exendin-4 into a bifunctional chelator did not negatively impact on the affinity of the probe for GLP-1R, it was decided to assess its ability to give a quantitative assessment of functional β-cell mass in a disease model. The model of choice was referred to as Dicer-KO. DICER is an RNAseIII enzyme which is required in the production of miRNA critical to the development of β-cells. The deletion of this enzyme can be induced by injection of tamoxifen and has been shown to reduce β-cell mass and trigger hypoglycaemia[4,5]. **GdEx** was administered to these mice and a control group which were also injected with tamoxifen but did not undergo the DICER deletion (Dicer-Ctrl). The resulting CNR values showed that there was statistically significant retention of the probe in the pancreases of the Dicer-Ctrl mice compared to the Dicer-KO mice, therefore suggesting that **GdEx** is capable of delineating individuals where decline of β-cell mass has taken place. This could potentially act as an early warning system for the beginnings of diabetes mellitus development, as well as contributing towards the debate in the literature around the extent to which β-cell mass decline contributes to manifestation of the disease.

One limitation of **GdEx** is that a substantial quantity of the probe is required for imaging. Although **GdEx** may be administered at half the clinical concentration of $[Gd(dota)]^-$ - 0.05 $mmolkg^{-1}$ compared to 0.1 $mmolkg^{-1}$ – the large molecular weight of the compound means that as much as 20 g would be required for an MRI scan in an average adult human, which is a concern as exenatide has been shown to result in nausea and vomiting in clinical trials even at the μgkg^{-1} scale[6,7]. Whilst this would limit any clinical translation of **GdEx**, this work has shown that the development of pancreas-specific GBCAs is possible and could enable alternative probes targeted to this vital organ to be produced: this would avoid

exposure of patients to ionising radiation and avoid some of the complex synthetic challenges associated with radiochemistry.

Future work in this area could explore alterations to the bioconjugation strategy employed through different peptides or other compounds with a high affinity for pancreatic β-cells. Furthermore, other receptors could be targeted: consider the focus on GPR40 discussed in Chapter 3 of this thesis. Alternative diabetes models could also be explored.

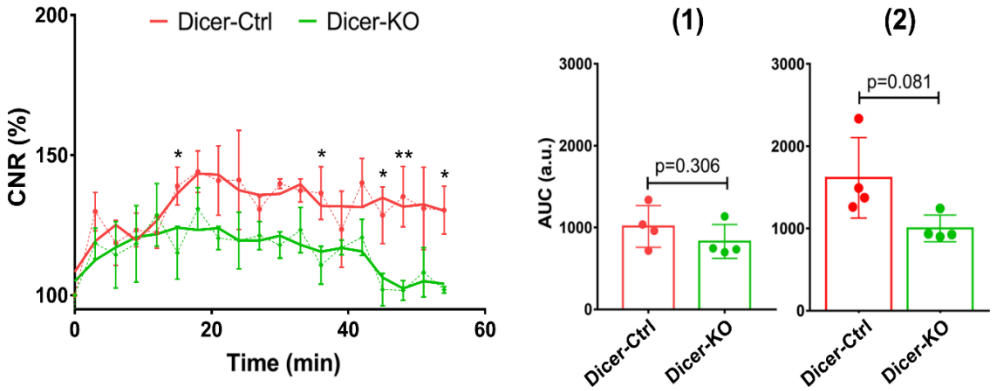


Figure 6.2: CNR values in Dicer-Ctrl and Dicer-KO mice, showing enhanced CNR after 21 minutes post injection (2), therefore suggesting retention of **GdEx** in the pancreas.

The success had with **GdEx** inspired the design of an additional probe, **GdZn**. This compound was extremely similar in structure to **GdEx**, but incorporated the amine DPA as a zinc-sensing unit. Zn^{2+} is found in high concentrations in the pancreas, where it helps to stabilise insulin storage as hexameric units, and the design of zinc-sensing MRI contrast agents has been carried out by many in the field seeking to monitor pancreatic β-cell function[8–11]. The synthesis of **GdZn** was successful and the probe was tested *in vivo* to examine its specificity and efficacy. The results, from two healthy, WT mice, were disappointing, with no visible uptake from the pancreas. It appeared that the probe failed to leave the bloodstream, which was attributed to possible formation of a ternary complex with serum albumin proteins and Zn^{2+}. Indeed, the extensive work published by the Sherry group indicates that this interaction is essential for an increase in CNR to be observed, as it results in an increase in τ_R and therefore in relaxivity[9–11].

There is the potential to modify and optimise this probe to enable some receptor binding to take place: this could be done through alternative zinc-sensing groups.

6.3. Lanthanide(III) Complexes of a Ligand Targeted to GPR40

The large quantities necessary for successful MRI scans using peptide-targeted GBCAs, coupled with their high cost and synthetic limitations drove an interest in the use of alternative targeting strategies. Given that GLP-1R agonists are typically peptides and the field is dominated by exendin-4 and its analogues, it was decided to look for an alternative receptor which could aid the delivery of compounds

to pancreatic β-cells. One such receptor was GPR40, a fairly recently discovered receptor found to be enriched in β-cells to a greater degree than GLP-1R, as well as being present in the brain and the ileum of the small intestine[12–16]. Several agonists for this receptor reached clinical trials for the treatment of diabetes, and an analysis of these compounds, combined with a recent SAR study by Yoon *et al*. revealed that GPR40 could be activated by indole rings functionalised with propionic acid arms and polar aryl substituents[16–19].

A relatively simple ligand system based on the macrocycle H_3do3a was designed which incorporated GPR40 targeting capability. This ligand, shown below, was synthesised at an overall yield of 5%.

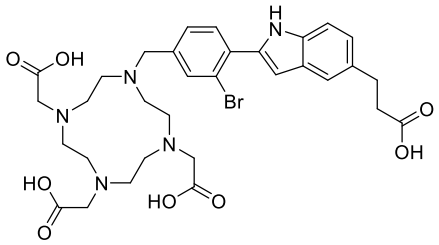


Figure 6.3: The structure of the target ligand, **GPR-L1**.

The gadolinium(III) complex of this ligand was considered an interesting alternative to **GdEx** due to its similar potential application as an MRI contrast agent. Comparisons could be drawn between the two compounds on the efficacy of each targeting methodology, enabling conclusions to be drawn about the most appropriate receptor to target with β-cell specific probes. The relaxivity of **[Gd(GPR-L1)]** was calculated as 9.22 $M^{-1}s^{-1}$. This value is substantially higher than that of **GdEx**, likely due to the heptadentate nature of the ligand enabling a greater hydration state and could potentially require a lower concentration of **[Gd(GPR-L1)]** to be used *in vivo*. Coupled with the much lower molecular weight, less than a fifth of that of **GdEx**, it is likely that clinical applications of **[Gd(GPR-L1)]** would require a much lower quantity of compound and therefore potentially avoid toxicity issues associated with high or repeated administrations of GBCAs such as NSF.

It was discovered that the aromatic targeting moiety of **GPR-L1** was fluorescent, with excitation of the free ligand at 366 nm resulting in emission at 484 nm. It was hypothesised that this property of the ligand could be used to assess the affinity of the probe for GPR40 *via in vitro* optical imaging. The gadolinium(III) complex was found to emit at 430 nm when excited at 326 nm. Through *in vitro* examination, it was established that the indole propanoic acid group determined by Yoon *et al*. could successfully enable binding to GPR40 and offered proof of the potency of this indole group, as well as paving the way for further β-cell imaging probes incorporating this motif.

Given that the photophysical properties of this ligand system, it was decided to assess its suitability for sensitisation of the luminescence of two lanthanide(III) ions: terbium(III) and europium(III). These two metal ions have found widespread use in the field of optical imaging. The complexes that **GPR-L1**

formed with these two metal centres could be excited at 391 nm and 323 nm respectively, which successfully resulted in sensitisation of phosphorescence from the metal centres. This could be seen from their time-gated emission spectra (**Figure 6.4**). Although the lanthanide(III)-based emission from both of these complexes is likely too weak to enable clinical applications, it was hypothesised that the lifetimes of the excited states within the system could be utilised to calculate the hydration states of the complexes and validate the relaxivity value obtained for [Gd(GPR-L1)].

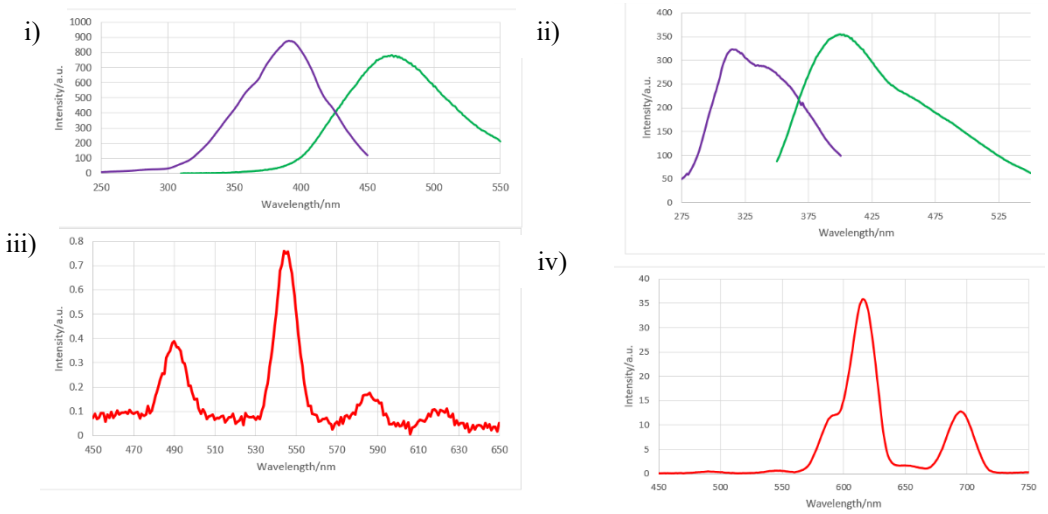


Figure 6.4: Top: Fluorescence spectra of i) **[Tb(GPR-L1)]** and ii) **[Eu(GPR-L1)]**, bottom: phosphorescence spectra of iii) **[Tb(GPR-L1)]** and iv) **[Eu(GPR-L1)]**.

The luminescence lifetime data which was acquired from these two complexes was somewhat confusing and unfortunately did not provide any clear validation of the hydration state of the Gd(III) complex, knowledge of which would be critical to its deployment as an MRI contrast agent. The hydration state calculated for the Eu(III) complex was 0.32, and no value could be reliably calculated for the Tb(III) complex. This is quite dramatically different from the expected value of 2, based on the denticity of **GPR-L1** and the relaxivity value of the Gd(III) complex. There was an increase in the calculated value of q for both species when degassed solvents were used – this was potentially indicative of some degree of excited state quenching by O_2, which should be investigated in any future studies. Variation in solvent polarity and oxygen solubility could also be carried out to ensure accurate data. However, the discrepancy in expected results could be due to weak Ln(III) sensitisation from the ligands. Additionally, other factors may be involved in the high relaxivity of the Gd(III) complex, including rotational correlation time.

There were substantial differences in the rates of formation of each of the complexes made using **GPR-L1**, with the Gd(III), Tb(III) and Eu(III) complexes requiring reaction times of 2, 3.5 and 11 days respectively. These vastly different kinetics may originate from some different properties of the Ln^{3+} ions themselves, the salts used as their source, solvent conditions, temperature and pH variations. An

extensive, systematic investigation into these factors, as well as forming complexes of the rest of the lanthanide series, could be carried out to establish the reason for this variation.

In addition to *in vitro* confirmation, the ability of complexes of **GPR-L1** to target pancreatic β-cells should be examined through thorough *in vivo* analysis. This could be done using the same WT/Dicer-Ctrl/Dicer-KO model employed to study the biodistribution properties of **GdEx** and would enable direct comparisons to be made between the two compounds. If successful, the versatility of the macrocyclic chelating unit of **GPR-L1** could be harnessed through complexation to a variety of metal ions. Manganese has garnered attention as a potential metal for use in MRI contrast agents, macrocyclic chelators for radioactive indium and yttrium isotopes could be utilised in SPECT or radiotherapy, perhaps for insulinoma treatment.

As with **GdEx**, there could certainly be scope to synthesise analogues of **GPR-L1** which are capable of sensing Zn^{2+} ions. This could be achieved through the development of ligand systems based on H_2do2a, which would enable a zinc-binding unit and the GPR40 targeting moiety to be incorporated. Furthermore, modifications to the ligand to increase ligand denticity and improve complex stability could also be pursued. Some of these possible future target compounds are shown below.

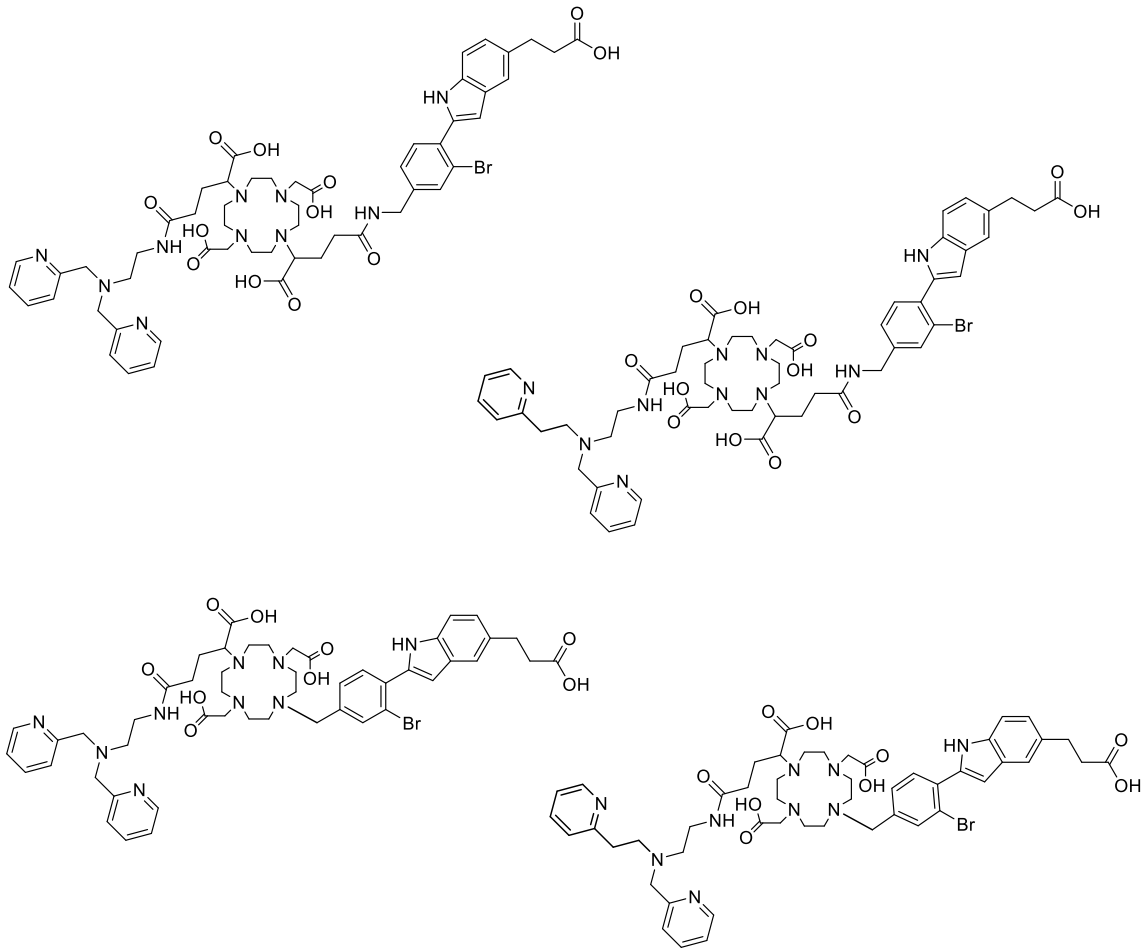


Figure 6.5: Possible future synthetic targets based on the GPR40 targeting group which was built into **GPR-L1** with additions designed to sense Zn^{2+} ions and enhance denticity to ensure more stable complex formation.

6.4. Exploration of Agonist Binding in GLP-1R

GLP-1R is a class B G-protein coupled receptor (GPCR)[20–23]. Its stimulation has been shown to result in an increase in insulin secretion and enhancement of β-cell proliferation which has led to great interest in the application of GLP-1R agonists as therapeutic agents for the treatment of diabetes[24–29]. Incorporation of GLP-1R agonists as targeting moieties is widespread in the field, as mentioned in Chapter 2 alongside the discussion of **GdEx**. However, there is limited understanding of the events which take place at the cellular level after agonist binding, with conflicting evidence around the relationship between agonist binding, receptor conformational change and internalisation and subsequent insulin production and release[1,3,30]. Exploration of these processes, and of the impact of ligand modification on receptor affinity and membrane localisation could aid the development of therapeutic agents for diabetes mellitus and contribute to our understanding of the disease.

A family of probes based on the potent GLP-1R agonist exendin-4 were synthesised using the mild, robust and high-yielding method of CuAAC chemistry. Five of these compounds were conjugated to a

luminescent Tb(III) complex. This complex could act as a FRET donor to GLP-1R receptors modified with a cyanine-based FRET acceptor, and this FRET pair was used to examine the proximity of agonist and receptor during binding events. Conformational changes are known to take place during ligand binding to GPCRs, and it was hoped that these exendin-4 derivatives could be used to explore the effect of amino acid substitution on these conformational changes, binding affinity and physiological activity. Each peptide unit was modified with a synthetic amino acid incorporating a propargyl group at the 12th position in the exendin-4 sequence, based on prior studies by Clardy *et al.*[31]. The affinity of some of these probes for GLP-1R was explored, with EC_{50} values of 2.4 and 5.6 nM found for the derivatives **Ex4-Pra^{12}**, consisting of the Tb(III) complex and modified exendin chain and another additionally including a C_{16} fatty acid chain, **Ex4-Pra^{12}-C$_{16}$** respectively. These values are significantly lower than the EC_{50} of the native agonist (0.1 nM) but still showed that it was possible to elicit a receptor binding response despite substantial modifications to the peptide ligand. The impact on receptor affinity of the other peptide modifications, indicated below in **Figure 6.6** and **Table 6.1**, would form a part of future work on this area of the project.

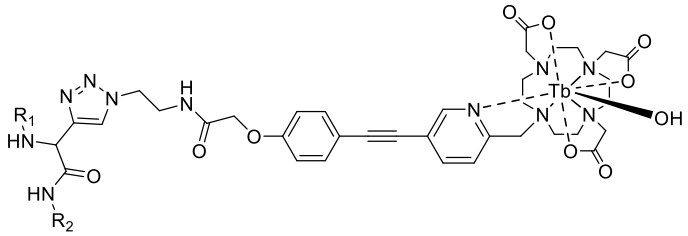


Figure 6.6: General structure of the conjugates synthesised.

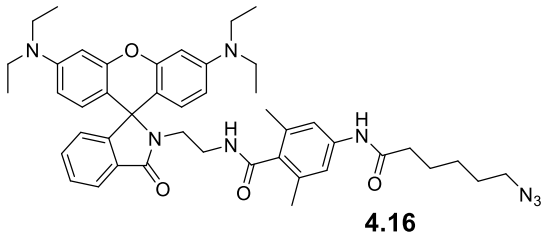
Peptide	R_1	R_2
Ex4-Pra^{12}	HisGlyGluGlyThrPhe ThrSerAspLeuSer	GlnMetGluGluGluAlaValArgLeuPheIleGluTrpLeuLysAsnGlyGlyProSerSer GlyAlaProProProSerNH$_2$
Ex4-Pra^{12}-C$_{16}$	HisGlyGluGlyThrPhe ThrSerAspLeuSer	GlnMetGluGluGluAlaValArgLeuPheIleGluTrpLeuLysAsnGlyGlyProSerSer GlyAlaProProProSerGlyLys-hexadecanoic acid
Ex9-Pra^{12}	AspLeuSer	GlnMetGluGluGluAlaValArgLeuPheIleGluTrpLeuLysAsnGlyGlyProSerSer GlyAlaProProProSerNH$_2$
Ex4-Phe^1-Pra^{12}	PheGlyGluGlyThrPhe ThrSerAspLeuSer	GlnMetGluGluGluAlaValArgLeuPheIleGluTrpLeuLysAsnGlyGlyProSerSer GlyAlaProProProSerNH$_2$
Ex4-Asp^3-Pra^{12}	HisGlyAspGlyThrPhe ThrSerAspLeuSer	GlnMetGluGluGluAlaValArgLeuPheIleGluTrpLeuLysAsnGlyGlyProSerSer GlyAlaProProProSerNH$_2$

Table 6.1: Nomenclature and amino acid sequences of the peptides discussed in this Chapter.

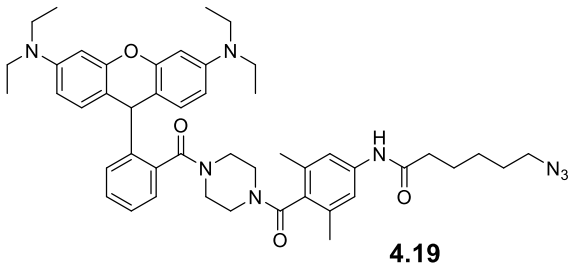
Both of these probes were additionally found to act as FRET donors to acceptor-labelled GLP-1R, indicating that they could be used to successfully examine the conformational changes associated with receptor binding events. There was a slight reduction in the FRET ratio recorded with, **Ex4-Pra^{12}-C$_{16}$** which suggests less effective agonist binding, a conclusion which is reaffirmed by the lower EC_{50} value for this probe. Comparison of the FRET ratios and receptor affinities of the entire compound family should be carried out in order to establish the relationship between different agonist amino acid substitutions, receptor affinities and the conformational changes that take place during binding events.

The distribution of the probes **Ex4-Pra^{12}-C$_{16}$** and **Ex4-Pra^{12}** in the plasma membrane was studied. Both compounds were shown to act as FRET donors to the compound NR12S, which mimics phospholipids. NR12S exhibits polarity-dependent changes in its emission wavelength and can be used to assess the structure of phospholipid membranes *via* its emission wavelength. Examination of cells expressing GLP-1R should be carried out to study how these probes could interact with certain regions of cell membranes. Cell membranes contain cholesterol-rich regions known as lipid rafts. The role of these lipid rafts is unclear, although it is hypothesised that they may be involved in cell signalling. Examination of the interaction between probes and membranes may aid our understanding of the role of lipid rafts and agonist binding in pancreatic β-cells.

Another key event in receptor binding is that of endosome formation and receptor internalisation. Endosomal pH is known to be acidic when compared to its external environment. An exendin-4-rhodamine conjugate containing a spirolactam ring was synthesised and found to exhibit pH-responsive emission, with a pK_a of 4.19 the compound was almost non-emissive at pH values above 5. As this was slightly too low to gain meaningful data from *in vitro* studies using the probe as an on-off fluorophore, modifications will be necessary in future to enhance the range over which the fluorophore could be utilised. An "always-on" variant containing a tertiary amine which would be unable to form a spirolactam system was also synthesised: peptide conjugations and pH titrations of this compound should be carried out to act as a control for the reversible system.



4.16



4.19

Figure 6.7: Compounds **4.16** and **4.19**. Compound **4.16** was designed as a pH-switchable analogue which may have a greater pKa than the previously synthesised compound, **4.9.**

There is evidence that increasing steric hindrance close to the spirolactam ring may raise the pK_a of the compound, and attempts were made to introduce this through the synthesis of the compounds shown in **Figure 6.7**. Unfortunately, they could not be coupled to the exendin-4 analogues described above through CuAAC chemistry, despite many variations of reaction conditions being attempted. There is

some evidence in the literature that reduced rhodol derivatives can act as pH-sensitive chemosensors in a similar way to rhodamine compounds, and future work in this area could focus on the synthesis of this alternative family of pH-sensitive dyes and their conjugation to GLP-1R binding peptides.

6.5. Near-Infrared Emissive Fluorescent Cyanine Dyes for Multi-Modal Imaging

The work outlined in Chapter 5 sought to develop a series of multi-modal probes for β-cell specific imaging. These were to be primarily based around a series of NIR emissive fluorophores for optical imaging, with the incorporation of ^{18}F or radiometal chelating sites to enable PET imaging. The concept of zinc-sensing was explored, with the hope that these compounds could be designed to respond to the presence of Zn^{2+}, which may be critical in the monitoring of β-cell function.

Initially, a series of three heptamethine cyanine dyes were synthesised with a range of zinc-sensing moieties. Introducing thiophene sensors, which may be more selective for Zn^{2+} than DPA, was found to push the emission of the fluorophores further unto the NIR, which could have advantages in optical imaging. However, the thiophene incorporating compounds were found to possess a reduced affinity for zinc(II) and exhibited little change in emission intensity in the presence of Zn^{2+}. As such, the alternative sensors were not pursued further, and the use of DPA was adopted exclusively in the cyanine dyes developed. Inclusion of additional binding units, in an analogous fashion to Nolan *et al.*[32–34], or exploration of other sensing groups such as macrocyclic chelates could be further explored. The inclusion of the carboxylic acid arms of the dye unit could also have interacted with Zn^{2+}, rather than the receptor unit. This could have been an error in methodology, which would be revisited if the experiments were to be repeated.

In the pursuit of an optical-PET imaging agent, two fluorinated cyanine dyes were synthesised, along with their tosylate analogues as precursors for radiolabelling. The di-fluorinated species was shown to exhibit an increase in emission intensity in the presence of Zn(II), with a relative increase of around 17% between the lowest and greatest emission intensities fitting this trend (**Figure 6.8**).

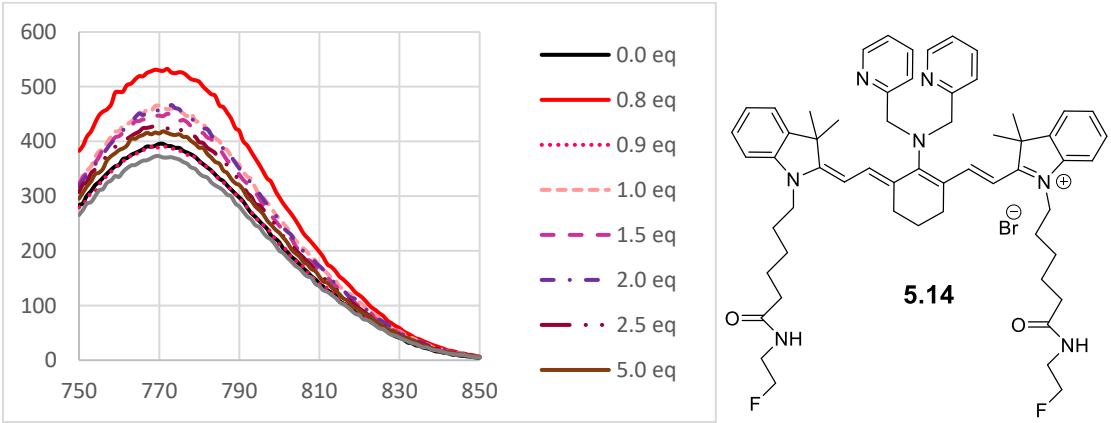


Figure 6.8: The difluorinated, zinc-sensing cyanine dye **5.14** (right) and selected data points from the fluorescence titration carried out with Zn^{2+} (left, n = 3, HEPES/MeCN (9:1), λ_{ex}= 728 nm).

Whilst there was a general trend of increased emission intensity at greater concentrations of Zn(II), this was by no means linear or ratiometric. Indeed, the lowest emission intensity was observed in the presence of 10 equivalents of Zn^{2+} and the greatest at 0.8 equivalents, which was extremely unexpected. It may be that the introduction of the metal ions and their obvious interaction with Zn^{2+} led to some unusual aggregation in solution, which has been observed in cyanine dyes in the literature due to their hydrophobic nature[35–37]. This could be further investigated through the use of less polar solvents, but ultimately could pose a significant hurdle to the application of these probes *in vivo*.

Radiolabelling of the tosylate precursor to **5.14** to give a potential PET agent was not successful, with degradation of the precursor occurring even at room temperature. This was attributed to attack of the fluoride anion present on the highly conjugated cyanine backbone, despite recent evidence from the literature that suggested other heptamethine compounds were robust under similar conditions[38]. The acidity of the α position in the carbonyl arms could have also resulted in deprotonation and subsequent decomposition. Reducing the length of these chains, based on hexanoic acid, could increase steric hindrance around the acidic α protons and potentially reduce the risk of deportation. The synthesis of a series of these dyes with varying arm lengths and an investigation of their stabilities under acidic conditions could be carried out to establish the underlying cause of the degradation of the cyanine and direct future dual modal probe synthesis.

In order to avoid the radiolabelling issues encountered with fluorination, it was decided to introduce a macrocyclic metal chelating unit, which could be complexed to metals like copper or zirconium which have positron emitting isotopes. Additionally, macrocyclic ligands are highly versatile, as has been explored throughout this thesis, and the introduction of a gadolinium(III) complex to the zinc-sensing cyanine unit was also sought after as a potential dual-modal MRI-optical imaging agent. This could successfully be achieved with a macrocycle-copper complex, although not with a zirconium or gadolinium analogue. Furthermore, no targeting moiety, such as the GPR40 targeting unit developed in Chapter 3, could not be introduced. This was attributed to the sensitive nature of the cyanines themselves, and if this were to be developed further a new synthetic route may need to be devised.

Ultimately, the heptamethine, zinc-sensing cyanine core devised in the final Chapter of this thesis could benefit the field through its versatile nature, with substantial scope for modification. Alternative zinc sensing units could be used to push the emission wavelength of these dyes into the NIR, an increasingly important window for optical imaging of biological systems. However, the sensitivity of the cyanine backbone to radiolabelling conditions and other synthetic procedures was a major hindrance. This could be adapted through a systematic evaluation of the structure of the dye to establish the underlying degradation mechanisms. Whilst no successful dual-modal imaging agent could be produced, there is certainly scope in this area for further improvements and developments to be made.

6.6. Final Remarks

This thesis has described the design, synthesis and testing of a family of compounds developed to enhance understanding of pancreatic β-cells. **GdEx**, a novel MRI contrast agent, is, to the best of our knowledge, the first reported gadolinium-based contrast agent to utilise exendin-4 as a targeting moiety. **GdEx** displays pancreas-specific contrast enhancement *in vivo*, as well as a significant difference in organ retention between healthy and β-cell depleted animals. Despite the high dosage required, **GdEx** represents a proof of concept: that pancreas-specific GBCAs may be developed and that these are capable of giving a qualitative indication of β-cell mass decline.

An alternative targeting strategy was employed through the development of the ligand **GPR-L1**, designed using an indole-propionic acid targeting moiety. This ligand was designed to target an alternative receptor to **GdEx** and to examine the differences between the use of a peptide and a small molecule as a targeting vector. **GPR-L1** was found to be a versatile ligand, and the Gd(III), Tb(III) and Eu(III) complexes successfully isolated. The former exhibited a high relaxivity and was found *in vitro* to bind to cells overexpressing the GPR40 receptor. The ligand itself was capable of sensitising the luminescence of both terbium(III) and europium(III), enabling potential future developments in optical imaging using this ligand. Following successful confirmation of the affinity of the Gd(III) complex of **GPR-L1** for GPR40, there is scope to develop an additional family of zinc-sensing imaging agents incorporating this targeting strategy.

Further *in vivo* work with **[Gd(GPR-L1)]** could enable a comparison with **GdEx** and allow further exploration of the efficacy of targeting pancreatic β-cells with small molecules and peptides respectively.

Exendin-4 and its analogues found further application in the study of conformational changes in the structure of GLP-1R. A family of compounds were synthesised based on conjugates of these peptide analogues and a luminescent Tb(III) complex. These probes can act as FRET donors to acceptor-labelled GLP-1R and will be used in future to explore how the receptor changes during agonist binding events, as well as examining the membrane structure of β-cells and how structures such as cholesterol rich regions of the plasma membrane are involved in cell signalling. Two rhodamine derivatives, one of which was sensitive to pH, were synthesised and conjugated to a modified version of exendin-4. The pH switchable derivative was found to be weakly fluorescent at pH values above 4.19, with much more intense emission below this value due to spirolactam ring opening. Further alterations were made in an attempt to raise this value, rendering these compounds more applicable to the study of endocytosis and receptor internalisation pathways.

A series of modifications were made to a NIR emissive cyanine dye framework to explore the potential for the development of dual-modal optical/PET probes. A zinc-sensing cold analogue of such a compound was produced, but unfortunately could not be successfully radiolabelled. The exploration of

alternative zinc-sensing moieties and functionalisation strategies could be used in future pursuit of NIR compound for optical imaging of β-cells.

6.7. References

1 B. Jones, T. Buenaventura, N. Kanda, P. Chabosseau, B. M. Owen, R. Scott, R. Goldin, N. Angkathunyakul, I. R. Corrêa, D. Bosco, P. R. Johnson, L. Piemonti, P. Marchetti, A. M. J. Shapiro, B. J. Cochran, A. C. Hanyaloglu, A. Inoue, T. Tan, G. A. Rutter, A. Tomas and S. R. Bloom, *Nat. Commun.,* 2019, **9**, (1), 1602.

2 T. Buenaventura, S. Bitsi, W. E. Laughlin, T. Burgoyne, Z. Lyu, A. I. Oqua, H. Norman, E. R. McGlone, A. S. Klymchenko, I. R. Corrêa, A. Walker, A. Inoue, A. Hanyaloglu, J. Grimes, Z. Koszegi, D. Calebiro, G. A. Rutter, S. R. Bloom, B. Jones and A. Tomas, *PLoS Biol.*, 2019, **17**, e3000097.

3 T. Buenaventura, N. Kanda, P. C. Douzenis, B. Jones, S. R. Bloom, P. Chabosseau, I. R. Corrêa, D. Bosco, L. Piemonti, P. Marchetti, P. R. Johnson, A. M. J. Shapiro, G. A. Rutter and A. Tomas, *Diabetes*, 2018, **67**, 385–399.

4 A. Martinez-Sanchez, M. S. Nguyen-Tu and G. A. Rutter, *Mol. Endocrinol.*, 2015, **29**, 1067–1079.

5 G. A. Rutter, T. J. Pullen, D. J. Hodson and A. Martinez-Sanchez, *Biochem. J.*, 2015, 466, 203–218.

6 E. Coakley, Imperial College London, 2018.

7 M. S. Fineman, L. Z. Shen, K. Taylor, D. D. Kim and A. D. Baron, *Diabetes. Metab. Res. Rev.*, 2004, **20**, 411–417.

8 G. J. Stasiuk, F. Minuzzi, M. Sae-Heng, C. Rivas, H. Juretschke, L. Piemonti, P. R. Allegrini, D. Laurent, A. R. Duckworth, A. Beeby, G. A. Rutter and N. J. Long, *Chem. – A Eur. J.*, 2015, **21**, 5023–5033.

9 A. F. Martins, V. Clavijo Jordan, F. Bochner, S. Chirayil, N. Paranawithana, S. Zhang, S. T. Lo, X. Wen, P. Zhao, M. Neeman and A. D. Sherry, *J. Am. Chem. Soc.*, 2018, **140**, 17456–17464.

10 A. C. Esqueda, J. A. López, G. Andreu-de-Riquer, J. C. Alvarado-Monzón, J. Ratnakar, A. J. M. Lubag, A. D. Sherry and L. M. De León-Rodríguez, *J. Am. Chem. Soc.*, 2009, **131**, 11387.

11 A. J. M. Lubag, L. M. De Leon-Rodriguez, S. C. Burgess and A. D. Sherry, *Proc. Natl. Acad. Sci. U. S. A.*, 2011, **108**, 18400–18405.

12 S. Edfalk, P. Steneberg and H. Edlund, *Diabetes*, 2008, **57**, 2280–2287.

13 P. Steneberg, N. Rubins, R. Bartoov-Shifman, M. D. Walker and H. Edlund, *Cell Metab.*, 2005, **1**, 245–258.

14 H. Shapiro, S. Shachar, I. Sekler, M. Hershfinkel and M. D. Walker, *Biochem. Biophys. Res. Commun.*, 2005, **335**, 97–104.

15 M. G. Latour, T. Alquier, E. Oseid, C. Tremblay, T. L. Jetton, J. Luo, D. C-H Lin and V. Poitout, *Diabetes*, 2007, **56**, 1087–1094.

16 M. Z. Khan and L. He, *Neuropharmacology*, 2017, 113, 639–651.

17 N. Negoro, S. Sasaki, S. Mikami, M. Ito, M. Suzuki, Y. Tsujihata, R. Ito, A. Harada, K. Takeuchi, N. Suzuki, J. Miyazaki, T. Santou, T. Odani, N. Kanzaki, M. Funami, T. Tanaka, A. Kogame, S. Matsunaga, T. Yasuma and Y. Momose, *Chem. Lett*, 2010, **1**, 290–294.

18 T. Araki, M. Hirayama, S. Hiroi and K. Kaku, *Diabetes, Obes. Metab.*, 2012, **14**, 271–278.

19 D. O. Yoon, X. Zhao, D. Son, J. T. Han, J. Yun, D. Shin and H. J. Park, *ACS Med. Chem. Lett.*, 2017, **8**, 1336–1340.

20 S. Runge, H. Thøgersen, K. Madsen, J. Lau and R. Rudolph, *J. Biol. Chem.*, 2008, **283**, 11340–11347.

21 S. R. J. Hoare, *Drug Discov. Today*, 2005, 10, 417–427.

22 C. R. Underwood, P. Garibay, L. B. Knudsen, S. Hastrup, G. H. Peters, R. Rudolph and S. Reedtz-Runge, *J. Biol. Chem.*, 2010, **285**, 723–730.

23 D. Donnelly, *Br. J. Pharmacol.*, 2012, **166**, 27–41.

24 U. Werner, G. Haschke, A. W. Herling and W. Kramer, *Regul. Pept.*, 2010, **164**, 58–64.

25 L. J. Miller, P. M. Sexton, M. Dong and K. G. Harikumar, *Int. J. Obes. Suppl.*, 2014, **4**, S9–S13.

26 A. Jodal, R. Schibli and M. Béhé, *Eur. J. Nucl. Med. Mol. Imaging*, 2017, **44**, 712–727.

27 J. P. Gutzwiller, B. Göke, J. Drewe, P. Hildebrand, S. Ketterer, D. Handschin, R. Winterhalder, D. Conen and C. Beglinger, *Gut*, 1999, **44**, 81–86.

28 M. A. Pfeffer, B. Claggett, R. Diaz, K. Dickstein, H. C. Gerstein, L. V. Køber, F. C. Lawson, L. Ping, X. Wei, E. F. Lewis, A. P. Maggioni, J. J. V. McMurray, J. L. Probstfield, M. C. Riddle, S. D. Solomon and J.-C. Tardif, *N. Engl. J. Med.*, 2015, **373**, 2247–2257.

29 D. J. Drucker and M. A. Nauck, *Lancet*, 2006, 368, 1696–1705.

30 M. M. Fletcher, M. L. Halls, P. Zhao, L. Clydesdale, A. Christopoulos, P. M. Sexton and D. Wootten, *Biochem. Pharmacol.*, 2018, **156**, 406–419.

31 S. M. Clardy, E. J. Keliher, J. F. Mohan, M. Sebas, C. Benoist, D. Mathis and R. Weissleder, *Bioconjug. Chem.*, 2014, **25**, 171–177.

32 E. M. Nolan and S. J. Lippard, *Acc. Chem. Res.*, 2009, **42**, 193–203.

33 E. M. Nolan, J. W. Ryu, J. Jaworski, R. P. Feazell, M. Sheng and S. J. Lippard, *J. Am. Chem. Soc.*, 2006, **128**, 15517–15528.

34 E. M. Nolan and S. J. Lippard, *Inorg. Chem.*, 2004, **43**, 8310–8317.

35 A. Mishra, R. K. Behera, P. K. Behera, B. K. Mishra and G. B. Behera, *Chem. Rev.*, 2000, **100**, 1973–2011.

36 A. Louie, *Chem. Rev.*, 2010, **110**, 3146–3195.

37 V. E. Shershov, M. A. Spitsyn, V. E. Kuznetsova, E. N. Timofeev, O. A. Ivashkina, I. S. Abramov, T. V. Nasedkina, A. S. Zasedatelev and A. V. Chudinov, *Dye. Pigment.*, 2013, **97**, 353–360.

38 R. Ting, T. A. Aguilera, J. L. Crisp, D. J. Hall, W. C. Eckelman, D. R. Vera and R. Y. Tsien, *Bioconjug. Chem.*, 2010, **21**, 1811–1819.

Chapter 7

Experimental Procedures

7.1. General Experimental Considerations

Solvents and reagents were of analar or reagent grade and were purchased from Sigma-Aldrich Chemical Co., VWR International, Acros Organics or Strem Chemical Co. and used without further purification. Anhydrous solvents were acquired from solvent towers within the department and stored over 3 Å molecular sieves. Thin-layer chromatography was conducted using pre-coated Merck Kieselgel 60, F254 plates. Flash chromatography used silica (60 Å pore size). Where specified, automated flash chromatography was performed using a Biotage Isolera Four unit and 10 g, 25 g, 50 g or 100 g SNAP KP-Sil or SNAP Ultra cartridges. Reverse phase automated flash chromatography utilised Biotage Isolera Four unit and a SNAP KP-Sil or SNAP Ultra 12 g C_{18} cartridge.

7.2. General Spectroscopic Methods

^{1}H-NMR and ^{13}C-NMR spectra were recorded on a Bruker AMX-400 spectrometer at room temperature and assigned where possible using 2D correlation spectroscopy. Spectra were analysed using MestReNova software and internally referenced to residual solvent peaks. Chemical shifts are quoted in parts per million (ppm), coupling constants (*J*) are quoted in Hz and multiplicities are abbreviated as: s = singlet, d = doublet, t = triplet, dd = doublet of doublets, dt = doublet of triplets, qu = quartet or m = multiplet, where substantial overlap of resonances or complex coupling of signals did not allow for precise assignment. Broadened signals are marked as br.

Electrospray Time-of-Flight and high-resolution mass spectra were obtained using a Waters LCT Premier by Dr. Lisa Haigh of the mass spectrometry facilities of Imperial College London, Department of Chemistry. MALDI-ToF spectra were obtained on a Micromass MALDI Micro MX spectrometer. LCMS analyses and purifications were performed on a Waters 2767 LCMS machine equipped with a photodiode array and Waters 3000 mass detector for ES^{+}/ES^{-} analyses. Analytical separations were performed on a Waters XBridge C_{18} column (5 µm, 4.6 x 100 mm) using a 1.2 $mLmin^{-1}$ flow and an eluent system of MeCN and H_2O (+ 0.1% formic acid). MassLynx and OpenChrom software packages were used for chromatographic analysis.

Infrared spectra were collected in the solid state using a Perkin Elmer Spectrum 100 FTIR Spectrometer.

7.2.1. Photophysical Methods

UV-vis absorption spectra were recorded on a Perkin Elmer 650 spectrometer in quartz cuvettes.

Fluorescence excitation and emission spectra were obtained using a Varian Cary Eclipse spectrophotometer with settings specified on a case by case basis. For pH measurements a Jenway model 3510 pH/mV/temperature meter was used that had been calibrated against pH 10.00, pH 7.00 and pH 4.00 buffers.

Lanthanide-based lifetimes were measured using a Varian Cary Eclipse spectrophotometer in the phosphorescence mode, using 100 μM or 1 mM solutions in H_2O and D_2O. The integrated emission intensity was recorded after excitation of the samples at 350 nm or 391 nm. The gate time was fixed at 0.1 ms with both excitation and emission slits set at 20 nm. The resulting decay curves were fitted to a single exponential decay in Origin.

7.2.2. Relaxometric Measurements

Gadolinium(III) complexes were dissolved in water at different molar concentrations. The solutions and a water standard were added into a glass capillary of 1.7 mm diameter, sealed and inserted into an NMR tube containing D_2O. Concentrations of Gd(III) present were assessed by measuring the difference in solvent shifts according to the magnetic susceptibility measurements conducted using the Evans method[1]. T_1 measurements were carried out by Dr. Peter Haycock using a Bruker Advance 400 spectrometer and inversion recovery measurements. Relaxivity values were calculated from the samples using a procedure described in the literature[2].

7.3. *In Vitro* Procedures

All *in vitro* procedures were carried out by Dr Shuai Zha at Hong Kong Baptist University.

7.3.1. *In Vitro* Toxicity Tests

HEK293 and HEK293 transfected with FFAR1 cells (1×10^6) were treated with **3.18** for 24 h with various concentrations (1, 5, 10, 50, 100, and 500 μM). The cells, incubated in 96-well plates, were rinsed with PBS and incubated with 0.5 mg/mL 3-(4,5-Dimethylthiazol-2-yl)-2,5-diphenyltetrazolium bromide (MTT) solution. The cells treated with MTT for 3 h. After that, the formazan crystals were dissolved in dimethylsulfoxide (DMSO) with shaking for 1 min. Lastly, the absorbance of the solution was recorded with a Biotek PowerWave XS microplate reader at a wavelength of 570 nm.

7.3.2. *In Vitro* Confocal Imaging

HEK293 and HEK293 transfected with FFAR1 cells (1×10^5) were initially seeded in confocal dishes for 24 h. Then the cells were incubated with 50 μM **3.18** for 6 h, 12 h, 24 h and washed with PBS twice before imaging. All the confocal images were obtained on a Leica TCS SP8 confocal laser-scanning microscope equipped with a Ti:sapphire laser. **3.18** was excited by 700 nm multi-photons wavelength for imaging and recorded the emission from 400 nm to 550 nm.

7.4. *In Vivo* Procedures

All *in vivo* work was carried out by Dr Aida Martinez-Sanchez and Dr Nicoleta Baxan at the Imperial College Centre for Translational and Experimental Medicine.

Male C57BL/6J mice were purchased from Charles River Laboratories (UK). Dicer-KO ($Dicer^{fl/fl}$, Cre-ER positive, heterozygous) and littermate controls Dicer-ctrl ($Dicer^{fl/fl}$, Cre-ER negative) were generated as previously described[3]. 2-5 animals were housed in ventilated cages with a 12-hour light/dark cycle and free access to standard chow diet in a pathogen-free facility (Imperial College Central Biomedical Service). 8-10-week-old animals were injected intraperitoneally with five doses of 2 mg tamoxifen (Sigma-Aldrich).

All *in vivo* procedures were approved by the UK Home Office Animals Scientific Procedures Act, 2986 (HO Licence PPL PA03F7F0F). Glucose levels were measured after imaging using an Accucheck Performa nano from blood samples from the tail.

7.4.1. Magnetic Resonance Imaging

Mice were anaesthetized in an anaesthesia box with 1-5% vol isofluorane in O_2. A tail-vein catheter was placed under anaesthesia (~2% vol) and maintained in the animals throughout the scan to allow administration of the probe and ensure the MR images were acquired at the same location before and after contrast administration.

All MRI scans were conducted on a pre-clinical 9.4 T scanner (94/20 USR Bruker BioSpec, Ettlingen, Germany) equipped with a 40 mm quadrature mouse body transceiver. Mice were positioned prone in a dedicated mouse bed and maintained under anaesthesia. Respiration and body temperature were continuously monitored through the entire imaging session (SA Instruments, Stony Brook, NY, USA). Body temperature was maintained at 36.5° by a circulating warm water heat mat. Data were acquired with Paravision 6.0.1 (Bruker, BioSpin). As a standard, the coronal plane was chosen, and the adjacent organs (kidney, spleen) were used as essential landmarks.

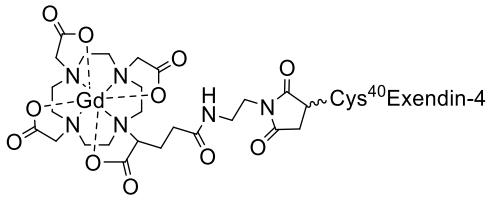
Dynamic T_1 weighted images (TR/TE = 160/2.360 ms, voxel size (140 x 140 x 600) μm^3) were acquired every 3 minutes to assess the **GdEx** kinetic uptake, retention and washout from the pancreas. Specifically, after 4 baseline images, **GdEx**/$[Gd(dota)]^-$ (1.12 µmol/animal in 150 µl of saline) was delivered intravenously and a series of T_1 images of the same acquisition parameters and geometry were acquired up to 54 minutes post-injection.

7.4.2. MR Data Analysis

The pancreas was outlined in each T_1 weighted image primarily based on its anatomical location relative to neighbouring organs. Namely, the spleen and superior aspect of the left kidney were used to identify the tail of the pancreas. At every time series, the mean intensity of outlined pixels of the pancreas and of the spleen were computed along with the standard deviation of image noise. The signal intensity difference between pancreas and spleen was then scaled to the standard deviation of image noise. The resulting parameter was referred to as contrast to noise ratio (CNR) and the results were presented as percentage of CNR change compared to the baseline values.

Statistical analysis was performed using GraphPad Prism 7.0. To better visualize the signal distribution of each time course, smoothing was performed by averaging two values on each side and using a second order polynomial smoothing[4]. Two-way ANOVA with Fisher least significant difference (LSD) test was used for time course analysis with each individual time point analysed respectively. Unpaired Student's t-test was performed for area under the curve (AUC) analysis.

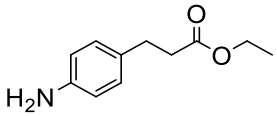
7.5. Synthesis of Compounds in Chapter 2



Gd-dota(ga)-maleimide-Cys^{40}Exendin-4 (GdEx): Cys^{40}Exendin-4 (0.040 g, 9.39 µmol) was dissolved in PBS (pH 7.4, 3.5 mL). H_4dota(ga)-maleimide (0.007 g, 11.53 µmol) was added and the solution incubated at 3 °C. After 24 hours, the reaction mixture was lyophilised to leave a white solid. This solid was re-dissolved in H_2O (5 mL) and $GdCl_3{\cdot}6H_2O$ (0.009 g, 25.29 µmol) was added, and the pH brought to 6 by addition of NaOH (aq., 0.1 M) before the reaction mixture was left to stir at room temperature. After 19 hours, LCMS indicated partial complexation, so an additional portion of $GdCl_3{\bullet}6H_2O$ (0.013 g, 34.97 µmol) was added, bringing the pH to 5. The pH was readjusted to 6 by addition of NaOH (aq., 0.1 M) and the reaction mixture left to stir at room temperature. After a further 22 hours, LCMS indicated complete conversion of starting material and the reaction mixture was lyophilised, leaving a white solid. Automated flash chromatography (C_{18} cartridge, 99.9% H_2O/0.1% TFA to 99.9% MeCN/0.1% TFA) gave **GdEx** as a white solid (0.022 g, 4.42 µmol, 47%).

ESI MS (ES+) *m/z* for $C_{212}H_{320}GdN_{56}O_{73}S_2$:$[M]^{5+}$ - calculated = 1008, found = 1009.37, $[M]^{4+}$ - calculated = 1260.00, found = 1261.35 $[M]^{3+}$ - calculated = 1680.00, found = 1679.74.

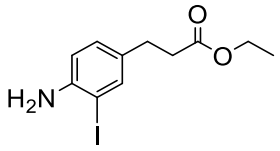
7.6. Synthesis of Compounds in Chapter 3



Ethyl 3-(4-aminophenyl)propanoate[5] (3.1): 4-aminophenyl propanoic acid (0.24 g, 1.43 mmol) was dissolved in EtOH (50 mL). H_2SO_4 (conc., 0.5 mL) was added and the yellow reaction mixture left to stir under reflux at 90 °C. After 17 hours, the solvent was removed *in vacuo* to leave a yellow oil. This oil was re-dissolved in DCM (30 mL) and washed with $NaHCO_3$ solution (sat., 20 mL) and H_2O (20 mL). The combined aqueous phases were washed with DCM (30 mL) and the combined organic phases dried over $MgSO_4$. The solvent was removed *in vacuo* to leave **3.1** as a yellow oil (0.23 g, 1.17 mmol, 82%).

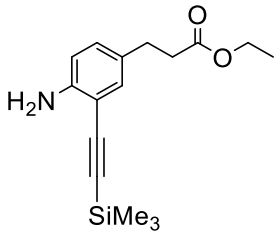
^{1}H NMR ($CDCl_3$ 400 MHz) δ/ppm = 6.99 (d, $^3J_{HH}$ = 8.4 Hz, 2H, Ar-H), 6.65 – 6.60 (m, 2H, Ar-H), 4.12 (q, $^3J_{HH}$ = 7.1 Hz, 2H, $COOCH_2CH_3$), 3.57 (br s, 2H, NH_2), 2.84 (t, $^3J_{HH}$ = 7.8 Hz, 2H, CH_2COOEt), 2.56 (t, $^3J_{HH}$ = 7.8 Hz, 2H, $ArCH_2$), 1.23 (t, $^3J_{HH}$ = 7.1 Hz, 3H, $COOCH_2CH_3$).

Data corresponds to literature[5].



Ethyl 3-(4-amino-3-iodophenyl)propanoate[6] (3.2): Compound **3.1** (0.18 g, 0.95 mmol) was dissolved in dry DMF (40 mL) and cooled to 0 °C. N-iodosuccinimide (0.26 g, 1.14 mmol) was added, forming a bright yellow solution which was left to warm to room temperature and stir under N_2. After 17 hours, a colour change to dark brown had taken place. EtOAc (50 mL) was added to the reaction mixture, which was then washed with H_2O (2 x 50 mL) and brine (50 mL). The combined organic phases were dried over $MgSO_4$ and the solvent removed *in vacuo* to leave a brown oil. Column chromatography using a Biotage was performed (50% to 20% hexane in EtOAc) and gave a red oil, which was dried under high vacuum to give **3.2** (0.26 g, 0.83 mmol, 87%).

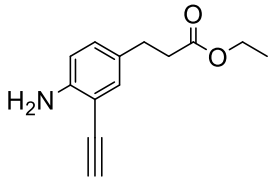
^{1}H NMR ($CDCl_3$ 400 MHz): δ/ppm = 7.48 (d, $^3J_{HH}$ = 1.9 Hz, 1H, Ar-H), 6.98 (dd, $^3J_{HH}$ = 8.1 Hz, $^4J_{HH}$ 1.9 Hz, 1H, Ar-H), 6.67 (d, $^3J_{HH}$ = 8.1 Hz, 1H, Ar-H), 4.12 (q, $^3J_{HH}$ = 7.1 Hz, 2H, $COOCH_2CH_3$), 3.99 (br s, 2H NH_2), 2.79 (t, $^3J_{HH}$ = 7.7 Hz, 2H, CH_2COOEt), 2.54 (t, $^3J_{HH}$ = 7.7 Hz, 3H, $ArCH_2$), 1.24 (t, $^3J_{HH}$ = 7.1 Hz, 3H, $COOCH_2CH_3$).
Data corresponds to literature[6].



Ethyl 3-(4-amino-3-((trimethylsilyl)ethynyl)phenyl)propanoate[6] (3.3): Compound **3.2** (0.26 g, 0.83 mmol) was dissolved in dry THF (40 mL). $PdCl_2(PPh_3)_2$ (0.03 g, 0.04 mmol) was added, followed by CuI (0.01 g, 0.06 mmol), TEA (0.58 mL, 0.42 g, 4.15 mmol) and TMS acetylene (0.17 mL, 0.12 g, 1.25 mmol). The resulting brown solution was left to stir under N_2 at 60 °C. After 20 hours, H_2O (40 mL) was added and the reaction mixture was extracted with EtOAc (50 mL). The aqueous phase was washed with EtOAc (2 x 30 mL) and the combined organic phases dried over $MgSO_4$. The solvent was removed *in vacuo* to leave a brown oil. This oil was filtered through a silica plug, with **3.3** eluting in 20% EtOAc in hexane. The solvent was removed *in vacuo* to leave **3.3** as a brown solid (0.24 g, 0.83 mmol, quant).

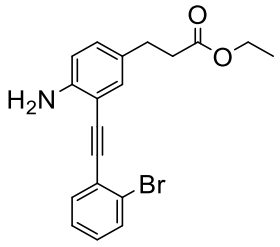
^{1}H NMR ($CDCl_3$, 400 MHz): δ/ppm = 7.14 (d, $^4J_{HH}$ = 2.0 Hz, 1H, Ar-H), 6.95 (dd, $^3J_{HH}$ = 8.3, $^4J_{HH}$ 2.2 Hz, 1H, Ar-H), 6.61 (d, $^3J_{HH}$ = 8.3 Hz, 1H, Ar-H), 4.10 (q, $^3J_{HH}$ = 7.1 Hz, 2H, $COOCH_2CH_3$), 2.79 (t, $^3J_{HH}$ = 7.7 Hz, 2H, CH_2COOEt), 2.53 (t, $^3J_{HH}$ = 7.8 Hz, 2H, $ArCH_2$), 1.23 (t, $^3J_{HH}$ = 7.1 Hz, 3H, $COOCH_2CH_3$), 0.25 (s, 9H, Me_3Si).

Data corresponds to literature[6].



Ethyl 3-(4-amino-3-ethynylphenyl)propanoate[6] (3.4): Compound **3.3** (0.17 g, 0.60 mmol) was dissolved in THF (20 mL), forming a light brown solution. NBu_4F (0.66 mL, 1.0 M in THF) was added and the resultant black reaction mixture left to stir at room temperature. After 4 hours, MeOH (5 mL) was added and the solvent removed *in vacuo* to leave a dark brown oil. Column chromatography using a Biotage (20% EtOAc in petroleum ether) gave **3.4** as a yellow oil (0.09 g, 0.41 mmol, 69%).

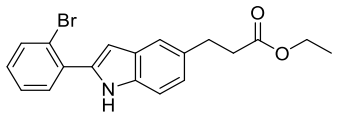
^{1}H NMR ($CDCl_3$, 400 MHz): δ/ppm = 7.16 (d, $^3J_{HH}$ = 2.0 Hz, 1H, Ar-H), 6.99 (dd, $^3J_{HH}$ = 8.3 Hz, $^4J_{HH}$ 2.1 Hz, 1H, Ar-H), 6.63 (d, $^3J_{HH}$ = 8.3 Hz, 1H, Ar-H), 4.15 (br s, 2H, NH_2), 4.12 (q, $^3J_{HH}$ = 7.2 Hz, 2H, $COOCH_2CH_3$), 3.36 (s, 1H HC≡CAr), 2.80 (t, $^3J_{HH}$ = 7.8 Hz, 2H, CH_2COOEt), 2.55 (t, $^3J_{HH}$ = 7.1 Hz, 2H, $ArCH_2$), 1.23 (t, $^3J_{HH}$ = 7.2 Hz, 3H, $COOCH_2CH_3$).
Data corresponds to literature[6].



Ethyl 3-(4-amino-3-((2-bromophenyl)ethynyl)phenyl)propanoate[6] (3.5): Compound **3.4** (0.03 g, 0.16 mmol) was dissolved in dry DMF (30 mL). TEA (0.20 mL, 0.15 g, 1.60 mmol) was added, followed by 1,2-dibromobenzene (0.04 mL, 0.08 g, 0.40 mmol), CuI (0.01 g, 0.03 mmol) and $PdCl_2(PPh_3)_2$ (0.02 g, 0.03 mmol), forming a yellow solution which was left to stir at 80°C under N_2. After 21 hours, H_2O (40 mL) was added and the reaction mixture extracted with EtOAc (3 x 40 mL). The combined organic phases were washed with brine (3 x 50 mL) before being dried over $MgSO_4$ before the solvent was removed *in vacuo* to leave a brown oil. Column chromatography using a Biotage (25% EtOAc in petroleum ether to 100% EtOAc) gave **3.5** as a yellow oil (0.12 g, 0.13 mmol, 82%).

^{1}H NMR (CDCl3, 400 MHz): δ/ppm = 7.62 (dd, $^3J_{HH}$ = 8.1, 1.0 Hz, 1H, Ar-H), 7.56 (dd, $^3J_{HH}$ = 7.7 Hz, $^4J_{HH}$ = 1.6 Hz, 1H, Ar-H), 7.31 (td, $^3J_{HH}$ = 7.7, $^4J_{HH}$ = 1.2 Hz, 2H, Ar-H), 7.24 (d, $^3J_{HH}$ = 2.0 Hz, 1H, Ar-H), 7.18 (td, $^3J_{HH}$ = 7.9 Hz, $^4J_{HH}$ =1.7 Hz, 1H, Ar-H), 6.67 (d, $^3J_{HH}$ = 8.3 Hz, 1H, Ar-H), 4.40 (s, 2H, NH_2), 4.13 (q, $^3J_{HH}$ = 7.1 Hz, 2H, $COOCH_2CH_3$), 2.84 (t, $^3J_{HH}$ = 7.8 Hz, 2H, CH_2COOEt), 2.57 (t, $^3J_{HH}$ = 7.8 Hz, 2H, $ArCH_2$), triplet from $COOCH_2CH_3$ lost under solvent peak.

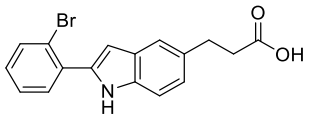
Data corresponds to literature[6].



Ethyl 3-(2-(2-bromophenyl)-1H-indol-5-yl)propanoate[6] (3.6): Ethyl 3-(4-amino-3-((2-bromophenyl)ethynyl)phenyl)propanoate (0.18 g, 0.57 mmol) was dissolved in EtOH (20 mL). $AuCl_3$ (0.03 g, 0.10 mmol) was added and the resulting brown solution left to stir at 60 °C. After 4.5 h, the solvent was removed *in vacuo* to leave a brown solid. This solid was re-dissolved in hexane and EtOAc (3:1 ratio, 40 mL) and filtered through a silica plug. The filtrate was retained and reduced *in vacuo*, leaving a yellow oil. Automated flash chromatography (25% EtOAc in petroleum ether to 100% EtOAc) gave **3.6** as a yellow oil (0.15 g, 0.41 mmol, 87%).

^{1}H NMR ($CDCl_3$, 400 MHz): δ/ppm = 8.59 (br s, 1H, NH), 7.68 (d, $^3J_{HH}$ = 8.1 Hz, 1H, Ar-H), 7.60 (d, $^3J_{HH}$ = 7.4 Hz, 1H, Ar-H), 7.49 (s, 1H, Ar-H), 7.39 (d, $^3J_{HH}$ = 7.4 Hz, 1H, Ar-H), 7.35 (d, $^3J_{HH}$ = 8.5 Hz, 1H, Ar-H), 7.21 (t, $^3J_{HH}$ = 7.7 Hz, 1H, Ar-H), 7.08 (d, $^3J_{HH}$ = 8.2 Hz, 1H, Ar-H), 6.75 (d, $^3J_{HH}$ = 2.1 Hz, 1H, Ar-H), 4.14 (q, $^3J_{HH}$ = 7.6 Hz, 2H, $COOCH_2CH_3$), 3.06 (t, $^3J_{HH}$ = 8.1 Hz, 2H, CH_2COOEt), 2.68 (t, $^3J_{HH}$ = 8.0 Hz, 2H, $ArCH_2$), 1.25 (t, $^3J_{HH}$ = 7.1 Hz, 3H, CH_2CH_3).

Data corresponds to literature[6].

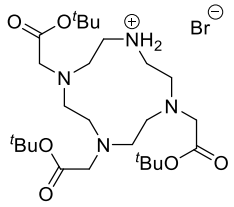


3-(2-(2-Bromophenyl)-1*H*-indol-5-yl)propanoic acid[6] (3.7) : Compound **2** (0.15 g, 0.41 mmol) was dissolved in MeOH (20 mL) and NaOH (0.02 g, 0.55 mmol) in H_2O (10 mL) added, forming a pale yellow solution which was left to stir at 40 °C. After 20 hours, TLC indicated that the reaction had gone to completion. HCl (0.1 M, 5 mL) was added and the solvent removed *in vacuo* to leave a brown solid. Automated flash chromatography (C_{18} cartridge, 50% H2O/50% MeCN + 0.1% FA, isocratic conditions) gave **3.7** as a white solid (0.11 g, 0.34 mmol, 82%).

^{1}H NMR (DMSO-d_6, 400 MHz): δ/ppm = 12.09 (br s, 1H, COOH), 11.31 (s, 1H, NH), 7.78 (dd, $^3J_{HH}$ = 8.0 Hz, $^4J_{HH}$ = 1.1 Hz, 1H, Ar-H), 7.64 (dd, $^3J_{HH}$ = 7.7 Hz, $^4J_{HH}$ = 1.7 Hz, 1H, Ar-H), 7.50 (t, $^3J_{HH}$ = 7.7 Hz , $^4J_{HH}$ = 1.2 Hz, 2H, Ar-H), 7.40 (s, 1H, Ar-H), 7.34 – 7.30 (m, 3H, Ar-H), 7.01 (dd, $^3J_{HH}$ =

8.4 Hz, $^4J_{HH}$ = 1.6 Hz, 1H, Ar-H), 6.74 (d, $^3J_{HH}$ = 1.4 Hz, 1H, Ar-H), 2.90 (t, $^3J_{HH}$ = 7.7 Hz, 2H, CH_2COOH), 2.59 (t, $^3J_{HH}$ = 7.5 Hz, 2H, $ArCH_2$)

LR ESI-MS: Calculated for M = $C_{17}H_{14}BrNO_2$: $[M+H]^+$ expected = 344.02, found = 344.00.



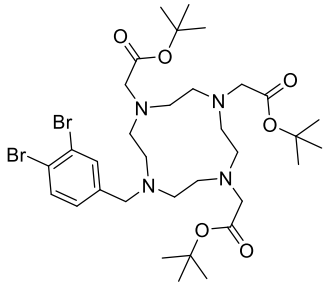
Tri-tert-butyl 2,2',2''-(1,4,7,10-tetraazacyclododecane-1,4,7-triyl)triacetate hydrobromide, ^{t}Bu$_3$-DO3A•HBr[7] (3.8): Cyclen (5.00 g, 29.02 mmol) was suspended in DMA (60 mL) and NaOAc (7.86 g, 95.77 mmol) added. The suspension was cooled to -20 °C and tert-butyl bromoacetate (14.14 mL, 18.68 g, 95.77 mmol) in DMA (20 mL) added dropwise over 40 minutes. The reaction mixture was left to stir vigorously. After 17 hours, an additional portion of DMA (10 mL) was added. After a total reaction time of 19.5 hours, the reaction mixture was poured into H_2O (325 mL) and stirred for 5 minutes, forming a clear solution. $KHCO_3$ (7.50 g, 74.91 mmol) was added in portions, resulting in the formation of a white precipitate. This precipitate was isolated by filtration and dissolved in $CHCl_3$ (250 mL). The solution was washed with H_2O (2 x 50 mL) and the combined organic phases dried over $MgSO_4$. The $MgSO_4$ was removed by filtration and the dark orange filtrate concentrated *in vacuo* to around 30 mL. Et_2O (240 mL) was added, resulting in the formation of a white precipitate, which was isolated by filtration and dried under vacuum to yield **3.8** as a white solid (10.22 g, 17.63 mmol, 61%).

^{1}H NMR (400 MHz, $CDCl_3$): δ/ppm = 10.05, (br s, 1H, NH), 3.37 (s, 4H, ^{t}BuOCOCH_2), 3.29 (s, 2H, ^{t}BuOCOCH_2), 3.10 (s, 4H, ^{t}BuOCOCH_2NCH_2), 2.94 (m, 8H, ^{t}BuOCOCH_2NCH_2), 2.88 (br s, 4H, CH_2NHCH_2), 1.46 (s, 18H ^{t}BuOCO), 1.45 (s, 9H, ^{t}BuOCO).

^{13}C NMR (101 MHz, CDCl3): δ/ppm = 170.3, 169.4, 81.6, 81.4, 65.6, 57.8, 51.0, 48.9, 47.3, 37.9, 35.0, 28.0, 21.4, 15.1.

HR ESI-MS: Calculated for $[M]^+ = C_{26}H_{51}N_4O_6^+$ expected = 515.3803, found 515.3796.

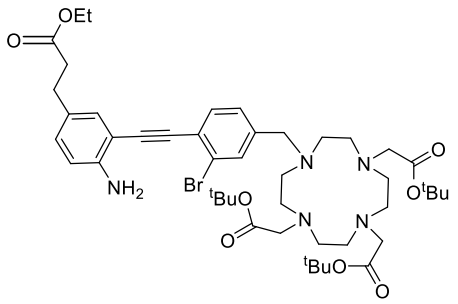
Data corresponds to literature[7].



Tri-tert-butyl 2,2',2''-(10-(3,4-dibromobenzyl)-1,4,7,10-tetraazacyclododecane-1,4,7-triyl)triacetate (3.9): 1-2-dibromo-4(bromomethyl)benzene (0.15 g, 0.45 mmol) was dissolved in MeCN (60 mL). Compound **3.8** (0.25 g, 0.43 mmol) was added, followed by K_2CO_3 (0.21 g, 1.49 mmol). The reaction mixture was left to stir at 95 °C under N_2. After 26 hours, TLC suggested that the reaction had not gone to completion. The temperature of the reaction mixture was increased to 110 °C. After a further 19 hours, TLC indicated that the reaction had still not reached completion. An additional portion of K_2CO_3 (0.46 g, 3.32 mmol) was added. After 24 hours, TLC showed consumption of starting material. The reaction mixture was filtered to remove K_2CO_3 and the solvent removed *in vacuo* to leave a brown solid. Automated flash chromatography (5% MeOH in DCM to 50% MeOH in DCM) gave **3.9** as a white solid (0.18 g, 0.24 mmol, 57%).

^{1}H NMR ($CDCl_3$, 400 MHz):δ/ppm = 7.93 (d, $^3J_{HH}$ = 2.0 Hz, 1H, Ar-H),7.52 – 7.49 (m, 1H, Ar-H), 7.25 – 7.23 (m, 1H, Ar-H), 3.30 – 2.14 (br m, 24H, ArCH_2, NCH_2CO and NCH_2CH_2N), 1.42 (s, 18H, COO^{t}Bu), 1.39 (s, 9H, COO^{t}Bu).

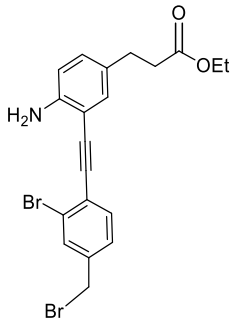
LR ESI-MS: Calculated for M = $C_{33}H_{54}Br_2N_4O_6$ $[M+H]^+$: expected = 763.63, found 763.25.



Tri-tert-butyl 2,2',2''-(10-(4-((2-amino-5-(3-ethoxy-3-oxopropyl)phenyl)ethynyl)-3-bromobenzyl)-1,4,7,10-tetraazacyclododecane-1,4,7-triyl)triacetate (3.10a): Compound **3.4** (0.03 g, 0.13 mmol) was dissolved in dry DMF (10 mL). Dry DIPA (10 mL) was added, followed by tri-tert-butyl 2,2',2''-(10-(3,4-dibromobenzyl)-1,4,7,10-tetraazacyclododecane-1,4,7-triyl)triacetate (0.43 g, 0.56 mmol), CuI (6.70 mg, 0.04 mmol) and $PdCl_2(PPh_3)_2$ (0.02 g, 0.03 mmol). The yellow reaction mixture was heated to 70 °C under N_2. After 23 hours, EtOAc (50 mL) was added. The reaction mixture was washed with H_2O (2 x 50 mL) and brine (50 mL) before the combined organic phases were dried over $MgSO_4$. The solvent was removed *in vacuo* to leave a brown oil. Automated flash chromatography (hexane to EtOAc) gave **3.10** as a green oil (0.08 g, 0.08 mmol, 35%).

^{1}H NMR ($CDCl_3$, 400 MHz): δ/ppm = 7.67 (s, 1H, Ar-H), 7.48 (d, $^3J_{HH}$ = 7.2 Hz, 2H, Ar-H), 7.18 (d, $^3J_{HH}$ = 15.7 Hz, 2H, Ar-H), 6.97 – 6.89 (m, 1H, Ar-H), 6.63 (d, $^3J_{HH}$ = 7.7 Hz, 1H, Ar-H), 3.59 - 3.38 (m, 14H), 2.80 (s, 18H, CH_2), 2.64 – 2.43 (m, 8H, CH_2), 1.81 - 1.52 (m, 5H, CH_2), 1.40 (s, 29H O^{t}Bu).

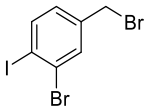
LR-ESI-MS for M = $C_{46}H_{68}BrN_5O_8$: Calculated $[M + H]^+$: 899.98, found: 900.40.



Ethyl 3-(4-amino-3-((2-bromo-4-(bromomethyl)phenyl)ethynyl)phenyl)propanoate (3.12a): Compound **3.4** (0.07 g, 0.33 mmol) was dissolved in dry DMF (20 mL). 1,2-dibromobenzene (0.23 g, 0.71 mmol) was added, followed by $Pd(PPh_3)_4$ (0.03 g, 0.03 mmol), CuI (0.02 g, 0.08 mmol) and triethylamine (0.45 mL, 3.20 mmol). The orange reaction mixture was left to stir at 80 °C under N_2. After 21 hours, EtOAc (50 mL) was added. The reaction mixture was washed with H_2O (2 x 50 mL) and brine (2 x 50 mL). The combined organic phases were dried over $MgSO_4$ and the solvent removed *in vacuo* to leave a yellow oil. Automated flash chromatography (hexane to EtOAc to MeOH) gave **3.12a** as a brown oil (0.03 g, 0.06 mmol, 17%).

^{1}H NMR ($CDCl_3$, 400 MHz):δ/ppm = 7.62 (d, $^3J_{HH}$ = 1.9 Hz, 1H, Ar-H), 7.58 (d, $^3J_{HH}$ = 8.1 Hz, 1H, Ar-H), 7.20 (d, $^3J_{HH}$ = 2.0 Hz, 1H, Ar-H), 7.15 (d, $^3J_{HH}$ = 8.5 Hz, 1H, Ar-H), 7.03 (dd, $^3J_{HH}$ = 8.3, $^4J_{HH}$ = 2.1 Hz, 1H, Ar-H), 6.66 (d, $^3J_{HH}$ = 8.3 Hz, 1H, Ar-H), 4.26 (br s, 2H, NH_2), 4.15 (q, $^3J_{HH}$ = 7.1 Hz, 2H, $COOCH_2CH_3$), 2.84 (t, $^3J_{HH}$ = 7.7 Hz, 2H, CH_2), 2.58 (t, $^3J_{HH}$ = 7.7 Hz, 2H, CH_2), 2.27 (s, 2H, $ArCH_2Br$), 1.25 (t, $^3J_{HH}$ = 2.0 Hz, 3H, $COOCH_2CH_3$).

LR ESI-MS: For M = $C_{20}H_{19}Br_2NO_2$: Calculated $[M + H]^+$ = 465.98, found 465.30.



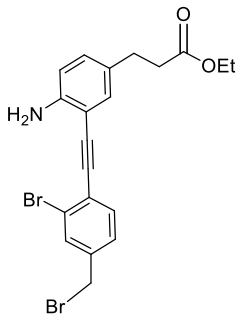
2-Bromo-4-(bromomethyl)-1-iodobenzene (**3.13)**: 3-Bromo-4-iodotoluene (1.20 mL, 8.42 mmol) was dissolved in $CHCl_3$ (30 mL). NBS (1.86 g, 10.44 mmol) was added followed by AIBN (0.02 g, 0.14 mmol), forming a yellow solution which was left to stir at 80 °C under N_2. During heating, a colour change from yellow to red to brown was observed over 2 hours. After 22 hours, the reaction mixture was orange in colour. Additional portions of AIBN (0.06 g, 0.34 mmol) and NBS (1.71 g, 9.63 mmol) were added. After a further 23 hours, the reaction mixture was red in colour. The solution was allowed to cool to room temperature before being washed with water (3 x 50 mL). The combined organic phases were dried over $MgSO_4$ and the solvent removed *in vacuo* to leave a red oil. Automated flash chromatography (hexane to EtOAc) gave a red solid (1.53 g). This solid was re-dissolved in EtOAc (20

mL) and the solution washed with sodium thiosulphate solution (sat., aq., 25 mL). The organic phase was reduced *in vacuo* to leave **3.13** as a white crystalline solid (1.17 g, 3.12 mmol, 37%).

^{1}H NMR ($CDCl_3$,400 MHz): δ/ppm = 7.82 (d, $^3J_{HH}$ = 8.1 Hz, 1H, Ar-H), 7.65 (d, $^4J_{HH}$ = 2.0 Hz, 1H, Ar-H), 7.02 (dd, $^4J_{HH}$ = 8.1 Hz, $^3J_{HH}$ = 2.1 Hz, 1H, Ar-H), 4.37 (s, 2H, ArCH_2Br).

^{13}C NMR (101 MHz, $CDCl_3$) δ/ppm = 140.5, 139.4, 132.9, 129.9, 129.0, 101.2, 31.5.

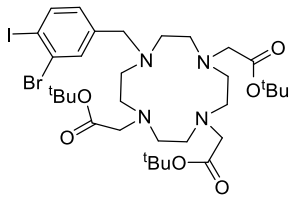
HR-ESI-MS for M = $C_7H_5Br_2I$: Calculated $[M + H]^+$: 373.7797, found: 373.7803.



Ethyl 3-(4-amino-3-((2-bromo-4-(bromomethyl)phenyl)ethynyl)phenyl)propanoate (3.12b):
Compound **3.13** (0.20 g, 0.54 mmol) was dissolved in dry DMF (5 mL). Ethyl 3-(4-amino-3-ethynylphenyl)propanoate (0.05 g, 0.2 mmol) was added, followed by $PdCl_2(PPh_3)_2$ (0.02 g, 0.03 mmol), CuI (0.02 g, 0.08 mmol) and dry DIPA (20 mL), forming a yellow solution which was left to stir under N_2 at 70 °C. After 22 hours, EtOAc (50 mL) was added and the reaction mixture washed with water (2 x 50 mL) and brine (50 mL). The combined organic phases were dried over $MgSO_4$ and the solvent removed *in vacuo* to leave a yellow oil. Automated flash chromatography (hexane to EtOAc, then to MeOH, followed by DCM to 10% MeOH in DCM) gave **3.12b** as a yellow oil (0.03 g, 0.06 mmol, 26%).

^{1}H NMR ($CDCl_3$, 400 MHz) δ/ppm = 7.65 (d, $^4J_{HH}$ = 1.1 Hz, 1H, Ar-H), 7.46 (d, $^3J_{HH}$ = 7.9 Hz, 1H, Ar-H), 7.31 (dd, $^3J_{HH}$ = 7.9, $^4J_{HH}$ = 1.5 Hz, 1H, Ar-H), 7.22 (d, $^3J_{HH}$ = 2.0 Hz, 1H, Ar-H), 6.99 (dd, $^3J_{HH}$ = 8.2, $^4J_{HH}$ = 2.1 Hz, 1H, Ar-H), 6.66 (d, $^3J_{HH}$ = 8.3 Hz, 1H, Ar-H), 4.40 (br s, 2H, NH_2), 4.13 (q, $^3J_{HH}$ = 7.1 Hz, 2H, COOCH_2CH$_3$), 3.62 (s, 2H, ArCH_2), 2.83 (t, $^3J_{HH}$ = 7.7 Hz, 2H, ArCH$_2$CH_2), 2.57 (t, $^3J_{HH}$ = 7.8 Hz, 2H, ArCH_2CH$_2$), 1.24 (t, $^3J_{HH}$ = 7.1 Hz, 3H, COOCH$_2$CH_3).

LR-ESI-MS for M = $C_{20}H_{19}Br_2NO_2$: Calculated $[M + Na]^+$: 488.19, found: 488.20.

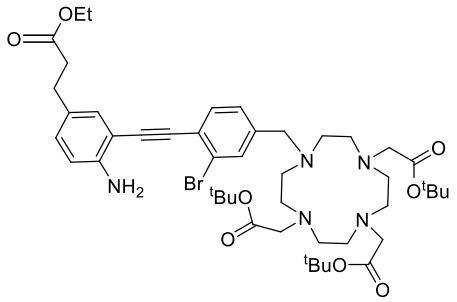


Tri-tert-butyl 2,2',2''-(10-(3-bromo-4-iodobenzyl)-1,4,7,10-tetraazacyclododecane-1,4,7-triyl)triacetate (**3.14**): Compound **3.8** (0.15 g, 0.26 mmol) was dissolved in MeCN (60 mL). Compound **3.13** (0.10 g, 0.35 mmol) was added, followed by K_2CO_3 (0.70 g, 5.10 mmol), forming a white solution which was left to stir at 100 °C under N_2. After 70 hours, the reaction mixture was allowed to cool to room temperature and filtered to remove K_2CO_3. The solvent was removed *in vacuo* to leave an orange residue. Automated flash chromatography (DCM to 2% MeOH in DCM) gave **3.8** as a yellow solid (0.17 g, 0.20 mmol, 80%).

^{1}H NMR ($CDCl_3$, 400 MHz): δ/ppm = 7.88 (dd, $^3J_{HH}$ = 8.3 Hz, $^4J_{HH}$ = 1.9 Hz, 1H, Ar-H), 7.69 (d, $^3J_{HH}$ = 8.0 Hz, 1H, Ar-H), 7.04 (dd, $^3J_{HH}$ = 8.3 Hz, $^4J_{HH}$ = 1.9 Hz, 1H, Ar-H), 3.45 – 1.98 (m, 28H, CH_2), 1.35 (s, 27H, O^{t}Bu).

^{13}C NMR ($CDCl_3$, 101 MHz): δ/ppm = 211.4, 167.4, 157.3, 142.9, 132.6, 131.5, 118.0, 103.7, 87.4, 83.1, 56.2, 52.1, 28.2, 28.0.

HR-ESI-MS for M = $C_{33}H_{54}BrIN_4O_6$: Calculated $[M + H]^+$: 809.2350, found: 809.2355.



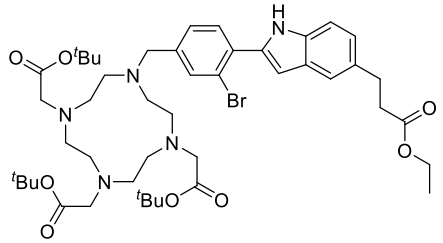
Tri-tert-butyl 2,2',2''-(10-(4-((2-amino-5-(3-ethoxy-3-oxopropyl)phenyl)ethynyl)-3-bromobenzyl)-1,4,7,10-tetraazacyclododecane-1,4,7-triyl)triacetate (3.10b): Compound **3.4** (0.18 g, 0.83 mmol) was dissolved in dry DMF (40 mL). Dry DIPA (5 mL) was added, followed by compound **3.14** (0.81 g, 1.00 mmol), CuI (15.90 mg, 0.08 mmol) and $PdCl_2(PPh_3)_2$ (58.90 mg, 0.08 mmol) forming a yellow solution which was heated to 80 °C under N_2. After 22 hours, the temperature was increased to 110 °C. After a further 2 hours EtOAc (50 mL) was added to the brown reaction mixture. The reaction mixture was washed with H_2O (2 x 50 mL) and brine (2 x 50 mL) before the combined organic phases were dried over $MgSO_4$. The solvent was removed *in vacuo* to leave a yellow oil. Automated flash chromatography (DCM to 50% MeOH in DCM) gave **3.10b** as a yellow oil (0.31 g, 0.35 mmol, 42%).

^{1}H NMR (400 MHz, $CDCl_3$) δ/ppm = 7.44 (d, $^3J_{HH}$ = 7.9 Hz, 1H, Ar-H), 7.35 (d, $^3J_{HH}$ = 9.2 Hz, 1H, Ar-H), 7.10 (d, $^3J_{HH}$ = 1.8 Hz, 1H, Ar-H), 6.94 (dd, $^3J_{HH}$ = 8.2, 1.8 Hz, 1H, Ar-H), 6.68 (d, $^3J_{HH}$ = 8.3 Hz, 1H, Ar-H), 4.51 (s, 1H, ArCH_2), 4.05 (q, $^3J_{HH}$ = 7.1 Hz, 1H, CH_2CH$_3$), 3.08 – 2.91 (m, 4H, CH_2), 2.86 (d, $^3J_{HH}$ = 6.5 Hz, 1H, CH_2), 2.80 – 2.70 (m, 3H, CH_2), 2.66 (d, $^3J_{HH}$ = 20.1 Hz, 3H, CH_2), 2.54 – 2.45

(m, 3H, C$\underline{H}_2$), 2.44 – 2.22 (m, 4H, C$\underline{H}_2$), 2.22 – 2.11 (m, 2H, C$\underline{H}_2$), 1.40 (s, 27H, $^t\underline{Bu}$O), 1.21 (t, $^3J_{HH}$ = 7.1 Hz, 3H, CH$_2$C$\underline{H}_3$).

^{13}C NMR (101 MHz, $CDCl_3$) δ/ppm = 173.4, 172.9, 172.5, 162.5, 147.2, 139.1, 134.8, 134.1, 132.7, 131.3, 130.5, 129.5, 129.1, 125.2, 124.8, 114.8, 106.7, 92.6, 91.9, 83.1, 82.4, 60.4, 58.9, 58.1, 56.0, 55.7, 53.5, 52.4, 50.4, 49.9, 36.5, 36.2, 31.4, 29.9, 28.0, 27.8, 20.2, 18.4, 14.2, 13.6.

HR-ESI-MS: Calculated for M = $C_{46}H_{69}N_5O_8Br$: $[M+H]^+$ expected = 898.4330 found = 898.4332.

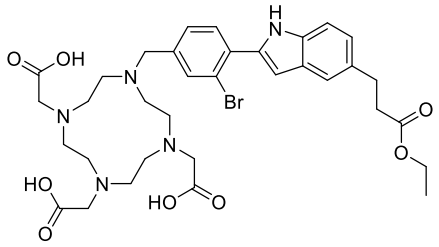


Tri-tert-butyl 2,2',2''-(10-(3-bromo-4-(5-(3-ethoxy-3-oxopropyl)-1H-indol-2-yl)benzyl)-1,4,7,10-tetraazacyclododecane-1,4,7-triyl)triacetate (3.11b): Compound **4** (0.31 g, 0.34 mmol) was dissolved in EtOH (40 mL). $AuCl_3$ (25.80 mg, 0.09 mmol) was added, forming a brown solution which was left to stir at 80 °C. After 4 hours, the solvent was removed *in vacuo* to leave a brown solid. Automated flash chromatography (DCM to 20% MeOH in DCM) yielded **3.11b** as a yellow oil (0.19 g, 0.21 mmol, 62%).

^{1}H NMR (400 MHz, $CDCl_3$) δ/ppm = 7.47 (d, $^3J_{HH}$ = 7.9 Hz, 1H, Ar-$\underline{H}$), 7.39 (d, $^3J_{HH}$ = 7.9 Hz, 1H, Ar-$\underline{H}$), 7.15 (d, $^3J_{HH}$ = 1.8 Hz, 1H, Ar-$\underline{H}$), 6.98 (dd, $^3J_{HH}$ = 8.2, 1.7 Hz, 1H, Ar-$\underline{H}$), 4.44 (s, 1H), 4.09 (q, $^3J_{HH}$ = 7.1 Hz, 2H, C$\underline{H}_2$CH$_3$), 3.14 (s, 2H), 2.94 (m, 5H, C$\underline{H}_2$), 2.85 – 2.72 (m, 4H, C$\underline{H}_2$), 2.65 (s, 2H, C$\underline{H}_2$), 2.52 (d, $^3J_{HH}$ = 7.5 Hz, 2H, C$\underline{H}_2$), 2.44 – 2.08 (m, 7H, C$\underline{H}_2$), 1.76 (d, $^3J_{HH}$ = 8.0 Hz, 1H), 1.44 (d, $^3J_{HH}$ = 9.0 Hz, 27H, $^t\underline{Bu}$O), 1.21 (t, $^3J_{HH}$ = 7.1 Hz, 4H, CH$_2$C$\underline{H}_3$).

^{13}C NMR (101 MHz, $CDCl_3$) δ/ppm = 173.6, 172.5, 138.9, 135.7, 135.5, 133.7, 132.7, 131.7, 131.3, 130.0, 128.3, 125.2, 123.9, 123.1, 121.2, 119.5, 112.2, 103.3, 83.1, 83.1, 82.4, 60.4, 58.6, 56.2, 56.0, 55.7, 53.5, 49.8, 37.0, 36.2, 31.6, 31.3, 28.0, 27.9, 22.7, 14.3, 14.2.

HR-ESI-MS: Calculated for M = $C_{46}H_{69}N_5O_8Br$: : $[M+H]^+$ expected = 898.4330 found = 898.4335.

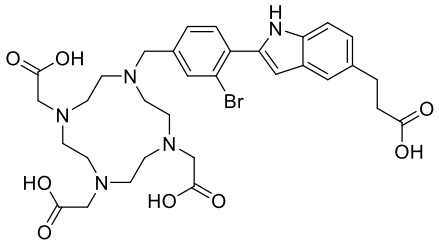


2,2',2''-(10-(3-Bromo-4-(5-(3-ethoxy-3-oxopropyl)-1H-indol-2-yl)benzyl)-1,4,7,10-tetraazacyclododecane-1,4,7-triyl)triacetic acid (**3.15)**: Compound **3.11b** (0.14 g, 0.16 mmol) was dissolved in DCM (4 mL). TFA (4 mL) was added, forming a brown solution which was left to stir at room temperature. After 17 hours, an additional portion of DCM (1 mL) and TFA (1 mL) was added. After a further 4 hours, the solvent was removed *in vacuo* to leave a brown oil. Automated flash chromatography (DCM to MeOH to MeOH + 0.5% TEA) gave **3.15** as a yellow oil (0.08 g, 0.11 mmol, 69%).

^{1}H NMR (400 MHz, CD_3OD) δ/ppm = 8.03 – 7.94 (m, 1H, Ar-H), 7.66 (dd, $^{3}J_{HH}$ = 27.2, $^{4}J_{HH}$ = 9.9 Hz, 2H, Ar-H), 7.40 (s, 1H, Ar-H), 7.33 (d, $^{3}J_{HH}$ = 8.3 Hz, 1H, Ar-H), 7.03 (d, $^{3}J_{HH}$ = 8.5 Hz, 1H, Ar-H), 4.65 – 4.13 (m, 3H, CH_2), 4.12 – 4.01 (m, 1H, CH_2), 3.99 – 3.35 (m, 12H, CH_2), 3.29 (d, *J* = 2.3 Hz, 21H, CH_2), 2.98 (t, $^{3}J_{HH}$ = 7.8 Hz, 2H, CH_2), 2.80 (d, $^{3}J_{HH}$ = 7.2 Hz, 2H, CH_2), 2.62 (t, $^{3}J_{HH}$ = 7.6 Hz, 2H, CH_2), 1.29 (d, $^{3}J_{HH}$ = 10.0 Hz, 1H, CH_3).

^{13}C NMR (101 MHz, CD_3OD) δ/ppm = 260.0, 248.6, 243.5, 237.3, 232.8, 219.4, 211.5, 199.3, 191.7, 184.2, 176.6, 168.8, 162.0, 152.1, 140.7, 129.4, 117.3, 103.4, 86.5, 66.1, 64.4, 56.2, 51.6, 35.0, 29.1, 21.9.

HR-ESI-MS: Calculated for M = $C_{34}H_{45}N_5O_8Br$: $[M+H]^+$ expected = 730.2452 found = 730.2461.



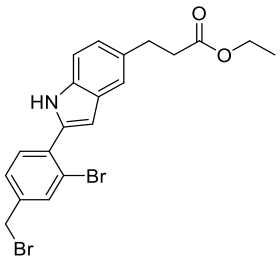
2,2',2''-(10-(3-Bromo-4-(5-(2-carboxyethyl)-1H-indol-2-yl)benzyl)-1,4,7,10-tetraazacyclododecane-1,4,7-triyl)triacetic acid (GPR-L1/3.16): Compound **3.15** (0.08 g, 0.11 mmol) was dissolved in MeOH (20 mL). NaOH (0.11 g, 2.73 mmol) in H_2O (5 mL) was added, forming a yellow solution which was left to stir at 50 °C. After 22 hours, the reaction mixture was allowed to cool to room temperature and the MeOH removed *in vacuo*, leaving a yellow solution. This solution was brought to pH 2 by addition of HCl (aq., 2.0 M) before the solvent was removed *in vacuo* to leave

a brown solid. Automated flash chromatography (C_{18} cartridge, H_2O + 0.1% TFA to MeCN + 0.1% TFA) gave **3.16** as a brown oil (39.10 mg, 0.06 mmol, 51%).

^{1}H NMR (400 MHz, CD_3OD) δ/ppm = 7.84 (d, $^3J_{HH}$ = 13.7 Hz, 2H, Ar-H), 7.60 – 7.49 (m, 2H, Ar-H), 7.45 – 7.35 (m, 1H, Ar-H), 7.27 (d, $^3J_{HH}$ = 1.9 Hz, 1H, Ar-H), 7.11 (dd, $^3J_{HH}$ = 8.3, 2.0 Hz, 1H, Ar-H), 6.94 (d, $^3J_{HH}$ = 8.3 Hz, 1H, Ar-H), 4.36 – 3.22 (m, 28H, CH_2), 3.03 (m, 17H, CH_2), 2.75 (t, $^3J_{HH}$ = 7.4 Hz, 3H, CH_2), 2.47 (t, $^3J_{HH}$ = 7.5 Hz, 2H, CH_2).

^{13}C NMR (101 MHz, CD_3OD) δ/ppm = 176.95, 163.07, 161.93, 161.55, 135.39, 133.74, 132.75, 127.03, 119.19, 116.33, 58.60, 58.41, 54.44, 36.97, 31.44.

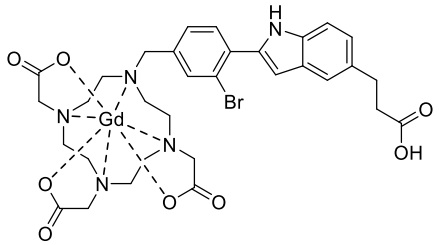
HR-ESI-MS: Calculated for M = $C_{32}H_{41}N_5O_8Br$: $[M+H]^+$ expected = 702.2138 found = 702.2117.



Ethyl 3-(2-(2-bromo-4-(bromomethyl)phenyl)-1H-indol-5-yl)propanoate (3.17): Compound **3.12b** (0.01 g, 0.03 mmol) was dissolved in EtOH (10 mL). $AuCl_3$ (5.80 g, 0.02 mmol) was added, forming a yellow solution which was left to stir at 80 °C. After 17 hours, the reaction mixture was red in colour. The solvent was removed *in vacuo* to leave a brown solid. Automated flash chromatography (DCM to 25% MeOH in DCM) gave **3.17** as a purple solid (8.70 mg, 0.02 mmol, 62%).

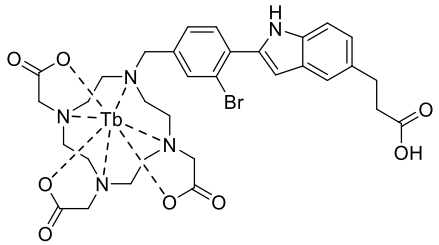
^{1}H NMR ($CDCl_3$, 400 MHz) δ/ppm = 7.66 (dd, $^3J_{HH}$ = 12.8 Hz, $^4J_{HH}$ = 7.7 Hz, 2H, Ar-H), 7.59 – 7.52 (m, 2H, Ar-H), 7.46 (td, $^3J_{HH}$ = 7.9, $^4J_{HH}$.2.9 Hz, 2H, Ar-H), 7.36 – 7.32 (m, 1H, Ar-H), 4.24 (q, $^3J_{HH}$ = 5.6, 2H, $COCH_2CH_3$), 4.14 (br s, 1H, NH), 3.64 (s, 2H, $ArCH_2Br$), 3.03 (m, 2H, $ArCH_2CH_2$), 2.73 – 2.58 (m, 2H, $ArCH_2CH_2$), 2.40 – 2.24 (m, 3H, $COCH_2CH_3$).

LR-ESI-MS for M = $C_{20}H_{19}Br_2NO_2$: Calculated $[M + H]^+$: 466.19, found: 466.80.



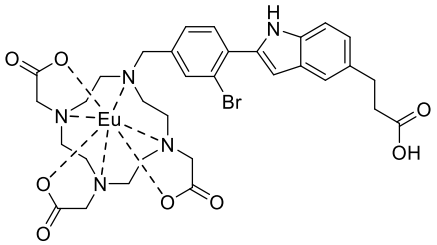
[Gadolinium (2,2',2''-(10-(3-bromo-4-(5-(3-ethoxy-3-oxopropyl)-1H-indol-2-yl)benzyl)-1,4,7,10-tetraazacyclododecane-1,4,7-triyl)triacetate)] ([Gd(GPR-L1)]/3.18): GPR-L1 (14.00 mg, 19.90 μmol) was dissolved in MeOH (10 mL). $Gd(NO_3)_3 \cdot 6H_2O$ (14.40 mg, 31.90 μmol) was added and the pH brought to 6.5 by addition of NaOH (0.10 M, aq.) and the reaction mixture left to stir at 50 °C. After 48 hours, the solvent was removed *in vacuo* to leave a yellow solid. Reverse phase automated chromatography (99.9% H_2O + 0.1% TFA to 99.9% MeCN + 0.1% TFA) gave **1** as a yellow solid (3.20 mg, 3.64 μmol, 18%).

HR-ESI-MS: Calculated for M = $C_{32}H_{37}BrGdN_5O_8$ - Expected $[M+H]^+$ = 857.1139 found = 857.1123.



[Terbium (2,2',2''-(10-(3-bromo-4-(5-(3-ethoxy-3-oxopropyl)-1H-indol-2-yl)benzyl)-1,4,7,10-tetraazacyclododecane-1,4,7-triyl)triacetate)] ([Tb(GPR-L1)]/3.19): GPR-L1 (10.00 mg, 14.20 μmol) was dissolved in H_2O (5 mL). $Tb(OTf)_3$ (11.40 mg, 18.80 μmol) was added and the reaction mixture brought to pH 6.5 by addition of NaOH (0.10 M, aq.) and left to stir at room temperature. After 21 hours, LCMS indicated only partial complexation. An additional portion of $Tb(OTf)_3$ (9.80 mg, 16.20 μmol) was added and the pH readjusted to 6.5. After a further 72 hours, LCMS indicated total complexation. The solvent was removed *in vacuo* to leave a yellow solid. Reverse phase automated chromatography (99.9% H_2O + 0.1% TFA to 99.9% MeCN + 0.1% TFA) gave **2** as a yellow solid (6.26 mg, 7.10 μmol, 50%).

HR-ESI-MS: Calculated for M = $C_{32}H_{37}BrTbN_5O_8$: Expected $[M+H]^+$ = 858.1152 found = 858.1141.



[Europium (2,2',2''-(10-(3-bromo-4-(5-(3-ethoxy-3-oxopropyl)-1H-indol-2-yl)benzyl)-1,4,7,10-tetraazacyclododecane-1,4,7-triyl)triacetate)] ([Eu(GPR-L1]/3.20): **GPR-L1** (3.90 mg, 5.6 µmol) was dissolved in H_2O (5 mL). $EuCl_3$ (3.00 mg, 11.60 µmol) was added and the red reaction mixture adjusted to pH 6 by addition of NaOH (0.1 M, dropwise) before being left to stir at room temperature. After 67 hours, LCMS indicated no reaction progress and an additional portion of $EuCl_3$ (6.60 mg, 25.50 µmol) was added and the pH readjusted to 6 before the reaction mixture was left to stir at room temperature. After a further 24 hours, an additional portion of $EuCl_3$ was added and the pH readjusted to 6. After a further 7 days, MALDI-MS suggested the presence of product. The reaction mixture was lyophilised to leave a brown solid. Reverse phase automated flash chromatography (H_2O to MeCN + 0.1% TFA) gave **3.20** as a brown solid (2.10 mg, 2.5 µmol, 45%).

HR-ESI-MS: M = $C_{32}H_{37}Br^{153}EuN_5O_8$, expected $[M+H]^+$ = 852.1116, found = 852.1115.

7.7. Synthesis of Compounds in Chapter 4

7.7.1. General Considerations

Many of the compounds discussed in Chapter 4 of this thesis are complex peptides with extended amino acid sequences. For the sake of simplicity, they are referred to in the experimental summary by an abbreviation, with the table below summarising the amino acid sequence of each peptide. All of the peptides contained a synthetic amino acid variant incorporating a propargyl alkyne at the 12th position to enable peptide functionalisation *via* copper-catalysed alkyne-azide cycloaddition (CuAAC) chemistry.

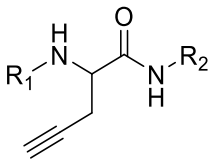


Figure 7.1: General structure of peptides used, displaying the modified amino acid at the 12th position.

The peptides used in this synthesis were provided by Dr. Ben Jones at the Imperial College Centre for Translational and Experimental Medicine.

Peptide	R_1	R_2
Ex4-Pra^{12}	HisGlyGluGlyThrPhe ThrSerAspLeuSer	GlnMetGluGluGluAlaValArgLeuPheIleGluTrpLeuLysAsnGlyGlyProSerSer GlyAlaProProProSerNH$_2$
Ex4-Pra^{12}-C$_{16}$	HisGlyGluGlyThrPhe ThrSerAspLeuSer	GlnMetGluGluGluAlaValArgLeuPheIleGluTrpLeuLysAsnGlyGlyProSerSer GlyAlaProProProSerGlyLys-hexadecanoic acid
Ex9-Pra^{12}	AspLeuSer	GlnMetGluGluGluAlaValArgLeuPheIleGluTrpLeuLysAsnGlyGlyProSerSer GlyAlaProProProSerNH$_2$
Ex4-Phe^1-Pra^{12}	PheGlyGluGlyThrPhe ThrSerAspLeuSer	GlnMetGluGluGluAlaValArgLeuPheIleGluTrpLeuLysAsnGlyGlyProSerSer GlyAlaProProProSerNH$_2$
Ex4-Asp^3-Pra^{12}	HisGlyAspGlyThrPhe ThrSerAspLeuSer	GlnMetGluGluGluAlaValArgLeuPheIleGluTrpLeuLysAsnGlyGlyProSerSer GlyAlaProProProSerNH$_2$

Table 7.1: Abbreviations and amino acid sequences of the peptides used, with R_1 and R_2 referring to the sequences in **Figure 7.1**.

The terbium(III) complex which was conjugated to each of these peptides was provided by Yue Wu, a synthetic chemist working under Professor Gary Ka-Leung Wong at Hong Kong Baptist University. This complex contained an azide group to enable CuAAC chemistry and is shown in **Figure 7.2**. It is referred to in the experimental text as **Yue286**.

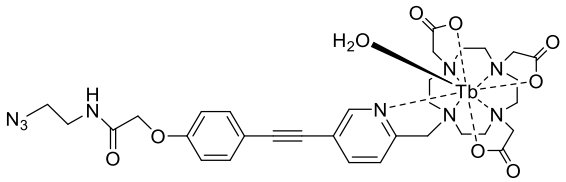


Figure 7.2: The Tb(III) complex provided by Yue Wu (**Yue286**).

7.7.2. Experimental Procedures

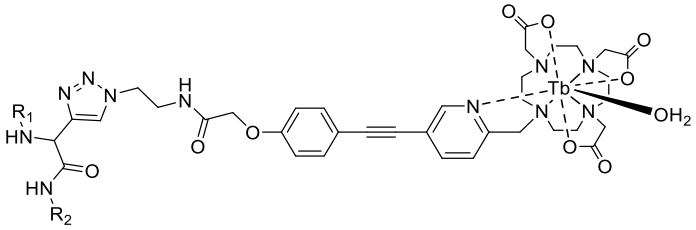


Figure 7.4: General structure of the conjugates synthesised.

Ex4-Pra^{12}-Tb (**4.1**): **Yue286** (0.60 mg, 0.70 μmol) was dissolved in H_2O (5 mL). **Ex4-Pra^{12}** (1.50 mg, 0.36 μmol) was added, followed by $CuSO_4 \cdot 5H_2O$ (4.50 mg, 18.02 μmol) and sodium ascorbate (0.60 mg, 3.03 μmol), forming a yellow solution which was left to stir at room temperature. After 24 hours, LCMS indicated product formation and the reaction mixture was lyophilised, leaving a green solid. Reverse phase automated flash chromatography (H_2O to MeCN + 0.1% TFA) gave **4.1** as a white solid (1.70 mg, 0.34 μmol, 94%).

LC-MS: MW = 5007.15, found 836.0637 $[M]^{6+}$, 1001.6753 $[M]^{5+}$, 1247.8477 $[M]^{4+}$, 1663.4458 $[M]^{3+}$, 5004.0000 $[M]^{+}$.

Ex4-Pra^{12}-C$_{16}$-Tb (4.2): **Ex4-Pra^{12}-C$_{16}$** (1.50 mg, 0.33 μmol) was dissolved in H_2O (5 mL) NaOH (aq., 0.1 M, 2 drops) was added to aid solubility. **Yue286** (0.80 mg, 0.94 μmol) was added, followed by CuI (12.40 mg, 65.01 μmol), forming a yellow solution which was left to stir at room temperature. After 22 hours, LCMS indicated product formation and the reaction mixture was lyophilised, leaving a green solid. Reverse phase automated flash chromatography (H_2O to MeCN + 0.1% TFA) gave **4.2** as a white solid (0.90 mg, 0.17 μmol, 50%).

LC-MS: MW = 5461.75, found 1089.20 $[M]^{5+}$, 1361.20 $[M]^{4+}$, 1814.90 $[M]^{3+}$, 5458.00 $[M]^{+}$.

Ex9-Pra^{12}-Tb (4.3): **Yue286** (0.43 mg, 0.50 μmol) was dissolved in H_2O (5 mL). **Ex9-Pra^{12}** (1.50 mg, 0.45 μmol) was added, followed by $CuSO_4 \cdot 5H_2O$ (0.10 mg, 0.40 μmol) and sodium ascorbate (0.20 mg, 1.01 μmol), forming a yellow solution which was left to stir at room temperature. After 24 hours, LCMS indicated that no reaction had taken place. An additional portion of by $CuSO_4 \cdot 5H_2O$ (19.30 mg, 0.08 mmol) was added, followed by sodium ascorbate (9.80 mg, 0.05 mmol). After a further 15 hours, LCMS indicated product formation and the reaction mixture was lyophilised, leaving a green solid. Reverse phase automated flash chromatography (H_2O to MeCN + 0.1% TFA) gave **4.3** as a white solid (1.70 mg, 0.41 μmol, 91%).

LC-MS: MW = 4206.37, found 1047.80 $[M]^{4+}$, 1396.70 $[M]^{3+}$.

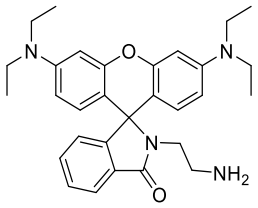
Ex-Phe^{1}-Pra^{12}-Tb (4.4): **Yue286** (0.40 mg, 0.50 μmol) was dissolved in H_2O (5 mL). **Ex-Phe^{1}-Pra^{12}** (1.50 mg, 0.36 μmol) was added followed by NaOH (aq., 0.1 M, 4 drops), $CuSO_4 \cdot 5H_2O$ (10.50 mg, 42.10 μmol) and sodium ascorbate (5.30 mg, 0.03 mmol), forming a yellow solution which was left to stir at room temperature. After 2 days, LCMS showed no reaction progress. Additional portions of $CuSO_4 \cdot 5H_2O$ (10.50 mg, 42.10 μmol) and sodium ascorbate (5.30 mg, 0.03 mmol) were added. After a further 4 days, LCMS indicated product formation and the reaction mixture was lyophilised, leaving a green solid. Reverse phase automated flash chromatography (H_2O to MeCN + 0.1% TFA) gave **4.4** as a white solid (1.30 mg, 0.26 μmol, 72%).

LC-MS: MW = 5017.18, found 1254.30 $[M]^{4+}$, 1672.00 $[M]^{3+}$, 5013.00 $[M]^{+}$.

Ex-Asp^{3}-Pra^{12}-Tb (4.5): **Yue286** (0.90 mg, 1.10 μmol) was dissolved in H_2O (5 mL). **Ex-Asp^{3}-Pra^{12}** (1.80 mg, 0.45 μmol) was added, followed by $CuSO_4 \cdot 5H_2O$ (9.50 mg, 0.04 mmol) and sodium ascorbate (6.40 mg, 0.03 mmol), forming a yellow solution which was left to stir at room temperature. After 2 days, LCMS indicated no reaction progress and additional portions of $CuSO_4 \cdot 5H_2O$ (9.50 mg, 0.04 mmol) and sodium ascorbate (6.40 mg, 0.03 mmol) were added. After a further 4 days, LCMS indicated

product formation and the reaction mixture was lyophilised, leaving a green solid. Reverse phase automated flash chromatography (H_2O to MeCN + 0.1% TFA) gave **4.5** as a white solid (0.50 mg, 0.10 μmol, 28%).

LC-MS: MW = 4993.12, found 1248.30 $[M]^{4+}$, 1669.30 $[M]^{3+}$, 4989.00 $[M]^{+}$.

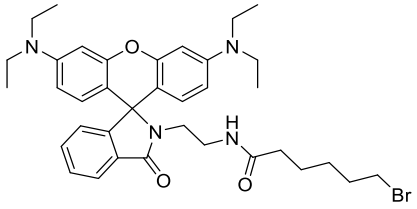


2-(2-Aminoethyl)-3',6'-bis(diethylamino)spiro[isoindoline-1,9'-xanthen]-3-one[8] (4.6): Rhodamine B (1.05 g, 2.20 mmol) was dissolved in EtOH (30 mL). Ethylenediamine (5 mL) was added, forming a pink solution which was left to stir under reflux at 90 °C. After 23 hours, the solvent was removed *in vacuo* to leave an orange residue, which was then re-dissolved in DCM and washed with H_2O (2 x 50 mL) and brine (100 mL). The combined organic phases were dried over $MgSO_4$ and the solvent removed *in vacuo* to leave **4.6** as an orange solid (0.95 g, 1.95 mmol, 93%).

^{1}H NMR (400 MHz, $CDCl_3$) δ/ppm = 7.90 – 7.82 (m, 1H, Ar-H), 7.48 – 7.39 (m, 2H, Ar-H), 7.06 (dd, $^3J_{HH}$ = 15.3, 7.4 Hz, 1H, Ar-H), 6.45 – 6.23 (m, 6H, Ar-H), 3.33 (q, $^3J_{HH}$ = 7.1 Hz, 7H, NCH_2CH_3), 3.27 (t, $^3J_{HH}$ = 5.6 Hz, 2H, NCH_2CH_2N), 2.73 (m, $^3J_{HH}$ = 5.0 Hz, 1H, NCH_2CH_2N), 1.16 (t, $^3J_{HH}$ = 7.0 Hz, 11H, NCH_2CH_3).
^{13}C NMR (101 MHz, $CDCl_3$) δ/ppm = 170.7, 153.4, 150.7, 150.6, 135.5, 130.5, 128.6, 128.4, 125.4, 124.7, 108.5, 104.3, 97.8, 65.0, 44.5, 41.3, 40.8, 12.7.

HR-ESI-MS: Calculated for M = $C_{30}H_{36}N_4O_2$ – expected $[M+H]^+$ = 485.2917 , found 485.2918.

Data corresponds to literature[8].



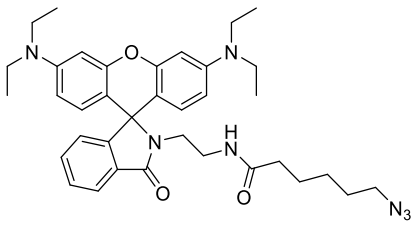
***N*-(2-(3',6'-Bis(diethylamino)-3-oxospiro[isoindoline-1,9'-xanthen]-2-yl)ethyl)-6-bromohexanamide (4.7)**: Compound **4.6** (0.47 g, 0.98 mmol) was dissolved in DCM (30 mL). DIPEA (0.34 mL, 1.96 mmol) was added, followed by HATU (0.37 g, 0.98 mmol) and 6-bromohexanoic acid (0.21 g, 1.08 mmol), forming an orange solution which was left to stir at room temperature. After 19 hours, the reaction mixture was washed with H_2O (2 x 50 mL) and brine (50 mL) before the combined

organic phases were dried over $MgSO_4$ and the solvent removed *in vacuo* to leave an orange solid. Automated flash chromatography (DCM to 25% MeOH in DCM) gave **4.7** as a pink oil (0.14 g, 0.22 mmol, 22%).

^{1}H NMR (400 MHz, $CDCl_3$) δ/ppm = 7.86 (dd, $^3J_{HH}$ = 5.7, $^4J_{HH}$ 2.7 Hz, 1H, Ar-H), 7.46 – 7.42 (m, 2H, Ar-H), 7.09 – 7.04 (m, 1H, Ar-H), 6.90 (t, $^3J_{HH}$ = 4.2 Hz, 1H, Ar-H), 6.42 – 6.21 (m, 6H, Ar-H), 3.69 (m, 2H, NCH_2CH_2N), 3.32 (m, 13H, NCH_2CH_2N, CH_2Br and NCH_2CH_3) 2.08 (t, $^3J_{HH}$ = 7.5 Hz, 2H, CH_2), 1.82 (p, $^3J_{HH}$ = 6.9 Hz, 2H, CH_2), 1.58 (p, $^3J_{HH}$ = 7.5 Hz, 2H, CH_2), 1.40 (p, $^3J_{HH}$ = 7.4 Hz, 2H, CH_2), 1.15 (t, $^3J_{HH}$ = 7.0 Hz, 13H, NCH_2CH_3).

^{13}C NMR (101 MHz, $CDCl_3$) δ/ppm = 173.0, 169.9, 165.8, 153.9, 153.5, 149.0, 133.0, 130.4, 128.4, 108.3, 104.7, 97.9, 65.9, 58.4, 53.5, 44.5, 40.5, 36.4, 33.8, 27.8, 24.8, 18.5, 12.7.

HR-ESI-MS: Calculated for M = $C_{36}H_{45}BrN_4O_3$ – expected $[M+H]^+$ = 661.2748 , found 661.2756.

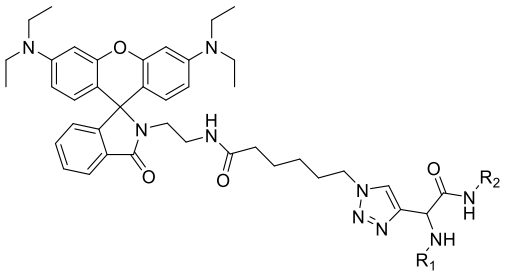


6-Azido-*N*-(2-(3',6'-bis(diethylamino)-3-oxospiro[isoindoline-1,9'-xanthen]-2-yl)ethyl)hexanamide (4.8): Compound **4.7** (0.14 g, 0.22 mmol) was dissolved in dry DMF (20 mL). NaN_3 (0.02 g, 0.35 mmol) was added, forming a bright pink solution which was left to stir at 60 °C. After 1 minute, the reaction mixture was pale orange in colour. After 17 hours, the reaction mixture was allowed to cool to room temperature and DCM (75 mL) added. The reaction mixture was washed with H_2O (5 x 50 mL) and the combined organic phases dried over $MgSO_4$. The solvent was removed *in vacuo* to leave a yellow oil. Automated flash chromatography (DCM to 10% MeOH in DCM) gave **4.8** as a pink solid (24.30 mg, 0.04 mmol, 18%).

^{1}H NMR (400 MHz, $CDCl_3$) δ/ppm = 7.91 – 7.88 (m, 1H, Ar-H), 7.47 - 7.45 (m, 2H, Ar-H), 7.10 – 7.04 (m, 1H, Ar-H), 6.93 - 6.89 (m, 1H, Ar-H), 6.47 – 6.24 (m, 6H, Ar-H), 3.36 – 3.31(m, 10H, NCH_2CH_2N and NCH_2CH_3), 3.24 (t, $^3J_{HH}$ = 7.0 Hz, 2H, NCH_2CH_2N), 2.10 (t, $^3J_{HH}$ = 7.6 Hz, 2H, CH_2), 1.67 – 1.50 (m, 5H, CH_2), 1.43 – 1.30 (m, 3H, CH_2), 1.17 (t, $^3J_{HH}$ = 7.0 Hz, 12H, NCH_2CH_3).

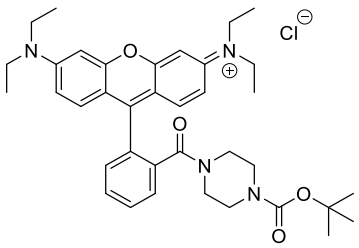
^{13}C NMR (101 MHz, $CDCl_3$) δ/ppm = 172.5, 169.6, 153.8, 153.2, 148.8, 132.7, 130.4, 128.3, 128.1, 123.8, 122.6, 108.2, 97.7, 65.5, 57.7, 53.6, 51.2, 44.3, 40.1, 36.4, 31.3, 28.5, 25.0, 18.3, 12.5.

HR-ESI-MS: Calculated for M = $C_{36}H_{45}N_7O_3$ – expected $[M+H]^+$ = 624.3662 , found 624.3668.



Ex4-Pra^{12}-SwitchRho (4.9): **Ex4-Pra^{12}** (1.50 mg, 0.36 µmol) was dissolved in H_2O (5mL). Compound **4.8** (2.40 mg, 3.90 µmol) was dissolved in H_2O/MeOH (1:3 ratio, 0.4 mL) and added, followed by sodium ascorbate (3.60 mg, 18.20 µmol) and $CuSO_4 \cdot 5H_2O$ (7.20 mg, 28.80 µmol), forming a pink solution which was left to stir at room temperature. After 5 days, LCMS indicated product formation. The reaction mixture was lyophilised to leave a pink solid. Automated flash chromatography (H_2O to MeCN + 0.1% TFA) gave **4.9** as a purple solid (1.50 mg, 0.31 µmol, 86%).

LC-MS: MW = 4777.87, found 955.80 $[M]^{5+}$, 1194.80 $[M]^{4+}$, 1592.70 $[M]^{3+}$, 4776.00 $[M]^+$.

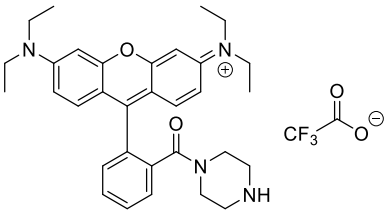


***N*-(9-(2-(4-(*Tert*-butoxycarbonyl)piperazine-1-carbonyl)phenyl)-6-(diethylamino)-3*H*-xanthen-3-ylidene)-*N*-ethylethanaminium chloride (4.10)**: Rhodamine B (1.01 g, 2.11 mmol) was dissolved in DCM (40 mL). HATU (0.82 g, 2.16 mmol) was added, followed by DIPEA (0.72 mL, 4.11 mmol) and *N*-Boc piperazine (0.51 g 2.75 mmol), forming a pink solution which was left to stir at room temperature. After 21 hours, the reaction mixture was washed with H_2O (3 x 50 mL) and the combined organic phases dried over $MgSO_4$. The solvent was removed *in vacuo* to leave a purple solid. Automated flash chromatography (DCM to 20% MeOH in DCM) gave **4.10** as a purple solid (0.59 g, 0.91 mmol, 43%).

^{1}H NMR (400 MHz, $CDCl_3$) δ/ppm = 7.66 – 7.60 (m, 2H, Ar-H), 7.52 – 7.46 (m, 1H, Ar-H), 7.32 – 7.27 (m, 1H, Ar-H), 7.18 (d, $^3J_{HH}$ = 9.5 Hz, 2H, Ar-H), 6.93 – 6.82 (m, 2H, Ar-H), 6.73 (s, 2H, Ar-H), 3.71 – 3.51 (m, 11H, NCH_2CH_3), 3.39 – 3.17 (m, 9H, $N(CH_2CH_2)_2N$), 1.38 (s, 10H, COO^tBu), 1.27 (t, $^3J_{HH}$ = 7.1 Hz, 13H, NCH_2CH_3)

^{13}C NMR (101 MHz, $CDCl_3$) δ/ppm = 167.7, 165.8, 157.7, 155.8, 155.6, 154.5, 135.1, 132.0, 130.7, 130.3, 130.2, 130.1, 127.6, 114.1, 113.7, 96.3, 80.5, 77.5, 77.2, 76.8, 58.2, 53.5, 47.3, 46.1, 41.8, 38.6, 28.3, 18.4, 12.5.

HR-ESI-MS: Calculated for $[M]^+ = C_{38}H_{48}BrN_4O_3$ – expected $[M]^+$ = 687.2910, found 687.2918.



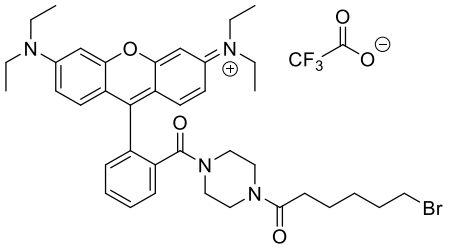
***N*-(6-(Diethylamino)-9-(2-(piperazine-1-carbonyl)phenyl)-3*H*-xanthen-3-ylidene)-*N*-ethylethanaminium triflate[9] (4.11)**: Compound **4.10** (0.59 g, 0.91 mmol) was dissolved in DCM (10 mL). TFA (10 mL) was added, forming a red solution which was left to stir at room temperature. After 23 hours the solvent was removed *in vacuo* to give **4.11** as a red oil (0.57 g, 0.91 mmol, quant.).

^{1}H NMR (400 MHz, $CDCl_3$) δ/ppm = 7.76 – 7.62 (m, 3H, Ar-H), 7.34 – 7.30 (m, 1H, Ar-H), 7.19 (d, $^3J_{HH}$ = 9.5 Hz, 2H, Ar-H), 6.97 (dd, $^3J_{HH}$ = 9.6, 2.2 Hz, 2H, Ar-H), 6.75 (d, $^3J_{HH}$ = 2.4 Hz, 2H, Ar-H), 3.77 – 3.53 (m, 14H, NCH_2CH_3 and $N(CH_2CH_2)_2N$), 1.32 (t, $^3J_{HH}$ = 7.1 Hz, 12H, NCH_2CH_3).

^{13}C NMR (101 MHz, CD_3OD): δ/ppm = 159.7, 157.7, 157.1, 136.0, 133.5, 132.2, 132.0, 131.9, 129.2, 115.9, 115.8, 115.3, 97.8, 76.8, 47.3, 39.3, 16.6, 13.2.

HR-ESI-MS: Calculated for $[M]^+ = C_{32}H_{39}N_4O_2$ – expected $[M]^+$ = 511.3100, found 511.3029.

Data corresponds to literature[9].



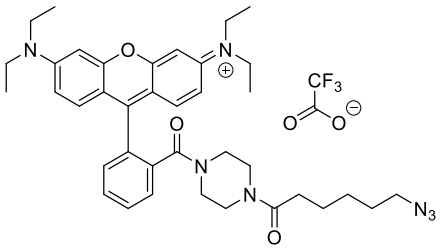
***N*-(9-(2-(4-(6-Bromohexanoyl)piperazine-1-carbonyl)phenyl)-6-(diethylamino)-3*H*-xanthen-3-ylidene)-*N*-ethylethanaminium triflate (4.12)**: Compound **4.11** (0.57 g, 0.91 mmol) was dissolved in DCM (40 mL). HATU (0.40 g, 1.95 mmol) was added, followed by 6-bromohexanoic acid (0.21 g, 1.07 mmol) and DIPEA (0.32 mL, 1.82 mmol), forming a pink solution which was left to stir at room temperature. After 21 hours, the reaction mixture was washed with water (2 x 50 mL) and the combined

organic phases dried over $MgSO_4$. The solvent was removed *in vacuo* to leave a purple solid. Automated flash chromatography (DCM to MeOH) gave **4.12** as a purple solid (0.20 g, 0.25 mmol, 27%).

^{1}H NMR (400 MHz, $CDCl_3$) δ/ppm = 7.75 – 7.59 (m, 3H, Ar-H), 7.30 (d, $^3J_{HH}$ = 10.5 Hz, 1H, Ar-H), 7.23 (d, $^3J_{HH}$ = 9.3 Hz, 1H, Ar-H), 7.17 (d, $^3J_{HH}$ = 9.5 Hz, 1H, Ar-H), 7.04 (d, $^3J_{HH}$ = 10.6 Hz, 1H, Ar-H), 6.93 (dd, $^3J_{HH}$ = 9.6, $^4J_{HH}$ = 2.1 Hz, 1H, Ar-H), 6.79 – 6.65 (m, 2H, Ar-H), 3.71 – 3.51 (m, 10H, CH_2Br and $N(CH_2CH_2)_2N$), 3.38 (q, $^3J_{HH}$ = 7.0 Hz, 8H, NCH_2CH_3), 2.33 (t, $^3J_{HH}$ = 7.4 Hz, 5H, $COCH_2$), 1.94 – 1.78 (m, 5H, CH_2), 1.68 – 1.61 (m, 4H, CH_2), 1.53 – 1.43 (m, 5H, CH_2), 1.29 (t, $^3J_{HH}$ = 7.0 Hz, 13H, NCH_2CH_3).

^{13}C NMR (101 MHz, $CDCl_3$) δ/ppm = 177.2, 165.8, 157.8, 157.7, 155.8, 132.4, 131.9, 130.2, 127.6, 114.5, 113.8, 96.3, 96.0, 77.5, 77.2, 76.8, 46.2, 41.1, 38.8, 34.1, 33.9, 33.6, 32.8, 32.5, 27.8, 27.7, 24.4, 24.0, 12.6.

HR-ESI-MS: Calculated for $[M]^+ = C_{32}H_{48}N_4O_3Br$ – expected $[M]^+$ = 687.2910, found 687.2918.

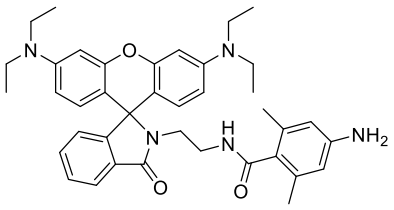


***N*-(9-(2-(4-(6-Azidohexanoyl)piperazine-1-carbonyl)phenyl)-6-(diethylamino)-3*H*-xanthen-3-ylidene)-*N*-ethylethanaminium triflate (4.13)**: Compound **4.12** (0.18 g, 0.21 mmol) was dissolved in dry DMF (40 mL). NaN_3 (0.03 g, 0.52 mmol) was added, forming a pink solution which was left to stir at 60 °C. After 18 hours, DCM (50 mL) was added and the reaction mixture washed with H_2O (3 x 75 mL) and brine (50 mL). The combined organic phases were dried over $MgSO_4$ and the solvent removed *in vacuo* to leave a pink solid. Automated flash chromatography (DCM to 25% MeOH in DCM) gave **4.13** as a purple solid (19.10 mg, 0.03 mmol, 12%).

^{1}H NMR (400 MHz, $CDCl_3$) δ/ppm = 8.01 (s, 2H, Ar-H), 7.71 – 7.60 (m, 2H, Ar-H), 7.51 (d, $^3J_{HH}$ = 6.2 Hz, 1H, Ar-H), 7.29 (s, 1H, Ar-H), 7.12 – 7.01 (m, 1H, Ar-H), 6.93 – 6.77 (m, 1H, Ar-H), 6.68 (s, 1H Ar-H), 3.59 (m, 6H, NCH_2CH_2N and CH_2CH_3), 3.45 – 3.40 (m, 2H, NCH_2CH_2N), 3.39 – 3.31 (m, 2H, NCH_2CH_2N), 3.31 – 3.18 (m, 3H, NCH_2CH_2N), 2.37 (t, $^3J_{HH}$ = 7.4 Hz, 2H, CH_2N_3), 1.63 (m, 8H, CH_2), 1.48 – 1.38 (m, 4H), 1.32 (t, $^3J_{HH}$ = 7.1 Hz, 12H, CH_2CH_3).

^{13}C NMR (101 MHz, $CDCl_3$) δ/ppm = 162.8, 157.9, 144.2, 130.4, 130.2, 129.9, 119.8, 109.5, 96.0, 95.9, 77.5, 77.2, 76.8, 53.6, 51.0, 46.2, 38.8, 36.7, 31.6, 28.7, 26.3, 24.4, 12.7.

HR-ESI-MS: Calculated for $[M]^+$ = $C_{38}H_{48}N_7O_3$ – expected $[M]^+$ = 650.3819, found 650.3809.

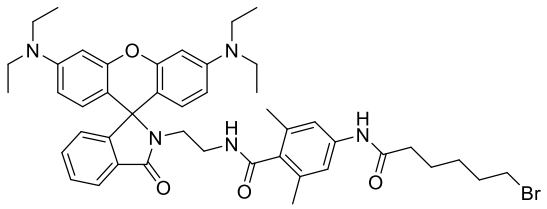


4-Amino-*N*-(2-(3',6'-bis(diethylamino)-3-oxospiro[isoindoline-1,9'-xanthen]-2-yl)ethyl)-2,6-dimethylbenzamide (4.14): Compound **4.6** (0.15 g, 0.30 mmol) was dissolved in DCM (30 mL). DIPEA (0.10 mL, 0.60 mmol) was added, followed by HATU (0.11 g, 0.30 mmol) and 4-amino-2,6-dimethyl benzoic acid (0.05 g, 0.30 mmol), forming an orange solution which was left to stir at room temperature. After 22 hours, the reaction mixture was washed with H_2O (2 x 50 mL) and brine (50 mL) and the combined organic phases were dried over $MgSO_4$ and the solvent removed *in vacuo* to leave a pale pink solid. Automated flash chromatography (DCM to 25% MeOH in DCM) gave **4.14** as a purple solid (0.10 g, 0.16 mmol, 53%).

^{1}H NMR (400 MHz, $CDCl_3$) δ/ppm = 7.87 – 7.80 (m, 1H, Ar-H), 7.45 – 7.37 (m, 2H, Ar-H), 7.07 – 7.01 (m, 1H, Ar-H), 6.66 (t, $^3J_{HH}$ = 4.5 Hz, 1H, Ar-H), 6.37 (d, $^3J_{HH}$ = 8.9 Hz, 2H, Ar-H), 6.32 (d, $^3J_{HH}$ = 2.6 Hz, 2H, Ar-H), 6.25 (s, 2H, Ar-H), 6.21 (dd, $^3J_{HH}$ = 8.9 Hz, $^4J_{HH}$ = 2.6 Hz, 2H, Ar-H), 3.36 (m, 2H, NCH_2), 3.28 (q, $^3J_{HH}$ = 7.1 Hz, 8H, ArNCH_2), 3.15 (m, 2H, NCH_2), 2.11 (s, 5H, ArCH_3), 1.12 (t, $^3J_{HH}$ = 7.1 Hz, ArNCH$_2$CH_3).

^{13}C NMR (101 MHz, $CDCl_3$) δ/ppm = 207.7, 171.2, 170.0, 154.1, 153.6, 149.3, 146.7, 136.0, 133.2, 130.8, 128.8, 128.7, 128.6, 128.6, 124.2, 123.2, 114.3, 108.7, 105.1, 98.2, 65.8, 58.5, 53.8, 50.8, 44.7, 40.7, 40.1, 39.0, 31.3, 19.8, 18.7.

HR-ESI-MS: Calculated for [M] = $C_{39}H_{45}N_5O_3$– expected $[M + H]^+$ = 632.301, found 632.3596.



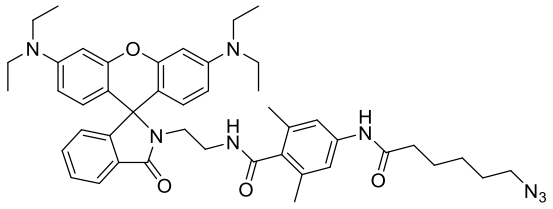
***N*-(2-(3',6'-Bis(diethylamino)-3-oxospiro[isoindoline-1,9'-xanthen]-2-yl)ethyl)-4-(6-bromohexanamido)-2,6-dimethylbenzamide (4.15)**: Compound **4.14** (0.28 g, 0.45 mmol) was

dissolved in DCM (40 mL). 6-Bromohexanoic acid (0.19 g, 0.98 mmol) was added, followed by HATU (0.34 g, 0.90 mmol) and DIPEA (0.31 mL, 1.78 mmol), forming a pink solution which was left to stir at room temperature. After 19 hours, TLC indicated that the reaction had not yet reached completion. An additional portion of 6-bromohexanoic acid (0.22 g, 1.14 mmol) was added, followed by HATU (0.36 g, 0.94 mmol) and DIPEA (0.60 mL, 3.44 mmol). After a further 4 hours, the reaction mixture was washed with H_2O (4 x 50 mL) and brine (50 mL) before the combined organic phase dried over $MgSO_4$. The solvent was removed *in vacuo* to leave a pink oil. Automated flash chromatography (DCM to 50% MeOH in DCM) gave **4.15** as a purple solid (0.19 g, 0.24 mmol, 54%).

^{1}H NMR (400 MHz, $CDCl_3$) δ/ppm = 7.80 (dd, $^3J_{HH}$ = 5.8, 2.3 Hz, 1H, Ar-H), 7.44 – 7.40 (m, 2H, Ar-H), 7.11 (s, 2H, Ar-H), 7.09 – 7.04 (m, 1H, Ar-H), 6.37 (d, $^3J_{HH}$ = 8.9 Hz, 2H, Ar-H), 6.32 (d, $^3J_{HH}$ = 2.5 Hz, 2H, Ar-H), 6.20 (dd, $^3J_{HH}$ = 8.9 Hz, $^4J_{HH}$ = 2.5 Hz, 2H, Ar-H), 3.27 (q, $^3J_{HH}$ = 7.0 Hz, 9H, NCH_2CH_3), 3.20 (m, 2H, NCH_2CH_2N), 2.32 (t, = 7.4 Hz, 2H, CH_2), 2.24 – 2.16 (m, 2H, CH_2), 2.11 (s, 6H, $ArCH_3$), 1.85 (m, 2H, NCH_2CH_2N), 1.69 (p, $^3J_{HH}$ = 7.5 Hz, 2H, CH_2), 1.46 (p, $^3J_{HH}$ = 7.5 Hz, 2H, CH_2), 1.30 (d, $^3J_{HH}$ = 6.7 Hz, 1H, CH_2), 1.12 (t, $^3J_{HH}$ = 7.0 Hz, 13H, NCH_2CH_3).

^{13}C NMR (101 MHz, $CDCl_3$) δ/ppm = 213.4, 207.3, 177.9, 157.4, 153.3, 128.4, 124.0, 118.5, 100.8, 97.6, 77.5, 77.2, 76.8, 44.3, 38.8, 33.7, 33.6, 32.6, 32.5, 31.4, 31.1, 27.9, 27.7, 24.7, 24.0, 19.6, 12.7.

HR-ESI MS: Calculated for M = $C_{45}H_{54}BrN_5O_4$, expected $[M + H]^+$ = 808.3281, found = 808.3320.

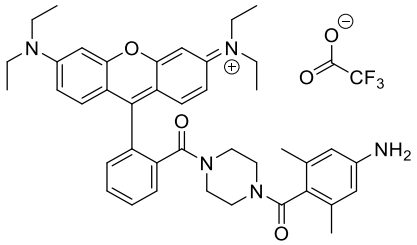


4-(6-Azidohexanamido)-*N*-(2-(3',6'-bis(diethylamino)-3-oxospiro[isoindoline-1,9'-xanthen]-2-yl)ethyl)-2,6-dimethylbenzamide (4.16): Compound **4.15** (10.50 mg, 0.01 mmol) was dissolved in dry DMF (20 mL). NaN_3 (0.04 g, 0.65 mmol) was added, forming a pink solution which was left to stir under N_2 at 60 °C. After 22 hours, the reaction mixture was allowed to cool to room temperature and H_2O (50 mL) added. After stirring for 5 minutes, the reaction mixture was extracted with DCM (50 mL). The organic phase was washed with H_2O (2 x 50 mL) and brine (50 mL). The combined organic phases were dried over $MgSO_4$ and the solvent removed *in vacuo* to leave **4.16** as a pink solid (9.70 mg, 0.01 mmol, 97%).

^{1}H NMR (400 MHz, $CDCl_3$) δ/ppm = 8.23 (s, 1H, Ar-H), 7.98 (s, 1H, Ar-H), 7.85 – 7.78 (m, 1H, Ar-H), 7.42 (qd, $^{3}J_{HH}$ = 7.5, $^{4}J_{HH}$ = 3.6 Hz, 2H, Ar-H), 7.06 (dd, $^{3}J_{HH}$ = 6.7, $^{4}J_{HH}$ = 1.6 Hz, 1H, Ar-H), 6.69 (t, $^{3}J_{HH}$ = 4.3 Hz, 1H, Ar-H), 6.38 (d, $^{3}J_{HH}$ = 8.9 Hz, 2H, Ar-H), 6.33 (d, $^{3}J_{HH}$ = 2.5 Hz, 2H, Ar-H), 6.21 (dd, $^{3}J_{HH}$ = 8.9, $^{4}J_{HH}$ = 2.6 Hz, 2H, Ar-H), 3.40 – 3.47 (m, 2H, $N(CH_2)_2N$), 3.28 (q, $^{3}J_{HH}$ = 7.0 Hz, 8H, NCH_2CH_3), 3.21 – 3.19 (m, 2H, $N(CH_2)_2N$), 2.34 – 2.26 (m, 3H, CH_2), 2.14 (s, 6H, $ArCH_3$), 1.70 (m, 2H, CH_2), 1.60 (m, 2H, CH_2), 1.46 – 1.35 (m, 2H, CH_2), 1.26 – 1.17 (m, 2H, CH_2), 1.13 (t, $^{3}J_{HH}$ = 7.0 Hz, 12H, NCH_2CH_3).

^{13}C NMR (101 MHz, $CDCl_3$) δ/ppm = 171.4, 170.3, 169.6, 162.6, 153.7, 153.3, 149.0, 138.3, 135.0, 133.4, 132.9, 130.5, 129.1, 128.4, 128.3, 128.3, 125.3, 124.0, 122.9, 118.6, 108.3, 104.7, 97.8, 77.5, 77.2, 76.8, 65.5, 51.3, 44.4, 40.5, 40.0, 38.7, 37.2, 36.7, 31.5, 29.8, 28.7, 26.4, 25.1, 21.5, 19.5, 12.6, 1.1.

HR-ESI MS: Calculated for M = $C_{45}H_{54}N_8O_4$, expected $[M + H]^+$ = 771.4341, found = 771.4346.

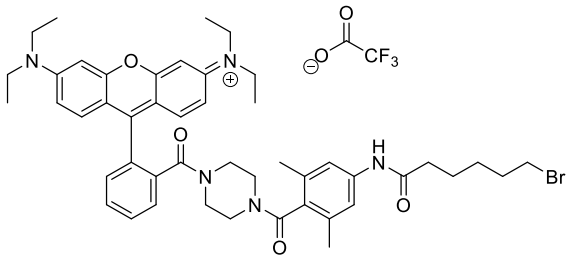


***N*-(9-(2-(4-(4-Amino-2,6-dimethylbenzoyl)piperazine-1-carbonyl)phenyl)-6-(diethylamino)-3*H*-xanthen-3-ylidene)-*N*-ethylethanaminium triflate (4.17)**: Compound **4.11** (0.10 g, 0.17 mmol) was dissolved in DCM (30 mL). 4-Amino-2,6-dimethylbenzoic acid (0.03 g, 0.20 mmol) was added, followed by DIPEA (0.06 mL, 0.34 mmol) and HATU (0.08 g, 0.21 mmol), forming a pink solution which was left to stir at room temperature. After 22 hours, the reaction mixture was washed with H_2O (2 x 50 mL) and brine (50 mL). The combined organic phases were dried over $MgSO_4$ and the solvent removed *in vacuo* to leave a purple solid. Automated flash chromatography (DCM to 25% MeOH in DCM) gave **4.17** as a purple solid (0.07 g, 0.09 mmol, 53%).

^{1}H NMR (400 MHz, $CDCl_3$) δ/ppm = 8.46 (dd, $^{3}J_{HH}$ = 4.3, 1.3 Hz, 1H, Ar-H), 8.16 (dd, $^{3}J_{HH}$ = 8.4 Hz, 1.3 Hz, 1H, Ar-H), 7.77 – 7.31 (m, 3H, Ar-H), 7.20 (d, $^{3}J_{HH}$ = 4.4 Hz, 1H, Ar-H), 7.01 – 6.69 (m, 3H, Ar-H), 6.32 – 6.16 (m, 1H, Ar-H), 4.82 (br s, 2H, NH_2), 3.70 – 3.57 (m, 12H, NCH_2CH_3), 2.82 – 2.36 (m, 8H, $N(CH_2CH_2)_2N$),), 2.01 (br s, 4H, $ArCH_3$),1.31 (t, $^{3}J_{HH}$ = 7.1 Hz, 8H, $ArNCH_2$).

^{13}C NMR (101 MHz, $CDCl_3$) δ/ppm = 207.2, 157.9, 155.8, 149.2, 135.0, 130.3, 119.8, 114.1, 77.5, 77.2, 76.8, 53.8, 46.3, 42.1, 31.1, 30.6, 19.3, 18.8, 17.5, 12.8, 12.2.

HR-ESI MS: Calculated for $[M]^+ = C_{41}H_{48}N_5O_3^+$, expected = 658.3742, found = 658.3757.

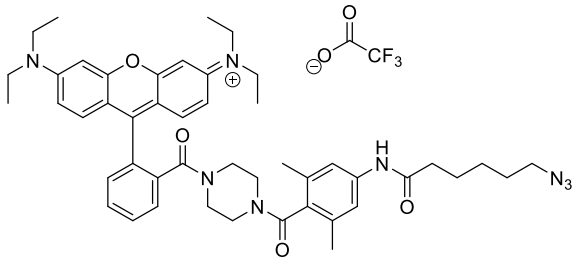


***N*-(9-(2-(4-(4-(6-Bromohexanamido)-2,6-dimethylbenzoyl)piperazine-1-carbonyl)phenyl)-6-(diethylamino)-3*H*-xanthen-3-ylidene)-*N*-ethylethanaminium triflate (4.18)**: Compound **4.17** (0.07 g, 0.09 mmol) was dissolved in DCM (30 mL). HATU (0.06 g, 0.16 mmol) was added, followed by 6-bromohexanoic acid (0.03 g, 0.14 mmol) and DIPEA (0.03 mL, 0.18 mmol), forming a pink solution which was left to stir at room temperature. After 18 hours, an additional portion of HATU (0.07 g, 0.17 mmol) was added, followed by 6-bromohexanoic acid (0.13 g, 0.67 mmol) and DIPEA (0.10 mL, 0.57 mmol). After a further 5 hours, the temperature of the reaction mixture was increased to 45 °C. After a further 19 hours, the reaction mixture was allowed to cool to room temperature before being washed with H_2O (3 x 50 mL) and brine (50 mL). The combined organic phases were dried over $MgSO_4$ and the solvent removed *in vacuo* to leave a pink oil. Automated flash chromatography (DCM to 50% MeOH in DCM) gave **4.18** as a purple solid (0.03 g, 0.03 mmol, 32%).

^{1}H NMR (400 MHz, $CDCl_3$) δ/ppm = 8.74 (d, $^3J_{HH}$ = 5.7 Hz, 1H, Ar-H), 8.39 (d, $^3J_{HH}$ = 9.7 Hz, 1H, Ar-H), 7.78 – 7.63 (m, 2H, Ar-H), 7.63 – 7.50 (m, 2H, Ar-H), 7.43 (dd, $^3J_{HH}$ = 8.4 Hz, $^4J_{HH}$ = 4.5 Hz, 1H, Ar-H), 7.40 – 7.31 (m, 1H, Ar-H), 7.26 – 7.17 (m, 2H, Ar-H), 6.90 (d, $^3J_{HH}$ = 10.3 Hz, 1H, Ar-H), 6.76 (s, 1H, Ar-H), 3.71 - 3.61 (m, 8H, N((CH_2)$_2$)$_2$N), 3.16 (q, $^3J_{HH}$ = 7.4 Hz, 8H, ArNCH_2CH$_3$), 2.18 (s, 7H, ArCH_3), 2.10 – 2.02 (m, 5H, CH_2), 1.98 – 1.91 (m, 6H, CH_2), 1.81 – 1.74 (m, 6H, CH_2), 1.61 (t, $^3J_{HH}$ = 7.4 Hz, 12H ArNCH_2CH$_3$).

^{13}C NMR (101 MHz, $CDCl_3$): δ/ppm = 211.6, 206.9, 193.0, 176.6, 155.8, 151.3, 129.4, 120.8, 81.3, 77.5, 77.2, 76.8, 69.0, 67.5, 66.4, 54.2, 53.6, 42.5, 33.7, 31.1, 27.9, 25.1, 24.5, 19.3, 18.7, 18.5, 17.5, 12.8, 12.2.

HR-ESI MS: Calculated for $[M]^+ = C_{47}H_{57}BrN_5O_4^+$, expected $[M]^+$ = 834.3588, found = 834.3572, found $[M]^{3+}$ = 278.1111.

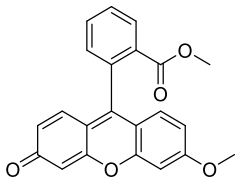


***N*-(9-(2-(4-(4-(6-Azidohexanamido)-2,6-dimethylbenzoyl)piperazine-1-carbonyl)phenyl)-6-(diethylamino)-3*H*-xanthen-3-ylidene)-*N*-ethylethanaminium triflate (4.19)**: Compound **4.18** (27.20 mg, 0.03 mmol) was dissolved in dry DMF (25 mL). NaN_3 (12.40 mg, 0.19 mmol) was added, forming a pink solution which was left to stir at 60 °C under N_2. After 18 hours, H_2O (50 mL) was added. The reaction mixture was extracted with DCM (50 mL) and the organic phase washed with water (4 x 100 mL) and brine (75 mL) before the combined organic phases dried over $MgSO_4$. The solvent was removed *in vacuo* to leave **4.19** as a purple solid (12.90 mg, 0.01 mmol, 49%).

^{1}H NMR (400 MHz, $CDCl_3$) δ/ppm = 8.02 (s, 1H, Ar-H), 7.81 – 7.64 (m, 2H, Ar-H), 7.64 – 7.47 (m, 3H, Ar-H), 7.43 – 7.29 (m, 2H, Ar-H), 7.21 – 7.13 (m, 2H, Ar-H), 6.88 (d, $^3J_{HH}$ = 11.9 Hz, 1H, Ar-H), 6.78 – 6.70 (m, 1H, Ar-H), 3.83 – 3.51 (m, 8H, ArNCH_2CH$_3$), 3.50 – 3.00 (m, 8H, N((CH_2)$_2$)$_2$N), 2.70 – 2.53 (m, 3H, CH_2), 2.35 (s, 2H, CH_2), 2.00 (s, 5H, ArCH_3), 1.97 – 1.87 (m, 2H, CH_2), 1.74 (m, 3H, CH_2), 1.51 – 1.41 (m, 3H, CH_2), 1.42 – 1.26 (m, 12H, ArNCH$_2$CH_3).

^{13}C NMR (101 MHz, $CDCl_3$) δ/ppm = 179.8, 164.3, 154.2, 153.1, 148.7, 137.8, 134.0, 130.9, 119.7, 118.9, 111.8, 106.3, 95.1, 85.0, 84.4, 83.3, 66.5, 59.7, 58.8, 57.9, 53.4, 46.2, 45.4, 44.6, 39.6, 32.8, 32.3, 31.1, 28.4, 24.0, 14.2, 1.2.

HR-ESI MS: Calculated for $[M]^+ = C_{47}H_{57}N_8O_4^+$, expected $[M]^+$ = 797.4503, found = 797.4492.



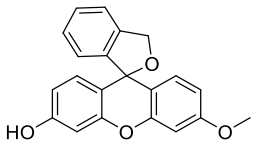
Methyl 2-(6-methoxy-3-oxo-3*H*-xanthen-9-yl)benzoate (4.20): Fluorescein (1.51 g, 4.55 mmol) was dissolved in DMF (25 mL). K_2CO_3 (1.70 g, 12.30 mmol) was added, followed by MeI (2 M in THF, 6.77 mL, 13.53 mmol), forming an orange solution which was left to stir at room temperature. After 21 hours, TLC indicated that the reaction had not yet reached completion. Additional portions of MeI (2 M in THF, 5.00 mL, 10.00 mmol) and K_2CO_3 (2.04 g, 14.76 mmol) were added. After a further 3 hours, H_2O (ice-cold, 50 mL) was added and the reaction mixture left to stir at 0 °C. After 30 minutes, the

reaction mixture was extracted with EtOAc (3 x 50 mL). The combined organic phases were washed with H_2O (50 mL) and brine (50 mL) before being dried over $MgSO_4$. The solvent was removed *in vacuo* to leave an orange solid. Automated flash chromatography (DCM to 25% MeOH in DCM) gave **4.20** as an orange solid (0.11 g, 0.31 mmol, 7%).

^{1}H NMR (400 MHz, $CDCl_3$) δ/ppm = 7.53 – 7.48 (m, 1H, Ar-H), 7.02 (td, $^3J_{HH}$ = 7.5, $^4J_{HH}$ = 1.3 Hz, 1H, Ar-H), 6.94 (td, $^3J_{HH}$ = 7.7, $^4J_{HH}$ = 1.3 Hz, 1H, Ar-H), 6.61 – 6.55 (m, 1H, Ar-H), 6.24 (d, $^3J_{HH}$ = 2.4 Hz, 1H, Ar-H), 6.14 (dd, $^3J_{HH}$ = 13.4, $^3J_{HH}$ = 9.3 Hz, 2H, Ar-H), 6.01 (dd, $^3J_{HH}$ = 8.9, $^4J_{HH}$ = 2.5 Hz, 1H, Ar-H), 5.76 (dd, $^3J_{HH}$ = 9.7, $^4J_{HH}$ = 1.9 Hz, 1H, Ar-H), 5.67 (d, $^3J_{HH}$ = 1.9 Hz, 1H, Ar-H), 3.18 (s, 3H, COOMe), 2.89 (s, 3H, OMe).

^{13}C NMR (101 MHz, $CDCl_3$) δ/ppm = 185.3, 165.3, 163.9, 162.2, 158.8, 154.0, 150.2, 134.3, 132.5, 130.3, 130.1, 129.5, 117.2, 114.6, 113.2, 105.3, 100.1, 55.8, 53.4, 52.1, 36.2, 31.1.

HR-ESI MS: Calculated for M = $C_{22}H_{16}O_5$: expected $[M + H]^+$ = 361.1071 found = 361.1063.



6'-Methoxy-3*H*-spiro[isobenzofuran-1,9'-xanthen]-3'-ol (4.21): Compound **4.20** (0.11 g, 0.31 mmol) was dissolved in dry THF (20 mL). The orange solution was cooled to 0 °C and $LiAlH_4$ (0.05 g, 1.24 mmol) was added and the reaction mixture left to stir at 0 °C. After 2.5 hours, the reaction mixture was left to stir at room temperature. After a further 2 hours, an additional portion of $LiAlH_4$ (0.13 g, 3.43 mmol) was added. TLC showed no reaction progress after a further 17 hours and the reaction mixture was again cooled to 0 °C. A third portion of $LiAlH_4$ (fresh bottle, 0.07 g, 1.83 mmol) was added, resulting in some effervescence. After 5 hours, with the reaction mixture kept at 0 °C, a fourth portion of $LiAlH_4$ (0.11 g, 2.82 mmol) was added. After one hour, Na_2SO_4 (9.00 g, 63.22 mmol) was added and the reaction mixture left to stir and warm to room temperature. After 30 minutes, the reaction mixture was filtered over a pad of celite and washed with DCM (75 mL). The filtrate was reduced *in vacuo* to leave a yellow solid. This solid was re-dissolved in MeOH (20 mL). *p*-Chloranil (0.30 g, 1.22 mmol) was added, forming a yellow solution which was left to stir at room temperature. After 15 hours, the formation of a yellow precipitate was observed. This precipitate was removed *via* filtration and the filtrate reduced *in vacuo* to leave a yellow solid. Automated flash chromatography (DCM to 25% MeOH in DCM) gave **4.21** as a yellow solid (0.11 g, 0.31 mmol, quant.)

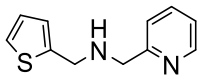
^{1}H NMR (400 MHz, CD_3CN) δ/ppm = 7.57 – 7.19 (m, 5H, Ar-H), 6.88 – 6.49 (m, 5H, Ar-H), 3.80 (s, 3H, OMe), 3.09 (s, 2H, $ArCH_2O$).

^{13}C NMR (101 MHz, CD_3CN) δ/ppm = 165.1, 153.5, 153.4, 149.6, 141.4, 138.8, 137.7, 136.7, 127.1, 126.2, 97.6, 82.6, 82.3, 79.8, 55.5, 55.3, 55.2, 54.9, 54.6, 54.4, 49.9, 30.1, 28.7.

HR-ESI MS: Calculated for M = $C_{21}H_{16}O_4$: expected $[M + H]^+$ = 333.1127, found = 333.1127.

7.8. Synthesis of Compounds in Chapter 5

The ligand H_3do3a-NH_2 was synthesised according to literature procedures and provided by Dr. Tamara Boltersdorf[10,11].



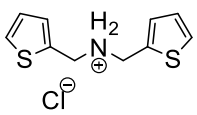
1-(Pyridin-2-yl)-*N*-(thiophen-2-ylmethyl)methanamine[12] (5.1):: Thiophene-2-methylamine (1.00 mL, 1.10 g, 9.75 mmol) was dissolved in MeCN (40 mL). 2-bromomethylpyridine hydrobromide (2.55 g, 10.09 mmol) was added, followed by K_2CO_3 (4.17 g, 30.20 mmol), forming a pale pink solution which was left to stir at 110 °C. After 65 hours, a colour change from pink to orange had occurred. The solvent was removed *in vacuo* to leave an orange residue. This residue was re-dissolved in DCM (30 mL) and filtered to remove insoluble salts. The solvent was removed *in vacuo* to leave an orange oil. Flash chromatography was performed using a Biotage (DCM to 20% MeOH in DCM) to give **5.1** as a yellow oil (1.33 g, 6.53 mmol, 67%).

^{1}H NMR (400 MHz, $CDCl_3$): δ/ ppm = 8.56 – 8.53 (m, 1H, Ar-H), 7.68 (q, $^{3}J_{HH}$ = 1.4 Hz, 1H, Ar-H), 7.35 (dt, $^{3}J_{HH}$ = 7.8 Hz, $^{4}J_{HH}$ = 1.0 Hz, 1H, Ar-H), 7.26 – 7.23 (m, 1H, Ar-H), 7.17 (m, 1H, Ar-H), 6.98 – 6.97 (m, 1H, Ar-H), 6.97 (s, 1H, Ar-H), 3.92 (s, 1H, $NHCH_2py$), 3.87 (s, 2H, $NHCH_2th$), 2.09 (s, 1H, NH).

^{13}C NMR (101 MHz, $CDCl_3$): δ/ppm = 159.4, 148.8, 136.6, 126.6, 125.9, 124.8, 122.7, 122.1, 59.5, 52.3.

HR-ESI MS: Calculated for M = $C_{11}H_{12}N_2S$, expected $[M+H]^+$ = 205.0794, found = 205.0790.

Data corresponds to literature[12].



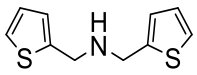
Bis(thiophen-2-ylmethyl)ammonium chloride (5.2): Thiophene-2-methylamine (1.00 mL, 1.10 g, 9.75 mmol) was dissolved in toluene (50 mL). Thiophene-2-carboxaldehyde (1.33 mL, 1.62 g, 9.75

mmol) was added, forming a yellow solution which was heated to 130 °C and left to stir under reflux with a Dean and Stark trap. After 2 hours, the solvent was removed *in vacuo* and the yellow residue re-dissolved in EtOH (50 mL) and cooled to 0°C. $NaBH_4$ (0.41 g, 10.73 mmol) was added and the reaction mixture left to stir and warm to room temperature. After 17 hours, the reaction mixture was poured over ice (~ 100 g), resulting in a colour change from yellow to white. The solution was acidified by addition of HCl (conc., 10 mL), inducing the formation of a white precipitate. This precipitate was isolated by filtration and dried under high vacuum to give **5.2** as a white solid, (1.73 g, 8.28 mmol, 85%).

^{1}H NMR (400 MHz, D_2O): δ/ppm = 7.46 (d, $^3J_{HH}$ = 5.1 Hz, 2H, Ar-H), 7.17 (d, $^3J_{HH}$ = 3.4 Hz, 2H, Ar-H), 7.04 – 7.01 (m, 2H, Ar-H), 4.40 (s, 4H, $ArCH_2NH_2$).

^{13}C NMR (101 MHz, D_2O): δ/ppm = 132.1, 129.7, 128.8, 44.8.

HR-ESI MS: Calculated for $[M]^+ = C_{10}H_{12}NS_2^+$, expected = 210.0406, found = 210.0403.

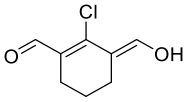


Bis(thiophen-2-ylmethyl)amine (5.3) : Compound **5.2** (0.68 g, 3.23 mmol) was dissolved in H_2O (30 mL) and the pH of the solution brought from 5 to 9 by addition of NaOH solution (1.0 M). The solution was washed with DCM (70 mL) and the combined organic phases dried over MgSO4. The solvent was removed *in vacuo* to leave **5.3** as a yellow oil (0.27 g, 1.29 mmol, 40%).

^{1}H NMR (400 MHz, $CDCl_3$): δ/ppm = 7.22 (dd, $^3J_{HH}$ = 1.27, 5.00 Hz, 2H, Ar-H), 6.97 – 6.93 (m, 4H, Ar-H), 4.03 (s, 4H, $ArCH_2NH$), 1.75 (s, 1H, NH).

^{13}C NMR (101 MHz, $CDCl_3$): δ/ppm = 143.6, 126.8, 124.7, 47.1.

HR-ESI MS: Calculated for $M = C_{10}H_{11}NS_2$, expected $[M + H]^+$ = 210.0406, found 210.0402.

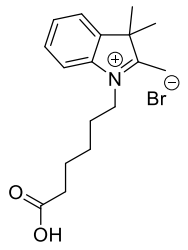


(*E*)-2-Chloro-3-(hydroxymethylene)cyclohex-1-ene-1-carbaldehyde[13] (5.4): DMF (25 mL) was cooled to 0 °C under N_2. $POCl_3$ (7.04 mL, 11.55 g, 75.26 mmol) was added, slowly, to form a pale pink solution which was left to stir at room temperature. After 30 minutes, cyclohexanone (2.57 mL, 2.00 g, 20.34 mmol) was added and the dark red reaction mixture left to stir under N_2 at 50 °C. After 5 hours, the reaction mixture was removed from heating and poured into a beaker of ice (75.2 g). The solution was left to stir at room temperature. After one hour, formation of a yellow precipitate was observed.

After 17 hours, the precipitate was isolated by filtration and washed with H_2O (20 mL) before being recrystallised with DCM, giving **5.4** as a yellow, crystalline solid (1.12 g, 6.49 mmol, 32%).

^{1}H NMR (400 MHz, DMSO-d_6): δ/ppm = 10.84, (br s, 1H, C<u>H</u>O), 9.05, (br s, 1H, CO<u>H</u>), 3.34 (s, 2H, C=C(<u>H</u>)OH), 2.35 (t, $^3J_{HH}$ = 6.11 Hz, 3H, (C<u>H$_2$</u>CH$_2$C<u>H$_2$</u>)), 1.58 (quin., $^3J_{HH}$ = 6.25 Hz, 2H, (CH$_2$C<u>H$_2$</u>CH$_2$)).

Data corresponds to literature[13].



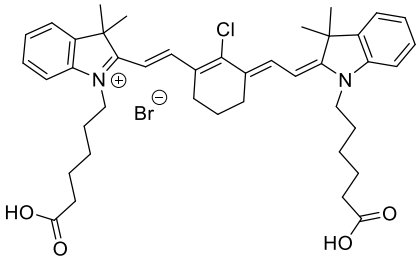
1-(5-Carboxypentyl)-2,3,3-trimethyl-3*H*-indol-1-ium bromide[13] (5.5): 2,3,3 trimethyl indolenine (8.03 mL, 50.00 mmol) was dissolved in nitromethane (30 mL), forming an orange solution. 6-Bromohexanoic acid (9.75 g, 50.00 mmol) was added, forming a pink solution which was left to stir under N_2 at 80 °C. After 21 hours, the solvent was removed *in vacuo* to leave a pink oil. Et_2O (200 mL) was added, resulting in the formation of a pink precipitate. This precipitate was isolated by filtration, giving **5.5** as a pink solid (9.74 g, 27.50 mmol, 55%).

^{1}H NMR (400 MHz, DMSO-d_6) δ/ppm = 7.97 (d, $^3J_{HH}$ = 8.9 Hz, 1H, Ar-<u>H</u>), 7.84 (d, $^3J_{HH}$ = 8.7 Hz, 1H, Ar-<u>H</u>), 7.62 (d, $^3J_{HH}$ = 8.9 Hz, 2H, Ar-<u>H</u>), 4.53 – 4.35 (m, 2H, C<u>H$_2$</u>COOH), 2.83 (s, 3H, C<u>H$_3$</u>C=N), 2.23 (t, $^3J_{HH}$ = 7.2 Hz, 2H, NC<u>H$_2$</u>), 1.90 – 1.75 (m, 2H, C<u>H$_2$</u>), 1.63 – 1.53 (m, 2H, C<u>H$_2$</u>), 1.53 (s, 6H, C<u>H$_3$</u>), 1.47 – 1.36 (m, 2H, C<u>H$_2$</u>).

^{13}C NMR (101 MHz, DMSO-d_6) δ/ppm = 196.5, 174.3, 144.9, 141.9, 141.1, 129.4, 129.0, 127.8, 126.0, 123.5, 122.2, 118.3, 115.5, 54.2, 53.4, 48.6, 47.4, 40.2, 39.9, 39.7, 39.5, 39.3, 39.1, 38.9, 35.0, 33.5, 33.4, 32.0, 27.1, 27.0, 25.4, 24.0, 23.6, 22.3, 22.0, 15.0, 14.0.

HR-ESI MS: Calculated for $M^+ = C_{17}H_{24}NO_2^+$, expected = 274.1802, found = 274.1795.

Data corresponds to literature[13].



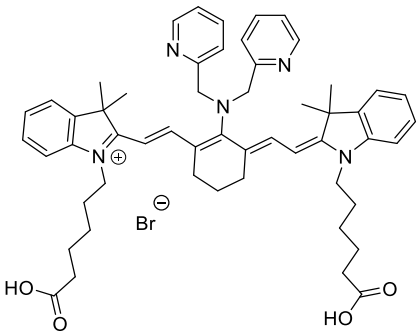
1-(5-carboxypentyl)-2-((*E*)-2-((*E*)-3-(2-((*E*)-1-(5-carboxypentyl)-3,3-dimethylindolin-2-ylidene)ethylidene)-2-chlorocyclohex-1-en-1-yl)vinyl)-3,3-dimethyl-3*H*-indol-1-ium bromide[13] (5.6): Compound **5.4** (1.12 g, 6.49 mmol) was dissolved in EtOH (65 mL) and compound **5.5** (4.66 g, 13.12 mmol) added, along with NaOAC (1.60 g, 19.47 mmol). The reaction vessel was wrapped in foil and left to stir at 70 °C. After 80 minutes, the solvent was removed *in vacuo* to give a blue-green oil which was stored under foil in a freezer. The crude compound was purified by flash chromatography (10% - 75% MeOH in DCM) to give **5.6** as a green solid (3.13 g, 4.09 mmol, 63%).

^{1}H NMR (400 MHz, $CDCl_3$): δ/ppm = 8.33, (d, $^3J_{HH}$ = 14.04 Hz, 2H, HC=CH), 7.42 – 7.15, (m, 8H, Ar-H), 6.21 (d, $^3J_{HH}$ = 14.05 Hz, 2H, HC=CH), 4.12 (t, $^3J_{HH}$ = 7.28 Hz, 4H, NCH_2), 2.72 (m, 2H, CH_2CH=), 2.46 (t, $^3J_{HH}$ = 6.22 Hz, 2H, α-CH_2COOH), 2.01 (br s, 2H, CH_2), 1.86, (m, 4H, δ-CH_2), 1.77 (m, 4H, β-CH_2), 1.71 (s, 12H, (Ar-(CH_3)$_2$), 1.55 (m, 4H, γ-CH_2).

^{13}C NMR (101 MHz, $CDCl_3$): δ/ppm = 172.4, 150.9, 144.5, 142.2, 141.1, 129.0, 128.0, 125.4, 122.4, 111.1, 101.4, 77.5, 77.2, 76.8, 49.4, 44.5, 34.9, 28.3, 27.1, 26.7, 26.4, 24.8, 20.8.

HR-ESI MS: Calculated for $[M]^+$ = $C_{42}H_{52}N_2O_4Cl$: expected = 683.3616 found = 683.3622.

Data corresponds to literature[13].



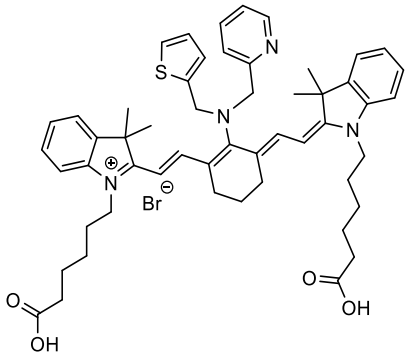
2-((*E*)-2-((*E*)-2-(bis(pyridin-2-ylmethyl)amino)-3-(2-((*E*)-1-(5-carboxypentyl)-3,3-dimethylindolin-2-ylidene)ethylidene)cyclohex-1-en-1-yl)vinyl)-1-(5-carboxypentyl)-3,3-dimethyl-3*H*-indol-1-ium bromide (5.7): Compound **5.6** (0.52 g, 0.68 mmol) was dissolved in DMF (70 mL). Dipicolylamine (1.50 mL, 1.36 g, 6.80 mmol) was added and the reaction mixture left to stir under N_2 at 70 °C. After 4.5 hours, the reaction mixture was allowed to cool to room temperature before

being poured into Et_2O (1 L) and stirred violently. After 40 minutes, formation of a blue precipitate was observed. This precipitate was collected by filtration onto a sintered glass funnel, before being washed with Et_2O (100 mL) and EtOAc (100 mL). The blue solid was washed into an rbf with MeOH (75 mL) and the solvent removed *in vacuo* to give the crude product as a blue solid. Flash chromatography (10% - 75% MeOH in DCM) gave pure **5.7** as a blue solid (0.27 g, 0.29 mmol, 43%).

^{1}H NMR (400 MHz, $CDCl_3$): δ/ppm = 8.70 (d, $^3J_{HH}$ = 4.37 Hz, 2H, HC=CH), 7.93 (td, $^3J_{HH}$ = 7.65 Hz $^4J_{HH}$ = 1.64 Hz, 2H, Ar-H), 7.61 (d, $^3J_{HH}$ = 13.50 Hz, 2H, Ar-H), 7.37 – 7.28 (m, 7H, Ar-H), 7.17 (m, 1H, Ar-H), 7.11 (t, $^3J_{HH}$ = 7.46 Hz, 2H, Ar-H), 6.98 (d, $^3J_{HH}$ = 7.96 Hz, 2H, Ar-H), 5.94 (d, $^3J_{HH}$ = 13.31 Hz, 2H, HC=CH), 4.74 (s, 4H, CH_2CH=), 3.92 (m, 4H, NCH_2Ar), 2.57 (m, 4H, α-CH_2COOH), 2.38 (m, 4H, δ-CH_2), 1.97 (m, 4H, β-CH_2), 1.48 (m, 4H, (γ-CH_2), 1.43 (s, 12H, Ar-(CH_3)$_2$), 1.31 (m, 2H, CH_2) 1.24 (t, $^3J_{HH}$ = 7.03 Hz, 4H, NCH_2).

^{13}C NMR (101 MHz, $CDCl_3$): δ/ppm = 180.4, 172.3, 166.4, 165.1, 150.9, 144.5, 142.0, 141.2, 129.1, 128.1, 125.4, 122.4, 119.7, 111.1, 101.4, 94.7, 89.1, 53.7, 49.3, 44.5, 34.8, 28.4, 27.3, 27.0, 26.0, 24.6, 21.1.

HR-ESI MS: Calculated for $[M]^+ = C_{54}H_{64}N_5O_4$: expected = 846.4958 found = 846.4970.



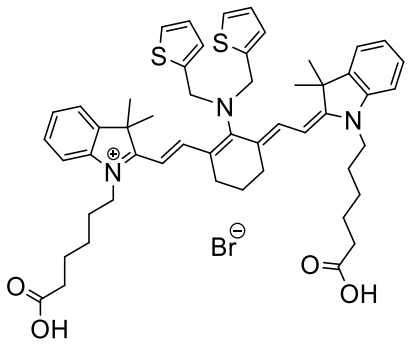
1-(5-Carboxypentyl)-2-((*E*)-2-((*E*)-3-(2-((*E*)-1-(5-carboxypentyl)-3,3-dimethylindolin-2-ylidene)ethylidene)-2-((pyridin-2-ylmethyl)(thiophen-2-ylmethyl)amino)cyclohex-1-en-1-yl)vinyl)-3,3-dimethyl-3*H*-indol-1-ium bromide (5.8): Compound **5.6** (0.30 g, 0.40 mmol) was dissolved in DMF (40 mL). Compound **5.1** (0.82 g, 4.02 mmol) was added and the reaction mixture left to stir at 70 °C under N_2, with the flask covered in foil. After 4 hours, the reaction mixture was allowed to cool to room temperature before being poured into vigorously stirred Et_2O (1 L). After 45 minutes, formation of a blue precipitate was observed. This precipitate was isolate by filtration to leave a blue solid. Flash chromatography (DCM to MeOH) gave **5.8** as a blue solid (0.21 g, 0.22 mmol, 55%).

^{1}H NMR (400 MHz, CD_3OD): δ/ppm = 8.43 (d, $^3J_{HH}$ = 14.1 Hz, 1H, N=CCH=CH), 7.73 (d, $^3J_{HH}$ = 13.1 Hz, 1H, N=CCH=CH), 7.52 (d, $^3J_{HH}$ = 7.4 Hz, 1H, Ar-H), 7.46 – 7.41(m, 1H, Ar-H), 7.35 – 7.27 (m, 1H, Ar-H), 7.14 – 7.03 (m, 3H, Ar-H), 6.30 (d, $^3J_{HH}$ = 14.2 Hz, 2H, ArCH=CH), 5.90 (d, $^3J_{HH}$ = 13.3

Hz, 2H, N=CC<u>H</u>=CH), 5.02 (s, 2H, pyC<u>H</u>$_2$), 4.20 (s, 2H, thC<u>H</u>$_2$) 4.16 (t, $^3J_{HH}$ = 7.4 Hz, 2H, Cα<u>H</u>$_2$), 3.96 (t, $^3J_{HH}$ = 7.4 Hz, 2H, Cα<u>H</u>$_2$), 2.74 (t, $^3J_{HH}$ = 6.5 Hz, 2H, Cε<u>H</u>$_2$), 2.56 (t, $^3J_{HH}$ = 6.5 Hz, 2H, Cε<u>H</u>$_2$) 2.20 (m, 4H, cyclic C<u>H</u>$_2$), 1.98 (m, 2 H, cyclic C<u>H</u>$_2$), 1.89 – 1.78 (m, 8H, Cβ<u>H</u>$_2$ and Cδ<u>H</u>$_2$), 1.77 (s, 6H, C<u>H</u>$_3$), 1.71 – 1.66 (m, 6H, Cγ<u>H</u>$_2$), 1.52 (s, 6H, C<u>H</u>$_3$).

^{13}C NMR (101 MHz, $CDCl_3$): δ/ppm = 183.7, 172.5, 150.7, 147.8, 144.6, 142.4, 140.9, 129.2, 1285, 128.0, 125.3, 122.4, 111.1, 107.7, 101.6, 93.2, 69.3, 49.5, 44.4., 34.8, 28.4, 27.0, 26.3, 24.6.

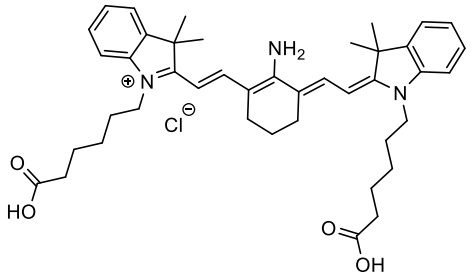
HR-ESI MS: Calculated for $[M]^+ = C_{53}H_{63}N_4O_4S$: expected = 851.4570 found = 851.4558.



2-((*E*)-2-((*E*)-2-(bis(thiophen-2-ylmethyl)amino)-3-(2-((*E*)-1-(5-carboxypentyl)-3,3-dimethylindolin-2-ylidene)ethylidene)cyclohex-1-en-1-yl)vinyl)-1-(5-carboxypentyl)-3,3-dimethyl-3*H*-indol-1-ium bromide (5.9): Compound **5.3** (0.27 g, 1.29 mmol) was dissolved in DMF (40 mL) and **5.6** (0.10 g, 0.13 mmol) added, forming a dark green solution which was left to stir at 70 °C under N_2 with the flask wrapped in foil. After 4 hours, the reaction mixture was poured into Et_2O (1 L) and left to stir vigorously. After one hour, formation of a green precipitate was observed. This precipitate was isolated by filtration. Flash chromatography (DCM to 20% MeOH in DCM) gave **5.9** as a blue-green solid (0.01 g, 0.01 mmol, 5%).

^{1}H NMR (400 MHz, CD_3OD): δ/ppm = 8.44 – 8.38 (m, 2H, N=CC<u>H</u>=CH), 7.51 – 7.49 (m, 2H, Ar-<u>H</u>), 7.41 – 7.37 (m, 2H, Ar-<u>H</u>), 7.33 – 7.24 (m, 4H, Ar-<u>H</u>), 6.93 – 6.88 (m, 2H, Ar-<u>H</u>), 6.30 – 6.22 (m, 2H, ArC<u>H</u>=CH), 4.14 (m, 2H, Cα<u>H</u>$_2$), 3.60 (s, 2H, thC<u>H</u>$_2$N), 2.71 – 2.66 (m, 2H, Cε<u>H</u>$_2$), 2.22 (m, 2H, cyclic C<u>H</u>$_2$), 1.83 – 1.71 (m, 8H, Cβ<u>H</u>$_2$ and Cδ<u>H</u>$_2$), 1.70 (s, 6H, C<u>H</u>$_3$), 1.46 – 1.45 (m, 4H, cyclic C<u>H</u>$_2$), 1.25 (m, 4H, Cγ<u>H</u>$_2$).

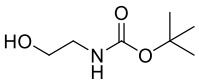
LR-ESI MS: Calculated for M = $C_{52}H_{61}N_3O_4S_2$ (zwitterion): expected $[M+NH_4]^+$ = 874.20, found = 874.00.



2-((*E*)-2-((*E*)-2-Amino-3-(2-((*E*)-1-(5-carboxypentyl)-3,3-dimethylindolin-2-ylidene)ethylidene)cyclohex-1-en-1-yl)vinyl)-1-(5-carboxypentyl)-3,3-dimethyl-3*H*-indol-1-ium chloride (5.10): Compound **5.6** (0.31 g, 0.41 mmol) was dissolved in MeCN (50 mL). Potassium phthalimide (0.08 g, 0.44 mmol) was added and the reaction mixture left to stir at 90 °C under N_2 with the rbf wrapped in foil. After 18 hours, the reaction mixture was allowed to cool to room temperature. $N_2H_4{\cdot}2HCl$ (0.06 g, 0.54 mmol) in H_2O (16 mL) was added and the reaction mixture left to stir at 60 °C under N_2, again with the flask wrapped in foil. After a further 23 hours, the solvent was removed *in vacuo* to leave a purple solid. Flash chromatography (DCM to 30% MeOH in DCM) gave **5.10** as a purple solid (0.15 g, 0.21 mmol, 54%).

^{1}H NMR (400 MHz, CD_3OD): δ/ppm = 8.19 (d, $^3J_{HH}$ = 10.7 Hz, 2H, N=CC<u>H</u>=CH), 7.26 (d, $^3J_{HH}$ = 7.9Hz, 2H, Ar-<u>H</u>), 7.20 (t, $^3J_{HH}$ = 7.7 Hz, 2H, Ar-<u>H</u>), 6.94 (t, $^3J_{HH}$ = 7.5 Hz, 2H, Ar-<u>H</u>), 6.86 (d, $^3J_{HH}$ = 7.9 Hz, 2H, Ar-<u>H</u>), 5.59 (d, $^3J_{HH}$ = 12.00 Hz, 2H, ArC<u>H</u>=CH), 3.79 (t, $^3J_{HH}$ = 7.5 Hz, 4H, Cα<u>H</u>$_2$), 2.60 (t, $^3J_{HH}$ = 6.1 Hz, 4H, Cε<u>H</u>$_2$), 2.30 (t, $^3J_{HH}$ = 7.3 Hz, 4H, cyclic C<u>H</u>$_2$), 1.86 (t, $^3J_{HH}$ = 6.0 Hz, 2H, cyclic C<u>H</u>$_2$), 1.73 – 1.69 (m, 8H, Cβ<u>H</u>$_2$ and Cδ<u>H</u>$_2$), 1.65 (s, 12H, C<u>H</u>$_3$), 1.47 (m, 4H, Cγ<u>H</u>$_2$).

LR-ESI MS: Calculated for M = $C_{42}H_{53}N_3O_4$ (zwitterion), $[M+H]^+$ expected = 664.91, found = 665.40.



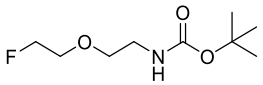
***Tert*-butyl (2-hydroxyethyl)carbamate[14] (5.11)**: Ethanolamine (0.50 mL, 8.29 mmol) was dissolved in DCM (20 mL) and cooled to 0 °C. Triethylamine (1.73 mL, 9.12 mmol) was added, followed by Boc_2O (2.04 g, 10.10 mmol). The reaction mixture was allowed to warm temperature and left to stir. After 18 hours, TLC suggested that the reaction had reached completion. NH_4Cl solution (aq., sat., 50 mL) was added and the reaction mixture extracted with EtOAc (100 mL). The organic phase was washed with brine (50 mL) before being dried over $MgSO_4$. The solvent was removed *in vacuo* to leave **5.11** as a yellow oil (1.32 g, 8.16 mmol, 98%).

^{1}H NMR ($CDCl_3$, 400 MHz): δ/ppm = 4.96 (br s, 1H, N<u>H</u>), 3.69 (t, $^3J_{HH}$ = 4.8 Hz, 2H, C<u>H</u>$_2$OH), 3.28 (q, $^3J_{HH}$ = 4.8 Hz, 2H, C<u>H</u>$_2$NH), 1.44 (s, 9H, COO^t<u>Bu</u>).

^{13}C NMR (101 MHz, $CDCl_3$): δ/ppm = 157.0, 122.4, 98.2, 61.9, 50.3, 43.0, 28.4.

HR-ESI MS: Calculated for M = $C_7H_{15}NO_3$: expected $[M + Na]^+$ = 184.0944 found = 184.0946.

Data corresponds to literature[14].

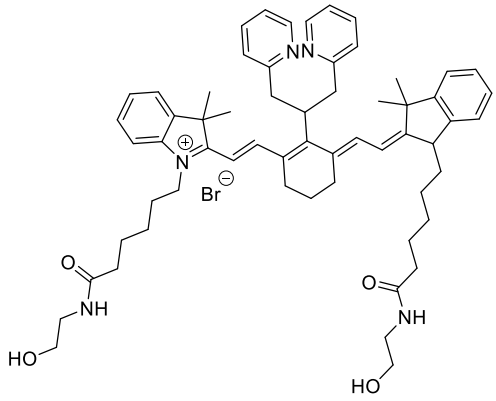


***Tert*-butyl (2-(2-fluoroethoxy)ethyl)carbamate[15] (5.12)**: Compound **5.11** (2.32 g, 14.38 mmol) was dissolved in dry DMF (30 mL). 2-Fluoroethyl *p*-toluenesulfonate (1.00 g, 4.58 mmol) was added and the solution cooled to 0 °C. NaH (0.53 g, 22.18 mmol) was added and the resulting yellow solution left to stir and warm to room temperature. After 19 hours. H_2O (50 mL) was added to the bright yellow reaction mixture. The solution was extracted with EtOAc (2 x 30 mL) and the combined organic phases washed with H_2O (40 mL) and brine (50 mL) before being dried over $MgSO_4$. The solvent was removed *in vacuo* to leave a yellow oil. Automated flash chromatography (20% EtOAc in petroleum ether to 50% EtOAc in petroleum ether, followed by 40% EtOAc in petroleum ether, isocratic conditions) gave **5.12** as a colourless oil (0.17 g, 0.80 mmol, 17%).

^{1}H NMR ($CDCl_3$, 400 MHz): δ/ppm = 4.64 – 4.60, (m, 1H, C$\underline{H_2}$F), 4.52 – 4.48, (m, 1H, C$\underline{H_2}$F), 3.75 – 3.73 (m, 1H, FCH$_2$C$\underline{H_2}$O), 3.68 – 3.66 (m, 1H, FCH$_2$C$\underline{H_2}$O), 3.57 (t, $^3J_{HH}$ = 5.0 Hz, 2H, OC$\underline{H_2}$CH$_2$N), 3.26 – 3.21 (m, 2H, OC$\underline{H_2}$CH$_2$N), 1.56 (s, 9H, COO$^t\underline{Bu}$).

^{19}F NMR ($CDCl_3$, 377 MHz): δ/ppm = -221.42 (tt, $^2J_{FH}$ = 47.4 Hz, 28.6 Hz, 1F, $\underline{F}$CH$_2$).

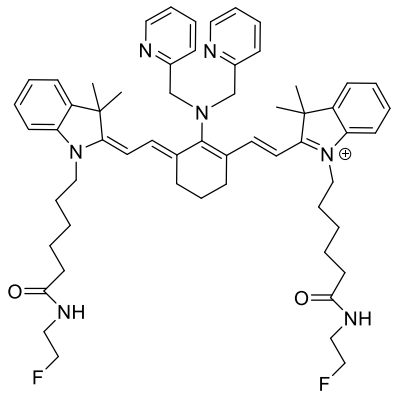
Data corresponds to literature[15].



2-((*E*)-2-((*E*)-2-(1,3-Di(pyridin-2-yl)propan-2-yl)-3-(2-((*Z*)-3-(6-((2-hydroxyethyl)amino)-6-oxohexyl)-1,1-dimethyl-1,3-dihydro-2*H*-inden-2-ylidene)ethylidene)cyclohex-1-en-1-yl)vinyl)-1-(6-((2-hydroxyethyl)amino)-6-oxohexyl)-3,3-dimethyl-3*H*-indol-1-ium bromide (5.13):
Compound **5.7** (0.02 g, 0.02 mmol) was dissolved in DMF (30 mL). Ethanolamine (0.02 mL, 0.04 mmol) was added, followed by DIPEA (0.07 mL, 0.04 mmol) and HATU (0.02 g, 0.05 mmol), forming a dark green solution which was left to stir at room temperature. After 25 hours, TLC suggested that

the reaction had gone to completion. The reaction mixture was poured into Et_2O (1 L), which was stirred vigorously. After 2 hours, this solution was cooled to 0 °C, which resulted in the formation of a dark blue precipitate. This precipitate was isolated by filtration before being washed into an rbf with MeOH. The solvent was removed *in vacuo* to leave **5.13** blue solid (2.43 mg, 2.40 μmol, 12%).

LR ESI-MS: Calculated for M = $C_{60}H_{75}N_5O_4$ (zwitterion). Expected $[M+H]^+$ = 931.30, found = 932.58.



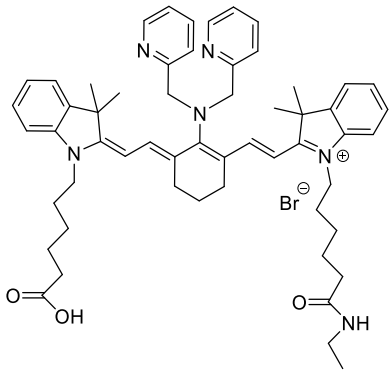
2-((*E*)-2-((*E*)-2-(Bis(pyridin-2-ylmethyl)amino)-3-(2-((*E*)-1-(6-((2-fluoroethyl)amino)-6-oxohexyl)-3,3-dimethylindolin-2-ylidene)ethylidene)cyclohex-1-en-1-yl)vinyl)-1-(6-((2-fluoroethyl)amino)-6-oxohexyl)-3,3-dimethyl-3*H*-indol-1-ium bromide (5.14): Compound **5.7** (0.13 g, 0.14 mmol) was dissolved in DMF (20 mL). HATU (0.09 g, 0.24 mmol) was added, followed by 2-fluoroethylamine hydrochloride (0.09 g, 0.90 mmol) and DIPEA (0.08 mL, 0.48 mmol), forming a dark blue solution which was left to stir at room temperature. After 18 hours, additional portions of HATU (0.18 g, 0.46 mmol) and 2-fluoroethylamine hydrochloride (0.16 g, 1.60 mmol) and DIPEA (0.15 mL, 0.86 mmol) were added and the reaction mixture left to stir for a further 6 hours, after which the reaction mixture was poured into Et_2O (1.00 L) and left to stir. After 16 hours, formation of a blue precipitate was observed. This precipitate was isolated by filtration. Automated flash chromatography (DCM to MeOH) gave **5.14** as a blue solid (0.11 g, 0.11 mmol, 69%).

^{1}H NMR ($CDCl_3$, 400 MHz): δ/ppm = 8.72 (d, $^3J_{HH}$ = 6.5 Hz, 2H, Ar-H), 7.81 – 7.73 (td, $^3J_{HH}$ = 7.6 Hz, $^4J_{HH}$ = 1.8 Hz, 2H, Ar-H), 7.66 (d, $^3J_{HH}$ = 13.6 Hz, 2H, HC=CH), 7.39 – 7.27 (m, 8H, Ar-H), 7.13 (td, $^3J_{HH}$ = 7.5, $^4J_{HH}$ = 1.8 Hz, 2H, Ar-H), 6.97 (d, $^3J_{HH}$ = 8.0 Hz, 2H, Ar-H), 6.16 (br s, 2H, CONH), 5.89 (d, $^3J_{HH}$ = 13.6 Hz, 2H, HC=CH), 4.76 (s, 4H, ArCH_2N), 4.46 (dt, $^2J_{FH}$ = 47.5 Hz, $^3J_{HH}$ = 5.1 Hz, 4H), 3.88 (t, $^3J_{HH}$ = 7.6 Hz, 4H, ArNCH_2) 3.72(t, $^3J_{HH}$ = 7.6 Hz, 4H, NHCOCH_2), 3.55 (dq, $^3J_{FH}$ = 26.2 Hz, $^3J_{HH}$ = 5.4 Hz 4H, FCH_2CH_2), 2.57 (t, $^3J_{HH}$ = 6.4 Hz, 4H. CH_2CHCH_2), 2.26 (t, $^3J_{HH}$ = 7.4 Hz, 4H, CH_2), 1.94 (m, 2H, CH_2CHCH_2), 1.81 – 1.72 (m, 8H, CH_2CH_2), 1.44 (s, 12H, CH_3).

^{19}F NMR ($CDCl_3$, 377 MHz): δ/ppm = -225.82 (dd, $^2J_{FH}$ = 47.2 Hz, $^3J_{FH}$ = 26.3 Hz, 2F).

^{13}C NMR ($CDCl_3$, 101 MHz): δ/ppm = 162.2, 156.7, 150.1, 143.7, 142.6, 140.3, 137.4, 128.6, 124.7, 123.9, 123.7, 123.1, 122.0, 109.6, 97.0, 83.1, 81.4, 77.4, 77.0, 76.7, 60.3, 55.9, 48.1, 45.6, 43.8, 39.9, 36.0, 28.6, 26.6, 25.2, 21.9, 18.5, 12.7.

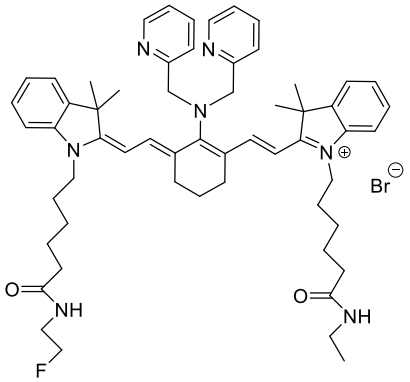
LR-ESI-MS: Calculated for M = $C_{58}H_{72}F_2N_7O_2$, expected $[M+H]^+$ = 937.57, found = 937.60.



2-((*E*)-2-((*E*)-2-(Bis(pyridin-2-ylmethyl)amino)-3-(2-((*E*)-1-(5-carboxypentyl)-3,3-dimethylindolin-2-ylidene)ethylidene)cyclohex-1-en-1-yl)vinyl)-1-(6-(ethylamino)-6-oxohexyl)-3,3-dimethyl-3*H*-indol-1-ium bromide (5.15): Compound **5.7** (0.10 g, 0.11 mmol) was dissolved in DCM (20 mL). DIPEA (0.04 mL, 0.23 mmol) was added, followed by HATU (0.05 g, 0.12 mmol) and ethylamine hydrochloride (0.01 g, 0.13 mmol), forming a blue solution which was left to stir at room temperature. After 23 hours, the reaction mixture was poured into Et_2O (750 mL) and left to stir. After 6 hours, formation of a blue precipitate was observed. This precipitate was isolated by filtration. Automated flash chromatography (DCM to 25% MeOH) gave **5.15** as a blue solid (0.03 g, 0.03 mmol, 26%).

^{1}H NMR ($CDCl_3$, 400 MHz): δ/ppm = 8.73 – 8.68 (m, 1H, Ar-H), 8.51 (d, $^3J_{HH}$ = 4.6 Hz, 1H, Ar-H), 7.83 – 7.73 (m, 1H, Ar-H), 7.69 – 7.56 (m, 3H, Ar-H), 7.40 – 7.27 (m, 3H, Ar-H), 7.21 – 7.09 (m, 3H, Ar-H), 7.01 (d, $^3J_{HH}$ = 7.8 Hz, 1H, HC=CH), 6.96 (d, $^3J_{HH}$ = 7.9 Hz, 1H, HC=CH), 5.90 (d, $^3J_{HH}$ = 13.6 Hz, 1H, HC=CH), 4.74 (s, 2H, ArCH_2N), 3.91 (s, 2H, ArCH_2N), 2.56-2.50 (m, 2H, CH_2), 2.45 – 2.34 (m, 4H, CH_2), 2.34 – 2.25 (m, 2H, CH_2), 1.95 (dd, $^2J_{HH}$ = 13.0 Hz, $^3J_{HH}$ = 6.5 Hz, 2H, CH_2), 1.85 – 1.76 (m, 2H, CH_2), 1.76 – 1.63 (m, 6H, CH_2), 1.59 (s, 6H, CH_3), 1.57 (s, 6H, CH_3), 1.12 (t, $^3J_{HH}$ = 7.2 Hz, 3H, NCH_2CH_3).

LR-ESI-MS: Calculated for M = $C_{56}H_{68}N_6O_3$, expected $[M+H]^+$ = 874.21, found = 874.50.

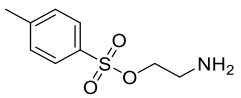


2-((*E*)-2-((*E*)-2-(Bis(pyridin-2-ylmethyl)amino)-3-(2-((*E*)-1-(6-((2-fluoroethyl)amino)-6-oxohexyl)-3,3-dimethylindolin-2-ylidene)ethylidene)cyclohex-1-en-1-yl)vinyl)-1-(6-(ethylamino)-6-oxohexyl)-3,3-dimethyl-3*H*-indol-1-ium bromide (5.16): Compound **5.15** (0.03 g, 0.03 mmol) was dissolved in DCM (20 mL). 2-fluoroethylamine (6.40 mg, 0.06 mmol) was added, followed by HATU (0.02 g, 0.05 mmol) and DIPEA (0.02 mL, 0.09 mmol), forming a blue solution which was left to stir at room temperature. After 24 hours, the solvent was removed *in vacuo* to leave a blue solid. Automated flash chromatography (DCM to MeOH) gave **5.16** as a blue solid (8.60 mg, 29%).

^{1}H NMR ($CDCl_3$, 400 MHz): δ/ppm = 8.71 (d, $^{3}J_{HH}$ = 4.7 Hz, 1H, Ar-H), 8.55 – 8.48 (m, 1H, Ar-H), 7.76 (t, $^{3}J_{HH}$ = 8.5 Hz 1H, Ar-H), 7.68 – 7.63 (m, 2H, HC=CH), 7.37 – 7.28 (m, 4H, Ar-H), 7.23 – 7.13 (m, 4H, Ar-H), 7.02 – 6.92 (m, 1H, Ar-H), 5.97 – 5.77 (m, 2H, HC=CH), 4.75 (t, $^{3}J_{HH}$ = 7.1 Hz, 4H, NHCOCH_2), 4.48 (dd, $^{2}J_{FH}$ = 47.5 Hz, $^{3}J_{HH}$ = 4.7, 2H, FCH_2), 3.92 – 3.82 (m, 2H, CH_2), 3.73 (s, 2H, ArCH_2), 2.91 (m, 2H, CH_2), 2.60 – 2.47 (m, 2H, CH_2), 2.47 – 2.29 (m, 2H, CH_2), 2.27 – 2.17 (m, 2H, CH_2), 1.96 – 1.88 (m, 1H, CH_2), 1.82 – 1.58 (m, 8H, CH_2), 1.47 (s, 6H, CH_3), 1.45 (s, 6H, CH_3), 1.10 (t, $^{3}J_{HH}$ = 8.5 Hz, 3H, CH_3).

^{19}F NMR ($CDCl_3$, 377 MHz): δ/ppm = -224.07 (t, $^{2}J_{FH}$ = 47.1 Hz, 1F).

LR-ESI-MS: Calculated for M = $C_{58}H_{72}FN_6O_3$, expected $[M + H]^+$ = 920.25, found = 920.60.

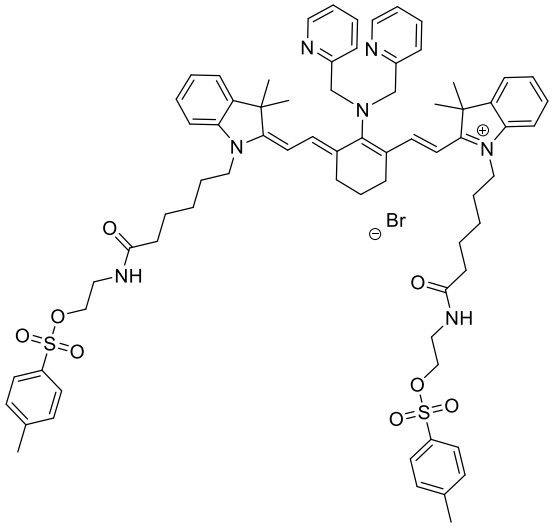


2-Aminoethyl 4-methylbenzenesulfonate (5.17): Ethanolamine (0.25 mL, 3.89 mmol) was dissolved in DCM (20 mL). *p*-Tosyl chloride (0.87 g, 4.54 mmol) was added, followed by pyridine (0.63 mL, 7.78 mmol), forming a yellow solution which was left to stir at room temperature. After 3 hours, the solvent was removed *in vacuo* to leave an off-white residue. Automated flash chromatography (DCM to MeOH) gave **5.17** as a yellow oil (0.24 g, 1.12 mmol, 29%).

^{1}H NMR ($CDCl_3$, 400 MHz): δ/ppm = 7.69 (t, $^{3}J_{HH}$ = 8.3 Hz, 2H, Ar-H), 7.21 (t, $^{3}J_{HH}$ = 8.5 Hz, 2H, Ar-H), 6.16 (br s, 1H, NH_2), 3.60 (t, $^{3}J_{HH}$ = 4.8 Hz 2H, $CH_2CH_2NH_2$), 2.99 (t, $^{3}J_{HH}$ = 5.2 Hz, 2H, $CH_2CH_2NH_2$), 2.33 (s, 3H, CH_3Ar).

^{13}C NMR (101 MHz, $CDCl_3$): δ/ppm = 144.0, 137.0, 130.2, 127.5, 61.7, 45.6, 22.0.

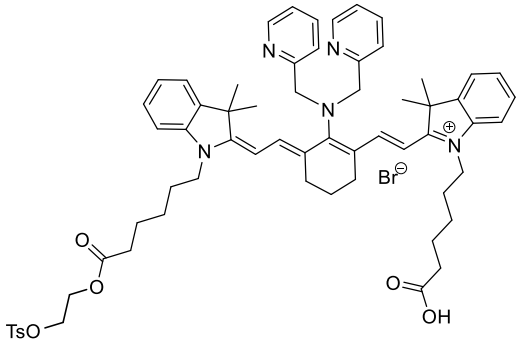
HR-ESI-MS: Calculated for M = $C_9H_{13}NO_3S$, expected $[M + Na]^+$ = 238.0508, found = 238.0504.



2-((*E*)-2-((*E*)-2-(Bis(pyridin-2-ylmethyl)amino)-3-(2-((*E*)-3,3-dimethyl-1-(6-oxo-6-((2-(tosyloxy)ethyl)amino)hexyl)indolin-2-ylidene)ethylidene)cyclohex-1-en-1-yl)vinyl)-3,3-dimethyl-1-(6-oxo-6-((2-(tosyloxy)ethyl)amino)hexyl)-3*H*-indol-1-ium bromide (5.18): Compound **5.7** (0.17 g, 0.18 mmol) was dissolved in DCM (20 mL). Compound **5.17** (0.09 g, 0.40 mmol) was added, followed by HATU (0.08 g, 0.20 mmol) and DIPEA (0.03 mL, 0.18 mmol), forming a blue solution which was left to stir at room temperature. After 22 hours, the solvent was removed *in vacuo* to leave a blue solid. Automated flash chromatography gave **5.18** as a blue solid (0.03 g, 0.02 mmol, 11%).

^{1}H NMR ($CDCl_3$, 400 MHz): δ/ppm = 8.71 (d, $^{3}J_{HH}$ = 4.1 Hz, 1H, Ar-H), 7.79 (d, $^{3}J_{HH}$ = 7.7 Hz, 1H, Ar-H), 7.77 – 7.71 (t, $^{3}J_{HH}$ = 8.2 Hz, 3H, Ar-H), 7.65 (d, $^{3}J_{HH}$ = 13.3 Hz, 1H, HC=CH), 7.38 – 7.33 (m, 1H, Ar-H), 7.30 (t, $^{3}J_{HH}$ = 8.2 Hz 5H, Ar-H), 7.13 (t, $^{3}J_{HH}$ = 7.4 Hz, 1H, Ar-H), 6.98 (d, $^{3}J_{HH}$ = 7.9 Hz, 1H, Ar-H), 5.92 (d, $^{3}J_{HH}$ = 13.6 Hz, 1H, HC=CH), 5.16 (t, $^{3}J_{HH}$ = 6.3 Hz, 1H, CH_2), 4.94 (t, $^{3}J_{HH}$ = 5.9 Hz, 1H, CH_2), 4.75 (s, CONH, 1.99H), 4.41 (d, $^{3}J_{HH}$ = 7.0 Hz, 1H, CH_2), 4.11 (t, $^{3}J_{HH}$ = 5.3 Hz, 2H, CH_2), 3.96 – 3.85 (m, 2H, CH_2), 3.68 (t, $^{3}J_{HH}$ = 5.1 Hz, 1H, OCH_2), 3.18 (m, 2H, CH_2), 3.12 (s, 4H, $ArCH_2$), 3.09 – 3.05 (m, 2H, CH_2NH), 2.57 (m, 2H, CH_2), 2.41, (s, 6H, $ArCH_3$), 2.33 (m, 2H, CH_2), 1.94 (t, $^{3}J_{HH}$ = 6.5 Hz, 2H, CH_2), 1.85 – 1.75 (m, 2H, CH_2), 1.75 – 1.63 (m, 4H, CH_2).

LR-ESI-MS: Calculated for M = $C_{72}H_{85}N_7O_8S_2$, expected $[M + H]^+$ = 1241.64, found = 1241.60.

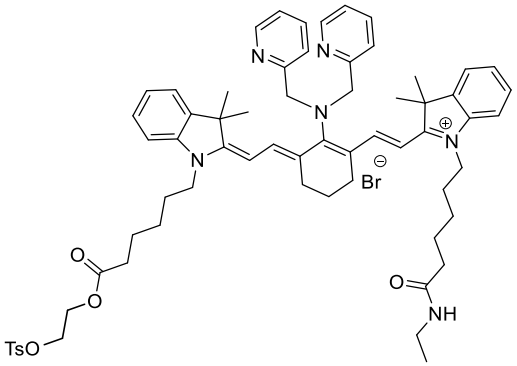


2-((*E*)-2-((*E*)-2-(Bis(pyridin-2-ylmethyl)amino)-3-(2-((*E*)-3,3-dimethyl-1-(6-oxo-6-(2-(tosyloxy)ethoxy)hexyl)indolin-2-ylidene)ethylidene)cyclohex-1-en-1-yl)vinyl)-1-(5-carboxypentyl)-3,3-dimethyl-3*H*-indol-1-ium bromide (5.19): Compound **5.7** (16.90 mg, 0.18 mmol) was dissolved in DCM (10 mL). DIPEA (3.50 µL, 0.02 mmol) was added, followed by 2-aminoethyl 4-methylbenzenesulfonate (3.90 mg, 0.02 mmol), forming a blue solution which was left to stir at room temperature. After 17 hours, the solvent was removed *in vacuo* to leave a blue solid. Automated flash chromatography (DCM to MeOH) gave **5.19** as a blue solid (10.20 mg, 0.01 mmol, 50%).

^{1}H NMR ($CDCl_3$, 400 MHz) δ/ppm = 7.76 (d, $^3J_{HH}$ = 2.0 Hz, 2H, Ar-H), 7.64 (d, $^3J_{HH}$ = 8.1 Hz, 1H, HC=CH), 7.42 (d, $^3J_{HH}$ = 8.4 Hz, 1H, Ar-H), 7.32 (s, 6H, Ar-H), 7.12 (s, 3H, Ar-H), 6.97 (d, $^3J_{HH}$ = 13.0 Hz, 2H, Ar-H), 5.90 (d, $^3J_{HH}$ = 11.7 Hz, 1H, HC=CH), 4.75 (s, 9H, CH_2), 3.97 – 3.88 (m, 2H, CH_2), 3.21 – 3.10 (m, 6H, CH_2), 2.94 (d, $^3J_{HH}$ = 3.7 Hz, 2H, CH_2), 2.80 (s, 3H, CH_2), 2.64 – 2.50 (m, 14H, CH_2), 2.45 – 2.26 (m, 29H, $ArCH_3$ and CH_2), 2.03 (d, $^3J_{HH}$ = 17.9 Hz, 6H, CH_2), 1.94 (d, $^3J_{HH}$ = 9.9 Hz, 3H, CH_2), 1.82 – 1.67 (m, 12H, CH_3)

^{13}C NMR ($CDCl_3$, 101 MHz) δ/ppm = 221.9, 185.0, 179.6, 170.1, 167.8, 142.6, 140.9, 130.8, 127.8, 123.4, 97.8, 95.9, 92.3, 89.3, 72.6, 55.3, 46.1, 29.8, 26.2, 21.5.

HR-ESI-MS: Calculated for $M^+ = C_{63}H_{74}N_5O_7S^+$, expected = 1043.5469 found = 1043.5476.

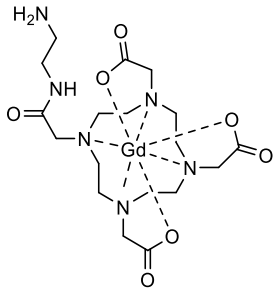


2-((*E*)-2-((*E*)-2-(Bis(pyridin-2-ylmethyl)amino)-3-(2-((*E*)-3,3-dimethyl-1-(6-oxo-6-(2-(tosyloxy)ethoxy)hexyl)indolin-2-ylidene)ethylidene)cyclohex-1-en-1-yl)vinyl)-1-(6-(ethylamino)-6-oxohexyl)-3,3-dimethyl-3*H*-indol-1-ium bromide (5.20): Compound **5.19**, (10.20 mg, 9.10 µmol) was dissolved in DCM (10 mL). HATU (5.40 mg, 14.20 µmol) was added, followed by ethylamine hydrochloride (2.70 mg, 33.10 µmol) and DIPEA (5.80 µL, 27.40 µmol), forming a dark blue solution which was left to stir at room temperature. After 4 hours, the solvent was removed *in vacuo* to leave a blue solid. Automated flash chromatography (DCM to MeOH) gave **5.20** as a blue solid (7.40 mg, 6.43 µmol, 71%).

^{1}H NMR (400 MHz, $CDCl_3$) δ/ppm = 8.71 (d, $^{3}J_{HH}$ = 4.1 Hz, 1H, Ar-H), 7.81 – 7.70 (m, 4H, Ar-H), 7.67 – 7.58 (m, 1H, HC=CH), 7.40 – 7.26 (m, 3H, Ar-H), 7.13 (d, $^{3}J_{HH}$ = 7.9 Hz, 1H, Ar-H), 7.03 – 6.91 (m, 5H, Ar-H), 6.85 (d, $^{3}J_{HH}$ = 8.0 Hz, 1H, HC=CH), 4.75 (s, 3H, CH_2 and CONH), 4.16 – 4.08 (m, 2H, CH_2), 3.93 – 3.86 (m, 1H, CH_2), 3.26 (m, 3H, CH_2), 2.60 – 2.52 (m, 5H, CH_2 and CH_3), 2.41 (s, 2H, CH_2), 2.34 (s, 1H CH_2), 2.25 – 2.17 (m, 1H), 1.35 (s, 9H, ArCH_3), 1.24 (s, 13H, CH_3).

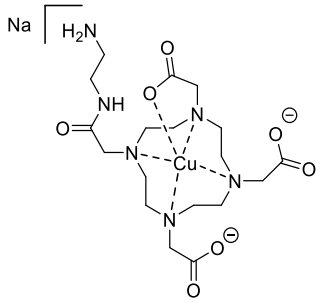
^{13}C NMR (101 MHz, $CDCl_3$) δ/ppm = 240.4, 230.6, 207.0, 167.2, 162.1, 138.8, 134.8, 131.9, 98.9, 97.2, 64.5, 55.6, 53.6, 51.0, 48.7, 43.6, 38.8, 36.4, 28.8, 18.7, 17.4, 12.6.

HR-ESI-MS: Calculated for M^+ = $C_{65}H_{79}N_6O_6S^+$, expected = 1070.5293, found = 1070.5374.

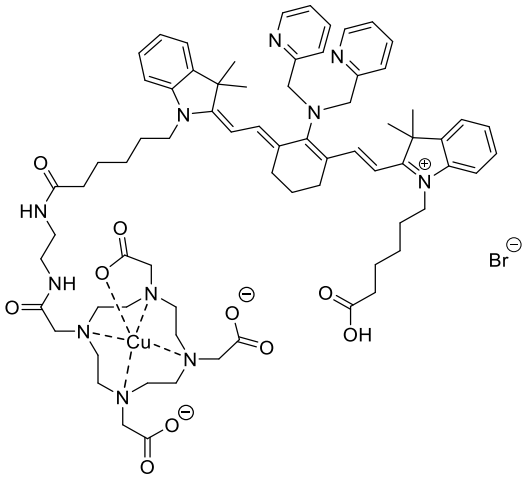


Gadolinium 2,2',2''-(10-(2-((2-aminoethyl)amino)-2-oxoethyl)-1,4,7,10-tetraazacyclododecane-1,4,7-triyl)triacetate (5.21): **H_3do3a-NH_2** (22.50 mg, 50.40 µmol) was dissolved in H_2O (5 mL).

$GdCl_3 \cdot 6H_2O$ (27.10 mg, 72.90 µmol) was added and the reaction mixture brought to pH 8 by addition of NaOH (0.1 M, aq.). After 22 hours, the solvent was removed *in vacuo* to leave a white solid. Reverse phase automated flash chromatography (99.9% H_2O + 0.1% TFA to 99.9% MeCN + 0.1% TFA) gave **5.21** as a white solid (16.00 mg, 26.60 µmol, 59%).

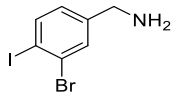


Sodium [Copper 2,2'-(7-(2-((2-aminoethyl)amino)-2-oxoethyl)-10-(carboxymethyl)-1,4,7,10-tetraazacyclododecane-1,4-diyl)triacetate] (5.22): H_3do3a-NH_2 (15.40 mg, 34.50 µmol) was dissolved in H_2O (5 mL). $CuSO_4 \cdot 5H_2O$ (27.10 mg, 72.90 µmol) was added and the reaction mixture brought to pH 6 by addition of NaOH (0.1 M, aq.). After 17 hours, the solvent was removed *in vacuo* to leave a blue solid. Reverse phase automated flash chromatography (99.9% H_2O + 0.1% TFA to 99.9% MeCN + 0.1% TFA) gave **5.22** as a blue solid (5.40 mg, 10.19 µmol, 30%).



CyDPA-[Cu(do3a-NH_2)] (5.23): Compound **5.7** (13.40 mg, 14.50 µmol) was dissolved in DMF (10 mL). Compound **5.22** (5.40 mg, 10.19 µmol) was added, followed by HATU (5.00 mg, 13.10 µmol) and DIPEA (1.90 µL, 10.70 µmol), forming a dark blue solution which was left to stir at room temperature. After 22 hours, the reaction mixture was poured into Et_2O (400 mL) and left to stir. After 3 hours, formation of a dark blue precipitate was observed. This precipitate was isolated by filtration before being washed into an rbf with MeOH. The solvent was removed *in vacuo* to leave a blue solid. Reverse phase automated flash chromatography (99.9% H_2O + 0.1% TFA to 99.9% MeCN + 0.1% TFA) gave **5.23** as a blue-green solid (4.30 mg, 3.23 µmol, 30%).

LR-ESI-MS: Calculated for $M^+ = [C_{72}H_{93}CuN_{11}O_{10}]^+$ - Expected [M + 2Na] = 1382.15, found $[M]^{4+}$ at ~346 and $[M]^{3+}$ at ~ 466.

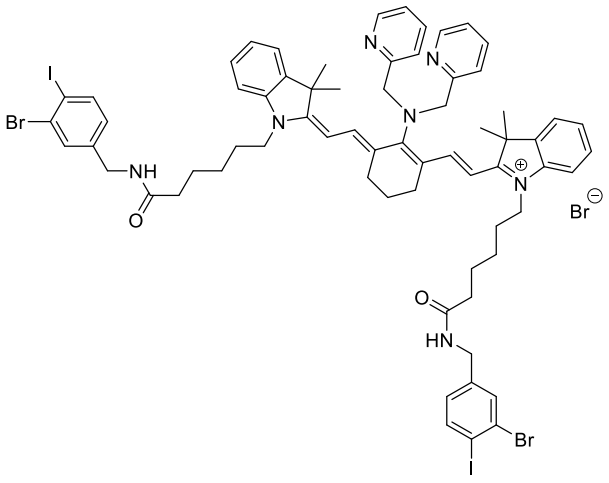


(3-Bromo-4-iodophenyl)methanamine (5.24): Compound **3.13** (0.15 g, 0.40 mmol) was dissolved in dry DMF (10 mL). Potassium phthalimide (0.10 g, 0.55 mmol) was added and the reaction mixture left to stir at 120 °C under N_2. After 16 hours, the reaction mixture was poured into H_2O (300 mL) at 0 °C, forming a white suspension which was washed with EtOAc (3 x 50 mL). The combined organic phases were dried over $MgSO_4$ and the solvent removed *in vacuo* to leave a white solid. This solid was re-suspended in EtOH (75 mL) and hydrazine hydrate (0.04 mL, 0.76 mmol) added, forming a white suspension which was left to stir at 90 °C. After 7 hours, H_2O (50 mL) was added. The EtOH was removed *in vacuo* and HCl (10%, 40 mL) added to the resultant solution, which was left to stir at 90 °C. After 16 hours, the reaction mixture was allowed to cool to room temperature. The solution was basified by addition of NaOH before being extracted with DCM (2 x 75 mL). The combined organic phases were dried over $MgSO_4$ and the solvent removed *in vacuo* to leave a white solid. Automated flash chromatography (DCM to 25% MeOH in DCM) gave **5.24** as a yellow oil (0.12 g, 0.39 mmol, 98%).

^{1}H NMR ($CDCl_3$, 400 MHz) δ/ppm = 7.77 (d, $^3J_{HH}$ = 8.1 Hz, 1H, Ar-H), 7.59 (d, $^3J_{HH}$ = 2.0 Hz, 1H, Ar-H), 6.94 (dd, $^3J_{HH}$ = 8.1 Hz, $^4J_{HH}$ = 2.0 Hz, 1H, Ar-H), 3.80 (s, 2H, ArCH_2), 1.56 (s, 3H, NH_2).

^{13}C NMR ($CDCl_3$, 101 MHz) δ/ppm = 145.0, 140.0, 131.2, 127.1, 98.3, 45.1.

HR-ESI-MS: Calculated for M = C_7H_7NBrI - Expected $[M+H]^+$: 311.8897 found: 311.8886.



2-((*E*)-2-((*E*)-2-(Bis(pyridin-2-ylmethyl)amino)-3-(2-((*E*)-1-(6-((3-bromo-4-iodobenzyl)amino)-6-oxohexyl)-3,3-dimethylindolin-2-ylidene)ethylidene)cyclohex-1-en-1-yl)vinyl)-1-(6-((3-bromo-4-iodobenzyl)amino)-6-oxohexyl)-3,3-dimethyl-3*H*-indol-1-ium bromide, **(5.25)**: Compound **5.24** (27.40 mg, 90.00 µmol) was dissolved in DCM (20 mL). DIPEA (13.90 µL, 80.00 µmol), HATU (33.40 mg, 90.00 µmol) and compound **5.7** (74.70 mg, 80.00 µmol), forming a dark blue solution which was left to stir at room temperature. After 16 hours, the solvent was removed *in vacuo* to leave a blue solid. Automated flash chromatography (DCM to MeOH) gave **5.25** as a blue solid (36.60 mg, 24.20 µmol, 30%).

^{1}H NMR ($CDCl_3$, 400 MHz) δ/ppm = 8.71 – 8.64 (m, 1H, Ar-H), 8.46 (d, $^{3}J_{HH}$ = 4.7 Hz, 1H, Ar-H), 8.39 (d, $^{3}J_{HH}$ = 3.4 Hz, 3H, Ar-H), 8.25 (t, $^{3}J_{HH}$ = 6.2 Hz, 1H, Ar-H), 8.11 (d, $^{3}J_{HH}$ = 8.3 Hz, 3H, Ar-H), 7.71 (td, $^{3}J_{HH}$ = 7.6, $^{4}J_{HH}$ = 1.9 Hz, 1H, Ar-H), Ar-H, 7.64 – 7.54 (m, 2H, Ar-H), 7.45 (d, $^{3}J_{HH}$ = 2.1 Hz, 1H, HC=CH), 7.34 – 7.27 (m, 2H, Ar-H), 7.23 (dd, $^{3}J_{HH}$ = 7.5, $^{4}J_{HH}$ = 5.4 Hz, 2H, Ar-H), 7.17 – 7.11 (m, 4H, Ar-H), 6.98 (d, $^{3}J_{HH}$ = 7.9 Hz, 1H, Ar-H), 6.88 – 6.84 (m, 1H, CH_2), 5.90 (d, $^{3}J_{HH}$ = 13.5 Hz, 1H, HC=CH), 4.72 (s, 2H), 4.32 (s, 1H, CH_2), 4.29 (d, $^{3}J_{HH}$ = 5.9 Hz, 2H, CH_2), 3.91 (d, $^{3}J_{HH}$ = 8.0 Hz, 2H, CH_2), 3.72 (hept, $^{3}J_{HH}$ = 6.7 Hz, 3H, CH_2), 3.11 (q, $^{3}J_{HH}$ = 7.4 Hz, 3H, CH_2), 2.47 (t, $^{3}J_{HH}$ = 6.5 Hz, 1H, CH_2), 2.36 (t, $^{3}J_{HH}$ = 7.4 Hz, 2H, CH_2), 1.84 – 1.58 (m, 5H, CH_2), 1.24 (s, 7H, CH_3).

^{13}C NMR ($CDCl_3$, 101 MHz) δ/ppm = 173.8, 169.4, 157.0, 150.1, 149.3, 148.3, 142.7, 141.8, 140.4, 140.0, 139.8, 137.5, 137.2, 135.2, 131.9, 129.4, 128.7, 128.2, 127.7, 123.9, 123.2, 123.0, 121.9, 119.4, 109.9, 77.5, 77.2, 76.8, 60.3, 53.3, 52.1, 50.8, 48.2, 43.8, 42.3, 41.8, 36.0, 29.8, 28.8, 26.8, 25.4, 25.1, 12.2.

7.9. References

1 D. M. Corsi, C. Platas-Iglesias, H. Van Bekkum and J. A. Peters, *Magn. Reson. Chem.*, 2001, **39**, 723–726.

2 M. Rohrer, H. Bauer, J. Mintorovitch, M. Requardt and H.-J. Weinmann, *Comparison of Magnetic Properties of MRI Contrast Media Solutions at Different Magnetic Field Strengths*, 2005, vol. 40.

3 A. Martinez-Sanchez, M. S. Nguyen-Tu and G. A. Rutter, *Mol. Endocrinol.*, 2015, **29**, 1067–1079.

4 A. Savitzky and M. J. E. Golay, *Anal. Chem.*, 1964, **36**, 1627–1639.

5 A. Kunfi, V. Szabó, Á. Mastalir, I. Bucsi, M. Mohai, P. Németh, I. Bertóti and G. London, *ChemCatChem*, 2017, **9**, 3236–3244.

6 D. O. Yoon, X. Zhao, D. Son, J. T. Han, J. Yun, D. Shin and H. J. Park, *ACS Med. Chem. Lett.*, 2017, **8**, 1336–1340.

7 B. Jagadish, G. L. Brickert-Albrecht, G. S. Nichol, E. A. Mash and N. Raghunand, *Tetrahedron Lett.*, 2011, **52**, 2058–2061.

8 X. Zhang, Y. Shiraishi and T. Hirai, *Org. Lett.*, 2007, **9**, 5039–5042.

9 L. Yuan, W. Lin, Z. Cao, J. Wang and B. Chen, *Chem. - A Eur. J.*, 2012, **18**, 1247–1255.

10 W. S. Perry, S. J. A. Pope, C. Allain, B. J. Coe, A. M. Kenwright and S. Faulkner, *Dalt. Trans.*, 2010,

39, 10974–10983.

11 T. Boltersdorf, J. Ansari, E. Y. Senchenkova, L. Jiang, A. J. P. White, M. Coogan, F. N. E. Gavins and N. J. Long, *Dalt. Trans.*, 2019, **48**, 16764–16775.

12 I. A. Koval, M. Huisman, A. F. Stassen, P. Gamez, O. Roubeau, C. Belle, J. L. Pierre, E. Saint-Aman, M. Lüken, B. Krebs, M. Lutz, A. L. Spek and J. Reedijk, *Eur. J. Inorg. Chem.*, 2004, **20**, 4036–4045.

13 S. Luo, X. Tan, Q. Qi, Q. Guo, X. Ran, L. Zhang, E. Zhang, Y. Liang, L. Weng, H. Zheng, T. Cheng, Y. Su and C. Shi, *Biomaterials*, 2013, **34**, 2244–2251.

14 W. G. Devine, R. Diaz-Gonzalez, G. Ceballos-Perez, D. Rojas, T. Satoh, W. Tear, R. M. Ranade, X. Barros-Álvarez, W. G. J. Hol, F. S. Buckner, M. Navarro and M. P. Pollastri, *ACS Infect. Dis.*, 2017, **3**, 225–236.

15 T. W. Price, G. Firth, C. J. Eling, M. Kinnon, N. J. Long, J. Sturge and G. J. Stasiuk, *Chem. Commun.*, 2018, **54**, 3227–3230.

Chapter 8

Appendix: Table of Rights and Permissions

Page No.	Type of work:	Name of work	Source of work	Copyright holder and contact	permission requested on	I have permission yes /no	Permission note
20	Figure	Figure 1.1	Global aetiology and epidemiology of type 2 diabetes mellitus and its complications, *Nature Reviews Endocrinology*, volume 14, pages 88–98(2018)	© Springer Nature	26/04/2020	yes	Licensed for reproduction in a thesis.
30	Figure	Figure 1.4	Ligand design strategies to increase stability of gadolinium-based magnetic resonance imaging contrast agents, *Nature Communications*, volume 10, Article number: 1420 (2019)	© Springer Nature	n/a	yes	Published under Open Access
31	Figure	Figure 1.5	Ligand design strategies to increase stability of gadolinium-based magnetic resonance imaging contrast agents, *Nature Communications*, volume 10, Article number: 1420 (2019)	© Springer Nature	n/a	yes	Published under Open Access

80	Figure	Figure 2.7	Synthesis and *in vivo* behaviour of an exendin-4-based MRI probe capable of β-cell-dependent contrast enhancement in the pancreas, *Dalton Trans.*, 2020, **49**, 4732	© Royal Society of Chemistry	n/a	yes	Formal permission not required for authors provided appropriate reference is given in the text.
81	Figure	Figure 2.8	Synthesis and *in vivo* behaviour of an exendin-4-based MRI probe capable of β-cell-dependent contrast enhancement in the pancreas, *Dalton Trans.*, 2020, **49**, 4732	© Royal Society of Chemistry	n/a	yes	Formal permission not required for authors provided appropriate reference is given in the text.
82	Figure	Figure 2.9	Synthesis and *in vivo* behaviour of an exendin-4-based MRI probe capable of β-cell-dependent contrast enhancement in the pancreas, *Dalton Trans.*, 2020, **49**, 4732	© Royal Society of Chemistry	n/a	yes	Formal permission not required for authors provided appropriate reference is given in the text.

83	Figure	Figure 2.10	Synthesis and *in vivo* behaviour of an exendin-4-based MRI probe capable of β-cell-dependent contrast enhancement in the pancreas, *Dalton Trans.*, 2020, **49**, 4732	© Royal Society of Chemistry	n/a	yes	Formal permission not required for authors provided appropriate reference is given in the text.
97	Figure	Figure 3.1	High-resolution structure of the human GPR40 receptor bound to allosteric agonist TAK-875, *Nature*, volume 513, pages124–127(2014)	© Springer Nature	17/01/2020	yes	
99	Figure	Figure 3.3	SAR Studies of Indole-5-propanoic Acid Derivatives To Develop Novel GPR40 Agonists *ACS Med. Chem. Lett.* 2017, 8, 12, 1336–1340	© Springer Nature	07/01/2021	yes	See certificate below
130	Figure	Figure 4.1	**Mechanisms of peptide and nonpeptide ligand binding to Class B G-protein-coupled receptors**	© Elsevier	16/04/2020	yes	

			Drug Discovery Today Volume 10, Issue 6, 15 March 2005, Pages 417-427				
145	Figure	Figure 4.16	Switchable Nile Red-Based Probe for Cholesterol and Lipid Order at the Outer Leaflet of Biomembranes *J. Am. Chem. Soc.* 2010, 132, 13, 4907–4916	© American Chemical Society	07/01/ 2021	yes	See certificate below
146	Figure	Figure 4.17	Switchable Nile Red-Based Probe for Cholesterol and Lipid Order at the Outer Leaflet of Biomembranes *J. Am. Chem. Soc.* 2010, 132, 13, 4907–4916	© American Chemical Society	07/01/ 2021	yes	See certificate below
150	Figure	Figure 4.20	Rhodamine B Equilibria *J. Am. Chem. Soc.* 1956, 78, 19, 4872–4878	© American Chemical Society	07/01/ 2021	yes	See certificate below

Copyright Clearance Center | RightsLink®

Home | Help | Email Support | Thomas Clough

SAR Studies of Indole-5-propanoic Acid Derivatives To Develop Novel GPR40 Agonists

Author: Dong-Oh Yoon, Xiaodi Zhao, Dohyun Son, et al
Publication: ACS Medicinal Chemistry Letters
Publisher: American Chemical Society
Date: Dec 1, 2017

Copyright © 2017, American Chemical Society

PERMISSION/LICENSE IS GRANTED FOR YOUR ORDER AT NO CHARGE

This type of permission/license, instead of the standard Terms & Conditions, is sent to you because no fee is being charged for your order. Please note the following:

- Permission is granted for your request in both print and electronic formats, and translations.
- If figures and/or tables were requested, they may be adapted or used in part.
- Please print this page for your records and send a copy of it to your publisher/graduate school.
- Appropriate credit for the requested material should be given as follows: "Reprinted (adapted) with permission from (COMPLETE REFERENCE CITATION). Copyright (YEAR) American Chemical Society." Insert appropriate information in place of the capitalized words.
- One-time permission is granted only for the use specified in your request. No additional uses are granted (such as derivative works or other editions). For any other uses, please submit a new request.

If credit is given to another source for the material you requested, permission must be obtained from that source.

BACK | CLOSE WINDOW

Copyright Clearance Center | RightsLink®

Home | Help | Email Support | Thomas Clough

Switchable Nile Red-Based Probe for Cholesterol and Lipid Order at the Outer Leaflet of Biomembranes

Author: Oleksandr A. Kucherak, Sule Oncul, Zeinab Darwich, et al
Publication: Journal of the American Chemical Society
Publisher: American Chemical Society
Date: Apr 1, 2010

Copyright © 2010, American Chemical Society

PERMISSION/LICENSE IS GRANTED FOR YOUR ORDER AT NO CHARGE

This type of permission/license, instead of the standard Terms & Conditions, is sent to you because no fee is being charged for your order. Please note the following:

- Permission is granted for your request in both print and electronic formats, and translations.
- If figures and/or tables were requested, they may be adapted or used in part.
- Please print this page for your records and send a copy of it to your publisher/graduate school.
- Appropriate credit for the requested material should be given as follows: "Reprinted (adapted) with permission from (COMPLETE REFERENCE CITATION). Copyright (YEAR) American Chemical Society." Insert appropriate information in place of the capitalized words.
- One-time permission is granted only for the use specified in your request. No additional uses are granted (such as derivative works or other editions). For any other uses, please submit a new request.

If credit is given to another source for the material you requested, permission must be obtained from that source.

BACK | CLOSE WINDOW

Copyright Clearance Center | RightsLink®

Home | Help | Email Support | Thomas Clough

Rhodamine B Equilibria

Author: R. W. Ramette, E. B. Sandell
Publication: Journal of the American Chemical Society
Publisher: American Chemical Society
Date: Oct 1, 1956

Copyright © 1956, American Chemical Society

PERMISSION/LICENSE IS GRANTED FOR YOUR ORDER AT NO CHARGE

This type of permission/license, instead of the standard Terms & Conditions, is sent to you because no fee is being charged for your order. Please note the following:

- Permission is granted for your request in both print and electronic formats, and translations.
- If figures and/or tables were requested, they may be adapted or used in part.
- Please print this page for your records and send a copy of it to your publisher/graduate school.
- Appropriate credit for the requested material should be given as follows: "Reprinted (adapted) with permission from (COMPLETE REFERENCE CITATION). Copyright (YEAR) American Chemical Society." Insert appropriate information in place of the capitalized words.
- One-time permission is granted only for the use specified in your request. No additional uses are granted (such as derivative works or other editions). For any other uses, please submit a new request.

If credit is given to another source for the material you requested, permission must be obtained from that source.

BACK | CLOSE WINDOW



From the journal:
Dalton Transactions

Synthesis and *in vivo* behaviour of an exendin-4-based MRI probe capable of β-cell-dependent contrast enhancement in the pancreas†

Thomas J. Clough,[a] Nicoleta Baxan,[b] Emma J. Coakley,[a] Charlotte Rivas,[a] Lan Zhao,[bc] Isabelle Leclerc,[d] Aida Martinez-Sanchez,*[d] Guy A. Rutter*[de] and Nicholas J. Long*[a]

Author affiliations

Abstract

Global rates of diabetes mellitus are increasing, and treatment of the disease consumes a growing proportion of healthcare spending across the world. Pancreatic β-cells, responsible for insulin production, decline in mass in type 1 and, to a more limited degree, in type 2 diabetes. However, the extent and rate of loss in both diseases differs between patients resulting in the need for the development of novel diagnostic tools, which could quantitatively assess changes in mass of β-cells over time and potentially lead to earlier diagnosis and improved treatments. Exendin-4, a potent analogue of glucagon-like-peptide 1 (GLP-1), binds to the receptor GLP-1R, whose expression is enriched in β-cells. GLP-1R has thus been used in the past as a means of targeting probes for a wide variety of imaging modalities to the endocrine pancreas. However, exendin-4 conjugates designed specifically for MRI contrast agents are an under-explored area. In the present work, the synthesis and characterization of an exendin-4-dota(ga)-Gd(III) complex, **GdEx**, is reported, along with its *in vivo* behaviour in healthy and in β-cell-depleted C57BL/6J mice. Compared to the ubiquitous probe, [Gd(dota)]$^-$, **GdEx** shows selective uptake by the pancreas with a marked decrease in accumulation observed after the loss of β-cells elicited by deleting the microRNA processing enzyme, DICER. These results open up pathways towards the development of other targeted MRI contrast agents based on similar chemistry methodology.



Reproduced material should be attributed as follows:

- For reproduction of material from NJC:
  Reproduced from Ref. XX with permission from the Centre National de la Recherche Scientifique (CNRS) and The Royal Society of Chemistry.
- For reproduction of material from PCCP:
  Reproduced from Ref. XX with permission from the PCCP Owner Societies.
- For reproduction of material from PPS:
  Reproduced from Ref. XX with permission from the European Society for Photobiology, the European Photochemistry Association, and The Royal Society of Chemistry.
- For reproduction of material from all other RSC journals and books:
  Reproduced from Ref. XX with permission from The Royal Society of Chemistry.

If the material has been adapted instead of reproduced from the original RSC publication "Reproduced from" can be substituted with "Adapted from".

In all cases the Ref. XX is the XXth reference in the list of references.

If you are the author of this article you do not need to formally request permission to reproduce figures, diagrams etc. contained in this article in third party publications or in a thesis or dissertation provided that the correct acknowledgement is given with the reproduced material.

Reproduced material should be attributed as follows:

- For reproduction of material from NJC:
  [Original citation] - Reproduced by permission of The Royal Society of Chemistry (RSC) on behalf of the Centre National de la Recherche Scientifique (CNRS) and the RSC
- For reproduction of material from PCCP:
  [Original citation] - Reproduced by permission of the PCCP Owner Societies
- For reproduction of material from PPS:
  [Original citation] - Reproduced by permission of The Royal Society of